

Dissertation

submitted to the

Combined Faculty of Mathematics, Engineering and Natural Sciences

at Heidelberg University

for the degree of

Doctor of Natural Sciences

Put forward by

Albrecht Wulf Henning Kamlah

born in: Hamburg, Germany

Oral examination: 25.05.2023

The impact of the stellar evolution of single and binary
stars on the global, dynamical evolution of dense star
clusters across cosmic time

Insights from gravitational N -body simulations

Referees:

apl. Prof. Dr. Rainer Spurzem

Prof. Dr. Friedrich Röpke

Abstract

Star clusters in the Universe represent dense, self-gravitating and typically dynamically collisional environments of thousands to millions of stars. They populate galactic discs, halos and even galactic centres across the cosmos and are postulated to act as a fundamental unit in a hierarchy of cosmic structure formation. Importantly, they are typically much denser than their host galaxy, which makes them incredibly fascinating astronomical objects. Unlike their surroundings, stars and compact objects within in star clusters experience frequent dynamical encounters, form dynamical binary stars, merge by emitting gravitational waves, are ejected due to three-body dynamics and in rare cases even collide directly. As a result, star clusters are factories of all exotic binary stars, from, e.g. Thorne-Zytkow objects and Cataclysmic Variables to compact binary stars such as the elusive black hole-neutron star binaries. Furthermore, for increasing particle number, unique gravitational effects of collisional many-body systems begin to dominate the early cluster evolution that lead to a contracting and increasingly rapidly rotating core of the star clusters containing massive and binary stars, compact objects and an expanding halo of lower mass stars. Star clusters are therefore not only a laboratory for gravitational many-body physics, but also stellar evolution of single, binary and higher-order stars. All of these physical processes cannot be disentangled - they reinforce each other and many happen on similar time-scales. In this thesis, I aim to shed some light on the impact that stellar evolution has on the global dynamics of star clusters using direct gravitational N -body and Hénon-type Monte-Carlo simulations of star clusters. I focus on the evolution of metal-poor stellar populations (population II) that are present in globular clusters and extremely metal-poor stellar populations (population III) found in the oldest star clusters in the Universe.

Zusammenfassung

Sternhaufen im Universum stellen dichte, selbstgravitierende und typischerweise dynamisch kollidierende Umgebungen dar, die aus Tausenden bis Millionen von Sternen bestehen. Sie bevölkern galaktische Scheiben, Halos und sogar galaktische Zentren im gesamten Kosmos und bilden eine grundlegende Einheit in einer Hierarchie der kosmischen Strukturbildung. Außerdem sind sie in der Regel viel dichter als ihre Wirtsgalaxie, was sie zu unglaublich faszinierenden astronomischen Objekten macht. Anders als ihre Umgebung erleben Sterne und kompakte Objekte in Sternhaufen häufige dynamische Streuungen, bilden dynamische Doppelsterne, verschmelzen unter Aussendung von Gravitationswellen, werden durch Dreikörperdynamik herausgeschleudert und stoßen in seltenen Fällen sogar direkt zusammen. Infolgedessen sind Sternhaufen Fabriken aller exotischen Doppelsterne, von z.B. Thorne-Zytkow-Objekten und kataklysmischen Variablen bis hin zu kompakten Doppelsternen, beispielsweise Doppelsterne, die aus schwarzen Löchern und Neutronensternen bestehen. Darüber hinaus fangen mit zunehmender Teilchenzahl einzigartige Gravitationseffekte von kollidierenden Vielteilchensystemen an die frühe Entwicklung des Haufens zu dominieren, die zu zusammenziehenden und zunehmend schneller rotierenden Kernen der Sternhaufen führen, die bevorzugt massereiche Sterne und kompakte Objekte sowie Doppelsterne enthalten, und einem sich ausdehnenden Halo aus Sternen und kompakten Objekten geringerer Masse. Sternhaufen sind daher nicht nur ein Labor für die Gravitationsvielteilchenphysik, sondern auch für die Sternentwicklung von Einzel- und Doppelsternen sowie hierarchischen Sternensystemen höherer Ordnung. Alle diese physikalischen Prozesse können nicht isoliert betrachtet werden - sie verstärken sich in Sternhaufen gegenseitig und viele passieren auf ähnlichen Zeitskalen. In dieser Arbeit möchte ich den Einfluss der Sternentwicklung auf die globale Dynamik von Sternhaufen mit Hilfe von direkten gravitativen N-Körper und Hénon-Typ Monte-Carlo Simulationen von Sternhaufen genauer studieren. Ich konzentriere mich auf die Entwicklung von metallarmen Sternpopulationen (Population II), die in Kugelsternhaufen und extrem metallarme Sternpopulationen (Population III), die die ältesten Sternpopulationen im Universum bilden.

Acknowledgements

When I started the PhD two and a half years ago at the peak of the first Corona epidemic in Europe and the world, I faced significant uncertainty both in professional and personal life. When I started the PhD, the long-term funding was unclear and short to mid-term alternatives such as funded research stay abroad were simply not possible. Reflecting on my time as a PhD researcher, it now appears almost miraculous to me that two and a half years later I can submit and defend this thesis. I fully acknowledge that this would not at all have been possible without the continued advice, assistance and collaboration of some amazing people and I have to extend my deep gratitude to them.

First of all, I want to thank my doctoral advisor Rainer Spurzem for first taking me on as a master student in a joint project with Wolfram Kollatschny in Goettingen and Beijing. This incredibly rewarding time particularly in China was the reason why I then took the opportunity to do a PhD with him in Heidelberg. The humble beginnings of learning about the N -body code and running first modest simulations during my master thesis have evolved into many different and relevant research projects in my PhD over the past years ultimately culminating in this thesis. Without Rainer opening many scientific doors and sharing his deep knowledge and impressive expertise on a large variety of astrophysics and computational physics subjects, I would not have been able to develop the same level of understanding of these subjects. He was always available for coding and astrophysics problems and I would like to thank him for that, especially always taking the time to think about my questions deeply and replying swiftly.

Furthermore, I want to extend my deep gratitude to Nadine Neumayer, who took me under her wing during my second year of the PhD by providing funding for the remainder and even beyond it. The funding provided me with a stress-free framework compared with my first year and I could fully concentrate on my work. Thanks to her funding I could produce my first-author and the many co-author publications, which were absolutely essential in completing the program and more importantly, under the financially secure circumstances I got my passion for the subject back. Additionally, her scientific input has been very valuable for me in particular regarding observations. Thank you!

Next, I want to thank Mirek Giersz for always being available for collaboration and scientific discussion. His scientific feedback and insights were among the most useful that I have received during my PhD time. I approached him with many ideas for simulations and coding and he always reacted positively and encouragingly. It has been an absolutely pleasure writing the papers together and collaborating on the MOCCA stellar evolution.

I would like to also thank Peter Berczik, who was always available for one on one meetings on a large variety of astrophysics questions, especially with respect to galactic dynamics, and, which was especially important for me, coding problems and the initialisation of star cluster simulations in a very straightforward manner. I learned a lot during the process. The few encounters at ARI that have had were always enjoyable and a welcome break from the daily routine.

Furthermore, I want to thank Manuel Arca Sedda. I profited a lot from our frequent scientific exchanges and collaborations, especially with respect to compact object mergers, gravitational wave physics and related phenomena.

Additionally, I want to thank Andreas Just, for volunteering to be part of my thesis committee alongside Nadine and Rainer. His input has been crucial to stay on track during the program. It has been a pleasure to work together especially following his supervision of my Bachelor thesis.

I would like to acknowledge all my other collaborators. The Population-III stellar evolution was thankfully provided by Ataru Tanikawa, whom I really enjoyed working with due to his high level of professionalism and integrity. Francesco Flammini Dotti has been very helpful in discussing and simulating rotating star clusters and generating research results. Additionally, I learned some crucial Italian to order myself pasta and coffee from him and Gaia Fabj, who I also acknowledge herewith. Here, I also thank Katja and Kseniia as office mates, who always created a pleasant and collegial atmosphere during our time together at ARI. I want to thank Nils Hoyer, who provided me with the opportunity to participate in his exciting projects surrounding nuclear star clusters with JWST. Furthermore, I would like to express my gratitude to Alina Böcker, Nils Hoyer and Ben Rudgley for helping with the formatting of the thesis. I am indebted to the whole

MOCCA team, who have not been explicitly mentioned so far, Lucas Hellstroem, Abbas Askar, Arek Hypki, Greg Wiktorowicz, Agostino Leveque and Diogo Belloni as well as Debatri Chatthopdhyay and Jarrod Hurley by extension for the fruitful and enjoyable collaboration over these years.

I want to thank my main collaborators in China: Pang Xiaoying, with whom it has been an absolute pleasure to work together with and Shu Qi, who has been a great help with running simulations. I thank Wang Long for the productive collaboration on some of the published simulations. Furthermore, I thank Li Zhongmu and Bhusan Kayastha for their collaboration comparing N -body simulations and population synthesis.

Additionally, I thank the executive committee of the German Astronomical Society, especially Michael Kramer, Thomas Kraupe, Klaus Reinsch, Renate Hubele and Steven Haemmerich for the productive work together. I would also like to thank Friedrich Roepke for kindly volunteering to review my thesis and Sabine Reffert and Luca Amendola for offering their time to participate in my defense as examiners. I acknowledge the computing (time) and data resources at JSC and MPCDF, as well as the MPCDF's team for collaborating on benchmarking the codes.

Most importantly, I start thanking with all my friends and family in Germany and abroad who have been there for me during this time - thank you! When times were tough my parents always offered their wisdom and the right advice to carry on. Thank you for being there during the crucial moments. I deeply thank my fiancée Vera for being there for each other during the past years, which were never that easy. You have helped me keep my life in a healthy balance and keeping a positive outlook for the future. Without you this would have been a very tough time.

Contents

| | |
|--|-----------|
| Contents | xi |
| GENERAL INTRODUCTION | 1 |
| 1 Motivation, scientific rationale and outline | 3 |
| 1.1 Motivation and scientific rationale | 3 |
| 1.2 Thesis outline | 5 |
| ASTROPHYSICAL INTRODUCTION | 9 |
| 2 Star clusters across cosmic time | 11 |
| 2.1 What are star clusters? | 11 |
| 2.1.1 Nuclear star clusters | 12 |
| 2.1.2 Globular star clusters | 14 |
| 2.1.3 Open star clusters | 18 |
| 2.1.4 Population III star clusters | 19 |
| 2.2 The formation of star clusters | 20 |
| 2.2.1 Initial conditions for star cluster simulations | 26 |
| 2.2.2 Initial stellar mass function | 29 |
| 2.2.3 Initial binary population | 30 |
| 2.2.4 Multiple stellar populations | 33 |
| 2.2.5 McLUSTER | 34 |
| 2.2.6 Initial star cluster rotation | 35 |
| 2.3 The life and fate of star clusters | 37 |
| 2.3.1 Gravothermal catastrophe | 37 |
| 2.3.2 Gravogyro catastrophe and its coupling with the gravothermal catastrophe | 40 |
| 2.3.3 Pre-core collapse star cluster evolution | 43 |
| 2.3.4 Post-core collapse star cluster evolution | 48 |
| 3 Astrophysics within star clusters | 55 |
| 3.1 Single stellar evolution | 55 |
| 3.1.1 Two fundamental principles of stellar evolution | 59 |
| 3.1.2 Time-scales, energy conservation and homology | 60 |
| 3.1.3 Fundamental parameters - mass and composition | 64 |
| 3.1.4 Mass change of stars - stellar winds | 64 |
| 3.1.5 Discretizing ZAMS mass in stellar evolution | 65 |
| 3.1.6 Formation of compact objects and their natal masses, kicks and spins | 68 |
| 3.2 Binary stellar evolution | 73 |
| 3.2.1 Stellar Spin and orbital changes due to mass loss or gain | 74 |
| 3.2.2 Effects of tidal damping | 74 |
| 3.2.3 Dynamical mass transfer and its stability | 76 |
| 3.2.4 Common-envelope evolution | 79 |
| 3.2.5 Mergers and general relativistic merger recoil kicks | 80 |
| 3.2.6 Accretion or merger induced collapse | 82 |
| 3.2.7 Gravitational radiation and magnetic braking | 83 |

| | | |
|---|--|----------------|
| 3.2.8 | Stellar types and binary classes in classical SSE & BSE | 84 |
| 4 | Stellar dynamics of star clusters | 89 |
| 4.1 | The gravitational N -body problem | 89 |
| 4.1.1 | The gravitational two-body problem | 90 |
| 4.1.2 | Hyperbolic encounters between stars | 93 |
| 4.1.3 | Relaxation revisited | 96 |
| 4.1.4 | Inelastic encounters between stars | 98 |
| 4.1.5 | The gravitational three-body problem | 99 |
| 4.2 | Statistical treatment of star clusters | 101 |
| 4.2.1 | Collisionless stellar dynamics | 102 |
| 4.2.2 | Collisional stellar dynamics | 104 |
| COMPUTATIONAL METHODS FOR COLLISIONAL DYNAMICS | | 113 |
| 5 | Direct N-body methods | 115 |
| 5.1 | From <code>NBODY1</code> to <code>NBODY6++GPU</code> and <code>NBODY7</code> - the growth of an industry | 115 |
| 5.2 | Summary <code>NBODY</code> codes | 118 |
| 5.3 | Time profile of <code>NBODY6++GPU</code> | 119 |
| 5.4 | Basic features and <code>NBODY</code> units | 121 |
| 5.5 | Methods and algorithms in <code>NBODY6++GPU</code> | 123 |
| 5.5.1 | 4 th -order Hermite integration | 123 |
| 5.5.2 | Block time-steps scheme | 125 |
| 5.5.3 | Ahmad-Cohen (AC) neighbour scheme | 126 |
| 5.5.4 | Two-body regularisation and Kustaanheimo-Stiefel (KS) decision making | 128 |
| 5.5.5 | Hierarchical systems and three-body regularisation | 131 |
| 5.5.6 | Chain regularisation | 132 |
| 5.6 | Parallelization in <code>NBODY6++GPU</code> | 134 |
| 5.7 | Summary of <code>NBODY6++GPU</code> | 136 |
| 6 | Hénon-type Monte-Carlo methods | 139 |
| 6.1 | Hénon type method | 139 |
| 6.1.1 | Two-body relaxation in the Hénon type method | 142 |
| 6.1.2 | The effective scattering angle | 143 |
| 6.2 | Binaries and triples in a Hénon-type Monte-Carlo code | 145 |
| 6.2.1 | Single-single interactions | 146 |
| 6.2.2 | Binary and binary-binary interactions | 147 |
| 6.3 | Updating the positions and velocities | 148 |
| 6.4 | Calculating the gravitational potential | 148 |
| 6.5 | Energy conservation in a Hénon-type Monte Carlo code | 148 |
| 6.6 | On the reliability of direct N -body and Hénon-type Monte-Carlo methods for star cluster simulations | 149 |
| 6.7 | Summary of MOCCA | 151 |
| 7 | Orbit-averaged Fokker-Planck methods for axisymmetric systems | 153 |
| 7.1 | Flux conservation and flux coefficients | 153 |
| 7.2 | Background distribution | 156 |
| 7.3 | Rotating King models | 157 |
| 7.3.1 | Further work | 158 |

| | | |
|----------|---|------------|
| 8 | Combining stellar evolution with collisional N-body codes | 161 |
| 8.1 | Interpolation between tables | 161 |
| 8.2 | Interpolation/Fitting formulae | 162 |

STELLAR EVOLUTION IMPLEMENTATIONS IN NBODY6++GPU, MOCCA AND McLUSTER 167

| | | |
|----------|---|------------|
| 9 | Preparing the next gravitational million-body simulations | 169 |
| 9.1 | Abstract | 169 |
| 9.2 | Introduction | 169 |
| 9.3 | Methods | 172 |
| 9.3.1 | Simulations with NBODY6++GPU and MOCCA | 172 |
| 9.3.2 | Summary: stellar evolution updates (SSE AND BSE) in NBODY6++GPU and MOCCA | 172 |
| 9.4 | Initial models - delayedSNe-Uniform & rapidSNe-Sana | 174 |
| 9.5 | Results | 176 |
| 9.5.1 | Global dynamical evolution | 176 |
| 9.5.2 | Stellar evolution | 178 |
| 9.6 | Summary, conclusion and perspective | 190 |
| 9.6.1 | Summary: direct N -body (NBODY6++GPU) and Monte Carlo (MOCCA) simulations | 190 |
| 9.6.2 | Perspective on future stellar evolution (SSE & BSE) updates | 193 |
| 9.7 | Stellar and binary evolution levels A, B, C | 199 |
| 9.7.1 | Dynamical mass transfer and other processes in binary stars | 200 |
| 9.7.2 | Stellar winds | 202 |
| 9.7.3 | Remnant masses of compact objects | 203 |
| 9.7.4 | Compact object natal kick distributions | 206 |
| 9.7.5 | Compact objects natal spins | 208 |
| 9.8 | McLuster | 211 |
| 9.8.1 | Remnant-masses of compact objects | 212 |

THE IMPACT OF STELLAR EVOLUTION ON (NON-)ROTATING POPULATION-II STAR CLUSTERS 215

| | | |
|-----------|--|------------|
| 10 | Impact of stellar evolution on rotating star clusters | 217 |
| 10.1 | Abstract | 217 |
| 10.2 | Introduction | 217 |
| 10.2.1 | 2-D Fokker-Planck models vs. direct N -body simulations | 219 |
| 10.3 | Methods | 221 |
| 10.3.1 | NBODY6++GPU | 221 |
| 10.3.2 | McLUSTER & FOPAX | 221 |
| 10.4 | Initial conditions | 222 |
| 10.4.1 | Star cluster parameters | 222 |
| 10.4.2 | Stellar evolution parameters | 223 |
| 10.5 | Results | 224 |
| 10.5.1 | Global dynamical evolution | 224 |
| 10.5.2 | Escaper stars | 231 |
| 10.5.3 | Binary stars | 233 |
| 10.6 | Summary, conclusion and perspective | 240 |
| 10.6.1 | Summary | 240 |
| 10.6.2 | Conclusion | 241 |
| 10.6.3 | Perspective on future simulations | 242 |

| | |
|--|------------|
| THE EVOLUTION OF EXTREMELY MASSIVE, (NON-)ROTATING POPULATION-III STAR CLUSTERS | 245 |
| 11 Direct N-body simulations Population III star clusters | 247 |
| 11.1 Abstract | 247 |
| 11.2 Introduction | 247 |
| 11.3 Methods | 251 |
| 11.3.1 NBODY6++GPU | 251 |
| 11.3.2 McLUSTER & FOPAX | 252 |
| 11.3.3 SSE, BSE and Pop-III stellar evolution | 252 |
| 11.3.4 General relativistic merger recoil kicks | 255 |
| 11.4 Initial conditions | 256 |
| 11.4.1 Star cluster parameters | 256 |
| 11.4.2 Stellar evolution parameters | 258 |
| 11.5 Results | 259 |
| 11.5.1 Global dynamical evolution | 259 |
| 11.5.2 Stars and compact objects | 268 |
| 11.5.3 Binary stars | 271 |
| 11.5.4 Collision and coalescence events | 275 |
| 11.5.5 Escaper stars | 278 |
| 11.6 Summary, conclusion and perspective | 284 |
| 11.6.1 Summary | 284 |
| 11.6.2 Conclusion | 287 |
| | |
| SUMMARY, CONCLUSION AND OUTLOOK | 289 |
| | |
| 12 Summary | 291 |
| | |
| 13 Conclusion | 297 |
| | |
| 14 Outlook | 299 |
| | |
| APPENDIX | 301 |
| | |
| A Publications | 303 |
| A.1 Publications used in this thesis either published or submitted | 303 |
| A.2 Publications used that are in writing as of submission of PhD thesis | 303 |

List of Figures

| | | |
|------|---|-----|
| 2.1 | JWST and HST images of the NSC in the grand-design spiral galaxy M74 (NGC 628) | 12 |
| 2.2 | Compilation of dynamically and spectroscopically modeled NSC masses | 14 |
| 2.3 | The action-space map for the Milky Way GCs. | 15 |
| 2.4 | Colour-composite image of NGC 3201 from the WFI instrument on the ESO/MPG 2.2-m telescope | 15 |
| 2.5 | Half-mass initial density as a function of particle number for key N -body simulations | 16 |
| 2.6 | Spitzer and JWST MIRI images of the LMC | 17 |
| 2.7 | Ground-based image of the Hyades OC | 18 |
| 2.8 | Orion Nebula as seen with JWST NIRC <i>am</i> instrument revealing star and planet formation. | 20 |
| 2.9 | The galaxy-wide initial stellar mass function (gwIMF) | 29 |
| 2.10 | Diagram showing the Sana binary mass ratio distribution q | 31 |
| 2.11 | The stellar multiplicity fractions as a function of primary mass | 31 |
| 2.12 | Diagram showing the geometry of the orbit in binary star | 31 |
| 2.13 | Results of the kinematic analysis for 47 Tuc (NGC 104) | 35 |
| 2.14 | Ellipticity profile ϵ for the GC ω Cen (NGC 5139) | 35 |
| 2.15 | Diagram of the gravothermal instability in an isolated, isothermal gas spheres | 38 |
| 2.16 | Diagram showing the gravothermal oscillations | 39 |
| 2.17 | Diagram of the gravogyro instability in a rotating, isolated, initially isothermal gas cylinder | 41 |
| 2.18 | Time evolution of the particle and angular momentum distributions of a star cluster | 42 |
| 2.19 | Schematic diagram illustrating the process of dynamical friction | 45 |
| 2.20 | Isosurfaces of the total potential of star cluster in a constant tidal field | 50 |
| 2.21 | Spatial distribution of a combined sample of 109 bona fide stream members of the GC Pal 5 | 51 |
| | | |
| 3.1 | Energy transport in a star via radiation and convection within a star | 56 |
| 3.2 | Schematic illustration of the MLT approximation | 58 |
| 3.3 | Schematic illustration of the onion-like structure of a star | 60 |
| 3.4 | Mass-loss rates as function of luminosity for an RSG star | 65 |
| 3.5 | Initial-final-mass-relations of the BHs | 68 |
| 3.6 | Remnant mass natal kick prescriptions | 69 |
| 3.7 | Crab Nebula (SN 1054) taken by Hubble Space Telescope. | 70 |
| 3.8 | Plot showing the magnitude of dimensionless spin parameter | 73 |
| 3.9 | Schematic diagram of binary motion | 74 |
| 3.10 | Schematic diagram of RLOF overflow in detached, semi-detached and contact binaries. | 75 |
| 3.11 | Different modes of mass exchange between stars in a binary system | 77 |
| 3.12 | Post-CE planetary nebulae with a compact binary as central object in NGC 6778 | 79 |
| 3.13 | Conceptual image presenting the general relativistic merger recoil velocity (distribution) | 81 |
| 3.14 | Tycho's Supernova (SN 1572) in the X-ray band | 82 |
| 3.15 | Schematic diagram of isolated compact binary formation. | 84 |
| 3.16 | CMD of the GC NGC 3201 | 85 |
| 3.17 | Artistic impression of the SS 443, an eclipsing X-ray binary. | 87 |
| 3.18 | Possible observable differences between different seeding scenarios of mBHs for galactic nuclei | 88 |
| | | |
| 4.1 | Diagram showing the geometry of a Kepler ellipse or orbit of two stars | 90 |
| 4.2 | Schematic diagram of the two-body problem between two stars | 90 |
| 4.3 | Schematic diagram showing a hyperbolic encounter. | 94 |
| 4.4 | Schematic diagram of the three-body problem between two stars | 99 |
| 4.5 | Various types of dynamical three-body encounters | 100 |

| | | |
|------|---|-----|
| 4.6 | Diagram showing the scattering of a star out of and into a unit phase-space volume | 106 |
| 5.1 | Pie chart showing the time fractions in the Nbody6++GPU code | 121 |
| 5.2 | Exemplary block time steps in Nbody6++GPU for four stars. | 125 |
| 5.3 | Relative energy error as the function of the number of steps for the Hermite scheme | 127 |
| 5.4 | Ahmad-Cohen neighbour scheme, regular and irregular force integration. | 128 |
| 5.5 | Diagram illustrating the Nbody6++GPU communication with the hardware. | 135 |
| 6.1 | Schematic diagram showing the Hénon-type Monte-Carlo method | 141 |
| 6.2 | Schematic diagram of the Hénon type coordinate system. | 142 |
| 7.1 | Schematic diagram illustrating the coordinate transformation | 153 |
| 7.2 | Figure showing the time evolution normalised by the half-mass relaxation time-scale | 158 |
| 8.1 | Diagram showing the complete stellar evolution for the SSE code. | 165 |
| 9.1 | Time evolution of the half-mass, tidal, core radii and core masses | 177 |
| 9.2 | Time evolution of the logarithm of the Lagrangian radii | 177 |
| 9.3 | HRD for all four simulations at 10 Gyr. | 177 |
| 9.4 | Time evolution over 10 Gyr of the logarithmic (compact) binary fractions | 180 |
| 9.5 | Initial-Final mass relation (IFMR) for the escaping compact objects. | 181 |
| 9.6 | Initial-Final mass relations (IFMR) for the escaping compact objects. | 181 |
| 9.7 | Plot showing the mass of the compact objects in relation to their distance to the density centre $r_{\text{dens}}(\text{pc})$ | 186 |
| 9.8 | Cumulative distributions for compact object distances to the density centre $r_{\text{dens}}(\text{pc})$ for all four simulations at (1,3,6,9,10) Gyr. | 187 |
| 9.9 | Plot showing the final escape speeds $v_{\text{esc}}(\text{kms}^{-1})$ of the compact objects (WDs, NSs, BHs) for the Nbody-delayedSNe-Uniform and the Nbody-rapidSNe-Sana simulations. | 188 |
| 9.10 | Plot showing the natal kick speeds $v_{\text{kick}}(\text{kms}^{-1})$ of the NSs and BHs (not recorded for WDs), as well as the final escape speeds $v_{\text{esc}}(\text{kms}^{-1})$ | 188 |
| 9.11 | Cumulative histogram showing the mass ratio at times (1,2,5,9,10) Gyr of the binaries | 188 |
| 9.12 | Cumulative histogram showing the semi-major axis $a(\text{AU})$ at times (1,2,5,9,10) Gyr of the binaries for all four simulations. | 189 |
| 9.13 | Histogram showing the eccentricity e^2 at times (1,2,5,9,10) Gyr of the binaries | 189 |
| 9.14 | Table showing the stellar evolution levels A, B and C. | 204 |
| 9.15 | Table showing the options in the SSE & BSE stellar evolution with respect to the parameters in Nbody6++GPU. | 209 |
| 9.16 | Table showing the options in the SSE & BSE stellar evolution with respect to the parameters in MOCCA. | 210 |
| 9.17 | HRDs for the McLUSTER samples | 212 |
| 9.18 | IFMRs of the BHs from the McLUSTER samples | 213 |
| 10.1 | Plot showing the total cluster mass, tidal and half mass radii and core mass | 225 |
| 10.2 | Plot showing the Lagrangian radii and the average mass | 235 |
| 10.3 | Plot showing the ratios of the principal axis of the moment of inertia tensor | 236 |
| 10.4 | Plot showing the deviation from sphericity of the star cluster models | 237 |
| 10.5 | Plot showing the total mass of the four mass groups | 237 |
| 10.6 | 3-D scatter plot showing the spatial distribution of the mass group in all eight simulations at 0.0 Myr | 238 |
| 10.7 | Plot showing over 1 Gyr the number of escapers | 239 |
| 10.8 | Plot showing the average mass of the escapers | 239 |
| 10.9 | Plots showing the number of binary stars | 239 |

| | | |
|-------|--|-----|
| 11.1 | Plot showing the Pop-III stellar evolution for masses, luminosities and radii from 8 to 300 Solar masses. | 253 |
| 11.2 | Plot showing the total cluster mass, the tidal, core and half-mass radii | 260 |
| 11.3 | Plot showing the Lagrange radii and the average mass | 261 |
| 11.4 | Plot showing the total mass of the four mass groups | 262 |
| 11.5 | Plots showing the number of stars n_{stars} , the number MS stars n_{MS} , the number MS stars n_{CHeB} , the number ShHeB stars n_{ShHeB} , the number NS stars n_{NS} , the number BH stars n_{BH} in the six panels for all eight simulations with and without GR recoil kicks for $\omega_0 = 0.0, 0.6, 1.2, 1.8$, respectively. The time axis is plotted logarithmically to show the details of the much more rapid early cluster evolution. The models with GR recoil kicks (GRk models) are plotted as solid lines and the models without GR recoil kicks (noGRk models) are plotted as dash-dotted lines. | 265 |
| 11.6 | Plots showing the initial-final-mass relation (IFMR) with the mass of the BH | 266 |
| 11.7 | Plots showing the initial-final-mass relation (IFMR) with the mass of the BH | 269 |
| 11.8 | Plots showing the number of binary stars and the number of compact binary stars | 272 |
| 11.9 | Plots showing several binary distributions from top to bottom at 500 Myr of simulation time | 273 |
| 11.10 | Plot showing all of the coalescence and all of the collision events | 277 |
| 11.11 | Plot showing the time-evolution of the cumulative number of the coalescence | 278 |
| 11.12 | Plot showing the time primary and secondary masses | 279 |
| 11.13 | Plot showing general relativistic (GR) recoil kick velocity | 279 |
| 11.14 | Plots showing the cumulative numbers of escaping single stars | 281 |
| 11.15 | Plots showing the cumulative numbers of escaping binary member stars | 283 |

List of Tables

| | | |
|------|--|-----|
| 4.1 | Exemplary and very approximate time-scales for several stellar systems. | 98 |
| 5.1 | Table showing important algorithmic, hardware and software development stepping stones | 117 |
| 5.2 | Table showing the comparison of the N _{BODY} codes | 119 |
| 5.3 | Profiling model developed for N _{BODY6++GPU} | 120 |
| 7.1 | Initial conditions of rotating King models with $W_0 = 6$ | 158 |
| 9.1 | Initial models for the (MOCCA and N _{BODY6++GPU}) simulations. | 174 |
| 9.2 | Table listing the orbital properties of some degenerate binaries surviving inside the cluster | 183 |
| 10.1 | Initial parameters that are identical across all eight initial models for the N _{BODY6++GPU} simulations. | 222 |
| 10.2 | Model identifiers (Model ID) for the eight N _{BODY6++GPU} simulations. | 223 |
| 11.1 | Initial parameters that are identical across all eight initial models for the N _{BODY6++GPU} simulations. | 256 |
| 11.2 | Model identifiers (Model ID) for the eight N _{BODY6++GPU} simulations. | 257 |
| 11.3 | Absolute numbers of stars, n_{stars} , ShHeB stars, n_{ShHeB} , NSs, n_{NS} and BHs, n_{BH} at 500 Myr for all eight N _{BODY6++GPU} simulations. The column headers have been abbreviated - G corresponds to the GRk and noG corresponds to the noGRk models. | 264 |
| 11.4 | Absolute numbers of remaining binaries | 271 |
| 11.5 | Absolute numbers of coalescence and collision events occurring in all simulations | 276 |
| 11.6 | Table showing the number of escaping objects from all simulations | 280 |

GENERAL INTRODUCTION

Motivation, scientific rationale and outline **1**

1.1 Motivation and scientific rationale

| | |
|---|---|
| 1.1 Motivation and scientific rationale | 3 |
| 1.2 Thesis outline | 5 |

Star clusters are spectacular and ubiquitous objects in the known Universe. Their stellar densities are typically so high that the stars that they host interact dynamically via strong and weak encounters many more times than stars in their host galaxies. As a result, star clusters are factories for the production of all sorts of exotic astrophysical phenomena and stars, from accretion and merger induced supernovae to intermediate mass hole production and growth as well as blue straggler star formation and stripped Helium and Wolf-Rayet like stars. In short, star clusters take a central role in modern multi-messenger astronomy over the entire electromagnetic and gravitational wave spectrum. Furthermore, the high densities of star clusters also imply that they are at the edge of computational astrophysics in terms of what is feasible and possible on modern hardware as well as programming and using modern astrophysics software.

Star clusters are extremely well studied objects both theoretically (Arca Sedda et al., 2019; Askar et al., 2017; Giersz et al., 2015; D. C. Heggie, 1975; Khalisi et al., 2007; Portegies Zwart & McMillan, 2002; Rizzuto, Naab, Spurzem, Arca-Sedda, Giersz, et al., 2021; Rizzuto, Naab, Spurzem, Giersz, et al., 2021; Wang et al., 2016) and observationally (Cantat-Gaudin et al., 2014; Giesers et al., 2018, 2019; Kamann, Bastian, et al., 2018; Lada & Lada, 2003; Martinazzi et al., 2014). However, despite over a century of efforts to resolve their global evolution and internal dynamics a complete picture of star cluster dynamics in combination with state-of-the-art stellar evolution is still not within reach.

Although becoming increasingly sophisticated, observational studies using astrophysical instruments such as Multi Unit Spectroscopic Explorer (MUSE) (Giesers et al., 2018, 2019; Husser et al., 2016; Kamann, Bastian, et al., 2018, 2020; Kamann, Giesers, et al., 2020; Kamann, Husser, et al., 2018) and Gaia (Bianchini et al., 2013a, 2018, 2019; de Boer et al., 2019; K.-W. Huang & Koposov, 2021; Kuhn et al., 2019) are not sufficient on their own to resolve the complete evolution of globular clusters across cosmic time, because they effectively only take snapshots of these clusters today. These observations must therefore be supplemented with astrophysical simulations (Krumholz et al., 2019). Simulations of such star clusters fundamentally aim to solve the equations of motion describing N bodies moving under the influence of their own self-gravity. For this purpose a variety of computational approaches have been developed beginning in the first half of the last century. The two main methods in the regime of around $10^5 - 10^7$ particles that stand out today are either related to direct N -body simulation or Monte-Carlo modelling (S. J. Aarseth & Lecar, 1975; S. J. Aarseth et al., 1974; Giersz & Heggie, 1994a; Spurzem, 1999). Direct N -body simulation, which is the orbit

integration of many particles in a self-gravitating bound star cluster, is the most suitable method to understand relaxation (Larson, 1970a, 1970b) and evolutionary processes in the regime of star clusters. Here, statistical physics still plays a role and more approximate models may be used. These models are based on the Fokker-Planck equation, which can be solved either directly or by a Monte-Carlo Markov-Chain method (Askar et al., 2017; Cohn, 1979; Giersz, 1998; Giersz et al., 2015; M. Hénon, 1975; Kremer, Ye, et al., 2020; Kremer et al., 2021; Merritt, 2015; Stodołkiewicz, 1982, 1986). In Kamlah, Leveque, et al. (2022) I tackle the following question:

How do different simulation methods of star clusters compare when using updated stellar evolution methods?

Present-day detectors and data processing methods have made it furthermore possible to resolve the photometry and kinematics of individual stars (even in components of binary and higher-order hierarchical stars) in star clusters (Giesers et al., 2018, 2019). These observations reveal global bulk rotation of the star clusters and even resolve the rotational kinematics of the extremely dense star cluster cores. On top of this, the kinematic patterns of multiple populations in star clusters can and have been mapped out in numerous studies (Bianchini et al., 2016a, 2018, 2019; Ferraro et al., 2018; Kamann, Bastian, et al., 2018; Kamann, Husser, et al., 2018; Kamann et al., 2016, 2019; Lanzoni, Ferraro, Mucciarelli, Pallanca, Lapenna, et al., 2018; Lanzoni, Ferraro, Mucciarelli, Pallanca, Tiongco, et al., 2018; Sollima et al., 2019; M. Tiongco et al., 2021; M. A. Tiongco et al., 2019). Nowadays, we are also beginning to resolve the complex interaction between a star cluster and its tidal field and the imprint that the tidal field may leave on the internal cluster dynamics (M. A. Tiongco et al., 2016a, 2016b, 2017, 2018). Recently, Lahén et al. (2020) ran simulations of young massive star clusters forming in metal-poor starburst dwarf galaxies and found that the star clusters have significant angular momentum upon formation. In these simulations, the more massive star clusters tend to have larger angular momentum. But they also find that the angular momentum is not always aligned with flattening, thereby indicating a complex kinematic structure overall. Both observations and other simulations support these results and find that star clusters show significant fractality (Ballone et al., 2020; Pang, Li, et al., 2021), and internal rotation at birth in general (Ballone et al., 2021). Velocity anisotropy has been observed in star clusters with detected elongated structures (Pang, Li, et al., 2021; Pang et al., 2020), and these structures might be induced by rotation. Related to the above, I attempt to answer this question in Kamlah, Spurzem, et al. (2022):

How does stellar evolution (mass loss) impact the global dynamics of (non-)rotating star clusters?

Gravitational runaway mergers between stars and compact objects happen throughout cosmic time in dense star clusters. They can be separated into a "fast" and a "slow" regime following Greene et al.

(2020). In the fast regime (a couple of million years from star cluster formation and natal gas expulsion), gravitational runaway mergers can happen during early star cluster evolution, when stars evolve and merge either through binary stellar evolution or dynamical collisions (Gieles et al., 2018; Portegies Zwart & McMillan, 2002; Reinoso et al., 2018; Reinoso et al., 2021; Sakurai et al., 2017; Wang et al., 2022). The slow regime (around 100 Myr to billions of years from star cluster formation and natal gas expulsion) is populated by gravitational runaway mergers that occur between black holes. Gravitational runaway mergers of both kinds are postulated to produce intermediate mass black holes with masses of order $10^2 M_{\odot}$ to $10^4 M_{\odot}$. Both the fast and the slow regimes have been confirmed extensively by simulations of dense star clusters using various methods and both mechanisms are instrumental to growing intermediate mass black holes (see e.g. Arca Sedda, Mapelli, et al., 2020; Arca Sedda et al., 2019; Di Carlo, Mapelli, Bouffanais, et al., 2020; Di Carlo, Mapelli, Giacobbo, et al., 2020; Di Carlo et al., 2021; Giersz et al., 2015; Leveque, Giersz, Arca-Sedda, & Askar, 2022; Maliszewski et al., 2022; Rizzuto, Naab, Spurzem, Giersz, et al., 2021; Rizzuto et al., 2022; Rodriguez et al., 2019). Moreover, massive Population III stars have been postulated to produce seed intermediate mass black holes with masses of order $10^2 M_{\odot}$ through direct collapse above the pair instability mass gap (see e.g. Bromm, 2013; Bromm & Larson, 2004; Haemmerlé et al., 2020; Woosley, 2017). (Extremely massive) Population III stars can merge with other Pop-III stars in their host clusters before collapse to produce even more massive black holes above the pair-instability mass gap during the fast gravitational runaway merger phase, as outlined above (see e.g. Katz et al., 2015; Reinoso et al., 2018; Reinoso et al., 2021; Sakurai et al., 2017; Tanikawa, Chiaki, et al., 2022; Wang et al., 2022). Therefore, metal-poor Pop-III star clusters at high redshifts ($z \gtrsim 10$) hosting stellar populations with a top-heavy initial mass function (see e.g. Sharda & Krumholz, 2022) are very strong candidates for the production of black hole seeds for galactic nuclei and their nuclear star clusters (Askar et al., 2021, 2022; Greene et al., 2020; Neumayer et al., 2020; Schleicher et al., 2022). With this in mind, in Kamlah et al. (2023, in prep.), I attempt to shed more light on the following question:

Can massive seed black holes for galactic nuclei form in extremely metal-poor star clusters and does initial star cluster rotation influence this process?

The remainder of the thesis is centered on these three questions. Additionally, I want to stress that I am biased towards simulations of star clusters as my research primarily uses them as a tool to gain insights into star cluster and stellar evolution. Whenever it is appropriate, especially when initialising my star cluster simulations, I will draw from and mention the relevant observations, but I do not focus on them.

1.2 Thesis outline

The thesis is structured as follows:

- ▶ In [Chapter 2](#) I outline the astrophysical context my research. I start with [Section 2.1](#), where I define star clusters and elaborate on their place in the greater cosmological picture. I continue with [Section 2.2](#) where I briefly touch on the formation of star clusters as this has consequences for the initial conditions of my star cluster models and I also explain the methodology of setting up these conditions with `MCLUSTER`. I end [Chapter 2](#) with explaining the evolution and death of star clusters and define many related time-scales that measure these processes in [Section 2.3](#), where especially highlight the pre-core collapse evolution of star clusters, which is the focus of my work that are included in this thesis.
- ▶ [Chapter 3](#) deals with the evolution of single stars across the entire mass spectrum in [Section 3.1](#) and the subsections therein. Binary stars and their evolutionary processes and associated time-scales are discussed in [Section 3.2](#) and the related subsections.
- ▶ [Chapter 4](#) describes the dynamics of stars under the influence of all surrounding stars, i.e. stellar dynamics in a self-gravitating many-body system. I start with the gravitational two-body problem and three-body problem in [Section 4.1.1](#) and [Section 4.1.5](#) and re-introduce the relaxation process in [Section 4.1.3](#) based on [Section 4.1.2](#). This leads naturally into the statistical treatment of star clusters in [Section 4.2](#), where I outline the nature of dynamically collisionless systems in [Section 4.2.1](#) and most importantly the nature of dynamically collisional systems in [Section 4.2.2](#).
- ▶ In [Chapter 5](#) I introduce the methods that I use most in my work, i.e. direct N -body methods and the associated state-of-the-art code `NBODY6++GPU`. I start with a historical overview of key developmental steps of this method in [Section 5.1](#) and [Section 5.2](#). I continue focusing on `NBODY6++GPU` and its performance in [Section 5.3](#) and I continue by highlighting its basic feature in [Section 5.4](#) and the algorithms in [Section 5.5](#). I finish with a description of the various parallelization techniques used in the code in [Section 5.6](#).
- ▶ [Chapter 6](#) deals with the second method for star cluster simulation that I use in my work, namely Hénon-type Monte-Carlo methods and the related code `MOCCA`. I start with a distinction between the Hénon and Spitzer-type methods and explain how two-body relaxation is dealt with in [Section 6.1.1](#) as well as the effective scattering angle in [Section 6.1.2](#). Strong interactions between binaries and single stars are explained in [Section 6.2](#) and subsections therein. In [Section 6.3](#) and [Section 6.4](#) I explain how the positions and velocities of the particles are advanced in time with Monte-Carlo methods, as well as

how the gravitational potential is calculated with updates to the original method to guarantee energy conservation in [Section 6.5](#). Lastly, I offer a brief account on the reliability of direct N -body methods from [Chapter 5](#) and the methods in this chapter in simulations.

- ▶ is dedicated to solving the orbit-axisymmetric Fokker-Planck equation in cylindrical coordinates to model axisymmetric star clusters. After introducing particle flux conservation form of the equation in [Section 7.1](#) and the workings of the code FOPAX, I elaborate on the rotating King models that are the basis of my work on rotating star clusters in [Section 7.3](#). I finish with a brief account on how that method has been updated and used more recently in [Section 7.3.1](#).
- ▶ In [Chapter 8](#) I explain how the stellar evolution processes from [Chapter 3](#) are combined with the direct N -body methods from [Chapter 5](#) and Hénon-type Monte-Carlo methods from [Chapter 6](#), which happens mostly by interpolating between tables in [Section 8.1](#) or stellar evolution fitting formulae presented in [Section 8.2](#), which I also use in my work.
- ▶ [Chapter 9](#) is based on my publication Kamlah, Leveque, et al. (2022) and my first research question in [Section 1.1](#). Here I focus on a comparison between direct N -body simulations presented in [Chapter 5](#) and Hénon-type Monte-Carlo methods introduced in [Chapter 6](#) with the updated stellar evolution, see also [Section 8.2](#) in both codes that is also presented in the publication. The chapter is in publication-style format, but the method is not fully repeated as it is already explained in earlier chapters.
- ▶ In [Chapter 10](#) I present my second first-author paper Kamlah, Spurzem, et al. (2022). This chapter focuses on the second research question from [Section 1.1](#) which includes a detailed comparison of rotating King models and methods from with direct N -body methods from [Chapter 5](#) and the stellar evolution presented in [Chapter 9](#). Again, it is in publication-style format with omissions where necessary to avoid repetition.
- ▶ [Chapter 11](#) is centered around my first-author publication that I am preparing Kamlah et al. (2023, in prep.). In this chapter I present the implementation of completely new stellar evolution tracks by Tanikawa et al. (2020). I run simulations of rotating King models and methods from with direct N -body methods from [Chapter 5](#). As the preceding two chapters, this chapter is also in publication-style format.
- ▶ Finally, in [Chapter 12](#) I summarize my thesis with answering the three research questions outlined above directly. In [Chapter 13](#), I offer some reflections on the state of (my) star cluster simulations. In [Chapter 14](#) I give a brief account on how I am currently developing further with respect to the work

presented here and what projects are on the horizon.

ASTROPHYSICAL INTRODUCTION

Some of the material in this section is part of the review paper on computational methods of collisional stellar systems submitted in collaboration with my PhD supervisor, Rainer Spurzem, as seen in Spurzem and Kamlah (2023). The material taken from that work and put into this thesis are the sections that I was mostly responsible for beyond the proof-reading of the manuscript that I both did on each other's sections.

2.1 What are star clusters?

Since star clusters of various make-ups are the object of interest and investigation in my work, it is worthwhile to describe and parameterise them first. It is now known to the astronomical community that star clusters can be found everywhere in the known Universe; they populate halos, disks and even bulges and centres of galaxies. Already Galileo Galilei discovered that our own galaxy, the Milky Way, is in fact

"...nothing else than a congeries of innumerable stars distributed in clusters. To whatever region of it you direct your spyglass, an immense number of stars immediately offer themselves to view, of which very many appear rather large and very conspicuous but the multitude of small ones is truly unfathomable." Galileo Galilei (1610), Sidereus Nuncius ("Starry Messenger")

This fundamental realisation without the use of the theoretical and observational tools of modern astronomy, optics and physics, has echoed in its relevance until today, although the picture of star clusters and their environments has naturally become more complex with new discoveries since. In their recent review, Krumholz et al. (2019) sum up the importance of star clusters as such: *"star clusters stand at the intersection of much of modern astrophysics: the interstellar medium, gravitational dynamics, stellar evolution, and cosmology"* (directly cited from the abstract). However, despite centuries full of efforts to understand them, a complete picture of star cluster formation, evolution and dynamics is still not within reach.

If you believe in the Socratic method, you will know that *"the beginning of wisdom is the definition of terms"*. Therefore, I will start with defining star clusters. However, despite astronomers acknowledging the fundamental importance of them for many centuries, defining what a star cluster resembles in nature is generally a tricky business and many definitions that overlap to varying degrees can be found in the literature. The underlying difficulty of defining star clusters stems from the fact that they span huge density, mass and age scales (Krumholz et al., 2019). Therefore, you can only give very general definitions and I like the following three, which are not mutually

- 2.1 What are star clusters? . . . 11
- 2.1.1 Nuclear star clusters . . . 12
- 2.1.2 Globular star clusters . . . 14
- 2.1.3 Open star clusters 18
- 2.1.4 Population III star clusters 19
- 2.2 The formation of star clusters 20
- 2.2.1 Initial conditions for star cluster simulations 26
- 2.2.2 Initial stellar mass function 29
- 2.2.3 Initial binary population 30
- 2.2.4 Multiple stellar populations 33
- 2.2.5 McLUSTER 34
- 2.2.6 Initial star cluster rotation 35
- 2.3 The life and fate of star clusters 37
- 2.3.1 Gravothermal catastrophe 37
- 2.3.2 Gravogyro catastrophe and its coupling with the gravothermal catastrophe 40
- 2.3.3 Pre-core collapse star cluster evolution 43
- 2.3.4 Post-core collapse star cluster evolution 48

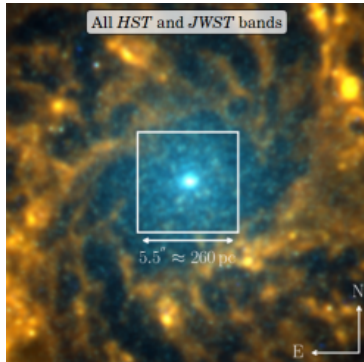


Figure 2.1: Colour image of the NSC in the grand-design spiral galaxy M74 (NGC 628) using various of the JWST and HST bands across the UV to mid-IR regime, highlighting star-formation by using the continuum-subtracted HST ACS F658N ($H\alpha$) filter. Dust lanes, where star formation occurs, are clearly visible. The squared box of side length 5.5 pc in the third panel shows the region that are considered for the fit of the NSC (Figure adapted from Hoyer et al. (2022)).

exclusive, but rather complementary. According to Portegies Zwart et al. (2010) star clusters can be simply thought of as stellar ensembles that fall under the category of so-called self-gravitating systems, which are, generally speaking, systems that are held together by the gravitational forces that are only produced by the bodies that they consist of. If they are old, which implies that they have evolved dynamically to a sufficient degrees, star clusters can also be defined to be stellar ensembles with their member stars having a statistical small-separation excess (Krumholz et al., 2019). In their recent review, Spurzem and Kamlah (2023) define star clusters as coeval associations of stars that are the birth places of most if not all stars. In fact, I will return to this in Section 2.2 and subsections therein. Leaning on these three definitions, I define star clusters as follows:

Definition 2.1.1 (Star cluster) *A star cluster is a self-gravitating stellar association of coeval stars, whose member stars exhibit a statistical small-separation excess compared with other stellar ensembles in the Universe, such as their host galaxies.*

While this definition is as precise as necessary and as general as possible, star clusters are generally classified further into several categories, which are highlighted in the next subsections starting with the most massive star clusters in the Universe and ending with the least massive ones that one can actually observe and ending with the still elusive Population-III star clusters.

2.1.1 Nuclear star clusters

A recent and excellent review on nuclear star clusters (NSCs) is presented in Neumayer et al. (2020) and I note that the afore-cited review by Krumholz et al. (2019) excludes NSCs. I am leaning on Neumayer et al. (2020) in my description of NSCs from hereon.

As their name implies, NSCs inhabit the innermost central regions and dynamical centres of galaxies. An impressive example of a NSC is shown in Figure 2.1 compiled from recent James Webb Space Telescope (JWST) and Hubble Space Telescope (HST) data (Hoyer et al., 2022). Whether or not a galaxy contains a NSC depends strongly on the galaxy mass where late-type galaxies in the Local Volume (LV)¹ with masses up to $10^{6.5} M_{\odot}$ have a nucleation fraction² of practically 0 % and where late-type galaxies with masses from $10^{7.5} M_{\odot}$ upwards approach nucleation fractions of 100 % (Hoyer et al., 2021). However, nucleation appears to seize again for galaxies with masses above $10^{11.5} M_{\odot}$. Hoyer et al. (2021) also find a dependence of nucleation fraction on Hubble-type³, insofar that LV dwarf early-types have a higher nucleation fractions than dwarf late-type galaxies. In general, very massive early-type galaxies have much lower nucleation fractions than their very massive late-type counterparts (Neumayer et al., 2020).

In the following, I summarise some of the defining features of NSCs that are relevant for my thesis work. NSCs have extreme stellar densities reaching surface densities of $10^6 M_{\odot} \text{pc}^{-2}$ and even beyond that in the most massive known NSCs (Neumayer et al., 2020).

1: The LV is defined as a sphere of radius of around 10 Mpc centred on the Local Group (LG). The LG, in turn, is the collection of 100 nearby galaxies to which the MW belongs. The LV includes more than 1200 known galaxies, many of which congregate in well known groups (Koribalski et al., 2018).

2: the nucleation fraction gives the occupation fraction of galaxies hosting a NSC as a function of galaxy stellar mass (Hoyer et al., 2021; Neumayer et al., 2020).

3: This refers to the Hubble-type classification based one galaxy morphology published by Hubble (1926). He erroneously thought that elliptical galaxies (early-type) generally evolve into spiral galaxies (late-type) and thus still today I am mostly stuck with these definitions.

Furthermore, NSCs are extremely luminous and even surpass the luminosities of globular clusters (GCs; [Section 2.1.2](#)) by several orders of magnitudes. The mass of a NSC strongly correlates positively with their host galaxy masses, where the slope of the correlation depends on the Hubble-type (early- vs. late-type) of the host galaxy. These correlations can be seen in [Figure 2.2](#). The most massive known NSCs have masses up to $10^9 M_{\odot}$ ([Neumayer et al., 2020](#), and sources therein).

Crucially, for my work, some NSCs are observed to be rapidly rotating ([Feldmeier et al., 2014](#); [Feldmeier-Krause et al., 2017](#)) with the strength of the rotation measured $(v_{\text{rot}}/\sigma)_{r_{\text{eff}}}$ approaching values of 1 for the NSC in NGC 4244 ([Seth et al., 2008](#)) with a corresponding ellipticity $(e)_{r_{\text{eff}}}$ approaching values beyond 0.5⁴. In general, all NSCs show some imprint of cluster rotation in their kinematics and ellipticities and are mostly pressure-supported star clusters. The rapid rotators do not appear to be the norm at least from current observations ([Neumayer et al., 2020](#)).

We know of the presence of supermassive black holes (SmbBHs) at the centres of galaxies with masses over $10^{10} M_{\odot}$ ([Kormendy & Ho, 2013](#)). Below that galaxy mass, [Neumayer et al. \(2020\)](#) summarise speculations that NSCs replace SmbBHs in dominating the host galaxy's global evolution. However, in some cases SmbBHs or massive black holes (mBHs) and NSCs co-exist⁵, which can be directly observed in our NSC at the centre of the MW (Event Horizon Telescope Collaboration, [2019](#); [Feldmeier-Krause et al., 2017](#); [Genzel et al., 2010](#); [Neumayer et al., 2020](#))⁶. How these SmbBHs form is still one of the great mysteries of astronomy (see the reviews by [Greene et al., 2020](#); [Rees, 1984](#), and sources therein) and my simulations presented in this thesis shed some light on this issue in [Kamlah, Spurzem, et al. \(2022\)](#) and [Kamlah et al. \(2023, in prep.\)](#).

Pioneering direct N -body simulations of NSCs with centrally located and accreting SmbBHs were conducted by [Panamarev et al. \(2019\)](#) with the simulation target being the aforementioned MW NSC⁷. Due to their relevance and also because I am anticipating follow-up simulations of NSCs in the (very) near future, I am briefly highlighting these. The main motivation for this simulation was the existence of young and massive stars in the inner-most region of the MW ([Genzel et al., 2010](#)). The motion of these stars suggests the presence of a SmbBH (see also [GRAVITY Collaboration et al., 2018](#)). It is important to note that the actual simulation of the NSC has around 10^6 particles, which still is an underestimate for the real number of stars in the MW NSC and NSCs in general. Through scaling techniques, [Panamarev et al. \(2019\)](#) assume that each particle actually represents a group of 65 particles and thus they get the a more realistic particle number of 6.5×10^7 particles and a total cluster mass of about $4 \times 10^7 M_{\odot}$ with the mass of the SmbBH properly set at $4 \times 10^6 M_{\odot}$. These simulations were then evolved up to 6.7 Gyr and still remain to be the only direct N -body simulations today⁸ of the MW NSC (or any NSC with an accreting SmbBH over many relaxation times⁹). A bit more on other simulations of NSCs up to this day can be read up our review in [Spurzem and Kamlah \(2023\)](#). Although, NSCs are not the explicit star cluster types of research in my thesis, they are relevant for four reasons here by extending and

4: $(v_{\text{rot}}/\sigma)_{r_{\text{eff}}}$, where v_{rot} are the rotational velocity and σ are the velocity dispersion, respectively, and the ellipticity $(e)_{r_{\text{eff}}}$ are measured at the effective radii of the NSCs. The effective radii are also known as the half-light radii of star clusters and contain half the total star cluster's light (e.g. [Ryon et al., 2017](#)). The ellipticity of star cluster is measured as $e = 1 - \frac{a}{b} = 1 - q$, where q represents the principal axis (a, b) ratio of the star cluster (e.g. [Theis & Spurzem, 1999](#)).

5: from hereon, I discretize the black hole mass spectrum as such:

- ▶ $M_{\text{SmbBHs}} < 10^2 M_{\odot}$,
- ▶ $10^2 M_{\odot} \leq M_{\text{ImBHs}} < 10^4 M_{\odot}$,
- ▶ $10^4 M_{\odot} \leq M_{\text{mBHs}} < 10^6 M_{\odot}$,
- ▶ $10^6 M_{\odot} \leq M_{\text{SmbBHs}}$,

where smBHs denotes stellar-mass, ImBHs denotes intermediate-mass, mBHs denotes massive and SmbBHs denotes supermassive black holes (BHs).

6: The SmbBH at the MW centre has a mass of around $4 \times 10^6 M_{\odot}$ and the NSC has a mass of around $3 \times 10^7 M_{\odot}$.

7: In the Heidelberg/Beijing research group of [Rainer Spurzem](#), I also refer to them now as Dragon-I NSC simulations, for reasons I will explain later.

8: the method of direct N -body simulation is defined in [Chapter 5 \(Direct N-body methods\)](#).

9: the term relaxation time(-scale) is defined in [Definition 2.2.4](#).

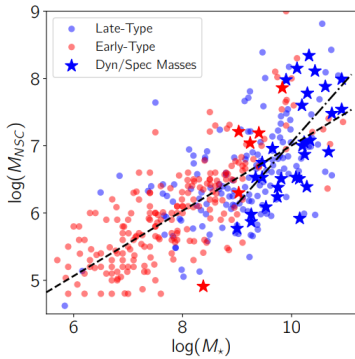


Figure 2.2: Figure showing the compilation of dynamically and spectroscopically modeled NSC masses from Erwin and Gadotti (2012). Their data is shown with stars, while all other masses are derived from colors using stellar population models with Chabrier or Kroupa initial-mass functions (IMFs; Georgiev et al., 2016; Ordenes-Briceño et al., 2018; Sánchez-Janssen et al., 2019; Spengler et al., 2017). Galaxies have been divided by their Hubble types into early and late types (Figure and caption taken from Neumayer et al., 2020).

10: number of clusters per galaxy mass unit (see e.g. Harris, 1996)

extrapolating the results from my simulations:

1. The rotating star cluster models presented in my paper Kamlah, Spurzem, et al. (2022) and especially my models in my upcoming publication of rotating, extremely massive and metal-poor (Population-III) star clusters presented in Kamlah et al. (2023, in prep.) can be treated to some degree as small mock models of NSCs due to their inclusion of star cluster bulk rotation leading to some models with comparable velocity dispersions.
2. One of the proposed channels of the growth of NSCs is the so-called 'dry-merger' scenario (e.g. Arca Sedda et al., 2018). Such a scenario for the build-up of NSCs has been proposed for a few decades (e.g. Tremaine et al., 1975) and with ample observational and theoretical evidence in both the Galactic but also extragalactic NSCs (e.g. Antonini, 2013, 2014; Arca-Sedda & Capuzzo-Dolcetta, 2017; Fahrion et al., 2020; Feldmeier-Krause et al., 2020). It involves the infall or inspiral of GCs into the NSC and therefore, a hierarchical build-up of NSCs from then onward.

Such a scenario has been proposed to explain the observed off-shift between the centre of a mid-IR structure from the respective JWST filter system with respect to the optical centre of the NSC in M74 (Hoyer et al., 2022). Furthermore, especially the aforementioned models of rotating, extremely massive and metal-poor (Population-III) star clusters from Kamlah et al. (2023, in prep.) could contribute the first galactic nuclei and their NSCs in such a dry-merger scenario and by extension the first high red-shift quasars in the Universe.

3. As discussed above, NSCs may harbour ImBHs, mBHs and even SmbBHs with their origins becoming increasingly uncertain for increasing BH mass. My simulations from Kamlah et al. (2023, in prep.) show self-consistent ImBH growth in Pop-III star clusters.
4. Lastly, the updated stellar evolution prescriptions presented in my paper Kamlah, Leveque, et al. (2022) are one important step in more up-to-date direct N -body simulations of NSCs compared with Panamarev et al. (2019).

I will come back to these points in the later chapters.

2.1.2 Globular star clusters

The following section is adapted and expanded from our review Spurzem and Kamlah (2023).

GCs are thought to be the oldest objects in our Galaxy, their age covering a large fraction of the age of the Universe, and they are considered as fossil records of the time of early galaxy formation. GCs in the MW have masses above $10^4 M_{\odot}$ and ages of above 6 Gyr (Krumholz et al., 2019). GCs of variable age are found near all galaxies (except for the smallest dwarfs) and their specific frequency¹⁰ differs as a function of galaxy type, highlighting the close relation between cluster and galaxy formation. The approximately 150 globular clusters of our own Milky Way have been studied in much more detail for their proximity. Figure 2.3 shows the action-space map

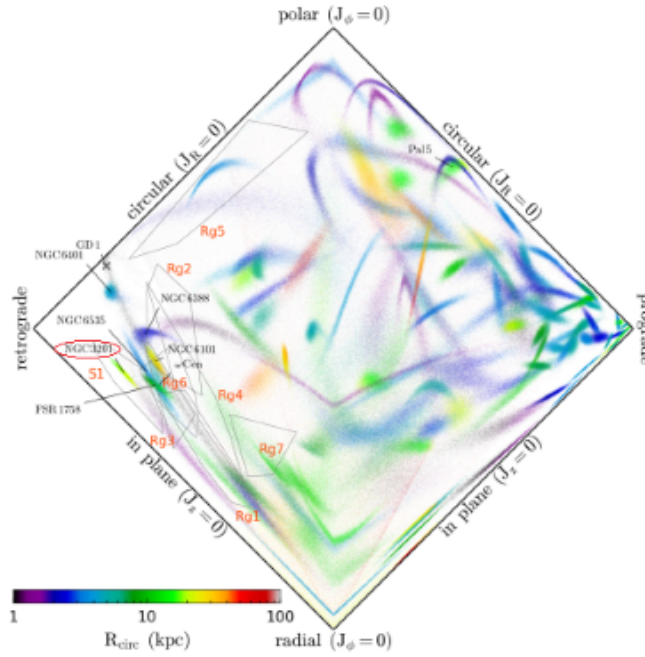


Figure 2.3: The action-space map for the GCs in the MW (Vasiliev, 2019) and retrograde substructures (Myeong et al., 2018a). The GD-1 stream (Grillmair & Dionatos, 2006) is also marked with a cross based on a representative 6D phase space information from Webb and Bovy (2019). The horizontal axis is J_ϕ/J_{tot} , and the vertical axis is $J_z - J_R/J_{\text{tot}}$, analogous to Figure 5 of Vasiliev (2019). Colour marks the circular orbit radius for the corresponding total energy $R_{\text{circ}}(E_{\text{tot}})$. Each object is shown with 1000 Monte Carlo representations of the orbit as drawn from the observational errors. The geometry of the figure can be thought as a projection of the energy-scaled 3D action-space, viewed from the top. NGC 3201, which is a simulation target of mine by using smaller mock models of this cluster (Kamlah, Leveque, et al., 2022; Kamlah, Spurzem, et al., 2022) is on a retrograde orbit, which suggests that it is part of an accretion event of the “Sequoia” dwarf galaxy onto the MW galaxy (Myeong et al., 2018a, 2018b, 2019) (Caption adapted and Figure taken from Myeong et al. (2019)).

for the GCs in the MW (Myeong et al., 2019; Vasiliev, 2019). This map reveals that some GCs are on pronounced retrograde orbits around the MW including the most massive MW GC ω Cen (NGC 5139), which is postulated to be nucleus of the accreted “Sequoia” dwarf galaxy (Bekki & Freeman, 2003) and the GC NGC 3201, on which I model my star rotating and non-rotating star cluster models presented in Kamlah, Leveque, et al. (2022) and Kamlah, Spurzem, et al. (2022). It is therefore possible that also NGC 3201, see also Figure 2.4, originates from the Sequoia dwarf galaxy and was accreted in the same event as ω Cen. This also implies that GCs are not only fundamental building blocks in galaxy evolution, but also tracers of the galaxy’s cosmological history, which make all the more worthwhile to study in greater detail (Reina-Campos et al., 2019, 2020, 2021).

Today, star-by-star observations with HST, and proper motion studies using Gaia with high resolution spectroscopy to determine their stellar velocity dispersions (Bianchini et al., 2013a, 2016b, 2018) are possible. Small and big galaxies in the LV have systems of GCs, e.g. the Andromeda galaxy and the Magellanic clouds.

Globular clusters in huge quantities have been detected around massive galaxies like M87 (Doyle et al., 2019; Tamura et al., 2006a, 2006b), and at higher redshifts (T. Zick et al., 2020; T. O. Zick, Kriek, et al., 2018; T. O. Zick, Weisz, & Boylan-Kolchin, 2018) or other bright central cluster galaxies (Harris et al., 2017) or at sites of star formation



Figure 2.4: Figure showing the colour-composite image of the GC NGC 3201, obtained with the WFI instrument on the ESO/MPG 2.2-m telescope at La Silla (Credit: ESO <https://www.eso.org/public/images/ngc3201/>).

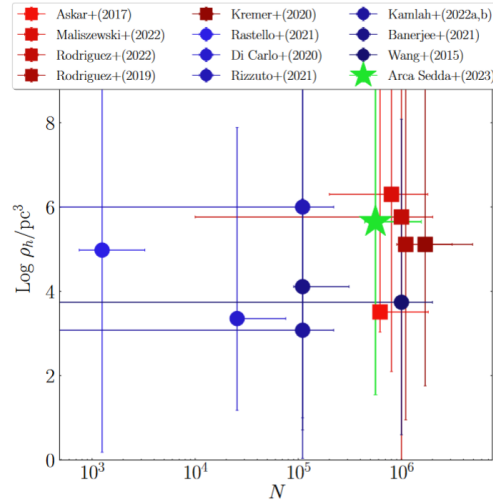


Figure 2.5: Plot showing the logarithm of the half-mass initial density $\text{Log}(\rho_h/\text{pc}^3)$ as a function of particle number N for key N -body simulations. The DRAGON-II cluster database Arca Sedda and et al. (2023a, in prep.) is represented by the green star. The red squares show results from important Hénon-type Monte-Carlo simulations, see also Chapter 6, from Askar et al. (2017), Kremer, Ye, et al. (2020), Maliszewski et al. (2022), and Rodriguez et al. (2019, 2022). Likewise, the blue dots show important direct N -body simulations, see also Chapter 5, from Banerjee (2021a), Di Carlo, Mapelli, Bouffanais, et al. (2020), Rastello et al. (2021), and Rizzuto, Naab, Spurzem, Giersz, et al. (2021) and including my own in Kamlah, Leveque, et al. (2022) and Kamlah, Spurzem, et al. (2022). (Figure taken from Arca Sedda and et al. (2023a)).

near the Antenna galaxies. Still this is – in cosmological scales – our neighborhood. We arrive at two important questions:

- ▶ Do clusters form normally following the cosmic star formation history, which peaks at redshifts of around two (Reina-Campos et al., 2019)?
- ▶ Or do massive clusters form preferentially as special objects at much higher redshifts Boylan-Kolchin (see e.g. $z \sim 6$ in 2018)?

Computer simulations of structure formation in the Universe begin to resolve GC scales (Ramos-Almendares et al., 2020), but they cannot compensate the current lack of deep observations. Only recently gravitational lensing from galaxy clusters has helped to identify candidates for proto-GCs at redshifts of $z > 3$ (Vanzella et al., 2017), and more recently even out to $z = 6$ (Vanzella et al., 2019, 2020; Vanzella et al., 2021). Current instruments such as James Webb Space Telescope (JWST) and future instruments such as Extremely Large Telescope (ELT), among others, will improve the situation significantly.

GCs are undoubtedly some of the most relevant targets for (my) star cluster simulations for many reasons:

1. The particle number of around 3×10^5 for low-mass GCs such as NGC 2298 up to 10^7 for high-mass GCs (or dwarf galactic nuclei) such as ω Cen (see e.g. Baumgardt & Hilker, 2018) required for simulating realistic GCs as those found in the MW is at the edge of what is possible today with modern massively parallelised software for direct N -body simulations, e.g. NBODY6++GPU (Wang et al., 2015), PETAR (Wang, Iwasawa, et al., 2020) and (B)FROST (Rantala et al., 2021), on modern Hardware such as the JUWELS (GPU) Booster at JSC or the

Raven GPU cluster at MPCDF*.

2. The GCs in the MW are abundant¹¹ and old meaning that many stellar exotica, binaries, IMBHs or BH / compact object subsystems have likely formed within them. Furthermore, GCs are comparatively well studied with observations. An area where observations have picked up, in particular, through increased angular resolution and sensitivity of spectrographs is the identification of stellar binaries (see e.g. Giesers et al., 2018, 2019; Kamann, Giesers, et al., 2020). Binary stars are an extremely important component of star clusters, because they form a dynamically active population which has a dramatic impact on the evolution of the host cluster (see e.g. R. Elson et al., 1987; D. C. Heggie, 1975; M. Hénon, 1961).
3. The GC NGC 3201 seen in Figure 2.4 is the star cluster from which I construct mock models for the star cluster simulations presented in Kamlah, Leveque, et al. (2022) and Kamlah, Spurzem, et al. (2022). NGC 3201 is an old and metal-poor GC, which has a mass today of about $1.49 \times M_{\odot}$ (Baumgardt & Hilker, 2018). NGC 3201 has, apart from ω Cen (NGC 5139), the largest half-light and core radius of all globular clusters in Kamann, Husser, et al. (2018) even though NGC 3201 is much less massive than, for example, 47 Tuc (NGC 104). This finding in itself sparks the suspicion that there must be a significant population of hard binaries and / or a compact black hole subsystem in the core of this cluster that counteracts core-collapse, which indeed has been verified observationally (Giesers et al., 2018, 2019) and theoretically (Askar et al., 2018; Giesers et al., 2019; Kremer, Ye, et al., 2018).

Furthermore, Young massive clusters (YMCs) can be characterised as less dense than GCs and they are typically sites of recent or ongoing star with metal-rich stellar populations. They typically have masses above $10^4 M_{\odot}$ and ages below 100 Myr. Krumholz et al. (2019) classify them as the most massive Open star clusters, see Section 2.1.3, however, they also admit that it is unclear if YMCs will actually evolve into GCs or not, see also Section 2.3. YMCs have a chemical composition that is typically more evolved than that of a GC and they also typically less massive than GCs upon birth. YMCs are usually situated in the galactic disk of their host galaxy unless they are formed through galaxy mergers. YMCs in Large Magellanic cloud (LMC), which is a satellite galaxy of our MW, see Figure 2.6 for a Spitzer Space Telescope's Infrared Array Camera (Spitzer) and a JWST MIRI image of the LMC, are the target of the DRAGON-II direct N -body simulation, where I am co-author (Arca Sedda & et al., 2023a, 2023b, 2023c, in prep.). Here, Figure 2.5 shows where these DRAGON-II simulations fit in the wider landscape of initial conditions for both important Hénon-type Monte-Carlo simulations (Chapter 6) such as the MOCCA Survey DataBase I from Askar et al.

11: the MW only has one NSC by definition and that is obscured by dust and other sources in the line-of-sight to Earth.

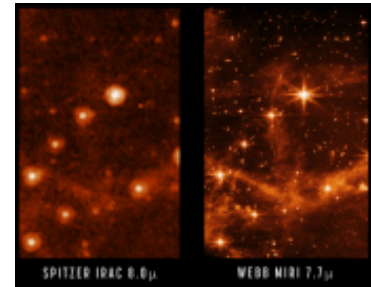


Figure 2.6: Spitzer Space Telescope's Infrared Array Camera (8.0μ) and JWST MIRI (7.7μ) images of the LMC, which reveals the incredible resolution capabilities of JWST and also the stunning star-forming structures and gas in the LMC (Credit: NASA/JPL-Caltech, left, NASA/ESA/CSA/STScI, right https://blogs.nasa.gov/webb/wp-content/uploads/sites/326/2022/05/spitzer_vs_webb_LMC.pdf).

* These are the machines that I have used predominantly for my research:

- ▶ JUWELS Booster <https://apps.fz-juelich.de/jsc/hps/juwels/booster-overview.html>
- ▶ Raven <https://docs.mpcdf.mpg.de/doc/computing/raven-user-guide.html>

(2017) and the CMC Catalog from Kremer, Ye, et al. (2020) as we all as key modern direct N -body simulations (Chapter 5) including the DRAGON-I simulations (Wang et al., 2015). It is clear from this plot that the DRAGON-II simulations present direct N -body simulations that are unparalleled in their computational effort even compared with the DRAGON-I simulations, even though the maximum particle number has not been significantly surpassed. This is due to the fact that the half-mass density of the DRAGON-II simulations is two orders of magnitude larger than that of the DRAGON-I simulations, which increases the required computing effort significantly.

2.1.3 Open star clusters



Figure 2.7: Ground-based image of the Hyades OC (Credit: NASA, ESA, and STScI. <https://esahubble.org/images/heic1309c/>).

12: In other words, we do not observe OCs that are old.

Open star clusters (OCs), such as the Hyades OC shown in Figure 2.7, are much more abundant in the MW than GCs with over 1100 of them having been identified so far (see e.g. Krumholz et al., 2019). Furthermore, unlike GCs, with new data from particularly Gaia and new statistical techniques mostly related to machine learning, new OCs are being discovered in large abundances even to this day in the MW (see e.g. Pang, Li, et al., 2021; Pang, Yu, et al., 2021; Piatti et al., 2023).

OCs in the MW are less dense and less massive than GCs (Krumholz et al., 2019) with most having masses below $5000 M_{\odot}$ and ages below 6 Gyr. Additionally, they occupy the disk of the MW galaxy unlike GCs that are preferentially found in the Galactic halo. OCs are also typically much younger than GCs¹², which might simply be due to the fact that the region where OCs form and due to their lower mass and their lower densities they are much more easily disrupted by external potentials and also on faster time-scales, see Section 2.3 and Forbes et al. (2018), Kruijssen (2014), and Krumholz et al. (2019). Therefore, one could assume that OCs and GCs are not in any way different in their (star) formation, see also Section 2.2, but due to some key structural parameters and their internal and external dynamics, the GCs that I observe today have survived and the OCs that have formed at the same time have not. In this way, GCs and OCs overlap certainly in the underlying physical processes and thus if I view them from this angle, the traditionally drawn lines between GCs and OCs occupying distinct loci in age, size and mass parameter spaces in the greater framework of cosmological and galactic evolution and structure formation are becoming blurred. However, Krumholz et al. (2019) maintain that a crucial difference exists between GCs and OCs. Unlike OCs, GCs have anti-correlations in light element abundances and also they exhibit multiple stellar populations, see also Section 2.2.4.

OCs are very friendly to direct N -body simulations compared with GCs, because of their low particle numbers, low densities and comparatively smaller life-times. Therefore, a large number of such simulations have been conducted to this day (see e.g. Pang, Shu, et al., 2022). My work does not focus on OCs as both publications Kamlah, Leveque, et al. (2022) and Kamlah, Spurzem, et al. (2022) need large particle numbers to yield statistically sensible time-evolution for global properties, such as binary fractions. Furthermore, the

Monte-Carlo method does not work well for low particle numbers N , see also [Chapter 6](#). I have mentioned OCs here for completeness.

2.1.4 Population III star clusters

I furthermore classify the first star clusters that have existed in our Universe as Population III (Pop-III) star clusters. The name of these clusters derives from the fact that the first stars in the Universe are classified as Pop-III stars. Pop-III star clusters are the object my studies presented in Kamlah et al. (2023, in prep.).

At large red-shifts the distinction between OCs and GCs dissolve in observations and theoretical modelling (Krumholz et al., 2019). Observations of Pop-III stars or their remnants or their host clusters remain elusive, because of the extreme distances from us. Recently, a possible detection of an extremely massive Pop-III star at $z = 6.2$ was announced by Schauer et al. (2022), but this detection needs follow-up studies to be conclusive. Earlier an observation with MUSE Deep Lensed Field (MDLF) targeting the Hubble Frontier Field (HFF) galaxy cluster MACS J0416 of a Pop-III stellar complex at $z = 6.629$ was claimed by Vanzella et al. (2020) and Vanzella et al. (2021). In general, however, direct observations of Pop-III stars and their host clusters will remain elusive even considering the ground-breaking results expected from JWST (Katz et al., 2022; Rydberg et al., 2013). On the other hand, de Souza et al. (2013) claim that some hundred SNe detections by JWST may be enough to constrain the IMF of Pop-III stars. Schauer et al. (2020) provide a further discussion on this issue. In the future, the wide field near-IR surveys by Euclid (Laureijs et al., 2011; Tanikawa, Moriya, et al., 2022) and the Nancy Grace Roman Space Telescope (RST) are postulated to yield much better resolution than JWST on direct collapse BHs above the pair instability mass gap because of their greater fields of view (Lazar & Bromm, 2022; Vikaeus et al., 2022).

In the absence of unambiguous observations of Pop-III stars and their environments, it remains difficult to constrain the parameter spaces for Pop-III star and star cluster formation (see e.g. Klessen, 2019). Fraser et al. (2017) attempted to fit an IMF to observed stars and collated detailed abundances of 29 Pop-III stars from the literature to infer the IMF. They found that the IMF is similar to those of Pop-I/-II populations. However, the authors cautioned against drawing strong conclusions due to low N statistics. Therefore, to constrain the IMF of Pop-III stars hydrodynamic models are often used to make up for this deficiency (see e.g. Chon & Omukai, 2020; Chon et al., 2021; Hirano et al., 2015; Hirano & Bromm, 2017, 2018a; Hirano et al., 2014; Latif et al., 2022; Sharda et al., 2021; Stacy et al., 2016; Sugimura et al., 2020; Susa, 2019; Susa et al., 2014). Similarly, the binary fraction and (initial) binary statistics of such star clusters is subject to significant uncertainty (Liu, Meynet, & Bromm, 2021; Stacy & Bromm, 2013). Furthermore, the Pop-III binary properties also depend on the environment, in which the star clusters, which hosts them, forms (e.g. Hirano & Bromm, 2018b; Sugimura et al., 2020).

Pop-III star clusters are extremely promising sources for producing seed black holes for galactic nuclei, see also the brief introduction in

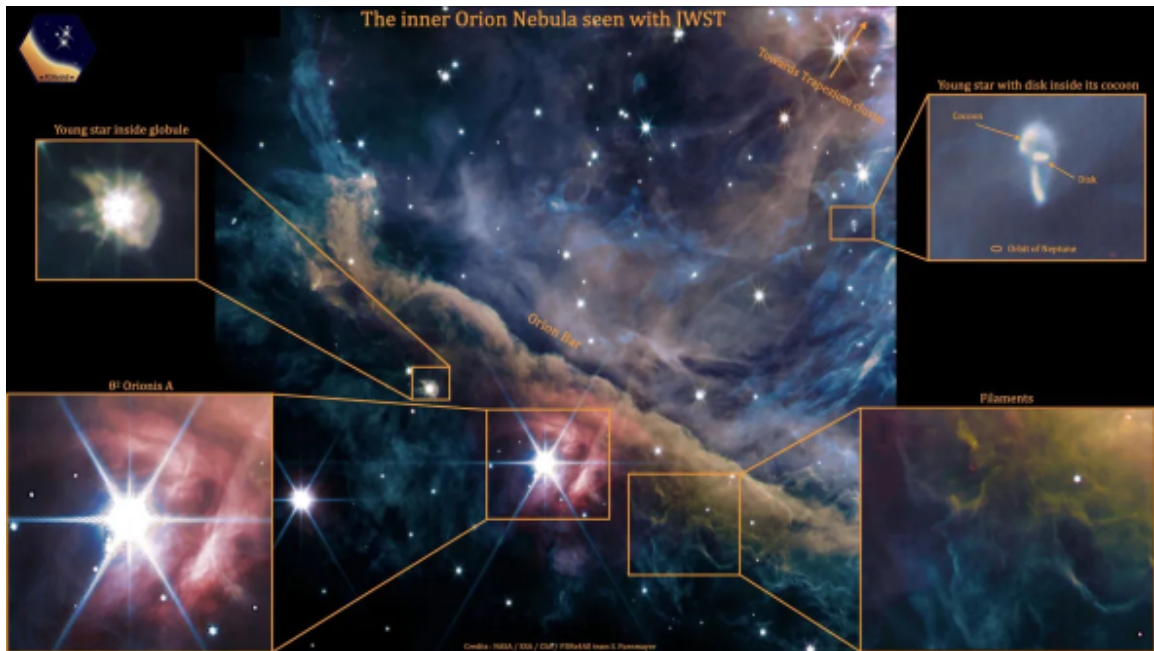


Figure 2.8: Orion Nebula (ONC) as seen with JWST NIRCcam instrument revealing star and planet formation with many fascinating objects annotated in the image. Depending on the author the ONC might not even be classified as a cluster (Krumholz et al., 2019). a) **Young star with disk inside its cocoon:** this shows a planet forming disks of gas and dust around a young star. These disks are being dissipated or “photo-evaporated” due to the strong radiation field of the nearby stars of the Trapezium creating a cocoon of dust and gas around them. Almost 180 of these externally illuminated photo-evaporating disks around young stars (also known as Proplyds) have been discovered in the Orion nebula, and HST-10 (the one in the picture) is one of the largest known. The orbit of Neptune is shown for comparison. b) **Filaments:** The entire image is rich in filaments of different sizes and shapes. The inset here shows thin, meandering filaments that are especially rich in hydrocarbon molecules and molecular hydrogen. c) **θ^2 Orionis A:** The brightest star in this image is θ^2 Orionis A, a star that is just bright enough to be seen with the naked eye from a dark location on Earth. Stellar light that is reflecting off dust grains causes the red glow in its immediate surroundings. d) **Young star inside globule:** When dense clouds of gas and dust become gravitationally unstable, they collapse into stellar embryos that gradually grow more massive until they can start nuclear fusion in their core – they start to shine. This young star is still embedded in its natal cloud. Several images in different filters were combined to create this composite image: F140M and F210M (blue); F277W, F300M, F323N, F335M, and F332W (green); F405N (orange); and F444W, F480M, and F470N (red) that represent emissions from ionized gas, hydrocarbons, molecular gas, dust and scattered starlight. (Credit: NASA / ESA / CSA; Data reduction and analysis: PDRs4All ERS Team <https://pdrs4all.org/>; Graphical processing: S. Fuenmayor & O. Berné.).

Chapter 1 and Figure 3.18. Some pioneering simulations with direct N -body methods on these clusters were already conducted by Wang et al. (2022).

2.2 The formation of star clusters

In this section, I already introduce some concepts, which will be derived in much more detail in Chapter 4. It is not necessary to read that chapter before this one, but need these concepts already to follow the formation and evolution of a star cluster.

Our understanding of how star clusters form appears now to be integral to the process of star formation itself, since all stars form in ensembles in some hierarchical fashion (see e.g. Grudić, Hopkins, et al., 2018; Grudić et al., 2023; Krumholz et al., 2019; Lada & Lada, 2003; Lada et al., 2010; Marks & Kroupa, 2011; McKee & Ostriker, 2007). An impressive image of the star formation processes being observed in the ONC, therefore in a star cluster (if you believe some authors, see also Krumholz et al. (2019)), is shown in Figure 2.8. In general, these stellar ensembles or clusters dissolve into the galactic

background over time triggered by tidal interactions in combination with stellar dynamics and stellar evolution (Krumholz et al., 2019), see also Section 2.3.

The nursery for star clusters are assumed to be Giant Molecular Clouds ((GMCs); see e.g. Larson, 1981; Pang et al., 2020), which are gravitationally bound (Sun et al., 2018). Therefore, they avoid tidal disruption, which for a GMC in our MW with a flat rotation curve (RC) means that the cloud density must exceed twice the galaxy background density (Chernoff & Weinberg, 1990). Star clusters are ‘born’ out of these GMCs in clumps, which are local regions of over-density. This fragmentation produces filaments that fragment further into denser cloud cores. These cloud cores contract and within them, the first proto-clusters form (Kroupa, 2008; Krumholz et al., 2019; Urquhart et al., 2018). These clumps have masses ranging from very small values up to about $10^5 M_{\odot}$. From MW surveys I know that the clumps that are currently around are not massive enough to form GCs. However, starburst (dwarf and nuclear) galaxies or any disk galaxy with a high enough gas fraction is expected to have GMCs with enough mass to produce clumps massive enough to nurse GCs¹³.

Proto-stars form within proto-clusters (Kroupa, 2011), see also Figure 2.8. These proto-stars accrete gas and need about $t_{ps} = 10^5$ yr to accumulate 95% of their masses (Wuchterl & Tscharnuter, 2003). It is not entirely clear if the stars already form mass segregated here or not; proto-stars at the centre of the proto-clusters should have more gaseous material to accrete (Bonnell et al., 2007; Zinnecker & Yorke, 2007). At some point the proto-stars begin to lose mass via proto-stellar outflows (Matzner & McKee, 2000; Offner & Chaban, 2017). It is worthwhile to have a look at the main drivers of terminating proto-star formation after the collapse of the clumps in the GMC, as some of these processes are linked to stellar evolution processes after the first proto-stars have formed. The quantity describing this process is the so-called

Definition 2.2.1 (Star formation efficiency) *The star formation efficiency (SFE) ϵ_* measures the mass fraction of star-forming gas converted into stars (Lada & Lada, 2003):*

$$\epsilon_* = \frac{M_*}{M_{\text{gas}} + M_*}, \quad (2.1)$$

where M_* is the total stellar mass and M_{gas} is the mass of unprocessed gas.

First of all, gas is removed in the form of proto-stellar outflow, because this process breaks up the dense regions in removing 2/3 of the proto-stellar cores (Offner & Chaban, 2017). These outflows are of very low velocity and only relevant for the smallest clusters of $M \leq 100 M_{\odot}$.

If there are massive stars forming in the cluster with masses even above $100 M_{\odot}$, other processes play a major role:

- Massive stars can undergo Supernova explosions (SNe), which are introduced more thoroughly in Section 3.1.6. They release

13: In general, there is a lot of literature available on the exact formation of gas into stars (see e.g. McKee & Ostriker, 2007). In Nbody6++GPU you typically already start with a distribution of fully formed and Virialised ensemble of stars, see also Section 2.2.5. Therefore, I will not go in much more detail into this issue. However, it needs to be said that gas and stellar material may over time migrate and enrich the cluster leading to new star formation and multiple stellar populations within stars, see also Section 2.2.4. Consequently, one also has to take my Nbody6++GPU models in Kamlah, Leveque, et al. (2022) and Kamlah, Spurzem, et al. (2022) and Kamlah et al. (2023, in prep.) with a grain of salt; they are mostly isolated clusters with a background galaxy as a source of a passive tidal field, which is set in the initialisation of the simulation without gas in- or outflow. However, there exist a version of Nbody6, called GASEX, which can be used to add gas into the simulation (Kroupa, 2001). Additionally, there is a version called Nbody6++TID, which treats tidal forces correctly for non-circular orbits using a 3D tidal tensor approximation for tidal forces (Ernst et al., 2007).

enormous amounts of energy almost in an instant ($t_{\text{SNe}} \simeq (2 - 3) \text{ Myr}$). However, during this time, the gas surrounding the exploding star might even birth new stars, so it is uncertain, what impact these explosions ultimately have on the gas removal.

- ▶ Another process that might play a role is the so-called photo-ionization feedback. This process refers to ionizing photons being released by stars and effectively heating up the surrounding gas and accelerating it to the “champagne flow”, which will leave the cluster, unless hindered by gravity or some other process. There also exist another back-reaction, when in this way ionised material bounces off neutral surfaces in the so-called rocket effect. This might eject more star forming material from the cluster.
- ▶ Direct radiation pressure is less powerful than photo-ionization pressure, but does still play a role. It comes from a fully formed zero-age stellar population, which emits light at mostly UV lengths. Since the Interstellar medium (ISM) is opaque most of the radiation momentum is transferred into the gas molecules and thus the gas is accelerated and driven outwards.

14: For clusters with higher masses and densities, then according to Grudić, Guszejnov, et al. (2018) and Grudić, Hopkins, et al. (2018) through simulations found that these three processes named above become ineffective in order of photo-ionization first, then direct radiation pressure and lastly SNe. Another process called indirect radiation pressure dominates at certain mass and density scales. This process involves the interstellar dust, which can absorb and re-emit radiation in the IR regime. The opacity of IR dust is of orders of two magnitudes smaller than that of UV, however, if the IR radiation encounters regions with sufficiently high column density, then this region might be opaque to IR radiation. As is the case with direct radiation pressure and UV photons, the IR photons transfer their momentum to the interstellar dust and therefore accelerate it and the dust then at some point re-emits IR photons and so on. According to Thompson et al. (2015), the resulting net force is much larger than the resulting net force of direct radiation pressure.

The above feedback mechanisms cap the amount of gas that can actually be transformed into stars¹⁴ and Lada and Lada (2003) find that ϵ_* ranges between $0.2 \leq \epsilon_* \leq 0.4$. Overall, proto-stellar outflows are dominant on these scales (a couple of pc) and terminates further star formation. This has been confirmed in (Kroupa et al., 2001), where bound remnants remain for $\epsilon_* = 0.3$ (lower limit). It is not clear if this happens before or after many of the denser cloud cores merge to form a massive embedded cluster, which happens on a time-scale of around 0.5 Myr. What is clear is that many generations of proto-stars form in the formation of the star cluster (Kroupa, 2008) (see also Section 2.2.4).

Definition 2.2.2 (time-scale for gas removal) *The time-scale for gas removal from the embedded star cluster is given by τ_{gas} .*

Whether the cluster survives the formation phase (remains bound) depends on the spatial distribution of gas and stars and on τ_{gas} (Kroupa, 2008; Krumholz et al., 2019; Smith et al., 2011, 2013), see Definition 2.2.2. If the most massive stars are O and B stars, these expel the embedded star cluster nebula by ionising over the gas expulsion time-scale τ_{gas} (0.5-1.5) Myr (Kroupa, 2008).

Definition 2.2.3 (crossing time-scale) *The time-scale for a star to cross the star cluster is given by τ_{cr} :*

$$\tau_{\text{cr}} = \frac{r_{\text{h}}}{\sigma_{\text{h}}}, \quad (2.2)$$

where σ_{h} is the typical velocity associated with the root mean square random motion (velocity dispersion) taken in the embedded cluster at the half-mass radius r_{h} ¹⁵.

15: radius containing 50 % of the (current) total mass.

If Virial equilibrium prevails, we have $\sigma_h^2 \approx GM_h/r_h$ (where the sign \approx here and henceforth means “approximately equal” or “equal within an order of magnitude”), thus

$$\tau_{\text{cr}} \approx \sqrt{\frac{r_h^3}{GM_h}}. \quad (2.3)$$

Global dynamical adjustments of the star cluster system, like oscillations, are connected with crossing time-scale.

It is furthermore important to introduce here one of the most important time-scales in star cluster evolution, which is the relaxation time-scale. Unlike most laboratory gases stellar systems are not usually in thermodynamic equilibrium, neither locally nor globally. Radii of stars are usually extremely small relative to the average inter-particle distances of stellar systems (e.g. the radius of the sun is $r_\odot \approx 10^{10}$ cm, a typical distance between stars in our galactic neighbourhood is of the order of 10^{18} cm). Only under rather special conditions in the centres of galactic nuclei and during the short high-density core collapse phase of a globular cluster, stellar densities might become large enough that stars come close enough to each other to collide, merge or disrupt each other. Therefore it is extremely unlikely under normal conditions that two stars touch each other during an encounter; encounters are elastic gravitational scatterings¹⁶. The mean inter-particle distance is large compared to $p_0 = 2Gm/\sigma^2$, which is the impact parameter for a 90° deflection in a typical encounter of two stars of equal mass m , where the relative velocity at infinity is $\sqrt{2}\sigma$, with local 1D velocity dispersion σ , see also already [Definition 4.1.4](#). Thus most encounters are small-angle deflections.

16: Following Binney and Tremaine (2008a) I define that encounters are gravitational perturbation of the orbit of one star by another. A collision describes the state of stars actually physically touching on another.

Definition 2.2.4 (relaxation time-scale) *The relaxation time τ_{rx} is defined as the time after which the root mean square velocity increment due to such small angle gravitational deflections is of the same order as the initial velocity dispersion of the system. We use the local relaxation time as defined by (Chandrasekhar, 1942)*

$$\tau_{\text{rx}} = \frac{9}{16\sqrt{\pi}} \frac{\sigma^3}{G^2 m \rho \ln(\gamma N)}. \quad (2.4)$$

G is the gravitational constant, ρ the mean stellar mass density, σ the 3D velocity dispersion, N the total particle number.

This definition was used by Bettwieser and Spurzem (1986) and Larson (1970a), because it naturally occurs when computing collisional terms, if the velocity distribution function is written as a series of Legendre polynomials (Spurzem & Takahashi, 1995), with numerical factors being unity¹⁷. Other definitions of relaxation can be found frequently, for example in L. Spitzer (1987). They differ only by numerical factors, except for the so-called

17: for equipartition terms of lowest order (Spurzem & Takahashi, 1995) or only little different from unity, such as 9/10 for the collisional decay of anisotropy (Bettwieser & Spurzem, 1986).

Definition 2.2.5 (Coulomb logarithm) $\ln(\gamma N)$, *which may take different functional forms. For common forms of the Coulomb logarithms only γ is of order unity, but may take different values*¹⁸.

18: e.g. 0.11 (Giersz & Heggie, 1994a), or 0.4 (L. Spitzer, 1987). It is often found in formulae for scattering rates from $1/r$ potentials, such as the gravitational potential of a point mass or the electrostatic potential of a point charge.

Assuming Virial equilibrium a fundamental proportionality turns out:

$$\frac{t_{\text{rx}}}{t_{\text{dyn}}} \propto \frac{N}{\ln(\gamma N)}. \quad (2.5)$$

(cf. e.g. L. Spitzer (1987)). As a result, for very large N , dynamical equilibrium is attained much faster than thermodynamic equilibrium. Therefore, even if treating them as “gaseous” spheres, stellar systems evolve qualitatively different from stars; in stars the thermal time-scale is short compared to the dynamical timescale (Bettwieser & Sugimoto, 1984), which is the time a particle takes to orbit the cluster at the half-mass radius (see e.g. Rodriguez et al., 2022). Another interesting consequence of the long thermal timescale in star clusters is that anisotropy¹⁹ can prevail for many dynamical times. If one assumes a purely kinetic temperature definition, it ensues that in star clusters the temperatures (or velocity dispersions) can remain different for different coordinate directions over many dynamical times. For example, in a spherical system (using polar coordinates) the radial velocity dispersion of stars (“temperature”) σ_r^2 could be different from the tangential one σ_t^2 . For the relaxation time above the 3D velocity dispersion $\sigma^2 = \sigma_r^2 + 2\sigma_t^2$ is used. If axisymmetric or triaxial the tangential velocity dispersion can be decomposed into two different dispersions $2\sigma_t^2 = \sigma_\theta^2 + \sigma_\phi^2$.

I return to the question whether the cluster survives the gas expulsion phase or not. The relation between τ_{gas} from Definition 2.2.2 and τ_{cr} and from Definition 15 can yield some indication of how the embedded star cluster evolves:

- ▶ $\tau_{\text{gas}} \ll \tau_{\text{cr}}$, then the embedded star cluster does not survive gas expulsion.
- ▶ $\tau_{\text{gas}} \gg \tau_{\text{cr}}$, then the embedded star cluster survives gas expulsion as the expulsion is relatively slow. As a result, the cluster radius r expands by a factor of around of five²⁰.

In general, τ_{gas} becomes longer than τ_{cr} as the cluster increases in mass. This fact implies that low mass cluster ($< 10^5 M_\odot$) undergo a rapid dynamical evolution that results in cluster disintegration, while clusters above that mass undergo adiabatic expansion (Kroupa, 2005; Kroupa, 2008). From observations of young clusters, I know that most of the residual gas is indeed removed within one τ_{cr} (Kroupa, 2005) and around 90% of all clusters disperse. On the other hand, I still observe over 150 GCs in our MW and so evidently these GCs have survived the gas expulsion phase (Baumgardt & Hilker, 2018). If the resulting cluster has a low velocity dispersion, then the initial substructure is erased in the ensuing collapse. On the contrary, if the velocity dispersion is high, then the cluster will retain much of the initial substructure. Young star clusters that do exhibit substructures are much rarer, however, than young star clusters that do not (Goodwin & Whitworth, 2004). But those clusters that have a substructure have additional binding energy that might assist its survival and ϵ_* could be as low as 0.2 (Allison et al., 2009; Fellhauer & Kroupa, 2005).

19: Interest in anisotropy was recently sparked by anisotropic mass segregation in rotating star clusters, both globular and nuclear (Kamlah, Spurzem, et al., 2022; Szölggyen & Kocsis, 2018; Szölggyen et al., 2019, 2021; Tornamenti et al., 2019).

20: This is the model if $\epsilon = 0.2$ and $\tau_{\text{gas}} \rightarrow \infty$ (Kroupa, 2008).

Definition 2.2.6 (time-scale of the pre-cluster cloud-core contrac-

tion) The time-scale of the pre-cluster cloud-core contraction until the stellar feedback termination $\tau_{\text{cl,form}}$ is about the time over which the cluster forms.

The ratio $\tau_{Q0.5} = \tau_{\text{cl,form}}/\tau_{\text{cr}}$ determines whether the proto-stars reach Virial equilibrium

$$2K + W = 0 \rightarrow Q = \frac{K}{|W|} = 0.5, \quad (2.6)$$

where K is the kinetic energy of the stars in the cluster, W is the potential energy and Q is the Virial ratio, before gas expulsion or not:

1. $\tau_{Q0.5} < 1 \rightarrow$ the proto-stars cannot reach Virial equilibrium²¹ before gas removal.
2. $\tau_{Q0.5} > 1 \rightarrow$ the proto-stars reach Virial equilibrium before gas removal.

21:

- ▶ $Q < \frac{1}{2} \rightarrow$ collapsing,
- ▶ $Q > \frac{1}{2} \rightarrow$ expanding.

Which of the two is more likely, depends on whether molecular clouds and star clusters are on a single free-fall time-scale τ_{ff} or on many free-fall time-scales.

Definition 2.2.7 (free-fall time-scale) *the characteristic time-scale τ_{ff} that would take a body to collapse under its own gravitational attraction, if no other forces existed to oppose the collapse, which for a spherically symmetric distribution of stars is given by*

$$\tau_{\text{ff}} = \sqrt{\frac{3\pi}{32\rho G}}, \quad (2.7)$$

where ρ is the average mass density.

Furthermore, I can define the

Definition 2.2.8 (time-scale of star cluster formation) *This time-scale τ_{SF} accounts for the star formation history and measures the total time of star cluster formation.*

If I then account for the fraction of the GMC's mass, which is transformed into stars per free-fall time of that cloud and, which is given by ϵ_{ff} , then I have

$$\tau_{\text{SF}} = \epsilon_* \frac{\tau_{\text{ff}}}{\epsilon_{\text{ff}}} \quad (2.8)$$

τ_{SF} is now seen to be a few τ_{ff} . Since GMCs are rarely located in isolation, but rather in gaseous filaments, there exist a steady supply of gas forming material, which flows into the star-forming region and accretes onto the proto-cluster, which then causes instantaneous star formation. This is known as the conveyor belt effect. The time-scale of this inflow is typically much larger than τ_{ff} , because it is subject to much larger structures and therefore much longer dynamical times. Once this inflow ceases, however, the final time for star formation and gas removal is ultimately only determined by ϵ_{ff} and the feedback effects mentioned above. All of this happens for

22: But this is not a contradiction, since the dissipation of angular momentum via relaxation in the presence of tidal fields of quickly rotating proto-clusters can lead to very slow rotation rates (see e.g. Akiyama & Sugimoto, 1989).

a couple of million years for the distinct star clusters to form. This process leads to significant angular momentum of the proto-cluster, although it has also been found that other cluster do not seem to rotate (Kuhn et al., 2019)²². It has been known for over a century that star clusters even today show significant imprints of rotation, which can, for example, be observed in deviations in the shapes of star clusters from sphericity (Bianchini et al., 2013b; C. W. Chen & Chen, 2010; Frenk & Fall, 1982; Harris, 1976; Harris, 1996; I. King, 1961; Kopal & Slouka, 1936; Kormendy, 1985; Lupton et al., 1987; Pease & Shapley, 1917; Shapley, 1930; Shapley & Sawyer, 1927; White & Shawl, 1987). Moreover, present-day detectors and data processing methods have made it possible to resolve the photometry and kinematics of individual stars all the way down to the cluster centre revealing rotational kinematics of event multiple stellar populations (Bianchini et al., 2016a, 2018, 2019; Ferraro et al., 2018; Giesers et al., 2018, 2019; Kamann, Bastian, et al., 2018; Kamann, Husser, et al., 2018; Kamann et al., 2016, 2019; Lanzoni, Ferraro, Mucciarelli, Palla, Lapenna, et al., 2018; Lanzoni, Ferraro, Mucciarelli, Palla, Tiongco, et al., 2018; Sollima et al., 2019; M. Tiongco et al., 2021; M. A. Tiongco et al., 2019). Additionally, both observations and simulations support these results and find that star clusters show significant fractality (Ballone et al., 2020; Pang, Li, et al., 2021), and internal rotation at birth in general (Ballone et al., 2021; Lahén et al., 2020). Velocity anisotropy has been observed in star clusters with detected elongated structures (Pang, Li, et al., 2021; Pang et al., 2020), which might be induced by rotation. Today, it is still not entirely clear if observations are in harmony with the predicted rotation rate distribution. However, most star clusters are considered to be pressure-supported today. This means that the random stellar motions dominate the bulk and rotational motions (Kroupa, 2008).

The first gas-free cluster population emerges after around 10 – 100 Myr. Now, other mass loss mechanisms come into play, mainly stellar winds and tidal interactions, which depend on the ratio of the cluster concentration of cluster to its tidal radius.

2.2.1 Initial conditions for star cluster simulations

Defining appropriate global initial conditions for star cluster simulations is highly non-trivial as the formation of a star cluster and the stars within it depend on a large number of parameters that are very uncertain due to a lack of better theoretical understanding and or observations. In the following, I give an overview of the most important parameters in this context for N -body simulation of star clusters. Embedded cluster and some time-scales In this stage of cluster evolution, the star cluster and its stars are still embedded in the residual gas just after star formation has ceased. This phase lasts for around 0.5 Myr (Baumgardt, Kroupa, & Parmentier, 2008), after which the gas mass decreases exponentially.

In the following, M_{ecl} is the mass of the stars in the cluster.

Definition 2.2.9 (energy-equipartition/mass segregation time-s-

cale) The energy-equipartition/mass segregation time-scale between massive and average stars τ_{ms} is given by

$$\tau_{\text{ms}} = \frac{\bar{m}}{m_{\text{max}}} \tau_{\text{rx}} \quad (2.9)$$

where \bar{m} is the average mass, m_{max} is the mass of the most massive star and τ_{rx} is the relaxation time-scale from [Definition 2.2.4](#).

I now assume that the stars are of age τ_{age} , then if

- ▶ $\tau_{\text{cr}} > \tau_{\text{age}}$, then the cluster is very close to its initial configuration, because it has not dynamically mixed yet,
- ▶ $\tau_{\text{cr}} < \tau_{\text{age}}$, then the system mixed but has not yet fully relaxed.

In my simulations in Kamlah, Leveque, et al. (2022) and Kamlah, Spurzem, et al. (2022) and Kamlah et al. (2023, in prep.), I always start at around (10-100) Myr after the GMC's collapse with

- ▶ a fully formed stellar population in a cluster that has expelled all its gas and no more gas is flowing in,
- ▶ a cluster that exhibits no mass-segregation, fractal or other sub-structures,
- ▶ a stellar population that is in Virial equilibrium initially.

Initial 6D phase space distribution

In order to initialise an N -body star cluster simulation, I need to distribute the N particles in 6D phase space. A statistical approach as described in [Chapter 1.2](#) is taken to realize a stellar cluster which follows the probability density distribution $f(\vec{r}, \vec{v}, t)$. The full 6D distribution function is rarely known explicitly; when assuming a steady state²³ when solving Jeans's theorem (Binney & Tremaine, 2008b) allows us to express f as a function of integrals of motion²⁴ of a single star moving in the gravitational potential $\Phi(r)$. For now I assume spherical symmetry, so I have for example specific energy and specific angular momentum:

$$f = f(\vec{r}, \vec{v}) = f(E, L), \quad (2.10)$$

which are defined as

$$E = \frac{v^2}{2} + \Phi(r), \quad (2.11)$$

$$L = |\vec{r} \times \vec{v}|. \quad (2.12)$$

(cf. [Chapter 6](#)). Deviations from spherical symmetry can be taken into account as well, see for example [Section 2.2.6](#) for the importance of initial bulk rotation.

Definition 2.2.10 (Self-consistent distribution functions) *Examples of self-consistent distribution functions are given by*

$$f(E) = F_n E^{n-3/2}, \quad (2.13)$$

23: f does not depend on time.

24: These are functions of only the phase-space coordinates that are constant along an orbit of the star, see also Binney and Tremaine (2008a).

where n is an integer index and F_n a normalization factor to make sure $f(E)$ is properly normalized as probability density function. For $n = 5$ this realizes the famous Plummer model (Plummer, 1915), and for $n = 7/4$ another famous solution, a density cusp (Bahcall & Wolf, 1976; Frank & Rees, 1976) around supermassive black holes is found Preto et al. (2004).

In Binney and Tremaine (2008a) these models from Definition 2.2.10 are also called stellar polytropes, because their density distribution is the same as a gaseous polytrope (Chandrasekhar, 1939) of the same index n . Analytical density distributions exist for $n = 0$, $n = 1$, and $n = 5$ (Kippenhahn et al., 2012), but for stellar systems such as star clusters only $n = 5$ is physically useful.

The theory of gaseous spheres also knows the isothermal solution, which is obtained for $n = \infty$; in stellar dynamics the equivalent is the isothermal sphere

$$f(E) = F_\infty \exp(-E/\sigma^2) \quad (2.14)$$

Here σ^2 is the r.m.s. stellar velocity dispersion, analogous to the temperature in a gaseous sphere. These models have some problems, because their radial extent is unlimited in the case of Plummer and isothermal models. For the isothermal models even their mass is infinite. Therefore, and since real star clusters are often subject to a tidal cutoff due to the host galaxy, a tidal cutoff radius is introduced, which is connected to a tidal cutoff energy. If at the cutoff radius the gravitational potential of an isolated star cluster would be Φ_0 , then a relative potential Ψ and a relative energy ε are defined by

$$\Psi = \Phi - \Phi_0, \quad (2.15)$$

$$\varepsilon = E - \Phi_0. \quad (2.16)$$

In that way the star cluster extends from the center out to $\varepsilon = 0$ (and $\Psi = 0$), and I define the *lowered* isothermal distributions

Definition 2.2.11 (King distribution)

$$f(\varepsilon) = \begin{cases} f_\infty \exp(-\varepsilon/\sigma^2) & \varepsilon < 0 \quad (E < \Phi_0) \\ 0 & \varepsilon \geq 0 \quad (E \geq \Phi_0), \end{cases} \quad (2.17)$$

where f_∞ is the normalization factor that has to be chosen appropriately.

and I also define

Definition 2.2.12 (Plummer distribution)

$$f(\varepsilon) = \begin{cases} f_5 \varepsilon^{7/2} & \varepsilon < 0 \quad (E < \Phi_0) \\ 0 & \varepsilon \geq 0 \quad (E \geq \Phi_0), \end{cases} \quad (2.18)$$

where f_5 is the normalization factor that has to be chosen appropriately.

25: Some authors prefer to change the sign of E (or ε), such that bound objects have a positive value. I do not follow this here to avoid confusion, see also Spurzem and Kamlah (2023).

The model in Definition 2.17 is the widely used King model from I. R. King (1966a)²⁵.

Even in spherical symmetry the distribution function could be 2D,

since I have E and $|L|$ as constants of motion²⁶; it corresponds to the possibility that in spherical star clusters still at any given radius r the radial and tangential velocity dispersion may be different. So, a more general approach for the distribution function in case of an isothermal sphere is

Definition 2.2.13 (Michie distribution)

$$f(\varepsilon) = \begin{cases} f_\infty \exp(-L^2/L_0^2) \exp(-\varepsilon/\sigma^2) & \varepsilon < 0 \quad (E < \Phi_0) \\ 0 & \varepsilon \geq 0 \quad (E \geq \Phi_0), \end{cases} \quad (2.19)$$

which is known as Michie distribution from Michie (1963).

Numerical solutions of the Fokker-Planck equations in 2D are based on such 2D distribution functions and Michie models could serve as potential initial models, see Sect. ??²⁷.

King models (1D) are extensively used for initialising star cluster simulations (see e.g. Kamlah, Leveque, et al., 2022; Rizzuto, Naab, Spurzem, Arca-Sedda, Giersz, et al., 2021; Rizzuto, Naab, Spurzem, Giersz, et al., 2021). While the Plummer model needs two parameters (mass M and scale radius $r_h \approx 1.305 r_{pl}$), the King model needs three parameters (mass M , scale radius r_{pl} and dimensionless central potential W_0). For intermediate King models ($2.5 \leq W_0 \leq 7.5$), the Plummer models are very similar ($r_{h,Plummer} = 0.366 r_{h,King}$ I. R. King, 2008). I note that Gieles and Zocchi (2015) developed a new family of lowered isothermal models called the LIMEPY models.

Based on the 1D models of King a generalization in 2D for rotating star clusters is now being used and often described as rotating King models (see Section 2.2.6 and citations there).

Numerical star cluster solutions cannot be directly constructed from $f(E)$ or $f(E, L)$, because E depends explicitly on r and implicitly through the gravitational potential (Eq. 6.28). Therefore, in order to be self-consistent, the gravitational potential has to be determined by a velocity space integration over the distribution function and then Poisson's equation solved to obtain the stellar density as function of radius (see e.g. Binney & Tremaine, 2008a, for examples). In a final step a random procedure has to be used to obtain stellar positions and velocities. If density or gravitational potential are analytically known functions as is the case for the Plummer model in Definition 2.2.12, then the entire self-consistent model can be constructed in one loop using random numbers (see e.g. S. J. Aarseth et al., 1974, for such a procedure).

2.2.2 Initial stellar mass function

In order to initialise star cluster simulations, I need to draw the zero age main sequence (ZAMS) masses from an assumed distribution. For this purpose, I use an initial stellar mass function (IMF), a "Hilfskonstrukt" (Kroupa & Jerabkova, 2018; Kroupa et al., 2013), as a mathematical formulation of an idealised stellar population that has formed from a singular star formation event. I will discuss in Section

26: These are functions that may also depend on time in addition to phase-space coordinates, see also Binney and Tremaine (2008a).

27: It is interesting to note that the most well known 1D King distribution is actually based on the older, even more general (since 2D) Michie model; Ivan King himself gives an account of this in I. R. King (1981).

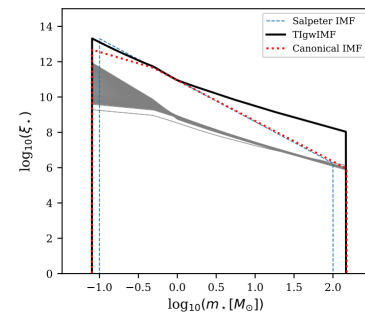


Figure 2.9: The galaxy-wide initial stellar mass function (gwIMF) of each 10 Myr star formation epoch (thin lines) and the time-integrated gwIMF for all formation, TIgwIMF, for a galaxy with a final mass of $M_{\text{dyn}} = 10^{11.9} M_{\odot}$. The gwIMF for the first and the last star formation epoch are highlighted by slightly thicker lines. The canonical IMF as given by Kroupa (2001) and the power-law IMF given by Salpeter (1955) are shown as the red-dotted and blue-dashed lines, respectively Yan et al. (Caption and figure taken from 2021).

28: For example, in Kamlah, Spurzem, et al. (2022) I model stars with metallicity of $Z = 5.1 \times 10^{-4}$ (Pop-II) and in Kamlah et al. (2023, in prep.) I model stars with metallicity of $Z = 2.0 \times 10^{-10}$ (Pop-III).

2.2.4 that this is not the case in nature. An excellent review on the IMF and its construction has been provided by Hopkins (2018) and it also explores the universality of the IMF as an “unchanging distribution regardless of environment and over the entirety of cosmic history”. They conclude that in general the IMF is not universal. This has consequences for the initial conditions of star cluster simulations across cosmic time and I need to model the IMF of different stellar populations individually²⁸.

Definition 2.2.14 (Initial mass function - IMF) *The IMF was established as a concept in a pioneering work by Salpeter (1955) as a quantisation of stellar masses in the Universe (Kroupa & Jerabkova, 2019), see also Figure 2.9 for example so-called galaxy-wide initial stellar mass functions. In general, the number of stars in the IMF is given by*

$$\xi_*(m) = \frac{dN}{dm}, \quad (2.20)$$

where dN is the number of stars formed in a small region, i.e. an embedded-cluster-forming molecular cloud core, in the mass interval m to $m + dm$ (Jeřábková et al., 2018).

Typically, I express the IMF as a (multi-)power law (powers are typically denoted by “ α ”) depending on the stellar population that I want to model. For example, for Population-I (Pop-I) stars I typically choose an IMF from Kroupa (2001), Chabrier (2003) or Maschberger (2013); they are quite similar. Our standard Nbody-codes, such as Nbody6++GPU or Nbody7 provide tools to initialize a star cluster model with generalized Salpeter or Kroupa(Kroupa, 2001) IMF’s, in a mass range from 0.08 to 100 or 150 M_\odot . Note that also the initialization of lower mass objects has been prepared in the codes by Pavel Kroupa. The IMF for Pop-I stars, in spite of many observations over the last decades, is still quite uncertain (see e.g. Hopkins, 2018, and sources therein).

For Population-III (Pop-III) stars, the IMF is very different. It becomes increasingly top-heavy for decreasing metallicity (Bromm, 2013; Bromm & Larson, 2004; Bromm et al., 2002; Jeřábková et al., 2018; Kroupa et al., 2020; Marks et al., 2012; Stacy et al., 2016). However, I do not have observations of Pop-III stars²⁹ and therefore, I do not have statistics from which to conclude an IMF. A flat IMF with $\alpha \approx -1.0$ between 8 M_\odot and 300 M_\odot for Pop-III stars has been proposed by Lazar and Bromm (2021). However, Fraser et al. (2017) use a Salpeter IMF (Salpeter, 1955) of slope $\alpha \approx -2.35$ with a maximum mass of around 87 M_\odot instead. I will have to wait for observations of Pop-III stars or their remnants before I can reliably constrain their IMF.

29: yet, although even with the James Webb Space Telescope (JWST) it will be a difficult or impossible undertaking (Rydberg et al., 2013). On the other hand, de Souza et al. (2013) claim that some hundred SNe detections by JWST may be enough to constrain the IMF of Pop-III stars. See also Schauer et al. (2020) for a further discussion

2.2.3 Initial binary population

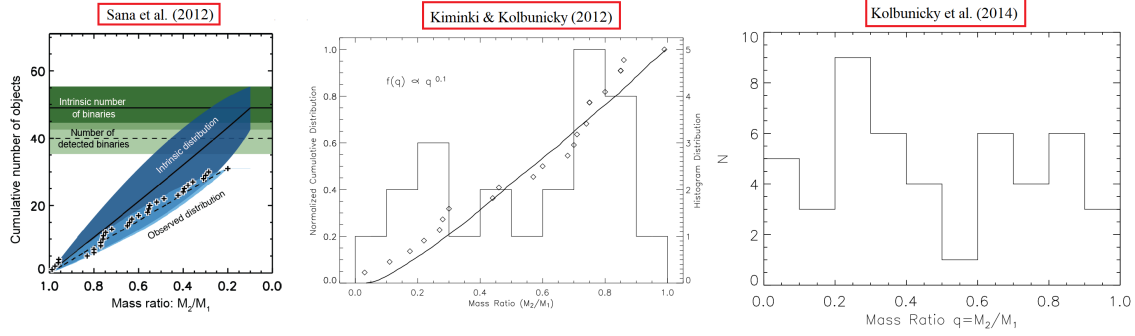


Figure 2.10: Diagram showing the Sana binary mass ratio distribution q . Left panel: Cumulative number of binary mass ratios for a sample of 71 O-type objects, of which 40 are identified binaries. The horizontal solid line and the associated dark green area indicate the most probable intrinsic number of binaries (49 in total) and its 1σ uncertainty, corresponding to an intrinsic binary fraction $f_{\text{bin}} = 0.69 \pm 0.09$. The horizontal dashed line indicates the most probable simulated number of detected binaries: 40 ± 4 , which agrees very well with the actual observed number of binaries (40 in total). Middle panel: Normalized cumulative distribution (diamonds) and conventional histogram for the observed orbital mass ratios. The solid curve is the normalized cumulative distribution for the best Monte-Carlo code fit, $\alpha = 0.1$ for n of 114 B3–O3 primary stars. Right panel: Statistical distribution of mass ratios for 48 known massive binaries in Cygnus OB2, based on Monte Carlo realizations over allowed inclination angles. All three studies show the uniform pairing for massive O-B stars (Compiled from figures by Kolbunicky et al. (2012, 2014) and Sana et al. (2012)).

Almost all stars form in binary systems and some in higher order multiple systems (Goodwin & Kroupa, 2005; Kroupa, 2008; Milone, Piotto, Bedin, Cassisi, et al., 2012), see also Figure 2.11. As with the IMF in Section 2.2.2, there is some debate on the universality of an initial binary population (IBP), i.e. that the IBP is independent of environment, in which binaries form (Belloni, Askar, et al., 2017; Marks et al., 2015). It is typically quietly assumed in the initialisation of star cluster simulations that the IBP is independent of environment, at least in simulations of clusters made up of Pop-I stars (see e.g. Askar et al., 2017; Kamlah, Leveque, et al., 2022). Although, I would expect this to vary for decreasing metallicity and higher red-shift, because the environments and also the primordial gas from which the stars form have very different properties from Pop-I stars (see e.g. Stacy & Bromm, 2013; Stacy et al., 2012).

The IBP evolves on a cluster crossing time-scale τ_{cr} from Definition 15. The widest binaries that form are dynamically disrupted, while in star clusters the hardest binaries harden further (D. C. Heggie, 1975; Hills, 1975). This leads to a pronounced SN-Ia rate in star clusters (Shara & Hurley, 2002). Binaries generally dominate the global, dynamical evolution of the star cluster by close Newtonian few-body interactions (binary-single and binary-binary encounters D. Heggie & Hut, 2003; Mapelli, 2018a).

A distinction is made following Belloni, Askar, et al. (2017) and Kroupa (1995b, 2008) between a birth stellar population, where all proto-stars are embedded in circum-protostellar material, and an initial stellar population, which consists of pre-main-sequence (pre-MS) stars and which are not embedded in surrounding proto-stellar material. The birth population evolves due to processes that are too rapid for N -body computations and results in the initial stellar population. The process from an initial binary population to a fully formed main-sequence star population is called pre-main-sequence eigen-evolution (tidal circularisation R. A. Mardling and Aarseth (2001); 10^5 yr) and this eigen-evolution is closely associated with

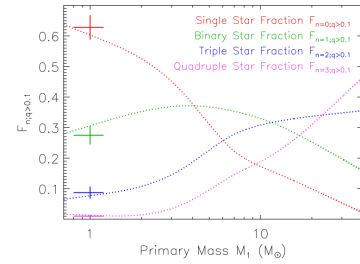


Figure 2.11: The stellar multiplicity fractions as a function of primary mass (dotted lines), including the single star fraction $F_n = 0; q > 0.1$ (red), binary star fraction $F_n = 1; q > 0.1$ (green), triple star fraction $F_n = 2; q > 0.1$ (blue), and quadruple star fraction $F_n = 3; q > 0.1$ (magenta). Given a primary mass M_1 , our model assumes the multiplicity fractions follow a Poisson distribution across the interval $n = [0, 3]$ in a manner that reproduces the measured multiplicity frequency $f_{\text{mult};q>0.1} = \sum_{n=1}^3 F_n; q>0.1$. For solar-type stars, this model matches the measured values (solid) within their uncertainties. Regardless of the uncertainties in the multiplicity fractions, $< 10\%$ of O-type stars are single while $> 55\%$ are born in triples and/or quadruples Moe and Di Stefano (Caption and Figure taken from 2017).

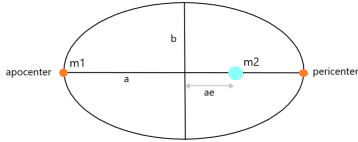


Figure 2.12: Diagram showing the geometry of the ellipse. The semi-major axis a , eccentricity e and the semi-minor axis $b = (1 - e^2)^{\frac{1}{2}} a$. Marked are also the location of the apocenter and pericenter in the orbit.

short-period low-mass or late-type binaries and not the high-mass binaries, for which the birth and the initial binary distributions are typically assumed to remain identical (Belloni, Askar, et al., 2017; Duquennoy & Mayor, 1991; Duquennoy et al., 1991; Kroupa, 1995b, 2008; Kroupa et al., 2013; Küpper et al., 2011a; Railton et al., 2014).

Definition 2.2.15 (Four central binary parameters) *Dynamically speaking, a binary star depends on four parameters (Kroupa, 2008), see also Figure 2.12:*

1. system mass $m_{\text{sys}} = m_1 + m_2$,
2. period P and correspondingly its semi-major axis a (via Kepler's third law),
3. mass ratio $q = m_2/m_1 \leq 1$
4. eccentricity $e = (r_{\text{apo}} - r_{\text{peri}})/(r_{\text{apo}} + r_{\text{peri}})$,

where r_{apo} and r_{peri} are the apocentric and pericentric distances, respectively.

Thus, a complete initial binary population in a star cluster depends on the stellar IMF $\xi_*(m)$ from Section 2.2.2, the period distribution $f_P(\log P)$, the mass ratio distribution $f_q(q)$ and the eccentricity distribution $f_e(e)$ (Belloni, Askar, et al., 2017; Kroupa, 2008; Moe & Di Stefano, 2017):

1. $f_P(\log P)$: Kroupa (1995b) showed that

$$f_P(\log P) = \eta \cdot \frac{\log(P) - \log(P_{\min})}{\delta + (\log(P) - \log(P_{\min}))^2}, \quad (2.21)$$

where $P_{\min} = 10$ days, $\delta = 45$, $\eta = 2.5$ and $P_{\max} = 2.188 \times 10^8$ days, because the initial binary fraction f_b is 100% (Goodwin & Kroupa, 2005). Adjustments to this distribution were later made for high mass stars with $m > 5 M_{\odot}$ following (Oh et al., 2015; Sana et al., 2012), where for these stars $f_P \propto (\log(P))^{-0.55}$ with $P_{\min} = 1.412$ days and $P_{\max} = 3.162 \times 10^3$ days.

2. f_e : Typically, I distribute the binaries thermally, meaning angular momenta are distributed equally $f_e = 2e$ (Kroupa, 1995b), although this might greatly over predict observed merger rates according to (Geller et al., 2019).
3. f_q : The binary stars with members below $5 M_{\odot}$ are distributed randomly and for masses above $5 M_{\odot}$, the binary mass ratios are distributed uniformly via $0.1 < q < 1.0$ (Kiminki et al., 2012; Kobulnicky et al., 2014; Sana et al., 2012; Sana & Evans, 2011), see also Figure 2.10.

In direct N -body simulations a large number of initial binaries is computationally expensive. Therefore, instead of a 100 % primordial binary fraction and a ‘‘Kroupa’’ (Kroupa, 1995b) binary period distribution, a much lower primordial binary fraction is used in initial models for long-term evolution of star clusters (order of 5 % - 20 %; but see some Monte Carlo simulations which start with

much higher number of binaries). This is not a problem, because the Kroupa period distribution includes many wide binaries. They are dynamically ionized (disrupted) in a time scale very short compared to the relaxation time scale. Therefore Monte Carlo simulations (even if they start with much larger initial number of binaries) and direct N -body models converge quickly, as can be seen in (Kamlah, Leveque, et al., 2022).

With `PeTAR` (Wang, Kroupa, et al., 2020; Wang, Nitadori, & Makino, 2020b), which uses Slow Down Algorithmic Chain Regularisation (SDAR) (Wang, Nitadori, & Makino, 2020a)³⁰, it is now possible within reasonable computing time to use a very large number of binaries in the simulations. The treatment of interacting and relativistic binaries in `PeTAR` is not equivalent to the one used in `NBODY`. Currently tests and comparisons of both codes with respect to binary evolution are ongoing.

In summary of what I discussed so far in Section 2.2.1 to Section 2.2.3, during the initialisation of N -body simulations I need to distribute the stars in 6D phase space, draw their masses from some IMF, and distribute primordial binaries according to IBP (Kroupa, 2008; Küpper et al., 2011a; Küpper et al., 2011b). Furthermore, I generally need to make a decision if our star cluster is mass segregated at the beginning of the simulation (Baumgardt, De Marchi, & Kroupa, 2008; Fregeau et al., 2002; Šubr et al., 2008), shows fractality (Goodwin & Whitworth, 2004) and if it is or is not in Virial equilibrium initially. Below I highlight two more areas of active research when it comes to simulations of star clusters and their initialisation: multiple stellar populations in Section 2.2.4 and initial bulk rotation of the star cluster in Section 2.2.6, respectively.

2.2.4 Multiple stellar populations

Modern observational methods have made it possible to resolve multiple stellar populations (MSPs) in globular clusters, which can mostly be inferred from photometric diagrams such as CMDs from multi-band HST photometry (see e.g. Anderson & King, 2000; Anderson et al., 2008; Gratton et al., 2012; Milone, Piotto, Bedin, Cassisi, et al., 2012; Milone et al., 2013; Milone, 2020; Milone & Marino, 2022). Nowadays, MSPs have been confirmed in around 70 Galactic and extragalactic clusters (Milone, Marino, Da Costa, et al., 2020; Milone, Marino, Mastrobuono-Battisti, & Lagioia, 2018; Milone, Marino, Renzini, et al., 2018, 2020; Milone, Marino, et al., 2017; Milone, Piotto, et al., 2017; Milone, Vesperini, et al., 2020; Milone, 2020; Milone & Marino, 2022).

In Section 2.2.2 I already made the simplifying assumption that stars form from a singular event. However, for example, the ONC, see also Figure 2.8, exhibits an age spread in its stellar population (Palla et al., 2007; Pflamm-Altenburg & Kroupa, 2006; Pflamm-Altenburg & Kroupa, 2007) and in fact most clusters already form in regions that have experienced previous star formation (Kroupa, 2008). Stars from previous generations³¹, may then be captured in the potential by the newly formed star cluster and I would then observe an age spread in the stellar population. But there are other proposed channels to form MSPs. For example, Wang, Kroupa, et al. (2020) discuss the

³⁰: slow-down also exist in classical `NBODY` codes.

³¹: especially high mass stars that have slowed down due to dynamical friction over the course of the star cluster's evolution.

possibility with the use of direct N -body simulations that stellar mergers might produce age spreads through rejuvenation of stars and these mergers will lead to observed top-heavy mass functions with MSPs (Marks et al., 2012). Hong, de Grijs, et al. (2017) focus on NGC 1806 in the LMC, see also Figure 2.6 and NCG 411 in the Small Magellanic Cloud (SMC). They use direct N -body methods and compare two formation models: the first assumes that a second generation of stars are formed inside a cluster of first generation of stars using the gas accumulated from the external intergalactic medium and the second models assumes a minor merger model of unequal mass of first to second generation stars. They find that both scenarios reproduce the observed spatial distributions with the second generation is more concentrated than the first (C. Li et al., 2016a, 2016b).

From the examples above, we can see that MSPs have very diverse origins. Nevertheless, we have also seen that dynamical simulations of their host environments can be extremely useful in unravelling formation channels and the dynamical properties of MSPs. Our direct `NBODY6++GPU` code allows for the distinction between different populations by defining a corresponding label for each star; this has been used by (Hong, Vesperini, et al., 2017) to constrain the dynamical origin of multiple populations in intermediate-age clusters in the LMC and SMC³² MOCCA simulations have been published (Hypki et al., 2022) hosting two generations of stars as above in tidally filling and underfilling clusters. They are able to reproduce the observed fractions and properties of second generation stars in MW GCs. A serious limitation is that there is still no good way known to handle encounters and mixing of material from different populations in stellar collisions and binary mass overflow interactions in any of the codes.

32: Another rarely used feature of `NBODY6++GPU`, but see Bialas et al. (2015), is that it can start with individual population data for every star (age, metallicity, population index).

In the simulations presented in this thesis and Kamlah, Leveque, et al. (2022) and Kamlah, Spurzem, et al. (2022) and Kamlah et al. (2023, in prep.) I only use one stellar population that has formed from a singular star formation event.

2.2.5 McLUSTER

This section is taken from Kamlah, Leveque, et al. (2022). I use `McLUSTER` in all of my publications, i.e. Kamlah, Leveque, et al. (2022) and Kamlah, Spurzem, et al. (2022) and Kamlah et al. (2023, in prep.).

The original `McLUSTER` software is an open source code, which is used to either set up initial conditions for N -body computations or to generate artificial star clusters for direct investigation (Küpper et al., 2011a). The `McLUSTER` output models can be read directly into the `NBODY6++GPU` and MOCCA simulations as initial models. This makes `McLUSTER` the perfect tool to initialise realistic star cluster simulations. After choosing the initial number of objects for each sub-population and the binary content within each, I can then choose structural parameters, such as the cluster density distribution (King, Plummer, Subr, EFF, Nuker) (R. A. W. Elson et al., 1987; I.

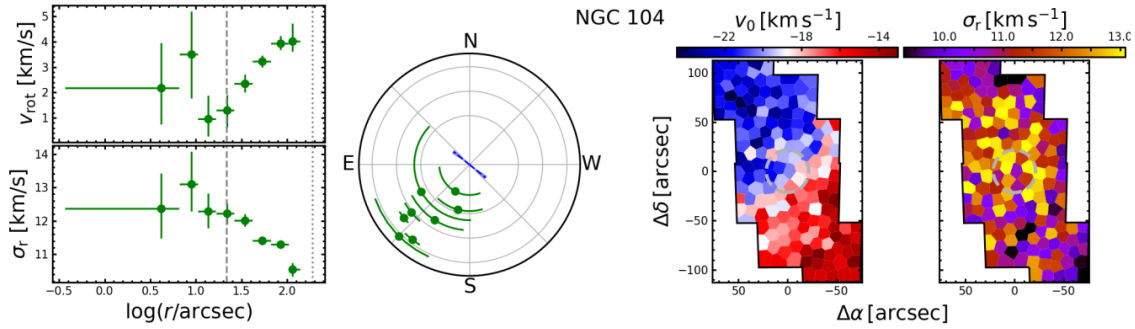


Figure 2.13: Results of the kinematic analysis for 47 Tuc (NGC 104). The left panels show the radial rotation and dispersion profiles, respectively. The dashed and dotted vertical lines indicate the core and half-light radii of each cluster, all values were taken from Harris (1996). The central panel shows the position angle of the rotation curve and its uncertainty for each radial bin. A blue dashed line is used to indicate the cluster’s photometric semi-major axis angle, with the blue-shaded area indicating the uncertainty and the length of the line scaling with cluster ellipticity. The right panels show Voronoi binned maps (Voronoi binning is also known as Dirichlet tessellation. They use a partitioning of a plane with n points into convex polygons such that each polygon contains exactly one generating point and every point in a given polygon is closer to its generating point than to any other.) of the mean velocity and the velocity dispersion across the footprint covered by the MUSE data. The dashed circles indicate again the core radii of the clusters (Figure and caption taken from Kamann, Husser, et al., 2018).

King, 1962; I. R. King, 1966a; Plummer, 1911; Šubr et al., 2008), mass segregation (Baumgardt, De Marchi, & Kroupa, 2008), fractal dimensions (Goodwin & Whitworth, 2004) and the Virial ratio. Furthermore, I may choose from many IMFs and respective limits (Kroupa, 2001). For the primordial binaries, I may choose from several binary mass ratio (Kiminki et al., 2012; Kobulnicky & Fryer, 2007; Kobulnicky et al., 2014; Kouwenhoven et al., 2007; Moe & Di Stefano, 2017; Sana et al., 2013; Sana & Evans, 2011), semi-major axis (Duquennoy & Mayor, 1991; Kroupa, 2008), period (Kroupa, 1995a, 2008; Moe & Di Stefano, 2017; Oh et al., 2015; Sana et al., 2013; Sana & Evans, 2011) and eccentricity (Duquennoy & Mayor, 1991; Kroupa, 1995b, 2008, 2009; Sana & Evans, 2011) distributions setting minimum and maximum initial separations in the process and eigen-evolution processes (Belloni, Giersz, et al., 2017; Belloni, Zorotovic, et al., 2017; Kroupa, 1995b; Kroupa et al., 1993). Lastly, I may put the star cluster model in a tidal field, such as one from a point-like MW galaxy. However, these are set in the simulations by Nbody6++GPU or MOCCA directly. In principle, there are many different options available to create star clusters with up to 10 different stellar sub-populations, each having their own distinct properties. However, for this to properly work, a large number of bugs were fixed in this version of McLUSTER. These extensive changes are reserved for a separate publication as seen in Leveque, Giersz, Banerjee, et al. (2022).

2.2.6 Initial star cluster rotation

The inclusion of initial bulk rotation in direct Nbody simulations of collisional stellar systems is still unusual (see e.g. Arca-Sedda et al., 2021; Askar et al., 2017; Di Carlo, Mapelli, Bouffanais, et al., 2020; Di Carlo, Mapelli, Giacobbo, et al., 2020; Di Carlo et al., 2019, 2021; Hong et al., 2013; Kamlah, Leveque, et al., 2022; Rizzuto, Naab, Spurzem, Arca-Sedda, Giersz, et al., 2021; Rizzuto, Naab, Spurzem, Giersz, et al., 2021; Wang et al., 2016)), although it has been known for

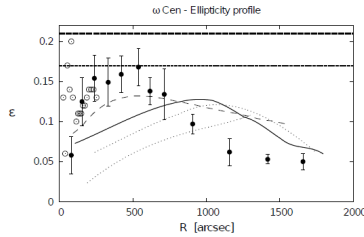


Figure 2.14: Ellipticity profile for the GC ω Cen (NGC 5139). Open circles mark the observed ellipticities from Anderson and van der Marel (2010), black dots those from Geyer et al. (1983). The solid line represents the predicted profile derived from the rotating axisymmetric model from Bianchini et al. (2013b), whereas the thin dotted curves correspond to the models used to test the sensitivity of the selection procedure. Dotted and dashed horizontal lines indicate the average values from WS87 and CC10, respectively. Finally, the long-dashed line represents the ellipticity profile for the best-fit rotating Wilson (1975) model from Sollima et al. (2009) (Figure and caption taken from Bianchini et al., 2013b).

33: assuming that the system rotates around the z -axis initially and ignoring a third integral, which in some cases can be approximated by the total angular momentum of a star L^2 (Lupton & Gunn, 1987), because a third integral is generally not analytically known.

34: derived from L_{z0} (see e.g. Einsel & Spurzem, 1999).

35: see Table 1 in Einsel and Spurzem (1999), and note that the second column is erroneously labeled, it contains the percentage contained in rotational energy; i.e. for $\omega_0 = 0.6$ we have 20% of the total kinetic energy in form of ordered rotational motion.

over a century that star clusters even today show significant imprints of rotation, which can, for example, be observed in deviations in the shapes of star clusters from sphericity, see e.g. Figure 2.14 (see e.g. Bianchini et al., 2013b; C. W. Chen & Chen, 2010; Frenk & Fall, 1982; Harris, 1976; Harris, 1996; I. King, 1961; Kopal & Slouka, 1936; Kormendy, 1985; Lupton et al., 1987; Pease & Shapley, 1917; Shapley, 1930; Shapley & Sawyer, 1927; White & Shawl, 1987).

Moreover, present-day detectors and data processing methods have made it possible to resolve the photometry and kinematics of individual stars all the way down to the cluster centre revealing rotational kinematics of event multiple stellar populations (Bianchini et al., 2013a, 2016a, 2019; Ferraro et al., 2018; Giesers et al., 2018, 2019; Kamann, Bastian, et al., 2018; Kamann, Husser, et al., 2018; Kamann et al., 2016, 2019; Lanzoni, Ferraro, Mucciarelli, Palla, Lapenna, et al., 2018; Lanzoni, Ferraro, Mucciarelli, Palla, Tiongco, et al., 2018; Sollima et al., 2019; M. Tiongco et al., 2021; M. A. Tiongco et al., 2019), see Figure 2.13. Additionally, both observations and simulations support these results and find that star clusters show significant fractality (Ballone et al., 2020; Pang, Li, et al., 2021), and internal rotation at birth in general (Ballone et al., 2021; Lahén et al., 2020). Velocity anisotropy has been observed in star clusters with detected elongated structures (Pang, Li, et al., 2021; Pang et al., 2020), which might be induced by rotation.

So, how do we initialise rotating collisional stellar systems? Sometimes it is assumed that there exists a kind of “Maxwell’s demon” that simply switches the direction of initial particle velocities to induce angular momentum to a N -body system and assuming the preservation of the spherical distribution function (see e.g. I. King, 1962; Plummer, 1911; Wilson, 1975) and angular momentum in the process (see e.g. Lingam, 2018; Lynden-Bell, 1960). This procedure is not physical. We instead need distribution functions that depends at least on two integrals of motion, such as the total energy E and the total angular momentum in the z -direction L_z ³³. Such rotating equilibrium models were developed by Einsel and Spurzem (1999), J. Goodman (1983), Longaretti and Lagoute (1996), and Varri and Bertin (2012). They can be considered as generalizations of standard King models (I. R. King, 1966a), see also Definition 2.17, because their energy dependence is a lowered isothermal, and the additional term for the second independent variable is $\exp(-L_z/L_{z0})$, which is analogous to Michie (1962) from Definition 2.2.13. L_{z0} is a scaling constant; usually a dimensionless rotation parameter ω_0 is used³⁴. The models are axisymmetric, with a rigid rotation of the inner parts of the cluster, a maximum of the rotation curve close to the half-mass radius, and a differentially decreasing rotation curve outside in the halo. Rotation supports only a fraction of the total kinetic energy³⁵. Evolved star clusters obtained from these initial models agree quite well with observed clusters (Fiestas et al., 2006). Due to the 2D velocity distribution function an anisotropy is possible between the velocity dispersions in radial direction (in cylindrical coordinates) and in rotational φ direction; the models are isotropic between radial and vertical direction and were subsequently used in 2D Fokker-Planck (FP) modelling and direct N -body simulation (Ernst et al., 2007; Fiestas & Spurzem, 2010; Fiestas et al., 2006, 2012; Hong

et al., 2013; Kamlah, Spurzem, et al., 2022; Kim et al., 2002; Kim et al., 2004, 2008). Note that the models by Varri and Bertin (2012) are using a different form of the distribution function based on the Jacobian of a cluster rotating around the galaxy, but they are as well generalizations of King models for rotation with similar properties. They also have been used as initial models for direct NBODY models (Livernois et al., 2022; M. Tiongco et al., 2021; M. A. Tiongco et al., 2016a, 2016b, 2017, 2018, 2019, 2022). Furthermore, semi-analytic models exist that Panamarev and Kocsis (2022), Szölggyen and Kocsis (2018), and Szölggyen et al. (2019, 2021) used to study the formation and evolution of rotating stellar or black hole disks in nuclear star clusters. Most of the aforementioned studies find evidence for the gravogyro catastrophe and its coupling to the gravothermal catastrophe (Akiyama & Sugimoto, 1989; Hachisu, 1979, 1982; Inagaki & Hachisu, 1978), discussed in Section 2.3. Lastly, I note that due to the assumption of spherical symmetry most of the current Monte Carlo methods for collisional dynamics are currently unable to evolve initially rotation star cluster models, such as those described above (see e.g. Askar et al., 2017; Cohn, 1979; Giersz, 1998; Giersz et al., 2015; M. Hénon, 1975; Kremer, Ye, et al., 2020; Kremer et al., 2021; Merritt, 2015; Stodołkiewicz, 1982, 1986). A restricted Monte Carlo method for rotating, axisymmetric star clusters (usable even for general geometry, but see problem below) has been presented by Vasiliev (2015). It uses Spitzer’s Monte Carlo method Section ??, which distinguishes it from currently common Monte Carlo codes. But it has some more serious deficiency, because the random relaxation scatterings are applied only in v_{\parallel} and v_{\perp} obtained from a fully isotropic spherically symmetric background. In 2D FP models of axisymmetric rotating star clusters (Einsel & Spurzem, 1999) the background distribution function used for the computation of diffusion coefficients is fully self-consistent and there are five different diffusion coefficients obtained, instead of only two.

2.3 The life and fate of star clusters

In this section, I assume that the star clusters are initially rotating as is generally expected from simulations and observations, see Section 2.2.6 and the sources therein. Furthermore, both Kamlah, Spurzem, et al. (2022) and Kamlah et al. (2023, in prep.) evolve rotating star cluster models. For the non-rotating star clusters, the gravitational phenomena that rotating star clusters experience, diminish and can mostly be conveniently ignored unless angular momentum is transferred externally into the star cluster due a merger with another rotating star cluster, for example. But first, two important physical processes have to be highlighted, the gravothermal catastrophe in Section 2.3.1 and the gravogyro catastrophe and their coupling in Section 2.3.2³⁶. These three sections are mainly taken from Kamlah, Spurzem, et al. (2022).

36: Some authors refer to these processes ‘instabilities’ instead of ‘catastrophes’. I adopt the term catastrophe since that is what the theoreticians that studied these initially referred to them as (see e.g. Antonov, 1960, 1961, 1962; Hachisu, 1979, 1982; Hachisu & Sugimoto, 1978; Inagaki & Hachisu, 1978; Lynden-Bell & Wall, 1962; Lynden-Bell & Wood, 1968).

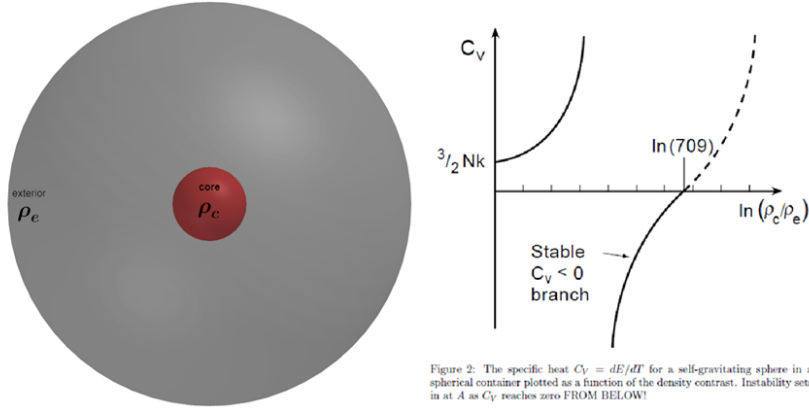


Figure 2: The specific heat $C_V = dE/dT$ for a self-gravitating sphere in a spherical container plotted as a function of the density contrast. Instability sets in at A as C_V reaches zero FROM BELOW!

Figure 2.15: Diagram of the gravothermal instability in an isolated, isothermal gas sphere. Below a certain density contrast between the central density ρ_c (sphere of radius r_c) and the density at the edge of the sphere (sphere of radius r_e) ρ_e ($\rho_e/\rho_c < 1/709$), he showed that there exists no global maximum to the entropy S at any fixed energy E (Right figure and caption adapted from Lynden-Bell, 1999).

2.3.1 Gravothermal catastrophe

To understand the gravogyro catastrophe, it is didactically sensible to first illustrate the gravothermal catastrophe. It has been known that adding energy to a star cluster will make it cool down and expand (Lynden-Bell, 1999). This process was first proposed by Antonov (1960, 1961, 1962). He found that an isothermal gas sphere is the most probable state (maximum entropy S) of an initially spherical self-gravitating system of N particles with energy E . However, he additionally found that this is not a global maximum. Below a certain density contrast between the central density ρ_c (sphere of radius r_c) and the density at the edge of the sphere (sphere of radius r_e) ρ_e ($\rho_e/\rho_c < 1/709$), he showed that there exists no global maximum to the entropy S at any fixed energy E . Such a sphere can be seen in Definition 2.15. This effect is purely gravitational in nature and disappears in the absence of gravity (Lynden-Bell, 1999).

Lynden-Bell and Wood (1968) then developed the thermodynamic theory of self-gravitating gas spheres. Using linear response theories, they were able to demonstrate that for certain configurations of such systems, there exists no equilibrium state. Furthermore, they showed that the specific heat capacity $C_V = dE/dT$ of the system becomes infinitely negative at around $3/100 \lesssim \rho_e/\rho_c$ and approaches and ultimately reaches zero when the density contrast limit predicted by Antonov (1962) is reached. Systems of self-gravitating gas spheres between the two limits are stable at fixed E and r_E and they possess a negative heat capacity C_V . For larger density contrasts than $1/709$, the system is unstable (no maximum entropy S).

The following thought experiment is adapted from Lynden-Bell (1999). We can consider an isothermal gas sphere in a density contrast that eventually results in a negative specific heat capacity C_V as an analogy to a star cluster in order to understand the gravothermal catastrophe. We assume that the gas sphere expands adiabatically. We would observe a gas sphere with a much denser core than halo. As a result, mostly only the gas in the halo of the sphere will adiabatically expand. Consequently, the drop in temperature by the gas in the

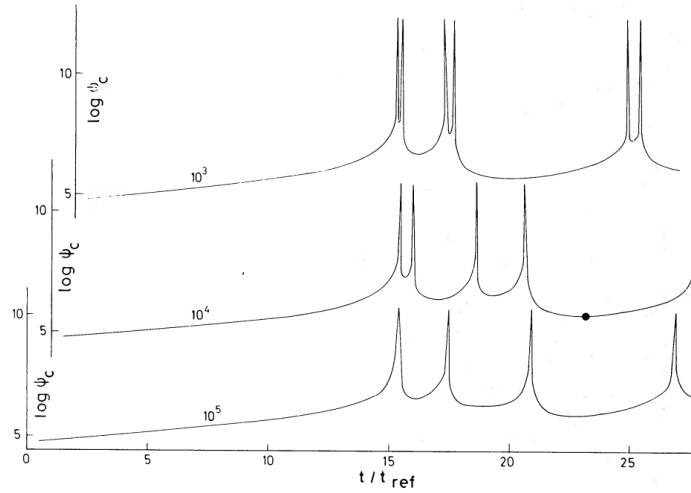


Figure 2.16: Diagram showing the gravothermal oscillations. The “central” density ψ_c is plotted against the non-dimensional time t/t_{ref} with $t_{\text{ref}} = 0.06(MR_h^3/G)^{1/2}/(m\log(0.4N))$ is the standard half-mass relaxation time from J. Spitzer (1975), see also Definition 2.2.4 for the definition by Chandrasekhar (1942), where N is the number of the stars in the system, m is the mean stellar mass $m = M/N$, and R_h is the radius containing half of the mass, or $k = 2$ models with three different values of C as attached to each curve. Note, that if they were plotted with the same ordinate they would be close to each other despite the great differences in C . The model indicated with a filled circle will be compared with King’s model. The core oscillations are clearly visible here Bettwieser and Sugimoto (Figure taken and caption adapted from 1984).

halo occurs much faster than the drop in temperature of the gas in the core. Keep in mind, that the specific heat capacity of the total system, $C_{V,\text{total}}$ can be split up into the specific heat capacity of the gas in the core $C_{V,\text{core}}$ core and the specific heat capacity of the gas in the halo $C_{V,\text{halo}}$. Due to the resulting temperature gradient, heat will flow from the core to the halo of the gas sphere. As a result of the negative $C_{V,\text{core}}$ the core will then contract and become hotter. The gas in the halo will also get hotter but in contrast to the gas in the core, it expands, because it has a positive $C_{V,\text{halo}}$. If $C_{V,\text{halo}}$ is very large, then this process will proceed indefinitely (in theory). The core will continuously lose more and more heat and this will cause it to contract further and further. This process is called the gravothermal catastrophe under the condition that $C_{V,\text{total}}$ should continuously increase and reach zero once the boundary condition by (Antonov, 1962) ($\rho_e/\rho_c = 1/709$) is met.

We now understand what happens in an adiabatically expanding, self-gravitating isothermal gas sphere. But in the context of stellar dynamics and realistic star clusters, the situation is much more complex. When replacing the gas molecules with actual stars in the thought experiment above, we now deal with a isothermal, self-gravitating sphere of stars.

Definition 2.3.1 (Gravothermal catastrophe in a star cluster) *Heat in star clusters is exchanged by repeated gravitational two-body encounters between the stars. The timescale for these encounters is much shorter at the centre of the cluster than at the outskirts of the star cluster. Therefore, when a star cluster adiabatically expands it is subject to the gravothermal catastrophe. The stellar density at the centre and the temperature (velocity dispersion) increases at ever smaller scales while the density in the halo decreases. This collapse would produce extremely*

large stellar densities at the core of the star cluster (Hachisu & Sugimoto, 1978; Hachisu et al., 1978; Inagaki & Lynden-Bell, 1983; Lynden-Bell, 1999; Lynden-Bell & Eggleton, 1980).

We have to answer why we do not observe star clusters with such density profiles as described in [Definition 2.3.1](#) in the universe. Nowadays, we know that it stems from the fact that binary stars (and hierarchical systems) act as gravitational energy sources (see e.g. S. J. Aarseth, 1972, 1985; D. C. Heggie, 1975, 1984; M. Hénon, 1975) that can halt core-collapse. It has been shown that a collisional stellar system will evolve to a state of stars with predominantly radial orbits in the halo and a central core, which has an isotropic velocity distribution and possesses a central density that increases steadily (Bettwieser, 1983; Bettwieser & Spurzem, 1986; Cohn, 1980; M. Hénon, 1972a, 1972b; Larson, 1970a, 1970b). The inclusion of binary stars on the other hand has a drastic effect, see Bettwieser and Sugimoto (1984). They confirmed that binary formation happens near the centre of the star cluster and that they release energy. This effect causes the core to expand and to cool in temperature. The energy exchange between the core and the halo will result in an isothermal system. As a result, the gravothermal collapse occurs once more. This process may repeat many times in a simulation in the presence of binary stars and is also referred to as gravothermal oscillations (Bettwieser & Sugimoto, 1984; Lynden-Bell, 1999), see also [Figure 2.16](#).

So far, only closed-off systems were considered. If stars are allowed to escape the system by a series of weak gravitational encounters, a strong encounter or stellar evolution natal kicks, then this will accelerate the process of the gravothermal catastrophe and, ultimately, the whole system will disperse leaving behind only a single or a collection of extremely hard binary stars (Padmanabhan, 1990).

2.3.2 Gravogyro catastrophe and its coupling with the gravothermal catastrophe

The linear response theories developed by Lynden-Bell and Wood (1968) were first applied to rigidly rotating and isothermal self-gravitating gas cylinders by Inagaki and Hachisu (1978), see also [Figure 2.17](#). They were able to define certain stability criteria for such systems, but were unable to define the coupling of the heat to angular momentum transport. To shed more light on this issue, Hachisu (1979) used the theories by Hachisu and Sugimoto (1978) and demonstrated that an unstable system as set up above has a negative specific moment of inertia even though its specific heat capacity C_V is positive (gravothermally stable). This can be explained by visualising a fluid element in a rigidly rotating and self-gravitating, isothermal, low temperature gas cylinder from [Figure 2.17](#).

When angular momentum is removed from the fluid element, then its angular speed also decreases. The region contracts towards the rotation axis of the gas cylinder in the absence of sufficient centrifugal forces. The moment of inertia of this fluid element decreases as a result. If the decrease of moment of inertia or the

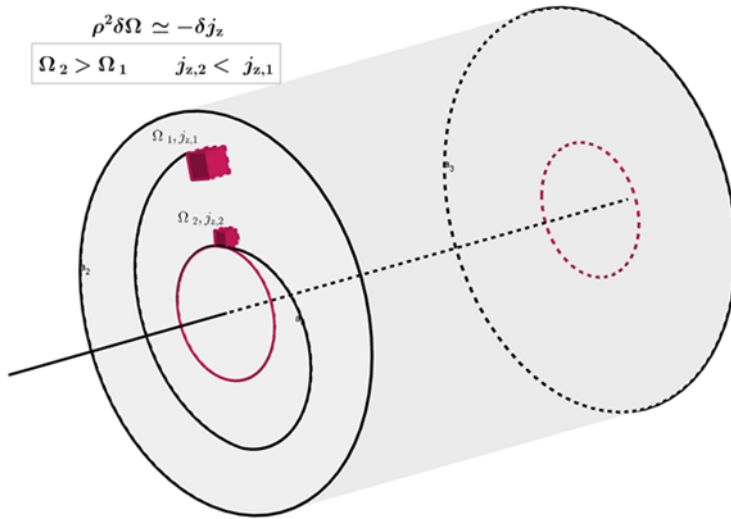


Figure 2.17: Diagram of the gravogyro instability in a rotating, isolated, initially isothermal gas cylinder. It shows a volume element highlighted in red with specific angular momentum $j_{z,1}$ and rotational speed Ω_1 that loses angular momentum due to a perturbation that can be measured with $\rho^2 \delta \Omega \simeq -\delta j_z$ (we assume here a low temperature limit and therefore the pressure term in the balance of force equation vanishes). Consequently, it contracts towards the rotation axis and has specific angular momentum $j_{z,2}$ and rotational speed Ω_2 . Since there is no pressure gradient from the inner parts of the cylinder to the outer parts, the angular speed of the volume element increases and we have $\Omega_2 > \Omega_1$ even though its specific moment of inertia decreases with $j_{z,2} < j_{z,1}$. Therefore, we speak of a negative specific moment of inertia.

degree of contraction are large enough, then the angular speed actually becomes greater than its value before the removal of angular momentum. Ignoring gravity this may be coined as an effective negative specific moment of inertia in analogy to the negative specific heat capacity of gravothermal systems, see [Section 2.3.1](#).

Definition 2.3.2 (Gravogyro catastrophe in star clusters) *Along these lines, Hachisu (1979) called the underlying process caused by the system's negative specific moment of inertia the gravogyro catastrophe in analogy to the gravothermal catastrophe discussed above (the angular velocity ω and the specific angular momentum j correspond to the temperature T and the specific entropy s Akiyama and Sugimoto (1989) The fluid element will contract towards the rotation axis until its angular momentum is exhausted due to its specific negative moment of inertia.*

Hachisu (1979) already predicted two further important effects without explicitly proving them:

1. The gravogyro catastrophe cannot proceed indefinitely since the contraction of the star cluster is halted by binary stars.
2. The heat transport from the inner regions of the star cluster to outer regions assists the gravogyro catastrophe, because a loss of heat is also associated with a loss of pressure from the fluid element and thus its contraction is accelerated.

Later, the theories by Hachisu (1979), Inagaki and Hachisu (1978), and Lynden-Bell and Wood (1968) were also applied to rotating and self-gravitating, isothermal gaseous disks and expanded to general

three-dimensional bodies by Hachisu (1982), who confirmed that the instabilities are originating from a coupling of the gravothermal and the gravogyro catastrophes. They found that in general configurations of rotating bodies, both the gravothermal and the gravogyro catastrophes will prevail if either one of the following conditions hold:

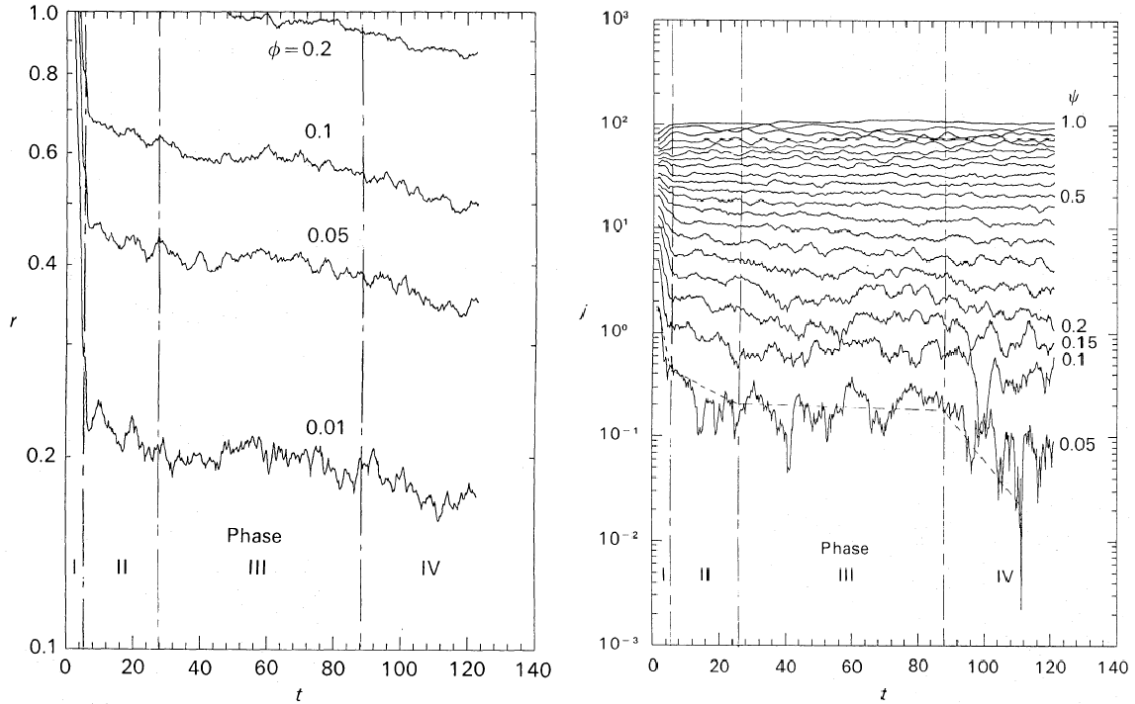


Figure 2.18: Diagram showing results from a $N = 1000$ direct N -body simulation by Akiyama and Sugimoto (1989). Left panel: time evolution of the particle distribution. Each line corresponds to a mass shell and is labeled according to the mass fraction. It covers four phases. Right panel: time evolution of the angular momentum j distribution. Each line shows the angular momentum averaged over the stars contained between two succeeding cylindrical mass shells. Attached to each line is the corresponding value of the mass fraction $\psi = 0.05$ (citeAkiyamaSugimoto1989).

1. The central concentration of the gas needs to be large enough,
2. Both the rotation is fast and the temperature of the gas is low enough.

37: $N = 1000$, which is very small for statistical purposes (Einsel & Spurzem, 1999).

38: This code is a precursor to the direct N -body code `NBODY6++GPU` (Wang et al., 2015, 2016).

Akiyama and Sugimoto (1989) conducted first direct N -body simulations³⁷ using the direct N -body code³⁸ `NBODY2` (S. J. Aarseth, 1985) used in the work presented here. Akiyama and Sugimoto (1989) already described the basic phenomena found a four-phase star cluster evolution, see also Figure 2.18 from the Phases I, II, III and IV are shown:

1. Phase I ($t = 0 - 5$): a phase of violent relaxation during which the N -body system collapses in the direction of the rotation axis at τ_{cr} , see also Definition 15. A *bar-like* structure develops that quickly disappears at $t = 5$ and subsequently a core-halo structure forms. Stars are redistributed according to their angular momentum and it is convective in nature, which can be seen in the right panel in Figure 2.18. It is important to note that the gravothermal catastrophe also begins at $t = 0$, but it is masked by the the phase of violent relaxation (Phase I) and the occurrence of the gravogyro catastrophe (Phase II).
2. Phase II ($t = 5 - 30$): the core-halo structure persists during this phase. A gravogyro catastrophe, which happens due to the stellar collisions and which is conductive in nature, of finite amplitude driven by the negative moment of inertia of a self-gravitating system through the transport of angular

momentum.

3. Phase III ($t = 30 - 90$): after $t = 30$, the gravogyro catastrophe levels off indefinitely as can be seen in the right panel in [Figure 2.18](#). This phenomenon marks a fundamental difference between the gravothermal and the gravogyro catastrophes:

The gravogyro catastrophe must level off because the angular momentum in the core is limited and the gravothermal catastrophe will never level off, because gravitational energy can be released indefinitely

When a system is expanding, then the density contrast decreases and as a result also the gravothermal catastrophe will level off in this system configuration (Hachisu et al., 1978). As can be seen in the left panel of [Figure 2.18](#), the density of the core has increased to a point, where the gravothermal collapse can occur sufficiently rapidly. During this contraction the remaining angular momentum is extracted from the star cluster core, as can also be inferred from the right panel of [Figure 2.18](#). As for the considerations surrounding the gravothermal catastrophe from [Section 2.3.1](#), where I split up the specific heat capacity of the system into a halo, $C_{V,\text{halo}}$, and into a core, $C_{V,\text{core}}$ contribution, the effective moment of inertia can be split up like-wise into a halo, J_{halo} , and into a core, J_{core} , contribution. In Phase III we ultimately have a core that is stable with a positive J_{core} and a halo that is unstable with a negative J_{halo} . This is because the time-scales in the star cluster halo for the conductive transport of angular momentum are much longer due the lower densities than in the core and so an effective gradient of ω persists there.

4. Phase IV ($t = 90 - \dots$): the densities in the core keep increasing as can be seen in the left panel of [Figure 2.18](#). As a result, the time-scales for gravothermal collapse become shorter. This collapse is restricted to the core of the star cluster simulation. The gradient of ω towards the star cluster centre increases again. Therefore, angular momentum is transported again from the core outwards, which can be see in the right panel in [Figure 2.18](#). This phenomenon means that the gravothermal catastrophe result in further angular momentum transport, while in Phases I and II the angular momentum transport drives the star cluster contraction. This leads to the fundamental realisation that

Definition 2.3.3 (Gravothermal-gravogyro catastrophe in star clusters) *The gravogyro and gravothermal catastrophes are inseparably coupled in star clusters and they ultimately reinforce each other. Therefore, it is adequate to describe the overall physical process as the gravothermal-gravogyro catastrophe.*

The core contracts on the local two-body relaxation time-scales.

Phases I-IV as outlined above cover the complete pre-core collapse

39: With the serious limitations that no primordial binaries, tidal field mass loss, stellar evolution or statistically sensible particle numbers were used.

phase of a small star cluster³⁹. Akiyama and Sugimoto (1989) lastly also concluded that such a series of evolutionary phases in combination with galactic tidal loss of stars would result in an overall loss of angular momentum from the cluster.

2.3.3 Pre-core collapse star cluster evolution

In the previous sections, I have already outlined much of what is needed to understand the pre-core collapse phase of a star cluster. In Kamlah, Spurzem, et al. (2022) and in Part 9.8.1 I will highlight some of my results that are directly relevant in this context. Here, I focus on a general and phenomenological discussion. I also already mention a lot material, which I explain in much more detail in Chapter 3. I reference the relevant sections where necessary, but there is naturally a little repetition.

I start with a star cluster that is in Virial equilibrium, not mass-segregated and that has primordial binaries. Unlike the simulation by Akiyama and Sugimoto (1989) that were used to explain the fundamental processes of the gravogyro, gravothermal catastrophes and the coupling between them, see Section 2.3.1 and Section 2.3.2 and which do not employ stellar evolution (mass loss), in realistic star clusters, the stars naturally undergo a large array of diverse, impactful and sometimes extreme stellar evolution processes.

Following the Virial theorem and assuming that the star cluster of energy content E , radius R and mass M keeps the same mass distribution, we find the following differential equation

$$\frac{dR}{R} = 2 \frac{dM}{M} - \frac{dE}{E}. \quad (2.22)$$

Stellar evolution mass loss by stellar winds

The shedding of outer layers from stars causes stellar winds, see also Section 3.1.4. These occur in all evolutionary phases and differ in magnitude, but are especially dominant in late evolutionary phases of massive stars such as Wolf-Rayet (WR) stars or Asymptotic Giant Branch (AGB) stars. The total mass loss from these processes generally surpasses that of Supernovae (SNe) depending on the stellar metallicity. At 1 Gyr into the star cluster's life already around 10% of mass has been lost by winds and the total wind mass loss reaches 50% by Hubble time (Krumholz et al., 2019), meaning it asymptotically decreases and reaches a maximum mass loss from the star cluster. The escaping mass leads to a change in kinetic energy and causes the star cluster to expand. This expansion makes it easier to remove light stars in wide orbits from the cluster over time. Rapid mass loss can also occur, such as when very young and hot stars blow away proto-stellar material, potentially making the cluster unbound. This partly explains why so many stars in the galactic disk are in open clusters.

The escaping mass dM leads to a change in kinetic energy dT of the star cluster:

$$dT = \frac{1}{2} dM (\langle v_e^2 \rangle - \langle v^2 \rangle) = \frac{3}{2} \langle v^2 \rangle dM = -dE. \quad (2.23)$$

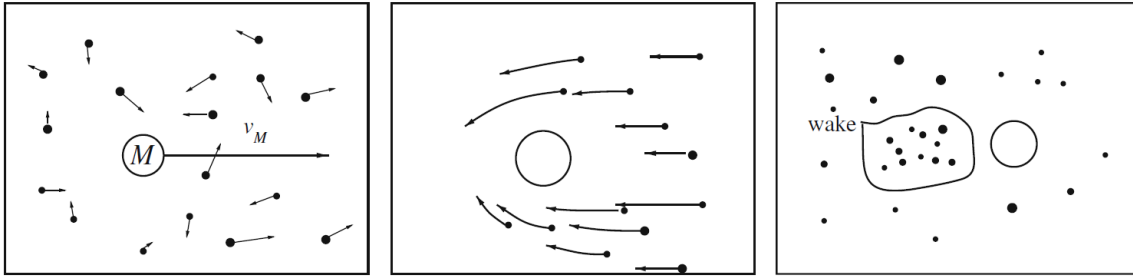


Figure 2.19: Schematic diagram of dynamical friction (Figure taken from Fellhauer, 2008).

Using $\langle v^2 \rangle = -2E/M$ and using Equation 2.22 it be shown that

$$R \propto \frac{1}{M}, \quad (2.24)$$

This means that this mass loss leads to a cluster expansion⁴⁰. However, mass loss also means that the tidal radius shrinks, because the cluster's mass decreases. These two processes combined mean that it becomes progressively easier with time to remove light stars in wide orbits from the cluster. The wind mass loss can also occur rapidly when, for example, very young and hot stars blow away the proto-stellar material. If half of the mass is blown away in this way, then the cluster becomes unbound and this explains partly why so many stars in the galactic disk reside in OCs.

40: factor of two or more during the lifetime of a cluster.

Stellar evolution mass loss by Supernova explosions

After the formation of a gas-free cluster population, around (3 – 40) Myr, the most massive stars in the cluster experience Supernova (SN) explosions. This results in a cluster mass loss of about 20% as detailed in Section 3.1.6. The mass loss is composed of gas with extremely high speeds that escape the cluster. Additionally, the asymmetry of the explosion and other factors can cause the remnant compact object (White Dwarf (WD), Neutron Star (NS), Black Hole (BH)) to receive high velocity kicks, which are dependent on its initial mass before the explosion. This can result in the compact object being expelled from the cluster (see e.g. Faucher-Giguère & Kaspi, 2006; Hobbs et al., 2005). NSs and BHs receiving high velocity kicks usually leave without hindrance, however, lighter WDs receiving smaller kicks may also be expelled later due to mass segregation, which is covered in an upcoming section. The kick distribution is a topic of ongoing research and debate in astrophysics, particularly in regards to preserving compact objects in binaries as potential gravitational wave sources (Banerjee et al., 2020; Belczynski et al., 2010).

Dynamical friction within star clusters and mass segregation

A process, which is central in self-gravitating systems with a mass spectrum and stellar dynamics in general is that of dynamical friction.

Definition 2.3.4 (Dynamical friction in star clusters) *Dynamical friction that was first studied by Chandrasekhar (1943a, 1943b, 1943c) in detail, is a deceleration of massive single and binary stars and compact objects in star clusters. It occurs whenever a massive object travels through another extended object, in this case a ‘sea’ of light-mass single and binary stars and compact objects (see also Binney & Tremaine, 2008a; Dosopoulou & Antonini, 2017; Fellhauer, 2008; Lingam, 2018).*

In [Figure 2.19](#), this process is shown. Here, dynamical friction occurs when a massive star (or a binary star) or compact object of mass M moves at speed v_M through an extended sea made up of lighter stars of masses m . This movement results in a gravitational interaction between the two. The lighter stars appear to be approaching from the front in the rest-frame of M and are deflected behind the object. The result of these many gravitational interactions is a reduction in the speed of M , while some of the deflected lighter particles m create a so-called wake behind M . This wake can be quantified and may cause additional drag on M , but this drag is not considered in the standard description of dynamical friction. According to Fellhauer (2008), the wake is a result of dynamical friction and not the cause of it. However, this is controversial, as dynamical friction is a self-reinforcing process. As will be explained later in [Definition 4.2.7](#), dynamical friction naturally emerges as the lowest-order term in the Taylor expansion of the encounter operator in the Fokker-Planck equation.

Depending on the density structure of the star cluster dynamical friction sometimes results in a circularisation of the orbit of a massive star (or a binary star) or compact object if the original orbit is eccentric around the star cluster’s centre. In homogeneous cores, there is no dynamical friction and therefore, there is no circularisation of the orbit due to dynamical friction.

Khalisi et al. (2007) present a detailed N -body study on this process by investigating stellar systems that have a two-component mass spectrum characterised by a parameter μ , which is the mass ratio of the heavy to light masses:

- ▶ $\mu \rightarrow 1$, then star cluster evolution occurs slowly since energy equipartition between the stars competes with a gravothermal collapse of the star cluster. Energy equipartition happens through dynamical encounters during which stars exchange energy and angular momentum and ultimately the stars will follow velocity distributions similar to Maxwell-Boltzmann distribution. This process is also known as relaxation, see [Definition 2.2.4](#).
- ▶ $\mu \sim 2$, then the two stellar populations decouple and the heavy mass stars sink towards the star cluster centre, i.e. the star cluster experiences mass segregation, resulting in a core-collapse.
- ▶ $\mu \gg 2$, then energy equipartition is never reached and since in this scenario in Khalisi et al. (2007) there are not a lot of high-mass stars. Therefore, dynamical friction causes mass segregation, which then supports a fast gravothermal catastrophe. Maximum mass segregation, which happens on the

times-scale τ_{ms} defined in [Definition 2.2.9](#) and which is a fraction of the relaxation time-scale τ_{rx} and it is achieved at the time when the star cluster core has collapsed maximally.

In my star cluster models presented in [Kamlah, Leveque, et al. \(2022\)](#) and [Kamlah, Spurzem, et al. \(2022\)](#) and [Kamlah et al. \(2023, in prep.\)](#) I always use a continuous mass spectrum between some limits, the point being that the systems here cannot be characterised by a parameter μ . However, in [Kamlah, Leveque, et al. \(2022\)](#) and [Kamlah, Spurzem, et al. \(2022\)](#) I use an IMF from [Kroupa \(2001\)](#), see also [Figure 2.9](#), which implies that there the highest mass star and the lowest mass star have four orders of magnitude in mass difference. Furthermore, there are a lot fewer of the high mass stars than low mass stars. This, in turn, implies that dynamical friction in these star clusters leads to mass segregation and accelerating core collapse. But I also use complex stellar evolution prescriptions, see also [Chapter 3](#) and the two subsections above, which change the masses and radii of the stars, which impact virtually all of the associated time-scales for the processes highlighted here, for example the local and half-mass relaxation time-scales or time-scales for mass segregation. The situation is further complicated in my rotating models in [Kamlah, Spurzem, et al. \(2022\)](#) and [Kamlah et al. \(2023, in prep.\)](#).

Here, the transfer of angular momentum from the high to the low mass stars associated with the gravogyro catastrophe from [Section 2.3.2](#) leads to a natural orbit decay of the high mass stars. Therefore, the pre-core collapse evolution is accelerated with increasing initial star cluster rotation (see e.g. [Einsel & Spurzem, 1999](#); [Hong et al., 2013](#); [Kamlah, Spurzem, et al., 2022](#); [Kim et al., 2008](#)).

Core-collapse and binary stars

I already described in detail what the core-collapse in a star cluster is and why it happens in [Section 2.3.1](#) and [Section 2.3.2](#). I already mentioned that binary stars can decelerate and brake the core collapsing entirely.

The internal energy of these binaries can “absorb” the increasing binding energy of the core collapse. Primordial binaries already exist pre-core collapse and their fraction relative to the total number of the stars in the cluster is called the binary fraction. Binaries can also form out of three-body encounters or two-body encounters. Encounters with binaries will change the orbits of stars, acting as a sink or a source of gravitational energy. Binaries are classified depending on if their binding energy E_b exceeds the mean kinetic energy of the stars, where σ is the mean velocity dispersion of the star cluster:

- ▶ Hard binaries: $E_b \gg m\sigma^2$
- ▶ Soft binaries: $E_b \ll m\sigma^2$

Definition 2.3.5 (Heggie’s law) *Soft binaries get softer and hard binaries get harder with increasing number of encounters (D. C. Heggie, 1975).*

The case of a three-body encounter of a hard binary with a field star is important in the evolution of the stellar core. A hard binary has a higher kinetic energy than the field star. Therefore, in the encounter kinetic energy will be transferred to the field star and the binary becomes more tightly bound. This is effectively an energy source in star clusters. The field star with increased kinetic energy, will move further away from the stellar core. Also, due to the semi-major axis of the hard binaries shrinking more and more, the cross-section of the binary shrinks and so does the probability of the hard binary being disrupted by an encounter. In fact,

Hardening of the binaries in the star cluster core can lead to a decrease of the core density.

This binary hardening of the binaries also makes X-ray binaries, see [Definition 3.2.10](#), more frequent in star cluster cores, since the existence of those requires the stars of the binaries to be spatial close together.

2.3.4 Post-core collapse star cluster evolution

Once the maximum core-collapse has been achieved, i.e. once the core expands again after collapse, I speak of the post-core collapse star cluster evolutionary phase, which typically lasts orders of magnitudes longer than the pre-core collapse phase, but, which is typically also much less violent in the presence of reasonably steady external tidal fields. Post-core collapse also implies that mass shells in the cluster have adjusted to a constant in- and outgoing mass flux. While the pre-core collapse phase is dominated by stellar evolution and the gravogyro-gravothermal catastrophe, the post-core collapse phase is dominated by two-body relaxation and tidal dissolution processes accelerated by the so-called binary burning process.

Definition 2.3.6 (Binary burning) *This process refers to the heating of the star cluster core in the late stages of core collapse due to the formation and the resulting superelastic scatterings in three-body encounters, see already [Section 4.1.5](#). Subsequently, a high-velocity star is ejected from the star cluster. (Hut, 1985; Kim et al., 2002)*

Overall, the discussion above can be related to the theorems described already in M. Hénon (1975), see also Breen and Heggie (2013). The evolution of the cluster system as a whole is governed by the energy flow through the half-mass radius r_h and it is independent of internal energy sources. The energy flow is approximately equal to

$$\frac{GM_{cl}^2/r_h}{\tau_{r_h}}, \quad (2.25)$$

where τ_{r_h} is the half-mass relaxation time-scale and M_{cl} is the cluster mass, and this is equal to the energy generated at the centre of the cluster, which is mainly generated due to binary stars. In general, stellar evolution causes mass loss and results in an increase of r_h . Additionally, the loss of mass by interaction and relaxation for very massive stars (without evolution) causes an increase in r_h . Because in the case of no evolution we have more massive stars than in the case of evolution, the core collapses deeper and earlier. Mass loss through evolution slows down the collapse that then continues further. To stop the core collapse (no evolution), it is necessary to eject out some of the most massive binary systems and the most massive stars. Then equilibrium occurs and both systems evolve similarly at the centre, generating similar energy. So if the mass of the system without stellar evolution is greater, then r_h must also be greater than in the case with stellar evolution.

Evaporation and ejections of stars from the star cluster

Not only compact objects get ejected from star clusters due to stellar evolution natal kicks. There are two further internal mechanisms (see also Binney & Tremaine, 2008a) that remove single and binary stars and compact objects from star clusters in the presence of tidal fields, which I employ in all of my simulations presented in Kamlah, Leveque, et al. (2022) and Kamlah, Spurzem, et al. (2022) and Kamlah et al. (2023, in prep.):

- ▶ Ejections: a process by a single strong encounter can give one of the stars a speed exceeding the local star cluster escape velocity. This has been mentioned earlier already in the context of binary stars regulating the star cluster's evolution, see also Definition 2.3.5. In fact, according to Weatherford et al. (2022) three-body binary formation may dominate high-speed ejections.
- ▶ Evaporation: a process by which a series of weak, distant uncorrelated encounters gradually increase the energy of a star, until a final weak encounter gives the star enough energy to escape mostly by being stripped from the cluster in a tidal interaction.

Therefore, through natal kicks, ejections and evaporation, the star cluster will lose additional mass throughout its life-time.

Escapers, in general, will lead to an irreversible leakage of stars from the star cluster. The result of this leakage are two stars or compact objects in an orbit around each-other. The evaporation time-scale may be estimated (J. Spitzer, 1940) by assuming that the escape speed from the star cluster at position \mathbf{x} is given by (see also Binney & Tremaine, 2008a)

$$v_e^2(\mathbf{x}) = -2\Phi(\mathbf{x}). \quad (2.26)$$

The mean-square escape velocity of the star cluster is then given by

$$\langle v_e^2 \rangle = -\frac{4W}{M} \quad (2.27)$$

Since we know from the Virial theorem that

$$2K = -W \rightarrow M\langle v^2 \rangle = -W, \quad (2.28)$$

we then get

$$\langle v_e^2 \rangle^{\frac{1}{2}} = 2\langle v^2 \rangle^{\frac{1}{2}}, \quad (2.29)$$

which means that the escape speed of a star from a star cluster in Virial equilibrium is just twice the root mean square velocity of the star cluster. Following Binney and Tremaine (2008a), the fraction of stars removed per time-step by escapers can be measured by some factor, which I call κ . I then get

$$\frac{dN}{dt} = -\frac{\kappa N}{\tau_{rel}} = -\frac{N}{\tau_{evap}}. \quad (2.30)$$

Definition 2.3.7 (evaporation time-scale) *This time-scale τ_{evap} is the characteristic time in which an **isolated** star cluster loses its member stars and can be approximated by*

$$\tau_{evap} = \frac{\tau_{rel}}{\kappa} \simeq 140\tau_{rel}, \quad (2.31)$$

where τ_{rel} is the relaxation time-scale.

From Definition 2.3.7 we can deduce that left uninterrupted, a star cluster will lose all its stars and compact objects on the order of $10^2\tau_{rel}$.

Tidal dissolution of a star cluster

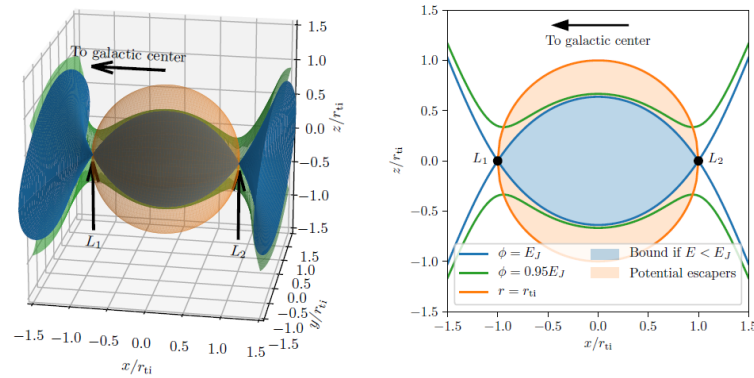


Figure 2.20: Isosurfaces of the total potential $\phi(x, y, z) = -\frac{GM}{\sqrt{x^2 + y^2 + z^2}} - \frac{\lambda_x}{2} \left(x^2 + \frac{\lambda_y}{\lambda_x} y^2 + \frac{\lambda_z}{\lambda_x} z^2 \right)$, where M is the cluster mass, $\lambda_x, \lambda_y, \lambda_z$ assuming the star cluster as a point-like mass distribution are the three eigenvalues of the tidal plus centrifugal tensor from Renaud et al. (2011). For a point-like star cluster embedded in a galaxy, seen in 3D (left) and in a cut through the $x - z$ plane (right). The cluster center is located at the origin, while the galaxy center is located at $(-R_g, 0, 0)$ for some distance R_g much larger than the physical size of the cluster. In the example shown, $\lambda_y = 0$ and $\lambda_x/\lambda_z = 1/3$. Blue shows the Jacobi surface, defined by $\psi = E_J$, while green shows a potential $\psi = 0.95E_J$, i.e., with energy 5% greater than the Jacobi energy, which is defined as $E_J = -(3/2)GM_c/r_{ti}$. Orange shows a sphere of radius $r = r_{ti} = \left(\frac{GM}{\lambda_x}\right)^{1/3}$. The Lagrange points L_1 and L_2 are as indicated. Stars inside the Jacobi surface, shaded blue in the right panel, are bound cluster members if their total energy $E < E_J$. Stars outside the Jacobi surface but at $r < r_{ti}$ (shaded orange), or those inside the Jacobi surface with $E \geq E_J$, are potentially unbound from the cluster, and can escape through the “windows” around L_1 and L_2 (Figure taken and caption adapted from Krumholz et al., 2019).

Although, I do not focus on tidal dissolution in my simulations in Kamlah, Leveque, et al. (2022) and Kamlah, Spurzem, et al. (2022) and Kamlah et al. (2023, in prep.) and do not run any of them until that point, it is worthwhile to briefly mention what will ultimately happen to a star cluster. I will introduce in Section 3.2.2 onwards how important tides are also to stellar evolution.

The central idea that I follow is that stars in the outer regions or halo of a star cluster are substantially affected more by a nearby mass distribution (such as a galaxy) than the inner regions of the star clusters. Tidal effects, which vary in magnitude with almost certainty across the life-time of the star cluster, can be classified as either continuous or steady, which accounts for the potential of the host galaxy, or spontaneous or shocks, for example, when the star cluster passes through the galactic disk or a GMC, while it orbits the host galaxy. Figure 2.20 shows the effective potential co-moving with a cluster orbiting with a galaxy by Taylor-expanding the galactic potential and adding this to the centrifugal acceleration in the rotating reference frame (Krumholz et al., 2019). The resulting potential has five saddle-points or so-called Lagrange points. Two of these L_1, L_2 are important and shown in Figure 2.20 and they lie at $L_{1,2} = (\pm r_{\text{ti}}, 0, 0)$, where

Definition 2.3.8 (Tidal radius) *The tidal radius of a star cluster is given by*

$$r_{\text{ti}} = \left(\frac{GM}{\lambda_x} \right)^{1/3}, \quad (2.32)$$

where M is the mass of the cluster, λ_x is the x -eigenvalue of the tidal plus centrifugal tensor from Renaud et al. (2011).

At L_1 and L_2 the acceleration due to the gravity of the cluster is equal to that due to the combination of galactic gravity and the centrifugal force (Krumholz et al., 2019).

Definition 2.3.9 (Jacobi energy and surfaces) *The value of the potential at L_1 and L_2 is the Jacobi energy*

$$E_J = -\frac{3GM_c}{2r_{\text{ti}}}, \quad (2.33)$$

and the locus where $\psi = E_J$ is called the Jacobi surface, see also Figure 2.20.

Stars within the Jacobi surface and with energies $E \geq E_J$ can only escape through a “window” L_1 and L_2 . From this discussion we know that in reasonably steady tidal fields and due to internal relaxation processes that lead to ejection of stars or evaporation, a star cluster will gradually dissolve into the galactic background, typically forming tidal streams as shown in for the GC Pal 5 in Figure 2.21, which may take even longer than Hubble time (see e.g. simulations by Weatherford et al., 2022).

However, star clusters are rarely exposed to constant tidal fields across their life-times. Depending on their position in a galaxy, the tidal forces that they experience might significantly vary in

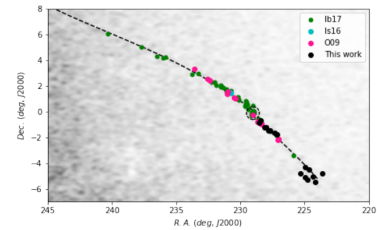


Figure 2.21: Spatial distribution of a combined sample of 109 bona fide stream members of the GC Pal 5 with the stream track of Ibata et al. (2016, 2017) under-laid. The stars closely follow the stream track until the edge of the leading tail, near $(\alpha, \delta) \sim (225^\circ, -5^\circ)$, where the fanning is observed. The dashed circle indicates the location of Pal 5 itself (Figure taken and caption adapted from Kuzma et al., 2022).

magnitude by a lot. A spontaneous and violent tidal event, such as a collision between a cluster and a GMC or a passage of a cluster through a galactic disk, will generally lead to an increase in the energies of the stars of the star cluster of mass M_c by some value Δv . I now assume that a star cluster crosses a GMC on its orbit. Summing over all the stars in the cluster gives the total change of energy ΔE

$$\Delta E = \frac{1}{2} M_c (\Delta v)^2. \quad (2.34)$$

Integrating over all impact parameters and introducing a geometric factor γ , which depends on geometry of star cluster, we receive for the cluster radius R_c of a cluster passing through a GMC of density ρ_{neb} , mass M_{neb} and radius R_{neb}

$$\frac{dR_c}{dt} = \frac{8\pi G}{3\gamma v} \rho_{\text{neb}} \frac{M_{\text{neb}} R_c^4}{M_c R_{\text{neb}}^2}, \quad (2.35)$$

which means that the cluster density ρ_c decreases with time. The life-time t_{shock} of a star cluster after a tidal shock is estimated via

$$t_{\text{shock}} = \frac{\gamma v}{6G} \frac{\rho_c R_{\text{neb}}^2}{\rho_{\text{neb}} M_{\text{neb}}} \propto \rho_c. \quad (2.36)$$

Therefore, the more concentrated a star cluster is the less it is affected by such a tidal shock. In other words, OCs are more affected by tidal shocks than GCs. Tidal shocks in general that include passages through a galactic disk strip stars from the star cluster halo.

For star clusters, which begin their gas-free evolution filling their tidal radius are much more prone to tidal disruption than tidally underfilling cluster⁴¹. Not surprisingly, the property whether the star clusters are tidally under- or overfilling approximately doubles the mass loss rate from the star cluster due from stellar evolution in the pre-core collapse evolution alone (Baumgardt & Makino, 2003). Clusters with low concentrations and already overfilling their tidal radii are extremely likely to completely dissolve during the pre-core collapse phase. This in turn implies that all GCs, which we observe today, must initially been tidally underfilling and have appropriate initial concentrations to curtail mass loss. This realisation is further substantiated by the fact that observations have shown that higher proportion of the older GC population, albeit not all of them, do indeed fill their tidal radii (Baumgardt & Makino, 2003).

The duration of a tidal shock event matters and the direction of the tidal field matter perhaps unsurprisingly. If a star cluster moves near-circular orbits in the galactic plane, then vertical motion above and below the galactic plane can be ignored and therefore the main source of tidal shocking comes from sudden encounters of GMCs, which can be instantaneous if the duration of the encounter is shorter than the crossing time-scale of the cluster (see e.g. J. Spitzer, 1975). If the orbit of the star cluster is different and it crosses the disk or even the galactic bulge along its orbit, then the star cluster invariably experiences a strongly changing tidal field. The star cluster will be subject to a so-called 1D pinch compression, which acts at a normal to the bulge or the disk (Gnedin & Ostriker, 1997). In general, GCs, which transit the bulge of a galaxy are subjected to much stronger

41: tidally underfilling and tidally overfilling star clusters are separated based on their initial concentration and ratio of their truncation radius to Jacobi radius.

tides, because of their vicinity to much denser galactic bulge and most likely, the galactic SmbH. Here they might lose a significant fraction of their mass in less than Hubble time (Madrid et al., 2017), see also Section 41 for such a scenario in the grand-spiral galaxy NGC 628 (Hoyer et al., 2022).

Dynamical friction of star clusters in an external (galactic) potential

Just as individual stars that exist in star clusters are subject to dynamical friction from Definition 2.3.4, so are star clusters in a galactic potential. Dynamical friction tends to cause loss of angular momentum from GCs and OCs, which as a result causes them to shrink their orbits around the Galactic centre. From the treatment of dynamical friction we know that massive bodies, in this case clusters, decelerate more quickly than lower mass clusters. Therefore, this is one of the only processes, which tends to disrupt or destroy massive clusters (see e.g. Bekki & Chiba, 2001). Furthermore, massive clusters tend to sink towards the Galactic centre, where the tidal forces increase, leading to smaller tidal radii and more tidal stripping until the cluster is eventually destroyed in well under Hubble time (see e.g. Gerhard, 2001; Madrid et al., 2017).

In Hoyer et al. (2022), we discuss such a scenario in the grand-spiral galaxy NGC 628, see also Figure 2.1, to explain an astrometric offset in the mid-IR from JWST data. The following section is adapted from Hoyer et al. (2022) and has been mainly written by myself.

We see the NSC and an in-falling star cluster, where the latter could be in a late stage of tidal disruption by the more massive NSC. Such a scenario for the build-up of NSCs has been proposed for a few decades (Tremaine et al., 1975) and is sometimes referred to as the “dry-merger” scenario (e.g. Arca Sedda et al., 2018) with ample observational and theoretical evidence in both the Galactic but also extragalactic NSCs (e.g. Antonini, 2013, 2014; Arca-Sedda & Capuzzo-Dolcetta, 2017; Fahrion et al., 2020; Feldmeier-Krause et al., 2020). The proposed scenario could occur as follows: the star cluster would form outside the nuclear region and spiral inwards due to dynamical friction. During this time, the star cluster can be considered self-gravitating, which implies that it evolved predominantly due to its internal collisional dynamics. During the in-fall of the cluster, it will experience gravothermal-gravogyro contraction and core-collapse (e.g. Kamlah, Spurzem, et al., 2022), mass segregate, and form a subsystem of black holes in its center, or even an intermediate-mass black hole, if the star cluster is massive enough. The most-massive stars accumulate in the star cluster’s center and lower-mass stars occupy the halo of the star cluster. Some of these low-mass stars will be stripped by the tidal field of the surrounding field or may be ejected through dynamical interactions, while the star cluster approaches the NSC. Some of the stripped or ejected stars might be visible as AGB with their strong, dust-driven stellar winds (see e.g. Decin, 2020, and sources therein) or in the near- to mid-infrared bands as single sources scattered around the NSC.

From N -body simulations by Arca Sedda et al. (2018), modeling the MW NSC and an in-falling star cluster, we know what the in-fall,

merger, and merger product phases look like in spatial coordinates (Figure 2 in Arca Sedda et al. (2018) and Figure 1 in Arca Sedda, Gualandris, et al. (2020)). If the in-falling star cluster has already crossed the effective radius of the NSC, after which the star cluster becomes entirely tidally disrupted and cannot be considered a self-gravitating system anymore (Arca Sedda, Gualandris, et al., 2020), the simulation snapshots could explain the potential astrometric offset. The star cluster's core would eventually fall into the core of the NSC and the remaining halo stars would tidally disperse. Among these would be AGB stars that may partly be responsible for the astrometric offset.

This is directly taken from Hoyer et al. (2022). One counter-argument is that it is unlikely to witness such an event: Arca Sedda, Gualandris, et al. (2020) simulated the in-fall of a star cluster on an NSC whose properties mimic the ones of the Milky Way NSC. They find that the star cluster enters a region 10 pc around the center of the NSC after 60 Myr and that the cluster is not a self-gravitating system anymore after another 1 Myr. Note that the bulge component in their simulation is likely more massive than the bulge-component and that the time scale for in-spiral will be longer. Nevertheless, the time scale will be short compared to the age of the cluster, ~ 8 Gyr.

Furthermore, radial migration from transient spiral density waves (see e.g. Binney & Tremaine, 2008b) are able to move stars or groups of stars, like our clusters, inwards or outwards in the galactic disk. However, this process does not destroy the cluster, since unlike tidal shocks by GMCs, the time it takes for a cluster to transit a spiral density wave is much longer than the cluster's internal crossing time (Gieles et al., 2007). If the cluster oscillates above and below the galactic disk, then it is less affected by this radial migration, as are clusters that have highly radial orbits anyway. Moving the cluster away or towards the GC also changes its angular momentum around the GC and according to Dehnen (2000), over a couple of billion years, this change can be substantial.

In the case that the galaxy, which the star cluster is orbiting has another galaxy close-by perturbing the disk, then this tidal perturbation can also affect the radial motion of the cluster (Quillen et al., 2009).

Overall, the radial motion of stars (or clusters) can be proven by comparing their metallicities to the local ISM metallicity. If they are different, then this star must have migrated from some other region. By measuring the phase-space coordinates of this star, one in theory could be able to reconstruct its origin (Cantat-Gaudin et al., 2018). In the future with the Gaia (DR3) release this year, it could be possible to further clarify this question.

Astrophysics within star clusters 3

This chapter is based primarily in its structure and content on the section 6 in my co-author living review paper in Spurzem and Kamlah (2023), for which I have been mostly responsible. Adjustments and especially extensions have been made in certain places, but they are not explicitly highlighted.

In realistic star cluster simulations as those presented in this thesis all stars undergo stellar evolution as time proceeds (Church et al., 2009). Therefore, a large array of stellar evolutionary processes must be integrated that affect all stars. I briefly outline the fundamentals of single stellar evolution in Section 3.1, because it is essential to understand the complexities that need to be modelled before I move on to an area, in which collisional N -body simulations really shine, which is binary stellar evolution outlined in Section 3.2 in dense star clusters.

3.1 Single stellar evolution

The discussion in this section is based mostly on the text book by Kippenhahn et al. (2012) and the review by Salaris and Cassisi (2017).

A star is commonly defined as a self-gravitating object of a hot plasma, which emits energy at the surface in form of photons (and from the inner regions in the form of neutrinos). Furthermore, it is spherically symmetric in the absence of rotation, magnetic fields and a sufficiently close companion or multiple companion stars that induce interior oscillations and bulges through tidal interaction or deforms the star through mass transfer (see also Section 3.2 for more details on these). These are typical assumptions in one-dimensional (1D from hereon) modelling of single stars and they yield four fundamental structure equations that govern stellar evolution under the assumption of hydrostatic equilibrium, which holds for most single stars.

Definition 3.1.1 (The four fundamental stellar structure relations)

$$\frac{\partial r}{\partial m} = \frac{1}{4\pi r^2 \rho} \quad (3.1a)$$

$$\frac{\partial P}{\partial m} = -\frac{Gm}{4\pi r^4} - \frac{1}{4\pi r^2} \frac{\partial^2 r}{\partial t^2} \approx -\frac{Gm}{4\pi r^4} \quad \text{hydrostatic equilibrium} \quad (3.1b)$$

$$\frac{\partial L_r}{\partial m} = \epsilon = \epsilon_{\text{nuc}} - \epsilon_\nu + \epsilon_g = \epsilon_{\text{nuc}} - \epsilon_\nu - c_p \frac{\partial T}{\partial t} + \frac{\delta}{\rho} \frac{\partial P}{\partial t} \quad (3.1c)$$

$$\frac{\partial T}{\partial m} = -\frac{GmT}{4\pi r^4 P} \nabla \quad (3.1d)$$

- 3.1 Single stellar evolution . 55
- 3.1.1 Two fundamental principles of stellar evolution . 59
- 3.1.2 Time-scales, energy conservation and homology . 60
- 3.1.3 Fundamental parameters - mass and composition . . 64
- 3.1.4 Mass change of stars - stellar winds 64
- 3.1.5 Discretizing ZAMS mass in stellar evolution 65
- 3.1.6 Formation of compact objects and their natal masses, kicks and spins . 68
- 3.2 Binary stellar evolution . 73
- 3.2.1 Stellar Spin and orbital changes due to mass loss or gain 74
- 3.2.2 Effects of tidal damping . 74
- 3.2.3 Dynamical mass transfer and its stability 76
- 3.2.4 Common-envelope evolution 79
- 3.2.5 Mergers and general relativistic merger recoil kicks 80
- 3.2.6 Accretion or merger induced collapse 82
- 3.2.7 Gravitational radiation and magnetic braking . . 83
- 3.2.8 Stellar types and binary classes in classical SSE & BSE 84

1: defined as the effective cross-section per unit mass seen by a photon, which may also be written as $\kappa = 1/(\rho\lambda)$, where λ is the mean-free path length and ρ is the density of the stellar material the photon passes through. The probability of interaction of a photon passing along a cylinder of cross-section equal to κ times the mass in the cylinder and length λ is set to unity. How opaque a star is depends on the star's density and temperature in a complex way, since at different densities and temperatures several scattering and absorption processes come into play.

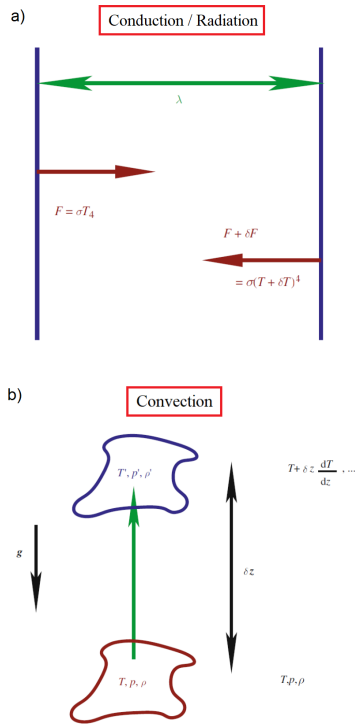


Figure 3.1: Diagram showing the energy transport in a star via radiation and convection; a) radiation (diffusion of photons): radiation, which is very similar to conduction (diffusion of particles, typically electrons), diffuses through the star as the star is locally at thermodynamic equilibrium (no steep temperature gradients) from hotter regions to cooler regions and on the way the photons are scattered, absorbed and emitted characterised by the quantity known as the mean-free path length. Here, a black body is assumed for the surfaces; b) convection (energy transport by bulk fluid motion): powered by the convective instability, where a bubble of fluid displaced upwards continues to rise if its density is less than that of its surroundings when it has reached pressure equilibrium adiabatically (Figure and caption adapted from Tout, 2008b).

which are written in Lagrangian coordinates, where mass $m = M_r$ is the coordinate and time t is the independent variable. r , P , L_r and T are the radius, the pressure, the luminosity at r and the temperature of the star, respectively, and are the dependent variables. I am ignoring magnetic fields here. Furthermore, there are dependent functions (also referred to as “microphysics”) in these equations, namely the density ρ , the Rosseland opacity κ^1 , the energy liberation rate per unit mass within the star ϵ , which can be split up into the energy generation due to nuclear reactions ϵ_{nuc} , the energy generation due to neutrino production ϵ_ν (minus sign is due to the fact that neutrinos generated in the stellar plasma escape the star almost immediately) and the energy generation due to gravothermal effects ϵ_g , i.e. the energy generation due to the expansion or contraction of the mass shell through the luminosity L_r . ϵ_g depends on the equation of state of the star, where in Equation 3.1c one of the possible variants is shown. These dependent function are functions of the dependent variables and the so-called composition variables also known as relative mass fractions, where traditionally X , Y , Z represent the relative mass fractions of Hydrogen (H), Helium (He), and all other ‘metals’ in the star (also called the metallicity of the star). Neutral H has $\mu = 1$, fully ionised H has $\mu = 1/2$ and fully ionised He has $\mu = 4/3$. When these metals are ‘fully’ ionised, then they contribute about half as a many particles as its atomic mass (each proton balances one electron). For metals I have therefore $\mu \approx 2$. For a fully ionised stellar mixture

$$\frac{1}{\mu} = 2X + \frac{3}{4}Y + \frac{1}{2}Z \quad \text{and} \quad X + Y + Z = 1 \quad (3.2)$$

Then the task is to solve an initial-value problem in time. Material on how to solve it can be found in Kippenhahn et al. (2012).

Strictly speaking, not only the stellar structure of a star changes with time, but also its chemical composition X_i and so one more equation must be added describing the stellar temporal chemical evolution:

$$\frac{\partial X_i}{\partial t} = \frac{m_i}{\rho} \left(\sum_j R_{ij} - \sum_k R_{ik} \right) - \frac{\partial}{\partial r} \left(\sigma^2 \frac{\partial X_i}{\partial r} \right), \quad (3.3)$$

where R_{ij} denotes the conversion rate of element i into j per unit volume, m_i is the atomic mass of element i and σ is the diffusion coefficient, which is derived from mixing length theory. Any deviation from hydrostatic equilibrium, i.e. changes to Equation 3.1b in Definition 1, will become especially important in (hard) binary stars. Energy transport in a star is either radiative or convective (where convective transport can also include some conduction, which is not that important) and it is important to define it for solving Equation 3.1d. A schematic figure of all the processes can be found in Figure 3.1:

1. Radiation

This process can be described as the diffusion of photons. Considering the spherical shells from one of which a photon is emitted isotropically and not necessarily directly towards the other surface, see also Figure 3.1 a), I find for the temperature gradient inside the star as a result of this process the radiative

transfer equation (∇ from Equation 3.1d):

$$\nabla := \frac{d \ln T}{d \ln P} = \nabla_{\text{rad}} = \frac{3}{16\pi a c G} \frac{\kappa L_r P}{m T^4}, \quad (3.4)$$

where a is the radiation density constant, c the speed of light, G the gravitational constant, κ the aforementioned Rosseland opacity, including also the contribution of electron conduction when appropriate.

2. Conduction

This process can be described as the diffusion of particles, which dominates in degenerate stars. This process is similar to radiative transfer, however, electrons transport the energy, which have much shorter mean-free path lengths, which leads to much larger opacities. Therefore, in non-degenerate stars radiative dominates conductive energy transfer. In degenerate stars, where virtually all neighbouring momentum states are occupied, the mean-free path lengths are very large and therefore these stars become superconducting and thus isothermal.

3. Convection

This process can be described by bulk motion of fluid at large temperature gradients, when radiative transfer is inefficient. A bubble of material is displaced vertically along the direction of gravity and rises to the surface, because of a large temperature gradient, see also Figure 3.1 b). The bubble rises, because it is less dense than the surrounding material due to its higher temperature and is said to be convectively unstable. In the beginning the bubble rises and the density changes adiabatically at constant entropy, because there is no heat exchange with surrounding material. However, as the bubble rises, the pressure inside the bubble must decrease in order to maintain hydrostatic equilibrium and therefore the fluid becomes unstable to convection. When I have a very powerful heat source in the star, such as the core which undergoes enormous rates of nuclear reactions, which lead to large temperature gradients, in the unstable region surrounding the heat source turbulent mixing of the fluid happens, which leads to an adiabatically stratified region of constant entropy, in which this convective bulk motion takes place. Following the discussion of Tout (2008b), the temperature gradient in the convective regions is written as

$$\frac{dT}{dr} = \nabla_{\text{ad}} \frac{T}{P} \frac{dP}{dr} + \Delta \nabla T, \quad (3.5)$$

where $\nabla \delta T$ is the super-adiabatic gradient. At the outer edge of the convective region, this gradient becomes very large and the acceleration of a convective packet reaches zero, however, the packet might still have some velocity and reach into non-convective zones. This is known as convective overshooting².

2: Convective overshooting extends the main-sequence lifetimes of stars, as more fuel is available for processing in the core afterwards. Moreover, they are more concentrated in their mass towards the stellar centre (Claret & Torres, 2016).

Whether the star is dominated by radiative or convective transport is decided by the following criteria:

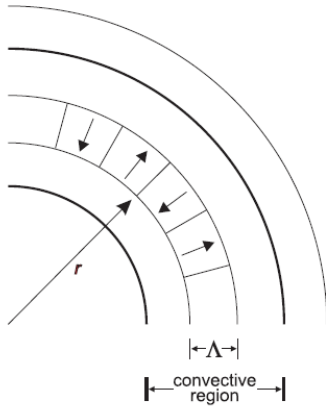


Figure 3.2: Schematic illustration of the MLT approximation to convective motion of bubbles. The mixing length Λ corresponds to the characteristic radial distance scale over which rising and falling convective elements / bubbles move before merging with the surrounding medium (Figure and caption taken from Salaris & Cassisi, 2017).

3: α_{MLT} is an extremely important parameter in mainstream 1D stellar evolution models. Depending on the choice of this parameter the theoretical evolution of all stars can be greatly influenced (Joyce & Chaboyer, 2018). I will return this in the construction of the stellar evolution fitting formulae for my star cluster simulations.

Definition 3.1.2 (Schwarzschild and Ledoux criteria) *The Schwarzschild stability criterion compares the temperature gradients in the radiative case with the temperature gradient by an adiabatic movement of matter elements:*

$$\nabla_{\text{rad}} < \nabla_{\text{ad}} \quad (3.6)$$

The Ledoux criterion also takes into account a possible gradient in the density and chemical composition of a star, which is more physically motivated, but it is at the same time less practical:

$$\nabla_{\text{rad}} < \nabla_{\text{ad}} - \frac{\chi_{\mu}}{\chi_T} \nabla_{\mu} \doteq \nabla_L, \quad (3.7)$$

where μ is the mean molecular weight of the stellar matter and $\chi_T = (d \ln(P)/d \ln(T))_{\rho, \mu}$; $\chi_{\mu} = (d \ln(P)/d \ln(\mu))_{\rho, T}$ and $\nabla_{\mu} \doteq d \ln(\mu)/d \ln(P)$ (see also Salaris & Cassisi, 2017). If some matter is unstable according to the Ledoux criterion, then convection will set in and will mix the material until stellar homogeneity. This process will diminish these gradients. Therefore, in practice the Schwarzschild criterion from Equation 3.6 is more commonly used.

In the case of convection, I simply have $\nabla = \nabla_c$. It stands today still that no complete theory of convection exists and the problem is approximated using mixing-length theory (MLT Böhm-Vitense, 1958). MLT describes the convective temperature gradient ∇_c surprisingly well despite a large number of unrealistic assumptions. Salaris and Cassisi (2017) summarise them as follows (see also Figure 3.2 for the geometry of the problem):

1. The convective bubbles have identical sizes of order of the mixing length Λ ;
2. Λ is much smaller than any other length scale of physical significance in the star such as the stellar radius r ;
3. the physical properties, i.e. temperature, density, pressure and chemical composition, of the bubbles differ only slightly from the surrounding medium;
4. Pressure equilibrium with the environment is maintained. This means that the velocities of the convective elements are small compared with the local sound speed in the local environment.

Definition 3.1.3 (mixing length parameter) *MLT is parameterised globally by α_{MLT} , which is the ratio of the mixing length Λ to the local pressure scale height h_P :*

$$\alpha_{\text{MLT}} = \frac{\Lambda}{h_P} \quad (3.8)$$

α_{MLT} needs to be calibrated, which is typically done based on the Sun's effective temperature and age³: this yields values of $\alpha_{\text{MLT}} \simeq 2$. Since convection is very efficient in deep stellar interiors and since the convective bubbles move adiabatically as a result, I typically assume:

$$\nabla_c \simeq \nabla_{\text{ad}}. \quad (3.9)$$

In the outermost layers, where the densities are much lower, convection is not so efficient. As a result, a lot of energy is lost by a convective bubble moving up and the energy transport is super-adiabatic even approaching the radiative gradient in the extreme:

$$\nabla_{\text{rad}} > \nabla_{\text{c}} > \nabla_{\text{ad}}. \quad (3.10)$$

The chemical composition of a star changes with time due to nuclear reactions in its interior. It can also be subject to convective mixing, sedimentation, rotation (angular momentum transport) and hydrodynamical instabilities. The inclusion of all of these effects is difficult, because it requires three-dimensional (3D from hereon) treatment; but most currently used stellar evolution codes, such as Modules for Experiments in Stellar Astrophysics (MESA Paxton et al., 2011, 2013, 2015, 2016, 2018, 2019) or HOngo Stellar Hydrodynamics Investigator (HOSHI Takahashi et al., 2016, 2018, 2019; Yoshida et al., 2019) are 1D.

3.1.1 Two fundamental principles of stellar evolution

The general evolution of a star following the assumptions above is governed by two fundamental principles, where I assume that the stars may be modelled as spherical gases that are in hydrostatic gases:

Definition 3.1.4 (Virial theorem for a mono-atomic stellar gas sphere in hydrostatic equilibrium) *The Virial theorem, which is a consequence of a self-gravitating sphere in hydrostatic equilibrium (which holds in most of the stars, see Equation 3.1b):*

$$E_g = -2E_i \quad (3.11)$$

where E_g is the gravitational energy and E_i is the integral over the specific internal energy and where a mono-atomic ideal gas is assumed⁴ where

$$\gamma = \left(\frac{d \ln(\rho)}{d \ln(P)} \right)_{\text{ad}} = \frac{5}{3} \quad (3.14)$$

is the adiabatic exponent of the gas. For mono-atomic gases $\zeta = 2$ and photon gases have $\zeta = 1$.

The Virial theorem implies that on contraction of a star that is modelled as an ideal gas, half of the liberated energy is radiated away and the other half is used to increase the internal energy (star is heating up). In other words, if stars lose energy from the surface, the star must contract (overall) and heat up, which is a consequence of its negative heat capacity. That does not mean that some parts (like the envelope) are not expanding over the evolution, but what is certain is that the largest part of the star is contracting over the life-time and heating up⁵. Therefore, these gas configurations have a negative specific capacity and are therefore very similar in simplistic modelling as star clusters (see e.g. Antonov, 1960, 1961, 1962; Lynden-Bell, 1960, 1962a, 1962b). The results are similar: because stars are losing energy from the surface, they experience gravothermal contraction

4: A mono-atomic ideal gas here has the equation of state

$$\frac{P}{\rho} = \left(\frac{2}{3} \right) u = \left(\frac{2}{3} \right) c_v T, \quad (3.12)$$

where u is the specific internal energy of the gas and c_v is the specific heat capacity at constant volume. For general gases, the equations of state is given by

$$3(P/\rho) = \zeta u (\zeta = 3(\gamma - 1)), \quad (3.13)$$

5: This is true, because

$$L = -\frac{dW}{dt} = (\zeta - 1) \frac{dE_i}{dt} \quad (3.15)$$

$$= \frac{dE_i}{dt} = -\frac{1}{2} \frac{dE_g}{dt}, \quad (3.16)$$

for I assume a mono-atomic gas with $\zeta = 2$.

(Lynden-Bell & Eggleton, 1980). Stars are losing energy from the surface and as a result they are getting increasingly hotter upon contraction. This effect is global meaning that individual parts of a star could be expanding, for example the envelope. The central regions, are contracting as a general rule of thumb.

Interestingly, massive stars, which are radiation pressure dominated and can be modelled in their envelopes by photon gases, which have $W = 0$ (see implications from Equation 3.16), approach the limit of an unbound structure, which is one of the reasons why they lose mass much more easily.

Definition 3.1.5 (Coulomb repulsion) *The Coulomb repulsion exists between positively charged nuclei, which are mostly fully ionized in stars. This barrier determines the sequence of nuclear burning phases. The larger the charge of the ion, the higher temperatures I need to overcome or in other words, I need higher and higher temperatures to produce heavier and heavier ions.*

Due to the Virial theorem in Equation 3.11 that leads to a general increase in the interior stellar temperature, nuclear burning phases follow a sequence of light to heavier elements, i.e. they start with H burning (the main sequence (MS) phase), followed by helium He burning (horizontal branch (HB) phase), the Carbon (C) burning phase and so on. This burning sequence stops when an iron (^{56}Fe) core is reached, because any further nuclear fusion is endothermic⁶. I obtain the well known “onion-like” stellar structure, as is illustrated very schematically in Figure 3.3: in the outer layers original stellar material is still processing (H fusing to He), while at the centre an Fe-core (and Ni core) forms simultaneously (if the stellar mass is large enough).

6: This is a typical assumption that is actual not quite true. It turns out that both ^{58}Fe and ^{62}Ni (Nickel) are more strongly bound than ^{56}Fe , with ^{62}Ni having the highest mean binding energy (Fewell, 1995).

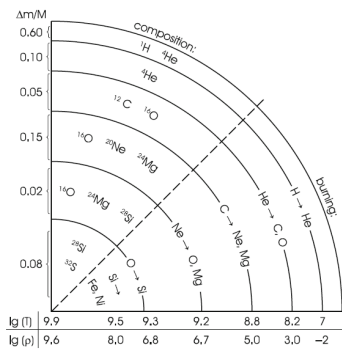


Figure 3.3: Schematic illustration (not to scale) of the “onion” in the interior of a highly evolved massive star. Along the vertical radius and below the horizontal radius some typical values of the mass, the temperature (in K), and the density (in gcm^{-3}) are indicated (Figure and caption taken from Kippenhahn et al., 2012).

3.1.2 Time-scales, energy conservation and homology

The following time-scales are extremely useful in characterising the evolution of stars and also

relating them to the time-scales of star cluster evolution:

Definition 3.1.6 (hydrostatic time-scale τ_{hydro}) *Let us assume that the internal stellar forces are not balanced anymore and the star is not in hydrostatic equilibrium anymore. I assume that the pressure within the star in Equation 3.1b is zero. The resulting time-scale to return to hydrostatic equilibrium is given by:*

$$\tau_{\text{hydro}} \approx \frac{1}{2}(G\bar{\rho})^{-1/2}, \quad (3.17)$$

where G is the gravitational constant and $\bar{\rho}$ is the mean stellar density.

To reiterate, from Equation 3.17 I can immediately see that τ_{hydro} only depends strongly on the mean stellar density $\bar{\rho}$. When assuming densities for Sun-like stars or more evolved stellar phases, I obtain that, in general, that stars return to hydrostatic equilibrium after

extremely short times comparatively speaking⁷. I note that according to Vasilyev et al. (2018), this model for τ_{hydro} is able to reproduce the pulsation periods (surface oscillations) of Cepheids, which are important Red Giant (RG) variable stars, quite well and therefore this time-scale has an actual use in practice.⁸

Definition 3.1.7 (Kelvin-Helmholtz (thermal) time-scale τ_{KH}) *Let us assume that the whole luminosity comes only from the internal energy, if the nuclear reactions are switched off. I also assume that the luminosity L stays constant at the current state for the duration of the thought experiment:*

$$\tau_{\text{KH}} \simeq \frac{GM^2}{2RL} \quad (3.20)$$

Definition 3.1.8 (nuclear time-scale τ_{nuc}) *Let us assume that the whole luminosity comes only from the nuclear energy reservoir within the star and that the luminosity stays constant at the current state for the duration of the thought experiment. I then have⁹:*

$$\tau_{\text{nuc}} = \frac{E_{\text{nuc}}}{L} \quad (3.21)$$

It is important to see how the time-scales that I have introduced relate to each other and such a comparison also helps to illustrate their utility. In most phases of stellar evolution, I have

$$\tau_{\text{hydro}} \ll \tau_{\text{KH}} \lesssim \tau_{\text{nuc}} \quad (3.22)$$

and mostly also even

$$\tau_{\text{KH}} \ll \tau_{\text{nuc}} \quad (3.23)$$

for MS and Core Helium Burning (CHeB) stars. In late stellar evolution phases I get

$$\tau_{\text{KH}} \rightarrow \tau_{\text{nuc}}. \quad (3.24)$$

According to Kippenhahn et al. (2012), τ_{nuc} is the most dominant time-scale during most of the star's lifetime, which implies that during long phases of nuclear burning as in our Sun, the star is in thermal equilibrium.

If I look at the global energy conservation of a star in stellar evolution:

$$\dot{W} = \frac{d}{dt}(E_{\text{kin}} + E_{\text{nuc}} + E_{\text{g}} + E_{\text{i}}) = -(L + L_{\nu}), \quad (3.25)$$

we arrive at the extremely useful homology relations for stars.

Definition 3.1.9 (homology relations) *Homology¹⁰ relations are simple analytic expressions that transform one solution of different stellar models that are calculated under similar assumptions into another solution. Two stars (0, 1) are said to be homologous to each other if the*

7: Examples for typical values of τ_{hydro} :

- ▶ MS Sun-like stars: 27 minutes
- ▶ Red Giant stars: 18 days
- ▶ White Dwarfs: 4.5 seconds

8: This is true because I know from Virial Theorem (see Equation 3.11):

$$L \simeq \left| \frac{dE_{\text{g}}}{dt} \right| \xrightarrow{\text{Virial theorem}} \frac{|E_{\text{g}}|}{L} \simeq \frac{E_{\text{i}}}{L}, \quad (3.18)$$

then I assume a sphere and obtain a simple value for E_{g} :

$$|E_{\text{g}}| \simeq \frac{GM^2}{2R}, \quad (3.19)$$

which then reinserted into Equation 3.18 yields Equation 3.20. For the Sun (and most other stars), this time-scale is of the order of 10 million years.

9: For an energy reservoir for Sun values of $\tau_{\text{nuc}} = 7 \times 10^{10}$ yrs

10: Etymologically speaking, this expression comes from ancient Greek and means "similarity laws"

following homology assumption holds (in Lagrangian coordinates):

$$\frac{m_1}{M_1} = \frac{m_0}{M_0} \rightarrow \frac{r_1}{R_1} = \frac{r_0}{R_0} \quad (3.26)$$

$$\rightarrow r \left(\frac{m}{M} \right) = R \times f_r \left(\frac{m}{M} \right) \quad (3.27)$$

$$\rightarrow P \left(\frac{m}{M} \right) = P_c \times f_P \left(\frac{m}{M} \right), \quad (3.28)$$

11: in the above Equation 3.27 f_r is a scaling function for radius r and f_P in Equation 3.28 is a scaling function for pressure

similarly for T, L_r , where the scaling functions¹¹ f_i are independent of the mass M of the star, but the constants are dependent on stellar mass and composition.

We find the following relationships for stars that are homologous to one another:

$$\frac{P}{m} \sim \frac{m}{r^4} \quad (3.29)$$

$$\frac{r}{m} \sim \frac{1}{r^2 \rho} \quad (3.30)$$

$$\frac{T}{m} \sim \frac{L_r}{r^4 T^3} \quad (3.31)$$

$$\frac{L_r}{m} \sim \epsilon \quad (3.32)$$

From the homology relations I can derive a mass-luminosity relation that is very fundamental in stellar physics. For MS stars, taking Equation 3.29, Equation 3.30 and the equation of state of the star, the homology analysis yields

Definition 3.1.10 (Mass-Luminosity-Relation for homologous stars)

$$L \simeq \mu^4 M^3, \quad (3.33)$$

where μ is the mean molecular weight ($rT \sim \mu m$) and I assume $m = M$.

This relation implies that the luminosity does not directly depend on energy generation ϵ ; also the proportionality factor is predominantly depends on the opacity of the stellar material, which in turn is determined by its chemical composition. If the energy generation in the star changes, it will adjust itself such that it has the same luminosity as before.

Furthermore, a mass-radius ($M-R$) relation is derived from the homology relations for stars.

Definition 3.1.11 (Mass-Radius-Relation for homologous stars)

The relation now depends on the energy generation too in contrast with the mass-luminosity ($M-L$) relation from Equation 3.33:

$$R \sim \mu^{0.61} M^{0.78} \quad \text{for the } pp\text{-cycle}, \quad (3.34)$$

$$R \sim \mu^{0.125} M^{0.5} \quad \text{for the CNO-cycle}, \quad (3.35)$$

where have the two main nuclear burning cycles on the MS, the pp -

and CNO-cycles, which are the two known main cycles by which stars convert H to He.

The $M-L$ relation from Definition 3.1.10, the $M-R$ relation from Definition 3.1.11 and the Stefan-Boltzmann law for black-body radiation, which is given by

$$L = 4\pi R^2 \sigma T_{\text{eff}}^4, \quad (3.36)$$

for a spherical star of radius R and effective temperature T_{eff} with σ being the Stefan-Boltzmann constant, I obtain equations for the luminosity of stars on the MS that depend only on the effective temperature:

$$\log_{10}(L) \propto 8 \log_{10}(T_{\text{eff}}) \quad (3.37)$$

We then obtain an equation for the MS and their lines of constant radii in the Hertzsprung-Russell diagram (HRD)¹²:

$$\log_{10}(L) \propto 4 \log_{10}(T_{\text{eff}}) \quad (3.38)$$

These lines are shallower than Equation 3.37. Equation 3.38 defines how stars on the MS lie in the HRD.

The lifetime of stars can be derived from the $M-L$ relation and $\tau_{\text{nuc}} \sim E_{\text{nuc}}/L \sim M/L$ to get

$$\tau_{\text{nuc}} \sim M^{-2}, \quad (3.39)$$

which reveals a central result in stellar evolution, which also has an enormous impact on the evolution star clusters, which are at the centre of my research thesis:

More massive stars are brighter, but have shorter lifespans. In phases beyond the MS, where He is burned in the core, the nuclear reaction energy release is smaller and the luminosities are generally larger, which leads to shorter lifetimes. Consequently, the total lifetime of a single star is dominated by its time spent on the MS.

Through the homology relations values of the central temperature T_c , central pressure P_c , and central density ρ_c of a star on the MS are obtained, which all depend on the stellar mass and the nuclear energy generation. Increasing stellar mass along the MS leads to:

1. an increase of central temperature T_c ,
2. a decrease of central density ρ_c if the CNO-cycle ($1.3 M_{\odot} \lesssim M$) is the dominant nuclear burning mechanism, while ρ_c increases if the pp-cycle ($M \lesssim 1.3 M_{\odot}$) dominates,
3. and a decrease of the central pressure P_c .

Hence, with increasing mass, stars along the MS are hotter and radiation pressure becomes increasingly dominant until it dominates completely for very high mass stars.

Finally, I discuss the homologous contraction of a gaseous sphere. This analysis yields a relation between the central temperature and central density. For ideal gases, their contraction lead to heating of the gas and for non-relativistic strongly degenerate gases, this contraction leads to cooling in a transition from non-degenerate

12: The HRD shows a correlation between the observable stellar properties of the stellar effective temperature T_{eff} and its luminosity L . Ejnar Hertzsprung discovered the differences in luminosity of red stars and separated them into "giants" and "dwarfs". Together with Henry Norris Russel, he devised the HR diagram, in which the stars and the properties of the spectra are plotted. L of a star in this diagram is a function of its spectral type, which in turn depends mainly on the star's surface temperature. The classification is done with the help of the star's absorption lines. The stars are subdivided in seven spectral classes (O, B, A, F, G, K, M), which in turn have ten sub-classes. These sub-classes have numbers. New discoveries have led to the adoption of the L and T spectral classes for the extremely faint red dwarfs and brown dwarfs, respectively.

to a strongly degenerate region, which leads to another important result:

Low mass stars will never ignite certain elements, because at some stage they become degenerate in the core and the central temperature drops upon further contraction.

3.1.3 Fundamental parameters - mass and composition

While they are incredibly useful to understand fundamental relations in stellar astrophysics, the homology relations (see Section 3.1.2) cannot be applied over the full evolution of the star and are typically only applied to MS stars. I need other ways to describe the full evolution of a star. In general, the fundamental parameters of stellar evolution are the zero-age (initial) MS (ZAMS) mass and the (homogeneous) chemical composition.

Other very important parameters independent of mass and composition are rotation and magnetic fields. (Fast) rotation can lead to additional interior mixing, which changes the chemical composition of the star. Magnetic fields may influence the pressure balance and interact with convection and rotation, which is probably most important for massive stars.

In the stellar evolution codes that I am using for this thesis, the masses, metallicities, stellar types and ages are the input parameters for the evolution of the intrinsic properties of the stars, see also Section 8.2 and Hurley et al. (2000).

3.1.4 Mass change of stars - stellar winds

The masses of all stars change throughout their lives through winds, parameterised by a stellar mass loss rate \dot{M} . Stellar winds are the outflows of matter leaving the stellar surface with an energy sufficient to escape from the star's gravity. The main question is what the nature of the force is that is powerful enough to overcome the star's gravity. Different types of stars have different winds. Recently, excellent reviews of the winds of lower mass stars were written by Decin (2020) and similarly of high mass stars by Vink (2021).

Definition 3.1.12 (Discretization of stellar mass loss rates) *It is useful to consider three classes of stars to differentiate between mass loss rates.*

- ▶ **Hot luminous stars (HLSs)**¹³
Massive MS or evolved stars ($R \sim 10 R_{\odot}$), have strong and fast (terminal wind velocities of $v_{\infty} \sim 2000 - 3000 \text{ km s}^{-1}$) stellar winds powered by radiative line driving. These HLSs have extremely high mass loss rates \dot{M} of $10^{-8} - 10^{-4} M_{\odot} / \text{yr}$.
- ▶ **Cool luminous stars (CMSs)**
For example, AGB stars ($R > 100 R_{\odot}$) have strong and slow

13: radiative line driving means radiative forces that are exerted on atomic lines, such as ionized C,N,O or Fe-group elements, which have orders of magnitudes of more lines than elements, such as H and He, that are still much more abundant in the HLSs even at late evolutionary stages. The resonance lines in the optically thick regions are located just a couple of R_{\odot} around the HLS)

$(v_\infty \leq 25 \text{ kms}^{-1})$ stellar winds that are pulsation-driven. These two have very high mass loss rates \dot{M} of $10^{-8} - 10^{-4} M_\odot/\text{yr}$.¹⁴

► **Solar-type stars (SLs)**

The stars have hot surrounding coronae and have a weak stellar wind that is a pressure-driven coronal wind of intermediate speeds ($v_\infty \leq 400 - 800 \text{ kms}^{-1}$). They have very low mass loss rates \dot{M} of $10^{-14} M_\odot/\text{yr}$.

Many stellar evolution models used inside N -body codes express wind acceleration by a Γ factor (see e.g. Giacobbo et al., 2018). Γ is defined as the ratio of radiative over gravitational acceleration. Radiative acceleration is due to radiative pressure and introduces an extra force acting on a spherically symmetric, isothermal wind. It is related to electron scattering Γ_e or dust scattering Γ_d , for example. These quantities are introduced into the momentum equation of an isothermal, spherically symmetric stellar wind, which leads to an effective gravitational acceleration $g_{\text{eff}}(r)$. Using $g_{\text{eff}}(r)$, I can calculate the escape velocities and these are lower by the introduction of the extra force. However, it depends very strongly on the distance to the stellar surface, where this additional force is introduced; the farther out it occurs, the less impactful it becomes on the overall stellar mass loss rate. Therefore, since dust grains form very close to the star¹⁵, these are very impactful on the mass loss rate. In red supergiants (RSGs), on the other hand, these grains form much farther out and therefore, dust-driven winds are generally not relevant here. Moreover, radiation transport and the chemistry in the wind are both essential to a full modelling of a stellar wind. It is important to state that in general, there is no full theory of stellar winds available (Decin, 2020). Furthermore, the layperson is overwhelmed by the large number of mass loss rate prescriptions derived predominantly from observations, which differ enormously in magnitude and slope (Decin, 2020), see also Figure 3.4 for an example RSG star and the impact of the choice of the mass loss recipe.

The choice of mass loss recipe has an enormous impact on the outcome of realistic N -body simulations and the dynamics of the star cluster as described in this review. As an astrophysical community, I am just at the beginning of unravelling the complexities of specific stellar winds, such as Wolf-Rayet (WR) stars (Sander & Vink, 2020) or the impact of pulsations and variability on winds in AGB and post-AGB stars (Trabucchi et al., 2019) before a fully self-consistent theory can be envisioned.

3.1.5 Discretizing ZAMS mass in stellar evolution

The mass ranges given below depend on the exact chemical composition of the stars. Discretization of stellar masses is very helpful in understanding the impact of ZAMS mass on stellar evolution. In the following, I put the stars into six distinct mass bins depending on their ZAMS masses.

14: CMSs are cool and therefore, it is believed that close to the stellar atmosphere, these stars can form dust grains, because the pulsations from the star can form regions of large density just above the stellar atmosphere. The dust grains absorb momentum and collide with surrounding gaseous species and thus you get a launch of a stellar wind.

15: as in the AGB star discussed as an example of a CMS in Definition 3.1.12

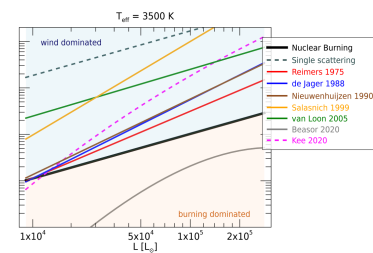


Figure 3.4: Mass-loss rate as a function of luminosity for a RSG star at a fixed temperature of 3500K. Empirical mass-loss rate relations are displayed with a full line, semi-empirical relations with a dash-dotted line, and theoretical relations with a dotted line. The rate at which hydrogen is consumed by nuclear burning, $\dot{M}_c = 1.02 \times 10^{-11} L_\odot$, is shown as thick black line; the single-scattering radiation pressure limit for an expansion velocity of 12 kms^{-1} is shown as dashed dark grey line. Stellar mass loss rules the evolution of the RSG stars if the wind mass-loss rate exceeds the nuclear burning rate, as indicated by the light-blue region; the hydrogen-burning dominated region is indicated by the light-orange region (caption and figure adapted from Decin (2020)).

Definition 3.1.13 (Brown Dwarfs (BDs): $M_{\text{Jup}} < M/M_{\odot} \lesssim 0.075$)
These stars do not reach the critical (central) temperature to supply their luminosity by nuclear H-burning, because they quickly reach a strong degeneracy and cannot contract and heat up any longer. They possess a lower limiting mass, which is $0.075 M_{\odot}$. They are fully convective stars.

In general, I do not consider BDs in N -body simulations, since I typically sample the stellar masses from a Kroupa (2001) IMF that has a lower mass limit of $0.08 M_{\odot}$. However, BDs can be produced by binary stellar evolution processes, see Section 3.2.

Definition 3.1.14 (Very low-mass (VLMS) stars: $0.075 < M/M_{\odot} \lesssim 0.4$)
VLMSs never reach the critical temperature for He-burning. They evolve extremely slowly and are fully convective, which means that the surface composition and structure influence the whole star. They evolve from ZAMS to cooling of a HeWD. In general, they leave the RGB once their core has grown to about 95% of their total mass. Due to their fully convective nature, they evolve along the Hayashi line¹⁶.

16: The Hayashi lines in the HRD are evolutionary stellar tracks of almost constant T_{eff} (Hayashi, 1961).

VLMSs are very abundant in my N -body simulations in presented in Kamlah, Leveque, et al. (2022) and Kamlah, Spurzem, et al. (2022). They are very important in regulating the angular momentum transport of star clusters and therefore, even though they are not very massive they can have a significant impact on the star cluster's evolution.

Definition 3.1.15 (Low-mass (LMS) stars: $0.4 < M/M_{\odot} \lesssim 2.5$)
These stars burn He in their degenerate cores¹⁷. While VLMS are fully convective, with increasing mass convection withdraws from the center and the convective envelope gets increasingly thinner, until it disappears at around $M \simeq 1.3 M_{\odot}$. At the center¹⁸, as T_c increases the mass, H-burning switches from predominantly pp-chains to the CNO-cycle. Here, core convection sets in at around $M \simeq 1.3 M_{\odot}$ and all stars above this mass have convective cores. These stars approach the RGB and evolution along the Hayashi-line and in the process the convective envelopes form and deepen with time. In such a star the convection mixes nuclear products (C,N,He) from the core to the surface, which is called the first dredge-up. On the RGB itself, the H-burning shell reaches a point of deepest convection, which increases the H-abundance in the shell. This process leads to a sudden decrease in luminosity at the deepest convection, which then increases again. Finally, the stars climb up the RGB and at the RGB-tip, He is ignited (outside of the stellar center) at a very similar luminosity for all LMSs. This ignition happens under degenerate (core) conditions in a so-called He flash, which is a violent and extremely luminous ($10^{10} L_{\odot}$) event. Following the He-flash, the star readjusts its core and lifts the degeneracy at beginning of the horizontal branch (HB). I have a lower luminosity and higher T_{eff} and core He-burning sets in (as it occurs in IMS).

17: Above $2.5 M_{\odot}$, He is ignited under non-degenerate conditions and this sets the upper limit for LMSs.

18: There are three commonly discussed dredge-ups, during which a convective layer extends from the stellar surface down to the interior:

1. dredge-up: occurs when a MS star enters the Red Giant Branch (RGB). The convective layer extends into previously burnt H layer, from where the He is mixed outwards and mixed with the still burning H.
2. dredge-up: occurs on the RGB if the star is massive enough. The convective envelope reaches into the H exhausted layers and CNO-cycle elements are convectively transported to the surface. Once this happens, the H-rich envelope reignites.
3. dredge-up: occurs on the Asymptotic Giant Branch (AGB) after the He-flash. He, C and isotopes created by the s -process are mixed to the stellar surface. If this process of dredging up repeats many times, the star is known as a Thermally Pulsating Asymptotic Giant Branch (TPAGB) star.

LMSs are also very abundant in the N -body simulations in presented

in Kamlah, Leveque, et al. (2022) and Kamlah, Spurzem, et al. (2022) and in Pop-I and Pop-II star clusters in general. As such much like VLMSs, they are very important in regulating the angular momentum transport of star clusters and the global evolution. Furthermore, they can donate significant mass in several binary stellar evolution processes, see also Section 3.2.

Definition 3.1.16 (High-mass (HMS) stars: $8 < M/M_{\odot} \lesssim 150$) *The physics of these stars is very difficult to model. Convective overshooting and semi-convection and additional processes, such as waves, mix material within the star, thus producing a practically fully convective star. As a result, the H- and He-burning cores are enlarged and extends the MS-lifetime. This process also raises the luminosity of the stars. The mass loss from these stars is strong at all phases of the evolution and in the extreme approaches the WR or He star mass loss $10^{-2} M_{\odot}/\text{yr}$ (Vink, 2021). For these massive stars, rotation is a crucial process, which influences the size of the core and mixes material to the surface and thus uncovers interior and layers that were already processed by nuclear fusion cycles. As a result, the star's evolution is affected significantly.*

A very high fraction of these stars are also found in binaries (Kiminki et al., 2012; Kobulnicky et al., 2014; Sana et al., 2012; Sana & Evans, 2011) and thus most of them are affected by binary processes outlined in Section 3.2. The strongest implication from a collisional dynamical perspective is that these stars may merge in primordial binaries to form even higher mass stars, before forming a compact remnant such as a smBH, ImBH or NS¹⁹. I have put the upper mass limit at $150 M_{\odot}$ but to decide whether there is an upper mass limit for the stellar mass in general, there are several criteria. For example, one might use the Eddington limit (Bestenlehner, 2020)²⁰. Sanyal et al. (2015) found that massive stars exceed the Eddington limit locally in the interior, but this only results in inflated envelopes and does not necessarily lead to massive mass loss (perhaps in combination with pulsations and eruptions). Another mechanism that might limit that upper mass is the ϵ -mechanism, which is important in radiative dominated envelopes as found in massive stars. In this mechanism it is proposed that increased pulsations may lead to shedding of the outermost layers of the massive star until a mass is reached until this mechanism is no longer relevant. From observations, I have the Humphreys-Davidson limit (Humphreys & Davidson, 1979), which indicates a lack of stars above some brightness taken as evidence for a lack of stars. However, in contrast to all of these upper limits, a star candidate with a mass of around $250 M_{\odot}$ was found in R136, the central cluster in the Tarantula Nebula of the Large Magellanic Cloud (LMC Bestenlehner et al., 2020).

Definition 3.1.17 (Extremely massive (EMS) stars: $150 < M/M_{\odot}$) *In collisional dynamical simulations, it is possible for stars to merge in the very early cluster evolution to produce stars with many hundreds of M_{\odot} or even above $1000 M_{\odot}$ (Banerjee, 2021b; Reinoso et al., 2021; Rizzuto, Naab, Spurzem, Arca-Sedda, Giersz, et al., 2021; Rizzuto, Naab, Spurzem, Giersz, et al., 2021; Tanikawa, Susa, et al., 2021; Wang*

19: Or they fall in the pulsational pair instability mass gap and produce no remnant, see Section 3.1.6.

20: This limit follows from the increasing radiation pressure that drive the stellar wind with increasing mass of stellar mass, see Kippenhahn et al. (2012). At the so-called Eddington luminosity the star becomes unbound:

$$L_{\text{Eddington}} = \frac{4\pi cGM}{\kappa}. \quad (3.40)$$

Since I know from Definition 3.1.10 that $L \sim M^3$, where the stars reach the opacity-dependent Eddington limiting luminosity. For HMSs, where electron scattering is the most efficient, the limiting mass is about $200 M_{\odot}$.

et al., 2022).

This physical process has many implications and for our modelling it means that I need robust stellar evolution models for these mass ranges. Practically speaking, I could use the PARSEC isochrones up to $350 M_{\odot}$ (Y. Chen et al., 2015; Spera et al., 2015), but depending on the initial stellar merger rate in simulations, I might even surpass this maximum mass. For very low metallicities ($10^{-2} \geq Z/Z_{\odot} \geq 10^{-8}$) and for masses up to $10^4 M_{\odot}$, new stellar evolution models have become available (Tanikawa et al., 2020). Particularly noteworthy is here that the metallicity range is such that these could also be used to model extremely dense (many collisions that produce EMSs) GC-like star clusters.

3.1.6 Formation of compact objects and their natal masses, kicks and spins

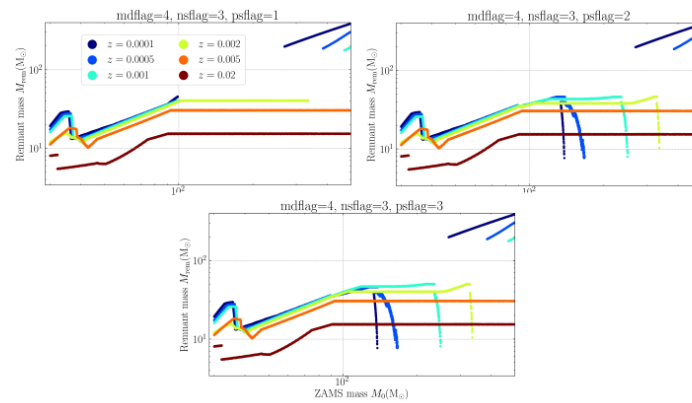


Figure 3.5: Initial-final-mass-relations (IFMRs) of the BHs from McLUSTER samples ($N = 2.5 \times 10^4$ single ZAMS stars) depending on six different metallicities ranging from $Z=0.0001$ to Solar metallicity at $Z=0.02$. The McLUSTER version uses level C stellar evolution (Kamlah, Leveque, et al., 2022). Shown are the recipes for the “strong” (psflag=1) on the top left (Belczynski et al., 2016), “weak” (psflag=2) on the top right (Leung, Blinnikov, et al., 2020; Leung et al., 2019) and the “moderate” (psflag=3) (P)PISNe on the bottom (Leung, Blinnikov, et al., 2020; Leung et al., 2019). The ZAMS stars suffer wind mass loss via metallicity-dependent winds (mdflag=4) (no bi-stability jump) from (Belczynski et al., 2010) and the core-collapse SNe are set to “rapid” (C. L. Fryer et al., 2012) (Figure adapted and caption taken from Kamlah, Leveque, et al. (2022) and it is also shown in a similar fashion in Spurzem and Kamlah (2023)).

Depending on the progenitor star core mass and by extension ZAMS mass, a compact object (WD, NS, BH) may form. Oftentimes binary processes are involved (Fragos et al., 2009; Willems et al., 2005; Wong et al., 2012, 2014), but these are discussed in Section 3.2. The following processes apply to all single stars in the relevant mass ranges.

The formation of a compact object is associated with a natal remnant mass, a natal kick and a natal spin, which are all subject to significant theoretical and observational uncertainty. Nevertheless, it is important to model these as accurately as possible, because the global dynamical evolution of a collisional stellar system critically depends on these.

The natal mass depends on a number of factors. I will only focus now on the collapse mechanism and its associated fallback onto the proto-remnant core and not the mass loss in the progenitor star, although it is also instrumental. The impact of the mass loss

has been discussed already in a previous section, see [Section 3.1.4](#). Traditionally, the natal masses of the WDs (and their three main sub-types HeWDs, COWDs, ONeWDs following [Hurley et al. \(2000\)](#)) and their dependence on the progenitor masses are modelled by ([Han et al., 1995](#); [Hurley & Shara, 2003](#); [Hurley et al., 2000](#))²¹. For NSs a maximum mass of around $2.5 M_{\odot}$ ([Linares, 2020](#); [Linares, 2018](#)) and the relationship follows typically [Hurley et al. \(2000\)](#), but the exact masses are unknown because of the large uncertainties mainly in the internal structure of a NS ([Lattimer & Prakash, 2004](#); [Lattimer, 2012](#)).

In addition to [Hurley et al. \(2000\)](#) the possibility of a so-called

21: There are also other newer and metallicity-dependent IFMRs for WDs that are not very different from the aforementioned ones (see e.g. [Cummings et al., 2018](#); [Meng et al., 2008](#)).

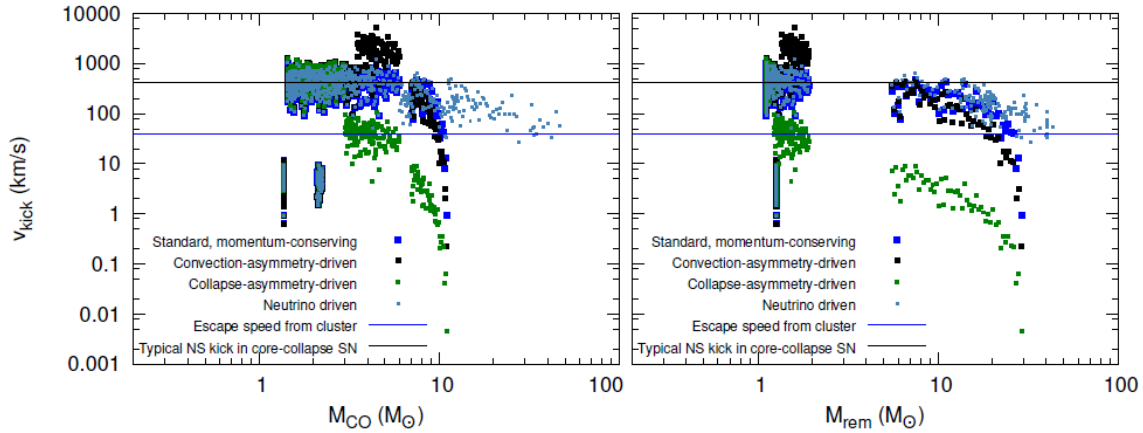


Figure 3.6: Plot showing natal kick prescriptions, v_{kick} (all of them are at least also available in `NBODY6++GPU`, `MOCCA`, `MCLUSTER` and `PETAR`), as generated by `NBODY7` in ([Banerjee et al., 2020](#)). A metallicity of $Z=0.0001$ is assumed here. The models feature rapid core-collapse SNe from ([C. L. Fryer et al., 2012](#)) and strong (P)PISNe from ([Belczynski et al., 2016](#)). Due to the logarithmic vertical axis, direct-collapse BHs with a fallback fraction, $f_{\text{fb}} = 1$ and $v_{\text{kick}} = 0$ are not shown in these panels. The sharp drop in v_{kick} with increasing m_{CO} or m_{rem} is the approach towards direct collapse. The typical v_{esc} for the $M_{\text{cl}}(0) \approx 5.0 \times 10^4 M_{\odot}$ and $r_{\text{h}}(0) \approx 2$ pc clusters considered here (blue, solid line). The velocity dispersion of the Maxwell distribution from all the kick models are scaled is 265.0 km s^{-1} from ([Hobbs et al., 2005](#)). It is apparent that for these settings the collapse asymmetry driven kicks will produce most (stellar mass) BHs below v_{esc} of the cluster. (Figure adapted from ([Banerjee et al., 2020](#)) and it is also shown in a similar fashion in [Spurzem and Kamlah \(2023\)](#)).

electron-capture SNe (ECSNe)²² that leads to the formation of a NS ([Ivanova et al., 2008](#); [Kiel et al., 2008](#); [Leung, Nomoto, & Suzuki, 2020](#); [Nomoto, 1984](#); [Nomoto, 1987](#); [Podsiadlowski et al., 2004](#)), which has very important properties that are discussed below, has been included in many stellar evolution and N -body codes ([Banerjee et al., 2020](#); [Belczynski et al., 2008](#); [Kamlah, Leveque, et al., 2022](#)). Most attention has arguably been paid to the remnant masses of BHs ([Belczynski et al., 2008](#); [Eldridge & Tout, 2004](#); [C. L. Fryer et al., 2012](#)) and a number of collapse mechanisms for certain mass ranges have been proposed. The remnants of such a SNe is shown in [Figure 3.7](#) from the famous Crab Nebula. Most widely used in simulations at the moment are the ‘rapid’ or ‘delayed’ core-collapse SNe models by [C. L. Fryer et al. \(2012\)](#) in combination with various (pulsational) pair instability SNe ((P)PISNe) stellar evolution recipes ([Belczynski et al., 2016](#); [C. L. Fryer et al., 2001](#); [Leung, Blinnikov, et al., 2020](#); [Leung et al., 2019](#); [Spera & Mapelli, 2017](#); [Woosley, 2017](#); [Woosley & Heger, 2021](#); [Yoshida et al., 2016](#)). I will highlight each of these briefly now, also because they are central in my comparison study presented in [Kamlah, Leveque, et al. \(2022\)](#).

22: This SNe occurs due electron-capture onto the isotope ^{24}Mg , which results in a removal of the electron-degeneracy pressure in the stellar core and therefore, in a sudden drop in pressure within the star.

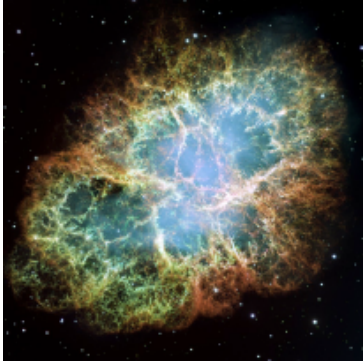


Figure 3.7: The Crab Nebula, which are the remnants of SN 1054, taken by the Hubble Space Telescope in visible light. This SNe was already recorded by middle-age Chinese astronomers in 1054. Tominaga et al. (2013) claim that the progenitor star, which was an AGB star, that was responsible for the Crab Nebula underwent an ECSNe and produced a NS. Credit: NASA/ESA.

23: the material that bounces off the proto-remnant core accelerates in-falling material and therefore does work and slows down in the process to a halt.

Definition 3.1.18 (core-collapse SNe) *These two mechanisms are extremes for the the convection-enhanced neutrino-driven paradigm based on current (2012) knowledge of SNe and gamma-ray burst explosions from C. L. Fryer et al. (2012).*

- ▶ **Rapid SNe mechanism:** fast convection explosions where explosions only occur if they happen in the first 250 ms after bounce.
- ▶ **Delayed SNe mechanism:** delayed-convection explosions which can occur over a much longer time-scale and it is assumed that it takes up to 20 s.

In general, the remnant formation process may be split three-fold according to C. L. Fryer et al. (2012):

1. Stellar collapse and bounce: the core compresses under its own weight, leading to electron capture removing degeneracy pressure and dissociation of core elements into α particles removing thermal support. This leads to the acceleration of the compression, electron capture and Fe dissociation. Consequently, I have a runaway collapse at extreme speeds close to c until the neutron degeneracy pressure (and other nuclear forces) halt the collapse. The in-falling material then bounces off of the proto-remnant core surface creating a shock wave until neutrino losses sap the shock wave's energy reservoir. This shock may happen multiple times.
2. Convective engine: for stars with masses above $11 M_{\odot}$ the instabilities form in region between the proto-NS surface, where the bounce occurs and the region where the bounced off material stalls²³:
 - ▶ Rayleigh-Taylor instability (see e.g. Kuranz et al., 2018),
 - ▶ Standing accretion shock instability (SASI; see e.g. Fernández, 2010).

These instabilities convert energy leaking out of the proto-NS in the form of neutrinos to kinetic energy, which results in the convective regions being pushed outwards. A SNe happens if the energy in this convective region overcomes the ram pressure of the in-falling stellar material. This is also known as convection-enhanced, neutrino-driven SNe.

3. Post-explosion fallback: crucially, the amount of fallback onto the proto-remnant core is determined by the time when the energy in the convective region overcomes the ram pressure. The amount of energy in the convective region is the amount of energy in the explosion (*assumption*). The mass of the fallback is the mass of the material that does work against the in-falling material subsequently decelerating.

The (P)PSiNe mechanisms shed the masses of extremely high mass stars stars prior too explosion by the creation of electron-positron pairs (see e.g. Woosley, 2017). These pairs effectively remove pressure from outward photons, until O (oxygen) in the stellar core ignites in

a flash, which creates a pulse and a thermonuclear reaction in the outward direction, after which the core stabilises. For the PPISNe mechanism, these pairs carry away around $10\text{--}25 M_{\odot}$, while for the PISNe, this mechanism completely disrupts the SNe²⁴ and I also may say it is a *failed* SNe²⁵.

Figure 3.5 shows a suite of small simulations when McLUSTER (Kamlah, Leveque, et al., 2022; Küpper et al., 2011a; Leveque, Giersz, Banerjee, et al., 2022) is used as a population synthesis tool with level C stellar evolution (as outlined in (Kamlah, Leveque, et al., 2022)). It shows all relevant remnant mass phases, which can be subdivided into a core-collapse SNe, PPISNe, PISNe and a direct collapse phase in increasing ZAMS mass (This is an extension of the core-collapse SNe models for ZAMS masses above which PISNe is ineffective; in our case an extension of the rapid SNe models by C. L. Fryer et al. (2012)). Two interesting conclusions can immediately be drawn here: first, the metallicity is incredibly important for the production of high mass BHs, because progenitor stars with high metallicities will contain more metal lines for radiative wind mass loss. Secondly, the (P)PISNe prescriptions available from theory can have an enormous impact on the abundance of BHs. This might particularly important in Pop-III star clusters, see Section 2.1.4, where IMBH progenitor stars are postulated to have large enough masses and crucially also low enough metallicities from birth to evolve by (P)PISNe from interior evolution alone (see e.g. Kamlah, Spurzem, et al., 2022; Wang et al., n.d.) for recent N -body simulations of these clusters; see Section 2.2.2 for a more general discussion of Pop-III stars in the initialisation of star cluster simulations.

The magnitude of natal kicks results in very general terms from an inherent asymmetry in the SNe process. Their magnitude is rather uncertain across the entire progenitor mass spectrum (Hansen & Phinney, 1997; Hobbs et al., 2005). Natal kicks affect the dynamical stability of a binary, which forms a compact object within it, and are even able to disrupt a binary completely. This fact also implies that a large amount of gravitational binding energy in binaries may be removed from the cluster in this way and this will consequently impact the global cluster evolution. In the following I briefly summarize the expected natal kick velocity magnitudes across the compact object mass spectrum:

- ▶ WDs are associated with low velocity kicks of the order of 10^0 kms^{-1} (Fellhauer et al., 2003; Jordan et al., 2012; Vennes et al., 2017).
- ▶ NSs may reach fallback-scaled kicks above 10^3 kms^{-1} through core-collapse mechanisms (Belczynski et al., 2008; C. L. Fryer et al., 2012). The exception is the ECSNe, which produces NSs with natal kicks of only 10^0 kms^{-1} ²⁶, meaning that they can be retained in a star cluster (simulation) (B. P. Abbott et al., 2017a; R. Abbott et al., 2020a; Clark, 1975; Kamlah, Leveque, et al., 2022; Manchester et al., 2005). It is important to note here that NSs can also be produced by binary processes involving mass transfer through accretion or mergers, which result in the accretion induced and merger induced SNe, respectively (see also Section 3.2). In most models, these SNe also result in natal kicks with very low magnitudes. In Kamlah, Leveque,

24: by the creation of multiple pulses in the above fashion.

25: Although, the actual existence of the (P)PISNe is still under debate, recently a strong candidate for such an even has been found by Woosley and Smith (2022).

26: This is the case because the low explosion energy and the extremely rapid outward expansion of SNe shocks and postshocks are preventing large natal kicks as was found in 2D/3D simulations of such explosions by Gessner and Janka (2018)

et al. (2022) I use the same magnitudes as for NSs produced by ECSNe following Gessner and Janka (2018).

- ▶ BHs receive kicks typically scaled by fallback during core-collapse SNe (Belczynski et al., 2008; C. L. Fryer et al., 2012).

Concerning the fallback of stellar material onto the proto-remnant core, it is important to know that the larger the fallback the lower resulting kick is (see e.g. Belczynski et al., 2008). Furthermore, in simulations, it is typically assumed that the asymmetry is produced by a dominant process (Banerjee et al., 2020; Banerjee, 2021a):

- ▶ convection-asymmetry driven kicks (C. L. Fryer & Young, 2007; Scheck et al., 2004, 2008),
- ▶ collapse-asymmetry driven kicks (Burrows & Hayes, 1996; C. L. Fryer, 2004; Meakin & Arnett, 2006, 2007),
- ▶ neutrino-driven natal kicks (Banerjee et al., 2020; Banerjee, 2021a; C. L. Fryer & Kusenko, 2006; G. M. Fuller et al., 2003).

These kicks result in different natal kick velocities and are therefore influential on the retention fractions of BHs in star cluster simulations (Banerjee et al., 2020), which can be seen in Figure 3.6 for a sample of NBODY7 simulations from Banerjee et al. (2020). It is apparent that for these settings the postulated collapse asymmetry driven kicks will produce most (stellar mass) BHs below v_{esc} of the cluster.

The natal spins of compact objects are important in general binary evolution (see also Section 3.2) and can also have significant impact on the mergers of compact objects, for example in a BH-BH merger (Morawski et al., 2018, 2019). In the following, I focus on BHs, but the same arguments can be extended to NSs and WDs and the discussion is largely taken from Kamlah, Leveque, et al. (2022). In general, the spin angular momentum of the parent star does not necessarily translate directly into the natal spin angular momentum of the BH upon collapse. To quantify the spin, Kerr (1963) define a dimensionless parameter a_{spin} that accounts for the natal spin angular momentum. Banerjee (2021a) assumes that the magnitude of a_{spin} for the BHs is set directly at the moment of birth without any related mass accretion or GR coalescence processes. I highlight three natal spin models that are available now in NBODY7, NBODY6++GPU, MCLUSTER, PETAR and MOCCA (see also Kamlah, Leveque, et al., 2022)

- ▶ FULLER model: this model leads to zero natal spins (Banerjee, 2021a) as here the Tayler-Spruit magnetic dynamo can essentially extract all of the angular momentum of the proto-remnant core leading to nearly non-spinning BHs (J. Fuller & Ma, 2019; J. Fuller et al., 2019; Spruit, 2002).
- ▶ GENEVA model: the basis for this model is the transport of the angular momentum from the core to the envelope. This is only driven by convection, because the GENEVA code does not have magnetic fields in the form of the Taylor-Spruit magnetic dynamo. This angular momentum transport is comparatively inefficient and leads to *high* natal spins for low to medium mass parent O-type stars, whereas for high mass parent O-type stars, the angular momentum of the parent star may already

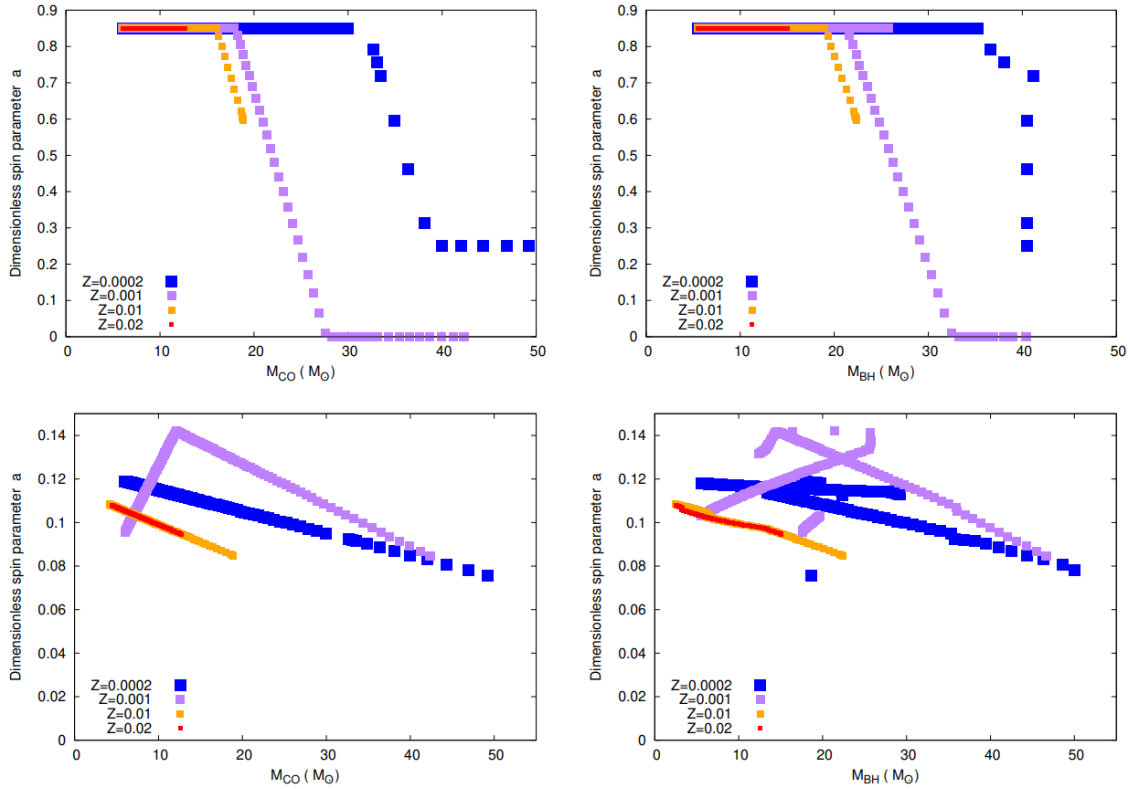


Figure 3.8: Plot showing the magnitude of dimensionless spin parameter, a_{spin} , of stellar-remnant BHs at birth (i.e., of BHs that have not undergone any mass accretion or GR coalescence after their formation) as a function of the progenitor star’s carbon-oxygen core mass, M_{CO} (left column), and the BH mass, M_{BH} (right column) (all of them are at least also available in `NBODY6++GPU`, `MOCCA`, `MCLUSTER` and `PETAR`), as generated by `NBODY7` in Banerjee (2021a).

Top panels: the N -body models corresponding to these panels employ the “GENEVA model” of Belczynski et al. (2020) for BH spin and comprise only single stars initially, whose ZAMS masses range from (0.08 – 150.0) M_{\odot} and which are distributed according to a standard Kroupa IMF (Kroupa, 2001). The models feature rapid core-collapse SNe from C. L. Fryer et al. (2012) and strong (P)PISNe from Belczynski et al. (2016). The models are shown for four metallicities, $Z = 0.0002, 0.001, 0.01,$ and 0.02 as indicated in the legends.

Bottom panels: the N -body models corresponding to these panels employ the “MESA model” of Belczynski et al. (2020) for BH spin. The other model characteristics are the same as those in the top panels except that the “weak” PPSN mass prescription (Leung et al., 2019) is utilized (resulting in the non-monotonic behaviour with respect to M_{BH} , which, here, extends up to $\approx 50 M_{\odot}$ as opposed to the models in the top panels where M_{BH} is capped at $\approx 40.5 M_{\odot}$ due to the use of Belczynski et al. (2016). (Figure adapted from Banerjee (2021a)) and it is also shown in a similar fashion in Spurzem and Kamlah (2023)).

have been transported away in stellar winds and outflows and thus the natal BH spins may be low (Banerjee, 2021a; Eggenberger et al., 2008; Ekström et al., 2012).

- MESA model: this model accounts for magnetically driven outflows and thus angular momentum transport (Banerjee, 2021a; J. Fuller et al., 2019; Paxton et al., 2011, 2015; Spruit, 2002). This model thus generally produces BHs with much *smaller* natal spins than the GENEVA model described above. The GENEVA and the MESA models and their metallicity dependence are shown in Figure 3.8.

3.2 Binary stellar evolution

In addition to the astrophysical processes that affect all stars in isolation, the proximity (orbital period $P_{\text{orb}} \leq 10^4$ days P. P. Eggleton, 1996) to another star or compact object through the frequent

encounters in collisional stellar systems or through intrinsic binary evolution, can affect the individual stars or compact objects dramatically and I need to account for these in the simulations. A population synthesis code should include them all (P. Eggleton, 2006).

3.2.1 Stellar Spin and orbital changes due to mass loss or gain

27: Hurley et al. (2002) note that this mechanism wind mass transfer is crucial for the evolution of many exotic binary stars, such as symbiotic stars, which typically consist of a semi-detached RG and a WD in this case undergoing wind mass

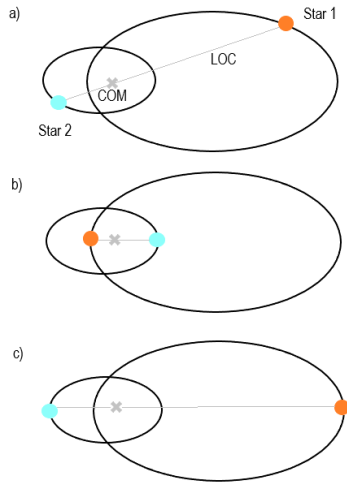


Figure 3.9: a) Schematic diagram of a binary star orbiting the common centre of mass (COM) with the mass of star 1 larger than star 2. The stars are joined by the line of centres (LOC); b) Star 2 is at periastron, therefore closest to star 1; c) Star 2 is at apastron, therefore furthest away from star 1. Mass transfer is more efficient at periastron than at apastron.

If two stars are in a binary, they can transfer mass via stellar winds²⁷ and therefore also transfer angular momentum even if they are not yet undergoing Roche-lobe overflow (RLOF P. Eggleton, 2006; Hurley et al., 2002; Tout, 2008a). If a secondary star accretes mass by passing through the wind of the primary star, it is spun up intrinsically by a fraction of the spin angular momentum that is lost by the donor star. The accretion rate is traditionally modelled by Bondi and Hoyle (1944), see the formula in Hurley et al. (2002):

$$\langle \dot{M}_{2A} \rangle = \frac{-1}{\sqrt{1-e^2}} \left(\frac{GM_2}{v_W^2} \right)^2 \frac{\alpha_W}{2\alpha^2} \frac{1}{(1+v^2)^{3/2}} \dot{M}_{1W}, \quad (3.41)$$

where $\langle \dot{M}_{2A} \rangle$ is the mean accretion rate by the secondary and \dot{M}_{1W} is the mean wind loss rate of the primary, $\alpha_W = 3.92 \times 10^8$ is a free parameter (Hurley et al., 2002), $v^2 = v_{orb}^2/v_W^2$, where v_W is the wind velocity, which is proportional to stellar surface escape velocity: $v_W^2 = 2\beta_W \frac{GM_1}{R_1}$, where β_W strongly depends on spectral type in many stellar evolution models (see e.g. Belczynski et al., 2008). The larger the star, the lower β_W . This quantity is observationally difficult to determine (Decin, 2020) and should be proportional to the escape velocity from the stellar surface of the star (Hurley et al., 2002).

The mass variations between companion stars also changes the orbital parameters of the binary star. In general, the eccentric orbit is circularised as a result of mass transfer being more effective at periastron than apastron, see Figure 3.9. Additionally, the accretor star is slowed down by drag induced by the wind it passes through and this dissipates angular momentum from the system. The orbital circularisation time-scale τ_{circ} as result of mass transfer is orders of magnitudes larger than the equivalent time-scale caused by tidal friction for the same binary star system.

3.2.2 Effects of tidal damping

Observations show that the rotation of close binary stars is synchronised with the orbital motion without any dynamical mass transfer having taken place (Lurie et al., 2017; Mazeh, 2008; Meibom & Mathieu, 2005). Therefore, there must exist a torque that transfers angular momentum between the stellar spin and the orbit in such a way that the binary approaches the observed equilibrium state that is characterised by corotation (spin-orbit synchronisation time-scale τ_{sync}) and a circular orbit (circularisation time-scale τ_{circ} Hurley et al., 2002; Hut, 1981; Tout, 2008a; Zahn, 1977). Alternatively, dissipation of energy might also lead to an accelerated in-spiral of the binary

stars (Hut, 1980; Rasio et al., 1996; Tout, 2008a).

When two binary star members are detached but sufficiently close, tidal interaction between them becomes important. The mere presence of a companion star causes a tidal force that elongates a star along the line between the centres of mass, thereby resulting in tidal bulges (see e.g. Hurley et al., 2002).

Definition 3.2.1 (Equilibrium tides) *When the binary component rotates uniformly with a circular orbital motion, then the tidal bulges on its stellar surfaces are steady and the stars are in hydrostatic equilibrium. This process ignores dissipation within the stars.*

However, when this condition no longer holds, the hydrostatic equilibrium is disrupted and the star undergoes forced stellar oscillations. This scenario is described by a combination of equilibrium and now also dynamical tides, the latter of which produce much smaller tidal bulges than the former and they can also take any orientation (P. Eggleton, 2006; P. P. Eggleton et al., 1998; Hurley et al., 2002; Siess et al., 2013; Zahn, 1970, 1974, 1975, 1977).

Definition 3.2.2 (Dynamical tides) *A star undergoes forced stellar oscillations in a binary star due to tidal interaction. This disrupts its hydrostatic equilibrium. Therefore, dynamically induced tidal bulges are induced in the star, which can take any orientation and are much smaller than the bulges created by the equilibrium tide, that also exist in the same star even in this scenario.*

Dissipative processes within a star cause the tides to be misaligned with the line of centres.

This results in a torque that transfers angular momentum between the stellar spin and the orbit (Hurley et al., 2002). This dissipation is non-conservative and happens on relatively long time-scales (P. Eggleton, 2006).

The dissipative processes within a star depend on the stellar structure. Typically, a distinction is made between stars with appreciably deep convective envelopes and stars with radiative envelopes. The tides dissipate energy and the binary system approaches an equilibrium state that is characterised by a circular orbit and corotation (Hurley et al., 2002; Hut, 1981; Tout et al., 2008; Zahn, 1977).

- ▶ Stars with appreciably deep *convective* envelopes: turbulent viscosity that acts on equilibrium tides (the same effect on dynamical tides is negligible (Zahn, 1975, 1977)) is the most efficient form of dissipation (Hurley et al., 2002; Hut, 1981; Kopal, 1978). The dissipation takes shorter than the nuclear burning time-scale τ_{nuc} (see Section 3.1.2) (Hurley et al., 2002; Zahn, 1989, 1991).
- ▶ In stars with *radiative* envelopes, radiative dissipation near the surface of the star causes an asymmetry in the internal stellar oscillations induced by tides and the tidal field itself. This leads to a torque that is necessary for the binary system to approach the equilibrium state (Hurley et al., 2002; Zahn, 1977, 1989, 1992)

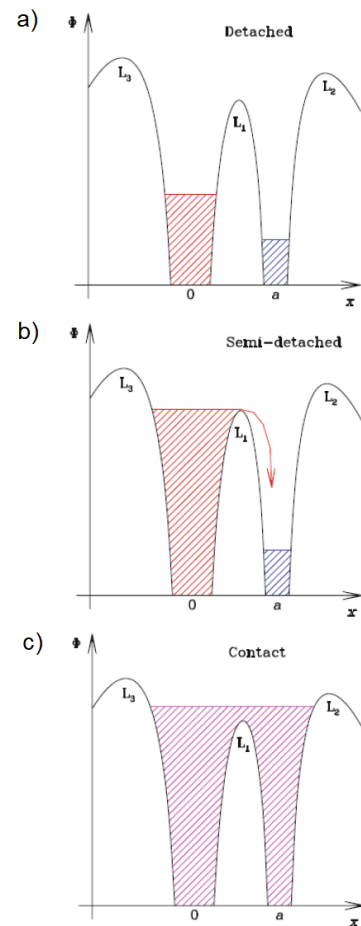


Figure 3.10: A schematic diagram showing the conditions for RLOF. In a), b) and c) there are two stars making up a binary, one positioned at 0 and one at a . $L_{1,2,3}$ are the three Lagrange points of the system; a) shows the potential Φ of the *detached* binary configuration along the z -axis, where neither star fills their Roche lobe; b) shows the potential of the *semi-detached* binary configuration along the z -axis, where RLOF happens; c) shows the potential of the *contact* binary configuration along the z -axis, where both stars fill their Roche lobes (Figure adapted from Tout (2008a)).

and in sufficiently close binaries this happens on shorter time-scales than the nuclear burning time-scale τ_{nuc} (Zahn, 1975). This radiative damping on the dynamical tides is the most efficient process to achieve the equilibrium state in binary stars with member stars that do not have an outer convective zone. However, if they do then the aforementioned turbulent friction on the equilibrium tides provides the primary torquing (Zahn, 1975, 1977, 1989).

τ_{sync} and τ_{circ} in binary stars with convective envelopes are typically orders of magnitude smaller than those with radiative envelopes (Hurley et al., 2002; Zahn, 1977):

$$\tau_{\text{sync,conv}} \ll \tau_{\text{sync,rad}} \quad \text{and} \quad \tau_{\text{circ,conv}} \ll \tau_{\text{circ,rad}}. \quad (3.42)$$

τ_{sync} and τ_{circ} are generally not equal except in a limiting case (Zahn, 1977):

$$\tau_{\text{sync}} \neq \tau_{\text{circ}} \quad (3.43)$$

If the stars are degenerate but have sufficient stellar structure, i.e. WDs and NSs, then the above two dissipative mechanisms cannot be used as the stellar structure is significantly different. WDs will have very low spins, because the progenitor AGB star has already spun down in its expansion. Furthermore, in WD-WD binaries, the orbit will already be circularised (in the absence of WD natal kicks Fellhauer et al., 2003) due to the stellar wind mass and thus angular momentum loss. For this reason only the synchronisation time-scale τ_{sync} due to degenerate damping is of importance here and it is only applicable for extremely close systems. τ_{sync} in WD-WD, WD-NS and NS-NS binaries could exceed the age of the Universe (Campbell, 1984; Hurley et al., 2002).

3.2.3 Dynamical mass transfer and its stability

Apart from mass transfer through stellar winds, mass transfer can also happen via Roche-lobe overflow (RLOF), a depiction of which is shown in Figure 3.10. This happens when the primary star fills it RL as a result of stellar expansion or in-spiral²⁸. The subsequent mass transfer then happens through the innermost Lagrange point. Typically, this process depends strongly on the mass ratio q of the binary (P. P. Eggleton, 1983):

$$\frac{R_{L1}}{a} = \frac{0.49q_1^{2/3}}{0.6q^{2/3} + \ln(1 + q_1^{1/3})}, \quad (3.44)$$

see also Figure 3.10, and RLOF happens in corotating, circularised binaries but in some instances, it can also occur in highly eccentric binaries, that are a result of tidal capture.

In the RLOF mass transfer, also angular momentum is transferred. The stability of the mass transfer traditionally determined by three logarithmic derivatives of radii with respect to the mass of the lobe-filling star following Webbink (1985, 2003).

28: In the discussion, I will use donor and primary interchangeably. The same is true for secondary and gainer.

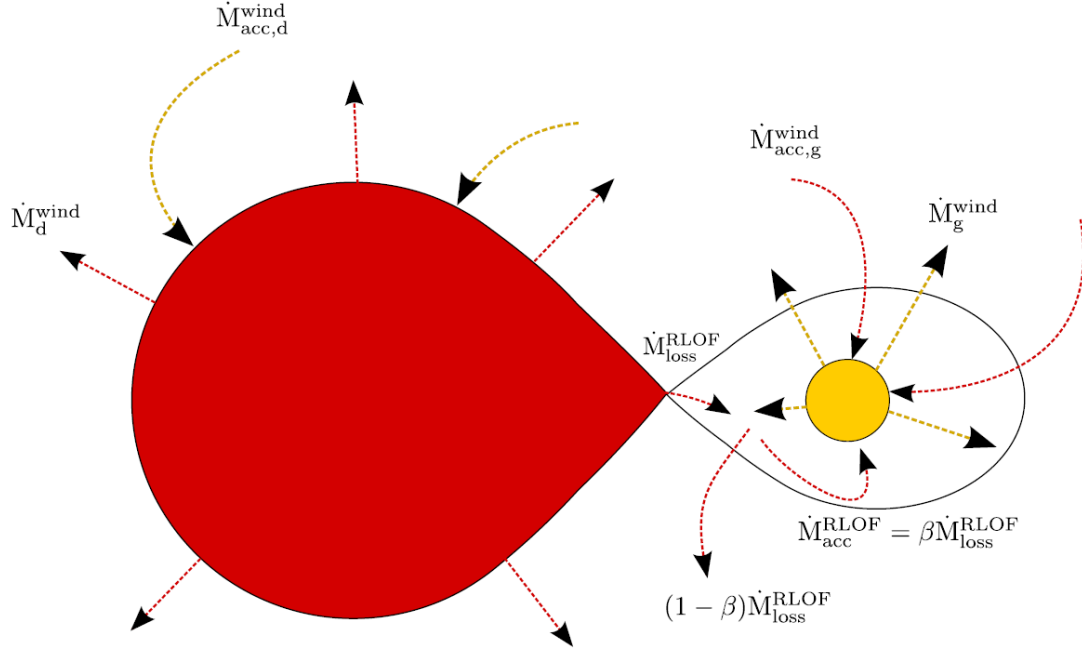


Figure 3.11: Different modes of mass exchange between stars in a binary system for the BINSTAR population synthesis code (Siess et al., 2013) that are similar for the stellar evolution codes based on Hurley et al. (2002) used in my thesis. \dot{M}_d^{wind} and $\dot{M}_{acc,d}^{wind}$ are the wind mass loss rate and the wind mass accretion rate (donated from the other star) of the primary star. \dot{M}_g^{wind} is the mass accretion rate that is given by $\dot{M}_g = -\beta\dot{M}_d > 0$, where $0 \leq \beta \leq 1$ to account for potential mass lost from the system in the models by Siess et al. (2013). \dot{M}_{loss}^{RLOF} is the mass donated from the donor via RLOF. However, not all of this mass is accreted and therefore, $\dot{M}_{acc}^{RLOF} = \beta\dot{M}_{loss}^{RLOF}$ and there is a mass loss from the binary system of $(1 - \beta)\dot{M}_{loss}^{RLOF}$. Lastly, the $\dot{M}_{acc,g}^{wind}$ is the mass gained by the accretor due to wind of the donor star (Figure taken from Siess et al., 2013).

Definition 3.2.3 The rate of change of the Roche lobe radius R_L for conservative mass transfer, in which the angular momentum of the system J and the total mass M are conserved is given by

$$\zeta_L = \left(\frac{\partial \log(R_L)}{\partial \log(M_1)} \right)_{M,J} = 2.13q - 1.67, \quad (3.45)$$

which means that all material, which is lost from the primary is accreted by the secondary (P. Eggleton, 2006).

From Equation 3.45, I know that as long as $M_1 > 0.78M_2$, the Roche lobe **shrinks** in response to RLOF and if $M_1 < 0.78M_2$, the Roche lobe **expands** in response to RLOF.

Definition 3.2.4 The rate of change of the donor star radius at constant entropy s and composition of each isotope X_i :

$$\zeta_{ad} = \left(\frac{\partial \log(R_1)}{\partial \log(M_1)} \right)_{s,X_i}. \quad (3.46)$$

From Equation 3.46, I know for stars with *radiative envelopes* with $\zeta_{ad} > 0$ they shrink due to mass loss. Stars with **convective envelopes** have $\zeta_{ad} < 0$ and therefore they expand on mass loss (see e.g. Tout, 2008a).

Definition 3.2.5 *The rate of change of the donor star radius at constant composition of each isotope X_i :*

$$\zeta_{\text{eq}} = \left(\frac{\partial \log(R_1)}{\partial \log(M_1)} \right)_{X_i}. \quad (3.47)$$

On thermal timescales, the star approaches full equilibrium with a new mass and with constant composition. For MS stars I have $\zeta_{\text{eq}} > 0$, which means that they shrink on mass loss and for red giants and stars crossing the HG, I have $\zeta_{\text{eq}} < 0$, which means that they expand (see e.g. Tout, 2008a).

The relationship between the three derivatives ζ_L , ζ_{ad} and ζ_{eq} determines the stability of dynamical mass transfer:

1. $\zeta_{\text{ad}} < \zeta_L \rightarrow \dot{M}$ increases rapidly, there is positive feedback and the mass transfer is unstable, the secondary star cannot accrete at such a high rate and it expands \rightarrow formation of a common envelope (CE; see Section 3.2.4) around the two stars (Ivanova et al., 2013; Ivanova, 2019; Paczynski, 1976). The time-scale for this process is the dynamical time-scale τ_{dyn} :

$$\left| \frac{\dot{M}_1}{M_1} \right| \rightarrow \tau_{\text{dyn}} = (10^1 - 10^2) \text{ yr}. \quad (3.48)$$

2. $\zeta_{\text{eq}} < \zeta_L < \zeta_{\text{ad}} \rightarrow \dot{M}$ decreases in its immediate response, but then expands on a thermal timescale²⁹:

$$\left| \frac{\dot{M}_1}{M_1} \right| \rightarrow \tau_{\text{th}} = (10^5 - 10^6) \text{ yr}. \quad (3.49)$$

3. $\zeta_L < \zeta_{\text{ad}} \ \& \ \zeta_L < \zeta_{\text{eq}} \rightarrow \dot{M}$ decreases initially, because the stellar radius decreases. RLOF happens again, when the donor fills its RL again. This process may happen either on the star's nuclear time-scale

$$\left| \frac{\dot{M}_1}{M_1} \right| \rightarrow \tau_{\text{nuc}} = (10^7 - 10^9) \text{ yr}, \quad (3.50)$$

or on the time-scale for the angular momentum to be lost from the system, as this will make the stars spiral inwards and so the donor will much easier fill its RL.

On the basis of these exponents alone, it is possible to make a number of arguments on the evolution of Cataclysmic Variables (CVs), Algols and other exotic binary stars.

Figure 3.11 shows a schematic depiction of the different modes of mass exchange between stars in a binary system discussed so far in Section 3.2.1, Section 3.2.2 and this section, i.e. the binary star undergoes RLOF and the member stars lose mass via winds and accrete mass from winds of the other binary member. Considering all the mass transfer processes involved, Siess et al. (2013) construct a mass transfer rate of the binary system:

$$\dot{M}_{\Sigma} = \dot{M}_{\text{acc,d}}^{\text{wind}} - |\dot{M}_{\text{d}}^{\text{wind}}| + \dot{M}_{\text{acc,g}}^{\text{wind}} - |\dot{M}_{\text{g}}^{\text{wind}}| - (1 - \beta) |\dot{M}_{\text{RLOF}}|, \quad (3.51)$$

29: This happens when sub-giants on the HG fill their RL, if they have a radiative or slightly convective envelopes. This is the case for Algols and also a formation scenario for blue straggler stars (BSS).

where the sub-script d denotes the donor and the sub-script g denotes the gainer (accretor) star. Similarly, due to the conservation of angular momentum, an equation for the rate of angular momentum change of each individual star of subscript i with $i = 1, 2$ can be constructed:

$$\dot{J}_i = \dot{J}_{\text{acc},i}^{\text{wind}} + \dot{J}_{\text{loss},i}^{\text{wind}} + \dot{J}_i^{\text{RLOF}} + \dot{J}_i^{\text{tides}}, \quad (3.52)$$

where \dot{J}_i^{tides} is the torque applied onto each star i with $\dot{J}_i^{\text{tides}} = I_i \dot{\Omega}_i$, where I_i is the moment of inertia of the respective star.

3.2.4 Common-envelope evolution

The process of common envelope evolution (CEE) is instrumental in compact binary and close binary formation (Ivanova et al., 2013; Ivanova, 2016, 2018; Ivanova, 2019; Paczynski, 1976).

Definition 3.2.6 (Common envelope) *A CE is the outcome when $\zeta_{\text{ad}} < \zeta_{\text{L}}$ in RLOF or when two stars collide, where one of the stars has a dense core. A CE happens when the primary star transfers more mass on dynamical time-scales than secondary can accept.*

The CE strongly depends on the instabilities in the RLOF preceding the formation of a CE (Olejak et al., 2021). The CE expands and thus rotates more slowly than the orbit of the secondary and primary star. This causes friction, the binary spirals in and transfers orbital energy to the envelope. Either so much energy in this process is transferred that the envelope is expelled completely resulting in a post-CE planetary nebula as observed in NGC 6778 as shown in Figure 3.12, leaving behind a close binary in corotation or in the process of in-spiral the binaries coalesce (P. Eggleton, 2006; Hurley et al., 2002; Tout et al., 1997).

The CE is traditionally modelled with the “ $\alpha_{\text{CE}}\lambda_{\text{CE}}$ ” energy-formalism (Hurley et al., 2002; Tout et al., 1997; Webbink, 1984), which assumes energy is conserved and where α_{CE} ($\alpha_{\text{CE}} < 1$ if no other energy sources other than the binding and orbital energy are present; it can be as high as $\alpha_{\text{CE}} = 5$ otherwise (Fragos et al., 2019)) is the “efficiency” of the energy re-use and λ_{CE} is a measure of the binding energy between the envelope and the core of the donor star and should depend on the type of the star, its mass and its luminosity (Claeys et al., 2014; Dewi & Tauris, 2000; Ivanova, 2019; Olejak et al., 2021). The total binding energy of the CE is given by

$$E_{\text{bind},i} = \frac{-G}{\lambda_{\text{CE}}} \left(\frac{M_1 M_{\text{env},1}}{R_1} + \frac{M_2 M'_{\text{env},2}}{R_2} \right), \quad (3.53)$$

where i denotes the initial state of the binding energy. The initial orbital energy of the cores is set to

$$E_{\text{orb},i} = -\frac{1}{2} \frac{GM_{\text{c1}}M'_{\text{c2}}}{a_i}, \quad (3.54)$$

where a_i denotes the initial semi-major axis just before the formation of the CE. The transfer of the angular momentum leads to a final

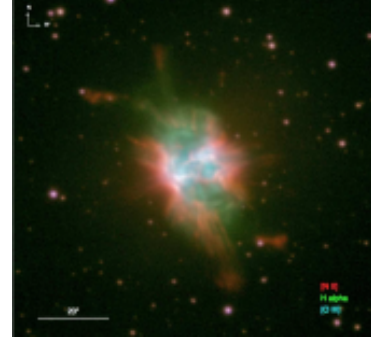


Figure 3.12: Post-CE planetary nebulae with a compact binary as central object in NGC 6778 from Guerrero and Miranda (2012) (Figure and caption taken from Ivanova et al., 2013).

semi-major axis a_f :

$$E_{\text{bind},i} = \alpha_{\text{CE}}(E_{\text{orb},i} - E_{\text{orb},f}) = -\alpha_{\text{CE}} \left(\frac{1}{2} \frac{GM_{\text{cl}}'}{M} \frac{a_f}{c_2} + \frac{1}{2} \frac{GM_{\text{cl}}'}{M} \frac{a_i}{c_2} \right). \quad (3.55)$$

This picture is very simplistic and does not take into account the myriad of processes that go on during CEE, which are also not fully understood yet (Ivanova & Nandez, 2016; Ivanova et al., 2013; Ivanova et al., 2020; Ivanova, 2019). On the other hand, the $\alpha_{\text{CE}}\lambda_{\text{CE}}$ energy-formalism is computationally very efficient and therefore it is widely used in population synthesis codes that require fast and robust stellar evolution computations (Belczynski et al., 2008; Breivik, Coughlin, et al., 2020; Claeys et al., 2014; Hurley et al., 2002; Kamlah, Leveque, et al., 2022; Mapelli, 2018b). Some of these also allow for recombination energy of hydrogen in the cool outer layers of the CE being transferred back into the binding energy of the CE. Recently, a new formalism has been developed by Trani et al. (2022), which solves a binary orbit under gas friction with numerical integration. This means that the authors do not approximate CE as an instantaneous process, unlike in many binary population synthesis (BPS) codes around. The new formalism, which can be easily implemented in BPS codes, provides a significant upgrade, which can explain observations of post-CE binaries which non-zero eccentricities (Kruckow et al., 2021).

In a binary consisting of a NS or a BH and a giant star, after the CE has been ejected and if the binary survives this phase, the H-rich envelope of giant stars might be stripped completely off. Now, the binary consists of a BH or a NS orbiting a naked He star. There might now be subsequent mass transfer from the naked helium star to the NS or BH. This post-CE RLOF mass transfer leaves behind a so-called “ultra-stripped” He star that explodes in an ultra-stripped SNe (Tauris, 2015; Tauris et al., 2013, 2017). This type of SNe is significantly different the typical core-collapse SNe and the process of ultra-stripping leads to a significant decrease in BH-NS and BH-BH mergers and a slight increase in NS-NS mergers (F. R. N. Schneider et al., 2021).

3.2.5 Mergers and general relativistic merger recoil kicks

An outcome of CEE may be the coalescence of the two binary stars. The subsequent merger product depends on the relative compactness of the two stars and thus it depends on the stellar evolutionary stage (Hurley et al., 2002; Tout et al., 1997). If similar in stellar type, then two stars mix completely. If one is much more compact than the other, then more compact core sinks to the centre and the other mixes with the envelope. An unstable Thorne-Żytkow object is created if the merger involves a NS or a BH (Thorne & Żytkow, 1977). Detailed calculations on the merger outcomes following coalescence and collisions, which are much less likely than coalescence, but still relevant in star clusters (see e.g. Rizzuto, Naab, Spurzem, Arca-Sedda, Giersz, et al., 2021; Rizzuto, Naab, Spurzem, Giersz, et al., 2021), depending on the initial stellar types have been tabulated in

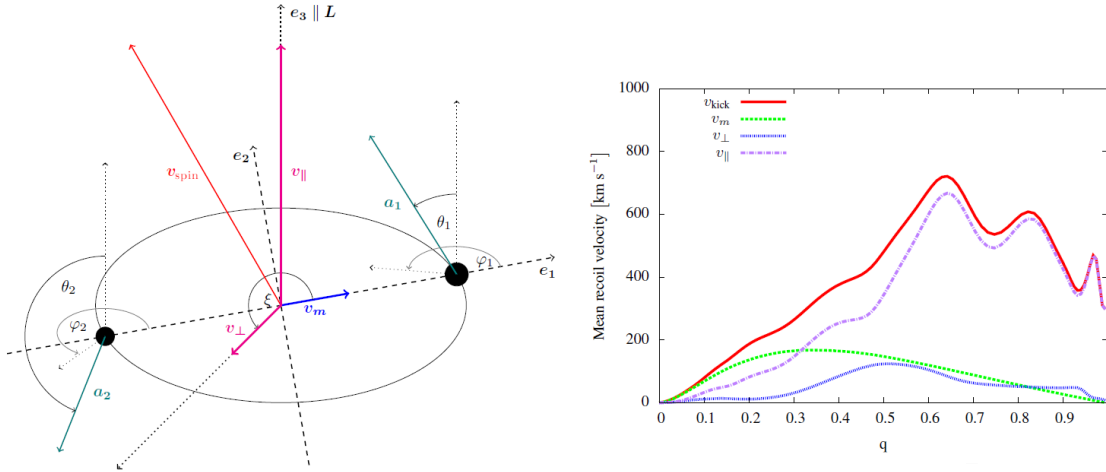


Figure 3.13: Left hand side: Conceptual picture presenting components of the recoil velocity. Dashed lines represent a Cartesian coordinate system in the orbital plane: \mathbf{e}_1 and \mathbf{e}_3 . A vertical dotted line is a line perpendicular to orbital plane (\mathbf{e}_3 , parallel to orbital angular momentum). The red vector is the kick component related to spin asymmetry, and magenta vectors are its projections on the plane and parallel to \mathbf{e}_3 . The blue vector represents the mass inequality contribution. The black filled circles represent a pair of BHs, their spins and orientation in a spherical coordinate system is illustrated. This drawing also reflects typical proportions between recoil velocity components.

Right hand side: Example of how each recoil velocity component depends on mass ratio q for a metallicity dependent spin vector from Belczynski et al. (2017). q is the only variable for the determination of v_m . Other components and the overall kick velocity depend also on spin magnitudes and orientations, in this case the mean value is plotted. As I can see, the major component is almost always v_{\parallel} , others only play a role for low q . (Figures and captions adapted from Morawski et al. (2018) (combination of Fig. 2 and Fig. 3) and it is also shown in a similar fashion in Spruzem and Kamlah (2023)).

Hurley et al. (2002). Generally, the mixing and the final masses of the merger products are highly uncertain and only approximations can be made according to our current knowledge (Kamlah, Leveque, et al., 2022; Olejak et al., 2020). There are recent attempts to unravel the masses and compositions of merger products of massive stars with hydrodynamical codes (Ballone et al., 2022; Costa et al., 2022) and they can be used to give approximate formulae for N -body or BPS codes in the future.

The merger of compact objects is associated with a general relativistic (GR) merger recoil kick due to the asymmetry in the GW (see also Kamlah, Leveque, et al. (2022) for a brief discussion with respect to Nbody6++GPU and MOCCA). The recoil velocity in this process depends on the mass ratio of the two participating compact objects and their spin vectors (Lousto et al., 2012) and can reach several hundreds kms^{-1} on average (Morawski et al., 2018, 2019), which is much larger than typical star cluster escape speeds. Figure 3.13 (from Morawski et al. (2018, 2019)) shows the a conceptual picture of the geometry of a GR merger recoil kick in a BH-BH merger and the dependence of the mean recoil velocity on the mass ratio q of the participating BHs for a metallicity dependent spin model from Belczynski et al. (2017). It can be seen that q has a huge impact on whether a GR merger recoil kick velocity exceeds the escape speed of the surrounding stellar (and gaseous) material or not. Equal mass mergers might be retained in nuclear star clusters (Schödel et al., 2014) and extreme mass ratio mergers might theoretically even be retained in open clusters (although IMBHs will probably not form there) Baker et al. (2007, 2008), Baumgardt and Hilker (2018), and Portegies Zwart et al. (2010). For (nearly) non-spinning BHs (FULLER model (J. Fuller & Ma, 2019)), the kick velocity is smaller than for

high spins. For non-aligned natal spins and small mass ratios, the asymmetry in the GW may produce GR merger recoils that reach thousands of kms^{-1} (Baker et al., 2008; van Meter et al., 2010). The calculation of the mass ratio is straightforward and the spins may be calculated from e.g. Hoffman and Loeb (2007) or Jiménez-Forteza et al. (2017).

Generally, the orbital angular momentum of the BH-BH dominates the angular momentum budget that contributes to the final spin vector of the post-merger BH and therefore, within limits, the final spin vector is mostly aligned with the orbital momentum vector (Banerjee, 2021a). In the case of physical collisions and mergers during binary-single interactions, the orbital angular momentum is not dominating the momentum budget and thus the BH spin can still be low. Banerjee (2021a) also includes a treatment for random isotropic spin alignment of dynamically formed BHs. Additionally, Banerjee (2021a) assumes that the GR merger recoil kick velocity of NS-NS and BH-NS mergers (Arca Sedda, 2020; Chattopadhyay et al., 2021) to be zero but assigns merger recoil kick to BH-BH merger products from numerical-relativity fitting formulae of van Meter et al. (2010), which is updated in Banerjee (2021b). The final spin of the merger product is then evaluated in the same way as a BH-BH merger.

The inclusion of these kicks in direct N -body simulations is still unusual (e.g. Di Carlo, Mapelli, Bouffanais, et al. (2020), Di Carlo, Mapelli, Giacobbo, et al. (2020), Di Carlo et al. (2019, 2021), Kamlah, Leveque, et al. (2022), Kamlah, Spurzem, et al. (2022), Rizzuto, Naab, Spurzem, Arca-Sedda, Giersz, et al. (2021), Rizzuto, Naab, Spurzem, Giersz, et al. (2021), and Rizzuto et al. (2022) all do not include these in addition to missing PN terms), but it is worth mentioning Arca-Sedda et al. (2021) do include the GR merger recoil kicks by posterior analysis. `NBODY7` S. J. Aarseth (2012), Banerjee et al. (2020), and Banerjee (2021a) on the other hand does include GR merger recoil kicks based on Hoffman and Loeb (2007) and Lousto et al. (2012). In MOCCA numerical relativity (NR) models (Campanelli et al., 2007; Hughes, 2009; Jiménez-Forteza et al., 2017; Rezzolla et al., 2008; van Meter et al., 2010) have been used to formulate semi-analytic descriptions for MOCCA and `NBODY` codes (Arca-Sedda et al., 2021; Banerjee, 2021a, 2021b; Belczynski & Banerjee, 2020; Morawski et al., 2018, 2019).

Recently, GR merger recoil kicks as outlined above have also been added to `NBODY6++GPU` as part of the DRAGON-II project (Arca Sedda & et al., 2023a, 2023b, 2023c, in prep.) following Campanelli et al. (2007) and Jiménez-Forteza et al. (2017) and with this code version, the whole kick process can be followed self-consistently. The `NBODY6++GPU` code version including Pop-III stellar evolution by Tanikawa et al. (2020) used in my upcoming work presented in Kamlah et al. (2023, in prep.) also showcases these kicks.

3.2.6 Accretion or merger induced collapse

In sufficiently close double degenerate COWD-COWD, ONeWD-ONeWD or COWD-ONeWD binary stars, high and dynamically stable RLOF mass accretion of hot CO-rich matter may lead to a heating of the outer layers of the secondary binary member, which

will result in the ignition of nuclear burning (Saio & Nomoto, 2004). If C-burning is ignited in the COWD envelope, the heat will be transported the stellar core by conduction

and then the secondary will evolve into an ONeWD (Saio & Nomoto, 1985; Saio & Nomoto, 1998), which will eventually collapse into a NS if the critical mass of the ONe core is surpassed ($(M_{\text{ecs}}=1.38 M_{\odot})$ Belczynski et al., 2008; Nomoto, 1984; Nomoto, 1987). This ONeWD collapse is referred to as accretion induced collapse (AIC), see Figure 3.14 as an impressive image of such an event. If, on the other hand, the ignition happens in the centre then the star will undergo a SN-Ia explosion, which leaves no remnant behind.

Double degenerate COWD binaries may also coalesce without undergoing dynamically stable mass transfer. During this process the less massive star forms a thick, turbulent accretion disk and the more massive COWD will accrete matter close to the Eddington limit. Here the C will be ignited on the envelope of the secondary and thus the outcome will be a ONeWD and no SN-Ia will happen (Saio & Nomoto, 2004). Again, if the ONe core mass surpasses M_{ecs} , then the ONeWD will collapse into a NS and this is known as a merger-induced collapse (MIC). Other pathways for MIC are mergers of a ONeWD with any type of WD companion if the resulting merger mass surpasses the critical mass for NS formation (Belczynski et al., 2008; Saio & Nomoto, 1998).

The distinction between AIC and MIC is made, because the former may be observed already through their stable mass transfer phase or in low-mass X-ray binary stars and the latter may be observed through gravitational waves observed with LISA (Ruiter et al., 2019).

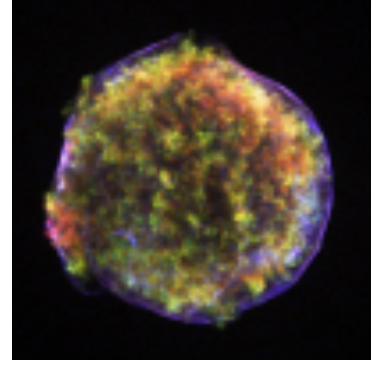


Figure 3.14: SN 1572 (B Cassiopeiae / B Cas), which is also known as Tycho's Supernova after the famous Danish astronomer Tycho Brahe as photographed with the Chandra X-ray Observatory (CXO Weisskopf et al., 2000). Tycho was inspired to label them novae (in his important astrophysical text *De nova stella* in 1573, where he refuted the Aristotelian model of an unchanging sky on the basis of SN 1572), because he thought that SN 1572 was the birth of a new star. In fact, I know now that SN 1572 is a type-Ia SNe triggered by stellar binary evolution processes involving WDs, see also Section 3.2. The image is taken from Warren et al. (2005).

3.2.7 Gravitational radiation and magnetic braking

Gravitational radiation emitted from sufficiently close binary stars ($P \leq 0.6$ days P. Eggleton, 2006) transports angular momentum away from the system and drives it to a mass transfer state that might result in coalescence (P. Eggleton, 2006; Hurley et al., 2002; Peters & Mathews, 1963). The effect this radiation has on the orbit of the binary (excluding PN terms) may be obtained by averaging the rates of energy loss and angular momentum loss over an approximately Keplerian orbit (P. Eggleton, 2006; Peters, 1964):

$$\left\langle \frac{da}{dt} \right\rangle = -\frac{64}{5} \frac{G^3 M_1 M_2 (M_1 + M_2)}{c^5 a^3 (1 - e^2)^{7/2}} \left(1 + \frac{73}{24} e^2 + \frac{37}{96} e^4 \right), \quad (3.56)$$

$$\left\langle \frac{de}{dt} \right\rangle = -\frac{304}{15} e \frac{G^3 M_1 M_2 (M_1 + M_2)}{c^5 a^4 (1 - e^2)^{5/2}} \left(1 + \frac{121}{304} e^2 \right), \quad (3.57)$$

where a and e are the semi-major axis and the eccentricity of the binary star of masses m_1 and m_2 , respectively. Gravitational radiation will circularise the orbit on the same time-scale as the orbit shrinks until coalescence. The associated merger time-scale is given by

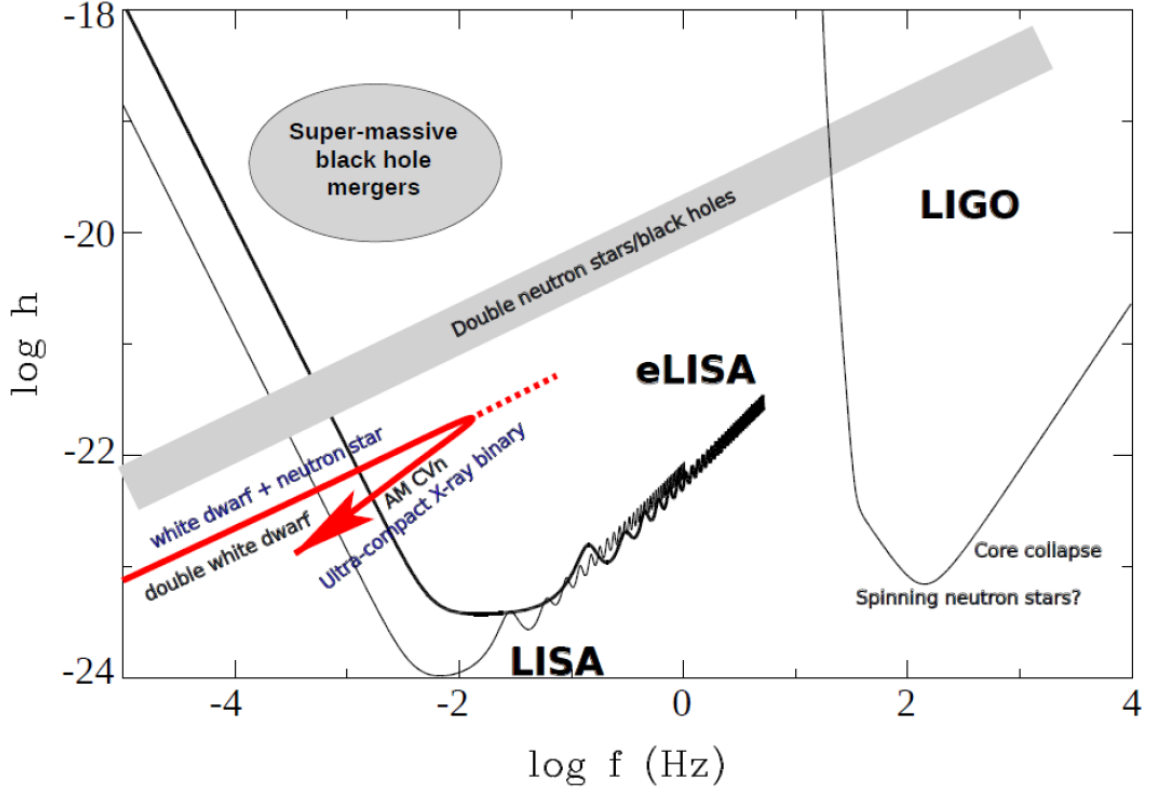


Figure 3.15: Sensitivity limits of GW detectors and the regions of the $f - h$ (frequency-strain) diagram occupied by some of the potential GW sources. Also shown are possible pathways for isolated WD-WD and BH-BH / NS-NS binaries to form. Also shown are so-called AM CVn systems and X-ray binaries, see Section 3.2.8. These signals are all highly speculative, since in dense, stellar systems with and without a central SmbH, binaries get disrupted by encounters or they form hierarchical systems, such as triples and so. If they are not destroyed in the process, the orbital parameters of the binaries may also be severely affected by encounters completely changing their CEE, see Section 3.2.4, for example. (Figure and caption taken from Postnov & Yungelson, 2014).

(Postnov & Yungelson, 2014)

$$\tau_{\text{GW}} \approx 4.8 \times 10^{10} \text{yr} \left(\frac{P_b}{\text{d}} \right)^{8/3} \left(\frac{\mu}{M_\odot} \right)^{-1} \left(\frac{M_1 + M_2}{M_\odot} \right)^{-2/3} (1 - e^2)^{7/2}, \quad (3.58)$$

where $\mu = M_1 M_2 / (M_1 + M_2)$ is the reduced mass of the binary. The spiralling in phase, the merger and the ring-down themselves may then be observable in a GW detector.

In co-rotating and sufficiently close binary stars, magnetic braking slows down the rotation of the individual star with a convective envelope, but also drains angular momentum from the orbit of the binary star, because tidal friction between the stars may conserve co-rotation (P. Eggleton, 2006; Mestel, 1968a, 1968b; Mestel & Spruit, 1987). As a result, this process will force a close binary to a state of RLOF within Hubble time. In some situations, this process is dominating binary evolution, such as in CVs above the orbital period gap (Belloni, Kroupa, et al., 2018; Schreiber et al., 2016; Zorotovic et al., 2016). In spin-spin period evolution ($P - \dot{P}$) of pulsars this process is also important (e.g. Kiel & Hurley, 2006, 2009). Both processes outlined above are non-conservative.

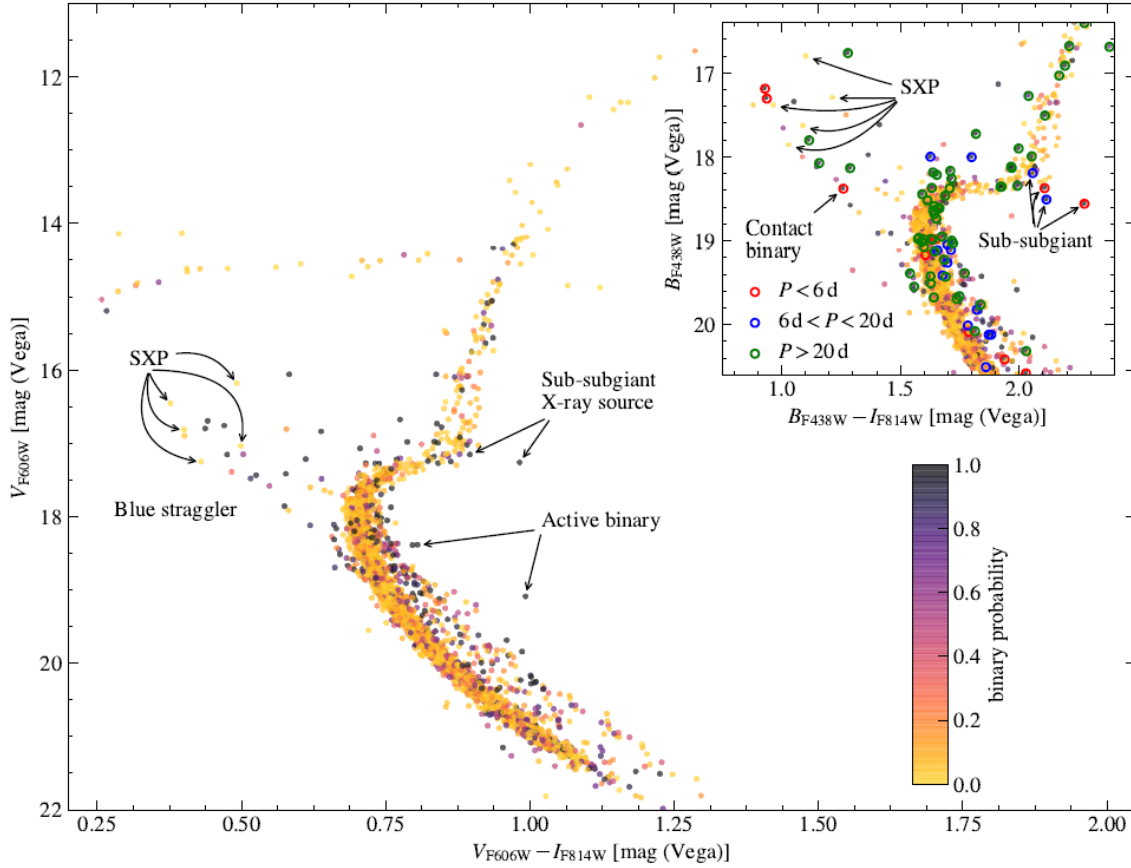


Figure 3.16: Colour-magnitude diagram of the members of GC NGC 3201 created with the photometry taken from the HST UV globular cluster survey (Nardiello et al., 2018; Piotto et al., 2015). Colour-coded is the binary probability obtained by our statistical method. Large panel: the full CMD of our sample using HST V_{F606W} and I_{F814W} equivalent filters is shown with Vega as the reference magnitude. Small panel: a detailed version of the main-sequence turn-off CMD region using V_{F438W} and I_{F814W} equivalent filters is displayed. Additionally, the period P range is indicated by coloured circles where THE JOKER (Giesers et al., 2018) was able to fit a well constrained Keplerian orbit. Also shown are some well-known binary types: BSSs, X-ray sources, active binaries and in terms of the research by Giesers et al. (2019) SXP (SX Phoenician-type variable) binaries, which are a sub-class of BSSs (Figure and caption taken from Giesers et al., 2019).

3.2.8 Stellar types and binary classes in classical SSE & BSE

In the interest of clarity, I outline some definitions of stars in the stellar evolution framework that I use for my work in the form of Single Stellar Evolution (SSE Hurley et al., 2000) and Binary Stellar Evolution (BSE Hurley et al., 2002). The stellar types, which are parameterised by KW, are divided as such (Hurley et al., 2000), but see also Kamlah, Leveque, et al. (2022) and Section 8.2:

- ▶ KW = 0 \doteq MS star $M \leq 0.7 M_{\odot}$
- ▶ KW = 1 \doteq MS star $M > 0.7 M_{\odot}$
- ▶ KW = 2 \doteq Hertzsprung Gap (HG)
- ▶ KW = 3 \doteq First Giant Branch (GB)
- ▶ KW = 4 \doteq Core Helium Burning (CHeB)
- ▶ KW = 5 \doteq Early Asymptotic Giant Branch (EAGB)
- ▶ KW = 6 \doteq Thermally Pulsating Asymptotic Giant Branch (TPAGB)
- ▶ KW = 7 \doteq Naked Helium Star MS (HeMS)
- ▶ KW = 8 \doteq Naked Helium Star Hertzsprung Gap (HeHG)

- ▶ $KW = 9 \doteq$ Naked Helium Star Giant Branch (HeGB)
- ▶ $KW = 10 \doteq$ Helium White Dwarf (HeWD)
- ▶ $KW = 11 \doteq$ Carbon-Oxygen White Dwarf (COWD)
- ▶ $KW = 12 \doteq$ Oxygen-Neon White Dwarf (ONeWD)
- ▶ $KW = 13 \doteq$ Neutron Star (NS)
- ▶ $KW = 14 \doteq$ Black Hole (BH)
- ▶ $KW = 15 \doteq$ massless remnant

I note, that `NBODY6++GPU` and `MOCCA` have another stellar type (for single stars), which is $KW=-1$, which assigns pre-MS stars (Railton et al., 2014). This treatment is valid for stars in the range $0.1 - 8.0 M_{\odot}$ at solar metallicity $Z_{\odot}=0.02$. Combinations of the above form a large variety of binary stars. There are some special binaries in the complete BSE picture that deserve a further definition and the in following KW_1 denotes the primary's stellar type and KW_2 denotes the secondary's stellar type.

Definition 3.2.7 (Blue Straggler Stars - BSS) *A BSS is a MS star, which through mass accretion or a merger process, appears younger on the HR and lies to the left of the MS turn-off point. SX Phoenixis-type variables (SXP) are a sub-class of BSSs that exhibit a very short period pulsating behaviour.*

Constraining the fractions of BSS in binaries and higher-order hierarchical stellar constellation in NGC 3201 was the original intent by Giesers et al. (2018) and in the process they also found smBHs in binaries, see also Giesers et al. (2019). Figure 3.16 shows a CMD of the GC NGC 3201 by Giesers et al. (2018), which shows a large and impressive variety of stellar binary types (also see below).

Definition 3.2.8 (Cataclysmic Variable - CV) *The secondary star in the binary is a WD with Roche-lobe filling primary companion, which is not degenerate. CVs can further be sub-divided by as such:*

- ▶ Classical CVs: $KW_1 \leq 1$,
- ▶ GK Persei systems (GK Per): $KW_1 = 2$,
- ▶ Symbiotic-like binaries (CV Symb): $3 \leq KW_1 \leq 6$,
- ▶ Subdwarf B binaries (SdB): $7 \leq KW_1 \leq 9$.

CVs are expected to be very abundant in star clusters and are therefore objects of frequent astrophysical study (see e.g. Belloni, Kroupa, et al., 2018; Schreiber et al., 2016; Zorotovic et al., 2016).

Definition 3.2.9 (Algol) *The secondary in the binary is a MS, which is accreting from a Roche-lobe filling companion. Algols³⁰ can further be sub-divided by as such:*

- ▶ Pre-Algol - $q_1 = M_1/M_2 > 1$,
- ▶ MS Algol - Primary is a MS star and $q_1 < 1$.
 - Hot Algol - $M_2 > 1.25 M_{\odot}$,
 - Cold Algol - $M_2 \leq 1.25 M_{\odot}$, could also appear as symbiotic binaries (see below).

30: Algol (also known as β Persei) is visible to the unaided naked eye and was possible discovered already by the Ancient Egyptians 3200 years ago and thought to be a single, variable star, also commonly referred to as the "Demon Star". It was associated with the Gorgon's head in Homer's *Iliad* and described as "...a ghastly sight, deformed and dreadful, and a sight of woe" (Homer (8th century BC), *Iliad* ("a poem about Ilium"). Today, I know that Algol is in fact a triple star system and the member stars are now known as Algol A, B and C (see e.g. Zavala et al., 2010)

Definition 3.2.10 (X-ray binaries) *The primary is a NS or BH accreting material from either stellar wind or RLOF, where the accretion luminosity L_X of the accretion disk exceeds the stellar luminosity L_\odot :*

$$L_X = \frac{GM_2\dot{M}_2}{2R_2} > L_\odot \quad (3.59)$$

X-ray binaries can then further be sub-divided into:

- ▶ Low-mass X-ray binary (LMXRB) - $M_1 < 2 M_\odot$,
 - ▶ White Dwarf X-ray binary (WDXRB) - Primary is WD,
 - ▶ Massive X-ray binary (MXRB) - $M_1 \geq 2 M_\odot$.
- transient XB and persistent XB - with

$$\log\left(\frac{L_{X,\text{crit}}}{L_\odot}\right) = \begin{cases} 1.62 + 1.07 (P/\text{h}) & \text{NS secondary,} \\ 2.22 + 1.07 (P/\text{h}) & \text{BH secondary,} \end{cases} \quad (3.60)$$

If $L_{X,\text{crit}} < L_X$, then it is a persistent XBp. If $L_{X,\text{crit}} > L_X$, then it is a soft transient XB (SXt). The instability of the accretion disk, which is affected by X-ray heating, so that accretion is possible to much lower mass transfer rates, making the XB soft transient.

The term X-ray binary stems from the fact that X-rays are emitted by the in-falling matter from

the primary onto the secondary upon the release of gravitational potential energy, see also [Figure 3.17](#) for an artistic impression of a famous eclipsing X-ray binary SS 443.

Definition 3.2.11 (Symbiotic stars (SySts)) *The secondary of the binary has stellar type $KW_2 \leq 12$, if the mass accretion by stellar winds produced from primary Giant exceeds $10 L_\odot$ or 1% of the primary luminosity:*

- ▶ **D-type symbiotic (D-SySt)** - Long period symbiotic binaries with a cool star primary $KW_1 = 6$. The binary is typically surrounded by a shell of dust.
- ▶ **S-type symbiotic (S-SySt)** - Short period symbiotic binaries with a normal Giant primary $KW_1 < 6$.

Belloni, Mikołajewska, et al. (2020) note that SySts are mostly disrupted by dynamical encounters in GCs and are therefore not observable at the present day. However, very recently Saeedi et al. (2022) detected one StSy in the GC 47 Tuc among other interesting 14 X-ray sources, which include 2 LMXBs, see [Definition 3.2.10](#), and 4 CVs, see [Definition 3.2.8](#).

Definition 3.2.12 (Double-degenerate binaries (DDs)) *These are any combinations of WD, NS, BH in binaries (WD-WD DD, NS-NS DD, BH-BH DD, NS-BH DD, WD-BH DD,...).*

- ▶ AM Canum Venaticorum (AM CVn) systems - DD system with a Roche-lobe filling primary WD:



Figure 3.17: Artistic impression of the SS 443, which is an eclipsing X-ray binary. The X-ray binary (MXRB) is postulated to consist of a smbH with a mass larger than $8.0 M_\odot$, which is accreting a $2.9 M_\odot$ star (+disk) (Cherepashchuk et al., 2021; Hillwig et al., 2004; MacAlpine et al., 2007) (Snapshot taken from animated video by DESY, Science Communication Lab.).

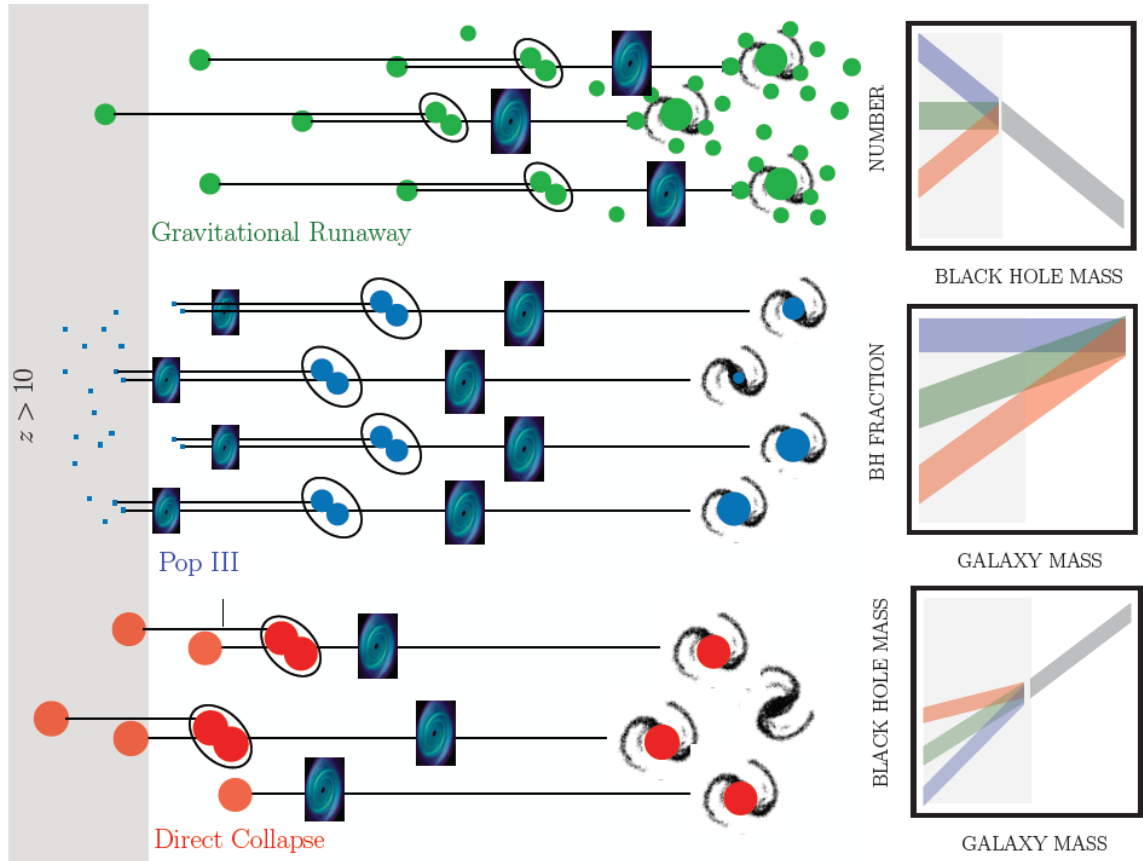


Figure 3.18: Possible observable differences between different seeding scenarios of mBHs for galactic nuclei. Early formation through direct collapse (red) or Pop-III stars (blue) occur at red-shift $z > 10$, while gravitational runaway (green) can happen throughout cosmic time. As cosmic structures evolve, the seed BHs will super mergers (black ovals) leading to the emission of GWs, as well as accretion episodes (blue disks) that could be observed as active galactic nuclei. At the present day, differences in BH mass functions, occupation fractions, and BH-galaxy scaling relations may ensue from different seeding channels, for simplicity here shown only for nuclear BHs. Grey bars in these relations show where I do not yet have observational constraints (Figure and caption taken from Greene et al., 2020).

- He DDRch - Primary is a HeWD with $KW_1 = 10$,
- CO DDRch - Primary is a HeWD with $KW_1 = 11$.
- ▶ NS DDRch - NS-NS binaries, which coalesce very quickly in gamma-ray bursts after entering RLOF.
- ▶ Low-mass White Dwarfs (LMWD) - Because of binary mass transfer, binary evolution may produce WDs of lower masses than would be possible for SSE $M_{WD} \leq 0.5 M_{\odot}$:
 - He LMWD - Primary is a He WD with $KW_1 = 10$,
 - CO LMWD - Primary is a He WD with $KW_1 = 11$.

DDs are among the most central objects of investigation in N -body simulations of star clusters and many studies more or less exclusively focus on these (see e.g. Arca Sedda & et al., 2023b, 2023c; Downing, 2012; Downing et al., 2010, 2011; Rizzuto, Naab, Spurzem, Giersz, et al., 2021; Rizzuto et al., 2022). This is mainly due to the emission of gravitational waves once they are sufficiently close that can be detected by detectors, see Section 3.2.7, but also due to the fact the star clusters are postulated to be factories for mBHs for galaxies through collisions and mergers of stars and compact objects (see e.g. Greene et al., 2020; Rees, 1984; Spurzem & Kamlah, 2023), see also Figure 3.18.

Although a lot has already been introduced about the physics of star clusters and their place in the cosmos, my work fundamentally focuses on simulations of them. Therefore, it cannot be avoided that the topic of gravitational N -body dynamics requires a chapter here. Generally speaking, an excellent introduction on the physics, the technical aspects and algorithms that are relevant in simulating the gravitational N -body problem are given by in publications by S. J. Aarseth (2003a), S. J. Aarseth et al. (2008), and Spurzem (1999). These texts in combination contain pretty fundamentally everything that is needed for dealing with the aspects of the stellar dynamics and computational methods for computing the evolution of star clusters. Further summaries and introductions to the field can be found in Binney and Tremaine (2008b) and Giersz and Spurzem (1994).

In this chapter I focus on the astrophysics of gravitational dynamics and in Part 11, I elaborate on the computational methods of solving the physical equations presented in this chapter.

| | |
|--|-----|
| 4.1 The gravitational N -body problem | 89 |
| 4.1.1 The gravitational two-body problem | 90 |
| 4.1.2 Hyperbolic encounters between stars | 93 |
| 4.1.3 Relaxation revisited | 96 |
| 4.1.4 Inelastic encounters between stars | 98 |
| 4.1.5 The gravitational three-body problem | 99 |
| 4.2 Statistical treatment of star clusters | 101 |
| 4.2.1 Collisionless stellar dynamics | 102 |
| 4.2.2 Collisional stellar dynamics | 104 |

4.1 The gravitational N -body problem

Starting from Newton's Law of Gravity, the equations of motion can deceptively simply be written down as

Definition 4.1.1 (Gravitational N -body problem)

$$\ddot{\mathbf{r}}_i = -G \sum_{j=1; j \neq i}^N \frac{m_j (\mathbf{r}_i - \mathbf{r}_j)}{|\mathbf{r}_j - \mathbf{r}_i|^3}, \quad (4.1)$$

for a particle of index i in a system containing N particles. Given initial conditions of masses m_i , positions \mathbf{r}_i , velocities \mathbf{v}_i for each particle at some time t_0 a system of dimension $3N$ of second-order differential equations is defined and solutions for \mathbf{r}_i may be obtained.

Therefore, the N -body problem can be defined as

Given initial values of N masses, coordinates and velocities, the task is to calculate the future orbits of these N masses.

The N -body problem appears innocuous, however it describes a large array of astrophysical situations from the stability of the Solar system and galaxies to the tidal dissolution of star clusters and the stellar dynamics occurring within star clusters. Two conserved quantities hold for such self-gravitating N -body system are the kinetic T + potential energy U and the angular momentum J of such

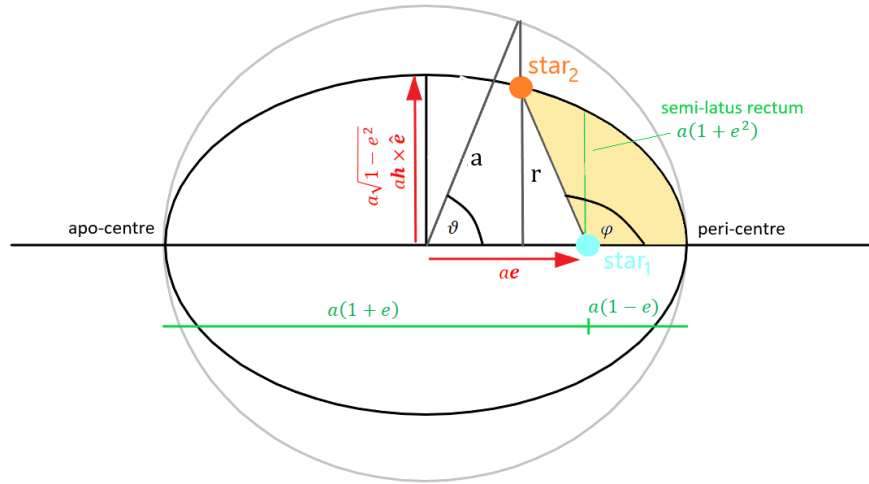


Figure 4.1: Diagram showing the geometry of a Kepler ellipse. There is a shaded area in light-yellow that is proportional to the mean anomaly λ .

a system of N bodies. These can be written down as

$$E = T + U = \frac{1}{2} \sum_{i=1}^N m_i \mathbf{v}_i^2 - \sum_{i=1}^N \sum_{j>1}^N \frac{G m_j m_i (\mathbf{r}_i - \mathbf{r}_j)}{|\mathbf{r}_j - \mathbf{r}_i|}, \quad (4.2)$$

$$J = \sum_{i=1}^N \mathbf{r}_i \times m_i \mathbf{v}_i. \quad (4.3)$$

Usually, as mentioned before, a tidal field introducing an additional external energy W adds an additional energy term in Equation 4.2. The task at hand is to find numerical solutions for consecutive time-steps.

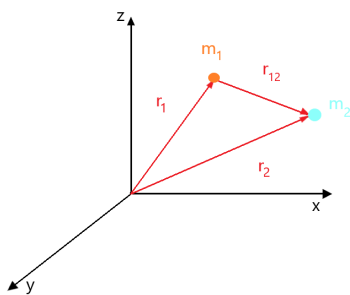


Figure 4.2: Schematic diagram of the two-body problem between two stars in Cartesian coordinates.

4.1.1 The gravitational two-body problem

I start the discussion, which follows Binney and Tremaine (2008a), with the simplest conceivable gravitational N and solve Equation 4.1 for $N = 2$. Consider two stars with indices $i = 1, 2$, masses m_i and position vectors \mathbf{r}_i moving at velocities $\dot{\mathbf{r}}_i$, see also Figure 4.2:

$$\ddot{\mathbf{r}}_1 = -G m_2 \frac{\mathbf{r}_2 - \mathbf{r}_1}{|\mathbf{r}_2 - \mathbf{r}_1|^3}, \quad (4.4)$$

$$\ddot{\mathbf{r}}_2 = -G m_1 \frac{\mathbf{r}_1 - \mathbf{r}_2}{|\mathbf{r}_1 - \mathbf{r}_2|^3}. \quad (4.5)$$

The two-body problem can also be formulated using the Hamilton formalism, where we consider the total energy of the three-body system in terms of gravitational and kinetic energy, which then results in 18 first-order differential equations using the generalized momenta \mathbf{p}_i and positions \mathbf{r}_i of the stars:

$$\frac{d\mathbf{r}_i}{dt} = \frac{\partial \mathcal{H}}{\partial \mathbf{p}_i}, \quad \frac{d\mathbf{p}_i}{dt} = -\frac{\partial \mathcal{H}}{\partial \mathbf{r}_i}, \quad (4.6)$$

where \mathcal{H} is the Hamiltonian:

$$\mathcal{H} = -\frac{Gm_1m_2}{|\mathbf{r}_1 - \mathbf{r}_2|} + \frac{\mathbf{P}_1^2}{2m_1} + \frac{\mathbf{P}_2^2}{2m_2}. \quad (4.7)$$

This treatment will be useful later for the purposes of regularization. Equation 4.7 can be transformed by setting

$$\mathbf{r} = \mathbf{r}_1 - \mathbf{r}_2, \quad (4.8)$$

$$\mathbf{R} = \frac{m_1\mathbf{r}_1 + m_2\mathbf{r}_2}{M} = \frac{m_1\mathbf{r}_1 + m_2\mathbf{r}_2}{m_1 + m_2}, \quad (4.9)$$

which gives the transformed Hamiltonian

$$\mathcal{H} = \frac{\mathbf{P}^2}{2M} + \frac{\mathbf{p}^2}{2\mu} - \frac{GM\mu}{|\mathbf{r}|} \quad (4.10)$$

where $\mathbf{P} = \mathbf{p}_1 + \mathbf{p}_2 = M\dot{\mathbf{R}}$, $\mathbf{p} = \mu\dot{\mathbf{r}}$, and where I have introduced the reduced mass

$$\mu \equiv \frac{m_1m_2}{m_1 + m_2} \quad (4.11)$$

For the two-body problem, I now have the following equations of motion

$$\dot{\mathbf{R}} = 0 \quad (4.12)$$

$$\ddot{\mathbf{r}} = -\frac{GM}{r^2}\hat{\mathbf{r}}. \quad (4.13)$$

Equation 4.13 is known as the Kepler problem. Note that Equation 4.10 only depends on $|\mathbf{r}|$, so only the magnitude of the vector describing the relative distance between the stars and not the direction of the vector. Therefore, the specific angular momentum

$$\mathbf{L} = \mathbf{r} \times \frac{\mathbf{p}}{\mu} \quad (4.14)$$

is conserved. The plane of the orbit of the two stars is always perpendicular to \mathbf{L} . The motion in the plane can also be transformed in a polar coordinate system (r, φ) , see also Figure 4.1. Then the equations of motion become

$$\ddot{r} - \frac{L^2}{r^3} = -\frac{GM}{r^2}, \quad (4.15)$$

$$\dot{\varphi} = \frac{L}{r^2} \rightarrow \frac{d}{dt} = \frac{L}{r^2} \frac{d}{d\varphi}. \quad (4.16)$$

Therefore, I get

$$\frac{L^2}{r^2} \frac{d}{d\varphi} \left(\frac{1}{r^2} \frac{dr}{d\varphi} \right) - \frac{L^2}{r^3} = -\frac{GM}{r^2}, \quad (4.17)$$

which can be re-written in terms of $u \equiv 1/r$ and that gives

$$\frac{d^2u}{d\varphi^2} + u = \frac{GM}{L^2}. \quad (4.18)$$

The equation can be multiplied by $du/d\varphi$ and integrating over φ , which results in

$$\frac{1}{2} \left(\frac{du}{d\varphi} \right)^2 + \frac{u^2}{2} - \frac{GM}{L^2} u = \frac{E}{L^2} = \text{constant}, \quad (4.19)$$

where E is the orbital energy of the unperturbed binary star in question. This orbital energy is conserved:

$$E = \frac{\mathbf{v}^2}{2} - \frac{GM}{r} \quad (4.20)$$

The solution to the differential equation 4.19 is given by

$$u(\varphi) = C \cos(\varphi - \varphi_0) + \frac{GM}{L^2}, \quad (4.21)$$

where C is some positive constant and φ_0 is some initial phase offset of the orbit, The following quantities help to quantify the orbit, see also Figure 4.1:

- eccentricity:

$$e \equiv \frac{CL^2}{GM} \geq 0 \quad (4.22)$$

- semi-major axis:

$$a \equiv \frac{L^2}{GM(1 - e^2)} \quad (4.23)$$

a and e describe the size and the shape of the Kepler ellipse and they are conserved along the orbit. With Equations 4.22 and 4.23, the solution for the conic sections can derived:

$$r(\varphi) = \frac{a(1 - e^2)}{1 + e \cos(\varphi - \varphi_0)}. \quad (4.24)$$

Equation 4.24 describes the Kepler ellipses shown in Figure 4.1. Equation 4.24 can deliver some insights:

- $e > 1$, $e = 1$ and $a = \infty$ give an unbound orbit.
- $e < 1$ gives bound orbits and this delivers periodic values of r with a period of 2π . Since E and L are both conserved along the orbit, the ellipse or the bound Kepler orbit are closed.

For the bound Kepler orbit the gravitational centre of attraction lies at one of the foci of the ellipse. The orbit may also be parameterised differently by setting

$$r = a(1 - e \cos(\vartheta)), \quad (4.25)$$

where the new phase ϑ , which is also known as the eccentric anomaly, is also shown in Figure 4.1. Furthermore, the true anomaly is simply given by $\varphi - \varphi_0$. The following relation can be derived from Equation 4.19:

$$\dot{r} = \sqrt{2E + 2\frac{GM}{r} - \frac{L^2}{r^2}} = \sqrt{GMa} r^{-1} e \sin(\vartheta) \quad (4.26)$$

Considering the time derivative of Equation 4.26

$$\dot{r} = ae \sin(\vartheta) \dot{\vartheta} \quad (4.27)$$

and putting that into Equation 4.26, we yield the following expression

$$\sqrt{\frac{GM}{a^3}} dt = (1 - e \cos(\vartheta)) d\vartheta. \quad (4.28)$$

Furthermore, we get

Definition 4.1.2 (Kepler's third law)

$$\Omega \equiv \sqrt{\frac{GM}{a^3}}, \quad (4.29)$$

where Ω is also known as the mean motion.

and the period

$$P = \frac{2\pi}{\Omega} = 2\pi a^{3/2} (GM)^{-1/2}. \quad (4.30)$$

lead to an equation for the mean anomaly λ , see also shaded area in Figure 4.1:

Definition 4.1.3 (Kepler's problem)

$$\Omega(t - t_0) = \lambda = \vartheta - e \sin(\vartheta), \quad (4.31)$$

which is also known as Kepler's equation.

Equation 4.31 can be solved to give the orbit of the stars. The eccentricity vector is also conserved along the orbit

$$\mathbf{e} \equiv \frac{\mathbf{v} \times (\mathbf{r} \times \mathbf{v})}{GM} - \hat{\mathbf{r}} = \left[\frac{\mathbf{v}^2}{GM} - \frac{1}{r} \right] \mathbf{r} - \frac{\mathbf{r} \cdot \mathbf{v}}{GM} \mathbf{v}. \quad (4.32)$$

This vector is perpendicular to the angular momentum \mathbf{L} and lies in the plane of the Kepler orbit and points towards the peri-centre, see also Figure 4.1. With the eccentricity vector the position of the star can be given along the orbit, see also Figure 4.1

$$\mathbf{r} = a[(\cos(\vartheta) - e)\hat{\mathbf{e}} + \mathbf{h} \times \hat{\mathbf{e}} \sin(\vartheta)] \quad \text{with} \quad \mathbf{h} \equiv \frac{\mathbf{L}}{\sqrt{GMa}}. \quad (4.33)$$

4.1.2 Hyperbolic encounters between stars

This section is based on Binney and Tremaine (2008a). The two-body problem discussed in Section 4.1.1 is very fundamental in the evolution of star clusters. As already mentioned in Definition 2.2.4, where the principle of relaxation is introduced for the first in this thesis, the evolution collisional, self-gravitating system is largely governed by two-body relaxation, or in other words, hyperbolic encounters between stars that can be modelled by unbound orbits of two stars. There are two stars of masses m and M with positions and velocities of

$$(\mathbf{x}_m, \mathbf{v}_m), \quad (4.34)$$

$$(\mathbf{x}_M, \mathbf{v}_M), \quad (4.35)$$

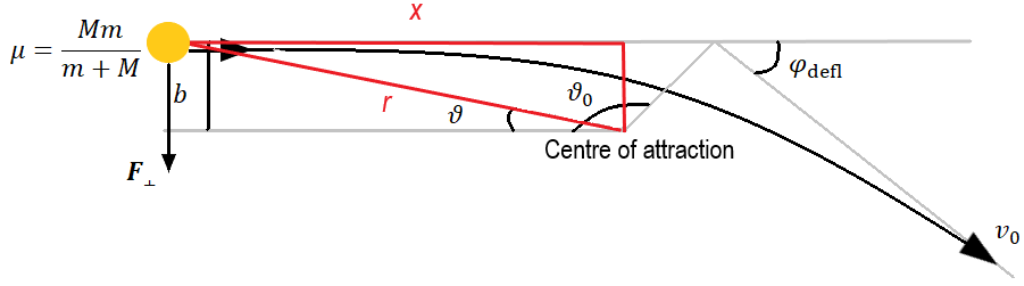


Figure 4.3: The trajectory of the reduced particle with mass μ during a hyperbolic encounter around the centre of gravitational attraction when travelling in a Kepler potential of another particle with mass $m + M$.

respectively. **Figure 4.3** then shows the trajectory of a ‘reduced’ particle that has mass

$$\mu = \frac{mM}{m + M}, \quad (4.36)$$

and that orbits in the Kepler potential of mass $m + M$. The equations of motions of this particle are

$$\left(\frac{mM}{m + M} \right) \ddot{\mathbf{r}} = -\frac{GMm}{r^2} \hat{\mathbf{e}}_r, \quad (4.37)$$

with $\mathbf{r} = \mathbf{x}_M - \mathbf{x}_m$. This can be rewritten with the reduced mass

$$\left(\frac{mM}{M + m} \right) \ddot{\mathbf{r}} = -\frac{GMm}{r^2} \hat{\mathbf{e}}_r \quad \text{or} \quad \mu \ddot{\mathbf{r}} = -\frac{G(M + m)\mu}{r^2} \hat{\mathbf{e}}_r \quad (4.38)$$

Now we have an equation of motion for a fictitious particles, which is called the ‘reduced’ particle that is also shown in **Figure 4.3**. The reduced particle travels in the Kepler potential of a fixed body of mass $M + m$. I denote the changes in the velocities of the masses m and M in the velocities as a result of the encounter as $\Delta \mathbf{v}_m$ and $\Delta \mathbf{v}_M$

$$\Delta \mathbf{v}_M - \Delta \mathbf{v}_m = \Delta \mathbf{v}. \quad (4.39)$$

It can be shown that in this in encounter the centre-of-mass (COM) of the two bodies is not affected by the encounter¹. Therefore, we have

$$M \Delta \mathbf{v}_M + m \Delta \mathbf{v}_m = 0. \quad (4.45)$$

Eliminating $\Delta \mathbf{v}_m$, we then get $\Delta \mathbf{v}_M$ as

$$\Delta \mathbf{v}_M = \frac{m}{M + m} \Delta \mathbf{v}. \quad (4.46)$$

The component of the initial separation vector that is perpendicular to the initial velocity vector $\mathbf{v}_0 = \mathbf{v}(t = -\infty)$ shown in **Figure 4.3** is known the impact parameter of the encounter and denoted by b . Then the conserved angular momentum per unit mass associated with the motion of the reduced particle is

$$L = b v_0.$$

1: For the system described here, the forces on stars according to Newton’s third law balance

$$\mathbf{F}_{Mm} = -\mathbf{F}_{mM}. \quad (4.40)$$

The COM in the isolated system is located at

$$\mathbf{x}_{\text{com}} = \frac{m\mathbf{x}_m + M\mathbf{x}_M}{M + m}. \quad (4.41)$$

Therefore, I get for the acceleration of the COM according to Newton’s second law

$$\frac{d^2 \mathbf{x}_{\text{com}}}{dt^2} = \frac{1}{M + m} \left(m \frac{d^2 \mathbf{x}_m}{dt^2} + M \frac{d^2 \mathbf{x}_M}{dt^2} \right) \quad (4.42)$$

$$\frac{d^2 \mathbf{x}_{\text{com}}}{dt^2} = \frac{1}{M + m} (\mathbf{F}_{Mm} + \mathbf{F}_{mM}) \quad (4.43)$$

The sum over \mathbf{F}_{Mm} vanishes since $\mathbf{F}_{Mm} = -\mathbf{F}_{mM}$ sums to zero. Thus

$$\frac{d^2 \mathbf{x}_{\text{com}}}{dt^2} = 0. \quad (4.44)$$

The COM of this isolated system moves at uniform velocity.

By considering again Equation 4.21, it can then be rewritten for the hyperbolic encounter for the problem considered here

$$\frac{1}{r} = C \cos(\vartheta - \vartheta_0) + \frac{G(M+m)}{b^2 v_0^2}, \quad (4.47)$$

where the angle ϑ is shown in Figure 4.3 and C and ϑ_0 are sensitive to the initial conditions of the hyperbolic encounter shown here. Equation 4.47 can be differentiated with respect to time:

$$\frac{dr}{dt} = C r^2 \dot{\vartheta} \sin(\vartheta - \vartheta_0), \quad (4.48)$$

and by using $r^2 \dot{\vartheta} = L$, Equation 4.48 is simply given by

$$C b V_0 \sin(\vartheta - \vartheta_0). \quad (4.49)$$

$\vartheta = 0$ is assumed to point towards the star as $t \rightarrow -\infty$. Equation 4.49 is then at $t = -\infty$ given by

$$-v_0 = C b v_0 \sin(-\vartheta_0). \quad (4.50)$$

Furthermore, Equation 4.48 at $t \rightarrow -\infty$ gives

$$0 = C \cos \vartheta_0 + \frac{G(M+m)}{b^2 v_0^2}. \quad (4.51)$$

Eliminating C between these equations, we obtain

$$\tan \vartheta_0 = -\frac{b v_0^2}{G(M+m)}. \quad (4.52)$$

The point of closest approach is reached when $\vartheta = \vartheta_0$. Figure 4.3 shows that in this scenario the angle by which the star is deflected by is given by

$$\varphi_{\text{defl}} = 2\vartheta_0 - \pi, \quad (4.53)$$

since the orbit is symmetrical about $\vartheta = \vartheta_0$.

Definition 4.1.4 (90° deflection radius) *The impact parameter b at $\varphi_{\text{defl}} = 90^\circ$ is given by*

$$b_{90^\circ} \equiv \frac{G(M+m)}{v_0^2}, \quad (4.54)$$

see also the discussion leading up to Definition 2.2.4.

Equation 4.54 can then be used to redefine Equation 4.52

$$\varphi_{\text{defl}} = 2 \tan^{-1} \left(\frac{G(M+m)}{b v_0^2} \right) = 2 \tan^{-1} \left(\frac{b_{90^\circ}}{b} \right). \quad (4.55)$$

The hyperbolic encounter in our situation conserves energy and therefore the relative velocity equals the initial speed v_0 . The velocity change Δv can be decomposed into the a contribution perpendicular, Δv_{\perp} , and parallel, Δv_{\parallel} , to the original relative velocity vector \mathbf{v}_0 .

With the use of trigonometry it can be shown that

$$|\Delta \mathbf{v}_\perp| = \frac{2v_0 (b/b_{90^\circ})}{1 + b^2/b_{90^\circ}^2} \quad (4.56)$$

$$|\Delta \mathbf{v}_\parallel| = \frac{2v_0}{1 + b^2/b_{90^\circ}^2}. \quad (4.57)$$

$\Delta \mathbf{V}_\parallel$ always points in the direction opposite to \mathbf{v}_0 . Equation 4.39 can then be decomposed and $\Delta \mathbf{v}_M$ is then given by

$$|\Delta \mathbf{v}_{M\perp}| = \frac{2mv_0}{M+m} \frac{b/b_{90^\circ}}{1 + b^2/b_{90^\circ}^2} \quad (4.58)$$

$$|\Delta \mathbf{v}_{M\parallel}| = \frac{2mv_0}{M+m} \frac{1}{1 + b^2/b_{90^\circ}^2}. \quad (4.59)$$

$\Delta \mathbf{v}_{M\parallel}$ always points in the direction opposite to \mathbf{v}_0 . In the limit of large impact parameters b , then

$$|\Delta \mathbf{v}_{M\perp}| = \frac{2Gm}{bv_0}. \quad (4.60)$$

In Section 4.1.3 below, this quantity will emerge in a slightly different fashion.

4.1.3 Relaxation revisited

The relaxation time-scale τ_{rx} was already introduced in Definition 2.2.4, but here it is derived from encounter theory. To formally calculate τ_{rx} , we look at the trajectories of stars and how they are changed by encountering other stars, distant and non-distant, on their paths. A schematic diagram of the discussion below can again be found in Figure 4.3.

Now the force acting on the incoming star can be decomposed into a transverse and longitudinal component yields for the transversal force component F_\perp

$$F_\perp = F \cos(90 - \vartheta) = \frac{Gm^2}{b^2 + x^2} \frac{b}{r} = \frac{Gm^2}{b^2} \left[1 + \left(\frac{vt}{b} \right)^2 \right]^{-3/2}, \quad (4.61)$$

which leads to a change in the transverse velocity

$$\delta v_\perp = \frac{Gm^2}{b} \int_{-\infty}^{+\infty} \left[1 + \left(\frac{vt}{b} \right)^2 \right]^{-3/2} dt = \frac{2Gm}{bv}. \quad (4.62)$$

Note that this is already given in Equation 4.60. Considering similar encounters of the star with impact parameter b with another N stars that are confined within a radius of R , as the star moves through the cluster, we get after one crossing time-scale τ_{cross} , see Definition 15, the number of encounters with impact parameters b can be written as

$$\delta n = \frac{N}{\pi R^2} 2\pi b db. \quad (4.63)$$

Since these encounters are random, the level of transverse velocity fluctuations δv_{\perp} can be written as

$$\delta v_{\perp}^2 = \left(\frac{2Gm}{bv} \right)^2 \frac{2N}{R^2} b db. \quad (4.64)$$

Integrating over all impact parameters b and setting a minimum impact parameter b_{\min} to avoid the singularity at $b = 0$, yields

$$\Delta v_{\perp}^2 = \int_{b_{\min}}^R \delta v_{\perp}^2 db = 8N \left(\frac{Gm}{Rv} \right)^2 \ln \left(\frac{R}{b_{\min}} \right) = 8N \left(\frac{Gm}{Rv} \right)^2 \ln(\Lambda), \quad (4.65)$$

where $\ln(\Lambda)$ is a weakly varying logarithmic trend, which is the previously introduced Coulomb logarithm, see Equation 2.5 and Definition 18. As mentioned previously, this logarithm may take many different functional forms. To account for relaxation, then this is achieved after n_{rx} crossings of the star cluster:

$$n_{\text{rx}} \left(\frac{\Delta v_{\perp}}{v} \right)^2 = n_{\text{rx}} \frac{8 \ln(\Lambda)}{N} \simeq 1. \quad (4.66)$$

With

$$\Lambda = \frac{R}{b_{\min}} = \frac{R}{Gm} v^2 \simeq N \quad (4.67)$$

$$\rightarrow n_{\text{rx}} \simeq \frac{N}{8 \ln(N)} \quad (4.68)$$

Using the expressions above we can relate the crossing time-scale τ_{cross} , see also Definition 15, and the relaxation time τ_{rx} , see also Definition 2.2.4, as follows:

$$\tau_{\text{rx}} = n_{\text{rx}} \tau_{\text{cross}} = \frac{N}{8 \ln(N)} \frac{R}{v}. \quad (4.69)$$

The process of relaxation can also be considered slightly differently. Due to the repeated hyperbolic encounters elaborated in this section stars in star clusters diffuse in phase space away from their original orbits to the point that after one τ_{rx} has no correlation with its original orbit before the first hyperbolic encounter. Therefore, a distinction can be made between so-called collisionless and collisional stellar systems.

If the life-time of the stellar system exceeds the relaxation time-scale of the system, then it is collisional. On the other hand, if the life-time of the stellar system is shorter than the relaxation time-scale of the system, then it is collisionless.

Now I briefly compare stellar systems and decide whether they should be treated as *collisionless* or *collisional*. This has been done for the main stellar systems in the Universe and the results are shown in Table 4.1. As can be seen in Table 4.1 that the star clusters that I

Table 4.1: Exemplary and very approximate time-scales for several stellar systems to illustrate whether the statistical treatment should be conducted using the collisionless Boltzmann equation (CBE) from Equation 4.99 or the collisional Fokker-Planck equation (FPE). τ_{rx} and τ_{cross} are calculated from Equation 4.69. The sizes given by effective radii r/pc and velocity dispersions given by σ/kms^{-1} as well as particle numbers N are rough estimates as the stellar systems presented here exist on huge size, mass and density scales (see e.g. Krumholz et al., 2019) or Chapter 2.

| Stellar system | N | r/pc | σ/kms^{-1} | $\tau_{\text{cross}}/\text{yr}$ | $\tau_{\text{rx}}/\text{yr}$ | age/ t_{rx} | CBE or FPE |
|----------------|-----------|---------------|--------------------------|---------------------------------|------------------------------|----------------------|------------|
| NSC | 10^7 | 10 | 50 | 2×10^5 | 10^{10} | ≤ 10 | FPE |
| GC | 10^5 | 4 | 10 | 4×10^5 | 4×10^8 | ≤ 10 | FPE |
| OC | 10^2 | 2 | 0.5 | 4×10^6 | 10^7 | ≤ 1 | CBE / FPE |
| Dwarf galaxy | 10^9 | 10^3 | 50 | 3×10^7 | 10^{17} | 10^{-7} | CBE |
| Massive galaxy | 10^{11} | 10^4 | 300 | 2×10^7 | 10^{14} | 10^{-4} | CBE |
| Galaxy cluster | 10^3 | 10^6 | 10^3 | 5×10^6 | 5×10^8 | 10^{-1} | CBE |

present in Kamlah, Leveque, et al. (2022) and Kamlah, Spurzem, et al. (2022) and Kamlah et al. (2023, in prep.) are generally collisional and require special treatment.

4.1.4 Inelastic encounters between stars

I briefly elaborate on inelastic encounters between stars, which is a natural consequence of the stars in the star clusters and simulations thereof not having zero radii, see also Section 3.2.5 for the ultimate consequences in terms of this fact in stellar evolution. In this chapter, I have so far assumed that the stars have finite radii.

The collision time-scale τ_{coll} gives the collision rate

$$\frac{1}{\tau_{\text{coll}}}, \quad (4.70)$$

which is the average number of collisions that one particular star experiences per time-step. It can be shown, see Binney and Tremaine (2008a), that the impact parameter between two stars of masses m during an inelastic encounter with r_{coll} being the radii of the stars is given by

$$b^2 = r_{\text{coll}}^2 + \frac{4Gmr_{\text{coll}}}{v_0^2}, \quad (4.71)$$

see also Figure 4.3 and a collision will occur if the distance between the two stars is smaller than b . Furthermore, through statistical arguments it can be shown that

$$\frac{1}{t_{\text{coll}}} = 4\sqrt{\pi}n\sigma \left(r_{\text{coll}}^2 + \frac{Gm}{\sigma^2} r_{\text{coll}} \right), \quad (4.72)$$

where n is the number density of stars and σ is the velocity dispersion of the stars. In Equation 4.72, the second term represents the enhancement in the collision rate due to

Definition 4.1.5 (Gravitational focusing) *which is the deflection of the trajectories of two stars by their mutual self-gravity ignoring other gravitational forces by perturbers.*

In dense star clusters as the ones presented in my work, gravitational focusing can enhance the collision rate. If r_{\star} is the stellar radius

the collision radius may simply be given by $r_{\text{coll}} = 2r_{\star}$. The escape speed from the stellar surface is given by

$$v_{\star, \text{esc}} = \sqrt{\frac{2Gm}{r_{\star}}}. \quad (4.73)$$

With the escape speed $v_{\star, \text{esc}}$, then Equation 4.72 can be rewritten as

$$\frac{1}{\tau_{\text{coll}}} = 16\sqrt{\pi}n\sigma r_{\star}^2 \left(1 + \frac{v_{\star, \text{esc}}^2}{4\sigma^2}\right) = 16\sqrt{\pi}n\sigma r_{\star}^2(1 + \Theta), \quad (4.74)$$

where we have introduced the Safronov number Θ is introduced as

$$\Theta \equiv \frac{v_{\star, \text{esc}}^2}{4\sigma^2} \quad (4.75)$$

Equation 4.74 typically underestimates the collision rate in star clusters due to three-body dynamics, see Section 4.1.5, which can result in a large variety of outcomes. Relating τ_{coll} to τ_{rx} gives

$$\frac{\tau_{\text{coll}}}{\tau_{\text{rx}}} = 0.4 \ln \Lambda \frac{\Theta^2}{1 + \Theta}. \quad (4.76)$$

Core-collapse of a star cluster typically happens within 300 central relaxation time-scales. Therefore, collisions between stars and compact objects can have a significant impact on the evolution of a star cluster if $\frac{\tau_{\text{coll}}}{\tau_{\text{rx}}} \leq 300$. Collisions (and coalescence) events between stars and compact objects are especially important in my work on Popu-III star clusters presented in Kamlah et al. (see e.g. 2023).

4.1.5 The gravitational three-body problem

Consider three stars with indices $i = 1, 2, 3$, masses m_i and position vectors \mathbf{r}_i moving at velocities $\dot{\mathbf{r}}_i$, see also Figure 4.4:

$$\ddot{\mathbf{r}}_1 = -Gm_2 \frac{\mathbf{r}_1 - \mathbf{r}_2}{|\mathbf{r}_1 - \mathbf{r}_2|^3} - Gm_3 \frac{\mathbf{r}_1 - \mathbf{r}_3}{|\mathbf{r}_1 - \mathbf{r}_3|^3}, \quad (4.77)$$

$$\ddot{\mathbf{r}}_2 = -Gm_3 \frac{\mathbf{r}_2 - \mathbf{r}_3}{|\mathbf{r}_2 - \mathbf{r}_3|^3} - Gm_1 \frac{\mathbf{r}_2 - \mathbf{r}_1}{|\mathbf{r}_2 - \mathbf{r}_1|^3}, \quad (4.78)$$

$$\ddot{\mathbf{r}}_3 = -Gm_1 \frac{\mathbf{r}_3 - \mathbf{r}_1}{|\mathbf{r}_3 - \mathbf{r}_1|^3} - Gm_2 \frac{\mathbf{r}_3 - \mathbf{r}_2}{|\mathbf{r}_3 - \mathbf{r}_2|^3}. \quad (4.79)$$

where G is the gravitational constant. This is a set of nine second-order differential equations. The three-body problem can also be formulated using the Hamilton formalism, where \mathcal{H} is the Hamiltonian:

$$\mathcal{H} = -\frac{Gm_1m_2}{|\mathbf{r}_1 - \mathbf{r}_2|} - \frac{Gm_2m_3}{|\mathbf{r}_3 - \mathbf{r}_2|} - \frac{Gm_3m_1}{|\mathbf{r}_3 - \mathbf{r}_1|} + \frac{\mathbf{p}_1^2}{2m_1} + \frac{\mathbf{p}_2^2}{2m_2} + \frac{\mathbf{p}_3^2}{2m_3}. \quad (4.80)$$

It will be easier in Chapter 5 to consider the three-body regularisation using this formalism.

Generally speaking the three-body problem does not have closed form solutions unlike the two-body problem introduced in Section

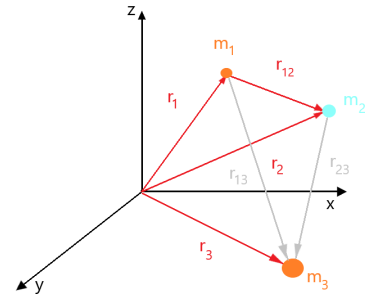


Figure 4.4: Schematic diagram of the three-body problem between two stars in Cartesian coordinates.

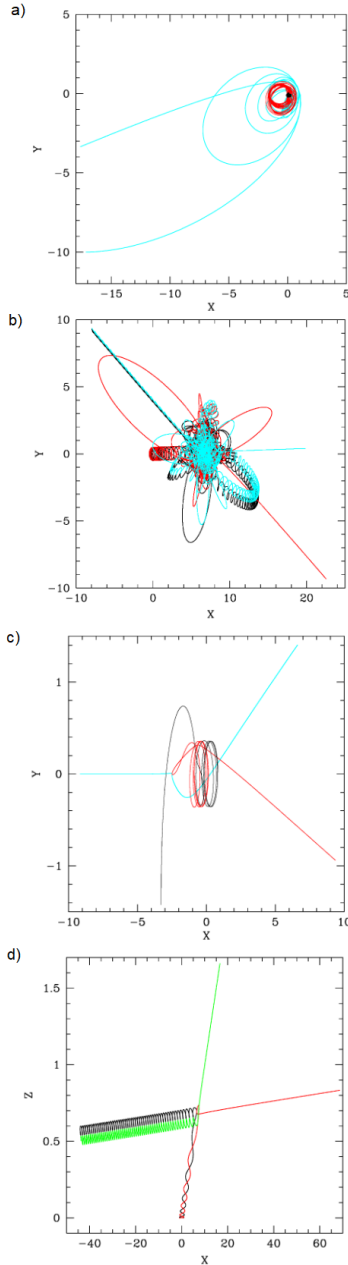


Figure 4.5: Figure showing various types of dynamical three-body encounters from dynamical simulations; The position axes are in N -body units: a) a dynamical flyby, b) resonant exchange, c) prompt exchange and d) ionization of a binary (Figure and caption taken from Mapelli, 2018a).

4.1.1. There exist some special configurations for which the three-body problem can be closed, but these will not occur in nature as the gravitational force cannot be shielded and thus even the most distant stars will perturb such a three-body configuration to some degree. Therefore, these will not be repeated here.

The interaction between three stars or compact objects is of fundamental importance in stellar and compact object dynamics on all scales (see e.g. Arca Sedda & et al., 2023b, 2023c; Bonetti et al., 2016, 2018; Fragione & Kocsis, 2020; Fragione & Loeb, 2019; Hoffman & Loeb, 2007; Thompson, 2011) and in general stellar evolution (see e.g. de Vries et al., 2014; Hamers et al., 2013; Hamers & Safarzadeh, 2020; Toonen et al., 2020; Toonen, 2019). Therefore, triples are of central importance in regulating star cluster evolution and we need to resolve at least the dynamics of a three-body interaction in simulations. The stellar evolution treatment of triple systems is generally much more complicated and it is difficult to include that in a gravitational N -body code (Hamers & Safarzadeh, 2020).

In fact, dynamical binaries cannot form from two stars simply encountering one another, because the orbit is always along a hyperbola, see discussion in Section 4.1.2.

The rate of binary formation by three-body encounters can be estimated following Binney and Tremaine (2008a). The velocity perturbation between two stars during a hyperbolic encounter may be written as

$$\delta v \sim \frac{Gm}{vb}, \quad (4.81)$$

where m is the mass of the binary, b is the impact parameter and v is the relative velocity between the two stars. This equation may be re-written as

$$\frac{\delta v}{v} \sim \frac{b_{90^\circ}}{b}, \quad (4.82)$$

by using Equation 4.54. Figure 4.5 illustrates a couple of three-body encounters. In general, if three stars in a star cluster at a common impact parameter b then by extension their change in relative velocity will also be of similar magnitude. If the result of such a triple encounter is a binary in a Keplerian orbit, then it follows that

$$\delta v \approx v \quad \text{with} \quad b \approx b_{90^\circ} \quad (4.83)$$

Based on this analysis, it is possible to estimate a time-scale for the n repeated three-body encounters at separation b_{90° or less.

$$\frac{1}{nb_{90^\circ}^2 v} \quad (4.84)$$

From simple geometric considerations, it is possible to estimate the probability that a third star also lies within a distance b_{90° , which is simply given by

$$nb_{90^\circ}^3 \quad (4.85)$$

Definition 4.1.6 (triple-encounter time-scale) *The time-scale τ_{3body} for a given star to suffer a triple encounter at a separation less than b_{90°*

is given by

$$\tau_{3body} \approx \frac{1}{n^2 b_{90}^5 v} \quad (4.86)$$

τ_{3body} from Definition 4.1.6 can be used to estimate the time-scale required for some star to form a binary with another star via such a triple encounter following J. Goodman and Hut (1993)

Definition 4.1.7 (dynamical binary formation time-scale) *The time-scale τ_{dynbin} for a given star to become part of a binary by a triple encounter is given by*

$$\tau_{dynbin} \approx \frac{v^9}{n^2 G^5 m^5}. \quad (4.87)$$

τ_{dynbin} may furthermore be related to τ_{rx} from Equation 4.69 by using the Virial theorem from Definition 4:

$$\frac{\tau_{dynbin}}{\tau_{rx}} \approx 10N^2 \ln(N) \quad (4.88)$$

or in other words, the total number of binaries formed within one relaxation time-scale is given by

$$\frac{N t_{rx}}{\tau_{dynbin}} \approx \frac{0.1}{N \ln N}. \quad (4.89)$$

This not very large and gets increasingly small for larger N . Therefore, the primordial binary fraction in a star cluster, see also Section 2.2.3, will continuously decrease over the life-time of a star cluster (see also Kamlah, Leveque, et al., 2022, for long-term simulations and the evolution of binary fractions).

Figure 4.5 shows the outcomes of some triple encounters. Mapelli (2018a) here distinguishes between three cases:

- ▶ Dynamical flyby: energy is exchanged between the binary and the single stars but the binary does not change its components.
- ▶ Resonant exchange: a binary exchanges one of its members with the intruder.
- ▶ Ionization: the binary breaks during the interaction.

All of these scenarios are possible and happen many times during the evolution of a star cluster, which also illustrates the necessity of full N -body simulations of star clusters for the search of gravitational wave sources instead of pure binary population synthesis.

4.2 Statistical treatment of star clusters

As the number of stars that are described increases from the two-body, see Section 4.1.1, and the three-body problem, see Section 4.1.5, statistical methods to describe their evolution in space and time. There exists one approximation that governs the evolution of the distribution function of such a system, the so-called Fokker-Planck

equation (FPE), which is at the heart of collisional dynamics and star cluster evolution. I begin, however, with the collisionless Boltzmann equation (CBE), which is the master equation of collisionless dynamics and from which the FPE naturally follows.

4.2.1 Collisionless stellar dynamics

Let's consider a star cluster that consists of N stars. I employ a statistical approach to find the probability of the location of a star in 6D phase-space with volume $d^3\mathbf{q}d^3\mathbf{p}$ that is centered on some location \mathbf{q} and some momentum \mathbf{p}^2

2: It can be shown that the distribution function has the same numerical value at a given phase-space point in any canonical coordinate system (see e.g. Binney & Tremaine, 2008a). Canonical coordinates satisfy the fundamental Poisson brackets:

$$[q^i, q^j] = 0 \quad (4.90)$$

$$[p_i, p_j] = 0 \quad (4.91)$$

$$[q^i, p_j] = \delta_{ij}, \quad (4.92)$$

where q_i denote the coordinates of the underlying manifold and the p_i values denote the underlying conjugate momenta.

A distribution function f needs to be defined such that $f(\mathbf{q}, \mathbf{p}, t)d^3\mathbf{q}d^3\mathbf{p}$ is the probability that at time t a randomly chosen star has phase-space coordinates in the given range.

I assume that all the stars in the star cluster identical and therefore $f(\mathbf{q}, \mathbf{p}, t)d^3\mathbf{q}d^3\mathbf{p}$ is the same for any star in the star cluster. $f(\mathbf{q}, \mathbf{p}, t)$ is normalised such that

$$\int f(\mathbf{q}, \mathbf{p}, t)d^3\mathbf{q}d^3\mathbf{p} = 1, \quad (4.93)$$

where the integral is taken over the whole phase-space. I note that the integral

$$\int d^3\mathbf{q}\rho(\mathbf{q}, t) = M, \quad (4.94)$$

is conserved and gives the total mass of the star cluster.

I treat $\mathbf{w} = (\mathbf{q}, \mathbf{p})$ as an arbitrary system of canonical coordinates from now on. A star moves through phase-space, so the probability of finding it at any given phase-space location evolves with time. A differential equation has to be derived that is satisfied by f as a consequence of this evolution. The probability of finding any star in the whole of the phase-space must at all times equal to one, see also Equation 4.93, and therefore a continuity equation, see also Equation 4.94 for mass conservation, exists to describe the conservation of this probability

Definition 4.2.1 (Continuity equation for stars)

$$\frac{\partial f}{\partial t} + \frac{\partial}{\partial \mathbf{w}} \cdot (f\dot{\mathbf{w}}) = 0. \quad (4.95)$$

This is analogous for the conservation of fluid mass in any fluid. Using the Hamilton formalism, which I already used in the section describing two-body, see Section 4.1.1, and the section describing three-body problem, see Section 4.1.5, to give the equations of motion for any given star

$$\dot{\mathbf{q}} = \frac{\partial \mathcal{H}}{\partial \mathbf{p}} \quad \text{and} \quad \dot{\mathbf{p}} = -\frac{\partial \mathcal{H}}{\partial \mathbf{q}} \quad (4.96)$$

it is possible to eliminate the $\dot{\mathbf{w}} = (\dot{\mathbf{q}}, \dot{\mathbf{p}})$ term from Equation 4.95:

$$\frac{\partial}{\partial \mathbf{q}} \cdot (f \dot{\mathbf{q}}) + \frac{\partial}{\partial \mathbf{p}} \cdot (f \dot{\mathbf{p}}) = \frac{\partial}{\partial \mathbf{q}} \cdot \left(f \frac{\partial \mathcal{H}}{\partial \mathbf{p}} \right) - \frac{\partial}{\partial \mathbf{p}} \cdot \left(f \frac{\partial \mathcal{H}}{\partial \mathbf{q}} \right) \quad (4.97)$$

$$= \dot{\mathbf{q}} \cdot \frac{\partial f}{\partial \mathbf{q}} + \dot{\mathbf{p}} \cdot \frac{\partial f}{\partial \mathbf{p}}, \quad (4.98)$$

which is substituted into Equation 4.95 to give

Definition 4.2.2 (Collisionless Boltzmann equation (CBE))

$$\frac{\partial f}{\partial t} + \dot{\mathbf{q}} \cdot \frac{\partial f}{\partial \mathbf{q}} + \dot{\mathbf{p}} \cdot \frac{\partial f}{\partial \mathbf{p}} = 0 \quad (4.99)$$

The CBE is a partial differential equation for the distribution function f as a function of 6 phase-space coordinates and time. I can also rewrite the CBE from Equation 4.99 as

$$\frac{df}{dt} = 0. \quad (4.100)$$

This implies that the “probability fluid” characterized by the distribution function f as it flows through phase space is in-compressible, just like an ideal fluid in the physical world, the phase-space density f of a fluid around the star always remains the same.

Binney and Tremaine (2008a) raise the following important issues with the description by Equation 4.99:

- In the CBE it is assumed that the stars are unchanging over their entire life-times, which we know is not true at the very least from Chapter 3: stars evolve, die and new stars may even be born over the life-time of the stellar ensemble that the CBE models:

$$\mathcal{H} = \frac{1}{2} \mathbf{p}^2 + \Phi(\mathbf{q}, t) \quad (4.101)$$

to yield

$$\frac{\partial f}{\partial t} + \mathbf{p} \cdot \frac{\partial f}{\partial \mathbf{q}} - \frac{\partial \Phi}{\partial \mathbf{q}} \cdot \frac{\partial f}{\partial \mathbf{p}} = 0. \quad (4.102)$$

Then, one can establish the following equation:

$$\frac{\partial f}{\partial t} + \mathbf{p} \cdot \frac{\partial f}{\partial \mathbf{x}} - \frac{\partial \Phi}{\partial \mathbf{q}} \cdot \frac{\partial f}{\partial \mathbf{p}} = B(\mathbf{q}, \mathbf{p}, t) - D(\mathbf{q}, \mathbf{p}, t), \quad (4.103)$$

where $B(\mathbf{q}, \mathbf{p}, t)$ and $D(\mathbf{q}, \mathbf{p}, t)$ are the rates per unit phase-space volume at which stars are born and die³. Only if

$$B(\mathbf{q}, \mathbf{p}, t) = D(\mathbf{q}, \mathbf{p}, t) = 0, \quad (4.104)$$

is the CBE from Equation 4.99 fulfilled. Thus, the CBE can only be applied to stellar ensembles over very short times or be applied to stellar ensembles which consists of e.g. low mass stars that evolve extremely slowly.

- The theoretical average number density of stars in an infinitesi-

³: Stars and compact objects can be ejected from star clusters, which in this definition also means that they effectively die.

4: coarse-grained means a piece-wise constant function, which is a result of probability density averaging in cells. The size of cells is typically assumed to be small, but finite, and does not tend to zero.

mal volume of phase-space is Nf . In practice all we can hope to measure is the number density in some volume of phase-space large enough to contain many stars. Therefore, we can assume that the density in such a volume is simply $N\bar{f}$, where \bar{f} is the coarse-grained distribution function⁴, which is the average of f within this volume. This assumption only holds if the stars in that phase-space volume are uncorrelated. In other words, by knowing the position \mathbf{q}_1 and momentum \mathbf{p}_1 of some star with index 1, it is not possible to deduce the position \mathbf{q}_2 and the momentum \mathbf{p}_2 of some other star with index 2. This is however not the case in reality since stars are gravitationally attracted to one another and are therefore correlated. Therefore, the probability distributions of individual stars in some phase-space are never fully separable.

While in collisionless systems such as galaxies we can assume uncorrelated distribution functions, because the probability of star encounters is extremely small, in stellar systems such as star clusters are so dense, that encounters play a significant role as I have already mentioned repeatedly in previous sections. Therefore, the correlations between stars cannot be easily ignored. This is one more reason why the CBE is a non-sufficient treatment of a star cluster, see also [Table 4.1](#).

4.2.2 Collisional stellar dynamics

For the purposes of star cluster dynamics, the CBE from Equation 4.99 will have to include a collisional term, which accounts of encounters between stars. Furthermore, a stellar system of a finite number of stars never fully conserves energy and angular momentum. Therefore, Equation 4.99 is insufficient for my purposes.

5: It is also certainly possibly to formulate all of the below in position-velocity space, but in statistical mechanics the position-momentum space is typically chosen.

From now on, a star cluster is represented by a state N stars by a point in a $6N$ -dimensional space, which is called the Γ -space in Binney and Tremaine (2008a). A point in this space is given three momentum coordinates and three position coordinates⁵ and is called a microstate and represents a Γ -point in Γ -space. In practice and also star cluster simulations, we are oftentimes concerned with global and averaged quantities such as the binary fractions as functions of simulation time (see e.g. Kamlah, Leveque, et al., 2022). Therefore, from a practical standpoint it is simpler to follow some probability distribution function in Γ -space and not individual stars or Γ -point in Γ -space.

Each star α with ($\alpha = 1, \dots, N$) is assigned a vector $\mathbf{w}_\alpha(\mathbf{q}_\alpha, \mathbf{p}_\alpha)$, of canonical coordinates $(\mathbf{q}_\alpha, \mathbf{p}_\alpha)$. Then the Γ -point of the whole system is given by the ensemble of star vectors \mathbf{w}_α . The probability that a Γ -point is found in a unit volume of Γ -space at time t is denoted by

$$f^{(N)}(\mathbf{w}_1, \dots, \mathbf{w}_N, t), \quad (4.105)$$

which is called the N -body distribution function, since the probability distribution function integrates to 1:

$$\int d^6\mathbf{w}_1 \cdots d^6\mathbf{w}_N f^{(N)}(\mathbf{w}_1, \dots, \mathbf{w}_N, t) = 1. \quad (4.106)$$

Employing the basic assumptions in the derivation from the CBE and assuming that the stars are identical, the N -body distribution function can be taken to be symmetric for all stars α, β . The treatment of $3N$ -dimensional vectors is analogous to the the treatment of 3-dimensional vectors, the analogues Equation 4.99 and the convective derivative from Equation 4.100 can be written as

Definition 4.2.3 (Liouville's / Gibb's equations)

$$\frac{\partial f^{(N)}}{\partial t} + \sum_{\alpha=1}^N \left(\dot{\mathbf{q}}_{\alpha} \cdot \frac{\partial f^{(N)}}{\partial \mathbf{q}_{\alpha}} + \dot{\mathbf{p}}_{\alpha} \cdot \frac{\partial f^{(N)}}{\partial \mathbf{p}_{\alpha}} \right) = 0 \quad (4.107)$$

$$\frac{\partial f^{(N)}}{\partial t} + \left[f^{(N)}, \mathcal{H}_N \right] = 0 \quad (4.108)$$

$$\frac{df^{(N)}}{dt} = 0. \quad (4.109)$$

These equations imply that the probability density of Γ -points $f^{(N)}$ around the Γ -point of a give a system always remains constant.

It can be shown from Definition 4.2.3 that energy equilibrium can never be achieved in self-gravitating N -body systems⁶. The use of the equations from Definition 4.2.3 becomes clear when relating them to Equation 4.99 and the convective derivative from Equation 4.100. First of all, a N -body distribution function is explicitly not separable⁷, because encounters between stars are relevant across the whole life-time of the star cluster. In other words, correlations between the one-body distribution functions that describe single stars are non-negligible and the probability of finding a star in a star cluster at a certain spatial and velocity coordinate is affected by all (nearby) stars. It can be shown that under the assumptions that

- ▶ N -body distribution function is separable,
- ▶ the number of stars $N \rightarrow \infty$,

the Liouville's / Gibb's equations from Definition 4.2.3 reduce to the CBE from Equation 4.99.

However, the N -body distribution function is not separable in collisional dynamics and therefore for $N \gg 1$

Definition 4.2.4 (Encounter operator) I define

$$\frac{df}{dt} = \Gamma[f] \neq 0, \quad (4.113)$$

where $\Gamma[f]$ is the encounter operator, given by

$$\Gamma[f(\mathbf{w}_1, t)] \equiv N \int d^6 \mathbf{w}_2 \frac{\partial \Phi_{12}}{\partial \mathbf{x}_1} \cdot \frac{\partial g(\mathbf{w}_1, \mathbf{w}_2, t)}{\partial \mathbf{v}_1}, \quad (4.114)$$

where $g(\mathbf{w}_1, \mathbf{w}_2, t)$ is the two-body correlation⁸ function, which measures the excess probability of finding a particle at \mathbf{w}_1 due to the presence of a particle at \mathbf{w}_2 . Φ_{12} is the gravitational potential of the two stars.

The encounter operator $\Gamma[f]$ from Equation 4.114 drives the rate of change of the phase-space density around a given star. $\Gamma[f]$

6: The following N -body distribution function is a solution to Definition 4.2.3:

$$f^{(N)}(\mathbf{w}_1, \dots, \mathbf{w}_N) = f[\mathcal{H}_N(\mathbf{w}_1, \dots, \mathbf{w}_N)]. \quad (4.110)$$

When the N -body distribution function was in thermal equilibrium, then it can be rewritten as

$$f^{(N)}(\mathbf{w}_1, \dots, \mathbf{w}_N) = C \exp[-\beta \mathcal{H}_N(\mathbf{w}_1, \dots, \mathbf{w}_N)], \quad (4.111)$$

with some positive constants C and β and this distribution function cannot satisfy the normalization condition that was imposed on the N -body distribution earlier, because either the spatial or the velocity integrals diverge in the normalization.

7: A separable N -body distribution function can be written as the product of one-body distribution functions:

$$f^{(N)}(\mathbf{w}_1, \dots, \mathbf{w}_N, t) = \prod_{\beta=1}^N f(\mathbf{w}_{\beta}, t). \quad (4.112)$$

8: Two random variables x and y are uncorrelated if their joint probability $p(x, y)$ can be factored into a product of the form $p(x)p(y)$.

can be derived in the following way. $\frac{df}{dt} = \Gamma[f] \neq 0$ for the one-body distribution function depends on the two-body distribution function. If the same equation was solved for the two-body distribution function instead, we find that equation depends on the three-body distribution function. This methodology can be continued for the three-body distribution function, which would then depend on the four-body distribution function and so on.

Definition 4.2.5 (BBGKY hierarchy) A sequence of equations based on

$$\frac{df}{dt} = \Gamma[f] \neq 0, \quad (4.115)$$

is obtained of rapidly increasing complexity, which expresses the rate of change of the distribution function $f^{(n)}$ in terms of the distribution function $f^{(n+1)}$. This is known as the BBGKY hierarchy.

9: named after N. N. Bogoliubov, M. Born and H. S. Green, J. G. Kirkwood, and J. Yvon.

However, a more physical approach, which I introduce now, truncates the BBGKY hierarchy⁹ at lowest order assuming that for most of the time all particles are uncorrelated with each other and only coupled via the smooth global gravitational potential (Spurzem & Kamlah, 2023).

I am now in a position to derive master equation of collisional stellar dynamics. To reiterate, under the influence of a smooth gravitational potential $\Phi(\mathbf{q})$ only, the distribution function $f(\mathbf{q}, \mathbf{p}, t)$ obeys the CBE from Equation 4.99. As a consequence, the phase-space probability density around a given star is unchanged. When dynamical encounters are taken in account, this phase-space probability density changes with time at a rate given by $\Gamma[f]$.

Following Binney and Tremaine (2008a), I let $\Psi(\mathbf{w}, \Delta\mathbf{w})d^6(\Delta\mathbf{w})\Delta t$ be the probability that a star with the phase-space coordinates $\mathbf{w} = (\mathbf{q}, \mathbf{p})$ is scattered through a dynamical encounter into the volume of phase space $d^6(\Delta\mathbf{w})$ during some very short time interval Δt . The transition probability Ψ induces the effects of encounters with other stars, but not the acceleration due to a smooth gravitational potential of the background stellar distribution, in my case a star cluster, which is accounted for in the CBE. The stars are classed into two subcategories

- ▶ Field stars: accounted for in the CBE and they create the smooth gravitational potential
- ▶ Subject star: we follow this star as it diffuses through phase-space under the influence of the field stars.

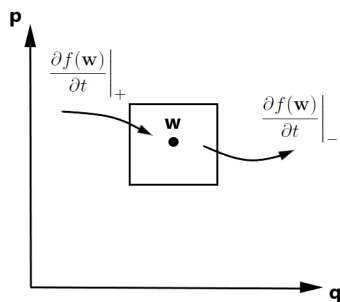


Figure 4.6: Diagram showing the scattering of a star in and out of a unit phase-space volume.

Consider a phase-space volume, centered around \mathbf{w} .

Then subject stars are scattered out of and into this unit phase-space volume at rates of

$$\frac{\partial f(\mathbf{w})}{\partial t} \Big|_{-} = -f(\mathbf{w}) \int d^6(\Delta\mathbf{w})\Psi(\mathbf{w}, \Delta\mathbf{w}), \quad (4.116)$$

$$\frac{\partial f(\mathbf{w})}{\partial t} \Big|_{+} = \int d^6(\Delta\mathbf{w})\Psi(\mathbf{w} - \Delta\mathbf{w}, \Delta\mathbf{w})f(\mathbf{w} - \Delta\mathbf{w}), \quad (4.117)$$

respectively, see also Figure 4.6. The sum of these two scattering relations yields

Definition 4.2.6 (Master equation of collisional dynamics) *The master equation and equals the encounter operator $\Gamma[f]$:*

$$\frac{df}{dt} = \Gamma[f] = \int d^6(\Delta\mathbf{w}) [\Psi(\mathbf{w}-\Delta\mathbf{w}, \Delta\mathbf{w})f(\mathbf{w}-\Delta\mathbf{w}) - \Psi(\mathbf{w}, \Delta\mathbf{w})f(\mathbf{w})], \quad (4.118)$$

where $\Psi(\mathbf{w} - \Delta\mathbf{w}, \Delta\mathbf{w})$ is the transition rate probability. The term master equation refers to a time evolution of a system, in this case a system that is described by a continuous probability distribution, which can be fully modelled in probabilistic combinations of states at any given time with the transition between states being determined by a transition matrix.

Equation 4.118 is not time-reversible¹⁰, since an expanded probability distribution via the encounter operator cannot shrink to a point. However, the exact description of the stellar system through the Liouville's / Gibb's equations from Definition 4.2.3 are time-reversible.

10: This is a consequence by the molecular chaos, which implies that the velocities of colliding particles are uncorrelated, and independent of position. Due to this missing correlation, the two-body distribution function can be written as the product of two one-body distribution functions. Here the distribution functions between the subject and field star are not correlated.

The scatterings in a star clusters are dominated by weak encounters that have $\delta v \ll v$.

This essential realisation helps to simplify Equation 4.118:

$$|\Delta(\mathbf{w})| \rightarrow 0. \quad (4.119)$$

Therefore,

$$\Psi(\mathbf{w} - \Delta\mathbf{w}, \Delta\mathbf{w})f(\mathbf{w} - \Delta\mathbf{w}) \quad (4.120)$$

may be expanded in a Taylor series¹¹,

$$\Psi(\mathbf{w} - \Delta\mathbf{w}, \Delta\mathbf{w})f(\mathbf{w} - \Delta\mathbf{w}) = \Psi(\mathbf{w}, \Delta\mathbf{w})f(\mathbf{w}) \quad (4.121)$$

$$- \sum_{i=1}^6 \Delta w_i \frac{\partial}{\partial w_i} [\Psi(\mathbf{w}, \Delta\mathbf{w})f(\mathbf{w})] \quad (4.122)$$

$$+ \frac{1}{2} \sum_{i,j=1}^6 \Delta w_i \Delta w_j \frac{\partial^2}{\partial w_i \partial w_j} [\Psi(\mathbf{w}, \Delta\mathbf{w})f(\mathbf{w})] + O(\Delta\mathbf{w}^3). \quad (4.123)$$

11: This procedure is also known as a Kramers-Moyal expansion of the master equation from Equation 4.118, which transform the integro-differential master equation in this to a second-order partial differential equation, because of the Fokker-Planck approximation.

As mentioned previously, there exists an approximation that truncates the BBKGY hierarchy from Definition 4.2.5 after the second-order terms.

Definition 4.2.7 (Fokker-Planck approximation and equation)

$$\Gamma[f] = - \sum_{i=1}^6 \frac{\partial}{\partial w_i} \{D[\Delta w_i] f(\mathbf{w})\} + \frac{1}{2} \sum_{i,j=1}^6 \frac{\partial^2}{\partial w_i \partial w_j} \{D[\Delta w_i \Delta w_j] f(\mathbf{w})\}, \quad (4.124)$$

where the diffusion coefficients are introduced:

$$D[\Delta w_i] = \int d^6(\Delta \mathbf{w}) \Psi(\mathbf{w}, \Delta \mathbf{w}) \Delta w_i, \quad (4.125)$$

$$D[\Delta w_i \Delta w_j] = \int d^6(\Delta \mathbf{w}) \Psi(\mathbf{w}, \Delta \mathbf{w}) \Delta w_i \Delta w_j, \quad (4.126)$$

which govern the rate t by which stars diffuse through phase-space as a result of dynamical encounters:

$D[\Delta w_i]$ represents a steady drift through phase-space and not a random walk. This drag process is the previously introduced dynamical friction (Chandrasekhar, 1942) from Definition 2.3.4.

- $D[\Delta w_i \Delta w_j]$ governs the rate at which the subject star executes a random walk in phase-space.

All of the dependence on the field-star distribution function is contained in the diffusion coefficients, which are functions only of the phase-space coordinates of the subject star. Equation 4.124 in combination with Equation 4.113 is the Fokker-Planck equation.

From the fact that scatterings in star clusters are dominated by weak encounters, it can also be shown that most of the scattering is due to local encounters with $b \ll R$, where R is the star clusters size or characteristic radius.

The majority of gravitational scatterings in a star cluster are due to weak, uncorrelated and local dynamical encounters.

The above has important consequences:

- As a result the encounter time-scale is short $\propto b/v$ and it is shorter than the crossing time-scale from Definition 15. Therefore, only the velocity of the subject star is affected by the encounter and not the position.
- During a dynamical encounter the two participating stars move on hyperbolic Keplerian orbits, see also Section 4.1.2.
- The impact of dynamical encounters on a star at \mathbf{x} can be calculated as if the star were embedded in an infinite homogeneous medium in which the density function is everywhere equal to the density function at \mathbf{x} .

For large N -body system with $N \gg 1$ such as the star clusters presented in Kamlah, Leveque, et al. (2022) and Kamlah, Spurzem, et al. (2022) and Kamlah et al. (2023, in prep.), the relaxation time-scale becomes much larger than the crossing time-scale of the star cluster.

Definition 4.2.8 (Orbit-averaging) *Changes in the distribution function caused by encounters are expected to be small over a single orbital period. It is therefore useful to separate the relatively slow changes in the phase-space coordinates through dynamical encounters and the comparatively rapid changes in the orbital motion of the stars in smooth gravitational potential.*

Orbit-averaging is typically done in action-angle space, see also [Figure 2.3](#). First, I need to introduce two fundamental concepts.

Definition 4.2.9 (Integrals & constants of motion) *Let (\mathbf{x}, \mathbf{v}) be the phase-space in Cartesian coordinates. A constant of motion in a gravitational potential is any function $C(\mathbf{x}, \mathbf{v}; t)$ of the phase-space coordinates and time that is constant along stellar orbits in the given gravitational potential, which implies*

$$C[\mathbf{x}(t_1), \mathbf{v}(t_1); t_1] = C[\mathbf{x}(t_2), \mathbf{v}(t_2); t_2] \quad (4.127)$$

for any times t_1 and t_2 . A subclass of constants of motion are integrals of motion that are any function of the phase-space coordinates $I(\mathbf{x}, \mathbf{v})$, which are constant along the orbit

$$I[\mathbf{x}(t_1), \mathbf{v}(t_1)] = I[\mathbf{x}(t_2), \mathbf{v}(t_2)] \quad (4.128)$$

Every integral of motion is a constant of motion, but not every constant of motion is an integral of motion.

For my purposes, especially in setting up the rotating King models from Einsel and Spurzem (1999) that I use in Kamlah, Spurzem, et al. (2022) and Kamlah et al. (2023, in prep.), it is important to consider the existence of integrals of motion in axisymmetric gravitational potentials. In such potential two analytical integrals of motions exist, which are the Hamiltonian \mathcal{H} or the total energy E and the z -component of the angular momentum, which is typically denoted by J_z and analytic expressions can be given for these. However, there exists a third integral of motion in flattened axisymmetric potentials, for which generally speaking no analytic expression exists. Such an integral of motion is also sometimes referred to as a non-classical integral of motion. The third integral of motion is only available in analytical form of the potential, which is the so-called Stäckel potentials (see e.g. Dejonghe & de Zeeuw, 1988). These potentials are beyond the treatment of this thesis. Furthermore, Lupton and Gunn (1987) showed that the total angular momentum along the orbit of a star J^2 can be considered a third integral for orbits in slightly flattened axisymmetric gravitational potentials, but a 15% deviation of the orbit has to be tolerated. The aforementioned models by Einsel and Spurzem (1999) that I use in my work crucially neglect a third integral of motion, because they assume that relaxation processes dominate the inner regions of a star cluster. But they note too that the more diffuse regions of the halo of a star cluster definitely depends on a third integral of motion. Therefore, this presents us with a very strong assumption, see also Einsel (1997) and J. J. Goodman (1983) for more details.

Integrals of motion can be used as coordinates in phase-space.

Definition 4.2.10 (Action-angle variables) *These are special sets of canonical coordinates and consist of three actions, which are momenta of the integrals of motion and their conjugate coordinates called angles. If an orbit of a star can be defined by complete set of these variables, it*

is called a regular orbit. Complete sets of action-angle variables cannot be defined a significant number of astronomically useful gravitational potentials.

Angle-action variables are typically denoted by

$$(\boldsymbol{\theta}, \mathbf{J}) \quad (4.129)$$

The momenta

$$\mathbf{J} = (J_1, J_2, J_3) \quad (4.130)$$

are the integrals of motion. Hamilton's equations for the motion of the momenta J_i are given by

$$0 = \dot{J}_i = -\frac{\partial \mathcal{H}}{\partial \theta_i}, \quad (4.131)$$

which in words means that \mathcal{H} is independent of the coordinates $\boldsymbol{\theta}$. Returning to the orbit-averaging from [Definition 4.2.8](#), the Fokker-Planck equation from [Equation 4.124](#) can be written in action-angle space:

Definition 4.2.11 (Fokker-Planck equation in action-angle space) *With the help of the the action-angle variables from [Equation eq.Angle-action variables](#), the orbit-averaged Fokker-Planck equation may be written as*

$$\frac{\partial f}{\partial t} + \dot{J}_i \frac{\partial f}{\partial J_i} + \dot{\theta}_i \frac{\partial f}{\partial \theta_i} = \Gamma[f] \quad (4.132)$$

The time derivatives \dot{J}_i and $\dot{\theta}_i$ refer to motion in the smooth potential (that is, neglecting encounters), and the encounter operator $\Gamma[f]$ from [Equation 4.113](#).

[Equation 4.132](#) is not yet orbit-averaged. This is done by introducing the operator

$$(2\pi)^{-3} \int d^3\theta \quad (4.133)$$

and operating with this on [Equation 4.132](#). Since all quantities are periodic in θ , all all terms involving $\partial/\partial\theta_i$ operator vanish across one orbit. This is also true for the term involving $\dot{\theta}_i(\partial/\partial\theta_i)$.

Definition 4.2.12 (Orbit-averaged Fokker-Planck equation) *The operator from [Equation 4.133](#) transforms [Equation 4.132](#) into*

$$\frac{\partial f}{\partial t} = \frac{1}{(2\pi)^3} \int d^3\theta \Gamma[f] = -\frac{\partial}{\partial J_i} \{f \bar{D} [\Delta J_i]\} + \frac{1}{2} \frac{\partial^2}{\partial J_i \partial J_j} \{f \bar{D} [\Delta J_i \Delta J_j]\}. \quad (4.134)$$

The diffusion coefficients from [Equation 4.125](#) and [Equation 4.126](#) become

$$\bar{D} [\Delta J_i] = \frac{1}{(2\pi)^3} \int d^3\theta D [\Delta J_i] \quad (4.135)$$

and

$$\bar{D} [\Delta J_i \Delta J_j] = \frac{1}{(2\pi)^3} \int d^3\theta D [\Delta J_i \Delta J_j], \quad (4.136)$$

respectively. This domain of the Fokker-Planck equation is now reduced from six phase-space coordinates and time to three actions and time.

The applications of solving the equations from [Definition 4.2.12](#) are given in [Chapter 1.2](#).

Furthermore, I reconsider the diffusion coefficients in Cartesian coordinates when they form functions of positions \mathbf{x} and velocities \mathbf{v} of the subject star with subscript a , where the mass of the subject star is m_a and the field stars have mass m :

$$D [\Delta v_i] = 4\pi G^2 m_a (m + m_a) \ln \Lambda \frac{\partial}{\partial v_i} h(\mathbf{x}, \mathbf{v}) \quad (4.137)$$

$$= 4\pi G^2 m_a (m + m_a) \ln \Lambda \frac{\partial}{\partial v_i} \int d^3 \mathbf{v}_a \frac{f_a(\mathbf{x}, \mathbf{v}_a)}{|\mathbf{v} - \mathbf{v}_a|} \quad (4.138)$$

$$D [\Delta v_i \Delta v_j] = 4\pi G^2 m_a^2 \ln \Lambda \frac{\partial^2}{\partial v_i \partial v_j} g(\mathbf{x}, \mathbf{v}) \quad (4.139)$$

$$= 4\pi G^2 m_a^2 \ln \Lambda \frac{\partial^2}{\partial v_i \partial v_j} \int d^3 \mathbf{v}_a f_a(\mathbf{x}, \mathbf{v}_a) |\mathbf{v} - \mathbf{v}_a|, \quad (4.140)$$

where $h(\mathbf{x}, \mathbf{v})$ and $g(\mathbf{x}, \mathbf{v})$ are the so-called Rosenbluth potentials (Rosenbluth et al., 1957). Again, the Coulomb logarithm $\ln \Lambda$ from [Definition 18](#) is found in the relations here with

$$\Lambda = \frac{b_{\max} v_{\text{typ}}^2}{G(m + m_a)}. \quad (4.141)$$

where v_{typ} is a typical velocity of stars in the system, and b_{\max} is the maximum impact parameter considered, which is typically the orbital radius. Here, it can be shown that if provided that the N -body distribution function f is given in terms of a convenient polynomial series as in Legendre polynomials the Rosenbluth potentials can be evaluated analytically to arbitrary order (see e.g. Giersz & Spurzem, 1994; Rosenbluth et al., 1957; J. Schneider et al., 2011; Spurzem & Takahashi, 1995). The use of these is briefly elaborated on in Spurzem and Kamlah (2023) and they are used in the procedure to derive the diffusion coefficients in Einsel and Spurzem (1999), which is why I have mentioned them here, see already [Chapter 1.2](#). The local Fokker-Planck equation can be written down in its standard form for the Cartesian coordinate system of the v_i :

$$\frac{\partial f}{\partial t} + \mathbf{v}_i \frac{\partial f}{\partial \mathbf{r}_i} + \vec{v}_i \frac{\partial f}{\partial \mathbf{v}_i} = \Gamma[f]. \quad (4.142)$$

$$\Gamma[f] = - \sum_{i=1}^3 \frac{\partial}{\partial v_i} [f(\mathbf{v}) D(\Delta v_i)] + \frac{1}{2} \sum_{i,j=1}^3 \frac{\partial^2}{\partial v_i \partial v_j} [f(\mathbf{v}) D(\Delta v_i \Delta v_j)]. \quad (4.143)$$

Still Equation 4.142 is a six-dimensional integro-differential equation; its direct numerical simulation in stellar dynamics can presently only be done by further simplification. For a self-gravitating system Equations 4.142 and 4.143 are not sufficient, since the knowledge of the gravitational potential of the system Φ is necessary. This can be seen above from the \vec{v}_i term - its computation requires to know the

gravitational force. How the computation of the potential depends on the employed method, which I explain in:

- ▶ Hénon-type Monte-Carlo methods in [Chapter 6](#). I use these methods in Kamlah, Leveque, et al. (2022).
- ▶ Orbit-averaged Fokker-Planck equation in axisymmetric systems in [Chapter 1.2](#). I use related methods in Kamlah, Spurzem, et al. (2022) and Kamlah et al. (2023, in prep.).

I finish the discussion on the physics of collisional stellar dynamics here, but much more material on this may be found in Binney and Tremaine (2008a, and sources therein), as well as in a much concise and review-like fashion in Spurzem and Kamlah (2023), but there with a focus on direct N -body integration, the main method of my work, which I use in all of the work presented in this thesis, see also [Chapter 5](#). I do not explain spherical gas and moment models, because I do not use these methods in the work presented in the thesis, but I highlight them here, because they have been instrumental in modelling star clusters (see e.g. Bettwieser, 1983; Bettwieser & Spurzem, 1986; D. C. Heggie, 1984; Louis & Spurzem, 1991; Lynden-Bell & Eggleton, 1980).

COMPUTATIONAL METHODS FOR COLLISIONAL DYNAMICS

This chapter is partly based on Spurzem and Kamlah (2023). In general, I use the terms ‘particles’ and ‘stars’ interchangeably in this part of the thesis. As already briefly highlighted in Section 4.2.2 these methods constitute the main tool for evolving star clusters in my research and are used in Kamlah, Leveque, et al. (2022) and Kamlah, Spurzem, et al. (2022) and Kamlah et al. (2023, in prep.). Therefore, this chapter is more exhaustive than the others explaining the computational methods I also use, see also Section 4.2.2. Direct N -body methods are based on solving Equation 4.1 directly, which is deceptively simple in theory. In general terms in order to integrate the orbits of stars in time under their mutual self-gravity the total gravitational potential at each star’s position is required. Poisson’s equation in integral form gives the gravitational potential $\Phi(\mathbf{r})$ generated at a point in coordinate space \mathbf{r} due to a smooth mass distribution $\rho(\mathbf{r})$

$$\Phi(\mathbf{r}) = -G \int \frac{\rho(\mathbf{r}')}{|\mathbf{r}' - \mathbf{r}|} d^3\mathbf{r}'. \quad (5.1)$$

A discrete particle distribution in N -body simulations is given by

$$\rho(\mathbf{r}) = \sum_{i=1}^N m_i \delta(\mathbf{r} - \mathbf{r}_i) \quad (5.2)$$

with N particles of mass m_i distributed at positions \mathbf{r}_i . Putting this into the integral Poisson equation from 5.1 we get Newton’s law for point masses:

$$\Phi(\mathbf{r}) = -G \sum_{j=1}^N \frac{m_j}{|\mathbf{r} - \mathbf{r}_j|} \quad (5.3)$$

5.1 From NBODY1 to NBODY6++GPU and NBODY7 - the growth of an industry

The title of this section is borrowed from the review by S. J. Aarseth (1999b), but slightly adjusted. A summary of important algorithmic, hardware and software development milestones is presented in Table 5.1. First N -body simulations were conducted in Heidelberg at Astronomisches Rechen-Institut in 1959 and published by Sebastian von Hoerner. In his two pioneering works von Hoerner (1960, 1963), among other interesting findings he confirmed that

- ▶ ignoring escaping stars, the relaxation time-scales in star clusters as proposed by Chandrasekhar (1942) earlier, see also Definition 2.2.4, holds,
- ▶ dynamical binary stars can form within star clusters. He called them a ‘nuisance’ later in his reflection on first N -body simulations published in von Hoerner (2001), because these

| | |
|---|-----|
| 5.1 From NBODY1 to NBODY6++GPU and NBODY7 - the growth of an industry | 115 |
| 5.2 Summary NBODY codes | 118 |
| 5.3 Time profile of NBODY6++GPU | 119 |
| 5.4 Basic features and NBODY units | 121 |
| 5.5 Methods and algorithms in NBODY6++GPU | 123 |
| 5.5.1 4 th -order Hermite integration | 123 |
| 5.5.2 Block time-steps scheme | 125 |
| 5.5.3 Ahmad-Cohen (AC) neighbour scheme | 126 |
| 5.5.4 Two-body regularisation and Kustaanheimo-Stiefel (KS) decision making | 128 |
| 5.5.5 Hierarchical systems and three-body regularisation | 131 |
| 5.5.6 Chain regularisation | 132 |
| 5.6 Parallelization in NBODY6++GPU | 134 |
| 5.7 Summary of NBODY6++GPU | 136 |

close stars require many more integration time-steps than more distant stars.

More or less simultaneous to von Hoerner's work, Sverre Aarseth, who is the father of the `NBODY` code family still in use today, developed a direct N -body integrator for galaxy clusters with gravitational softening based on Taylor series evaluation of the gravitational force up to its second derivative (S. J. Aarseth, 1963), see also Table 5.1. The latter was very important, because the gravitational softening could circumvent the problem of dynamically formed binary stars causing extreme numbers of orbit integrations, which was obstructing von Hoerner's work. The binary star issue was further revolutionized by the use of regularization methods using the Kustaanheimo-Stiefel (KS) regularization by Kustaanheimo and Stiefel (1965), which was implemented in `NBODY3` presented in S. J. Aarseth (1971). For the first time, this permitted the self-consistent treatment of many binary stars in a star cluster and this regularization technique is still in use today in `NBODY6++GPU` (Wang et al., 2015).

Roland Wielen developed another direct N -body code, which was presented in S. J. Aarseth et al. (1974) and then compared with Aarseth's aforementioned N -body codes (and a Monte-Carlo code). The code `NBODY5` published in S. J. Aarseth (1985) was the industry standard for several years later. It employed Taylor series using up to the third derivative of the gravitational force, in a divided difference scheme based on four time points, with individual particle time-steps. Also there were regularizations for more than two bodies, such as the classical chain regularization (Mikkola & Aarseth, 1990), and the Ahmad-Cohen (Ahmad & Cohen, 1973) neighbour scheme already in `NBODY5`. The main driver to the next version of a `NBODY` code was the invention of vector and parallel computers, which demanded an optimization towards hierarchically blocked time-steps and the Hermite scheme (Makino & Aarseth, 1992; McMillan, 1986), because it used only two time points instead of four in `NBODY5`, which made memory management significantly easier.

The code `NBODY6++GPU` (Wang et al., 2015), which I use in all of my work, is the massively parallel code from Aarseth's `Nbody` code family. I dedicate most of the remainder of this chapter to explaining the algorithm and some of the data structure of the code and I do not go into more detail here. The other `NBODY` code that is active development still today is `NBODY7` (S. J. Aarseth, 2012; Banerjee et al., 2020) also stems from this family, but it uses the algorithmic regularization chain method (Hellström & Mikkola, 2010; Mikkola & Aarseth, 1993; Mikkola & Merritt, 2008; Mikkola & Tanikawa, 1999a, 1999b). `NBODY7` is GPU accelerated, but has not yet the MPI parallelization of `NBODY6++` and `NBODY6++GPU`. Therefore, it is not optimised for massively parallel supercomputers and `NBODY6++GPU` remains to be currently one of the best available high accuracy, massively parallel, direct N -body simulation codes. Two very promising alternative and supposedly faster codes have been published during the preparation of this paper; the `PETAR` (Wang, Iwasawa, et al., 2020; Wang, Nitadori, & Makino, 2020a, 2020b) and `MSTAR/BI-FROST` (Rantala et al., 2020, 2021) codes, see also Table 5.1.

Table 5.1: Table showing important algorithmic, hardware and software development stepping stones in the development of direct *N*-body codes. The table is adapted from S. J. Aarseth (1999b), corrected in some places, but expanded to more recent developments. The abbreviations used are as follows:

- ▶ KS: Kustaanheimo-Stiefel
- ▶ AC: Ahmad-Cohen
- ▶ HARP-6 / GRAPE-6 : special-purpose computers named Hermite AcceleratoR Pipeline-6 / GRAvity piPE-6
- ▶ PN: Post-Newtonian
- ▶ SPMD / MPI: Single Program Multiple Data scheme/Message Passing Interface.
- ▶ AR: Algorithmic chain
- ▶ GPU: graphics processing unit
- ▶ SSE / AVX : Advanced Vector Extension/Streaming SIMD (Single Instruction, Multiple Data) Extension for vectorization in the CPU (central processing unit).
- ▶ P³T / SDAR: particle-particle particle-tree/Slow-Down Agolrithmic chain
- ▶ MSTAR / BiFrost: Minimum spanning tree + algorithmic chain / Binaries in Frost

| Year | Keyword | Reference |
|----------------|--|--|
| 1961 | Force polynomial | (S. J. Aarseth, 1963) |
| | Individual time steps | (S. J. Aarseth, 1963) |
| | Gravitational softening | (S. J. Aarseth, 1963) |
| 1966 | Spherical harmonics | (S. Aarseth, 1967) |
| 1969 | Two-body KS regularization | (Kustaanheimo & Stiefel, 1965) |
| 1972 | Three-body regularization | (S. J. Aarseth & Zare, 1974) |
| 1973 | Global regularization | (D. C. Heggie, 1974) |
| | AC neighbor scheme | (Ahmad & Cohen, 1973) |
| 1978 | Co-moving coordinates | (S. J. Aarseth, 1979) |
| 1979 | Regularized AC | (S. J. Aarseth, 1985) |
| 1980 | Planetary formation | (Lecar & Aarseth, 1986) |
| 1986 | Hierarchical block-time steps | (McMillan, 1986) |
| 1989 | Chain regularization | (Mikkola & Aarseth, 1990) |
| 1990 | Particle in box scheme | (S. J. Aarseth et al., 1993) |
| 1991 | Collisional tree code | (McMillan & Aarseth, 1993) |
| 1992 | Chain <i>N</i> -body interface | (S. J. Aarseth, 1994) |
| 1993 | Hermite integration | (Makino, 1991; Makino & Aarseth, 1992) |
| 1995 | Synthetic stellar evolution | (Tout et al., 1997) |
| | Tidal circularization | (R. A. Mardling, 1995a, 1995b) |
| | Slow chain regularization | (Mikkola & Aarseth, 1998) |
| 1996 | Hierarchical stability | (R. Mardling & Aarseth, 1999) |
| 1998 | Evolution of hierarchies | (R. Mardling & Aarseth, 1999) |
| | Stumpff KS method | (Mikkola & Aarseth, 1998) |
| 1999 | HARP-6 procedures | (S. J. Aarseth, 1999b) |
| | Symplectic integrators | (Mikkola & Tanikawa, 1999a, 1999b) |
| | <i>NBODY6++</i> SPMD / MPI acceleration | (Spurzem, 1999) |
| 2000 | Single stellar evolution in SSE | (Hurley et al., 2000) |
| 2002 | Binary stellar evolution in BSE | (Hurley et al., 2002) |
| 2003 | GRAPE-6 procedures | (Makino et al., 2003) |
| 2006 | 2.5PN in <i>NBODY5</i> | (Kupi et al., 2006) |
| 2007 | Direct <i>N</i> -body GPU acceleration | (Portegies Zwart et al., 2007) |
| 2008 | AR with PN terms | (Mikkola & Merritt, 2008) |
| 2010 | Updated AR for few-body problems | (Hellström & Mikkola, 2010) |
| 2012 | <i>NBODY</i> codes GPU acceleration | (Nitadori & Aarseth, 2012) |
| 2013 | MPI acceleration on GPU clusters / <i>PHIGPU</i> | (Berczik et al., 2013) |
| | 3.5PN in <i>NBODY6</i> | (Brem et al., 2013) |
| 2015 | SSE/AVX acceleration on GPU clusters | (Wang et al., 2015) |
| 2017 | Forward symplectic integrators (FSI) | (Dehnen & Hernandez, 2017) |
| 2020 | P ³ T with SDAR in <i>PeTAR</i> | (Wang, Nitadori, & Makino, 2020b) |
| | | (Wang, Iwasawa, et al., 2020) |
| 2021 | Minimum spanning tree MSTAR/BiFROST | (Rantala et al., 2021) |

5.2 Summary NBODY codes

As mentioned before, most of my work is produced using the parallel, direct force integration code `NBODY6++GPU` (Wang et al., 2015). Lets only consider single stars and no binaries or more complicated subsystems. As the number of simulated stars N grows, so does the number of computations to evaluate the force acting on each particle by a factor of N^2 . To speed up this calculation, `NBODY6++GPU` employs numerous of algorithms, which were developed reaching back many decades. As a summary, I will provide a brief introductory list, see also [Table 5.2](#):

1: 4th order integrator presents an optimal choice for performance and accuracy (Makino, 1991) compared with other orders such as the 6th and 8th order Hermite integrators (Nitadori & Makino, 2008).

2: The AZ regularisation is not used in `NBODY6++GPU` anymore, as it is only valid for small perturbations and the chain regularisation may be used for up to six members and takes care of perturbations.

3: In Kamlah, Leveque, et al. (2022), we note that there is an experimental version of the `NBODY6++GPU` code available on request, which uses a full post-Newtonian dynamics up to order PN3.5 including spins of compact objects, spin-orbit coupling to next-to-lowest order and spin-spin coupling to lowest order (Blanchet, 2014). It will provide more accurate orbital evolution and better predictions for gravitational waveforms in the final phases before coalescence. An early version of this code variant (only up to PN2.5) has been published in Brem et al. (2013) and Kupi et al. (2006).

1. Fourth-order Hermite integration scheme individual block-time steps¹ (Makino & Aarseth, 1992).
2. Kustaanheimo-Stiefel (KS) regularisation for strong interactions (Kustaanheimo & Stiefel, 1965).
3. Chain regularisation (Mikkola et al. 1993), which is the expanded Aarseth-Zare (AZ) three-body regularisation (S. J. Aarseth & Zare, 1974)²
4. Ahmad-Cohen (AC) neighbour scheme (Ahmad & Cohen, 1973).
5. Parallelization over many-core hardware (CPUs and GPUs) (Spurzem, 1999; Wang et al., 2015).
6. Post-Newtonian (PN) terms up to order 2.5 (Kupi et al., 2006) and general relativistic merger recoil kick (Arca Sedda & et al., 2023a, 2023b, in prep.)³.

Table 5.2: Table showing the comparison of the NBODY codes taken from Spurzem and Kamlah (2023). The abbreviations in the columns of the table are:

- ▶ ITS: Individual time-steps (S. J. Aarseth, 1985)
- ▶ ACS: Ahmad-Cohen neighbour scheme (Ahmad & Cohen, 1973)
- ▶ KS: KS-regularization of few-body subsystems (Kustaanheimo & Stiefel, 1965)
- ▶ HITS: Hermite scheme integration method combined with hierarchical block time-steps (Makino & Aarseth, 1992)
- ▶ PN: Post-Newtonian (S. J. Aarseth, 2012; Kupi et al., 2006; Mikkola & Merritt, 2008)
- ▶ AR: Algorithmic regularization (Mikkola & Merritt, 2008)
- ▶ CC: Classical chain regularization (Mikkola & Aarseth, 1998)
- ▶ MPI: Message Passing Interface, multi-node multi-CPU parallelization (Spurzem, 1999)
- ▶ GPU: use of GPU acceleration (Nitadori & Aarseth, 2012) (if also MPI: multi-node many GPU (Berczik et al., 2013))

| | ITS | ACS | KS | HITS | PN | AR | CC | MPI | GPU |
|-------------|-----|-----|----|------|----|----|----|-----|-----|
| NBODY1 | ✓ | | | | | | | | |
| NBODY2 | | ✓ | | ✓ | | | | | |
| NBODY3 | ✓ | | ✓ | | | | | | |
| NBODY4 | | | ✓ | ✓ | | | | | |
| NBODY5 | ✓ | ✓ | ✓ | | | | | | |
| NBODY6 | | ✓ | ✓ | ✓ | | | | | |
| NBODY6GPU | | ✓ | ✓ | ✓ | | | | ✓ | |
| NBODY6++ | | ✓ | ✓ | ✓ | | | ✓ | | |
| NBODY6++GPU | | ✓ | ✓ | ✓ | ✓ | | ✓ | ✓ | ✓ |
| NBODY7 | | ✓ | ✓ | ✓ | ✓ | ✓ | | | ✓ |

5.3 Time profile of NBODY6++GPU

Table 5.3 is reproduced from the the timing models for NBODY6++GPU from S.-Y. Huang et al. (2016), which is also shown in Spurzem and Kamlah (2023). The timing profiles here were obtained from a number of simulations using a range of particle numbers N and MPI process number N_p , where each MPI process also uses a GPU. In total, the profile was divided into eight different areas. From the fits and their fitting values, see Table 5.3, the following key conclusions can be drawn:

1. Regular and irregular force computation are very well parallelized ($\propto N_p^{-1}$);
2. Regular force computation still scales with approximately N^2 , but with a very small factor in front, due to the fast GPU processing.
3. MPI communication and synchronization provide a bottleneck, no further speedup possible for more than 8-16 MPI processes.
4. Also prediction and sequential parts on the host are bottlenecks if going for large N , because they scale approximately with $N^{1.5}$, and do not scale down with processor number.

According to Spurzem and Kamlah (2023) the timing model is already a few years old, the current code version has made progress in MPI parallelization of the prediction step. To improve the communication step scaling faster MPI or NVLINK⁴, which is wire-based serial multi-lane near-range communications link, would be very helpful. Figure 5.1 shows a similar information in principle than Table 5.3, but here the eye should inspect the relative weight of the different components, when increasing the number of MPI processes.

4: more information on this technology can be found here <https://www.nvidia.com/de-de/data-center/nvlink/>

Table 5.3: Profiling model developed for Nbody6++GPU reproduced from S.-Y. Huang et al. (2016) and also shown in Spurzem and Kamlah (2023). Note that all numerical factors in the fit depend on the specific hardware used - CPUs, GPUs, communication lines between CPU nodes and between CPU and GPU.

| Description | Timing variable | Expected scaling | | Fitting value [sec] |
|-------------------------------|-------------------|--|---|--|
| | | N | N_p | |
| Regular force computation | T_{reg} | $\mathcal{O}(N_{\text{reg}} \cdot N)$ | $\mathcal{O}\left(N_p^{-1}\right)$ | $(2.2 \cdot 10^{-9} \cdot N^{2.11} + 10.43) \cdot N_p^{-1}$ |
| Irregular force computation | T_{irr} | $\mathcal{O}(N_{\text{irr}} \cdot \langle N_{nb} \rangle)$ | $\mathcal{O}\left(N_p^{-1}\right)$ | $(3.9 \cdot 10^{-7} \cdot N^{1.76} - 16.47) \cdot N_p^{-1}$ |
| Prediction | T_{pre} | $\mathcal{O}(N^{kn_p})$ | $\mathcal{O}\left(N_p^{-k_{pp}}\right)$ | $(1.2 \cdot 10^{-6} \cdot N^{1.51} - 3.58) \cdot N_p^{-0.5}$ |
| Data moving | T_{mov} | $\mathcal{O}(N^{kn_m1})$ | $\mathcal{O}(1)$ | $2.5 \cdot 10^{-6} \cdot N^{1.29} - 0.28$ |
| MPI communication (regular) | T_{mcr} | $\mathcal{O}(N^{kn_{cr}})$ | $\mathcal{O}\left(kp_{cr} \cdot \frac{N_p-1}{N_p}\right)$ | $(3.3 \cdot 10^{-6} \cdot N^{1.18} + 0.12) \left(1.5 \cdot \frac{N_p-1}{N_p}\right)$ |
| MPI communication (irregular) | T_{mci} | $\mathcal{O}(N^{kn_{ci}})$ | $\mathcal{O}\left(kp_{ci} \cdot \frac{N_p-1}{N_p}\right)$ | $(3.6 \cdot 10^{-7} \cdot N^{1.40} + 0.56) \left(1.5 \cdot \frac{N_p-1}{N_p}\right)$ |
| Synchronization | T_{syn} | $\mathcal{O}(N^{kn_s})$ | $\mathcal{O}\left(N_p^{k_{ps}}\right)$ | $(4.1 \cdot 10^{-8} \cdot N^{1.34} + 0.07) \cdot N_p$ |
| Sequential parts on host | T_{host} | $\mathcal{O}(N^{kn_h})$ | $\mathcal{O}(1)$ | $4.4 \cdot 10^{-7} \cdot N^{1.49} + 1.23$ |

The coloured fields correspond to the code parts discussed above, but a little more segmented:

- ▶ Reg. and Irr. correspond to regular and irregular force computation in Table 5.3;
- ▶ Pred. is prediction;
- ▶ Move is data moving;
- ▶ Comm.R, Send.R., Comm.I. and Send.I is MPI communication (regular, irregular)
- ▶ Barr. is synchronization
- ▶ Init.B., Adjust, KS, refer to sequential parts on the host.

The bottom line that Spurzem and Kamlah (2023) draw is to stress that even for one million bodies the bottleneck of Nbody6++GPU is *NOT* the regular force, which would otherwise be extremely dominant in a sequential processing. The regular force is *NOT* the stumbling block for going to much higher particle number. The stumbling blocks are prediction and communication.

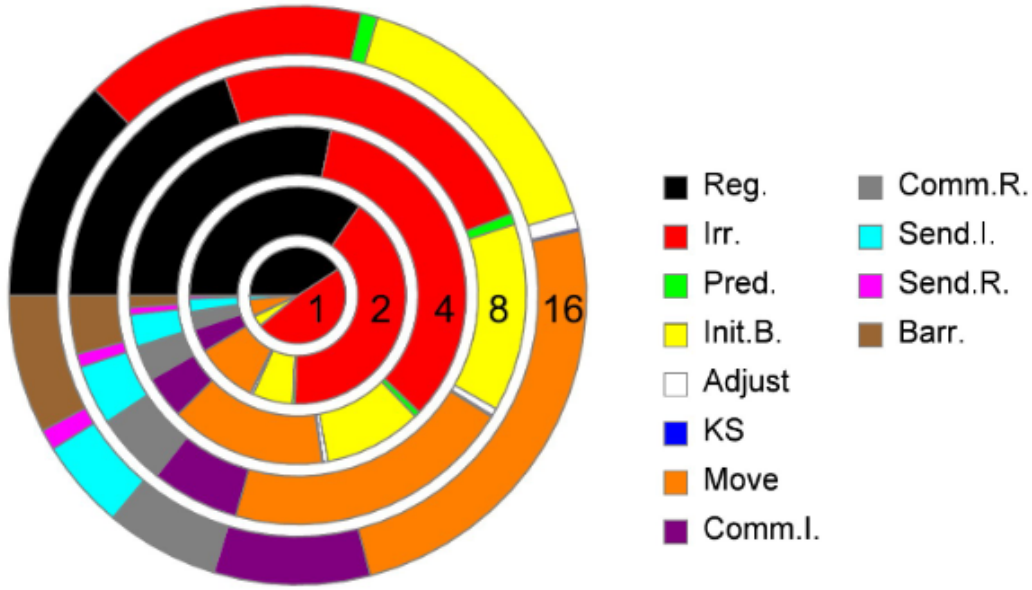


Figure 5.1: Pie chart showing the time fraction spent in different parts of the Nbody6++GPU code for a one million body simulation without initial (primordial) binaries, also shown in Spurzem and Kamlah (2023). Different rings show different number of MPI processes N_p (inside to outside 1, 2, 4, 8 and 16.), see also Table 5.3. Colours explained in main text.

5.4 Basic features and Nbody units

The Nbody codes have units defined for convenience using the average stellar mass $M_s[M_\odot]$ and the length scale or Virial radius $R_V[\text{pc}]$, see also S. J. Aarseth (2003a):

- Definition 5.4.1**
1. Fiducial length scale $\tilde{L}^* = 3 \times 10^{18}[\text{cm}]$
 2. Fiducial time scale $\tilde{T}^* = \sqrt{\frac{L^{*3}}{GM_\odot}}[\text{s}]$
 3. Fiducial velocity scale $\tilde{V}^* = 1 \times 10^{-5} \sqrt{\frac{GM_\odot}{L^*}}[\text{kms}^{-1}]$
 4. Star cluster time scale $T^* = 14.94 \times \sqrt{\frac{R_V^3}{NM_s}}[\text{Myr}]$
 5. Star cluster velocity scale $V^* = 6.557 \times 10^{-2} \sqrt{\frac{NM_s}{R_V}}[\text{kms}^{-1}]$

Converting Nbody units for a star cluster simulation for position r , velocity v and time t into real units $\tilde{r}[\text{pc}]$, $\tilde{v}[\text{kms}^{-1}]$, $\tilde{t}[\text{Myr}]$ is done via

$$\tilde{r} = R_V r \quad \tilde{v} = V^* v \quad \tilde{t} = T^* t. \quad (5.4)$$

The IMF from Definition 2.2.14 and the number of stars N and M_s and R_V define the star cluster simulated by Nbody6++GPU. After the assigning this data via the input file in the code, the kinetic K and the potential energy $U(U < 0)$ are evaluated. The initial velocities \tilde{v}_i are then scaled for each particle with index i according to

$$\mathbf{v}_i = \sqrt{\frac{Q_V |U|}{K}} \tilde{\mathbf{v}}_i = q \tilde{\mathbf{v}}_i, \quad (5.5)$$

where Q_V is typically 0.5 and an input parameter in the input file. Further standard units are defined as

1. Gravitational constant $G = 1$
2. Sum of the particle masses $\sum_i m_i = 1$
3. Total energy $E_0 = -0.25$ for bound systems, i.e., $Q_V < 1$

With this, the final scaling for the star with index i yields

$$\hat{\mathbf{r}}_i = \sqrt{\frac{q^2 K + U}{E_0}} \tilde{\mathbf{r}}_i = S^{-\frac{1}{2}} \tilde{\mathbf{r}}_i \quad \text{and} \quad \hat{\mathbf{v}}_i = S^{\frac{1}{2}} \tilde{\mathbf{v}}_i. \quad (5.6)$$

The final standard crossing time $T_{\text{cross}}[\text{Myr}]$, compare that with [Definition 15](#), is given by

$$T_{\text{cross}} = 2\sqrt{2}T^* \quad (5.7)$$

Additional input comes from the fact that `NBODY6++GPU` includes the treatment of binary stellar systems, see also [Section 2.2.3](#), which requires the variables of the eccentricity e , the semi-major axis a , relevant angles, periods and mass ratios. Due to the binding energies of the binaries the simple energy scaling from above cannot be applied. Therefore, the two stars that make up the binaries are combined into a single particle, of which there are N_b in the simulation and these can be scaled accordingly. The total number of particles in the simulation are therefore $N = N_s + 2N_b$.

`NBODY6++GPU` is able to resolve star clusters and related systems to a great detail of astrophysical realism. While this provides a competitive edge over other direct N -body codes and modelling methods, it also greatly increases the algorithmic and data complexity, because we need to keep track of each particle that have a unique particle ID throughout the simulation. Consequently, dealing with `NBODY6++GPU` is both astrophysically and computationally challenging.

The algorithms of how to treat close encounters and particle pairs are discussed later. I now briefly state how the code deals with data. When talking about regularisation in this context, I want to describe a mathematical procedure⁵, which enables us to find a global solution to a problem numerically, which was previously prevented by mathematical singularities.

5: usually coordinate transformation

1. KS regularisation

Binaries are treated via the aforementioned KS regularisation by Kustaanheimo and Stiefel (1965) and necessitates a new description. The new particle $N_{p,i}$ has the spatial coordinates of the COM of the individual stars that make up the binary and their relative motion is also saved, see also the discussion in [Section 4.1.1](#) for the geometry and dynamics of the problem. Triple stellar constellations, see also [Section 4.1.1](#), are reduced to a KS pair. In these so-called triples, the inner binary becomes the first member of the new KS pair and the third star becomes the second member of the new KS pair. To save the quantities associated with the outer component, so-called ghost stars or ghost particles are generated by the code, which have a mass equal to zero, but retain all other quantities of the star / particle. In quadruples, the method follows in an analogous manner. Here, two binary pairs become members the new KS pair and there are a ghost star for the COM and ghost binaries

for the individual binaries. This procedure can be extended to even higher-order systems, as long as they are dynamically stable.

2. Chain regularisation

Compact subsystems are described by the chain regularisation (Mikkola & Aarseth, 1993). Pairwise two-body KS regularisation is combined with treating distant particles⁶ as perturbers. At least two members of the compact subsystem are former components of KS binaries. At any given time-step, there can be an arbitrary number of KS pairs but only one compact subsystem (S. J. Aarseth et al., 2008).

6: measured from the particle, that is assigned the role of COM.

5.5 Methods and algorithms in NBODY6++GPU

In this section I expand on the main algorithms and methods within NBODY6++GPU. The time-line of invention of these ideas can be found in Table 5.1 and a summary of what is included in NBODY6++GPU compared with other NBODY code versions can be found in Table 5.2.

5.5.1 4th-order Hermite integration

Each star in the NBODY simulations experiences the combined acceleration \mathbf{a}_0 and the first derivative of the acceleration \mathbf{a}_0 , the so-called jerk, of all other stars in the simulation. I consider these at $t = 0$, see also Equation 4.1:

$$\mathbf{a}_{0,i} = - \sum_{i \neq j} Gm_j \frac{\mathbf{r}_{0,i} - \mathbf{r}_{0,j}}{|\mathbf{r}_{0,i} - \mathbf{r}_{0,j}|^3} = - \sum_{i \neq j} Gm_j \frac{\mathbf{R}}{R^3}, \quad (5.8)$$

$$\mathbf{a}_{0,i} = - \sum_{i \neq j} Gm_j \left[\frac{|\mathbf{v}_{0,i} - \mathbf{v}_{0,j}|}{|\mathbf{r}_{0,i} - \mathbf{r}_{0,j}|^3} + \frac{3(\mathbf{r}_{0,i} - \mathbf{r}_{0,j})(\mathbf{v}_{0,i} - \mathbf{v}_{0,j}) \cdot (\mathbf{r}_{0,i} - \mathbf{r}_{0,j})}{|\mathbf{r}_{0,i} - \mathbf{r}_{0,j}|^5} \right] \quad (5.9)$$

$$= - \sum_{i \neq j} Gm_j \left[\frac{\mathbf{V}}{R^3} + \frac{3\mathbf{R}(\mathbf{V} \cdot \mathbf{R})}{R^5} \right], \quad (5.10)$$

$$(5.11)$$

where the index i denotes the star in question and the j the indices of all other stars. However, these two terms are not sufficient to accurately calculate the new position of and velocity of a stars at time $t = 1$ after some time Δt . Further differentiating the above expression to give the higher-order corrective perturbative terms for $\mathbf{a}_{0,i}$ and $\mathbf{a}_{0,i}$ is very cumbersome. This has lead to the following force integration scheme:

Definition 5.5.1 (4th-order Hermite integration scheme) *The Hermite force integrations scheme has proven enormously successful in NBODY simulations (Makino & Aarseth, 1992). It is as a predictor-corrector method, since it calculates the trajectory of the particle by*

1. predicting a new position \mathbf{x}_1 and new velocity \mathbf{v}_1 for the next time step $t = 1$,
2. then correcting it by $\Delta\mathbf{x}$ and $\Delta\mathbf{v}$, respectively.

The Taylor series for the new predicted position \mathbf{x}_1 and the new velocity \mathbf{v}_1 of a star are corrected to 4th order in a time interval Δt , which yields

$$\mathbf{x}_1 = \mathbf{x}_0 + \Delta\mathbf{x} = \mathbf{x}_0 + \mathbf{v}_0\Delta t + \frac{\mathbf{a}_0}{2}\Delta t^2 + \frac{\dot{\mathbf{a}}_0}{6}\Delta t^3 + \boxed{\frac{\ddot{\mathbf{a}}_0}{24}\Delta t^4 + \alpha\frac{\ddot{\mathbf{a}}_0}{120}\Delta t^5}, \quad (5.12)$$

$$\mathbf{v}_1 = \mathbf{v}_0 + \Delta\mathbf{v} = \mathbf{v}_0 + \mathbf{a}_0\Delta t + \frac{\dot{\mathbf{a}}_0}{2}\Delta t^2 + \boxed{\frac{\ddot{\mathbf{a}}_0}{6}\Delta t^3 + \frac{\ddot{\mathbf{a}}_0}{24}\Delta t^4}, \quad (5.13)$$

where \mathbf{a} describes the acceleration and α in the last term of Equation 5.12 is some constant. The expressions in both equations that are boxed are known as the corrector and everything to the left are known as the predictor (together predictor-corrector method) of the new position \mathbf{x}_1 and the new velocity \mathbf{v}_1 of the star after a time-step Δt .

Equations 5.12 and 5.13 can be rewritten with $\alpha = 1$ and using Newmark's implicit method (Newmark, 1959) to yield the acceleration per unit mass \mathbf{a}_1 and the jerk $\dot{\mathbf{a}}_1$ acting on the particle after one time-step Δt :

$$\mathbf{a}_1 = \mathbf{a}_0 + \dot{\mathbf{a}}_0\Delta t + \frac{1}{2}\ddot{\mathbf{a}}_0\Delta t^2 + \frac{1}{6}\ddot{\mathbf{a}}_0\Delta t^3 \quad (5.14)$$

$$\dot{\mathbf{a}}_1 = \dot{\mathbf{a}}_0 + \ddot{\mathbf{a}}_0\Delta t + \frac{1}{2}\ddot{\mathbf{a}}_0\Delta t^2, \quad (5.15)$$

which is the standard Taylor series. The subscripts can be reversed and therefore, this formulation is time-symmetric. Note that the terms $\dot{\mathbf{a}}_0$ and \mathbf{a}_0 are already known but $\ddot{\mathbf{a}}_0$ and $\ddot{\mathbf{a}}_0$ are not. Therefore, we solve Equations 5.14 and 5.15 for $\ddot{\mathbf{a}}$ and $\ddot{\mathbf{a}}$:

$$\ddot{\mathbf{a}}_0 = -\frac{6}{\Delta t^2}(\mathbf{a}_0 - \mathbf{a}_1) - \frac{2}{\Delta t}(2\dot{\mathbf{a}}_0 + \dot{\mathbf{a}}_1), \quad (5.16)$$

$$\ddot{\mathbf{a}}_0 = \frac{12}{\Delta t^3}(\mathbf{a}_0 - \mathbf{a}_1) + \frac{6}{\Delta t^2}(\dot{\mathbf{a}}_0 + \dot{\mathbf{a}}_1). \quad (5.17)$$

Therefore, we can substitute Equations 5.16 and 5.17 into Equations 5.14 and 5.15. All of this means that we never had to explicitly calculate $\ddot{\mathbf{a}}_0$ or $\ddot{\mathbf{a}}_0$ but could express these in the known expressions in terms of \mathbf{a}_0 , \mathbf{a}_1 , $\dot{\mathbf{a}}_0$, $\dot{\mathbf{a}}_1$. This procedure is known as the Hermite scheme.

The local error in position \mathbf{x}_1 and the new velocity \mathbf{v}_1 within the two time-steps Δt is expected to be of order $\mathcal{O}(\Delta t^5)$, the global error for a fixed physical integration time scales with $\mathcal{O}(\Delta t^4)$ (Makino, 1991), see also Figure 5.3.

The number of iterations of evaluating and correcting the force acting on a particle n is usually chosen as 2, but $n = 3$ may also be worthwhile (S. J. Aarseth et al., 2008). For large number of particles in the simulation, these iterations of the perturbations is not performed again.

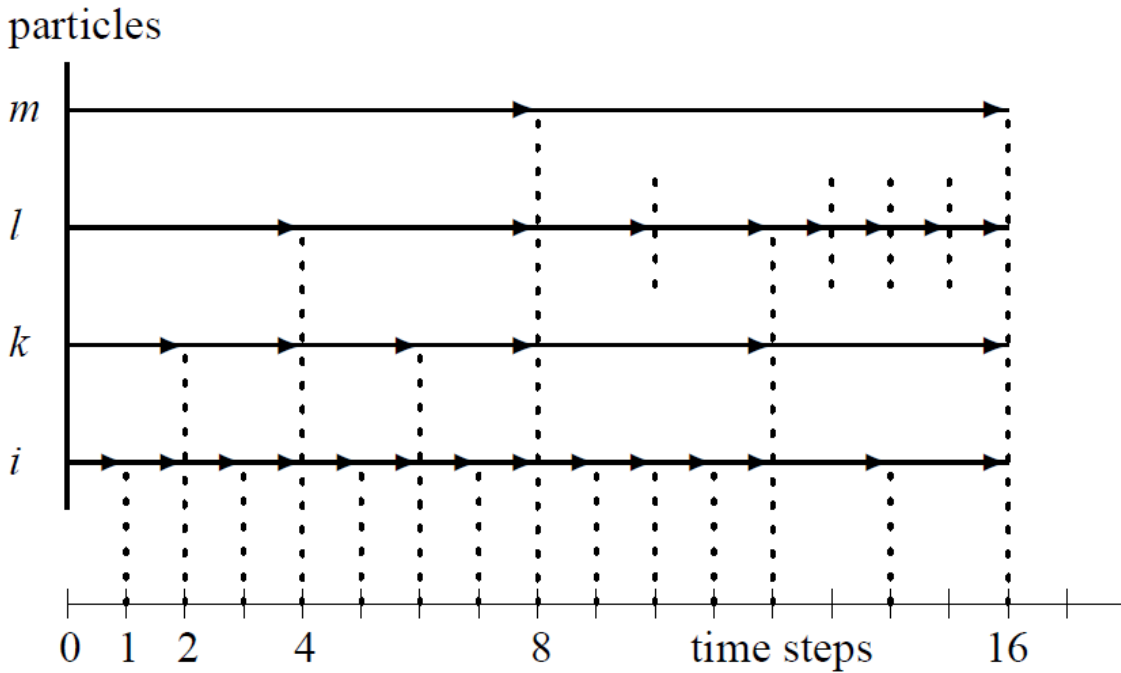


Figure 5.2: Exemplary block time steps in NBODY6++GPU for four stars, with the indices i, k, l, m , respectively, for 16 quantized time-steps in total. At the dotted vertical lines, Equations 5.12 and 5.13 are evaluated for the stars, respectively. The star indexed i has the smallest time step at the beginning, so its phase-space coordinates are determined at each of the 16 time-steps. The star indexed k has time steps that are twice as large, so that at every odd time-step its phase-space coordinates are simply extrapolated and at even time-steps, Equations 5.12 and 5.13 are evaluated again. Additionally, the time-step size is altered by factors of 2 or left unchanged after every integration cycle as can be seen for the particles i, k, l (Figure taken from the N -body manual).

But what do we do, if we are not only dealing with single stars, but also close encounters, binaries and other subsystems? This will be explained later in this chapter. The close encounter distance R_{cl} signals the code whether or not to switch on regularisation.

5.5.2 Block time-steps scheme

Each star (or particle) in a N -body simulation is characterised by its own time-scale - a binary star has an orbital period around the COM of a couple of days, while a star in the outer halo of a star cluster has an orbital period of million of years. The problem is that the stars with the shortest periods would demand force integrations for the stars with the longest periods as well in the traditional Hermite integration scheme introduced in the previous Section 5.5.1. This unnecessary effort results in an excessive computational effort, since we can usually assume that the trajectories of the stars in the outer halo are mostly smooth and do not vary a lot between the short time-scales of days. Therefore, so-called block time-steps are implemented in NBODY6++GPU. These can be understood when studying Figure 5.2, where four stars denoted by i, k, l, m over 16 time-steps are followed.

Definition 5.5.2 (Block time-steps) *The time-steps for each star are*

quantized, following the rule

$$\Delta t_n = \left(\frac{s_{\max}}{2} \right)^{n-1}, \quad (5.18)$$

where s_{\max} is set as some maximum permitted value. Furthermore, $T/\Delta t_n$ should be an integer number. This implies that in order to keep all particles synchronised as in Figure 5.2, the time-steps can only increase by a factor of 2.

But how does the code decide which time-step should be assigned to which star? In S. J. Aarseth (1985) the following formula was implemented in NBODY6++GPU for the time-step Δt_i for star with index i

Definition 5.5.3 (Block time-steps in NBODY6++GPU)

$$\Delta t_i = \sqrt{\eta \frac{|\mathbf{a}_{1,i}| |\ddot{\mathbf{a}}_{1,i}| + |\dot{\mathbf{a}}_{1,i}|^2}{|\dot{\mathbf{a}}_{1,i}| |\ddot{\mathbf{a}}_{1,i}| + |\ddot{\mathbf{a}}_{1,i}|^2}}, \quad (5.19)$$

where η is a constant that is typically set to a value between 0.01 to 0.04⁷.

7: This is talked about in the next section with regards to regular and irregular force integrations.

Equation 5.19 yields a well-defined large value when the force is small, for example, for the before-mentioned halo stars that are close to the tidal boundary. Furthermore, if two masses of stars approach each other they will usually have the same time-step after the quantisation from Equation 5.19, regardless of their individual masses.

The aforementioned subsystems like binaries, triples and higher-order subsystems are treated into this block time-step scheme only via their particle that accounts for their COM. The internal motion of these systems are subject to regularised integration. In Definition 5.5.1 it can be seen that Hermite method from used for a real N -body integration sustains generally an error of $\mathcal{O}(\Delta t^4)$ for the entire calculation. More about the time-steps and the optimal choice for these can be found in Spurzem and Kamlah (2023).

5.5.3 Ahmad-Cohen (AC) neighbour scheme

To further decrease the computation time, a so-called neighbour scheme (or two-time-step scheme) was introduced by Ahmad and Cohen (1973). In this scheme Equation 5.8 is split up into two parts, i.e. the *irregular* and *regular* force per unit mass:

$$\mathbf{a} = \mathbf{a}_{\text{irr}} + \mathbf{a}_{\text{reg}}, \quad (5.20)$$

where \mathbf{a}_{irr} corresponds to the acceleration the particle experiences due to particles n_p in the neighbourhood in some neighbour sphere of some neighbour radius r_s and \mathbf{a}_{reg} to the acceleration the particle experiences due to particles that are outside of that neighbourhood, see also Figure 5.4. To select neighbours, a balance needs to be found between a constant value of n and one that is flexible according to local conditions around the particle. It is intuitive to let r_s depend

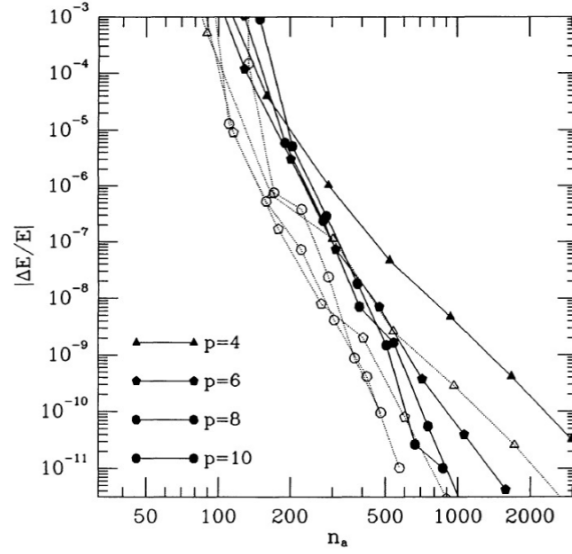


Figure 5.3: The relative energy error as the function of the number of steps. A time-step criterion using differences between predicted and corrected values is used, different from Equation 5.19. Dotted curves are for Hermite schemes, solid curves for Aarseth schemes. The step number p denotes the order of the integrator. Taken from Makino (1991), also shown in Spurzem and Kamlah (2023).

on the local density to further decrease the computational cost of the force integration. The neighbour radius in NBODY6++GPU is updated by the condition that an optimal neighbour number NNBOPT (free input parameter) should be reached. NNBOPT can be chosen to get the best performance, within reasonable limits which are $50 < \text{NNBOPT} < 200$ approximately. For low density regions also much smaller neighbour numbers than NNBOPT are permitted and special conditions apply if a particle is very massive or is fast approaching.

The regular force integration is undertaken for longer time-steps than the irregular force integration. At the end of each integration cycle of the regular force the full Hermite predictor-corrector method is undertaken for all particles. The neighbour sphere is re-evaluated and in NBODY6++GPU the typical number of particles within the sphere are 50 – 200, such as in all of my simulations presented here (Kamlah, Leveque, et al., 2022; Kamlah, Spurzem, et al., 2022) and in Kamlah et al. (2023, in prep.). Additionally, approaching particles within a surrounding shell satisfying the condition $\mathbf{R} \cdot \mathbf{V} < 0$ are included in the irregular force integration. The purpose of this buffer zone is to identify fast approaching particles before they are able to penetrate too far inside the neighbour sphere. As an aside, the neighbour list is also handy in identifying subsystems, which need to be regularised.

The AC scheme implies that there must be two time-scales for each particle; One time-scale for the irregular force integration t_{irr} and one time-scale for the regular force integration t_{reg} , see Figure 5.4. From Equation 5.19 we find that the parameter η takes the value $\eta_{\text{irr}} \approx 0.01$ for the irregular force integration and $\eta_{\text{reg}} \approx 0.02$ for the regular force integration.

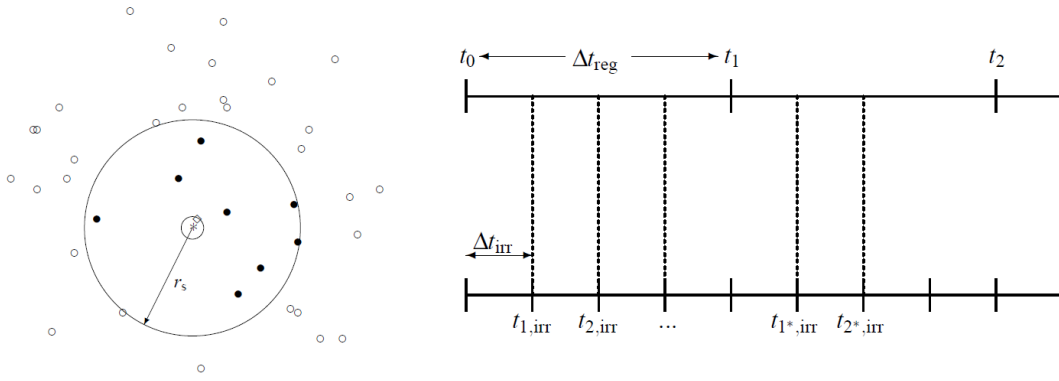


Figure 5.4: Left: Ahmad-Cohen (AC) neighbour scheme, regular and irregular force integration for some particle. The neighbour sphere of radius r_s is evaluated and the stars within its boundary and fast approaching stars that satisfy $\mathbf{R} \cdot \mathbf{V} < 0$ are included in the neighbour particle list, They are subject to the shot time-step irregular force integration. The stars outside of the sphere and stars that fulfill $\mathbf{R} \cdot \mathbf{V} \geq 0$ are subject to the long time-step regular force integration. Right: Illustration of the differing time-scales for the longer regular and the shorter irregular force integration time-scales (Figure taken from the *N*-body manual).

5.5.4 Two-body regularisation and Kustaanheimo-Stiefel (KS) decision making

As mentioned before, subsystems in the `NBODY6++GPU` simulations require special algorithmic treatment. But how does `NBODY6++GPU` decide when to trigger regularisation? To be regularised, the stars have to fulfill the following two criteria:

1. They are approaching each other.
2. Their mutual force is dominant.

In mathematical terms for two stars with indices k, l with masses m_k and m_l making up a perturbed binary, this is expressed via

$$\mathbf{R} \cdot \mathbf{V} > 0.1 \sqrt{GR(m_k + m_l)} \quad \text{and} \quad \gamma = \frac{|\mathbf{a}_{\text{pert}}| \cdot R^2}{G(m_k + m_l)} < 0.25, \quad (5.21)$$

where \mathbf{a}_{pert} is the vectorial differential force per unit mass exerted by other perturbing particles onto the candidate particle and γ is a parameter measuring the perturbations. R , \mathbf{R} and \mathbf{V} are defined as the scalar and vectorial distance with the relative velocity between the two particles. In the unperturbed case in `NBODY6++GPU` the analytical solutions for the Keplerian orbits are used. In the code they also fall into the category of mergers.

The internal motion of the perturbed particle pair⁸ is dealt with as such: Following Kustaanheimo and Stiefel (1965), the 3D spatial problem, for example in Cartesian coordinates, in the `NBODY` simulation is transformed into a 4D problem. This 4D space is also known as quaternion space and within it it is more convenient to describe and compute 3D rotations, which is computationally more efficient than other methods and avoids a lot of numerical errors. The transformation happens follows

$$R = u_1^2 + u_2^2 + u_3^2 + u_4^2. \quad (5.22)$$

8: In `NBODY6++GPU` this is a short-lived hyperbolic encounter, see also Section 4.1.2 or a hard binary

Additionally, a time transformation is undertaken via

$$dt = r d\tau. \quad (5.23)$$

The coordinate transformation is satisfied by

$$\mathbf{R} = \Lambda(\mathbf{u})\mathbf{u} = \begin{bmatrix} u_1 & -u_2 & -u_3 & u_4 \\ u_2 & u_1 & -u_4 & -u_3 \\ u_3 & u_4 & u_1 & u_2 \end{bmatrix} \mathbf{u}. \quad (5.24)$$

The new *regularised* velocities are given by

$$\mathbf{u}' = \frac{1}{2}\Lambda^T(\mathbf{u})\dot{\mathbf{R}}. \quad (5.25)$$

I now look at the two-body regularisation for the perturbed motion of two bodies with masses m_k and m_l around their COM. The acceleration is given by

$$\ddot{\mathbf{R}} = -\frac{m_k + m_l}{R^3}\mathbf{R} + \mathbf{P}, \quad (5.26)$$

where \mathbf{P} is the perturbation term. This is the equation governing the behaviour of a perturbed harmonic oscillator. The set of equations of motion is given by

$$\mathbf{u}'' = \frac{1}{2}h\mathbf{u} + \frac{1}{2}R\Lambda^T\mathbf{P} \quad h' = 2\mathbf{u}' \cdot \Lambda^T\mathbf{P} \quad t' = \mathbf{u} \cdot \mathbf{u}, \quad (5.27)$$

where h is the specific two-body energy. These equations describe the relative motion of the two bodies in the presence of external perturbations are well defined for $R \rightarrow 0$. The orbit about the centre of the star cluster is described the motion of the COM:

$$\ddot{\mathbf{r}}_{\text{cm}} = \frac{m_k\mathbf{P}_k + m_l\mathbf{P}_l}{m_k + m_l}. \quad (5.28)$$

This COM has a particle associated with it that is added to the list of particles of the simulation. The main idea is to take both members of the binary out of the main integration cycle, and replace them with their COM composite. This particle is then advanced in the usual integration. The two members of the regularised pair, which is also known as the KS pair, are relocated to the beginning of all vectors containing the particle data. The members of the KS pair have the corresponding individual coordinates

$$\mathbf{r}_k = \mathbf{r}_{\text{cm}} + \frac{\mu\mathbf{R}}{m_k} \quad \mathbf{r}_l = \mathbf{r}_{\text{cm}} - \frac{\mu\mathbf{R}}{m_l}, \quad (5.29)$$

with the reduced mass $\mu = \frac{m_k m_l}{(m_k + m_l)}$.

Algorithmically speaking, there are three processes that drive the regularisation:

1. Initialisation,
2. Integration,
3. Termination.

We are defining a close encounter via the following parameters

$$R_{\text{cl}} = \frac{4r_h}{NC^{1/3}} \quad \Delta t_{\text{cl}} = \beta \sqrt{\frac{R_{\text{cl}}^3}{m}}, \quad (5.30)$$

with the half-mass radius r_h , the before-mentioned central density contrast C and the experimental constant β . A particle of index k in the simulation with the time-step $\Delta t_k < \Delta t_{\text{cl}}$ has to have at least one particle within R_{cl} . The conditions from above that they are approaching each other and that their mutual force is dominant, still hold.

1. Initialisation

KS force polynomials are initialised in the same fashion as those of single particles in the simulation, except that we also need the explicit time derivatives of \mathbf{u} . Expanding $\Delta\tau$ as a Taylor series gives the time-step in physical units, which determines the schedule of the regularised solutions.

As stated before, the KS regularisation is undertaken for perturbed binaries, and therefore, a list of perturbers must be saved. Every time the binary stars pass the apocenter ($R_{\text{ap}} = a(1 + \epsilon)$), see [Figure 4.1](#), then within the tidal limit approximation particles that are found within a distance of

$$r_p = \sqrt[3]{\frac{2m_p}{m_b \gamma_{\text{min}}}} a(1 + \epsilon), \quad (5.31)$$

are the selected from the larger neighbour list. m_b is the mass of the binary and γ_{min} is the minimum perturbation⁹.

9: The minimum perturbation usually set to be of the order 10^{-6}

2. Integration

KS integration begins by predicting $\mathbf{u}, \mathbf{u}', \dots, \mathbf{u}^{(5)}$ and h, h', h'' . The perturbers are predicted to lowest order.

The physical coordinates $\mathbf{r}_k, \mathbf{r}_1, \mathbf{r}_k, \mathbf{r}_1$ are easily obtained and are used for the force computation. From there, the physical perturbation \mathbf{P} and its time derivative can be obtained $\dot{\mathbf{P}}$. We receive $\mathbf{P}' = R\dot{\mathbf{P}}$. We can now correct the previous prediction with the new values $\mathbf{u}, \mathbf{u}', \dots, \mathbf{u}^{(5)}$ and $h, h', \dots, h^{(4)}$. The conversion back to physical time is also carried out to highest order via a Taylor expansion. This results in the physical time-step:

$$\Delta t = \sum_{k=1}^6 \frac{1}{k!} t_0^{(k)} \Delta \tau^k. \quad (5.32)$$

3. Termination

Termination of hard binaries is appropriate for a strong perturbation, usually at a γ value of $\gamma \geq 0.5$. This perturbation would probably lead to switching to another dominant pair, for example, temporary capture, resonance or chain regularisation.

For soft binaries, a smaller value of γ is sufficient. After the KS pair is terminated, they are treated as standard single particles and their force polynomials are initialised as such.

Termination is delayed always until the end of the block-time

step for the whole NBODY6++GPU simulation, unless the particles collide.

5.5.5 Hierarchical systems and three-body regularisation

Hierarchical systems are systems in the simulation that make anything more than two particles¹⁰. Triples in NBODY6++GPU typically form when one two binaries have a strong encounter and one binary member star from the binary with higher E_b ($E_b < 0$) is ejected as a result, see also Section 4.1.5. The other binary member star is then captured by the stronger binary due to energy and angular momentum conservation rules¹¹.

10: or triples, quadruples,...

11: For quadruple systems the procedure is analogous.

- ▶ When is a hierarchical system deemed to be stable? A simplified criterion for the stability of the hierarchical system is the assumption that the inner semi-major axis is constant. One can then regularise the outer member with regard to the COM. Integration of the system then follows in the usual fashion at each apocenter turning point. Termination happens if the outer eccentricity changes sufficiently indicating further perturbations.
- ▶ How does NBODY6++GPU function for hierarchical systems? This involves many conditions:
 - After each turning point, if $\Delta t_{\text{cm}} < \Delta t_{\text{cl}}$, then this implies that the new hierarchy to form a hard outer binary.
 - After identifying the two most dominant neighbours, the outer two-body elements are constructed for the main perturber.
 - The perturbation on the outer orbit is checked, as well as the condition for a new hard binary.
 - If the outer component is also a binary, then a modified criterion is used depending on the ratio of the semi-major axes.

I elaborate on the three-body regularisation for strong interactions between three particles through the Aarseth-Zare (AZ) method (S. J. Aarseth & Zare, 1974). It is not used in NBODY6++GPU anymore but it can be considered as an intermediate step between the KS regularisation from Section 5.5.4 and the chain regularisation in Section 5.5.6. Instead, for hierarchical 3-body and 4-body subsystems the stability criterion of R. A. Mardling and Aarseth (2001) is used to decide about stability. If the system is stable, the inner binary is treated as analytic Kepler two-body problem.

Consider, three particles in the simulation with masses m_1, m_2 and m_3 . Basically now, two different KS solutions of m_1 and m_2 are employed with respect to the reference body m_3 . The Hamiltonian of the system is given by

$$\mathcal{H} = \sum_{k=1}^2 \frac{1}{2\mu_{k3}} \mathbf{p}_k^2 + \frac{1}{m_3} \mathbf{p}_1^T \cdot \mathbf{p}_2 - \frac{m_1 m_3}{R_1} - \frac{m_2 m_3}{R_2} - \frac{m_1 m_2}{R}, \quad (5.33)$$

where the three particles have coordinates \mathbf{r}_i and momenta $\mathbf{p}_1, \mathbf{p}_2$ and $\mathbf{p}_3 = -(\mathbf{p}_1 + \mathbf{p}_2)$. and where R defines the distance between m_1 and m_2 . $\mu_{k3} = (m_k m_3)/(m_k + m_3)$ is the reduced mass with respect to the reference particle. We have already seen this expression in a similar form in [Section 4.1.5](#) in Equation 4.80.

Analogous to the KS regularisation for two particles, we introduce quaternions for the coordinate transformation for the distances R_1 and R_2 via

$$\mathbf{Q}_k^2 = R_k \quad (k = 1, 2). \quad (5.34)$$

As in the KS regularisation, the time also needs to be transformed and another differential relation between physical time t and the regularised time τ is found

$$dt = R_1 R_2 d\tau. \quad (5.35)$$

Given the initial energy of the system E_0 , we can define a regularised Hamiltonian $\Gamma = R_1 R_2 (\mathcal{H} - E_0)$ with

$$\begin{aligned} \Gamma^* = \sum_{k=1}^2 \frac{1}{8\mu_{k3}} R_k \mathbf{P}_k^2 + \frac{1}{16m_3} \mathbf{P}_1^T \mathbf{A}_1 \cdot \mathbf{A}_2^T \mathbf{P}_2 \\ - m_1 m_3 R_2 - m_2 m_3 R_1 - \frac{m_1 m_2 R_1 R_2}{|\mathbf{R}_1 - \mathbf{R}_2|} - E_0 R_1 R_2, \end{aligned} \quad (5.36)$$

where \mathbf{A} is twice the transpose of the Levi-Civita matrix encountered and the regularised momenta are given by \mathbf{P}_k . Finally, the equations of motion are given by

$$\frac{d\mathbf{Q}_k}{d\tau} = \frac{\partial \Gamma^*}{\partial \mathbf{P}_k} \quad (5.37)$$

$$\frac{d\mathbf{P}_k}{d\tau} = -\frac{\partial \Gamma^*}{\partial \mathbf{Q}_k}. \quad (5.38)$$

These equations are regular for either $R_1 \rightarrow 0$ or $R_2 \rightarrow 0$. The singular terms are numerically smaller than the regular terms, provided $|\mathbf{R}_1 - \mathbf{R}_2| > \max(R_1, R_2)$. This implies that the reference particle with m_3 can be switched with another particle, given R is no longer the largest distance.

This three-body regularisation is only implemented in the `NBODY` code, if the chain regularisation, described in the following chapter is not available.

5.5.6 Chain regularisation

The basic idea comes directly from the three-body regularisation outlined in the previous [Section 5.5.5](#) (Mikkola & Aarseth, 1993). A subsystem in an `NBODY6++GPU` simulation is for chain regularisation if a hard binary is perturbed by a another star or another binary. It is scaled up from there. When the KS binary is terminated, the coordinates and momenta are expressed in the local COM frame of reference. Thus $N - 1$ chain vectors connect the particles experiencing the strongest pair-wise forces and are defined in terms

of the coordinates \mathbf{q}_k by

$$\mathbf{R}_k = \mathbf{q}_{k+1} - \mathbf{q}_k, \quad k = 1, \dots, N-1. \quad (5.39)$$

From Hamiltonian dynamics it is known that a generating function S is defined via a canonical transformation as

$$S = \sum_{k=1}^{N-1} \mathbf{W}_k \cdot (\mathbf{q}_{k+1} - \mathbf{q}_k), \quad (5.40)$$

where the relative physical momenta \mathbf{W}_k can be obtained recursively via

$$\mathbf{W}_k = \mathbf{W}_{k-1} - \mathbf{p}_k = \mathbf{W}_{k-1} - \frac{\partial S}{\partial \mathbf{q}_k}, \quad k = 2, \dots, N-2, \quad (5.41)$$

where $\mathbf{W}_1 = -\mathbf{p}_1$ and $\mathbf{W}_{N-1} = -\mathbf{p}_N$. We now want to consider a subsystem of n single particles of masses m_i and one dominant body of mass m_0 . The initial conditions q_i, p_i are expressed in the local COM reference frame. The relative coordinates \mathbf{q}_i with respect to m_0 introduced, the Hamiltonian is given by

$$\mathcal{H} = \sum_{i=1}^n \frac{\mathbf{p}_i^2}{2\mu_i} + \frac{1}{m_0} \sum_{i<j}^n \mathbf{p}_i^T \cdot \mathbf{p}_j - m_0 \sum_{i=1}^n \frac{m_i}{R_i} - \sum_{i<j}^n \frac{m_i m_j}{R_{ij}}, \quad (5.42)$$

where again $\mu_i = m_i m_0 / (m_i + m_0)$ is the reduced mass and $R_i = |\mathbf{q}_i|$. Comparing the above expression with Equation 5.36, then it is apparent that it is a generalisation for $n > 2$. Equation 5.41 can be plugged into Equation 5.42 and this gives

$$\begin{aligned} \mathcal{H} = \frac{1}{2} \sum_{k=1}^{N-1} \left(\frac{1}{m_k} - \frac{1}{m_{k+1}} \right) \mathbf{W}_k^2 - \sum_{k=2}^{N-1} \frac{1}{m_k} \mathbf{W}_{k-1} \cdot \mathbf{W}_k \\ - \sum_{k=1}^{N-1} \frac{m_k m_{k+1}}{R_k} - \sum_{1 \leq k \leq j-2}^N \frac{m_i m_j}{R_{ij}}, \end{aligned} \quad (5.43)$$

We can see that this formulation is independent of a reference body or star. We can regularise Equation 5.43 with the time regularisation via an inverse Lagrange energy

$$t' = \frac{1}{L} \quad (5.44)$$

gives the regularised Hamiltonian

$$\Gamma^* = t'(\mathcal{H} - E_0), \quad (5.45)$$

which can be differentiated in the usual way of equations of motion. As in the case of the KS relations we can recover the physical variables with

$$\mathbf{R}_k = \Lambda_k \mathbf{Q}_k, \quad (5.46)$$

$$\mathbf{W}_k = \frac{\Lambda_k \mathbf{P}_k}{2\mathbf{Q}_k^2}, \quad (5.47)$$

and from Equation 5.41 the momenta \mathbf{p}_k can be retrieved. For initialisation in the COM frame and evaluation of the total energy

E_0 , the chain vectors from Equation 5.39 must be constructed. The canonical variables \mathbf{Q}, \mathbf{P} are introduced as before and the integration can begin after specifying a suitably small time-step.

Decision-making here requires the following quantities:

- ▶ characteristic external perturbation γ_{ch} . If γ_{ch} is significant, then some perturber is included in the chain regularisation.
- ▶ gravitational radius R_{grav} , which is the effective size of the subsystem that undergoes chain regularisation. R_{grav} replaces in Equation 5.31 replacing the apocenter distance.

If a member has

$$\dot{R}_k^2 > \frac{2 \sum m_k}{R_k}, \quad (5.48)$$

$$R_k > 3R_{\text{grav}} \quad (5.49)$$

then it is subject to removal. As long as there are three or more members, the chain regularisation is continued. After any changes in the hierarchy, the chain regularisation is re-initialised. Any escaping single particle or binary can readily be identified by considering the distances at the beginning and end of the chain if $N > 3$. As in two-body regularisation, the internal integration is continued up to the next block-step time. The integral Ldt is inverted for an upper limit because thus the block-step is not exceeded. Note The time derivative does not have a Taylor series expansion. Termination is carried out if $\max(R_k) > 3R_{\text{cl}}$ for three particles or two hard binaries. If a more efficient KS treatment is available¹², then the chain regularisation is switched off.

12: that could be a strong interaction of two binaries

5.6 Parallelization in NBODY6++GPU

The GPU implementation and new features of the hybrid, parallel NBODY6++GPU are published in Wang et al. (2015). They found for number of million-body simulations, which are known as the DRAGON simulations, that NBODY6++GPU is generally 400–2000 times faster than NBODY6 using 320 CPU cores and 32 NVIDIA K20X GPUs¹³ (Wang et al., 2015). To achieve this immense speed-up, the following parallelisation techniques are applied in the code:

13: more information on these GPUs can be found here <https://www.techpowerup.com/gpu-specs/tesla-k20x.c2315>.

14: instead of the alternative, the ring algorithm. The big advantage compared to the ring algorithm is that since every MPI processor has the whole particle data set no extra time-consuming and algorithmically challenging communication between the MPI processors is necessary. But, obviously, the particle data set cannot be too large because of limited memory on each computing node.

15: Still somewhat state of the art is NBODY6GPU, which includes GPU acceleration of NBODY6 using CUDA kernels for single node servers (Nitadori & Aarseth, 2012). Many of these kernels written by Keigo Nitadori are still in current use, even for the massively parallel programs such as NBODY6++GPU, see also discussion in Spurzem and Kamlah (2023).

- ▶ MPI (Message Passing Interface): a long time before NBODY6++GPU was developed, NBODY6++ was published by Spurzem (1999), which used MPI parallelisation for the first time using a copy algorithm¹⁴. The irregular and regular forces in the AC neighbour scheme from Section 5.5.3 was successfully parallelized. Each MPI process has access to the complete particle data but calculates only an individual subset of the particle data. For NBODY6++GPU, MPI is designed for multi-node computing clusters, see also Figure 5.5.
- ▶ GPU (Graphics Processing Unit) with CUDA (Compute Unified Device Architecture)¹⁵: the GPU library is used for calculating the regular force, which dominates the direct integration, and potential energy calculation. The neighbour list is accumulated very efficiently by the GPU as well.

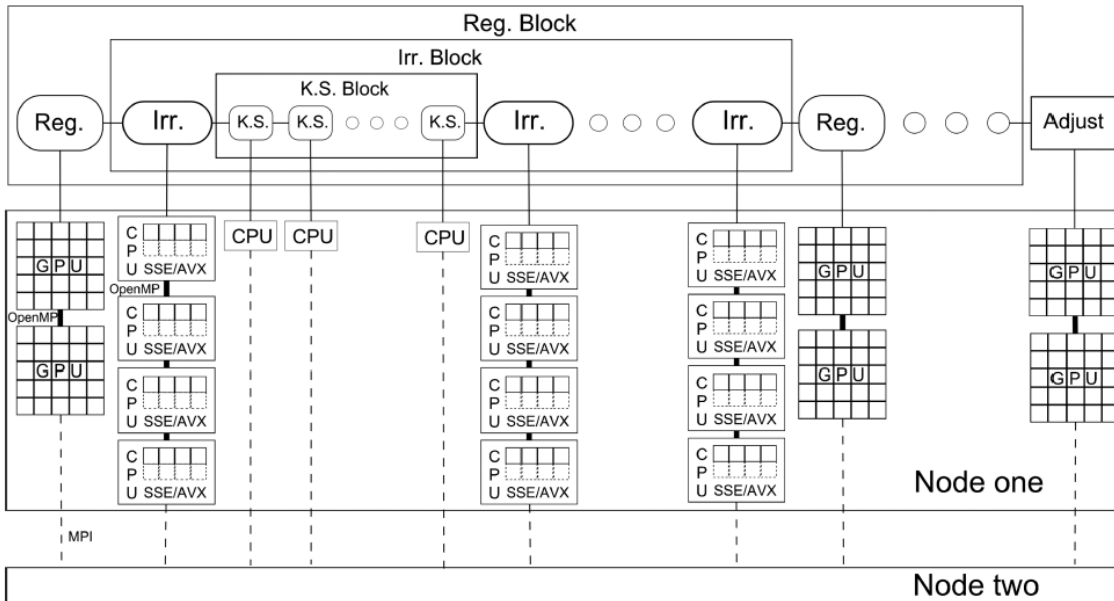


Figure 5.5: Diagram illustrating the NBODY6++GPU communication with the hardware: it shows one integration cycle in chronological order from left to right on one node. Based on the block time-steps, the integration cycle is divided into three steps: The KS calculation (K.S.) and the regular (Reg.) and irregular (Irr.) force integrations. The irregular force integration time-steps are sandwiched between the regular force integration time-steps and the KS regularizations time-steps are sandwiched between the irregular integration time-steps. Once several regular force integrations are completed, the ADJUST function is called. Inside one node, the regular force integration and ADJUST are parallelized by multiple GPUs. The irregular force integration is parallelized by AVX/SSE with OpenMP. MPI parallelization are done for all four parts between different nodes (Taken from Wang et al. (2015)).

- ▶ **OpenMP (Open Multi-Processing):** Like MPI and CUDA, OpenMP is another application programming interface (API) that supports multi-platform shared memory multiprocessing programming. Hybrid models of parallel programming can run on a computer cluster using both OpenMP and MPI, such that OpenMP is used for parallelism within a (multi-core) node while MPI is used for parallelism between nodes, see also Figure 5.5.
- ▶ **AVX/SSE (Advanced Vector Extension/Streaming SIMD Extension) for CPU:** AVX/SSE is effectively an instruction set for CPUs, which supports vector calculation in the specific cache. As mentioned before, the irregular force contribution is hard to parallelize due to the complexity of the AC neighbour scheme. The OpenMP parallel library is used together with AVX/SSE for neighbour particle prediction and the irregular force calculation still¹⁶.

In NBODY6++GPU the selection of active particles is done differently than before; A time-step sorting list algorithm is implemented. This is because that the time of selecting active particles can be much, much larger than the irregular force integration time. The exact method is described in (Wang et al., 2015).

As a result of the long historical development of the NBODY codes, see also Table 5.1, the NBODY6++GPU is a mixture of CUDA, C++ and Fortran 77 programming languages. As a result, the AVX/SSE and GPU libraries keep the individual copies of the particle data sets. The particles are therefore sometimes overlapping and inconsistent for different data copies distributed across several MPI processes (different time-steps for identical particles on different nodes). As a

16: Currently, the AVX/SSE implementations appear to be somewhat broken in NBODY6++GPU and erratic errors are produced from these routines during some simulations. New modern vectorizing compilers and additional OpenMP SIMD instructions might make the old AVX/SSE redundant in the future.

result, when synchronising the integration cycles, problems may be encountered. We need to make sure that every particle is predicted to a current time, before calling the stellar evolution routines, see [Chapter 8](#), KS and hierarchical regularisation, see [Section 5.5.4](#), because these are not parallelized and should have identical results on every node / every MPI processor, see [Figure 5.5](#).

Interesting is that the AC-scheme conflicts with the stellar evolution calculations. For example, when the star around which the neighbour sphere, [Figure 5.4](#), is constructed experiences mass loss or other stars in the neighbour sphere lose mass, then obviously the force this stars exerts on its surroundings decreases. Looking at [Figure 5.5](#), if mass loss happens at the irregular force integrations, then the neighbour sphere at the regular force integrations is erroneous and the regular force is inconsistent from then on. A correction with OpenMP needs to be undertaken for all particles that experience mass loss in their regular force and irregular force components. Sometimes mass loss is frequent and then the calculation performance is reduced significantly.

In the future, it would desirable to simulate larger and larger particle numbers, eventually ending up simulating a dwarf galaxy with 10^8 particles. However, the total wall clock time needs to be kept reasonable. Beyond hardware, software development and algorithmic advances this will require further optimisation of communication (speed) and data management. For example, when there are stars orbiting a SmBH (see e.g. Panamarev et al., 2019), the time-steps become very, very small, which increases the total wall clock time. Bandwidth and latency of the communication hardware will need to be improved, to reach higher float/s regimes. Currently, the main speed-up in Nbody6++GPU comes from the use of GPUs, which result in a reported 33 times (!) faster force calculation over not using them (Wang et al., 2015).

5.7 Summary of Nbody6++GPU

In this chapter *N*-body methods and in particular the code Nbody6++GPU were introduced in detail, so it is a good time to provide a brief summary. This section will also serve as part of the method section in [Chapter 9](#), [Chapter 10](#) and [Chapter 11](#) and will be referenced there. The state-of-the-art direct force integration code Nbody6++GPU, which is described in [Chapter 5](#) in great detail, is optimised for high performance GPU-accelerated supercomputing (Nitadori & Aarseth, 2012; Spurzem, 1999; Wang et al., 2015). This code follows a long-standing tradition in a family of direct force integration codes of gravitational *N*-body problems, which were originally written by Sverre Aarseth (see S. J. Aarseth, 1985; S. J. Aarseth, 1999a, 1999b, 2003b; S. J. Aarseth et al., 2008; Spurzem, 1999, and sources therein) and now spans a more than 60 year-long history of development, see [Table 5.1](#). The aforementioned code Nbody7 (S. J. Aarseth, 2012) also stems from this family, but it is its own serial code using the algorithmic regularization chain method (Hellström & Mikkola, 2010; Mikkola & Aarseth, 1993; Mikkola & Merritt, 2008; Mikkola & Tanikawa, 1999a, 1999b). It is not optimised for massively parallel

supercomputers, unlike NBODY6++GPU, which is currently one of the best available high accuracy, massively parallel, direct N -body simulation codes. Two very promising alternative and supposedly faster codes have been published during the preparation of this paper; the PETAR by Wang, Iwasawa, et al. (2020) and Wang, Nitadori, and Makino (2020a, 2020b) and BIFROST/MSTAR by Rantala et al. (2020, 2021) codes. These two codes are more recently developed and less mature.

NBODY6++GPU is optimised for large-scale computing clusters by utilising MPI (Spurzem, 1999), OpenMP and GPU (Nitadori & Aarseth, 2012; Wang et al., 2015) parallelisation techniques, see Section 5.6. In combination with intricate and highly sophisticated algorithms, see Section 5.5 and subsections therein, such as the KS regularisation (Kustaanheimo & Stiefel, 1965), the 4th-order Hermite scheme with hierarchical block time-steps (Hut et al., 1995; Makino, 1991, 1999; McMillan, 1986) and the AC neighbour scheme (Ahmad & Cohen, 1973), the code thus allows for star cluster simulations of realistic size without sacrificing astrophysical accuracy by not properly resolving close binary and/or higher-order subsystems of (degenerate) stars. With NBODY6++GPU we can include hard binaries and close encounters (binding energy comparable or larger than the thermal energy of surrounding stars) using two-body and chain regularization (Mikkola & Aarseth, 1998; Mikkola & Tanikawa, 1999a, 1999b), which permits the treatment of binaries with periods of days in conjunction and multi-scale coupling with the cluster environment. The AC scheme permits for every star to divide the gravitational forces acting on it into the regular component, originating from distant stars, and an irregular part, originating from nearby stars (“neighbours”). Regular forces, efficiently accelerated on the GPU, are updated in larger regular time steps, while neighbour forces are much more fluctuating and need update in much shorter time intervals. Since neighbour numbers are usually small compared to the total particle number, their implementation on the CPU using OpenMP (Wang et al., 2015) provides the best overall performance. Post-Newtonian dynamics of relativistic binaries is currently still using the orbit-averaged Peters & Matthews formalism (Peters, 1964; Peters & Mathews, 1963), as described e.g. in Arca-Sedda et al. (2021), Di Carlo, Mapelli, Bouffanais, et al. (2020), Di Carlo, Mapelli, Giacobbo, et al. (2020), Di Carlo et al. (2019, 2021), Rizzuto, Naab, Spurzem, Arca-Sedda, Giersz, et al. (2021), and Rizzuto, Naab, Spurzem, Giersz, et al. (2021). In those papers a collisional build-up of massive BHs, over one or even several generations of mergers, was found. The final merger of two massive BHs seen in the simulations is comparable to the most massive one observed by LIGO/Virgo (R. Abbott et al., 2020b).

Hénon-type Monte-Carlo methods

6

This chapter is partly based on Spurzem and Kamlah (2023), but more complete. Monte Carlo models of star clusters are the only ones which are still intensively used up to the present time with frequent publications (see e.g. Breivik, Mingarelli, & Larson, 2020; Kamlah, Leveque, et al., 2022; Kremer et al., 2021; Leveque, Giersz, Arca-Sedda, & Askar, 2022; Leveque, Giersz, Banerjee, et al., 2022; Ye et al., 2022), even though they are based on the Fokker-Planck approximation from Equations 4.124 and 4.113 in Definition 4.2.7, in the same way as Fokker-Planck, which I highlight for a special case in Chapter 7, or gaseous/moment models, which I do not elaborate on this thesis (see J. Schneider et al., 2011, for an overview). Monte-Carlo simulations provide data (and use input data) equivalent to N -body simulations: a set of particles with masses, positions and velocities at certain times. Detailed astrophysics such as full stellar evolution of single and binary stars has been included in Monte-Carlo models, which are largely the same, see Chapter 8 and Kamlah, Leveque, et al. (2022). It is important to know the strengths and limitations of the Monte-Carlo methods for star cluster simulation to appreciate the need to continuously benchmark Monte-Carlo with direct N -body simulations.

This chapter is mainly focused on the Monte-Carlo code MOnTe Carlo Cluster SimulAtor MOCCA (Giersz, 1998, 2001; Giersz et al., 2013, 2015; Hypki & Giersz, 2013) because I use that code in collaboration with the development team published in Kamlah, Leveque, et al. (2022). There exists a very similar, but competitor code called Cluster Monte-Carlo CMC with a recent paper summarising the latest iteration in Rodriguez et al. (2022) and see Joshi et al. (2000) and Pattabiraman et al. (2013) for earlier versions. Both are based on an evolved version of the original Hénon Monte-Carlo method (M. Hénon, 1971; M. H. Hénon, 1971), which was later re-introduced and developed further by Stodołkiewicz (1982, 1986). Today, they are used for star-by-star modelling¹ like the N -body methods described in Chapter 5, but every star is a particle in the Monte-Carlo simulation. Moreover, Freitag and Benz (2001) developed a new Hénon-type Monte-Carlo code that treated stellar collisions and centrally located, massive BHs differently. This code is not in use anymore, but many features were subsequently implemented in MOCCA and CMC (Rodriguez et al., 2022).

6.1 Hénon type method

Both the Hénon and Spitzer type method can work only for large particle numbers, i.e. particle numbers when the relaxation time-scale of the star cluster is much larger than the crossing time-scale, which is also one of the central assumptions in the Fokker-Planck approximation from Definition 4.2.7. As a consequence, the Hénon

| | |
|--|-----|
| 6.1 Hénon type method . . . | 139 |
| 6.1.1 Two-body relaxation in the Hénon type method | 142 |
| 6.1.2 The effective scattering angle | 143 |
| 6.2 Binaries and triples in a Hénon-type Monte-Carlo code | 145 |
| 6.2.1 Single-single interactions | 146 |
| 6.2.2 Binary and binary-binary interactions . . . | 147 |
| 6.3 Updating the positions and velocities | 148 |
| 6.4 Calculating the gravitational potential | 148 |
| 6.5 Energy conservation in a Hénon-type Monte Carlo code | 148 |
| 6.6 On the reliability of direct N -body and Hénon-type Monte-Carlo methods for star cluster simulations | 149 |
| 6.7 Summary of MOCCA | 151 |

1: Instead of “superstars”, i.e. one particle in the Monte-Carlo model could represent many real stars, which was used earlier.

and Spitzer type method work in a regime where the star cluster is dominated by distant, weak, two-body encounters instead a small number of strong encounters that may be expected in star clusters with particle numbers of 1000 or smaller. If in a star cluster there are many tightly bound binaries the theoretical foundation of the Fokker-Planck approximation (and consequently also of Monte Carlo models) breaks down, because we have strong correlations present. Practically it is observed (e.g. in N -body simulations) that close encounters between stars and binaries and between binaries have strong effect on the global dynamics of the system. Nevertheless Monte Carlo models have been quite successful by adding these effects into their models (using either statistical cross sections or few-body integrations for these events), see below.

As the name suggests Monte Carlo models are based on the principle that stars have an orbit in a known self-consistent potential; randomly perturbations are applied, which model the effect of relaxation by distant gravitational encounters. In fact, the current methods are Monte-Carlo Markov-chain methods, because they are predicting future outcomes, i.e. the particle's velocities and positions exclusively on the current particle's velocities and positions. Importantly, the current Monte-Carlo codes assume that this prediction is just as good as if the predictions of future velocities and positions were made on the basis of knowing the entire particle's trajectory from the beginning of the simulation. Therefore, this method fulfils the Markov property, i.e. the conditional probability distribution of the future particle's positions and velocities only depend on the present particle's positions and velocities. In this way, the current Hénon-type Monte-Carlo methods save a lot of resources and avoid the intractable problem. I will omit the Markov-chain in naming these methods from now on, but it is implicitly assumed.

Spitzer's method follows the orbits of stars in the global potential of the cluster and randomly applies kicks in velocity to the stars; at the end of a long series of papers they included binaries and a mass spectrum (J. Spitzer & Mathieu, 1980; J. Spitzer & Shull, 1975a, 1975b; J. Spitzer & Chevalier, 1973; J. Spitzer & Hart, 1971a, 1971b; J. Spitzer & Shapiro, 1972; J. Spitzer & Thuan, 1972).

Hénon's method, which the rest of this chapter focuses on, is using the phase space of constants of motion, see [Definition 4.2.9](#), of a star in a spherically symmetric potential, energy and angular momentum. Deflections are selected randomly, and their effect on angular momentum and energy computed and applied (M. Hénon, 1971; M. H. Hénon, 1971). It is already worthwhile and even important to point out already the very strong limiting assumptions in this modelling method.

Definition 6.1.1 (Assumptions in the Hénon's method) *Hénon's method makes the following central assumptions:*

- ▶ *The method assumes molecular chaos, see also Equation 4.118, which means that the distribution functions of field and subject stars are strictly separable and independent of each other.*
- ▶ *Only for large particle numbers with $N > 10^3$ is the method possible, where at least 10^5 yields statistically reliable results*

when compared with direct N -body simulations. This assumption is necessary for the Fokker-Planck approximation in [Definition 4.2.7](#) and orbit averaging the Fokker-Planck equation [Definition 4.2.12](#) in that the orbits of the stars are fixed at dynamical time-scales.

- ▶ The star cluster simulation is spherically symmetric at all times. It is necessary for the computation of new particle orbits, the determination nearest neighbors of the particles, and the computations of the star cluster potential.
- ▶ Hénon's method operates on the relaxation time-scale, which implies that every time-step in the simulation the star cluster model transitions from star cluster in Virial equilibrium to another.

From [Definition 6.1.1](#) we can already see when Hénon-type Monte-Carlo star cluster simulation methods experience problems:

- ▶ Any situation in which a star cluster might deviate from spherical symmetry can strictly speaking not be modelled by this method. Such situations might be, for example,
 - (Initially rotating) star clusters with flattened shapes, see [Section 2.2.6](#),
 - tidal tails of star clusters and general tidal fields,
 - bar formation / onset and evolution of triaxiality in star cluster's centres during violent relaxation.
- ▶ The assumption of molecular chaos breaks down when resonant effects need to be taken into account, such as dynamics around a central, massive BH or massive particles generally interacting with one another in star cluster cores.
- ▶ the Fokker-Planck approximation and orbit averaging break down for low particle numbers. Therefore, beyond the strong deviation from sphericity, the Hénon-type Monte-Carlo method cannot model the tidal dissolution of star clusters or OCs in general.
- ▶ The assumption of constant Virial equilibrium means that star cluster simulations with the Hénon-type Monte-Carlo method have to start after one relaxation time-scale. Additionally, effects such as star cluster mergers, tidal shocking etc. cannot be taken into account beyond the deviation from sphericity.

After such a long and non-exhaustive list of limitations of this modelling method, it begs the question why many people even today bother with developing it. The reason is that the this method is much less computationally expensive than direct N -body simulations (Downing, 2012; Giersz et al., 2008, 2013; Hypki & Giersz, 2013). The MOCCA Survey Database I (Askar et al., 2017), which provides a grid of about 2000 GC models, something that is currently unthinkable with direct N -body simulations, is a major outcome of the work with MOCCA and is also a testament to the strengths of this modelling approach, which has led to a large number of subsequent studies (Arca Sedda et al., 2019; Hong, Askar, et al., 2020; Hong, Vesperini, Askar, et al., 2020; Hong et al., 2018; Leveque et al., 2021; Morawski et al., 2018, 2019). With this database, we can choose appropriate initial conditions for realistic star cluster simulations using direct N -body methods. It is important to stress, that despite

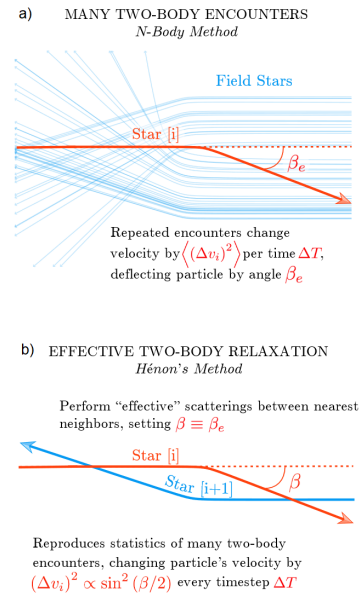


Figure 6.1: Schematic diagram showing the Hénon-type Monte-Carlo method: a) shows the cumulative effect of many two-body encounters between a subject star following the red trajectory and many surrounding field stars. b) shows the effective two-body relaxation that is calculated in the Hénon-type Monte-Carlo method, which simplifies this calculation to a single encounter between adjacent particles, where the deflection angle is selected to replicate statistical predictions utilizing Equation 6.12, see also [Definition 6.1.2](#) (Figure taken adapted from Rodriguez et al. (2022)).

some important physical simplification of the Hénon type Monte Carlo method listed in [Definition 6.1.1](#), the results of the MOCCA simulations agree very well with the results of N -body simulations for clusters with different initial number of stars (from 10^4 up to 10^6) and evolving in different host environments (Giersz et al., 2016; Giersz et al., 2013; D. C. Heggie & Giersz, 2014; Madrid et al., 2017; Wang et al., 2016). The agreement is not only good for the cluster global properties, but also for properties of the binary population (Geller et al., 2019; Rizzuto, Naab, Spurzem, Giersz, et al., 2021). I note that a similar database has been published by the CMC team called the CMC Cluster Catalog (Kremer, Ye, et al., 2020).

6.1.1 Two-body relaxation in the Hénon type method

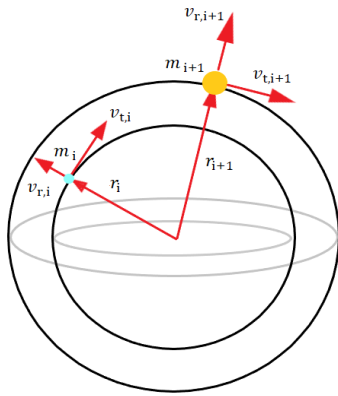


Figure 6.2: Schematic diagram showing the Hénon type coordinate system.

As is mentioned the two-body relaxation process is at the heart of the Hénon type method. I have already elaborated on this process twice, once in [Definition 2.2.4](#) and in much more detail in [Section 4.1.3](#). Therefore, a description of this processes will not be repeated here, and I will limit myself to the actual calculations that are related to relaxation in a Hénon type Monte-Carlo code for star cluster simulation.

In the Hénon type method, the 6-D velocities and positions are reduced to 3-D phase-space coordinates. Each particle is assigned a radial position r and it has two components of the velocity at r : the radial component v_r and the tangential component v_t as a result of spherical symmetry and Virial equilibrium, see [Figure 6.2](#). The code then tracks the constants of motion of each particle, i.e. the total energy E and the total angular momentum J , which are conserved over the dynamical time-scale τ_{dyn} due to the assumption of orbit averaging. The gravitational potential $\Phi(r)$ at radius r define a closed orbit for every particle in the star cluster. The Monte-Carlo time-step τ_{MC} enters the simulation at every time-step when a new orbit for every particle is randomly sampled, i.e. the three phase-space coordinates r , v_r and v_t .

As mentioned previously, the evolution of the star cluster is governed by the cumulative effect weak dynamical encounters. The orbits of the particles are affected on the relaxation time-scale τ_{rx} . At every τ_{MC} , the weak encounters lead to perturbations ΔE and ΔJ in each particle's E and J .

Definition 6.1.2 (Effective encounter and effective scattering angle) ΔE and ΔJ are calculated as a single effective encounter between each particle and its nearest neighbor in radius. As shown in [Figure 6.1 a](#)) from Rodriguez et al. (2022), in the COM frame of the weak two-body encounter, the magnitudes of the velocities are unchanged and the velocity vectors are deflected by the effective deflection / scattering angle β_e . Since the encounters are assumed to be elastic, the energy during the encounter is conserved. When viewed the frame of reference of the star cluster, each encounter exchanges E and J and it is necessary to ensure that each

effective encounter provides the accurate mean change in kinetic energy

$$(\Delta v_i)^2 \propto \sin^2 \left(\frac{\beta_e}{2} \right) \quad (6.1)$$

at the particle's location during the time-step ΔT , which requires the calculation of β_e of each particles and this gives the mean ΔE and ΔJ .

6.1.2 The effective scattering angle

The effective scattering angle β_e is calculated using the updated treatment by Joshi et al. (2000) and Stodołkiewicz (1982) and the description here leans on Rodriguez et al. (2022). An excellent introduction on the subject can also be found in Freitag (2008).

MOCCA sorts the particles in terms of increasing distance from the star cluster centre with $r_i < r_{i+1}$. As explained in Definition 6.1.2, the change in squared velocity for a single single encounter between adjacent particles is given by $(\Delta v_i)^2$ for the subject star with index i and mass m_i and the field star with mass m_f with index f and mass m_f , see Figure 6.1. It is quietly assumed here that all field star has the same mass and relative velocity, m_f and w , with respect to our test star, m_i . As was already seen in Section 4.1.2 at length, $(\Delta v_i)^2$ can be written in terms of the effective scattering angle β_e and the impact parameter b and the 90° deflection radius from Equation 4.54

$$(\Delta v_i)^2 = \frac{4m_f^2}{(m_i + m_f)^2} w^2 \sin^2 \left(\frac{\beta_e}{2} \right) \quad (6.2)$$

$$= \frac{4G^2 m_f^2}{w^2 b_{90^\circ}^2} \frac{1}{1 + (b/b_{90^\circ})^2}, \quad (6.3)$$

where $w = |\mathbf{v}_i - \mathbf{v}_f|$ is the relative speed of the particles at infinity. As shown in Figure 6.1 b), the velocity change over time caused by multiple weak interactions, one can analyze the field particles that particle i encounters while traveling through the cluster. The number of particles that particle i encounters at an impact parameter b during a time interval ΔT can be determined by multiplying the local number density of particles, n , by the volume swept out at that impact parameter b . When considering an infinitesimal annulus with an inner radius of b and an outer radius of $b + db$, this number can be expressed as

$$N_{\text{enc}} = 2\pi b m w \Delta T db, \quad (6.4)$$

where the length of the cylinder is the relative velocity of the particles, w , times ΔT , which is essentially equivalent to Equation 4.63. The product of Equations 6.4 and 6.3 should be integrated over all impact parameters

$$\langle (\Delta v_i)^2 \rangle \simeq 8\pi G^2 n \Delta T m_f^2 w^{-1} \ln(\Lambda), \quad (6.5)$$

where the Λ once again is the Coulomb logarithm from Definition 18, which depends on

$$\ln \Lambda = \ln(\gamma N), \quad (6.6)$$

2: γ is sensitive to the mass spectrum of the star cluster and needs to be adjusted accordingly (Freitag, 2008). The CMC value is possibly better for mass spectra with larger mass differences than the MOCCA value (priv. communication with Mirek Giersz).

where γ is an input parameter in Hénon-type method and the associated codes CMC with $\gamma = 0.01$ Rodriguez et al. (2022) and MOCCA with $\gamma = 0.02$ for multi-mass star clusters as default values Giersz and Heggie (1996) and Giersz et al. (2008)².

In order to get more realistic ranges of masses and velocities of the field stars, a distribution function is introduced that measures this

$$F(\mathbf{r}, \mathbf{v}, m) \quad (6.7)$$

with which the cumulative shift $\langle(\Delta v_i)^2\rangle$ can be rewritten as

$$\langle(\Delta v_i)^2\rangle = 8\pi G^2 n \Delta T \ln \Lambda \left\langle m_f^2 w^{-1} \right\rangle_F \quad (6.8)$$

with the average over the local phase-space distribution function

$$\left\langle m_f^2 w^{-1} \right\rangle_F \equiv \int F_i F_f m_f^2 w^{-1} d^3 \mathbf{v}_i d^3 \mathbf{v}_f dm_i dm_f. \quad (6.9)$$

where $F_i = F(\mathbf{r}_i, \mathbf{v}_i, m_i)$ is the distribution function of the subject stars and $F_f = F(\mathbf{r}_f, \mathbf{v}_f, m_f)$ is the distribution function of the field stars.

Definition 6.1.3 (Monte-Carlo method) *The determination of the scattering angle β_e involves solving*

$$\left\langle \frac{4m_f^2 w^2}{(m_i + m_f)^2} \right\rangle_F \sin^2 \left(\frac{\beta_e}{2} \right) \quad (6.10)$$

$$= 8\pi G^2 n \Delta T \ln \Lambda \left\langle m_f^2 w^{-1} \right\rangle_F, \quad (6.11)$$

which involves averaging the mass and velocity quantities over relevant distribution functions. According to M. Hénon (1971) averaging is not efficient and simply taking the values of the nearest neighbour of the subject particle with mass m_i . After sufficient time-steps, this procedure will represent a fair draw from the relevant distribution functions. Therefore, Equation 6.11 becomes

$$\sin^2 \left(\frac{\beta_e}{2} \right) = \frac{2\pi G^2 (m_i + m_{i+1})^2}{w^3} n \ln(\Lambda) \Delta T, \quad (6.12)$$

where n must be averaged over certain subsets of particles in the simulation, see also Figure 6.1, which can be rewritten in terms of the relaxation time-scale (Freitag & Benz, 2001).

From Equation 6.12, the scattering angles β_e for each particle pair partaking in the encounter can be used to calculate ΔE and ΔJ for each orbit. As depicted in Figure 6.1, the phase-space coordinates of the Hénon-type method gives the phase space coordinates of the two interacting particles by $(r_i, v_{r,i}, v_{t,i})$ and $(r_{i+1}, v_{r,i+1}, v_{t,i+1})$, with masses m_i and m_{i+1} , respectively. In line with Rodriguez et al. (2022) the reference frame such that the z-axis is parallel to \mathbf{r}_i and the (x, z) -plane contains \mathbf{v}_i . Converting these coordinates to Cartesian

coordinates, the two particle velocities are then

$$\mathbf{v}_i = (v_{t,i}, 0, v_{r,i}), \quad (6.13)$$

$$\mathbf{v}_{i+1} = (v_{t,i+1} \cos \phi, v_{t,i+1} \sin \phi, v_{r,i+1}), \quad (6.14)$$

where ϕ is a uniform random variate in the range $[0, 2\pi]$. The relative velocity \mathbf{w} is then:

$$\mathbf{w} \equiv \mathbf{v}_{i+1} - \mathbf{v}_i \quad (6.15)$$

$$= (v_{t,i+1} \cos \phi - v_{t,i}, v_{t,i+1} \sin \phi, v_{r,i+1} - v_{r,i}). \quad (6.16)$$

We now define vectors \mathbf{w}_1 and \mathbf{w}_2 with magnitude equal to $|\mathbf{w}|$, such that $\mathbf{w}_1 \times \mathbf{w}_2 = \mathbf{w}$. In this right-handed coordinate system, we have

$$\mathbf{w}_1 \equiv \left(\frac{-w_y w}{w_p}, \frac{w_x w}{w_p}, 0 \right), \quad (6.17)$$

$$\mathbf{w}_2 \equiv \left(\frac{-w_x w_z}{w_p}, \frac{-w_y w_z}{w_p}, w_p \right), \quad (6.18)$$

where $w_p = \sqrt{w_x^2 + w_y^2}$. The angle ψ is randomly selected $\in [0, 2\pi]$ between the plane of relative motion, defined by $(\mathbf{r}_{i+1} - \mathbf{r}_i, \mathbf{v}_{i+1} - \mathbf{v}_i)$, and the plane containing \mathbf{w} and \mathbf{w}_1 . The relative velocity after the dynamical encounter, \mathbf{w}^{new} , is then

$$\mathbf{w}^{\text{new}} = \mathbf{w} \cos \beta_e + \mathbf{w}_1 \sin \beta_e \cos \psi + \mathbf{w}_2 \sin \beta_e \sin \psi. \quad (6.19)$$

The particle velocities in the cluster frame after the dynamical encounter, $\mathbf{v}_i^{\text{new}}$ and $\mathbf{v}_{i+1}^{\text{new}}$ are

$$\mathbf{v}_i^{\text{new}} = \mathbf{v}_i - \left(\frac{m_{i+1}}{m_i + m_{i+1}} \right) (\mathbf{w}^{\text{new}} - \mathbf{w}), \quad (6.20)$$

$$\mathbf{v}_{i+1}^{\text{new}} = \mathbf{v}_{i+1} + \left(\frac{m_i}{m_i + m_{i+1}} \right) (\mathbf{w}^{\text{new}} - \mathbf{w}). \quad (6.21)$$

The new radial and transverse velocities for the first particle are

$$v_{r,i}^{\text{new}} = v_{z,i}^{\text{new}}, \quad (6.22)$$

$$v_{t,i}^{\text{new}} = \sqrt{\left(v_{x,i}^{\text{new}} \right)^2 + \left(v_{y,i}^{\text{new}} \right)^2}. \quad (6.23)$$

The new specific orbital energy and specific angular momentum for the particle with index i are then

$$E_i = \Phi(r_i) + \frac{1}{2} \left(\left(v_{r,i}^{\text{new}} \right)^2 + \left(v_{t,i}^{\text{new}} \right)^2 \right), \quad (6.24)$$

$$J_i = r_i v_{t,i}^{\text{new}}, \quad (6.25)$$

and in an analogous manner from particle $i + 1$.

6.2 Binaries and triples in a Hénon-type Monte-Carlo code

3: This assumption breaks down for low particle numbers and in dense star cluster cores, as was already stated in [Definition 6.1.1](#).

As mentioned repeatedly already in the thesis, strong dynamical encounters in star clusters can occur, especially in the much denser star cluster cores than the associated halos. However, the methodology outlined above relies on the weak encounter approximation and that orbit averaging can be applied and therefore, strong encounters are not part of the Hénon-type Monte-Carlo method and it is implicitly assumed that they are not statistically relevant³. There are two types of strong interactions in a Hénon-type Monte-Carlo code

- ▶ Single-single interactions,
- ▶ binary and binary-binary interactions,

which are all treated with the small- N scattering code FEWBODY (Fregeau et al., 2004). It employs the 8th order Runge-Kutta Prince-Dormand integrator to move the particles' positions. Additionally, there is an option to activate the complete pairwise KS regularization, see [Section 5.5.4](#) and [Section 5.5.5](#), within the simulation (S. J. Aarseth & Zare, 1974; Kustaanheimo & Stiefel, 1965). The program is capable of detecting stable hierarchical systems, which it represents as binary trees implying that each bound object (member in a binary) can only have two "children". The stability of these hierarchies is evaluated using the stability criterion by R. A. Mardling and Aarseth (2001). If the system is unstable, then the FEWBODY calculation is terminated. In the following two subsections, I briefly elaborate on how a Hénon-type Monte-Carlo code deals with these strong encounters. It is already useful to briefly point out how MOCCA separates strong from weak dynamical interactions, which still relies on criteria written up in Giersz (2001). Particles in the simulation either partake in the standard two-body relaxation described at length above or a strong interaction during one Monte-Carlo time-step. This is because the assumption in [Section 6.1.2](#) that the relative velocities between the field and subject stars are constant over one time-step is no longer valid. To integrate binary-single or binary-binary interaction we need to check the probability of such an interaction. If the random number is smaller than this probability the system is taken out of the standard two-body relaxation loop and integrated using the methods implemented in FEWBODY. To compute the probability, a simple two-body approximation is used. We can assume the maximum value for the pericenter distance during the first approach, which is always a multiplication of the binary semi-major axis. Knowing the maximum pericenter distance we can estimate the maximum impact parameter and then compute the interaction cross-section and probability. A similar, but not identical probability estimation is employed in CMC (Rodriguez et al., 2022). They use a similar sampling method but follow Fregeau and Rasio (2007) and Freitag and Benz (2002). After identifying the particles partaking in strong interactions, CMC also uses FEWBODY to integrate these systems.

6.2.1 Single-single interactions

CMC and MOCCA use the sticky-sphere approximation, where any two particles that touch radii collide. The cross-section for a pair of single stars with stellar masses m_i and m_{i+1} and stellar radii R_i and R_{i+1} can be expressed as

$$\Sigma_{\text{coll}} = \pi (R_i + R_{i+1})^2 \left(1 + \frac{2GM}{(R_i + R_{i+1})w^2} \right), \quad (6.26)$$

where $M = m_i + m_{i+1}$ (Rodriguez et al., 2022). In MOCCA, the outcome of such a collision is typically simply a new star with m_{new} , which is simply computed as $m_i + m_{i+1}$. The stellar phase is then modelled with the fitting formulae from SSE & BSE Hurley et al. (2000, 2002), see also Chapter 8. Compact objects are treated similarly.

6.2.2 Binary and binary-binary interactions

All of these interactions depend on the relative velocity, w , of the pair of interacting objects (singles or binaries) and the impact parameter at infinity, b . All of the interactions are integrated until a certain time limit is reached, which is approximately 10 s (corresponding to approximately 4000 integrations on the hardware then) in MOCCA (Hypki & Giersz, 2013) or if the system reaches a definite end-state. If there are strong encounters that cannot be resolved within these limits, these are then taken out of the FEWBODY treatment subsequently treated simply with the standard two-body relaxation procedure, but FEWBODY has a lot more stopping conditions that can be read up on Fregeau et al. (2004). Unlike CMC (see e.g. Rodriguez et al., 2018), the FEWBODY implementation in MOCCA does not have dissipative terms up to order PN2.5⁴.

Triple systems in FEWBODY are broken up into a binary and a single star. It is important to state the once the triple system is treated with FEWBODY, there are no tidal forces outside of the triple acting on any of the particles. Binary-single systems are chaotic as already highlighted in Section 4.1.5 and Figure 4.5. One of the outcomes of such an interaction that is chaotic and resonant can be the collision of two stars, which are treated similarly as the sticky-sphere approach from Equation 6.26.

Furthermore, as I already elaborated on in Section 4.1.2, dynamical binaries cannot form from two stars simply encountering one another, because the orbit is always along a hyperbola. Energy must be dissipated in some way. The excess kinetic energy may be carried away by a third or more stars leaving behind a dynamical binary in a bound orbit. The code decides on a hardness criterion, which is

$$\eta \equiv \frac{Gm_i m_{i+1}}{a \langle m \rangle \sigma^2}, \quad (6.27)$$

where a is the semi-major axis of the hypothetical binary, $\langle m \rangle$ is the average local mass, and σ is the average local velocity dispersion, which are both calculated with respect to some number of stars that are closest to the strong encounter. Then if stars pass the

4: However, FEWBODY in MOCCA might soon be replaced by TSUNAMI code (Trani & Spera, 2023), which might have terms up to order PN3.5. MOCCA with all dissipative terms switched on is about 3-5 times slower than without them (private comm. with Mirek Giersz).

hardness criterion, a dynamical binary forms out of the tripler interaction. If not then the aforementioned two-body relaxation or strong encounters are considered for the triple interaction.

6.3 Updating the positions and velocities

This brief paragraph is taken from Spurzem and Kamlah (2023). A each particle receives a new position and velocity at the end of τ_{MC} are randomly sampled according to the time the particle spends at a certain position on the orbit. If the spherically symmetric gravitational potential $\Phi(r)$ is known, the pericenter r_{min} and apocenter r_{max} of the orbit are known. At every point of the orbit r the radial velocity is known from

$$v_r = \pm \sqrt{2(E - \Phi(r)) - \frac{L^2}{r^2}} \quad (6.28)$$

The orbital integral defines the orbital time τ by

$$\frac{\tau}{2} = \int_{r_{\text{min}}}^{r_{\text{max}}} \frac{dr}{v_r} \quad (6.29)$$

With $p(r) = (2/\tau) \cdot (dr/v_r)$ one gets a probability distribution function, used to randomly pick a radial position r_i for the star on its orbit, which should be distributed according to $p(r)$.

6.4 Calculating the gravitational potential

This brief paragraph is also taken from Spurzem and Kamlah (2023). Let m_i be the stellar mass of stars ($i = 1, \dots, n$), then the spherically symmetric gravitational potential can be computed according to (M. Hénon, 1971)

$$\Phi(r) = G \left(-\frac{1}{r} \sum_{i=1}^k m_i - \sum_{i=k+1}^n \frac{m_i}{r_i} \right) \quad (6.30)$$

In addition to that two angles θ and ϕ are randomly picked, so as to have a three dimensional position of the star. Velocities are obtained from E , L , and $U(r_i)$ (one more random number needed). In that way a model star cluster is produced whose data structure is three dimensional - equivalent to that of an N -body simulation.

6.5 Energy conservation in a Hénon-type Monte Carlo code

At each time-step, the calculation of the updated gravitational potential is behind the updated energy and angular momentum that are a result of sampling the new positions and velocities of

each particle. Therefore, this introduces a energy drift that is non-negligible across many time-steps. Stodołkiewicz (1982) introduced a method to conserve the energy at each time-step. The change in energy for a particle can be written as

$$\Delta E_i^{\text{corr}} = \int \frac{\partial U(r_i)}{\partial t} dt. \quad (6.31)$$

This equation can approximately be written as the average of the change in the potential energy between the positions of the particle at the previous and current time-steps:

$$\int \frac{\partial U(r_i)}{\partial t} dt = \frac{[\Delta\Phi(r_i^{\text{prev}}) + \Delta\Phi(r_i^{\text{curr}})]}{2}, \quad (6.32)$$

where $\Delta\Phi \equiv \Phi^{\text{curr}} - \Phi^{\text{prev}}$, see Rodriguez et al. (2022).

Furthermore, the stellar orbits for the current time-step are calculated for the potential from the previous time-step. Therefore, when you update the orbit for some particle, the gravitational potential includes this particle on a different orbit. For heavy masses in the simulation, this can introduce a considerable error.

6.6 On the reliability of direct N -body and Hénon-type Monte-Carlo methods for star cluster simulations

It is worthwhile to comment on the general reliability of direct N -body simulations and Hénon-type Monte-Carlo simulations. The following paragraphs lean on Spurzem and Kamlah (2023).

This chapter has already listed the extremely strong assumption and the resulting shortcomings when simulating star clusters with Hénon-type Monte-Carlo codes in Section 6.1. Therefore, it is natural to assume that direct N -body simulation methods described in Chapter 5 are more reliable and they are by nature of the method. From Equation 5.19, we achieve any desired accuracy if needed, however, such a procedure is associated with an increasing computational cost and is also limited by the computer's accuracy. In practice, the accuracy is typically dependent on the globally conserved quantities such as the total energy and total angular momentum of the star cluster as well as the center of mass conservation. In Section 6.5 we have seen that such quantities are also relevant in Hénon-type Monte-Carlo codes concerning the long-term stability and corrections need to be made in each Monte-Carlo time-step to conserve them. For both methods, it needs to be said that these checks only check for numerical accuracy and not astrophysical realism, i.e., they are not a statement on the "true" individual trajectories of each particle. R. H. Miller (1964) already pointed out that repeated close encounters between stars lead to N -body systems that very quickly diverge from one another even with the same initial conditions. In other words, the separation of two trajectories increases exponentially with time. This known as the exponential instability and can only a fraction of the crossing time-scale of a star cluster. Therefore, a fully accurate

direct N -body integration of a star cluster would require of order $\mathcal{O}(N)$ decimal places (J. Goodman et al., 1993; Kandrup et al., 1994). Beyond standard weak, local two-body encounters that dominate the star cluster's evolution, collisional systems also host particles with highly chaotic orbits in non-integrable potentials, which can be the source of the exponential instability in numerical inaccuracy. Spurzem and Kamlah (2023) maintain that N -body simulations of star clusters or galactic nuclei do not always exploit the detailed configuration space of all particles and therefore, the situation is somewhat alleviated. Global averaged quantities such as binary fractions etc. are not sensitive to small variations of the initial configurations of star cluster simulations with variations of random seeds when sampling positions and velocities of particles (Giersz & Heggie, 1994a, 1994b; Giersz & Heggie, 1996, 1997). These papers also demonstrated good agreement with direct Fokker-Planck modelling. The impact of the random seed initialisation has also been nicely demonstrated in recent my co-author paper published as Z.-M. Li et al. (2023). Here, ten direct N -body simulations with different random seed initialisation show very similar compact binary fractions over long simulation times. The method of varying the random seed in the initialisation of the star cluster models was also partly and successfully used in Giersz and Spurzem (1994), which focused on the evolution of anisotropy and comparisons with the anisotropic gaseous models. Furthermore, the papers by Rizzuto, Naab, Spurzem, Giersz, et al. (2021) and Rizzuto et al. (2022) are good examples here, where the formation of intermediate mass black holes was analyzed over a large set of N -body simulations, using statistically independent initial models. This can also be said about the DRAGON-II simulations (Arca Sedda & et al., 2023a, in prep.) and the two-follow up studies on the binaries and GW events in Arca Sedda and et al. (2023b, 2023c, in prep.). The implication of this analysis is that it is much more reliable to focus on global, averaged quantities of star cluster simulations and preferably across multiple simulations and not to focus on detailed star by star analysis. Generally, the Hermite schemes might be updated to use time-symmetric methods comparable with general symplectic methods, which has been used for direct N -body simulations of planet formation and planetary systems (Kokubo et al., 1998; Makino et al., 1997) and for a hybrid N -body and Fokker-Planck simulation of planetesimal growth in protoplanetary disks (Amaro-Seoane et al., 2014; Glaschke et al., 2014). It works by following a small update using methods by Funato et al. (1996), Hut et al. (1995), and Makino et al. (1997). Mikkola and Aarseth (1998) stress that even with a newly applied classical method secular errors in the integration of close binaries can be strongly reduced. It stands that the 4th order integrator presents an optimal choice for performance and accuracy for star cluster simulation, but it is unsatisfactory for Solar system integration. Due to the inherently physically chaotic nature of star clusters remaining small secular errors can usually be tolerated. It means that the solution found in the computer always stays near a permitted solution of the underlying Hamiltonian, even if it does not stay on the one trajectory which belongs to the initial conditions (Quinlan & Tremaine, 1992). But a recent dynamical study has

reiterated that it may not be sufficient just to check a few globally conserved quantities, because that could be dominated by a few high energy objects (binaries) and could cover up errors in other parts of the system (Wang & Hernandez, 2021).

In summary, in star cluster simulations with direct N -body and Hénon-type Monte-Carlo methods the secular errors are being kept small relative to typical values of energy and angular momentum and an accurate reproduction of all individual stellar orbits is not generally required.

6.7 Summary of MOCCA

In this chapter Hénon-type Monte-Carlo methods and in particular the code MOCCA were introduced in detail, so it is adequate now to provide a brief summary. This section will also serve as part of the method section in [Chapter 9](#). Monte-Carlo methods are computationally much less taxing than direct N -body simulation (Downing, 2012; Giersz et al., 2008, 2013; Hypki & Giersz, 2013), but that comes at a cost. It is less realistic in the sense that it can only, for example, describe spherical systems, for more assumptions see [Section 6.1](#). This means that among other things rotation cannot be implemented in these Monte-Carlo simulations unlike direct N -body simulations (Amaro-Seoane et al., 2010; Einsel & Spurzem, 1999; Ernst et al., 2007; Fiestas & Spurzem, 2010; Hong et al., 2013; Kim et al., 2008; Spurzem, 2001). For the Monte-Carlo models of star cluster simulations in this paper we use the MOCCA (Giersz et al., 2013; Hypki & Giersz, 2013). This code is based on an improvement of the original Hénon-type Monte-Carlo Fokker-Planck method by Stodońkiewicz (1982, 1986) and in a further iteration by Giersz (1998, 2001) and ultimately by Giersz et al. (2013) and Hypki and Giersz (2013). This approach combines the statistical treatment of the process of relaxation with the particle based approach of direct N -body simulations. With this, they are able to model spherically symmetric star clusters over long dynamical times. Three- and four-body interactions in the star cluster simulation are computed separately by the FEWBODY code (Fregeau et al., 2004). Furthermore, the escapers from tidally limited star clusters are described by Fukushige and Heggie (2000). Here, the escaping stars stay in the system for some time depending on the excess energy above the escape energy.

The MOCCA Survey Database I (Askar et al., 2017), which provides a grid of about 2000 GC models, something that is currently unthinkable with direct N -body simulations, is a major outcome of the work with MOCCA and is also a testament to the strengths of this modelling approach, which has led to a large number of subsequent studies (Arca Sedda et al., 2019; Hong, Askar, et al., 2020; Hong, Vesperini, Askar, et al., 2020; Hong et al., 2018; Leveque et al., 2021; Morawski et al., 2018, 2019). With this database, we can choose appropriate initial conditions for realistic star cluster simulations using direct N -body methods. It is important to stress, that despite some important physical simplification of the Monte Carlo method, the

results of the MOCCA simulations agree very well with the results of N -body simulations for clusters with different initial number of stars (from 10^5 up to 10^6) and evolving in different host environments (Giersz et al., 2016; Giersz et al., 2013; D. C. Heggie & Giersz, 2014; Madrid et al., 2017; Wang et al., 2016). The agreement is not only good for the cluster global properties, but also for properties of the binary population (Geller et al., 2019; Rizzuto, Naab, Spurzem, Giersz, et al., 2021).

Orbit-averaged Fokker-Planck methods for axisymmetric systems 7

In this chapter I do not elaborate on the solving the orbit-averaged Fokker-Planck in spherical systems directly with and without isotropic velocity distributions. An account on these methods can be found in Freitag (2008) and also Binney and Tremaine (2008a). The Hénon-type Monte-Carlo methods assume spherical symmetry and involve the orbit-averaged Fokker-Planck equation, but they do not solve it directly, see Chapter 6. Instead I focus on systems with axial symmetry, because I am interested in rotating star clusters, which generally deviate from spherical symmetry and have flattened shapes, see Figure 2.14 and Section 2.2.6.

- 7.1 Flux conservation and flux coefficients 153
- 7.2 Background distribution 156
- 7.3 Rotating King models . 157
- 7.3.1 Further work 158

7.1 Flux conservation and flux coefficients

The general assumptions for orbit-averaging from Definition 4.2.8, which are also used in Hénon-type Monte-Carlo simulations in Definition 6.1.1, result in the orbit-averaged Fokker-Planck equation in Definition 4.2.12. The methodology in solving this equation in axisymmetry is based on the PhD thesis by J. J. Goodman (1983), which was further developed in Einsel and Spurzem (1999) and the details of the method can be found most exhaustively in the PhD thesis by Einsel (1997).

In the following, the distribution function depends only on the isolating integrals of motion (see Definition 4.2.9) energy E and the z -component of the angular momentum J_z , because the third integral of motion cannot be written down analytically except in special potentials, see discussion in Section 4.2.2. Therefore, the hypersurface that is constructed in phase space from E and J_z presents us with non-ergodicity.

Definition 7.1.1 (Ergodicity in stellar dynamics) *A stellar system that is ergodic, is a system that uniformly explores its energy surface in phase space. Therefore, the distribution function of stars is uniform on the energy hypersurface, but the motion of the individual stars generally is not (Binney & Tremaine, 2008a).*

Adopting the notation from Einsel and Spurzem (1999), the Fokker-Planck equation in action-angle space, which already has been given in Equation 4.132 can be written here as

$$\frac{\partial f}{\partial t} + \frac{\partial \phi}{\partial t} \frac{\partial f}{\partial E} = \Gamma[f], \quad (7.1)$$

where $\Gamma[f]$ is again the the encounter operator from from Equation 4.113 and where the gravitational potential ϕ is advanced in time according to the Poisson equation

$$\nabla^2 \phi = 4\pi G n \quad (7.2)$$

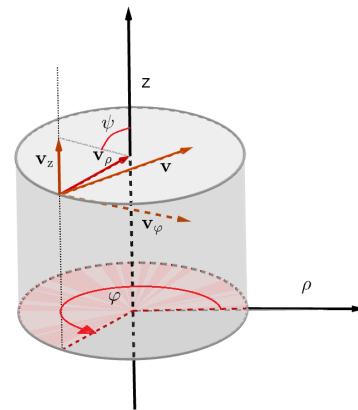


Figure 7.1: Schematic diagram illustrating the coordinate transformation for the space and velocity coordinates used in the computation of the diffusion coefficients in tensor form by Rosenbluth et al. (1957) in this chapter.

with n is the mass density of the system and $\Gamma[f]$ can be written under the Fokker-Planck approximation from [Definition 4.2.7](#) of weak, local encounters dominating the star cluster's evolution and allows for truncating the BBKGY hierarchy from [Definition 4.2.5](#) after the second-order terms Einsel and Spurzem (see Equation 3 in [1999](#)):

$$\Gamma[f] = \frac{1}{V} \left[-\frac{\partial}{\partial E} (\langle \Delta E \rangle f V) - \frac{\partial}{\partial J_z} (\langle \Delta J_z \rangle f V) \right. \quad (7.3)$$

$$\left. + \frac{1}{2} \frac{\partial^2}{\partial E^2} (\langle (\Delta E)^2 \rangle f V) + \frac{\partial^2}{\partial E \partial J_z} (\langle \Delta E \Delta J_z \rangle f V) \right. \quad (7.4)$$

$$\left. + \frac{1}{2} \frac{\partial^2}{\partial J_z^2} (\langle (\Delta J_z)^2 \rangle f V) \right], \quad (7.5)$$

where V is the volume element given by $2\pi/\rho$, with ρ the radius in cylindrical coordinates. As was stated repeatedly in the thesis, in star clusters τ_{rx} is much longer than τ_{dyn} , which allows for orbit averaging. Here, the orbit average is taken over over that area in the meridional plane that intersects with the hypersurface in phase space for which E and J_z are specified under the constraint that the kinetic energy in that plane is positive:

$$\frac{1}{2} (v_\rho^2 + v_z^2) \geq 0. \quad (7.6)$$

The volume of this hypersurface in cylindrical coordinates (ρ, z, φ) with associated velocity vector components (v_ρ, v_z, v_φ) , see [Figure 7.1](#) for the coordinates¹ is then given by

$$p(E, J_z) = 4\pi^2 \int_{A(E, J_z)} d\rho dz,$$

where the intersection from [Equation 7.6](#) is given by $A(E, J_z)$, i.e. a surface in the meridional plane, which is the interface between the hypersurface defined by (E, J_z) in phase-space with this meridional plane, which is the (ρz) -plane, see [Figure 7.1](#) and J. J. Goodman ([1983](#)). In other words, it is set of points on the meridional plane, which are accessible for stars with fixed energy and angular momentum:

$$A(E, J_z) = \left\{ (\rho, z) \mid E - \frac{J_z^2}{2\rho^2} \geq \Phi(\rho, z) \right\}, \quad (7.7)$$

which has no analytic expression. The factor in front of the integral of [Equation 1](#) is due to integration over the third velocity variable, e.g. $\psi = \arctan(v_\rho/v_z)$, which is the directional angle of the velocity in the meridional plane. Symmetry about the azimuthal direction in coordinate space was assumed. Then orbit-averaged² Fokker-Planck equation from [Equation 7.1](#) can be derived:

$$\frac{\partial f}{\partial t} + \frac{1}{p} \frac{\partial q}{\partial t} \frac{\partial f}{\partial E} = \Gamma[f] \quad (7.8)$$

with

$$q(E, J_z) = 2\pi^2 \iint_{A(E, J_z)} (v_\rho^2 + v_z^2) d\rho dz \quad (7.9)$$

1: Einsel and Spurzem ([1999](#)), derive the diffusion coefficients following Rosenbluth et al. ([1957](#)), see also [Equation 4.140](#). The Rosenbluth potentials $h(\mathbf{x}, \mathbf{v})$ and $g(\mathbf{x}, \mathbf{v})$ need to be rewritten in cylindrical coordinates to study rotating, axisymmetric systems in this procedure.

2: Since the trajectories of the stars are not closed it is not possible to take to orbital period of a star for the orbit averaging and the epicyclic frequency should be taken instead. However, because the system here is axisymmetric both the epicyclic frequencies in ρ and the z direction should be taken into account. Furthermore, since the method neglects the third integral of motion and even longer time-scale must be taken, i.e. that stars that are specified with (E, J_z, I_3) scatter with a significant probability onto (E, J_z, I'_3) , so that we have a smooth distribution function over the third integral of motion, which is the relaxation time-scale (Einsel, [1997](#)).

and note that the integrand is equal to

$$2(E - \phi) - \left(\frac{J_z^2}{\rho^2} \right) \quad (7.10)$$

and evaluates to zero on the boundary of A . $q(E, J_z)$ from Equation 7.9 can be seen as an quasi-adiabatic invariant³. This means that if we neglect dynamical encounters,

$$\left. \frac{\partial f}{\partial t} \right|_{q, J_z} = 0, \quad (7.11)$$

which in turn means that there exists a redistribution of energies in the system, however q and the angular momentum in the z -direction J_z are conserved. For the quasi-adiabatic invariance assumption to hold we need to take small enough time-steps. Then, we can then solve Equation 7.8 in two steps:

1. Fokker-Planck step: Computation of the system's evolution (see also Definition 5 and the equations there in flux conservation form of the Fokker-Planck equation) due to weak and local encounters at fixed gravitational potential using a sparse-matrix method to integrate the diffusion from Henyey et al. (1959) from gas / moment models by Spurzem (1994, 1996), a Chang-Cooper scheme to optimise for energy conservation from Chang and Cooper (1970) and a simple-centred difference scheme in the star cluster core by Takahashi (1995).
2. Vlasov step: Advancement of the distribution function f due to slow adiabatic changes⁴ in the gravitational potential with $f(q, J_z) = \text{constant}$. The density $n(\rho, z)$ (zeroth order moment) is then computed from

$$n(\rho, z) = \frac{2\pi}{\rho} \int_{\phi_c}^{E_{\text{tid}}} \int_{-\rho\sqrt{2E-2\phi}}^{\rho\sqrt{2E-2\phi}} f(E, J_z) dE dJ_z, \quad (7.12)$$

where the limits of the integral are E_{tid} , which is the energy at the tidal boundary $\phi(r_t) = E_{\text{tid}}$ and which is adjusted at every new time-step according to the mass of the star cluster, and ϕ_c , which is the central potential. Since we have the density, Poisson equation from Equation 7.2 can be solved now again with a sparse-matrix method from Henyey et al. (1959). The new gravitational potential is then used to calculate the hypersurface from $A(E, J_z)$ from Equation 7.7. We then this result to solve for $q(E, J_z)$ from Equation 7.9. Afterwards a new distribution function f is computed (see Einsel, 1997, for the most details).

The code that does the above is called FOPAX, but it is first mentioned by this name by the successor paper to Einsel and Spurzem (1999), which is Kim et al. (2002).

Definition 7.1.2 (flux conservation form of the Fokker-Planck equation) *The Fokker-Planck equation is transformed into particle flux ($\mathcal{F}_E, \mathcal{F}_{J_z}$) conservation form in order to improve conservation of several*

3: Actions are said to be adiabatically invariant if in the presence slow adiabatic potential variations, there is no lowest-order change in the area enclosed by the orbit (see e.g. Binney & Tremaine, 2008a). In our system, next to J_z the quantity $q(E, J_z)$ is also adiabatic invariant. But since only in the star cluster core, the relaxation time-scale is shorter than the orbital period can assume ergodicity on the hypersurface which is parameterized by (E, J_z) from Definition 7.1.1. In the halo of the cluster this is certainly not the case. This combined with the fact that when the potential changes between time-steps in an axi-symmetric system

4: These are assumed to quasi-stationary changes with contracting star cluster cores and expanding stellar halos. This expansion must be separated into sufficiently small time-steps so that the quasi-invariant $q(E, J_z)$ is conserved, which is reflected in Equation 7.8.

quantities that is more useful from a numerical viewpoint (Einsel, 1997):

$$\frac{df}{dt} = \frac{1}{p} \left(-\frac{\partial \mathcal{F}_E}{\partial E} - \frac{\partial \mathcal{F}_{J_z}}{\partial J_z} \right), \quad (7.13)$$

with the particle flux components that are given

$$\mathcal{F}_E = -\mathcal{D}_{EE} \frac{\partial f}{\partial E} - \mathcal{D}_{EJ_z} \frac{\partial f}{\partial J_z} - \mathcal{D}_E f \quad (7.14)$$

$$\mathcal{F}_{J_z} = -\mathcal{D}_{J_z J_z} \frac{\partial f}{\partial J_z} - \mathcal{D}_{J_z E} \frac{\partial f}{\partial E} - \mathcal{D}_{J_z} f, \quad (7.15)$$

where the factors $\mathcal{D}_{I_i I_i}$ are the so-called flux coefficients that must be calculated. By comparing them with Equation 7.5, they can be written down as

$$\mathcal{D}_{EE} = \frac{1}{2} \langle (\Delta E)^2 \rangle, \quad (7.16)$$

$$\mathcal{D}_{EJ_z} = \frac{1}{2} \langle \Delta E \Delta J_z \rangle, \quad (7.17)$$

$$\mathcal{D}_{J_z J_z} = \frac{1}{2} \langle (\Delta J_z)^2 \rangle, \quad (7.18)$$

$$\mathcal{D}_{J_z E} = \frac{1}{2} \langle \Delta E \Delta J_z \rangle \quad (7.19)$$

$$\mathcal{D}_E = -\langle \Delta E \rangle + \frac{1}{2} \frac{\partial}{\partial E} \langle (\Delta E)^2 \rangle + \frac{1}{2} \frac{\partial}{\partial J_z} \langle \Delta E \Delta J_z \rangle, \quad (7.20)$$

$$\mathcal{D}_{J_z} = -\langle \Delta J_z \rangle + \frac{1}{2} \frac{\partial}{\partial J_z} \langle (\Delta J_z)^2 \rangle + \frac{1}{2} \frac{\partial}{\partial E} \langle \Delta E \Delta J_z \rangle. \quad (7.21)$$

These are then rewritten using the Rosenbluth potentials involving covariant derivatives (Rosenbluth et al., 1957), which are more practical and the exact form can be found in Einsel (1997) and Einsel and Spurzem (1999)⁵.

7.2 Background distribution

The distribution function f appears twice in Equation 7.5 as a linear factor in front of the diffusion coefficients and within the diffusion coefficients themselves. Although f is the same it is conceptually split up into a background and foreground distribution function. The background distribution (for the field stars) appears in an integral over the velocity coordinates, because it is the distribution by which the subject / test stars are scattered. This integration yields a more robust solution compared with slight variations of the functional form of the background distribution. J. J. Goodman (1983) use a rotating, isotropic Maxwellian distribution for the background, which is then adopted by Einsel and Spurzem (1999)

$$f_b(\mathbf{v}) = \frac{n(\mathbf{r})}{[2\pi\sigma^2(\mathbf{r})]^{3/2}} \exp \left[-\frac{(\mathbf{v} - \Omega(\mathbf{r})\rho\mathbf{e}_\varphi)^2}{2\sigma^2(\mathbf{r})} \right]. \quad (7.22)$$

where n (density), Ω (angular velocity) and σ (one-dimensional velocity dispersion of the field star distribution) correspond to the zeroth-, first- and second-order moments of the distribution function

f , and are the density, angular velocity and velocity dispersion, respectively. With this equation Einsel and Spurzem (1999) derive analytic expressions for the diffusion coefficients from Definition 5 that have the (n, Ω, σ) as local parameters, which reduces the computational effort.

7.3 Rotating King models

We need fully self-consistent potential-density pairs, which have a suitable distribution function that depends on energy and angular momentum, by which we can create models with suitable rotation or flattening.

Definition 7.3.1 (Rotating King models) *For this purpose, Einsel and Spurzem (1999) introduce the so-called rotating King models*

$$f_{\text{rk}}(E, J_z) = \begin{cases} \text{const} \times (e^{-\beta E} - 1) \times e^{-\beta \Omega_0 J_z} & \text{if } E < E_{\text{tid}} \\ 0 & \text{if } E > E_{\text{tid}} \end{cases} \quad (7.23)$$

as a foreground distribution for the stars following (Lupton & Gunn, 1987), where $\beta = 1/(m\sigma_c^2)$ and the dimensionless angular velocity is given by $\omega_0 = \sqrt{9/4 \times \pi G n_c} \times \Omega_0$.

The rotating King models from Definition 7.3.1 are constructed iteratively by calculating the density and the potential one after the other. If the rotation of the model is not too large, this procedure typically converges (Einsel, 1997). This method is similar to Lupton and Gunn (1987), Prendergast and Tomer (1970), and Wilson (1975). Potential-density pairs for these models are created by relating β to the King parameter W_0 via $W_0 = \beta m(\psi - \psi_t)$, where ψ and ψ_t are the central King potential and the King potential at the truncation radius r_t as well as the number of stars and shells in the computation. Einsel and Spurzem (1999) then established a family of rotating King models that are parameterised by pairs of (W_0, ω_0) , see Table 7.1 for all models from Einsel and Spurzem (1999) for $(W_0 = 6)$, using numerical and computational methods by Cohn (1979), Henyey et al. (1959), and Spurzem (1994, 1996). Einsel and Spurzem (1999) found that with increasing initial angular velocity parameter ω_0 , the system is driven into strong mass loss and it contracts moderately, see Figure 7.2 b). Additionally, the dynamical ellipticity e_{dyn} of the models is shown in the same figure, which is taken from J. Goodman (1983) and, which is defined by

$$\frac{2T_{\text{rot}} + 3T_{\sigma_\phi} - T_\sigma}{T_\sigma - T_{\sigma_\phi}} = \frac{(1 + 2s^2) \arccos(s) - 3s\sqrt{1-s^2}}{s\sqrt{1-s^2} - s^2 \arccos(s)}, \quad (7.24)$$

where Einsel and Spurzem (1999) define the axis ratio, see also Section 2.1.1 of the oblate (not triaxial) ellipsoids with

$$s = \frac{b}{a} = 1 - e_{\text{dyn}}. \quad (7.25)$$

Table 7.1: Initial conditions of rotating King models from Einsel and Spurzem (1999) with $W_0 = 6$. $T_{\text{rot}}/T_{\text{kin}}$ is the ratio of bulk rotational energy to total kinetic energy in percent, $e_{\text{dyn}}(0)$ is the dynamical ellipticity, $r_{\text{tid}}/r_c(0)$ is the ratio of the tidal radius to core radius, $r_h/r_c(0)$ is the ratio of the half-mass radius to core radius, $\tau_{\text{rc}}(0)$ is the central relaxation time-scale and $\tau_{\text{rh}}(0)$ is the half-mass relaxation time-scale. All of these quantities are shown for $t = 0$ of system time units. Table is taken recreated from Einsel and Spurzem (1999), but crucially the column header for $T_{\text{rot}}/T_{\text{kin}}$ has been corrected by adding the percentage units. Otherwise, this would be very misleading, see also Spurzem and Kamlah (2023) for highlighting this.

| ω_0 | $T_{\text{rot}}/T_{\text{kin}}$ (%) | $e_{\text{dyn}}(0)$ | $r_{\text{tid}}/r_c(0)$ | $r_h/r_c(0)$ | $\tau_{\text{rc}}(0)$ | $\tau_{\text{rh}}(0)$ |
|------------|-------------------------------------|---------------------|-------------------------|--------------|-----------------------|-----------------------|
| 0.00 | 0.00 | -0.001 | 18.72 | 2.70 | 19.24 | 91.88 |
| 0.05 | 0.23 | 0.002 | 18.61 | 2.70 | 19.23 | 91.77 |
| 0.10 | 0.89 | 0.013 | 18.25 | 2.68 | 19.22 | 90.80 |
| 0.20 | 3.38 | 0.051 | 16.83 | 2.66 | 19.20 | 89.71 |
| 0.30 | 7.00 | 0.105 | 14.99 | 2.62 | 19.21 | 87.73 |
| 0.40 | 11.23 | 0.165 | 13.08 | 2.55 | 19.22 | 84.12 |
| 0.50 | 15.61 | 0.224 | 11.46 | 2.48 | 19.27 | 80.49 |
| 0.60 | 19.81 | 0.278 | 9.94 | 2.39 | 19.40 | 76.32 |
| 0.70 | 23.71 | 0.327 | 8.77 | 2.30 | 19.50 | 71.78 |
| 0.80 | 27.18 | 0.368 | 7.69 | 2.20 | 19.71 | 67.37 |
| 0.90 | 30.25 | 0.403 | 6.88 | 2.12 | 19.86 | 63.24 |
| 1.00 | 32.99 | 0.433 | 6.22 | 2.04 | 20.02 | 59.63 |

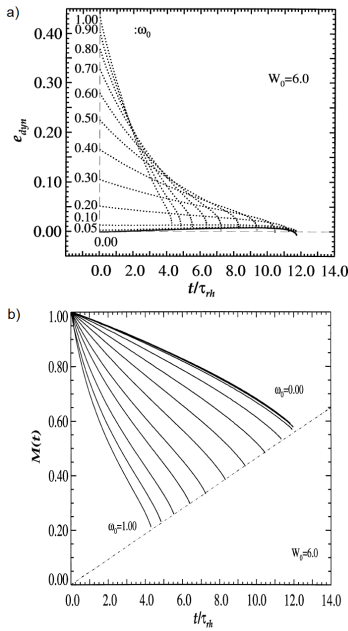


Figure 7.2: Figure showing the time evolution normalised by the half-mass relaxation time-scale t/τ_{rh} of the rotating King models from Equation 7.23 with $W_0=6.0$ and varying ω_0 values from Table 7.1. a) Evolution of dynamical ellipticity e_{dyn} as defined by J. Goodman (1983); b) Evolution of total mass retained. Figures compiled from Einsel and Spurzem (1999).

Furthermore, T_{rot} is the rotational energy, T_{σ_ϕ} is the energy contained in the azimuthal component of the velocity dispersion and T_σ is the energy associated with all components of the velocity dispersion. From Figure 7.2 a) it can be seen the models that rotate very strongly initially experience a strong decrease in dynamical ellipticity e_{dyn} . Moreover, the final state of all models is characterized by a lack of significant flattening. Einsel and Spurzem (1999) state that due to less effective mass loss in the moderately rotating models, i.e. the models with $\omega_0 \approx 0.5$, the less effective mass loss leads to smaller angular momentum loss via evaporation, see Section 2.3.4, beyond the tidal boundary and therefore, the respective curves cross each other at around $t/\tau_{rh} \sim 4$. But as J. J. Goodman (1983) already pointed out, the decrease in ellipticity is additionally a result of the expansion of the mass shells that retain their angular momentum, thereby decreasing their angular velocity in the process inversely to the actual radius of the shell.

Furthermore, the models exhibit the features for the gravogyro catastrophe, see Definition 2.3.2, found originally by Hachisu (1979): an increasingly faster rotating core, although angular momentum is transported outwards from the star cluster.

7.3.1 Further work

The work by Einsel and Spurzem (1999) was then improved through the inclusion of three-body binary heating by implementing statistical binary energy generation (Kim et al., 2002). They performed simulations of equal-mass systems without stellar evolution or tides, but nevertheless they confirmed that the collapse time could be significantly reduced due to rotation. (Kim et al., 2004) then im-

proved the research further by including a two-component mass spectrum. Ultimately, they were able to show that generally the angular momentum is transported from the high mass to the low mass group as long as dynamical friction (Chandrasekhar, 1943a, 1943b, 1943c; Dosopoulou & Antonini, 2017; Lingam, 2018) wins over the gravogyro catastrophe. In general, however, the underlying assumptions in the 2-D FP models by Einsel and Spurzem (1999) (neglect of third integral of motion, axisymmetry, see also Spurzem et al. (2005) for a discussion of tidal fields) require comparisons with direct N -body simulations. For this purpose, Kim et al. (2008) then investigated single mass component models and showed that the FP results are generally consistent with the N -body calculations. Their results also confirmed earlier N -body simulations by Ernst et al. (2007). The comparative studies between FP and direct N -body models were later expanded upon by Hong et al. (2013), who showed that the cluster evolution is accelerated by not only the initial rotation but also the mass spectrum of the cluster. They also demonstrated that the total angular momentum and the total mass of the cluster both decrease rapidly, while a bar-like structure forms and persists in the cluster centre. The formation of a bar and its subsequent fairly rapid dissolution was already found earlier in the pioneer simulations by Akiyama and Sugimoto (1989). Furthermore, it was confirmed that there is no conflict with observed limits of Galactic globular cluster rotation by expanding upon earlier comparisons between the FP models and observations from Fiestas and Spurzem (2010) and Fiestas et al. (2006).

Combining stellar evolution with collisional N -body codes

8

There are two main methods that stand out in practice concerning the integration of the complicated stellar evolution into N -body codes. Both of these, interpolation between tables or approximation of stellar evolution data by some interpolation (fitting) formulae as functions of mass, age and metallicity, has unique advantages and disadvantages that have been known for a long time (P. P. Eggleton, 1996). As it stands now, the two approaches are not in competition, but rather complement one another (Hurley et al., 2000).

| | |
|--|-----|
| 8.1 Interpolation between tables | 161 |
| 8.2 Interpolation/Fitting formulae | 162 |

8.1 Interpolation between tables

This method calculates stellar parameters from detailed evolutionary tracks (Pols et al., 1998). These evolutionary tracks are derived from 1D stellar evolution codes and are in tabular format. They are necessarily rather large and therefore, this approach has historically been limited by memory availability on hardware (Agrawal et al., 2020; P. P. Eggleton, 1996; Hurley et al., 2000). Unlike fitting formulae, stellar parameters from the given set of detailed tracks are calculated in real time with this method. Hence, one just needs to change the input stellar tracks to generate a new set of stellar parameters. It has been claimed that this approach is the most flexible, robust and efficient today when combining detailed stellar evolution with stellar dynamics (Agrawal et al., 2020).

Alongi et al. (1993), Bressan et al. (1993), Claret (1995), Claret and Gimenez (1995), Fagotto et al. (1994a, 1994b), Maeder and Meynet (1989), and Schaller et al. (1992) constructed such tables, which were later then expanded upon and refined by Pols et al. (1998). In the aforementioned works, the convective mixing or overshooting length l_{OV} presents another hurdle, which describes the average distance by which convective cells push into stable regions (or radiative regions from Schwarzschild condition (Biermann, 1932; Gabriel et al., 2014)) beyond the convective boundary (Joyce & Chaboyer, 2018; Pols et al., 1998; Schaller et al., 1992). This treatment was modified by Pols et al. (1998) and replaced with a “ ∇ prescription”, which is based on the stability criterion itself ($\delta_{OV} = 0.12$ was found to best reproduce observations (Hurley et al., 2000; Pols et al., 1997, 1998; Schroder et al., 1997)). This new criterion avoids physical discontinuities for disappearing classical convective cores. Further quantities that will influence the calibration of the luminosity L of a stellar evolution model are the nuclear reaction rates and the core Helium abundance Y . Another source of large uncertainty was left largely unchanged by Pols et al. (1998). This uncertainty has been described by Pols et al. (1998) as the “Achilles heel” in stellar evolution codes. This uncertainty is in the mixing length of α_{MLT} , which is derived from mixing-length theory Böhm-Vitense (1958) to describe heat transport in the convective regions of stars (Joyce & Chaboyer, 2018; Pasetto

et al., 2018) and has been introduced thoroughly in [Section 3.1](#). Pols et al. (1998) set $\alpha_{\text{MLT}}=2.0$ (based on the Solar model). But not all stars with convective regions exhibit identical convective properties and α_{MLT} can show large variations from star to star (Joyce & Chaboyer, 2018).

Even today methods stellar evolution by interpolation between tables are being developed with increasing success as hardware memory capabilities also improve:

- ▶ SEVN (Spera & Mapelli, 2017; Spera et al., 2015, 2019), which has been completed for binary evolution (Sicilia et al., 2021) has been used extensively to study the evolution gravitational wave source progenitor stars. Additionally, it is not available as SEVN2.0, which is integrated in PETAR (Wang, Iwasawa, et al., 2020).
- ▶ and COMBINE (Kruckow et al., 2018) codes, which also has binary evolution implemented (Kruckow, 2020; Kruckow et al., 2021) has also been used extensively to study the evolution gravitational wave source progenitor stars.
- ▶ METISSE code (Agrawal et al., 2020), which is based on the STARS (P. P. Eggleton et al., 1973; P. P. Eggleton, 1971, 1972, 1973; Pols et al., 1995, 1997; Schroder et al., 1997), MESA (Paxton et al., 2011, 2013, 2015, 2016, 2018, 2019) and BEC (Brott et al., 2011; Köhler et al., 2015; Szécsi et al., 2015, 2020; Yoon et al., 2006, 2012). Unlike SEVN or COMBINE, this code does not yet account for binary stars. In general, METISSE will be another promising candidate for combining full stellar dynamics with detailed stellar evolution.

8.2 Interpolation/Fitting formulae

A first attempt to incorporate simple stellar evolution fitting formulae in a direct N -body code was done by S. J. Aarseth (1996) on the basis of P. P. Eggleton et al. (1989). Later, as a successor to P. P. Eggleton et al. (1989) was created using the method developed by Pols et al. (1998). They based their code on the original Cambridge STARS stellar evolution program by P. P. Eggleton et al. (1973), P. P. Eggleton (1971, 1972, 1973), Pols et al. (1995, 1997), and Schroder et al. (1997). The result are the famous SINGLE STELLAR EVOLUTION (SSE) fitting formulae, which for the first time included metallicity as a free parameter (Hurley, 2008b; Hurley et al., 2000, 2013). [Figure 8.1](#) shows the complex discretization of stellar phases and the possible evolutionary pathways between them in the SSE package, see also [Section 3.2.8](#) for the definition of the stellar phases. The figure has been included, because this fundamental structure still remains in many stellar evolution production codes today (see below).

In general, such fitting formulae take much more care and thus time to set up than method of interpolating between tables (Church et al., 2009), because the movement of a star in the HRD is highly non-uniform and erratic. Furthermore, they are also less adaptable to changes in stellar tracks, for example, when they need to be adjusted due to some new discovery in astrophysics. On the other hand, the

SSE provides us with rapid, robust and analytic formulae, which can be easily modified and integrated into an N -body code along the lines of S. J. Aarseth (1996) and give stellar luminosity, radius and core mass of the stars as functions of mass, metallicity and age for all stellar evolutionary phases (Hurley et al., 2000; Railton et al., 2014).

However, these formulae necessarily also discard a lot of crucial stellar evolution information (Hurley, 2008b). For example, stellar mixing (collisions) depends on several timescales and internal stellar structure parameters (Olejak et al., 2020) and so they cannot be modelled directly by the fitting formulae and only the outcomes can be parameterised for stellar types of the individual stars along the lines of Hurley et al. (2002).

Despite these fundamental complications in stellar evolution modelling that persist to this day (see e.g. Agrawal et al., 2021; Joyce & Chaboyer, 2018; Pasetto et al., 2018; Tang & Joyce, 2021) and which translate directly into the continuous and differentiable fitting formulae (polynomial form from least square fitting (Hurley et al., 2000)), the SSE code has successfully, for the first time, provided us with a method by which we can evolve stars from zero-age main sequence (ZAMS) masses (0.1-100) M_{\odot} (the models from Pols et al. (1998) only reach 50 M_{\odot} , but the SSE formulae can be safely extrapolated to 100 M_{\odot} (Hurley, 2008b)) rapidly and accurately (within 5% of detailed stellar evolution models over all phases of the evolution (Hurley et al., 2000)) in N -body simulations throughout all evolutionary phases taking into account all of the astrophysical processes outlined in Section 3.1 and offering a metallicity range from 0.0001 to 0.03 with $Z_{\odot} \approx 0.02$ being Solar metallicity as an input parameter.

However, for a complete picture we also need to model the binary evolution processes outlined in Section 3.2. For the fitting formulae this is provided by the BINARY STELLAR EVOLUTION (BSE) code (Hurley, 2008a; Hurley et al., 2002, 2013), which is an add-on of the SSE package. This has been a huge success story and many full dynamical cluster simulations have utilised SSE & BSE to evolve the stars, e.g. Askar et al. (2017), Di Carlo, Mapelli, Bouffanais, et al. (2020), Di Carlo, Mapelli, Giacobbo, et al. (2020), Di Carlo et al. (2019, 2021), Kamlah, Leveque, et al. (2022), Rizzuto, Naab, Spurzem, Arca-Sedda, Giersz, et al. (2021), Rizzuto, Naab, Spurzem, Giersz, et al. (2021), and Wang et al. (2016). The SSE & BSE codes have been the foundation for many other binary population synthesis (BPS) codes:

- ▶ COMPAS (Team COMPAS et al., 2021)
- ▶ MSE (Hamers & Safarzadeh, 2020)
- ▶ MOBSE (Giacobbo & Mapelli, 2018, 2019; Mapelli, Spera, et al., 2020) and related code called ASPS also used in my co-author paper in Z.-M. Li et al. (2023),
- ▶ STARTRACK (Belczynski et al., 2020; Belczynski et al., 2002, 2008)
- ▶ COSMIC (Breivik, Coughlin, et al., 2020) and its implementations in CMC (Kremer et al., 2019; Rodriguez et al., 2022)
- ▶ BSE-LEVELC (Kamlah, Leveque, et al., 2022) and its implementation in McCLUSTER from Section 2.2.5 (Kamlah, Leveque, et al.,

2022; Küpper et al., 2011a).

The fitting formulae from the SSE code are also implemented in BPS code `BINARY_C` (Izzard et al., 2006, 2009; Izzard et al., 2004).

New fitting formulae have recently been constructed, which are derived from fitting to 1D HOSHI stellar evolution models (Takahashi et al., 2016, 2018, 2019; Yoshida et al., 2019) to extremely massive low metallicity (EMP; Pop-III) stars (Hijikawa et al., 2021; Tanikawa, Kinugawa, et al., 2021; Tanikawa, Susa, et al., 2021; Tanikawa et al., 2020). These are constructed such that they can be implemented into any of the BSE variants mentioned above in a straightforward fashion and therefore also into stellar dynamics codes such as `NBODY6++GPU` (Wang et al., 2015).

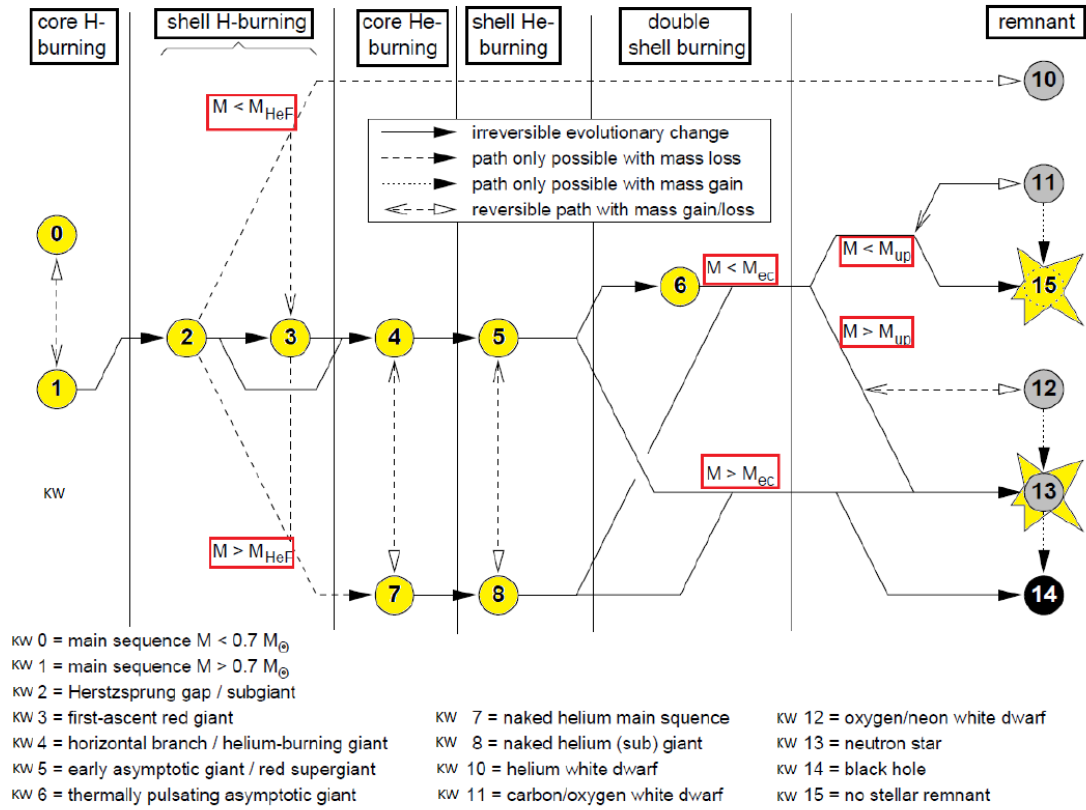


Figure 8.1: Diagram showing the complete stellar evolution for the SSE code. It shows the possible paths of evolution through the various single stellar evolution phases. The paths between the individual stellar types are marked as general *irreversible* paths and *irreversible* paths only possible with *mass loss* or *mass gain*. Furthermore, there are also *reversible* paths with *mass gain* or *mass loss*. The meaning of the masses is as follows: m_{HeF} is the mass of the star to constitute the development of a degenerate He core on the GB and ignite He in a degenerate He flash at the top of the GB. m_{ec} and m_{up} deal with the remnant masses and pathways of Supernovae (SNe), when the AGB evolution is terminated, which is after the CO-core mass reaches a limiting value and undergoes SNe. $m_{\text{up}} = 1.6 M_{\odot}$ and $m_{\text{ec}} = 2.25 M_{\odot}$ depend on metallicity of the star and refers to the mass-range, where C burning leads to the formation of a degenerate ONe-core. This might collapse due to electron-capture (EC) of ^{24}Mg and result in NS production, see Section 3.1.6. However, in almost all stars, mass loss in the TPAGB phase leads to a shedding of the envelope, so that the final remnant is a WD. If this mass is extreme, then we might get a mass-less remnant. If the mass of the core $M_{\text{c,BAGB}} < 1.6 M_{\odot}$, then the result is a COWD. With $M_{\text{c,BAGB}} \geq 1.6$, then we will get a ONeWD. If $M_{\text{c,BAGB}} > 2.25 M_{\odot}$, then the star is massive enough to form Fe core, which result in SNe, which end up either in a NS or a BH. If mass loss comes into the equation, then we might get NS production from stars within $m_{\text{up}} < M_{\text{c,BAGB}} < m_{\text{ec}}$. (Figure adapted from Hurley et al. (2000) and it is also shown in a similar fashion in Spurzem and Kamlah (2023)).

**STELLAR EVOLUTION IMPLEMENTATIONS IN
NBODY6++GPU, MOCCA AND McLUSTER**

Preparing the next gravitational million-body simulations **9**

This chapter is based on my publication Kamlah, Leveque, et al. (2022). It is not the full publication on its own as all of the underlying processes have already been explained to much greater detail in previous chapters and sections. However, I have kept most of the material to allow for a smooth and self-consistent presentation, i.e. the chapter can be understood without any of the chapters, of my results with appropriate references to previous chapters and references where necessary.

9.1 Abstract

We present the implementation of updated stellar evolution recipes in the codes `NBODY6++GPU`, `MOCCA` and `MCLUSTER`. We test them through numerical simulations of star clusters containing 1.1×10^5 stars (with 2.0×10^4 in primordial hard binaries) performing high-resolution direct N -body (`NBODY6++GPU`) and Monte-Carlo (`MOCCA`) simulations to an age of 10 Gyr. We compare models implementing either delayed or core-collapse supernovae mechanisms, a different mass ratio distribution for binaries, and white dwarf natal kicks enabled/disabled. Compared to `NBODY6++GPU`, the `MOCCA` models appear to be denser, with a larger scatter in the remnant masses, and a lower binary fraction on average. The `MOCCA` models produce more black holes (BHs) and helium white dwarfs (WDs), whilst `NBODY6++GPU` models are characterised by a much larger amount of WD-WD binaries. The remnant kick velocity and escape speed distributions are similar for the BHs and neutron stars (NSs), and some NSs formed via electron-capture supernovae, accretion-induced collapse or merger-induced collapse escape the cluster in all simulations. The escape speed distributions for the WDs, on the other hand, are very dissimilar. We categorise the stellar evolution recipes available in `NBODY6++GPU`, `MOCCA` and `MCLUSTER` into four levels: the one implemented in previous `NBODY6++GPU` and `MOCCA` versions (level A), state-of-the-art prescriptions (level B), some in a testing phase (level C), and those that will be added in future versions of our codes.

9.2 Introduction

The stellar environment in star clusters provides the ideal laboratory for investigating stellar binary evolution as well as GW physics. As outlined in [Chapter 2](#) and sections therein. This is because the densities are typically so high that stars can interact in close gravitational encounters or even physically collide with each other, see [Section 4.1.2](#) and [Section 4.1.4](#). These interactions support the presence of more tightly bound binary stars, which can act as a source

| | | |
|-------|---|-----|
| 9.1 | Abstract | 169 |
| 9.2 | Introduction | 169 |
| 9.3 | Methods | 172 |
| 9.3.1 | Simulations with <code>NBODY6++GPU</code> and <code>MOCCA</code> | 172 |
| 9.3.2 | Summary: stellar evolution updates (SSE AND BSE) in <code>NBODY6++GPU</code> and <code>MOCCA</code> | 172 |
| 9.4 | Initial models - <code>delayedSNe-Uniform</code> & <code>rapidSNe-Sana</code> | 174 |
| 9.5 | Results | 176 |
| 9.5.1 | Global dynamical evolution | 176 |
| 9.5.2 | Stellar evolution | 178 |
| 9.6 | Summary, conclusion and perspective | 190 |
| 9.6.1 | Summary: direct N -body (<code>NBODY6++GPU</code>) and Monte Carlo (<code>MOCCA</code>) simulations | 190 |
| 9.6.2 | Perspective on future stellar evolution (SSE & BSE) updates | 193 |
| 9.7 | Stellar and binary evolution levels A, B, C | 199 |
| 9.7.1 | Dynamical mass transfer and other processes in binary stars | 200 |
| 9.7.2 | Stellar winds | 202 |
| 9.7.3 | Remnant masses of compact objects | 203 |
| 9.7.4 | Compact object natal kick distributions | 206 |
| 9.7.5 | Compact objects natal spins | 208 |
| 9.8 | <code>McLuster</code> | 211 |
| 9.8.1 | Remnant-masses of compact objects | 212 |

of huge amounts of gravitational energy to the cluster, see [Section 2.3](#). This will result in enhanced mass-segregation: more massive stars and binaries sink to the centre of the system, where they undergo close gravitational encounters and in the case of high densities, stellar collisions, which has been predicted and tested theoretically (Arca Sedda et al., [2019](#); Askar et al., [2017](#); Giersz et al., [2015](#); D. C. Heggie, [1975](#); Khalisi et al., [2007](#); Portegies Zwart & McMillan, [2002](#); Rizzuto, Naab, Spurzem, Arca-Sedda, Giersz, et al., [2021](#); Rizzuto, Naab, Spurzem, Giersz, et al., [2021](#); Wang et al., [2016](#)) and verified observationally (Cantat-Gaudin et al., [2014](#); Giesers et al., [2018, 2019](#); Kamann, Bastian, et al., [2018](#); Lada & Lada, [2003](#); Martinazzi et al., [2014](#)). As already explained exhaustively in [Part 11](#), simulations of such star clusters fundamentally aim to solve the equations of motion describing N bodies moving under the influence of their own self-gravity. For this purpose a variety of computational approaches have been developed beginning in the first half of the last century. The two main methods in the regime of around $10^5 - 10^7$ particles that stand out today are either related to direct N -body simulation from [Chapter 5](#) or Monte-Carlo modelling from [Chapter 6](#) (S. J. Aarseth & Lecar, [1975](#); S. J. Aarseth et al., [1974](#); Giersz & Heggie, [1994a](#); Spurzem, [1999](#)). Direct N -body simulation, which is the orbit integration of the orbits of many particles in a self-gravitating bound star cluster, is the most suitable method to understand relaxation (Larson, [1970a, 1970b](#)) and evolutionary processes in the regime of star clusters, see [Section 6.6](#). Here, statistical physics still plays a role and more approximate models may be used. These models are based on the Fokker-Planck equation from [Equation 7.5](#), which can be solved either directly, see [Chapter 1.2](#) for solutions in axisymmetric systems, or by a Monte Carlo Markov-chain method (Askar et al., [2017](#); Cohn, [1979](#); Giersz, [1998](#); Giersz et al., [2015](#); M. Hénon, [1975](#); Kremer, Ye, et al., [2020](#); Kremer et al., [2021](#); Merritt, [2015](#); Stodółkiewicz, [1982, 1986](#)).

Beyond solving the equations of motion for the N bodies, the complete description of a *realistic* star cluster becomes much more complicated, because the stellar evolution of single and binary stars has an enormous impact on the dynamical evolution of star clusters as outlined in [Chapter 3](#). Single and binary stars may suffer significant mass loss over the lifetime of the cluster depending on their initial ZAMS mass and their metallicity, see [Section 3.1.4](#). This mass loss changes the potential of the star cluster and subsequently has an effect on the orbits of the stars. In our models of single stars, this mass loss is dominated by stellar winds and outflows (Hurley et al., [2000](#); Tout, [2008b](#)). In the models of binary stars, the member stars can interact with each other closely and other astrophysical processes involving dynamical mass transfer, tidal circularisation and stellar spin synchronisation happen (Hurley et al., [2002](#); R. A. Mardling & Aarseth, [2001](#); Tout, [2008a](#)), see also [Section 3.2](#) and subsections therein. In the case of compact objects repeated encounters between stars and binaries may lead to sudden orbit shrinking of a binary up to a point when finally a huge proportion of further orbit shrinking is due to the emission of gravitational radiation (Antonini & Gieles, [2020](#); Arca Sedda, Berry, et al., [2020](#); Brem et al., [2013](#); Faye et al., [2006](#); Mapelli, Santoliquido, et al., [2020](#)), see [Section 3.2.7](#). The

gravitational waves that accompany these subsequent gravitational inspiral events might be detectable with the (Advanced) Laser Interferometer Gravitational-Wave Observatory (aLIGO) (Aasi et al., 2015; B. P. Abbott, Abbott, Abbott, Acernese, Ackley, & Adams, 2018; B. P. Abbott et al., 2019), (Advanced) Virgo Interferometer (aVirgo) (B. P. Abbott, Abbott, Abbott, Acernese, Ackley, & Adams, 2018; B. P. Abbott et al., 2019; Acernese et al., 2015) if they emit signals coming from merging NSs (B. P. Abbott et al., 2017a, 2017b), stellar mass BHs (B. P. Abbott et al., 2016) or the process of core collapse in SNe (Ott, 2009). If, for example, the binary consists of two BHs then this gravitational wave inspiral may lead to the formation of IMBHs as has been confirmed in simulations (Arca Sedda et al., 2019; Banerjee, 2021a, 2021b; Di Carlo, Mapelli, Bouffanais, et al., 2020; Di Carlo, Mapelli, Giacobbo, et al., 2020; Di Carlo et al., 2019, 2021; Giersz et al., 2014, 2015; Rizzuto, Naab, Spurzem, Giersz, et al., 2021). A recent aLIGO and aVirgo detection of such an IMBH with a total mass of around $142 M_{\odot}$ (R. Abbott et al., 2020b) invites further simulations focusing on this particular aspect.

A subclass of star clusters that we aim to simulate across cosmic time are GCs, which I have already introduced in Section 2.1.2 in much more detail. Key features are repeated here. Our MW hosts over 150 of these (Baumgardt & Hilker, 2018; Harris, 1996). Their old age and relatively large numbers not only in our galaxy, but also in much more massive elliptical galaxies such as M87 (Doyle et al., 2019; Tamura et al., 2006a, 2006b), and at higher redshifts (T. Zick et al., 2020; T. O. Zick, Kriek, et al., 2018; T. O. Zick, Weisz, & Boylan-Kolchin, 2018) all suggest that they play an important role as a fundamental building block in a hierarchy of cosmic structure formation (Reina-Campos et al., 2019, 2020, 2021). Although becoming increasingly sophisticated, observational studies using astrophysical instruments such as MUSE (Giesers et al., 2018, 2019; Husser et al., 2016; Kamann, Bastian, et al., 2018, 2020; Kamann, Giesers, et al., 2020; Kamann, Husser, et al., 2018) and Gaia (Bianchini et al., 2013a, 2018, 2019; de Boer et al., 2019; K.-W. Huang & Koposov, 2021; Kuhn et al., 2019) are not sufficient on their own to resolve the complete evolution of GCs across cosmic time, because they effectively only take snapshots of these clusters today. These observations must therefore be supplemented with astrophysical simulations (Krumholz et al., 2019). Due to their typical sizes, simulations of GCs over billions of years are at the edge of high-resolution direct N -body simulations today, which are computationally possible and feasible. The DRAGON-I simulations were the first, direct gravitational million-body simulations of such a GC (Wang et al., 2016). This year, the DRAGON-II will be published, where I am co-author, see also Figure 2.5. It is clear from this plot that the DRAGON-II simulations present direct N -body simulations that are unparalleled in their computational effort even compared with the DRAGON-I simulations, even though the maximum particle number has not been significantly surpassed. This is due to the fact that the half-mass density of the DRAGON-II simulations is two orders of magnitude larger than that of the DRAGON-I simulations, which increases the required computing effort significantly. Similarly, the last direct million-body simulation of a NSC, which have similar particle number as the DRAGON-I, DRAGON-II simulations, but scaled

in a way to resemble a NSC, harbouring a central and accreting SMBH were performed by Panamarev et al. (2019). While Wang et al. (2015) made the technical programming advances necessary to perform million-body simulations with `NBODY6++GPU` in the first place by parallelising the integrations across multiple GPUs accelerating the (*regular*) direct force integrations and the energy checks to an unprecedented degree and while Panamarev et al. (2019) expanded the code to include a central and accreting SMBH, the stellar evolution prescriptions in both of these codes were largely unchanged.

To this end, we updated the stellar evolution routines in the direct-force integration code `NBODY6++GPU` (Wang et al., 2015), which are the SSE (Hurley et al., 2000) and BSE (Hurley et al., 2002) stellar evolution implementations, see Section 8.2. These updates mirror the updates in `NBODY7` by Banerjee et al. (2020) and Banerjee (2021a). The results are then compared with the Hénon-type Monte-Carlo code `MOCCA` (Giersz et al., 2013; Hypki & Giersz, 2013), which also conveniently models the evolution of single and binary stars with the SSE and BSE routines. This study is therefore also a continuation of the productive collaboration between the teams surrounding these modelling methods (Downing et al., 2010, 2011; Giersz et al., 2008, 2013; Rizzuto, Naab, Spurzem, Giersz, et al., 2021; Wang et al., 2016). Finally, in the appendix, we present an updated version of `McLUSTER` (Küpper et al., 2011a), which now includes a mirror of the stellar evolution available in `NBODY6++GPU`.

9.3 Methods

Concerning the methods I chose to briefly reiterate some of the key features of the codes that I use. The simple reason is that the related chapters are necessarily rather long and a quick guide here should help summarise the features and should assist particularly those readers that do not use these codes on regular basis. I acknowledge that for readers that know the codes well this might be repetitive, but they should simply skip the related sections.

9.3.1 Simulations with `NBODY6++GPU` and `MOCCA`

The star cluster models are evolved using the state-of-the-art direct force integration code `NBODY6++GPU`, which is optimised for high performance GPU-accelerated supercomputing (Nitadori & Aarseth, 2012; Spurzem, 1999; Wang et al., 2015) and also the Hénon-type Markov-Chain Monte-Carlo code `MOCCA` (Giersz et al., 2013; Hypki & Giersz, 2013). `NBODY6++GPU` is introduced extensively in Chapter 5 and a summary is given in Section 5.7, while `MOCCA` and the methods therein are introduced in Chapter 6 with a summary presented in Section 6.7. In the interest of brevity, the details will not be repeated here.

9.3.2 Summary: stellar evolution updates (SSE AND BSE) in NBODY6++GPU and MOCCA

In this paper we present updates in the SSE AND BSE routines in the two codes NBODY6++GPU & MOCCA. The details of these updates are shown in [Figure 9.15](#) and [Figure 9.16](#), respectively. These updates make MOCCA&NBODY6++GPU largely competitive in their stellar evolution with other codes that are used to simulate star clusters, such as the Monte-Carlo code CMC (Kremer, Chatterjee, et al., 2018; Kremer, Ye, et al., 2020; Kremer et al., 2019) with the COSMIC implementation (Breivik, Coughlin, et al., 2020) or the new, massively parallel direct N -body code PETAR (Wang, Nitadori, & Makino, 2020b). Furthermore, we are now in a position to model the full evolution of aLIGO/aVirgo gravitational wave sources and their progenitor stars up until the eventual merger according to our best current theoretical understanding. We also implemented the SSE AND BSE version that is shown in [Figure 9.15](#) into our version of MCLUSTER and we are now able to produce initial star cluster models that have proper evolution of multiple stellar populations (this will be elaborated in a further publication). The details are shown in Appendix B, where also two use-cases are demonstrated to confirm excellent agreement with the SSE AND BSE updates in NBODY7 and the results in Banerjee et al. (2020) and Banerjee (2021a). The SSE AND BSE implementation within our versions of NBODY6++GPU, MOCCA&MCLUSTER all contain, see [Chapter 3](#) for the related astrophysical processes and models:

- ▶ updated metallicity dependent stellar winds (Belczynski et al., 2010; Vink & de Koter, 2002, 2005; Vink et al., 2001),
- ▶ updated metallicity dependent core-collapse SNe, their remnant masses and fallback (Banerjee et al., 2020; C. L. Fryer et al., 2012),
- ▶ updated electron-capture supernovae (ECSNe), accretion-induced collapse (AIC) and merger-induced collapse (MIC) remnant masses and natal kicks (Gessner & Janka, 2018; Kiel et al., 2008; Nomoto, 1984; Nomoto, 1987; Nomoto & Kondo, 1991; Saio & Nomoto, 1985; Saio & Nomoto, 2004)
- ▶ (P)PISNe remnant masses (Belczynski et al., 2016; Belczynski et al., 2010; Woosley, 2017),
- ▶ updated fallback-scaled natal kicks for NSs and BHs (Banerjee et al., 2020; C. L. Fryer, 2004; C. L. Fryer et al., 2012; C. L. Fryer & Kusenko, 2006; C. L. Fryer & Young, 2007; G. M. Fuller et al., 2003; Meakin & Arnett, 2006, 2007; Scheck et al., 2004, 2008),
- ▶ and BH natal spins (see also Belczynski and Banerjee (2020) and Belczynski et al. (2020)) from
 - Geneva model (Banerjee, 2021a; Belczynski et al., 2020; Eggenberger et al., 2008; Ekström et al., 2012),
 - MESA model (Banerjee, 2021a; Belczynski et al., 2020; Paxton et al., 2011, 2015; Spruit, 2002),
 - and the Fuller model (Banerjee, 2021a; J. Fuller & Ma, 2019; J. Fuller et al., 2019).

The SSE AND BSE implementation within MOCCA contains, on top of the above:

- ▶ winds by Giacobbo et al. (2018),
- ▶ winds depending on surface gravity and effective temperature of a star by Schröder and Cuntz (2005),
- ▶ (P)PISNe from SEVN simulations by Spera and Mapelli (2017),
- ▶ an earlier treatment by Tanikawa et al. (2020) to model the evolution of extremely metal-poor and high mass POP III stars,
- ▶ and proper CV treatment and related dynamical mass transfer, magnetic braking and gravitational radiation criteria by Belloni, Schreiber, et al. (2018).

The SSE AND BSE algorithms of N_{BODY6++GPU} and McCLUSTER contain, on top of the list of the commonalities between the three codes:

- ▶ moderate and weak (P)PISNe by Leung et al. (2019),
- ▶ and WD kicks from Fellhauer et al. (2003).

9.4 Initial models - delayedSNe-Uniform & rapidSNe-Sana

We choose two initial models, which we generate with McCLUSTER (Küpper et al., 2011a), that satisfy the following conditions. Firstly, we do not want these models to be too dense, as we prefer that the dynamics does not overly interfere with the stellar evolution in the star cluster pre-core collapse evolution and secondly, we want the models to have a large tidal radius in order to curtail initial mass loss from the cluster models. With this, we arrive at the structural parameters listed in Table 9.1. We have a total number of 1.1×10^5 particles (i.e. stars), of which 2.0×10^4 are initially in primordial hard binaries. The number of binaries is thus 1.0×10^4 and the binary fraction is $f_b = 10\%$. The initial half-mass radius $r_{h,0}$ is set to 1.85 pc. The smaller particle number then introduces the problem of enhanced mass loss from the cluster. We therefore put the cluster on a circular orbit with a galacto-centric distance of 259.84 kpc in a MW-like point mass potential of $2.92 \times 10^{12} M_\odot$. This gives an initial tidal radius $r_{tid,0}$ of 500 pc in order to curtail this initial mass loss. The density model is a King model with a concentration parameter with $W_0 = 3.0$ (I. King, 1962) and since it is extremely tidally underfilling, it is very close to the corresponding isolated model.

Table 9.1: Initial models for the (MOCCA and N_{BODY6++GPU}) simulations.

| Parameter | N _{BODY6++GPU} & MOCCA |
|------------------------------|------------------------------------|
| Particle number | 110000 |
| Binary fraction f_b | 10.0% |
| Half mass radius r_h | 1.85 pc |
| Tidal radius r_{tid} | 500 pc |
| IMF | Kroupa IMF, (0.08 – 100) M_\odot |
| Metallicity Z | 0.00051 |
| Density model | King model, $w_0 = 3.0$ |
| Eccentricity distribution | Thermal |
| Semi-major axis distribution | flat in log |

The metallicity of the cluster is set to a low, but realistic (metallicity of the GC NGC3201 (Harris, 1996)) value of $Z = 0.00051$, meaning that 0.051 per cent of the mass in the cluster stars is not hydrogen or helium. The IMF is set in a range from $(0.08-100.0) M_{\odot}$, following Kroupa (2001). The binaries are initially thermally distributed in their eccentricities as is the current standard in N -body simulations (Kroupa, 2008). This, in general, may overpredict the merger rates significantly (Geller et al., 2019).

The binary semi-major axes follow flat distributions in the logarithm of the semi-major axis. The minimum and maximum of the semi-major axes distributions of the primordial binary population are set to the radius of the lowest mass star in the star cluster and 100 AU, respectively. This distribution of binary semi-major axes for hard binaries is reproduced from an initial distribution that includes many more, wider binaries initially in Kroupa (1995b).

The difference between the two distinct initial models that we use in this work arises from the choice of binary mass-ratio distribution and SN mechanism. For one model we use the uniform binary mass-ratio distribution q_{Uniform} and the delayed SNe mechanism and for the other we use the Sana binary mass-ratio distribution q_{Sana} (Kiminki et al., 2012; Kobulnicky et al., 2014; Sana et al., 2013; Sana & Evans, 2011) along with activating the rapid SNe treatment (C. L. Fryer et al., 2012) (both Level B: the parameters chosen are highlighted in orange in Figure 9.14, Figure 9.15 and Figure 9.16). To clarify, in the q_{Sana} mass ratio distribution, all the stars that have a mass above $5.0 M_{\odot}$ get paired with a secondary, such that the mass ratios are uniformly distributed in the range of $0.1 \leq q \leq 1.0$. The rest of the stars are paired randomly in their mass ratios. In this way, q_{Sana} and q_{Uniform} are actually quite similar in theory and we will find out if this is case through the simulations over time. An important point is that through the pairing algorithm for q_{Sana} in MCLUSTER (with `pairing=3`), we first select all stars and after that we pair them, so we strictly speaking do respect the IMF (Oh et al., 2015). These two separate models will be referred to as `delayedSNe-Uniform` and `rapidSNe-Sana` henceforth. In all other respects the stellar evolution settings of the two simulations are identical (Level B). The stellar evolution levels and their definitions may be understood from Figure 9.14, Figure 9.15 (NBODY6++GPU settings) and Figure 9.16 (MOCCA settings).

We do not enable any (P)PISNe schemes (parameters `psflag`, `piflag`) for the NBODY6++GPU and MOCCA simulations due to the maximum of the IMF at $100 M_{\odot}$ and the low initial cluster density (because of models with very low central density are expected only a few expected stellar mergers that produce stellar masses large enough to be progenitors of (P)PISNe BHs, compare Kremer, Spera, et al. (2020)). Furthermore, the NBODY6++GPU models have the WD natal kicks switched on following Fellhauer et al. (2003) and the MOCCA simulations do not assign natal kicks to the WDs. Moreover, the winds in the MOCCA simulations with `edd_factor=0` ignore the so-called bi-stability jump (see Appendix A2), whereas the NBODY6++GPU simulations with `mdflag=3` do not ignore it (Belczynski et al., 2010).

Following the original concept in Hurley et al. (2002), we define time

step parameters p_1, p_2, p_3 , to determine how many steps are done during certain evolutionary phases of stars (Note that Banerjee et al. (2020) use symbols `pts1`, `pts2` & `pts3` for these). Also MOCCA uses via BSE the same representation. p_1 describes the step used in the main sequence phase, p_2 in the sub-giant (BGB) and Helium main sequence phase, and p_3 in more evolved giant, supergiant, and AGB phases. For clarity we reproduce the equation in Hurley et al. (2002), where δt_k is the time step used to update the stellar evolution in the code, for stellar type k :

$$\delta t_k = p_k \begin{cases} t_{\text{MS}} & k = 0, 1 \\ (t_{\text{BGB}} - t_{\text{MS}}) & k = 2 \\ (t_{\text{inf},1} - t) & k = 3, t \leq t_x \\ (t_{\text{inf},2} - t) & k = 3, t > t_x \\ t_{\text{He}} & k = 4 \\ (t_{\text{inf},1} - t) & k = 5, 6, t \leq t_x \\ (t_{\text{inf},2} - t) & k = 5, 6, t > t_x \\ t_{\text{HeMS}} & k = 7 \\ (t_{\text{inf},1} - t) & k = 8, 9, t \leq t_x \\ (t_{\text{inf},2} - t) & k = 8, 9, t > t_x \\ \max(0.1, 10.0t) & k \geq 10 \end{cases} \quad (9.1)$$

The original choice in Hurley et al. (2000) was $p_{0,1} = 0.01$, $p_{2,7} = 0.05$, and $p_k = 0.02$ for all other k . During the following years, in widely used `NBODY6` codes and derivatives, and in standard BSE packages $p_{0,1}$ and p_4 have been increased to 0.05, probably to save some computing time. However, after comparison with `STARTRACK` (Belczynski et al., 2008) models with high time resolution, Banerjee et al. (2020) suggested $p_{0,1} = 0.001$, $p_2 = 0.01$ and $p_k = 0.02$ for all others. In Fig. 4 in Banerjee et al. (2020), we can see the difference that these time-step choices produce, by producing spikes in the initial-final mass relation for large progenitor ZAMS masses (ignoring (P)PISNe). Currently such small p_i does not pose any significant computational problem; but as seen in Banerjee et al. (2020) such problems with too large p_i only show up for very large stellar masses $M \gtrsim 100M_{\odot}$.

9.5 Results

9.5.1 Global dynamical evolution

We run each of the two initial models with `NBODY6++GPU` and MOCCA. Hence we have four distinct simulations to compare and contrast. We discuss in the following Figure 9.1 to Figure 9.3, to get an overview over the global evolution of the simulated star clusters. Figure 9.2 shows us that the core collapse happens a bit later in the MOCCA simulations and this is connected with the problems with the timescale. According to Hénon's principle, the rate of cluster evolution is governed by the heat flow through the half-mass radius. Therefore, for smaller r_h and half-mass relaxation time, t_h , in

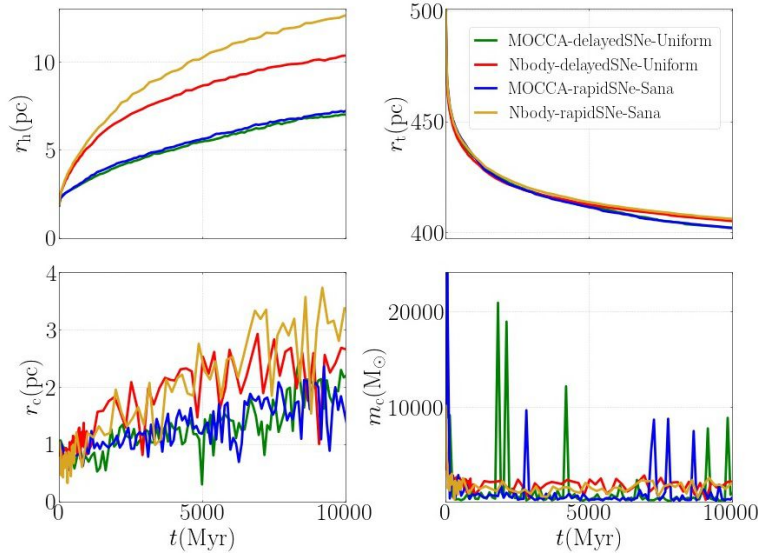


Figure 9.1: Time evolution of the half-mass radii r_h (pc) (top-left), the tidal radii r_t (pc) (top-right), core radii r_c (pc) (bottom-left) and core masses m_c (M_\odot) (bottom-right) for the four simulations. The Nbody - delayedSNe - Uniform, Nbody - rapidSNe - Sana, MOCCA - delayedSNe - Uniform and MOCCA - rapidSNe - Sana simulations are shown in red, yellow, green and blue, respectively.

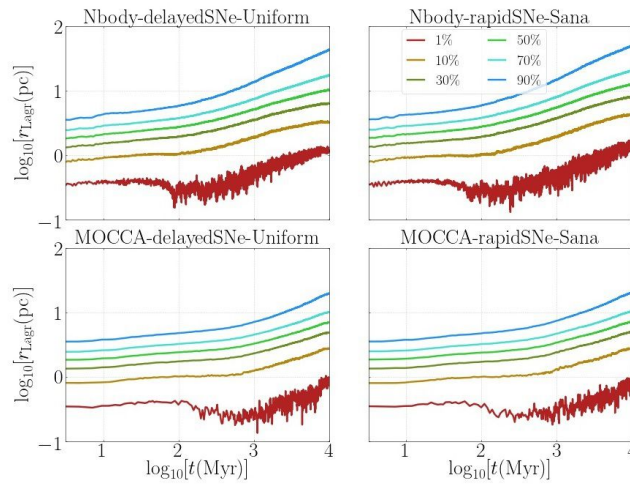


Figure 9.2: Time evolution of the logarithm of the Lagrangian radii r_{Lagr} (1, 10, 30, 50, 70, 90)% for the four simulations: Nbody - delayedSNe - Uniform (top-left), Nbody - rapidSNe - Sana (top-right), MOCCA - delayedSNe - Uniform (bottom-left) and MOCCA - rapidSNe - Sana (bottom-right).

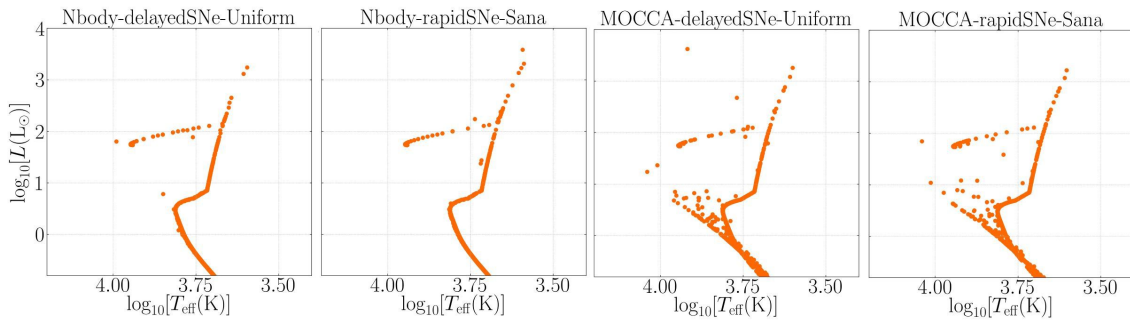


Figure 9.3: HRD for all four simulations at 10 Gyr. As can be seen from the HRDs of the MOCCA simulations, there are plenty of more blue stragglers in these than in the Nbody6++GPU simulations.

MOCCA than in the `NBODY6++GPU` models, the MOCCA models have to evolve faster and provide more energy in the core than their `NBODY6++GPU` counterparts. This leads to more dynamical interactions in the core and a small delay in the core-collapse time. Primordial binaries become active earlier as an energy source than in the direct N -body simulations. This can also be seen from the core radii, r_c , evolution of the cluster models and we see that the MOCCA simulations have a larger central density, which should lead to a larger number of dynamical interactions in MOCCA compared with the `NBODY6++GPU` runs. Likewise, this can be observed in the larger scatter in remnant masses in [Figure 9.6](#). In combination with the smaller r_h in the MOCCA models, which have a similar total mass (similar r_t in all) to those of the `NBODY6++GPU` models, this means that the energy flow across r_h is much larger in MOCCA than in the `NBODY6++GPU` runs. The denser models in the MOCCA simulations are evidenced further in the number of binaries in the simulations. The time evolution of the logarithm of the binary fraction for the four simulations is shown in the top-row of [Figure 9.4](#). Although the overall binary fractions are similar, the `NBODY6++GPU` simulations yield consistently larger fractions over 10 Gyr. This is due to more scattering events in MOCCA runs that disrupt binaries, which is mirrored by the denser cores and overall clusters in the MOCCA simulations, see [Figure 9.1](#). Moreover, looking at [Figure 9.6](#), one can see from the larger scattering in the remnant masses of all compact objects in the MOCCA simulations that there must have been more interactions between the stars that led to mass gain or loss. This is further evidenced by the Hertzsprung-Russel diagram (HRD) in [Figure 9.3](#) from all four simulations. We see many more blue stragglers in the HRDs of MOCCA compared with the `NBODY6++GPU` simulations. This means that there must have been collisions or mass transfer to rejuvenate the stars in order to make them blue stragglers. The likelihood of these formation channels is generally larger in denser systems.

9.5.2 Stellar evolution

Compact binary fractions

[Figure 9.4](#) shows, in addition to the overall binary fraction, the binary fractions of several other compact binaries in which at least one member is a compact object. Both compact binary fractions are dominated by WD binaries, where in the MOCCA simulations the WD binaries are mostly found as WD-MS binaries. In the `NBODY6++GPU` simulations, there also many WD binaries consisting of secondaries other than MSs, many of them also being WDs. In all simulations the overall WD binary fraction, as well as the WD-MS binary fraction increases over the whole 10 Gyr in contrast to the total star cluster binary fraction. The double-degenerate (DD) binary fraction for all simulations also increases continuously. This is dominated by WD-WD binaries, where the number of surviving WD-WD binaries in the `NBODY6++GPU` simulations is much larger than the number in the MOCCA simulations by a factor of about ten. This large discrepancy could be due to faster evolving and denser MOCCA star

cluster simulations, which ionise or force to merge more binaries. This is also evidenced by the lower overall binary fractions in the MOCCA models: see also the discussion above.

Further differences in WD binary fractions, especially the WD-MS binaries in [Figure 9.4](#), might additionally arise from the WD kicks that are switched on in the `NBODY6++GPU` simulations but not in the MOCCA models. In general, these WD kicks are the same for WD types in MOCCA and are assigned an arbitrary kick speed of `vkickwd`, unlike in `NBODY6++GPU`, which draws kicks for HeWDs and COWDs from a Maxwellian of dispersion `wksig1` and the kicks for the ONeWDs from a Maxwellian with dispersion `wksig2`. Both Maxwellians are truncated at `wkmax=6.0 kms-1`, where typically `wksig1=wksig2=2.0 kms-1` following (Fellhauer et al., 2003). The presence of these kicks in the `NBODY6++GPU` models might lead to increased disruption of WD-MS binaries and thus lead to the observed lower abundances. However, since MOCCA and `NBODY6++GPU` lead to faster and slower global evolution of the star cluster models, respectively, it is difficult to disentangle what actually produces these differences. So far, no cluster simulations on the scale of our simulations presented here have been undertaken investigating the stability of WD binaries in the presence of kicks in detail using both MOCCA and `NBODY6++GPU` and these need to be performed in the future.

From [Figure 9.4](#) we can see that near the beginning of all simulations there are small numbers of BH-MS binaries produced for all four simulations, where the `delayedSNe-Uniform` simulations produce more BH-MS binaries overall. Over the 10 Gyr evolution of our cluster simulations, the `MOCCA-delayedSNe-Uniform` simulation produces the most surviving BH-MS binaries, but the logarithmic binary fraction is still continuously decreasing. All simulations produce BH-BH binaries in similar numbers where these start forming after about 100 Myr. This suggests that BH-BH binary systems formed in dynamic interactions, since the last BH formed in a SNe was about 80 Myr earlier. At the end of all simulations, we have a surviving BH-BH, whose orbital parameters and masses may be inspected in [Table 9.2](#). All of these binaries are located very close to the cluster density centre, with masses of the same order of magnitude, with the highest mass BH in a BH-BH (and all BH binaries) being found in the `MOCCA-rapidSNe-Sana` model with mass $M_{\text{BH}} = 31.032 M_{\odot}$. The semi-major axes a of these BH-BH binaries are also all smaller than 100 AU: the closest BH-BH binary found in the `Nbody-delayedSNe-Uniform` simulation having a semi-major axis value of 53.129 AU. This is not small enough to have a merger within a Hubble time. The two BH-MS binaries in the `MOCCA-delayedSNe-Uniform` simulation both consist of an accreting BH with a low mass MS donor star of type `KW=0`. Therefore, these are not given in [Table 9.2](#).

The NS binaries are found further away from the density centre, the closest one coming from the `MOCCA-delayedSNe-Uniform` run with $r_{\text{dens}} = 2.018$ pc. The simulations do not produce any surviving NS-NS, NS-BH, or BH-WD binaries, the former of which are very elusive (Arca Sedda, 2020; Chattopadhyay et al., 2020, 2021; Drozda et al., 2020). The `MOCCA-rapidSNe-Sana` simulation

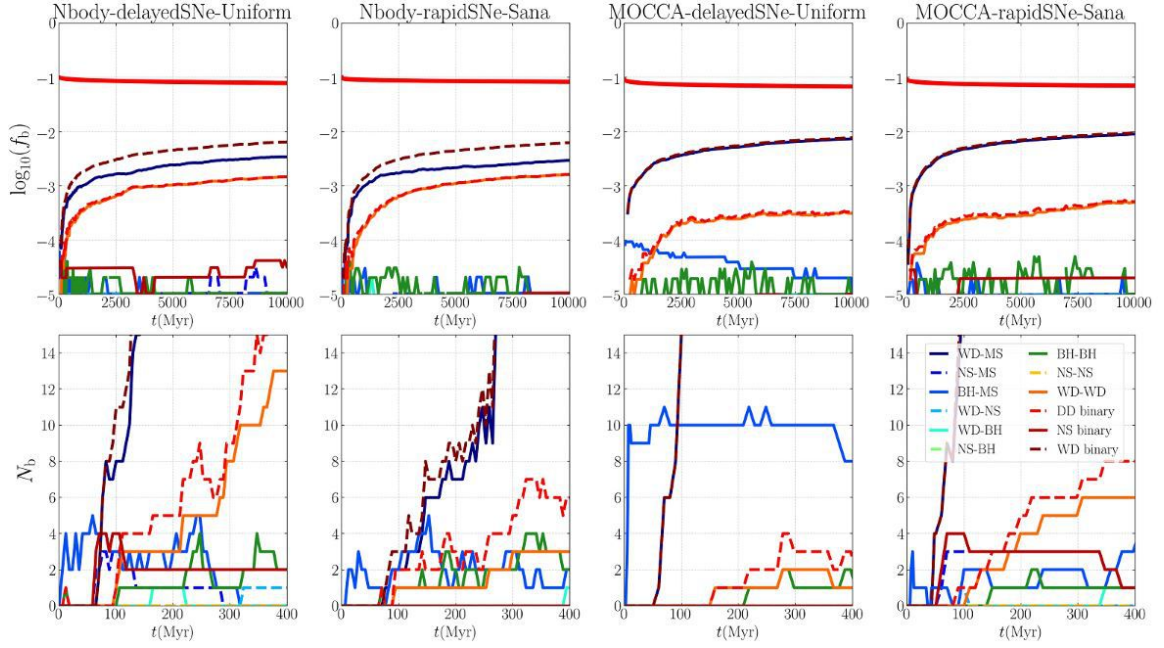


Figure 9.4: Time evolution over 10 Gyr of the logarithmic (compact) binary fractions (top row) for the Nbody-delayedSNe-Uniform, Nbody-rapidSNe-Sana, MOCCA-delayedSNe-Uniform and MOCCA-rapidSNe-Sana simulations from left to right, respectively. Shown in the top row as a thick red line are the overall logarithmic binary fractions. On the bottom row for the first 400 Myr the absolute number of the double-degenerate (DD), NS, WD, WD-MS, NS-MS, BH-MS, WD-NS, WD-BH, NS-BH, BH-BH, NS-NS and WD-WD binaries are shown.

produces one surviving BH-MS binary, whose parameters are given in Table 9.2. All simulations produce NS binaries, where at 10 Gyr we have mostly only NS-MS binaries surviving, apart from the Nbody6++GPU-delayedSNe-Uniform simulation, which also produces one NS-COWD binary: see Table 9.2. All NS masses in binaries are $1.26 M_{\odot}$ and thus these are either the result of a MIC, AIC or ECSNe.

Remnant masses

The remnant masses of the compact objects which have escaped the simulation are shown in the Initial-Final mass relation (IFMR) in Figure 9.5, where the initial mass is the ZAMS mass and the final mass denotes the compact remnant mass. These remnant masses are mainly determined by our choices of either the delayed SNe or the rapid SNe (C. L. Fryer et al., 2012) and the lack of an enabled (P)PSiNe mechanism. The masses of the compact objects in the MOCCA simulations appear to lie systematically above those of the Nbody6++GPU simulations. There exists one very high mass BH of mass $91.830 M_{\odot}$ for the MOCCA-rapidSNe-Sana simulation, which escaped at 1.298 Gyr. This BH has a complex history and it was subject to an initial binary merger due to stellar evolution. The progenitor stellar mass was $95.618 M_{\odot}$. If a (P)PSiNe scheme was enabled, then we would never reach these high BH masses of $91.830 M_{\odot}$. The resulting BH would have been capped at $40.5 M_{\odot}$ if we had used `psflag=1` & `piflag=2` (Belczynski et al., 2016), for example. Also shown in this figure, is an old IFMR from Belczynski et al. (2002). These black dots clearly lie below all the compact objects

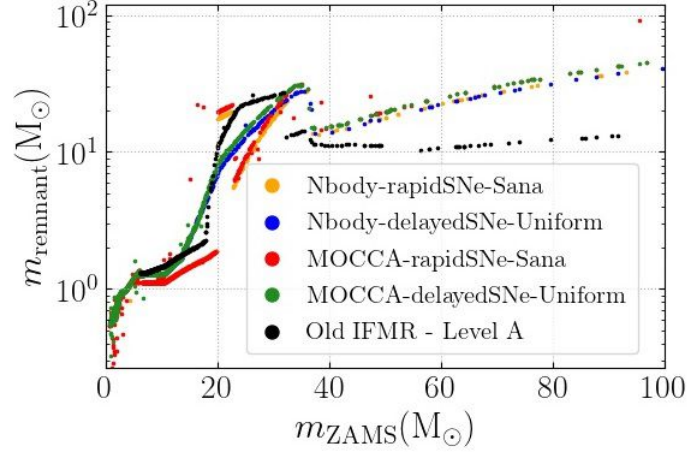


Figure 9.5: Initial-Final mass relation (IFMR) for the escaping compact objects. The Nbody-delayedSNe-Uniform, Nbody-rapidSNe-Sana, MOCCA-delayedSNe-Uniform and MOCCA-rapidSNe-Sana simulations are shown in red, green, blue and yellow, respectively. The black points show BH masses from another N -body simulation with Level A parameters (Belczynski et al., 2002).

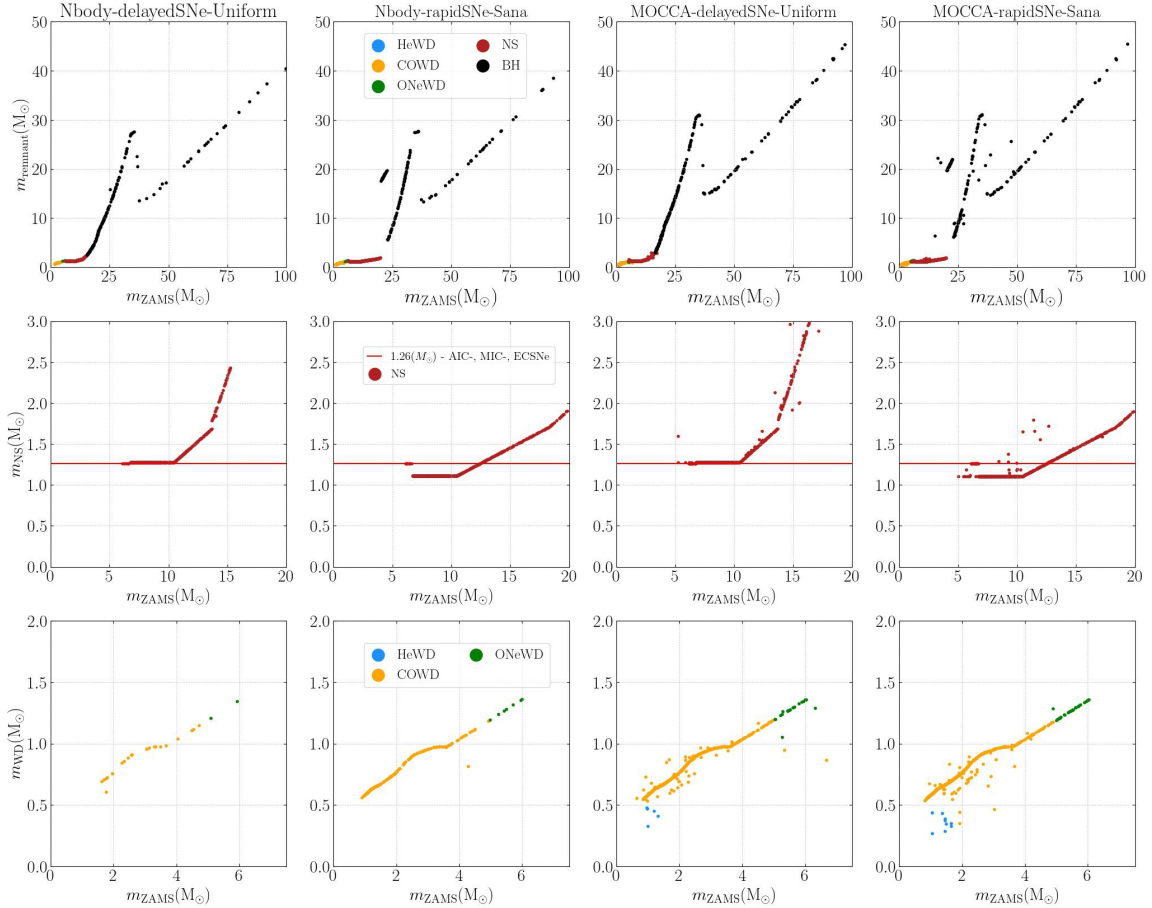


Figure 9.6: Initial-Final mass relations (IFMR) for the escaping compact objects. From left to right, there are shown the Nbody-delayedSNe-Uniform, Nbody-rapidSNe-Sana, MOCCA-delayedSNe-Uniform and MOCCA-rapidSNe-Sana simulations, respectively. From top to bottom, there are plotted the IFMRs for the BHs, NS and WDs, the IFMRs of the NSs only and the IFMRs for the WDs, respectively. The top IFMRs show excellent agreement with Banerjee et al. (2020) and C. L. Fryer et al. (2012). The bottom WD IFMR likewise compares well to Han et al. (1995), Hurley and Shara (2003), and Hurley et al. (2000). Interestingly, the IFMR shows some NSs escaping at a mass of $1.26 M_{\odot}$ (ECSNe, AIC or MIC) for all simulations even with small natal kicks following Gessner and Janka (2018).

from the new delayed and rapid SNe prescriptions in the range of $(30-100)M_{\odot}$. We also see that the difference in the delayed and rapid SNe prescription is mostly in the regime up to around $30.0 M_{\odot}$ at our metallicity of 0.00051. Therefore, the choice of `nsflag/compactmass` mostly affects the regime $< 30.0 M_{\odot}$. At larger ZAMS masses, all four simulations mostly coincide in their IFMRs. For the rapidSNe simulations, we see the double core-collapse hump, whereas for the delayedSNe simulations, we only see one hump (C. L. Fryer et al., 2012).

In Figure 9.6, we see a more detailed IFMR for each individual simulation, where we also zoom in on the NSs (middle row) and the WDs (bottom row) for all simulations. Apart from the already discussed larger spread in the remnant masses of the compact objects in the MOCCA simulations, the simulations show good consistency with each other, as well as the literature C. L. Fryer et al. (2012). This is also true for the WD masses, which are unaffected by the delayed or rapid SNe mechanisms and which follow the original SSE algorithm (Han et al., 1995; Hurley & Shara, 2003; Hurley et al., 2000). To add more depth to the analysis, see Figure 9.7 and Figure 9.8 for the masses of all the compact objects (BH, NS, ONeWD, COWD, HeWD) versus their distance to the density centre, r_{dens} , as well as the cumulative histograms of the compact object distances for the MOCCA and the Nbody6++GPU simulations, respectively. There are objects in these plots that extend beyond the tidal radius. This is due to the fact that the escape criterion in Nbody6++GPU removes stars once they are further than two times the tidal radius from the density centre. Overall, there are a lot more HeWDs both escaping and remaining inside the clusters of the MOCCA simulations over the full 10 Gyr. We know that HeWDs cannot be formed in the stellar evolution of single stars in a Hubble time. They can be formed only in binaries. In MOCCA models the central density is larger than in the N -body models, so it is expected that more frequent dynamical interactions force binaries to form HeWDs because of mass transfer. The COWD numbers and their distributions are similar for all simulations, but there are many more COWD-COWD binaries in the Nbody6++GPU simulations, mirroring findings in Figure 9.4. The mass and r_{dens} distributions of the ONeWDs for the MOCCA and Nbody6++GPU simulations are likewise similar, but there are more outlying ONeWDs for the MOCCA simulations, indicating and underlying the point made early about the MOCCA simulations having more interactions across their full evolution: see Figure 9.1 and Figure 9.6. The Nbody6++GPU simulations retain slightly larger numbers of NSs inside the cluster than the MOCCA simulations. Additionally, the Nbody6++GPU simulations only retain NSs of masses $1.26 M_{\odot}$, which is the mass that is assigned for NSs produced by an ECSNe, AIC or MIC. The MOCCA simulations have a much larger spread in the NS masses again underpinning the point that the MOCCA simulations are denser and lead to more interactions between the stars. The BH masses are distributed very dissimilarly. Firstly, the Nbody-delayedSNe-Uniform simulation retains the least BHs up until 10 Gyr; two single BHs and the BH-BH binary (see Table 9.2). This BH-BH binary is also the hardest of all BH-BH binaries remaining at 10 Gyr. The MOCCA-rapidSNe-Sana simulation retains

the largest number of BHs up until 10 Gyr (around 20 of which two are in a BH-BH binary). This BH-BH binary is the most massive (combined mass of around $60 M_{\odot}$) and also the most distant to the density centre of this cluster. The MOCCA-delayedSNe-Uniform and the Nbody-rapidSNe-Sana retain similar numbers of BHs and they are also distributed similarly.

Remnant natal kicks and escape speeds

Table 9.2: Table listing the orbital properties of some degenerate binaries surviving inside the cluster at time 10 Gyr with at least one member being a BH or a NS. Also shown is the expected merger timescale t_{GW} for the compact binaries computed from Peters (1964) and Peters and Mathews (1963). None of these compact binaries would be relevant for aLIGO or aVirgo detections.

| Simulation | type | $M_1(M_{\odot})$ | $M_2(M_{\odot})$ | e | $P(\text{days})$ | $a(\text{AU})$ | $r_{\text{dens}}(\text{pc})$ | $t_{\text{GW}}(\text{Gyr})$ |
|-----------------------|---------|------------------|------------------|-------|------------------|----------------|------------------------------|-----------------------------|
| Nbody-delayedSNe-Uni. | BH-BH | 22.586 | 17.145 | 0.415 | 22452 | 53.129 | 0.355 | 2.268×10^{10} |
| Nbody-delayedSNe-Uni. | MS-NS | 0.871 | 1.260 | 0.479 | 5271 | 7.600 | 1.727 | / |
| Nbody-delayedSNe-Uni. | NS-COWD | 1.260 | 0.892 | 0.729 | 56863 | 37.361 | 5.535 | 2.712×10^{12} |
| Nbody-rapidSNe-Sana | BH-BH | 18.275 | 20.969 | 0.953 | 24207 | 55.655 | 0.749 | 4.773×10^6 |
| Nbody-rapidSNe-Sana | NS-MS | 1.260 | 0.553 | 0.766 | 133522 | 62.343 | 12.920 | / |
| MOCCA-delayedSNe-Uni. | BH-BH | 29.910 | 19.747 | 0.940 | 31703 | 72.060 | 0.108 | 1.616×10^7 |
| MOCCA-delayedSNe-Uni. | NS-MS | 1.260 | 0.767 | 0.889 | 3517620 | 572.904 | 2.018 | / |
| MOCCA-rapidSNe-Sana | BH-BH | 29.905 | 31.032 | 0.329 | 22269 | 60.963 | 0.811 | 1.598×10^{10} |
| MOCCA-rapidSNe-Sana | BH-MS | 21.156 | 0.104 | 0.772 | 9223 | 23.845 | 3.3775 | / |
| MOCCA-rapidSNe-Sana | NS-MS | 1.260 | 0.343 | 0.801 | 153356 | 65.626 | 7.575 | / |

In Figure 9.9, the escape speeds v_{esc} of the compact objects in relation to their ZAMS mass are shown for the Nbody6++GPU simulations. The absolute number of the objects per stellar type are shown and we distinguish between objects coming from either a ZAMS single star or ZAMS binary. This information, as well as the kick speeds v_{kick} for the NSs and BHs for the MOCCA simulations, is also shown in Figure 9.10. For the MOCCA simulations, we computed the escape speeds v_{esc} from their escape energies infinitely far away from the cluster.

First, we discuss the WDs, for which we have the v_{esc} information readily available across all four simulations. All escaping HeWDs originate from ZAMS binaries in both simulations, which is expected from mass transfer in binaries and the production pathways of HeWDs in general. Their escape speeds reach a couple of hundred kms^{-1} in some instances for the Nbody6++GPU simulations. This is not the case for the MOCCA simulations. Comparing this with Figure 9.7 and Figure 9.8, there are still single HeWDs retained in both the Nbody6++GPU and MOCCA simulations, but a lot fewer for the Nbody6++GPU simulations than for the MOCCA simulations and on the other hand, many more HeWDs escape the Nbody6++GPU simulations than the MOCCA simulations.

Many more COWDs originating from ZAMS single stars escape than those with a ZAMS binary origin in the Nbody6++GPU runs. The same is true for the MOCCA simulations, but here many more COWDs originating from ZAMS single stars escape than from the Nbody6++GPU simulations. In the Nbody6++GPU simulations the escape speeds of the escaping COWDs from ZAMS binaries are much larger than those of the COWDs from ZAMS single stars. This

should be expected, because if the binary companion underwent a SNe event, the COWD or progenitor might have adopted the binary's high orbital speed. In the MOCCA simulation, however, the COWDs (and all other WD types) from ZAMS singles and ZAMS binaries escape with highly uniform v_{esc} . This needs to be investigated further in the future. In total, there are many more COWDs and ONeWDs retained for all simulations than those that escape (see [Figure 9.7](#) and ??). Consistently more ONeWDs escape the MOCCA simulations from singles and binary ZAMS stars. Future studies into the impact of WD natal kicks on binary stability, escape speeds and escaper number are needed going forward.

The BHs and NSs are affected by the delayed and rapid SNe as well as the fallback-scaled natal kicks, while the WDs are not. We see that compared with the Nbody6++GPU simulations, the distributions of the BH and NS escape speeds are very similar. The `KMECH=1` in Nbody6++GPU and the `bhflag_kick=nsflag_kick=3` settings in MOCCA for the fallback-scaled momentum conserving kicks, compare also [Figure ??](#) and [??](#), lead to very similar distributions in escape speeds. It also shows that escape speeds and the natal kick speeds of the MOCCA simulations are very similar. To clarify again, v_{kick} and v_{esc} describe the actual natal kick velocity and the velocity at escape from the cluster, respectively. The speeds for the escaping NSs in all four simulations reach up to 10^3 km s^{-1} .

The NSs produced from AIC, ECSNe and MIC lead to very low escape speeds as a result of the very low natal kicks, which we assign by using `ECSIG=sigmac=3.0 km s-1` from [Gessner and Janka \(2018\)](#). Even still, some of these NSs escape from all clusters without any significant acceleration. This may be due to evaporation, where a series of weak encounters finally leads to an escape of the NS, or by a strong dynamical ejection. Another reason might be their involvement in a binary, i.e., they were a member of a binary and the binary snaps due to the SN of its companion, causing the star to adopt the high orbital speed of the binary (similar to the proposed mechanism for the high v_{esc} for some HeWDs and COWDs in the Nbody6++GPU simulations).

The low mass BHs in the delayedSne simulations also reach 10^3 km s^{-1} , whereas the low mass BHs just at the transition between the NSs and BHs in the rapidSne simulations are very low, leading to a small gap in velocity distribution of the escaping BHs. This is due to the first of the two core-collapse humps in the remnant mass distribution of the rapid SNe scheme ([Banerjee et al., 2020](#); [C. L. Fryer et al., 2012](#)); the larger the fallback, the lower the natal kick of the NS or BH. Nevertheless, even some BHs in this gap escape all rapidSne simulations, which is a result of the low masses of the clusters and thus the low escape speeds. In realistically sized GCs, these BHs would probably not escape, unless through some hard encounter. The larger the ZAMS mass, the lower the resulting escape speed and natal kicks are, due to increasing fallback. This is why at the high end of the BH mass spectrum, the velocities become very small (only a couple of km s^{-1}) in all simulations.

Binary parameters

The only different initial binary parameters between the `delayedSNe-Uniform` and the `rapidSNe-Sana` simulations is the binary mass ratio distribution q , which is set to q_{Uniform} and q_{Sana} , respectively. The binary mass ratios for all four simulations at times (1,2,5,9,10) Gyr are presented in [Figure 9.11](#). The evolution across all simulations leads to very similar distributions at 10 Gyr with only a few very large binary mass ratios. We note that strictly speaking the q_{Uniform} and q_{Sana} initial distributions are very similar overall and thus it is not surprising, but rather reassuring, that this is indeed the case in the simulations. We also see similarities in the semi-major axes a of the binaries as shown in [Figure 9.12](#). The shape of the curve is roughly what we would expect, since they are distributed flat in $\log(a)$, however, for the `Nbody-rapidSNe-Sana` there is a small clustering at wide binaries in the cumulative distribution. This can more easily be seen as an unusual increase in the cumulative histogram of the binary eccentricities at low eccentricities in [Figure 9.13](#). This might be due to a change in regularisation, when the binaries move in and out of KS regularisation. Some testing has been done and we can confirm that this issue is definitely not related to stellar evolution and needs to be resolved in the future. Interestingly, this clustering does not seem to be present in the `Nbody-delayedSNe-Uniform` simulation. Therefore, it might be related to the hardware or technical parameters within the initialisation of the simulations. However, we did not change any of these between the two `NBODY6++GPU` simulations and therefore this seems unlikely. We need to explore this erratic issue further and resolve this.

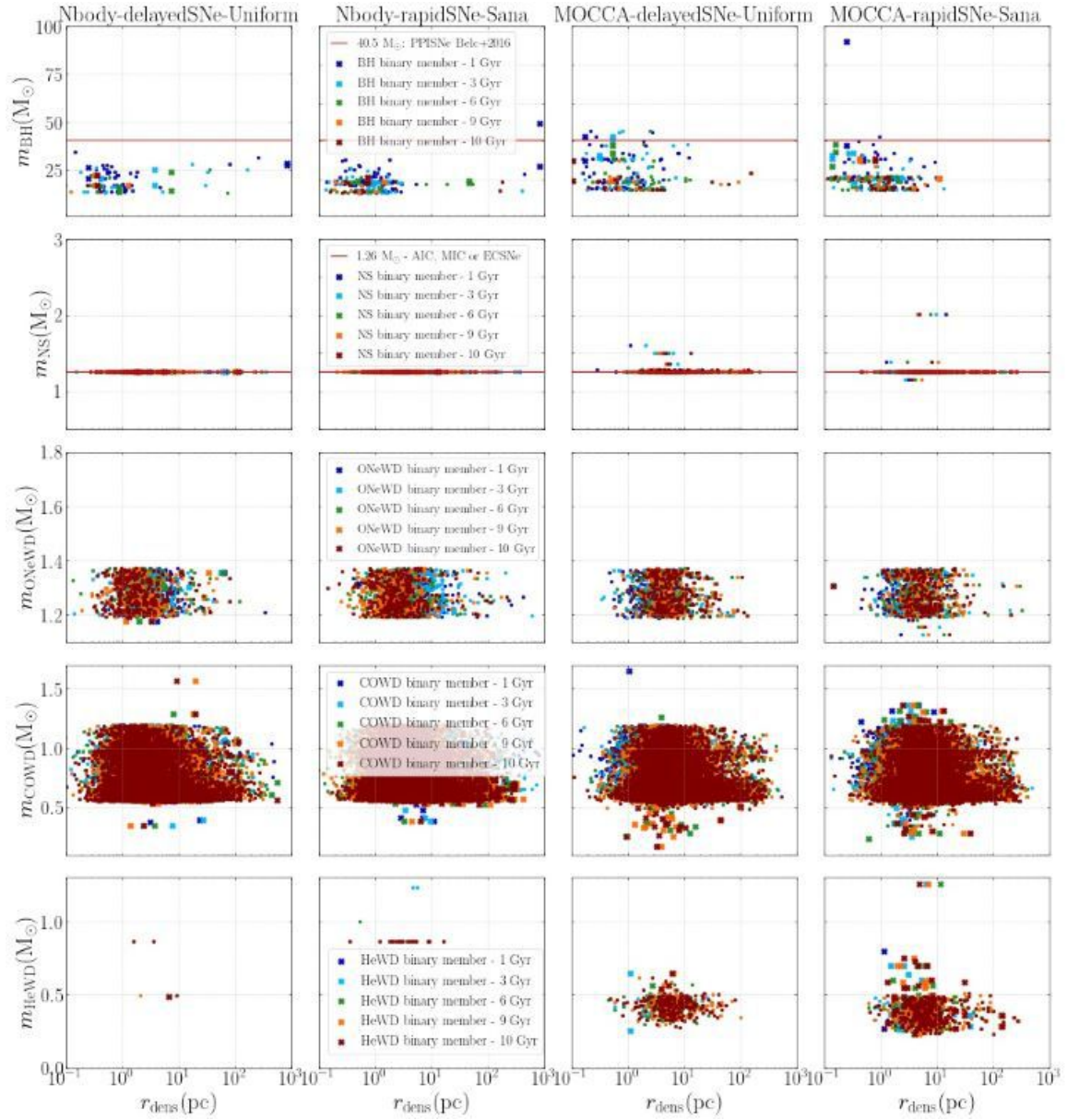


Figure 9.7: Plot showing the mass of the compact objects in relation to their distance to the density centre r_{dens} (pc) for all four simulations at (1,3,6,9,10) Gyr. From top to bottom the plots show the above information for the BHs, NSs, ONeWDs, COWDs and HeWDs, respectively. **BHs:** MOCCA retains more BHs than the Nbody6++GPU simulations and all four simulations retain a BH-BH binary at 10 Gyr. **NSs:** in the Nbody6++GPU runs only the ECSNe, AIC and MIC NSs are retained, whereas there is a larger spread in remnant masses in the MOCCA simulations (which might be due to a post-natal ECSNe, AIC, MIC NS accreting mass). **ONeWDs, COWDs:** the distributions across all four simulations are very similar. **HeWDs:** there are many more HeWDs retained in the MOCCA simulations than the Nbody6++GPU simulations at 10 Gyr.

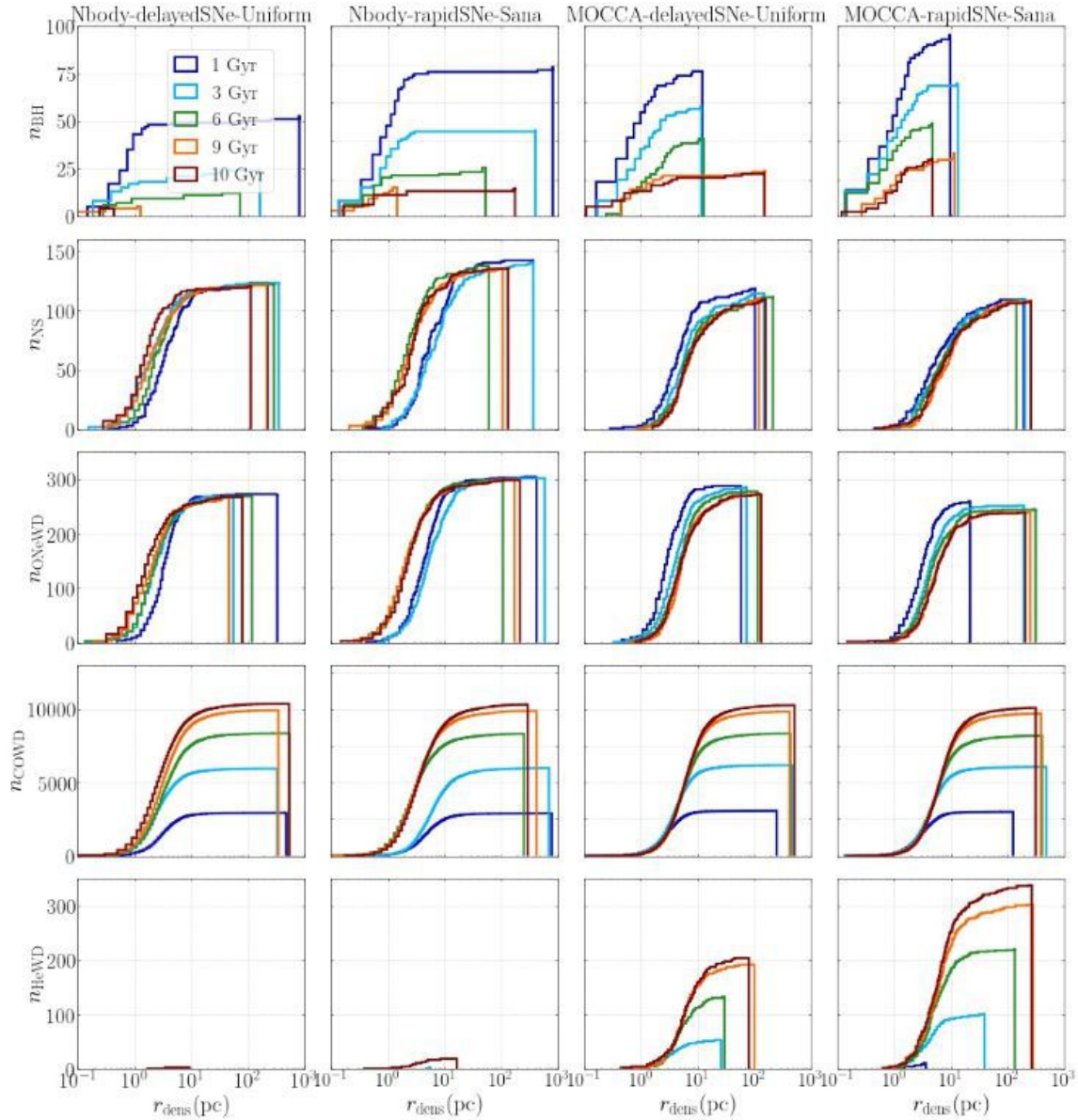


Figure 9.8: Cumulative distributions for compact object distances to the density centre $r_{\text{dens}}(\text{pc})$ for all four simulations at (1,3,6,9,10) Gyr. From top to bottom the plots show the above information for the BHs, NSs, ONeWDs, COWDs and HeWDs, respectively. **BHs:** Nbody6++GPU simulations retain consistently lower numbers of BHs with the Nbody -de-layedSNe -Uni form having the lowest by far (4). **NSs:** the Nbody6++GPU simulations have consistently slightly larger numbers of NSs retained, but the distributions are very similar. **OneWDs and COWDs:** distributions and numbers for these objects are very similar. **HeWDs:** much lower numbers of HeWDs in the Nbody6++GPU simulations than in the MOCCA simulations. If the enabled WD kicks in Nbody6++GPU were the reason, then we would expect to have equally lower numbers of ONeWDs and COWDs as well, but we do not.

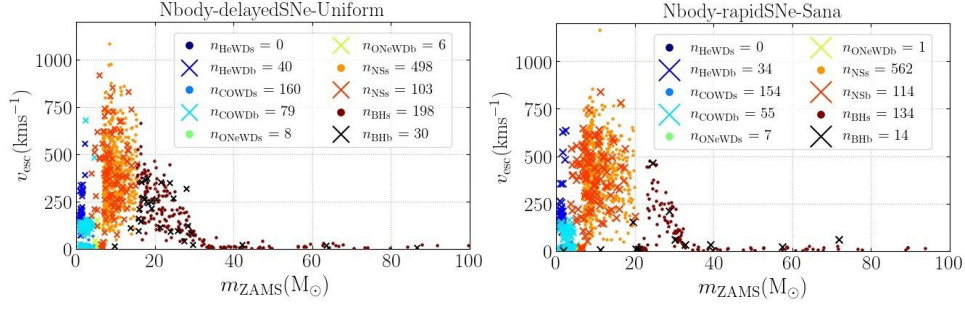


Figure 9.9: Plot showing the final escape speeds $v_{\text{esc}} (\text{kms}^{-1})$ of the compact objects (WDs, NSs, BHs) for the Nbody-delayedSNe-Uniform and the Nbody-rapidSNe-Sana simulations. Also shown in crosses are the compact objects that come from primordial ZAMS binary stars (n_{HeWDb} , n_{COWDb} , n_{ONeWDb} , n_{NSb} , n_{BHb}), whereas the smaller dots display compact objects originating from ZAMS single stars (n_{HeWDs} , n_{COWDs} , n_{ONeWDs} , n_{NSs} , n_{BHs}). The number counts n_{HeWDb} , n_{COWDb} , n_{ONeWDb} , n_{NSb} , n_{BHb} , n_{HeWDs} , n_{COWDs} , n_{ONeWDs} , n_{NSs} , n_{BHs} are recorded in the plot legend.

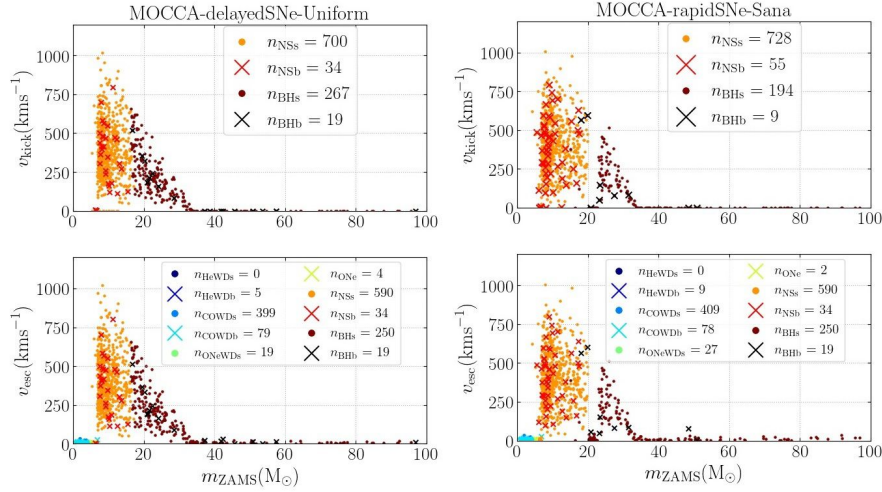


Figure 9.10: Plot showing the natal kick speeds $v_{\text{kick}} (\text{kms}^{-1})$ of the NSs and BHs (not recorded for WDs), as well as the final escape speeds $v_{\text{esc}} (\text{kms}^{-1})$ of all the compact objects (HeWDs, COWDs, ONeWDs, NSs, BHs) for the MOCCA-delayedSNe-Uniform (top two panels) and the MOCCA-rapidSNe-Sana (bottom two panels) simulations. Also shown in crosses are the compact objects that come from primordial ZAMS binary stars (n_{HeWDb} , n_{COWDb} , n_{ONeWDb} , n_{NSb} , n_{BHb}), whereas the smaller dots display compact objects originating from ZAMS single stars (n_{HeWDs} , n_{COWDs} , n_{ONeWDs} , n_{NSs} , n_{BHs}). The number counts n_{HeWDb} , n_{COWDb} , n_{ONeWDb} , n_{NSb} , n_{BHb} , n_{HeWDs} , n_{COWDs} , n_{ONeWDs} , n_{NSs} , n_{BHs} are recorded in the plot legend. The compact objects with a zero kick velocity have a constant value of 0.0001 kms^{-1} added to them to make them visible.

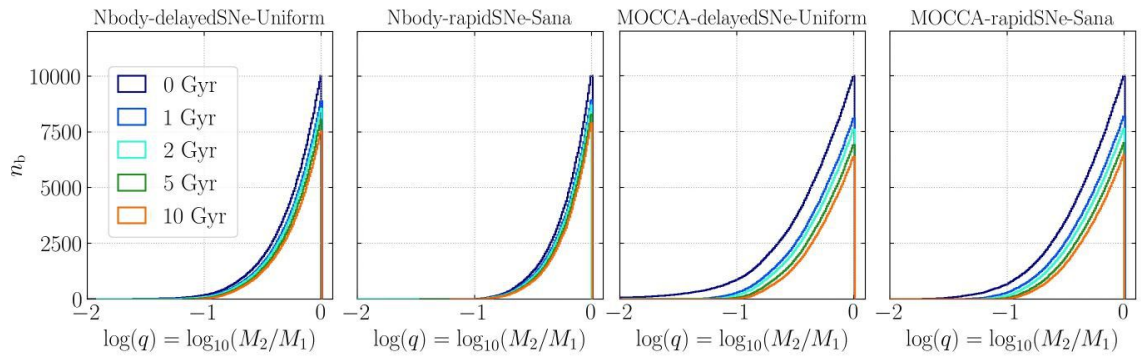


Figure 9.11: Cumulative histogram showing the mass ratio at times (1,2,5,9,10) Gyr of the binaries for all four simulations. The mass ratio q is calculated such that the lower mass M_2 is divided by the larger mass M_1 .

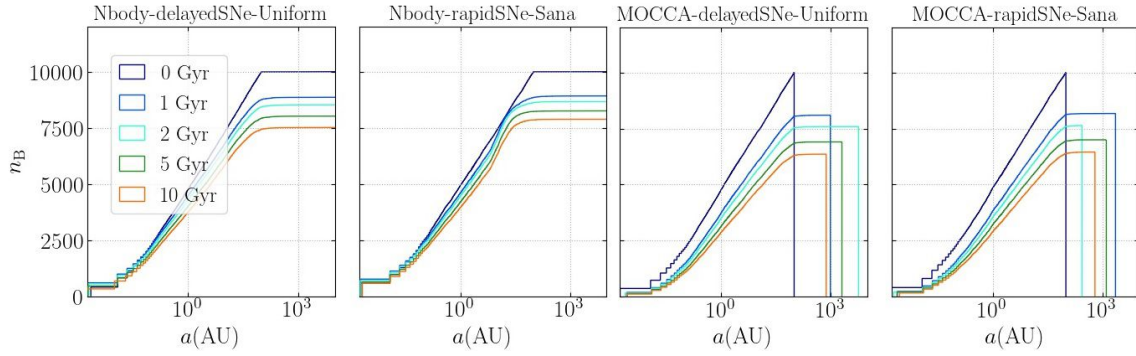


Figure 9.12: Cumulative histogram showing the semi-major axis a (AU) at times (1,2,5,9,10) Gyr of the binaries for all four simulations.

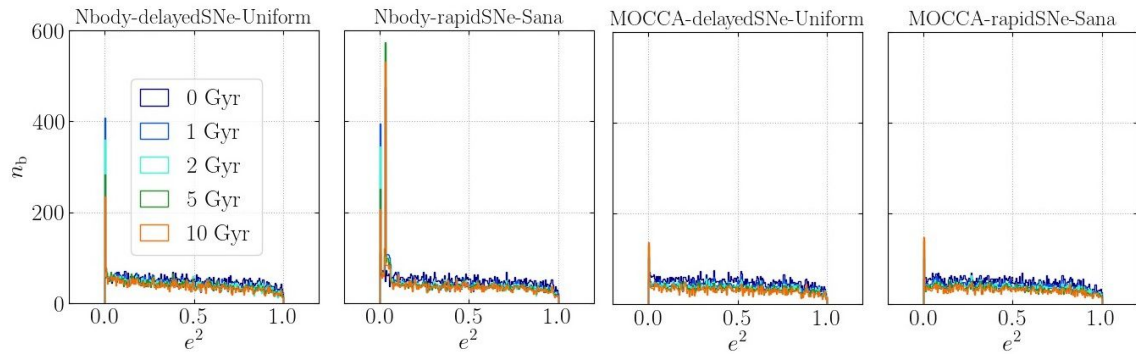


Figure 9.13: Histogram showing the eccentricity e^2 at times (1,2,5,9,10) Gyr of the binaries for all four simulations ($N(< e) \propto e^2$) for a thermal distribution (Duquennoy & Mayor, 1991)). The Nbody-rapidSNe-Sana simulation reveals a second peak, which might relate to regularisation or another complex origin.

9.6 Summary, conclusion and perspective

9.6.1 Summary: direct N -body (NBODY6++GPU) and Monte Carlo (MOCCA) simulations

We have compared direct N -body (NBODY6++GPU) and Monte Carlo (MOCCA) star cluster models for about 10 Gyr with our updated codes. We showcase the effect of parts of the updated stellar evolution, more specifically the delayed vs. rapid SNe as extremes for the convection-enhanced neutrino-driven SNe paradigm by C. L. Fryer et al. (2012) with standard momentum conserving fallback-scaled kicks in combination with metallicity dependent winds from Belczynski et al. (2010), Vink and de Koter (2002, 2005), and Vink et al. (2001) and low-kick ECSNe, AIC and MIC (Gessner & Janka, 2018; Ivanova et al., 2008; Leung, Nomoto, & Suzuki, 2020; Podsiadlowski et al., 2004). The BHs had no natal spins set (corresponding to the Fuller model in Banerjee (2021a) from J. Fuller and Ma (2019) and J. Fuller et al. (2019)). The initial model with the delayed SNe enabled had the binary mass ratios uniformly distributed (q_{Uniform}) and is dubbed `delayedSNe-Uniform`, whereas the initial model with the rapid SNe enabled, had the binary mass ratios distributed as inspired by observations following Kiminki et al. (2012), Kobulnicky et al. (2014), Sana et al. (2013), and Sana and Evans (2011) (q_{Sana}) and is dubbed `rapidSNe-Sana`. The MOCCA models did not employ WD kicks, whereas the NBODY6++GPU models used WD natal kicks following Fellhauer et al. (2003). The time-steps `pts1`, `pts2`, `pts3` of MOCCA represent fractions of stellar lifetimes in the main sequence, sub-giant, and more evolved phases that are taken as stellar-evolutionary time steps in the respective evolutionary stages and should, after calibrating them with `STARTRACK` (Belczynski et al., 2008), follow the suggestions by Banerjee et al. (2020): `pts1`=0.001, `pts2`=0.01 and `pts3`=0.02. In the NBODY6++GPU simulations, the time-steps `pts2`, `pts3` are all accounted for by `pts2`. Here, we chose `pts1`=0.05 and `pts1`=0.02. We make the following observations:

- Globally, the star cluster models evolve differently. The mass loss from NBODY6++GPU is slightly lower than that from the MOCCA simulations. The NBODY6++GPU simulations have consistently larger r_{Lagr} than the MOCCA simulations (see Figure 9.1). In particular, the half-mass radii are significantly larger than those in the MOCCA simulations. Figure 9.2 shows us that core collapse happens a bit later in the MOCCA simulations and this is connected with the time-scaling. In the Monte Carlo models the global cluster evolution rate is governed according to Hénon's principle by the heat flow through the half-mass radius. So for smaller half-mass radius and half-mass relaxation time in MOCCA than in NBODY6++GPU models, the MOCCA models have to evolve faster and provide more energy in the core than for the NBODY6++GPU approach. This leads to more dynamical interactions in the core and a small delay in the core-collapse time. Primordial binaries become active earlier as an energy source than in N -body. The MOCCA simulations have smaller half-mass radius and mass and there-

fore the half-mass relaxation time is also smaller. This means that the MOCCA models are overall dynamically older and have evolved faster. Furthermore, from the core radii evolution of the cluster models, we see that MOCCA simulations have a larger central density, which should lead to a larger number of dynamical interactions in these models compared with the `NBODY6++GPU` runs. All of this is also connected to the treatment of unbound stars in MOCCA. In MOCCA, when a star acquires a high enough energy in relaxation/interaction to become unbound it is immediately removed from simulations. In `NBODY6++GPU` this is not the case as stars need time to travel across the star cluster system to be removed to a distance of twice the tidal radius from the density centre. Since r_t is very large in our simulations (see [Table 9.1](#)), this may take a very long time (on the scale of Gyrs in some cases). During this time the star can undergo relaxation and become a bound star in the cluster yet again (Baumgardt, 2001). When this process is properly accounted for in MOCCA the evolution of Lagrangian radii in MOCCA and `NBODY6++GPU` are similar and a new version of the MOCCA code includes an upgrade to properly treat these escaped objects.

- ▶ From the core radii evolution of the cluster models, we see that MOCCA simulations have a larger central density over the whole simulation. This leads to a larger number of dynamical interactions in the MOCCA runs compared with the `NBODY6++GPU` runs, as can be inferred from the larger scatter in remnant masses in [Figure 9.6](#). Although the overall binary fractions are similar, the `NBODY6++GPU` simulations yield consistently larger fractions over 10 Gyr. Due to the denser MOCCA models, binaries will be disrupted and forced to merge at larger rates. Additionally, more blue straggler stars are shown in the HRDs of the MOCCA simulations, as can be seen in [Figure 9.3](#). This means that there must have been more interactions that lead to mass gain to produce these, i.e. this is a result of the denser MOCCA models. In [Figure 9.5](#), the masses of the escaping NSs for the MOCCA-`delayedSNe-Uniform` simulation are larger, simply because we found that the maximum NS mass was set to $3.0 M_{\odot}$, rather than $2.5 M_{\odot}$ in the other simulations. This maximum NS mass is taken as the upper limit of neutron star masses and follows from causality (Lattimer & Prakash, 2004). This is not a big a problem, however, since the IFMR for the delayed SNe is continuous in this regime. If we had instead set the maximum NS to $2.5 M_{\odot}$ then all the NSs in the mass range between $2.5 M_{\odot}$ and $3.0 M_{\odot}$ would be BHs with the same masses as the NSs. In the future gravitational million-body simulations, we will use $2.5 M_{\odot}$ in line with recent observations, such as Linares (2018).
- ▶ The differences in the time-step parameters (`pts1`, `pts2`, `pts3`) and the wind treatment (`mdflag=3≠edd_factor=0`, where `NBODY6++GPU` takes into account the bi-stability jump and the MOCCA simulations do not), in combination, might

lead to the slight upward shift in values in the IFMR in [Figure 9.5](#), which otherwise shows excellent agreement in the BHs, NSs and WDs masses across all simulations for both MOCCA & N_{BODY6++GPU}. Further investigations should be done into systematic shifts of the remnant masses between the MOCCA and N_{BODY6++GPU} code. Both of the IFMRs show excellent agreement with the theory from C. L. Fryer et al. (2012) and the N_{BODY7} results from Banerjee et al. (2020). Comparisons with old (Level A) stellar evolution treatments reveal that these core-collapse neutrino-driven SNe schemes produce much larger BH masses for increasing ZAMS masses than what was previously available (Belczynski et al., 2002) and provide a smooth transition to any of the available (P)PISNe treatments (see also [Figure ??](#)) if these are switched on.

- The fallback-scaled kick distributions for NSs and BHs likewise show excellent agreement across all masses as shown in [Figure 9.9](#) and [Figure 9.10](#). All simulations retain NSs formed from an ECSNe, AIC or MIC of mass $1.26 M_{\odot}$ (Belczynski et al., 2008) as we see in [Figure 9.7](#) and [??](#). But some of these also escape the cluster despite the low natal kick velocity that we set of $\text{eccsig}=\text{sigmac}=3.0 \text{ kms}^{-1}$ (Gessner & Janka, 2018) at similar escape speeds, which might be due to the low cluster densities, evaporation (a series of weak encounters), the kick itself or a combination of the above. Overall, the retention fractions and distributions, see [Figure 9.7](#), [??](#), of the compact objects across all simulations are very similar. The HeWDs are the big exception which are mostly retained in the MOCCA simulations, in contrast to N_{BODY6++GPU} where virtually all of them escape with large escape speeds. These escape speeds are, however, much larger than the largest permitted HeWD natal kick of 6.0 kms^{-1} (Fellhauer et al., 2003) that is set in the N_{BODY6++GPU} simulations and they are also much larger than the escape speeds for the HeWDs from the MOCCA simulations (see [Figure 9.10](#)). All of the escaped HeWDs originate from ZAMS binaries in both the MOCCA and the N_{BODY6++GPU} simulations. Many more COWDs from single ZAMS stars escape the MOCCA simulations than the N_{BODY6++GPU} simulations and the escape speeds are also much more similar and in many cases much lower than those of the N_{BODY6++GPU} runs. COWDs from ZAMS binaries escape all the simulations in similar numbers. The same statements can be made about the ONeWDs. The reasons why the v_{esc} distributions are so dissimilar cannot be attributed only to the WD kicks in the N_{BODY6++GPU} simulations, because the natal kicks are of very low velocity dispersion. Further studies with MOCCA and N_{BODY6++GPU} on the effects that WD natal kicks have on binary stability and WD production and retention fraction in OCs, GCs and NSCs should be done going forward to shed more light on this particular aspect using the two modelling methods.

Overall, from the detailed comparison, we find very good agreement between the two modelling methods (N_{BODY6++GPU} and MOCCA)

when looking at, for example, the remnant mass distributions. This provides mutual support for both methods in star cluster simulations and the stellar evolution implementations in both codes. However, there are also some significant differences in the global evolution of the star cluster simulations with the two modelling methods. An example of these is the striking differences in blue straggler stars from [Figure 9.3](#), the reasons for which are given above. The conclusion here relates to our initial models and the treatment of unbound stars in MOCCA vs. Nbody6++GPU simulations. In the future, we strongly suggest to not choose massively tidally underfilling initial cluster models with extremely large tidal radii, especially when using MOCCA simulations, to avoid problems with extremely large escape times for unbound objects. In any case, the results invite additional future comparative studies exploring the vast parameter space of star cluster simulations, also in the initial conditions, with direct N -body (Nbody6++GPU) and Monte Carlo (MOCCA) simulations using the updated stellar evolution.

9.6.2 Perspective on future stellar evolution (SSE & BSE) updates

We have identified the following pain points in our SSE & BSE implementations in Nbody6++GPU & McLuster and to a lesser extent MOCCA, where we still have some work to do. The version of MOCCA presented in this paper has the CV behaviour around the orbital period gap and the GR merger recoil and final post-merger spins, as well as some earlier implementation of modelling high mass and metal-poor Population III stars (Tanikawa et al., 2020) available. An even more up-to-date version by Belloni, Mikołajewska, et al. (2020) also has an advanced treatment of the wind velocity factor β_W as an option. Overall, we will include the stellar evolution routines listed below in the codes MOCCA, Nbody6++GPU & McLuster in the next iteration of stellar evolution updates and refer to these necessary updates below as Level D, see also Appendix A. The (technical) details of these implementations are not shown in [Figure 9.16](#) and are reserved for a future publication in the interest of brevity.

CVs and the orbital period gap

The proper behaviour of the CVs around the so-called *orbital period gap*, which is located at $2 \text{ hr} < P_{\text{orb}} < 3 \text{ hr}$ (Knigge, 2006; Schreiber et al., 2010; Zorotovic et al., 2016), cannot be reproduced by Nbody6++GPU, however, in MOCCA since the BSE modifications by Belloni, Schreiber, et al. (2018) and discussions by Belloni, Giersz, et al. (2017) are accounted for, this behaviour can be modelled according to our best current understanding. The BSE algorithm of Nbody6++GPU is still in its original form to treat CVs and includes only a simple description of the evolution of accreting WD binary systems given that comprehensive testing of degenerate mass-transfer phases was beyond the original scope of Hurley et al. (2002). The changes that need to be done and we are implementing at the moment in Nbody6++GPU require a lot of modifications.

Firstly, the original mass transfer rate onto *any* degenerate object ($KW \geq 10$) in MOCCA has been upgraded from Claeys et al. (2014), Hurley et al. (2002), and Whyte and Eggleton (1980) by including the formalism following Ritter (1988). The angular momentum loss in a close interacting CV that happens as a consequence of mass transfer is called the consequential angular momentum loss mechanism (CAML). Depending on the driving process behind the mass transfer it is either referred to as classical CAML (cCAML) (A. R. King & Kolb, 1995) or empirical CAML (eCAML) (Schreiber et al., 2016). The original BSE formalism can also be chosen (Hurley et al., 2002). The eCAML is more empirically motivated by including nova eruptions as the source of additional drag forces. Here the CAML is stronger for low mass WDs. Furthermore, Belloni, Schreiber, et al. (2018) introduced new, completely empirical normalisation factors for magnetic braking (MB) angular momentum loss and gravitational multipole radiation (GMR) angular momentum loss in the case of cCAML following Knigge et al. (2011) and in the case of eCAML, these normalisation factors for MB and GMR follow Zorotovic et al. (2016). The merger between a MS star and its WD companion is now treated with the variable `qdynflag`, for which if set to 0 the merger assumes no CAML, if set to 1 the merger depends on classical cCAML and if set to 2 the merger depends on empirical CAML (Schreiber et al., 2016). Moreover, Belloni, Kroupa, et al. (2018) improved the stability criteria for thermally unstable mass transfer depending on a critical mass ratio between the primary and secondary star (Schreiber et al., 2016) in the original BSE (Hurley et al., 2002), because the mass transfer rates for thermal timescale mass transfer are underestimated in the original BSE. All of these changes are further complemented by a large reduction in the time-steps for interacting binaries, depending on the factor that may be chosen freely. These upgrades in MOCCA, and soon to be included in `NBODY6++GPU`, will have the following impact. Firstly, the spins will be properly treated in response to the updated magnetic braking. Secondly, the inflation above and below the orbital period gap and the deflation in the orbital period gap of the donor primary star will be described correctly. Lastly, the processes of GR that lead to angular momentum loss and bloating *below* the orbital period gap and of MB, which leads to angular momentum and bloating *above* the orbital period period gap, will be accounted for.

More on magnetic braking

As mentioned above, the MB mechanisms were updated in Belloni, Schreiber, et al. (2018). The original version in Hurley et al. (2002) has been improved by Belloni, Schreiber, et al. (2018) to include the more rigorous treatment by Rappaport et al. (1983), which may be switched on in MOCCA. Then, this new implementation was applied to CVs in GCs in the MOCCA study in Belloni et al. (2019). This model was expanded further in Belloni, Schreiber, et al. (2020) by also adding the so-called reduced magnetic braking model, which extends the previous works to magnetic CVs. An issue that remains in both MOCCA and `NBODY6++GPU` is the limit for applying MB, which arrives from the fact that MB is only expected to operate in

MS stars with convective envelopes. This affects low-mass accreting compact object binaries, such as CVs and low-mass X-ray binaries. In *STARTRACK* (Belczynski et al., 2008), there is such a mass limit imposed. At metallicities of $Z \geq 0.02$, the maximum mass is set to $1.25 M_{\odot}$ and for low metallicities at $Z \leq 0.001$, i.e. also at the metallicity used in the simulations of this paper, this limit should be $0.8 M_{\odot}$. Additionally, unlike *STARTRACK*, the magnetic braking does not depend on the stellar type *KW* in *MOCCA* and in the *NBODY6++GPU* BSE algorithm, which should be the case, as the MB upper mass limit depends on it.

Extending SSE fitting formulae to extreme metal-poor (EMP) stars

In *N*-body simulations that use SSE & BSE to model the stellar evolution, any extrapolation beyond $100 M_{\odot}$ should be used with caution (Hurley et al., 2000). However, this mass can be reached in the initial conditions when an IMF above $100 M_{\odot}$ is used, e.g. Wang et al. (2021), or can be reached through stellar collisions Kremer, Spera, et al. (2020), especially in the beginning of the simulations (Di Carlo et al., 2019, 2021; Morawski et al., 2018, 2019; Rizzuto, Naab, Spurzem, Arca-Sedda, Giersz, et al., 2021; Rizzuto, Naab, Spurzem, Giersz, et al., 2021). The fact the masses in these simulations sometimes reach masses largely in excess of the original upper mass limit to the fitting process employed in Hurley et al. (2000) cannot simply be ignored. To this end, Tanikawa et al. (2020) devised fitting formulae for evolution tracks of massive stars from $8 M_{\odot}$ up to $160 M_{\odot}$ in extreme metal-poor environments ($10^{-8} \leq Z/Z_{\odot} \leq 10^{-2}$), which can be easily integrated into existing SSE & BSE code variants. These formulae are based on reference stellar models that have been obtained from detailed time evolution of these stars using the *HOSHI* code (Takahashi et al., 2016, 2019) and the 1-D simulation method described in Yoshida et al. (2019). In a further study with the same method Tanikawa, Susa, et al. (2021) provide fitting formulae of these stars that go up to even $1260 M_{\odot}$ and recently, these are now available up to $1500 M_{\odot}$ (Hijikawa et al., 2021). In general, BSE& SSE variants need this implementation, which is already available in *MOCCA* (although not fully tested), to accurately model the evolution of these extremely-metal poor stars (e.g. Population III) star clusters, high mass stars in some extremely metal poor GCs and to use IMFs, which go beyond $100 M_{\odot}$, e.g. Wang et al. (2021), for these clusters. Adding the Tanikawa et al. (2020) capability is especially interesting as for the first time we might be able to model extremely massive stars (many hundreds and even thousands of M_{\odot}) in massive GC environments. We note that there are likely some intrinsic differences between the standard SSE (Hurley et al., 2000) and the new fitting formulae by Tanikawa et al. (2020), because the former were fitted to the *STARS* stellar evolution program (P. P. Eggleton et al., 1973; P. P. Eggleton, 1971, 1972, 1973; Pols et al., 1995) results and latter to the afore-mentioned *HOSHI* code (Takahashi et al., 2016, 2019). This becomes particularly relevant when attempting to mix low mass stars ($M_{\odot} \leq 8$) modelled with the traditional fitting formulae in the SSE code and high mass stars modelled by Tanikawa et al. (2020). Moreover, the formulae by Tanikawa et al. (2020) are only valid for

masses larger than $8 M_{\odot}$ and thus we need a sensible transition between Hurley et al. (2000) and Tanikawa et al. (2020).

Masses of merger products

In the most recent version of `STARTRACK`, the merger products of certain stellar types were assigned new merger masses (Olejak et al., 2020). The problem in the old BSE (Hurley et al., 2002) arises from the fact that the mass of the product of a merger during dynamically unstable mass transfer, especially MS-MS merger, leads to $M \simeq M_{\text{accretor}}$. There are many contact or over-contact MS-MS binaries that appear to be stable. On the other hand, there are also blue straggler stars and very massive stars ($> 150 M_{\odot}$) that are believed to be merger products, e.g. stars R136a, R136b and 136c in the large Magellanic cloud (Bestenlehner et al., 2020) and the two stars WR 102ka in the Milky Way (Barniske et al., 2008; Hillier et al., 2001) are estimated to have masses exceeding $200 M_{\odot}$. To account for this, Olejak et al. (2020) have introduced formalisms along the lines of $M = M_{\text{accretor}} + f_x \times M_{\text{donor}}$, for a number of different merger scenarios involving different stellar types. Here f_x should be in the range of 0.5-1.0. This is still a very simple picture of stellar mergers and we need to elaborate on this approach. With the old BSE formalism, we may significantly reduce the cluster mass, which therefore also affects its evolution. This might be specially true when using the Sana orbital period distribution from `MCLUSTER` initial conditions (`adis=6`) (Kiminki et al., 2012; Kobulnicky et al., 2014; Sana et al., 2013; Sana & Evans, 2011), which has a lot of massive primordial MS-MS binaries with periods P_{orb} shorter than a few days.

GR merger recoil and final post-merger spins

The latest studies of IMBH growth with `NBODY6++GPU` (Di Carlo, Mapelli, Bouffanais, et al., 2020; Di Carlo, Mapelli, Giacobbo, et al., 2020; Di Carlo et al., 2019, 2021; Rizzuto, Naab, Spurzem, Arca-Sedda, Giersz, et al., 2021; Rizzuto, Naab, Spurzem, Giersz, et al., 2021) do not include a general relativistic merger recoil treatment (in addition to missing PN terms). But Arca-Sedda et al. (2021) have included the recoil kicks by a posteriori analysis. The GR merger recoil is also missing from the MOCCA Survey Database I (Askar et al., 2017). `NBODY7` and also the current development version of `NBODY6++GPU` contain a proper treatment of such velocity kicks. They depend on spins and mass ratio, and are caused due to asymmetric GW radiation during the final inspiral and merger process. Numerical relativity (NR) models (Campanelli et al., 2007; Hughes, 2009; Rezzolla et al., 2008; van Meter et al., 2010) have been used to formulate semi-analytic descriptions for MOCCA and `NBODY` codes (Arca-Sedda et al., 2021; Banerjee, 2021a, 2021b; Belczynski & Banerjee, 2020; Morawski et al., 2018, 2019). For (nearly) non-spinning BHs (Fuller model), the kick velocity is smaller than for high spins. In the case of large mass ratios the kick velocity is much smaller than for small mass ratios (Morawski et al., 2018, 2019) and therefore, in extreme

cases these post-merger BHs might even be retained in open clusters (Baker et al., 2007, 2008; Baumgardt & Hilker, 2018; Portegies Zwart et al., 2010; Schödel et al., 2014). For non-aligned natal spins and small mass ratios on the other hand, the asymmetry in the GW may produce GR merger recoils that reach thousands of kms^{-1} (Baker et al., 2008; van Meter et al., 2010).

Generally, the orbital angular momentum of the BH-BH dominates the angular momentum budget that contributes to the final spin vector of the post-merger BH and therefore, within limits, the final spin vector is mostly aligned with the orbital momentum vector (Banerjee, 2021a). In the case of physical collisions and mergers during binary-single interactions, the orbital angular momentum is not dominating the momentum budget and thus the BH spin can still be low. Banerjee (2021a) also includes a treatment for random isotropic spin alignment of dynamically formed BHs. Additionally, Banerjee (2021a) assumes that the GR merger recoil kick velocity of NS-NS and BH-NS mergers (Arca Sedda, 2020; Chattopadhyay et al., 2021) to be zero but assigns merger recoil kick to BH-BH merger products from numerical-relativity fitting formulae of van Meter et al. (2010) (which is updated in Banerjee (2021b)). The final spin of the merger product is then evaluated in the same way as a BH-BH merger.

With the updates above, in addition to the BH natal spins discussed above, `NBODY6++GPU` will be able to fully model IMBH growth during the simulation (unlike in post-processing with `MOCCA` as in Morawski et al. (2018, 2019)) in dense stellar clusters according to our best understanding. This is one of last remaining and important puzzle pieces in our SSE & BSE implementations that helps us to simulate IMBH formation and retention in star clusters and the corresponding aLIGO/aVirgo GW signal (R. Abbott et al., 2020b).

Wind velocity factor

The accretion of stellar winds in binaries depends on the wind velocity and a factor β_W . In the updated binary population synthesis (BPS) code `COSMIC` by Breivik, Coughlin, et al. (2020), the value β_W is allowed a broader range of values that actually do depend on stellar type following the `STARTRACK` code by Belczynski et al. (2008). In the `MOCCA` & `NBODY6++GPU` versions presented in this paper $\beta_W=0.125$, where this represents the lower limit and should roughly correspond to the wind from the largest stars of $900 R_\odot$ (Hurley et al., 2002). In the future, β_W will depend on the stellar type.

Pulsars and magnetic spin field from NSs

The `COSMIC` BPS code (Breivik, Coughlin, et al., 2020) includes new BSE additions that properly treat pulsars (Breivik, Coughlin, et al., 2020; Kiel et al., 2008; Ye et al., 2019) in an attempt to mirror observations of spin periods and magnetic fields of young pulsars (Manchester et al., 2005). Similarly, the `COMPAS` BPS code (Stevenson, Berry, & Mandel, 2017; Stevenson, Vigna-Gómez, et al., 2017) employs updated BSE and is used to study NS binaries, such as

the elusive BH-NS (Chattopadhyay et al., 2021) and NS-NS binaries (Chattopadhyay et al., 2020) using updated pulsar prescriptions. These updates are also present in the earlier BPS code BINPOP by Kiel et al. (2010), which is also based on the original BSE (Hurley et al., 2002). In detached binaries, a magnetic dipole radiation is assumed for the spin-period evolution whereas in non-detached binaries, a so-called magnetic field burying as a response to mass transfer is implemented (Kiel et al., 2008), where the magnetic field decays exponentially depending on the accretion time and the mass that is transferred (equation (7) in Breivik, Coughlin, et al. (2020)). Mergers that include a NS produce a NS with a spin period and magnetic field that is drawn again from the same initial distribution, except for millisecond pulsars (MSPs) which stay MSPs after mergers. The magnetic field of a NS cannot be smaller than 5×10^7 G (Kiel et al., 2008). In `NBODY6++GPU` & `MOCCA`, we need these updates to properly account for the spin and the magnetic field evolution of all pulsars.

Ultra-stripping in binary stars

After CE formation in a hard binary consisting of a NS or a BH and a giant star, the hydrogen-rich envelope of the giant star gets ejected, carrying large amounts of angular momentum with it (Tauris et al., 2013; Tauris et al., 2015). After the CE is ejected fully, the NS orbits a naked He star, after which further mass transfer via RLOF may happen (Tauris et al., 2017) depending on the RLOF criteria mentioned above. This leads to stripping of the envelope of the He star until it reaches a naked core of mass $1.5 M_{\odot}$ and explodes in a so-called ultra-stripped SNe (USSNe) (Tauris et al., 2013; Tauris et al., 2015). According to Tauris et al. (2017) most of these binaries survive the USSNe. Breivik, Coughlin, et al. (2020) have an implementation in `COSMIC`, which allows for this SNe pathway. In their models, the USSNe leads to an ejected mass of $0.1 M_{\odot}$. The resulting kick velocity dispersion is much lower than the kick velocity dispersion following Hobbs et al. (2005). In general, there should be a bi-modal kick distribution, where NSs with a mass above $1.33 M_{\odot}$ receive large kicks and NSs with masses below that receive small kicks with a kick velocity dispersion of about 20.0 km s^{-1} (Tauris et al., 2017). Since the USSNe appears to be central to BH-BH, BH-NS and NS-NS merger rates (F. R. N. Schneider et al., 2021), we will work on implementations in `NBODY6++GPU` & `MOCCA`. Very recently, F. R. N. Schneider et al. (2021) found that through extreme stellar stripping in binary stars (Tauris et al., 2013, 2017; Tauris et al., 2015) in their MESA models (Paxton et al., 2011, 2015), there is an overestimation by 90% in the BH-BH mergers and 25-50% in the BH-NS numbers if only any of the C. L. Fryer et al. (2012) prescriptions, rapid or delayed, are enabled. Overall, they predict a slight increase of 15-20% more NS-NS mergers. This will definitely have to be explored in the future in N-body simulations.

We are in the process of implementing the above into the `MCLUSTER` version presented in this paper and results are reserved for a future publication.

With the updates in the SSE & BSE algorithms of `MOCCA` &

NBODY6++GPU presented in this paper, we are now able to fully model realistic GCs accurately across cosmic time with direct N -body simulation and also Monte-Carlo models according to our current understanding of stellar evolution of binary and single stars. Thus, the next step is to test these updates with new direct million-body Dragon-type GC simulations, following on from Wang et al. (2016), and Dragon-like NSC simulations similar to Panamarev et al. (2019), and compare these with MOCCA modelling. In addition to NBODY6++GPU, we will in the future also use the PETAR code by (Wang, Iwasawa, et al., 2020; Wang, Nitadori, & Makino, 2020a, 2020b). This code also uses up-to-date SSE & BSE implementations in code structure similar to the original SSE & BSE (Hurley et al., 2000, 2002) and similar to MOCCA. These two direct N -body codes in combination with Monte-Carlo models from MOCCA all employing modern stellar evolution will yield unprecedented and exciting results into the dynamical and stellar evolution of star clusters of *realistic* size.

Finally, we note that a successor to SSE called the Method of Interpolation for Single Star Evolution METISSE (Agrawal et al., 2020) has recently been produced. This utilises advancements in astrophysical stellar evolution codes to provide rapid stellar evolution parameters by interpolation within modern grids of stellar models. Thus it offers the potential for an astrophysically more robust (and potentially faster) realistic alternative to the updated SSE implementation in NBODY6++GPU and MOCCA. However, a similar approach as presented by Agrawal et al. (2020) is not yet available for the BSE routines and thus we will have to wait for a binary stellar evolution version of METISSE. Similarly, the SEVN code (Mapelli, Spera, et al., 2020; Spera & Mapelli, 2017; Spera et al., 2019) and its binary version is still a work in progress and at this moment in time not ready to be fully implemented into our codes. Therefore, it is likely that the SSE & BSE presented here and the large number of variants of these codes are destined to stay relevant in the modelling of stellar evolution of single and binary stars for quite some time.

9.7 Stellar and binary evolution levels A, B, C

The stellar evolution levels and the corresponding options are shown in Figure 9.14, Figure 9.15 and Figure 9.16. The foundation for evolving a single star in the NBODY6++GPU and MOCCA codes and all subsequent updates is provided by the state-of-art population synthesis code SSE (Hurley et al., 2000, 2013). This appendix is devoted to summarise the extensive changes which have been made in the stellar evolution in MOCCA & NBODY6++GPU since Hurley et al. (2000, 2002). We categorise the existing stellar evolution routines in `levels`. This is because with the increasing number of recipes and complexity therein available, we found it difficult to document and communicate these quickly in our simulations. The stellar evolution options that are available in NBODY6++GPU and MOCCA as of the writing of this paper, are shown in Figure 9.14, Figure 9.15 and Figure

9.16, respectively. We divide the available stellar evolution recipes in `NBODY6++GPU` & `MOCCA` as such:

1. **Level A** - Stellar evolution settings that mirror in part the settings in the Dragon simulations of GCs (Wang et al., 2016) and NSCs (Panamarev et al., 2019) and also the `MOCCA` Survey DataBase I (Askar et al., 2017). Most of these are outdated and should be generally not be used anymore, see e.g Shu et al. (2021).
2. **Level B** - Stellar evolution settings that have been tested extensively and may be used without concern. A selection of these should be enabled in the next gravitational million-body simulations.
3. **Level C** - Stellar evolution settings that are available in the codes, but those that are not present in level B have not yet undergone sufficient testing and are therefore deemed experimental as of the writing of this paper.
4. **Level D** - Stellar evolution settings that will be added in the next iteration of stellar evolution updates, see also section 5.2 for details on these.

In the more distant future, we will sequentially add new levels (the next one would be level E), where we group further planned stellar evolution updates on top of the preceding level (in this case level D) in `NBODY6++GPU`, `MOCCA` & `McCLUSTER` together. We hope that this will greatly help in the documentation and aid the future user of the codes to properly choose SSE & BSE settings in his or her simulations.

9.7.1 Dynamical mass transfer and other processes in binary stars

In `NBODY6++GPU`, the dynamical mass transfer and the stability thereof in Roche-lobe overflow (RLOF) between binary stars is computed by `roche.f`, which calls subroutines for magnetic braking `magbrk.f`, for gravitational radiation `grrad.f` and for coalescing of RLOF or common-envelope evolution (CEE) binaries `coal.f`. The tidal circularisation and tidal spin synchronisation and associated timescales are set in `bsetid.f`, which still follow the original treatment by Hurley et al. (2002) and sources therein. In `MOCCA`, all of the above is included in the original `evol2b.f` (Hurley et al., 2002) with lots of more recent updates regarding the proper evolution of cataclysmic variables (CVs) (Belloni, Schreiber, et al., 2018). These updates may be switched off, however, with the parameters `camlflagMZ=qdynflagMZ=qtherflagMZ=0` (Belloni, Schreiber, et al., 2018). Therefore, we may still enable the same dynamical mass transfer and stability criteria in `NBODY6++GPU` and `MOCCA` based on (Hurley et al., 2002). Here, the stability of the mass transfer is determined by the original relations of radius-mass exponents ζ by (Webbink, 1985), which give critical mass ratios of the donor and

accretor star implemented in Hurley et al. (2002). In semi-detached binaries, the primary loses some mass via winds and the secondary can accrete the material if passing through it. This Bondi-Hoyle accretion rate Bondi and Hoyle (1944) (`acc2` in both codes) is sensitive to the wind velocity factor β_W (Hurley et al., 2002). β_W strongly depends on spectral type KW ; the larger the star, the lower β_W . In the BSE implementation of `NBODY6++GPU` (and `PeTar` and `Nbody7`) this is not the case, unlike in the latest versions of `MOCCA` (Belloni, Mikołajewska, et al., 2020), `StarTrack` (Belczynski et al., 2008) and `COSMIC` (Breivik, Coughlin, et al., 2020). The latter is also implemented in the latest version of `CMC` (Kremer, Spera, et al., 2020). We set `beta=0.125` in the simulations following Hurley et al. (2002), where this represents the lower limit and should roughly correspond to the wind from the largest stars of $900R_\odot$. The angular momentum factor for mass loss during RLOF in both codes is set by `gamm1` in `NBODY6++GPU` and `gamma` in `MOCCA` (Hurley et al., 2002). If positive `gamm1=gamma > 0`, then the lost material carries with it a fraction `gamma` of orbital angular momentum. If set to `gamm1=gamma=-1`, then the material carries with it specific angular momentum of the primary and if set to `gamm1=gamma=-2`, then the material is lost from system as if it was a wind from the secondary. The factor to reduce the spin angular momentum change owing to wind accretion is `xi` and the fraction of accreted matter retained in nova eruption is `epsnov` in both codes (Hurley et al., 2002).

Accretion rates onto a NS or BH (Eddington and Super-Eddington) are controlled by the parameter `eddfac` in both codes. Super-Eddington accretion rates are set by (`eddfac=100.0`) (Cameron & Mock, 1967). The Chandrasekhar mass of a WD is set to `MCH = 1.44 M_\odot` (Boshkayev et al., 2013; Mazzali et al., 2007). The maximum NS mass is set to `mxns ≤ 2.5 M_\odot` (Baym et al., 2018, 2019; Lattimer & Prakash, 2004; Linares, 2018). In the `mix.f` and `coal.f` subroutines of `NBODY6++GPU`, (Rizzuto, Naab, Spurzem, Giersz, et al., 2021) implemented a variable `FctorCl`, that controls the mass accretion if a big star ($KW \leq 9$) merges with a BH or NS. If `FctorCl=1`, then the whole star is accreted onto the BH or NS. Likewise, if `FctorCl=0`, then no mass is accreted. `MOCCA` has a similar variable available called `tzo`. We include a post-Newtonian (PN) orbit averaged dynamics treatment according to Peters (1964) and Peters and Mathews (1963) for binaries containing a NS or BH in `grrad.f` in `NBODY6++GPU` and `evol2b.f` in `MOCCA`.

The routine `comenv.f` and the respective parameters (second row in Figure 9.15 and Figure 9.16 for `NBODY6++GPU` and `MOCCA`, respectively) deal with the common envelope evolution following Hurley et al. (2002), which in turn follows Dewi and Tauris (2000) and Tauris et al. (2000). CEE is one of the possible outcomes of RLOF between close binary stars (Ivanova et al., 2013; Ivanova, 2016; Ivanova et al., 2020; Paczynski, 1976). At the end of CEE the envelope of the primary (in some cases also of the secondary) is stripped away and CEE terminates. It is described by two parameters α_{CE} and λ_{CE} ; the first one parameterizes what fraction of the orbital energy is used to liberate the envelope; the second one is a factor scaling the binding energy of the envelope. Both codes also allow the addition of some fraction of recombination energy to the binding energy in

order to lower the threshold for loss of the envelope, depending on the stellar type. The procedure used is similar, but not identical to Claeys et al. (2014).

Still today, both λ_{CE} and α_{CE} remain highly uncertain (De et al., 2020; Everson et al., 2020; Giacobbo & Mapelli, 2018, 2019; Langer et al., 2020; Morawski et al., 2018, 2019; Santoliquido et al., 2020). However, for low-mass stars, given their relatively large numbers in observed samples, such as the post-CE binaries identified by the Sloan Digital Sky Survey (Rebassa-Mansergas et al., 2012), reconstruction techniques and binary population synthesis have allowed us to infer, to some extent, a low value for α_{CE} , which is $\sim 0.2 - 0.3$ (Camacho et al., 2014; Cojocaru et al., 2017; Toonen & Nelemans, 2013; Zorotovic et al., 2010).

9.7.2 Stellar winds

The routine `mlwind.f` and the respective parameters (second row in Figure 9.15 and Figure 9.16 for `NBODY6++GPU` and `MOCCA`, respectively) deal with the mass loss from stars via winds and outflows. In `NBODY6++GPU` and `MOCCA` the choices of wind prescriptions are determined by `mdflag` and `edd_factor`, respectively. Stellar winds and their correct descriptions for our purposes are very important, because they are critical in determining the mass of the compact object progenitors and thus they have a large influence on the compact object mass distributions in the cluster themselves (Belczynski et al., 2010; Giacobbo et al., 2018; Kremer, Spera, et al., 2020). In `NBODY6++GPU` and `MOCCA`, the options of winds are very different in many places and therefore, these are listed independently below. First of all, for `NBODY6++GPU` and `mdflag` ≤ 2 we apply the mass loss of Nieuwenhuijzen and de Jager (1990) for massive stars over the entire HRD with a metallicity factor from Kudritzki et al. (1989). In the case of giant stars, `NBODY6++GPU` calculates the mass loss from Kudritzki and Reimers (1978) (with `neta`=0.477 suggested from McDonald and Zijlstra (2015)). Similarly, for the AGB stars and `mdflag` ≤ 2 BSE follows Vassiliadis and Wood (1993) and we apply the reduced Wolf-Rayet (WR)-like mass loss for small H-envelope masses from Hamann and Koesterke (1998), Hurley et al. (2000), and Reimers (1975). If `mdflag`=2, then the treatment of luminous blue variable (LBV) winds are added, which follow Humphreys and Davidson (1979) and Humphreys and Davidson (1994). For `mdflag`>2, these winds follow the LBV winds of Belczynski et al. (2020). If `mdflag`=3, then for massive and hot O and B-type stars, the code switches on the metallicity dependent winds by Belczynski et al. (2010), Vink and de Koter (2002, 2005), and Vink et al. (2001), who established their mass-loss rates for O and B-type from a grid of wind models across a wide range of metallicities ($10^{-5} < Z/Z_{\odot} < 10$). Caution is advised against the so-called bi-stability jump, which is the drastic change of the character of the driving (ionisation) line, because of a sudden change in the wind ionisation. There is the option available to have these winds without the bi-stability jump Belczynski et al. (2010) (temperature shifted to the edge of the jump) in `NBODY6++GPU` (`mdflag`=4). For more evolved stars starting from naked He stars with `KW` ≥ 7 , with `mdflag` ≥ 3 the metallicity dependent

WR wind factor from Vink and de Koter (2005) is used. For H-rich low mass stars, the mass loss rates remain unchanged Hurley et al. (2000).

In the MOCCA version of BSE, with `eddy_factor=0`, we use fixed α from Giacobbo et al. (2018) in the prescriptions by Belczynski et al. (2010). If `eddy_factor=1`, then the electron-scattered Eddington factor is taken from Gräfener and Hamann (2008) and the exponent of the dependence on metallicity is then calculated from Y. Chen et al. (2015) instead. The rest of the `mlwind.f` routine uses the same prescriptions for the stars for both `eddy_factor=0` and `eddy_factor=1`. The LBV-like mass loss beyond the Humphreys-Davidson limit follows Belczynski et al. (2010) and Humphreys and Davidson (1994). We apply the mass loss of Nieuwenhuijzen and de Jager (1990) for massive stars over the entire HRD with a metallicity factor from Kudritzki and Reimers (1978). In the case of giant stars, MOCCA calculates the mass loss from Kudritzki and Reimers (1978). If `neta>0` (`neta=0.477` from McDonald and Zijlstra (2015) is suggested), then this mass loss is based on Reimers (1975) and if `neta<0` it follows a more realistic setting by Schröder and Cuntz (2005), which takes into account the effective temperature and surface gravity of the star (here `neta=0.172` is suggested). The winds of the AGB stars follow Vassiliadis and Wood (1993) and we apply the reduced Wolf-Rayet (WR) like mass loss for small H-envelope masses from Hamann and Koesterke (1998), Hurley et al. (2000), and Reimers (1975). For massive and hot O and B-type stars, the code switches on the metallicity dependent winds by Belczynski et al. (2010), Vink and de Koter (2002, 2005), and Vink et al. (2001). For more evolved stars starting from naked He stars with $KW \geq 7$, the MOCCA BSE uses the metallicity dependent WR wind factor from Vink and de Koter (2005). We note that the MOCCA BSE does not account for the aforementioned bi-stability jump, so overall the treatment of the winds from MOCCA and `NBODY6++GPU` are most similar for `mdflag=4` \simeq `eddy_factor=0`. We note, that today the wind mass loss from very large mass stars in the regime of WR stars still remains very uncertain and is difficult to model (Higgins et al., 2021; Higgins & Vink, 2019; Sander & Vink, 2020; Sander et al., 2020; Vink, 2021). The same can also be said in general about stars on the lower mass end (Decin, 2020). It is likely that we will need to revise our stellar wind mass loss and terminal velocity models many times in the future with this in mind, especially, when we aim to properly model aLIGO/aVirgo GW source progenitor stars.

9.7.3 Remnant masses of compact objects

The routine `hrdiag.f` and the respective parameters (first row in Figure 9.15 and Figure 9.16 for `NBODY6++GPU` and MOCCA, respectively) deal with the post-SNe remnant masses of the NSs and BHs. In `NBODY6++GPU` and MOCCA the choices of the NS and BH remnant masses are determined by `nsflag` and `compactmass`, respectively. The updated stellar evolution now incorporates a selection of possible SNe pathways, which lead to a variety of remnant masses. In the present versions of the `hrdiag.f` routine, any of the five remnant-mass schemes following Belczynski et al. (2002,

| Code | | Nbody6++GPU | | | | | | MOCCA | | | | | |
|-------------|----------|--|--|--|----------|---|--|-------------------------|---------|--|--|--|--|
| BSE & SSE ? | | Stellar evolution level | | | | | | Stellar evolution level | | | | | |
| Relevance | Routine | Level A | Level B | Level C | Routine | Level A | Level B | Level C | Routine | Level A | Level B | Level C | |
| SSE | hrdiag.f | ecflag = 0 wdflag = 1 nsflag = 1 psflag = 0 | ecflag = 1 wdflag = 1 nsflag = 2,3,4 psflag = 0,1 | psflag = 2,3 | hrdiag.f | ecflag = 0 wdflag = 1 compactmass = 1 piflag = 0 | ecflag = 1 wdflag = 1 compactmass = 2,3,4 piflag = 0,2 | | | ecflag = 0 wdflag = 1 compactmass = 1 piflag = 0 | ecflag = 1 wdflag = 1 compactmass = 2,3,4 piflag = 0,2 | piflag = 1 | |
| SSE | m1wind.f | mdflag = 1 neta = 0.5 bwind = 0.0 flbv = 1.5 | mdflag = 2,3 neta = 0.5 bwind = 0.0 flbv = 1.5 | mdflag = 4 neta = 0.477 bwind = 0.0 flbv = 1.5 | m1wind.f | eddfactor = 0 neta = 0.5 bwind = 0.0 flbv = 1.5 | eddfactor = 0 neta = 0.5 bwind = 0.0 flbv = 1.5 | | | eddfactor = 0 neta = 0.5 bwind = 0.0 flbv = 1.5 | eddfactor = 0 neta = 0.5 bwind = 0.0 flbv = 1.5 | eddfactor = 1 neta = 0.477, -0.172 bwind = 0.0 flbv = 1.5 | |
| BSE | comenv.f | LAMBDA = 0.5 ALPHA1 = 3.0 | LAMBDA = 0.5 ALPHA1 = 3.0 | LAMBDA = 0.0 ALPHA1 = 1.0 | comenv.f | lambda = 0.5 alpha = 3.0 | lambda = 0.5 alpha = 3.0 | | | lambda = 0.5 alpha = 3.0 | lambda = 0.5 alpha = 3.0 | lambda = 0.0 alpha = 1.0 | |
| BSE | kick.f | bhflag = 0 KMECH = 1 disp = 30.0, 190.0, 265.0 ecsig = 20.0 wdsig1 = 2.0 wdsig2 = 2.0 wdkmax = 6.0 vfac = 0.0 | bhflag = 2 KMECH = 1,2,3 disp = 265.0 ecsig = 3.0 wdsig1 = 2.0 wdsig2 = 2.0 wdkmax = 6.0 vfac = 0.0 | bhflag = 3,4 KMECH = 4 disp = 265.0 ecsig = 3.0 wdsig1 = 2.0 wdsig2 = 2.0 wdkmax = 6.0 vfac = 0.0 | kick.f | sigmans = 30.0, 190.0, 265.0 sigmabh = 30.0, 190.0, 265.0 bhflag_kick = 0,1,2 nsflag_kick = 0,1,2 sigmac = 20.0 | sigmans = 265.0 sigmabh = 265.0 bhflag_kick = 3,4,5 nsflag_kick = 3,4,5 sigmac = 3.0 | | | sigmans = 265.0 sigmabh = 265.0 bhflag_kick = 3,4,5 nsflag_kick = 3,4,5 sigmac = 3.0 | sigmans = 265.0 sigmabh = 265.0 bhflag_kick = 6 nsflag_kick = 6 sigmac = 3.0 | | |
| BSE | roche.f | acc2 = 1.5 beta = 0.125 epsnov = 0.001 eddfac = 100.0 gamm1 = -1.0 xi = 1.0 | acc2 = 1.5 beta = 0.125 epsnov = 0.001 eddfac = 100.0 gamm1 = -1.0 xi = 1.0 | acc2 = 1.5 beta = 0.125 epsnov = 0.001 eddfac = 100.0 gamm1 = 0.0, -2.0 xi = 1.0 | roche.f | acc2 = 1.5 beta = 0.125 epsnov = 0.001 eddfac = 100.0 gamma = -1.0 xi = 1.0 | acc2 = 1.5 beta = 0.125 epsnov = 0.001 eddfac = 100.0 gamma = -1.0 xi = 1.0 | | | acc2 = 1.5 beta = 0.125 epsnov = 0.001 eddfac = 100.0 gamma = -1.0 xi = 1.0 | acc2 = 1.5 beta = 0.125 epsnov = 0.001 eddfac = 100.0 gamma = -1.0 xi = 1.0 | acc2 = 1.5 beta = 0.125 epsnov = 0.001 eddfac = 100.0 gamma = 0.0, -2.0, 3.0 xi = 1.0 | |

Figure 9.14: Table showing our stellar evolution levels A, B and C with respect to changes in the stellar evolution routines and the parameters in the codes Nbody6++GPU (left) and MOCCA (right). The parameters used in the simulations of this study (delayedSNe-Uniform & rapidSNe-Sana) are shown in orange. All excluded stellar evolution routines not shown in the table are largely identical to the original SSE and BSE (Hurley et al., 2000, 2002). The exact meaning of the parameters and the literature basis for the choice of these are given in Figure 9.15 for Nbody6++GPU and in Figure 9.16 for MOCCA. Level C includes stellar evolution settings that are available in the codes, but those that are not present in level B have not yet undergone sufficient testing and are therefore deemed experimental as of the writing of this paper.

2008), Eldridge and Tout (2004), and C. L. Fryer et al. (2012) may be chosen. In this paper the *rapid* (`nsflag=compactmass=3`) and *delayed* (`nsflag=compactmass=4`) SNe mechanisms are used as extremes for the convection-enhanced neutrino-driven SNe paradigm (C. L. Fryer et al., 2012).

In `hrdiag.f`, we can also set the pulsating pair instability SNe (PPISNe) resulting from electron-positron pair production and subsequent decreasing pressure support in massive He cores. These electron-positron pairs effectively remove pressure from outward photons, until the oxygen in the stellar core ignites in a flash, which creates a pulse and a thermonuclear reaction in the outward direction, after which the core stabilises. In even more massive He cores, the core does not stabilise and creates many of the above pulses, which leads to a failed or disrupted SNe, as the star is completely destroyed in the process. This is known as pair instability SNe (PISNe). Both of these processes are theoretically well understood (Belczynski et al., 2016; Brevik, Coughlin, et al., 2020; Kremer, Spera, et al., 2020; Leung, Blinnikov, et al., 2020; Leung et al., 2019; Woosley, 2017). In `NBODY6++GPU` and `MOCCA` `psflag` and `piflag` determine the BH remnant masses that are produced by a (P)PISNe. By setting `psflag=piflag=0`, the progenitor star in the He core mass range of $65.0 \leq m_{\text{He}}/M_{\odot} \leq 135.0$ is destroyed in the SN explosion (`KW=15`). With `psflag=1` or `piflag=2` the maximum He core mass is set to $45.0 M_{\odot}$, below which the PISNe is not activated (Belczynski et al., 2016). In their scheme, the BH mass from a PPISNe is set to $40.5 M_{\odot}$ from $45.0 M_{\odot}$ minus a 10% neutrino mass loss (Timmes et al., 1996). In the range of $45.0 \leq m_{\text{He}}/M_{\odot} \leq 135.0$ the star is destroyed by PISNe. Additionally, for `NBODY6++GPU` `psflag=2,3` the so-called *moderate* (P)PISNe and *weak* (P)PISNe following (Leung et al., 2019) may be set. These models again assume a 10% neutrino loss in the PPISNe and set for He core mass range of $40.0 \leq m_{\text{He}}/M_{\odot} \leq 65.0$ linearly increasing BH remnant masses dependent on the initial stellar mass. In the mass range of $60.0 \leq m_{\text{He}}/M_{\odot} \leq 62.5$, the BH remnant masses (including 10% neutrino loss) are $50.04 M_{\odot}$ for the weak and $46.08 M_{\odot}$ for the moderate PPISNe, respectively. These two (P)PISNe prescriptions are not yet available in `MOCCA`. With `piflag=1` we activate the remnant mass scheme by Spera and Mapelli (2017) in `MOCCA`, who fit the compact remnants as a function of the final He mass fraction and final He core mass (Woosley, 2017). However, they fitted the data using the `SEVN` code (Spera et al., 2015) and not any variant of the `BSE` and so this should be used with caution in `Nbody6++GPU` & `MOCCA`.

At the lower end of the progenitor mass spectrum, `NBODY6++GPU` and `MOCCA` have implementations of electron-capture SNe (ECSNe) (Gessner & Janka, 2018; Ivanova et al., 2008; Kiel et al., 2008; Leung, Nomoto, & Suzuki, 2020; Nomoto, 1984; Nomoto, 1987; Podsiadlowski et al., 2004), which are activated using `ecflag=1` in both codes for progenitor stars in the range of $8 \leq m/M_{\odot} \leq 11$. Detailed studies of the behaviour of these stars in direct N -body simulations may be found in Banerjee (2018) and Fragione and Banerjee (2020) and in CMC models in Ye et al. (2019). The progenitor stars build up He cores in a theoretical uncertain range of $1.4 \leq m_{\text{He}}/M_{\odot} \leq 2.5$ (Belczynski et al., 2008; Hurley et al., 2002; Podsiadlowski et al., 2004), where in

NBODY6++GPU and MOCCA we take $1.6 \leq m_{\text{He}}/M_{\odot} \leq 2.25$ from Hurley et al. (2002). In these cores, Ne and Mg capture electrons, thus effectively removing electron pressure from the cores, and if the stellar core mass (m_{cX}) surpasses the ECSNe critical mass of $1.372 M_{\odot}$ (Ivanova et al., 2008), the star collapses almost instantaneously, unlike the neutrino-driven core-collapse explosions. This instantaneous explosion also means that the ECSNe NS has no fallback mass leaving behind NSs with a characteristic mass of $m = 1.26 M_{\odot}$ (Belczynski et al., 2008). In binaries, accretion may lead to an accretion-induced collapse (AIC) (Nomoto & Kondo, 1991; Saio & Nomoto, 2004), when an ONeWD accretes material from a COWD or ONeWD and the resulting ONeWD exceeds the ECSNe critical mass (Hurley et al., 2002; Nomoto & Kondo, 1991). Similarly, if this mass is surpassed by a COWD-COWD or ONeWD-ONeWD merger, then the result is a merger-induced collapse (MIC) (Saio & Nomoto, 1985), which is treated the same as an AIC if the ECSNe critical mass is surpassed. The kicks for the ECSNe, AIC and MIC are all drawn from the same Maxwellian, see below. All the above paths generally produce NSs in binaries, which can often lead to subsequent RLOF and the production of low-mass X-ray binaries (LMXBs; in GCs see Clark (1975)) and millisecond pulsars (MSPs; in GCs see Manchester et al. (2005)).

9.7.4 Compact object natal kick distributions

The routines `kick.f` in NBODY6++GPU and `kickv.f` in MOCCA and the respective parameters (fourth row in Figure 9.15 and Figure 9.16 for NBODY6++GPU and MOCCA, respectively) deal with the (fallback-scaled) kick distributions of the compact objects. The purpose of updating this routine is to retain some of the compact objects in dense clusters of all sizes (OCs, GCs, NSCs) in order of increasing escape velocity v_{esc} (Baumgardt & Hilker, 2018; Portegies Zwart et al., 2010; Schödel et al., 2014) based on physically motivated SNe mechanisms. This is crucial since the simulations need to properly treat the formation of NSs and BHs in these environments (Giesers et al., 2018, 2019; Kuranov & Postnov, 2006; Portegies Zwart et al., 2010) and it makes the formation and survival of complex compact binaries such as NS-NS, and BH-BH possible (Banerjee et al., 2020; C. Fryer & Kalogera, 1997).

How these kicks are constrained remains uncertain and is highly theoretical. The origin of these kicks come from asymmetries either due to further in-falling material or accretion onto the proto-NS core and/or strong neutrino-driven convection during the long phase after the stalling of the first shockwave, which has bounced off of the proto-NS core. Traditionally, the kicks for the NSs are given by Hobbs et al. (2005), i.e. following a Maxwellian with a velocity dispersion of 265.0 km s^{-1} . However, before this work, a dispersion of 190.0 km s^{-1} by Hansen and Phinney (1997) was also frequently used. Drawing natal kicks from these Maxwellians with these velocity dispersions would effectively kick all NSs out of the cluster, which can be observed in the output of the Dragon simulations by Wang et al. (2016): they use a high and a low velocity dispersion,

265.0 kms^{-1} from Hobbs et al. (2005) and 30.0 kms^{-1} inspired by Manchester et al. (2005), respectively.

The LIGO/Virgo detections of the gravitational wave sources coming from a NS-NS binary (B. P. Abbott et al., 2017a, 2017b; R. Abbott et al., 2020a) or other NS binaries observed in star clusters (Benacquista & Downing, 2013) inspired the update of the natal kicks for these NSs. To this end, for the ECSNe, AIC and MIC, the kick distribution is now a Maxwellian with a velocity dispersion of 3.0 kms^{-1} (ECSIG in Nbody6++GPU and sigmac in MOCCA) following Gessner and Janka (2018), who used detailed 2-D and 3-D simulations to model these processes. We note that other groups, for example, the COSMIC developers (Breivik, Coughlin, et al., 2020) use 20.0 kms^{-1} and the MOBSE team (Giacobbo et al., 2018) use 15.0 kms^{-1} in previous simulations. The justification for the low velocity dispersions are that the ECSNe, AIC or MIC are modelled as instantaneous events (Hurley et al., 2002; Ivanova et al., 2008; Podsiadlowski et al., 2004).

All other NSs and BHs that do not undergo ECSNe, AIC or MIC have their kicks traditionally scaled by the before-mentioned fallback onto the proto-remnant core (Belczynski et al., 2008; C. L. Fryer et al., 2012), which most importantly implies that the larger the fallback, the lower the natal kick is and if $f_b=1$, then the natal kick is zero. This would be called a direct collapse or a *failed* SN. The variables to set the kicks are KMECH in Nbody6++GPU (which also necessitates setting bhflag ≥ 2 for all KMECH) and bhflag_kick for the BHs and nsflag_kick for the NSs in MOCCA. Therefore, in MOCCA we may enable separate kick mechanisms with different kick velocity dispersions (sigmans, sigmabh), whereas all the kicks in Nbody6++GPU excluding the ECSNe, AIC and MIC are drawn from the same Maxwellian with dispersion disp.

On top of the standard momentum-conserving kick mechanism (KMECH=1, bhflag_kick=nsflag_kick=3), there are the convection-asymmetry-driven (KMECH=2, bhflag_kick=nsflag_kick=4) (C. L. Fryer & Young, 2007; Scheck et al., 2004, 2008), collapse-asymmetry-driven (KMECH=3, bhflag_kick=nsflag_kick=5) (Burrows & Hayes, 1996; C. L. Fryer, 2004; Meakin & Arnett, 2006, 2007) and neutrino-driven natal kicks (KMECH=4, bhflag_kick=nsflag_kick=6) (Banerjee et al., 2020; C. L. Fryer & Kusenko, 2006; G. M. Fuller et al., 2003) options, where the authors assume *one* dominant kick mechanism in the SNe. In MOCCA and Nbody6++GPU, we also make this assumption. The equations for the kick velocity of the compact object in Nbody6++GPU and MOCCA mirror those in Nbody7 (Banerjee et al., 2020). We note that both MOCCA and Nbody6++GPU both have implementations for WD natal kicks (Fellhauer et al., 2003; Jordan et al., 2012; Vennes et al., 2017), but they are not the same. In MOCCA, these WD kicks are the same for WD types and are assigned an arbitrary kick speed of vkickwd, unlike in Nbody6++GPU, which draws kicks for HeWDs and COWDs from a Maxwellian of dispersion wdksig1 and the kicks for the ONeWDs from a Maxwellian with dispersion wdksig2. Both Maxwellians are truncated at wdkmax=6.0 kms^{-1} , where typically wdksig1=wdksig2=2.0 kms^{-1} following Fellhauer et al. (2003).

9.7.5 Compact objects natal spins

The aforementioned routines `kick.f` in `NBODY6++GPU` and `kickv.f` in `MOCCA` and the respective parameters (fourth row in [Figure 9.15](#) and [Figure 9.16](#) for `NBODY6++GPU` and `MOCCA`, respectively) also deal with the natal spins distributions of the BHs. In `NBODY6++GPU` these spins are controlled by the variable `bhflag`. The latest version of `NBODY6++GPU` includes updated *metallicity-dependent* treatments of BH natal spin (the natal NS spins are not changed from the original BSE), which follow those of Banerjee (2021a) and Belczynski et al. (2020). This is needed, because the spin angular momentum of the parent star does not necessarily translate directly into the natal spin angular momentum of the BH. We define a dimensionless parameter that accounts for the natal spin angular momentum following Kerr (1963). Like Banerjee (2021a), we assume the magnitude of this parameter for the BHs directly at their birth without any mass accretion of GR coalescence processes. The simplest model of BH natal spins, the Fuller model, produces zero natal spins (Banerjee, 2021a) (`bhflag=2`), as here the Tayler-Spruit magnetic dynamo can essentially extract all of the angular momentum of the proto-remnant core, leading to nearly non-spinning BHs (J. Fuller & Ma, 2019; J. Fuller et al., 2019; Spruit, 2002). The second spin model is the Geneva model (Banerjee, 2021a; Eggenberger et al., 2008; Ekström et al., 2012) (`bhflag=3`). The basis for this model is the transport of the angular momentum from the core to the envelope. This is only driven by convection, because the Geneva code does not have magnetic fields in the form of the Taylor-Spruit magnetic dynamo. This angular momentum transport is comparatively inefficient and leads to *high* natal spins for low to medium mass parent O-type stars, whereas for high mass parent O-type stars, the angular momentum of the parent star may already have been transported away in stellar winds and outflows and thus the natal BH spins may be low. The third and last spin model is the MESA model (`bhflag=4`), which also accounts for magnetically driven outflows and thus angular momentum transport (Banerjee, 2021a; J. Fuller et al., 2019; Paxton et al., 2011, 2015; Spruit, 2002). This generally produces BHs with much *smaller* natal spins than the Geneva model described above.

| Relevance | Routine | Parameter | Parameter option and source |
|-----------|----------|---|--|
| SSE | hrdiag.f | ecflag - Enables or disables ECSNe nsflag - Choices for how NS/BH masses are calculated psflag - No, strong, weak or moderate PPISNe wdflag - Choices for how the white dwarfs are cooled | ecflag = 0 → No ECSNe, ecflag = 1 → ECSNe from (Belczynski et al. 2008) nsflag = 0 → Use original SSE NS/BH mass (Hurley et al. 2000) nsflag = 1 → Use FeNi core mass from (Belczynski et al. 2002) nsflag = 2 → Use FeNi core mass from (Belczynski et al. 2008) nsflag = 3 → Remnant masses with rapid SNe (Fryer et al. 2012) nsflag = 4 → Remnant masses with delayed SNe (Fryer et al. 2012) nsflag = 5 → Remnant masses from (Eldridge & Tout 2004) psflag = 0 → No PPISNe/PISNe psflag = 1 → Strong PPISNe/PISNe (Belczynski et al. 2016) psflag = 2 → Weak PPISNe/PISNe (Leung et al. 2019a, 2020c) psflag = 3 → Moderate PPISNe/PISNe (Leung et al. 2019a, 2020c) wdflag = 0 → Mestel cooling (Mestel 1952) wdflag = 1 → Modified Mestel cooling (Tout et al. 1997) |
| SSE | mlwind.f | mdflag - Sets the wind mass-loss prescription meta - Reimers mass-loss coefficient for giant winds bwind - Companion-enhanced mass-loss factor flbv - Coefficient for LBV wind rate if mdflag > 2 | mdflag = 1 → Mass loss from (Hurley et al. 2000) mdflag = 2 → Mass loss added for LBVs (Humphreys & Davidson 1979) & (Belczynski et al. 2010) mdflag = 3 → Mass loss from (Belczynski et al. 2010) + Metallicity factor from (Vink et al. 2001) + Mass loss for hot, massive O/B stars from (Vink et al. 2001) mdflag = 4 → Mass loss without bi-stability jump (Belczynski et al. 2010) + Metallicity factor from (Belczynski et al. 2010) meta = 0.5 (Kudritzki & Reimers 1978), meta = 0.477 (McDonald & Zijlstra 2015) bwind = 0.0, (Hurley et al. 2002) flbv = 1.5 (Belczynski et al. 2010) |
| BSE | comenv.f | LAMBDA - Structural parameter for giant envelope and control of recombination energy used ALPHA1 - factor scaling the amount of orbital energy used for envelope liberation in CEE | lambda = 0.5, alpha = 3.0 (Giacobbo & Mapelli 2018) (A _{CE} : depends on stellar type and recombination energy; α_{CE} = ALPHA1) lambda = 0.0, alpha = 1.0 (A _{CE} : depends on stellar type, NO recombination energy used; α_{CE} = ALPHA1, see Appendix A1) |
| BSE | kick.f | bhflag - BH kicks, same as for CC NSs but reduced for momentum cons. if fallback kmech - NS, BH kick mechanism: standard momentum cons., convection-asymm., collapse-asymm. & neutrino driven disp - Dispersion in a Maxwellian velocity distribution or the maximum value for a flat distribution eccsig - Dispersion for ECSNe wdsig1 - Dispersion for He and CO WDs wdsig2 - Dispersion for ONe WDs wldmax - Maximum WD kick velocity, vfac - Option to scale by VSTAR | bhflag = 0 → No BH kicks bhflag = 1 → unscaled kicks: BHs & NSs (Belczynski et al. 2002) bhflag = 2 → fallback-scaled kicks for BHs and NSs (KMECH) bhflag = 3 → KMECH kicks + BH natal spins Geneva models (Banerjee et al. 2020; Banerjee 2021b) bhflag = 4 → KMECH kicks + BH natal spins MESA models (Banerjee et al. 2020; Banerjee 2021b) bhflag > 4 → KMECH kicks + BH natal spins Fullier model (Banerjee et al. 2020; Banerjee 2021b) KMECH = 1 → standard mom. conserving kick (Belczynski et al. 2008) KMECH = 2 → Convection-asymm.-driven kick (Banerjee et al. 2020) KMECH = 3 → Collapse-asymm.-driven kick (Banerjee et al. 2020) KMECH = 4 → Neutrino-driven kick (Banerjee et al. 2020) disp = 30.0 (Wang et al. 2016), disp = 190.0 (Hansen & Phinney 1997), disp = 265.0 (Hobbs et al. 2005) eccsig = 3.0 (Gessner & Janka 2018), wdsig1 = wdsig2 = 2.0, wldmax = 6.0 (Teilhauer et al. 2003) |
| BSE | roche.f | acc2 - Bondi-Hoyle wind accretion efficiency factor beta - Wind velocity factor epsnow - Fraction of material accreted onto a WD ejected in a nova eddfac - Eddington limit for accretion onto a degenerate object gam1 - Choices for angular momentum changes owing to RLOF mass-loss xi - Factor to reduce spin angular momentum change owing to wind accretion | acc2 = 1.5 Bondi & Hoyle (1944) beta = 0.125 → lower limit (Hurley et al. 2002) epsnow = 0.001 (Hurley et al. 2002) eddfac = 100 → 100x Eddington limit accretion rate (Hurley et al. 2002) gam1 = -2.0 → Super-Eddington mass transfer rates (Hurley et al. 2002) gam1 = -1.0 → Lost material carries with it the specific angular momentum of the primary (Hurley et al. 2002) gam1 > 0.0 → takes away a fraction gam1 of J_{orb} (Hurley et al. 2002) xi = 1.0 (Hurley et al. 2002) |

Figure 9.15: Table showing the options in the SSE & BSE stellar evolution with respect to the parameters in Nbody6++GPU. The parameters used in the simulations of this study (delayedSNe-Uniform & rapidSNe-Swana) are shown in orange. The parameters that are present in Nbody6++GPU version but not in MOCCA are shown in red. All the stellar evolution routines not listed here are largely identical to the original SSE and BSE (Hurley et al., 2000, 2002). The abbreviations are as follows: ECSNe - electron capture supernova, AIC - accretion-induced collapse, MIC - merger-induced collapse, PPISNe - pulsating pair instability supernova, PISNe - pair instability supernova, LBV - luminous blue variable, NS - neutron star, BH - black hole.

| | | | |
|-----|----------|--|--|
| SSE | hrdiag.f | <p>ecflag - Enables or disables ECSNe compactmass - Choices for how NS/BH masses are calculated piflag - No, strong or Spera PISNe wdflag - Choices for how the white dwarfs are cooled</p> | <p>ecflag = 0 → No ECSNe ecflag = 1 → ECSNe with remnant mass from (Belczynski et al. 2008) compactmass = 0 → Use original SSE NS/BH mass (Hurley et al. 2000) compactmass = 1 → Use FeNi core mass from (Belczynski et al. 2002) compactmass = 2 → Use FeNi core mass from (Belczynski et al. 2008) compactmass = 3 → Remnant masses with rapid SNe (Fryer et al. 2012) compactmass = 4 → Remnant masses with delayed SNe (Fryer et al. 2012) compactmass = 5 → Remnant masses from (Eldridge & Tout 2004) piflag = 0 → No PISNe/PISNe piflag = 1 → PISNe/PISNe (Spera & Mapelli 2017) piflag = 2 → Strong PISNe/PISNe (Belczynski et al. 2016) wdflag = 0 → Mestel cooling (Mestel 1952) wdflag = 1 → Modified Mestel cooling (Tout et al. 1997)</p> |
| SSE | mlwind.f | <p>edd_factor - Sets the wind mass-loss prescription meta - Reimers mass-loss coefficient for giant winds bwind - Companion-enhanced mass-loss factor flbv - Coefficient for LBV wind rate if mdflag > 2</p> | <p>edd_factor = 0 → Mass loss from (Belczynski et al. 2010; Chen et al. 2015) edd_factor = 1 → Mass loss from (Chen et al. 2015; Giacobbo et al. 2018) meta = 0.5 (Kudritzki & Reimers 1978), meta = 0.477 (McDonald & Zijlstra 2015) neta = -0.172 (Schröder & Cumz 2005) bwind = 0.0, (Hurley et al. 2002) flbv = 1.5 (Belczynski et al. 2010)</p> |
| BSE | comenv.f | <p>LAMBDA - Structural parameter for giant envelope and control of recombination energy used ALPHA1 - factor scaling the amount of orbital energy used for envelope liberation in CEE</p> | <p>lambda = 0.5, alpha = 3.0 (Giacobbo & Mapelli 2018) (ACS: depends on stellar type and recombination energy; ace = ALPHA1) lambda = 0.0, alpha = 1.0 (ACE: depends on stellar type, NO recombination energy used; ace = ALPHA1, see Appendix A1)</p> |
| BSE | kick.f | <p>nsflag_kick, bhflag_kick - BH kicks, same as for CC NSs but reduced for momentum cons. for fallback: standard momentum cons., convection-asymm. collapse-asymm. & neutrino driven sigmabh - NS/BH Maxwellian kick velocity dispersion sigmac - ECSNe/AIC/MIC Maxwellian kick velocity dispersion vki ckwd - He/CO/ONeWDs Maxwellian kick velocity dispersion</p> | <p>nsflag_kick, bhflag_kick = 0 → no kicks at all nsflag_kick, bhflag_kick = 1 → kicks for single NS formation only nsflag_kick, bhflag_kick = 2 → kicks for single and binary formation NS nsflag_kick, bhflag_kick = 3 → standard mom. conserving kick (Belczynski et al. 2008) nsflag_kick, bhflag_kick = 4 → Convection-asymm.-driven kick (Scheek et al. 2004; Fryer & Young 2007; Banerjee et al. 2020) nsflag_kick, bhflag_kick = 5 → Collapse-asymm.-driven kick (Fryer 2004; Meakin & Arnett 2006; Banerjee et al. 2020) nsflag_kick, bhflag_kick = 6 → Neutrino-driven kick (Fuller et al. 2003; Fryer & Kusenko 2006; Banerjee et al. 2020) sigmabh = 190.0 (Hansen & Phinney 1997), sigmans, sigmabh = 30.0 (Wang et al. 2016) sigmac = 3.0 (Gessner & Janka 2018) vki ckwd = 0.0, vki ckwd = 2.0 (Fellhauer et al. 2003)</p> |
| BSE | evol2b.f | <p>acc2 - Bondi-Hoyle wind accretion efficiency factor beta - Wind velocity factor epsnow - Fraction of material accreted onto a WD ejected in a nova eddfac - Eddington limit for accretion onto a degenerate object gamma - Choices for angular momentum changes owing to RLOF mass-loss xi - Factor to reduce spin angular momentum change owing to wind accretion</p> | <p>acc2 = 1.5 Bondi & Hoyle (1944) beta = 0.125 → lower limit (Hurley et al. 2002) epsnow = 0.0 (Hurley et al. 2002) eddfac = 100 → 100× Eddington limit accretion rate (Hurley et al. 2002) gamma = -2.0 → Super-Eddington mass transfer rates (Hurley et al. 2002) gamma = -1.0 → Lost material carries with it the specific angular momentum of the primary (Hurley et al. 2002) gamma > 0.0 → takes away a fraction gamma of J_{orb} (Hurley et al. 2002) gamma = 3 → following MB prescriptions by (Rappaport et al. 1983; Belloni et al. 2018b) xi = 1.0 (Hurley et al. 2002)</p> |

Figure 9.16: Table showing the options in the SSE & BSE stellar evolution with respect to the parameters in MOCCA. The parameters used in the simulations of this study (deLaydSNe-Uni form & rapidSNe-Sana) are shown in orange. The parameters that are present in MOCCA version but not in Nbody6++GPU are shown in red (the added CV and symbiotic star treatment by Belloni, Mikołajewska, et al. (2020) and Belloni, Schreiber, et al. (2018) are not listed here). All the stellar evolution routines not listed here are largely identical to the original SSE and BSE (Hurley et al., 2000, 2002). The abbreviations are as follows: ECSNe - electron capture supernova, AIC - accretion-induced collapse, MIC - merger-induced collapse, PISNe - pulsating pair instability supernova, PISNe - pair instability supernova, LBV - luminous blue variable, NS - neutron star, BH - black hole.

9.8 *McLuster*

In this paper we present the updated SSE & BSE routines in *McLUSTER*, a code that is used mainly for the initialisation of star cluster simulations and that is described in detail in Küpper et al. (2011a). These include all of the stellar evolution contained in the levels A, B and C. This version provides a framework, in which we can evolve the different stellar populations at the level of stellar evolution that is also discussed in this paper. This is helpful in the following way. If we want to study the evolution of clusters with multiple stellar populations as observed in Gratton et al. (2012), Kamann, Giesers, et al. (2020), Latour et al. (2019), and Milone, Piotto, Bedin, King, et al. (2012) using *NBODY6++GPU* and *MOCCA*, we can create initial models, where the first population of stars in the case of two populations has a slight offset in epoch and has thus undergone stellar evolution. This stellar evolution can then be modelled with the up-to-date stellar evolution routines contained in our SSE & BSE codes. In principle, however, this code may also be used as a pure population synthesis code, because by setting the epoch parameter we may age the population(s) up to any point in time and look at the detailed evolution of each single or binary star over the whole epoch. If used in this way, *McLUSTER* can be used for a large number of studies. It could shed light on the how stellar evolution levels affects the formation of BH-BH, BH-NS and NS-NS mergers or how they affect the development of low- and high-mass X-ray binaries (or their progenitors). Moreover, we can explore how stellar mergers would affect the overall mass function, and what the role of stellar evolution levels and orbital parameters in the determination of these are.

The parameters are set in `mcluster.ini` file. Here, we may switch on and off the stellar evolution by setting `BSE=1` or `BSE=0`. Below that all the options as outlined in Figure 9.15 are available. We note that the BHs have natal spins set by the parameter `bhspin` in the *McLUSTER* version, and these are set in the routines `evol1.f` for the single stars and in `evol2.f` for the binary stars. This is in part due to the different structure in the SSE & BSE in *NBODY6++GPU*. The *McLUSTER* version produces next to the `dat.10`, which may be used as an input file for the *NBODY6++GPU* simulations and the `single_nbody.dat` and `binary_nbody.dat` for the *MOCCA* simulations (through the appropriate choice of the parameter `outputf` in `mcluster.ini`), also the following files. First of all, if `BSE=1`, we get the output file `vkick.dat`, which contains the velocity kick information for all the compact objects in the population. The files `singles.dat` and `binaries.dat` contain furthermore, the luminosities, effective temperatures, core masses and radii, stellar radii, envelope masses and radii, stellar spins and all the velocity kick information for all the stars and not just the compact objects.

In the following two subsections, we present results from two small studies with our *McLUSTER* version. Future additions in this *McLUSTER* version may be found in the section 5.2 and are grouped together in the stellar evolution level D.

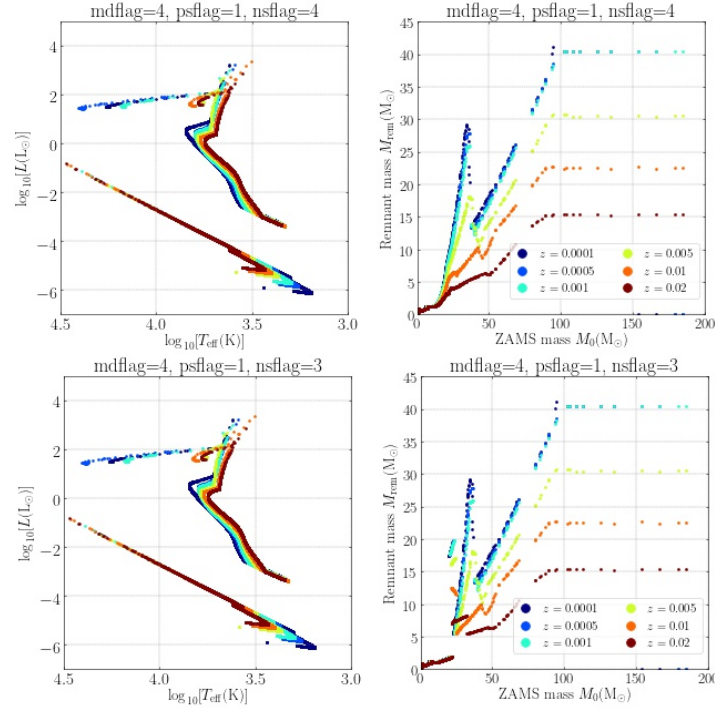


Figure 9.17: HRDs for the McLUSTER samples ($N = 1.0 \times 10^5$ single ZAMS stars) for all stars and the IFMRs of the compact objects depending on six different metallicities ranging from $Z=0.0001$ to Solar metallicity at $Z=0.02$. On top, the results for delayed SNe ($nsflag=4$) and on the bottom the results for the rapid SNe are shown ($nsflag=3$) (C. L. Fryer et al., 2012). The ZAMS stars suffer wind mass loss via $mdflag=4$ (no bi-stability jump) (Belczynski et al., 2010) and the (P)PISNe are set to $psflag=1$ from Belczynski et al. (2016).

9.8.1 Remnant-masses of compact objects

Delayed & rapid SNe and metallicity dependence

We simulate a star sample made up of only single ZAMS stars of size $N = 1.0 \times 10^5$ up to an epoch=12000.0, so 12 Gyr. The IMF is a Kroupa (2001) IMF between $(0.08-150.0)M_{\odot}$. We investigate a range of metallicities Z for the two extremes of the core-collapse SNe paradigm, the rapid $nsflag=3$ and the delayed $nsflag=4$ SNe (C. L. Fryer et al., 2012). The ZAMS stars suffer wind mass loss via $mdflag=4$, i.e. we ignore the bi-stability jump (Belczynski et al., 2010) (and the Reimer’s mass loss coefficient set to $\eta_{\alpha}=0.477$ (McDonald & Zijlstra, 2015)), and the (P)PISNe are set to $psflag=1$ from Belczynski et al. (2016). The specific time-steps $pts1$, $pts2$, $pts3$ follow suggestions from Banerjee et al. (2020). The random seeds in McLUSTER are the same ($seedmc=19640916$) for all samples and therefore, we are evolving the identical ZAMS sample each time.

The results are shown in Figure 9.17 for the delayed SNe on the top and the rapid SNe on the bottom. For both the remnant masses decrease continuously for increasing metallicity. This is mainly due to the fact that at lower metallicities the mass loss from the stars before undergoing a core-collapse SNe (or another evolutionary process that leads to a compact object) is lower than at large metallicities (Vink & de Koter, 2005; Vink et al., 2001). At metallicities as large as $Z=0.005$, the mass loss is so large and the resulting BH mass so low that the

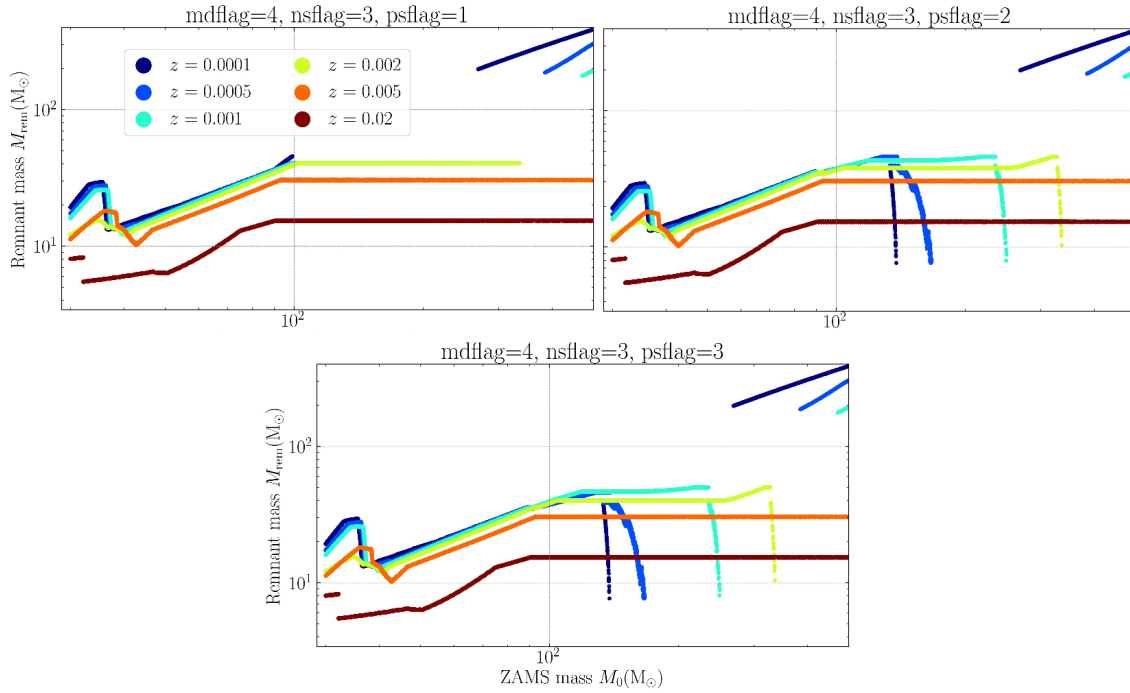


Figure 9.18: IFMRs of the BHs from the McLUSTER samples ($N = 2.5 \times 10^4$ single ZAMS stars) depending on six different metallicities ranging from $Z=0.0001$ to Solar metallicity at $Z=0.02$. Shown are the (P)PISNe recipes for $\text{psflag}=1$ on top (Belczynski et al., 2016), $\text{psflag}=2$ in the middle (Leung, Blinnikov, et al., 2020; Leung et al., 2019) and $\text{psflag}=3$ on the bottom (Leung, Blinnikov, et al., 2020; Leung et al., 2019). The ZAMS stars suffer wind mass loss via $\text{mdflag}=4$ (no bi-stability jump) (Belczynski et al., 2010) and the core-collapse SNe are rapid (C. L. Fryer et al., 2012).

(P)PISNe are not triggered at all, see Figure 9.18. The results mirror those from Banerjee et al. (2020) and therefore the implementations in Nbody7, which confirms an accurate implementation of Levels A, B and C in McLUSTER.

(P)PISNe and metallicity dependence

We simulate a star sample made up of only single ZAMS stars of size $N = 2.5 \times 10^4$ up to an epoch=12000.0, so 12 Gyr. The IMF is a Kroupa (2001) IMF between $(30.0-500.0)M_{\odot}$. We note that this is a large extrapolation of what should be considered safe in the original SSE & BSE (Hurley et al., 2000, 2002). But these masses are reached already in dense simulations, see Arca-Sedda et al. (2021), Di Carlo et al. (2021), Rizzuto, Naab, Spurzem, Arca-Sedda, Giersz, et al. (2021), and Rizzuto, Naab, Spurzem, Giersz, et al. (2021). We need the implementations in the SSE&BSE from Hijikawa et al. (2021), Tanikawa, Susa, et al. (2021), and Tanikawa et al. (2020) to properly model these stars in McLUSTER in the future. We investigate a range of metallicities Z (0.0001-0.02). The ZAMS stars suffer wind mass loss via $\text{mdflag}=4$, i.e. we ignore the bi-stability jump (Belczynski et al., 2010) (and the Reimer’s mass loss coefficient set to $\text{meta}=0.477$ (McDonald & Zijlstra, 2015)), and we subject the stars to the rapid SNe core-collapse prescription (C. L. Fryer et al., 2012). The specific time-steps pts1 , pts2 , pts3 follow suggestions from Banerjee et al. (2020). We investigate a range of metallicities Z for the available (P)PISNe recipes: $\text{psflag}=1$ (Belczynski et al., 2016), $\text{psflag}=2$ (Leung, Blinnikov, et al., 2020; Leung et al., 2019) and $\text{psflag}=3$

(Leung, Blinnikov, et al., 2020; Leung et al., 2019). The random seeds in `McLUSTER` are the same (`seedmc=19640916`) for all samples and therefore, we are evolving the identical ZAMS sample each time. The results are shown in [Figure 9.18](#). We see that the main difference between the three prescriptions is the onset of the (P)PISNe and the masses that result thereof. For low metallicities ($z < 0.001$), the Leung, Blinnikov, et al. (2020) and Leung et al. (2019) (P)PISNe produce high mass BHs for much larger ZAMS masses than the Belczynski et al. (2016) (P)PISNe. At metallicities as large as $Z=0.005$, the mass loss is so large and the resulting BH mass so low that the (P)PISNe are not triggered at all, see also [Figure 9.17](#). Here, the remnant masses then coincide for all `psflag` ($z > 0.005$). At large ZAMS and at the offset of the PISNe, the BH remnant masses are the same for `psflag`. Apart from initialising star cluster simulations with an IMF that is top-heavy and goes up to very large masses, e.g. Weatherford et al. (2021), these BH masses may be reached through initial stellar collisions and coalescence in primordial binaries (Kremer, Spera, et al., 2020). Alternatively, these may be reached dynamical through BH-BH mergers (Arca-Sedda et al., 2021; Di Carlo et al., 2019; Morawski et al., 2018, 2019; Rizzuto, Naab, Spurzem, Arca-Sedda, Giersz, et al., 2021; Rizzuto, Naab, Spurzem, Giersz, et al., 2021).

**THE IMPACT OF STELLAR EVOLUTION ON
(NON-)ROTATING POPULATION-II STAR
CLUSTERS**

Impact of stellar evolution on rotating star clusters

10

10.1 Abstract

We present results from a suite of eight direct N-body simulations, performed with `NBODY6++GPU`, representing realistic models of rotating star clusters with up to 1.1×10^5 stars. Our models feature primordial (hard) binaries, a continuous mass spectrum, differential rotation, and tidal mass loss induced by the overall gravitational field of the host galaxy. We explore the impact of rotation and stellar evolution on the star cluster dynamics. In all runs for rotating star clusters we detect a previously predicted mechanism: an initial phase of violent relaxation followed by the so-called gravogyro catastrophe. We find that the gravogyro catastrophe reaches a finite amplitude, which depends in strength on the level of the bulk rotation, and then levels off. After this phase the angular momentum is transferred from high-mass to low-mass particles in the cluster (both stars and compact objects). Simultaneously, the system becomes gravothermally unstable and collapses, thus undergoing the so-called gravothermal-gravogyro catastrophe. Comparing models with and without stellar evolution, we find an interesting difference. When stellar evolution is not considered, the whole process proceeds at a faster pace. The population of heavy objects tend to form a triaxial structure that rotates in the cluster centre. When stellar evolution is considered, we find that such a rotating bar is populated by stellar black holes and their progenitors. The triaxial structure becomes axisymmetric over time, but we also find that the models without stellar evolution suffer repeated gravogyro catastrophes as sufficient angular momentum and mass are removed by the tidal field.

10.2 Introduction

Present-day detectors and data processing methods have made it possible to resolve the photometry and kinematics of individual stars (even in components of binary and higher-order hierarchical stars) in star clusters (Giesers et al., 2018, 2019). These observations reveal global bulk rotation of the star clusters and even resolve the rotational kinematics of the extremely dense star cluster cores. On top of this, the kinematic patterns of multiple populations in star clusters can and have been mapped out in numerous studies (Bianchini et al., 2013a, 2016a, 2019; Ferraro et al., 2018; Kamann, Bastian, et al., 2018; Kamann, Husser, et al., 2018; Kamann et al., 2016, 2019; Lanzoni, Ferraro, Mucciarelli, Palla, Lapenna, et al., 2018; Lanzoni, Ferraro, Mucciarelli, Palla, Tiongco, et al., 2018; Sollima et al., 2019; M. Tiongco et al., 2021; M. A. Tiongco et al., 2019). Nowadays, we are also beginning to resolve the complex interaction between a star cluster and its tidal field and the imprint that the

| | | |
|--------|--|-----|
| 10.1 | Abstract | 217 |
| 10.2 | Introduction | 217 |
| 10.2.1 | 2-D Fokker-Planck models vs. direct N-body simulations | 219 |
| 10.3 | Methods | 221 |
| 10.3.1 | <code>NBODY6++GPU</code> | 221 |
| 10.3.2 | <code>MCLUSTER & FOPAX</code> | 221 |
| 10.4 | Initial conditions | 222 |
| 10.4.1 | Star cluster parameters | 222 |
| 10.4.2 | Stellar evolution parameters | 223 |
| 10.5 | Results | 224 |
| 10.5.1 | Global dynamical evolution | 224 |
| 10.5.2 | Escaper stars | 231 |
| 10.5.3 | Binary stars | 233 |
| 10.6 | Summary, conclusion and perspective | 240 |
| 10.6.1 | Summary | 240 |
| 10.6.2 | Conclusion | 241 |
| 10.6.3 | Perspective on future simulations | 242 |

tidal field may leave on the internal cluster dynamics (M. A. Tiongco et al., 2016a, 2016b, 2017, 2018).

With the use of these observations, we can refine existing theoretical models of star cluster dynamics. While supporting observational evidence of rotating and flattened star clusters accumulates, the majority of numerical and theoretical models of star clusters still rely on the simplistic assumption of spherical symmetry (e.g. Askar et al. (2017), Kamlah, Leveque, et al. (2022), Rizzuto, Naab, Spurzem, Arca-Sedda, Giersz, et al. (2021), Rizzuto, Naab, Spurzem, Giersz, et al. (2021), and Wang et al. (2016)), which are supported by a wide range of models with fully self-consistent energy and angular momentum distribution functions (e.g. I. King (1962), Plummer (1911), and Wilson (1975)). Moreover, some methods simply require spherical symmetry. This is the case for Monte Carlo models and the mainstream Monte-Carlo codes are currently unable to evolve initially rotating star cluster models (Askar et al., 2017; Cohn, 1979; Giersz, 1998; Giersz et al., 2015; M. Hénon, 1975; Kremer, Ye, et al., 2020; Kremer et al., 2021; Merritt, 2015; Stodołkiewicz, 1982, 1986). Here, we briefly point out that Vasiliev (2015) has developed a novel Monte Carlo method for simulating the dynamical evolution of stellar systems in arbitrary geometry.

Recently, Lahén et al. (2020) ran simulations of young massive star clusters forming in metal-poor starburst dwarf galaxies and found that the star clusters have significant angular momentum upon formation. In these simulations, the more massive star clusters tend to have larger angular momentum. But they also find that the angular momentum is not always aligned with flattening, thereby indicating a complex kinematic structure overall. Both observations and other simulations support these results and find that star clusters show significant fractality (Ballone et al., 2020; Pang, Li, et al., 2021), and internal rotation at birth in general (Ballone et al., 2021). Velocity anisotropy has been observed in star clusters with detected elongated structures (Pang, Li, et al., 2021; Pang et al., 2020), and these structures might be induced by rotation.

Akiyama and Sugimoto (1989) already described the basic phenomena in a surprisingly small 1000 body direct N -body simulation; they found a four-phase star cluster evolution: “(1) violent relaxation; (2) a gravogyro catastrophe, introduced in detail in Section 2.3.2, of finite amplitude driven by the negative moment of inertia of a self-gravitating system through the transport of angular momentum; (3) a leveling off of the gravogyro instability where the transport of angular momentum is driven by coexisting, yet still slow, gravothermal instability; and (4) a relatively rapid gravothermal collapse”, directly cited from the abstract of Akiyama and Sugimoto (1989). The gravothermal instability is introduced in detail in Section 2.3.1 with the implications of both the gravogyro and gravothermal instabilities listed in detail Section 2.3.3 and Section 2.3.4. In the following years the focus shifted to the derivation of rotating equilibrium models, by J. Goodman (1983), Longaretti and Lagoute (1996), and Varri and Bertin (2012). These models are an extension of standard King models, adding a rotational parameter and a dependency of the distribution function on the angular momentum, and we denote them in the following as rotating King models. Such models were

used as initial models for numerical solutions of the corresponding 2-D orbit-averaged Fokker-Planck (FP) equation. These models showed that not only the birth distribution, but also the long-term dynamical evolution of a star cluster is significantly affected by its initial bulk rotation, and follow-up work included binary heating and a stellar mass spectrum (Fiestas et al., 2006; Kim et al., 2002; Kim et al., 2004, 2008). Direct N -body models were resumed by Ernst et al. (2007) and Hong et al. (2013), in the first place to compare and check the numerical solutions of the FP equation. Rotation in nuclear star clusters was studied using the FP model (Fiestas & Spurzem, 2010; Fiestas et al., 2012) and by N -body and semi-analytic models of Szölggyen and Kocsis (2018) and Szölggyen et al. (2019, 2021) - they were interested into the formation and evolution of rotating stellar or black hole disks in nuclear star clusters. Large and long term N -body simulations of star clusters, similar to globular clusters, were only recently published by Livernois et al. (2022) and M. A. Tiongco et al. (2022), though with some restrictions on the stellar mass function. In this paper we present and discuss the results of direct N -body simulations of rotating star clusters with and without stellar evolution. The models feature primordial (hard) binaries, a continuous mass spectrum, differential rotation, and tidal mass loss induced by the overall gravitational field of the host galaxy.

This section is structured as follows: in Section 10.2.1, we summarize the research status on rotating star clusters, the methods used up-to-date and the existing research gaps. In Section 10.3 we discuss the methodology and in Section 10.4 we outline the initial conditions for the simulations. In Section 10.5 we present the simulation results and in Section 10.6 we summarize and conclude the work and we give a perspective on future work and open questions.

10.2.1 2-D Fokker-Planck models vs. direct N -body simulations

The following theory, simulations and methods are introduced in detail Chapter 1.2. Expanding on the solvers for the 2-D orbit-averaged Fokker-Planck (FP) equation in (E, J_z) space developed by J. Goodman (1983), Einsel and Spurzem (1999) modelled the evolution of rotating stellar systems while assuming cylindrical coordinates and ignoring the existence of a third integral of motion. They propose a rotating King model in the form of

$$f_{\text{rk}} \propto \left(e^{\beta E} - 1 \right) \times e^{-\beta \Omega_0 J_z} \quad (10.1)$$

as a background distribution for the stars following Lupton and Gunn (1987), where $\beta = 1/(m\sigma_c^2)$ and the dimensionless angular velocity is given by $\omega_0 = \sqrt{9/4 \times \pi G n_c} \times \Omega_0$. Potential-density pairs (see e.g. Binney and Tremaine (2008b)) for these models are created by relating β to the King parameter W_0 via $W_0 = \beta m(\psi - \psi_t)$, where ψ and ψ_t are the central King potential and the King potential at the truncation radius r_t as well as the number of stars and shells in the computation. Einsel and Spurzem (1999) then established a family of rotating King models that are parameterised by pairs

of (W_0, ω_0) using numerical and computational methods by Cohn (1979), Henyey et al. (1959), and Spurzem (1994, 1996). Einsel and Spurzem (1999) found that with increasing initial angular velocity parameter ω_0 , the system is driven into strong mass loss and it contracts moderately. Furthermore, the models exhibit the features for the gravogyro catastrophe found originally by Hachisu (1979): an increasingly faster rotating core, although angular momentum is transported outwards from the star cluster.

The work by Einsel and Spurzem (1999) was then improved through the inclusion of three-body binary heating (Kim et al., 2002). They performed simulations of equal-mass systems without stellar evolution or tides, but nevertheless they confirmed that the collapse time could be significantly reduced due to rotation. Kim et al. (2004) then improved the research further by including a two-component mass spectrum. Ultimately, they were able to show that generally the angular momentum is transported from the high mass to the low mass group as long as dynamical friction (Chandrasekhar, 1943a, 1943b, 1943c; Dosopoulou & Antonini, 2017; Lingam, 2018) wins over the gravogyro catastrophe. In general, however, the underlying assumptions in the 2-D FP models by Einsel and Spurzem (1999) (neglect of third integral of motion, axisymmetry, see also Spurzem et al. (2005) for a discussion of tidal fields) require comparisons with direct N -body simulations. For this purpose, Kim et al. (2008) then investigated single mass component models and showed that the FP results are generally consistent with the N -body calculations. Their results also confirmed earlier N -body simulations by Ernst et al. (2007). The comparative studies between FP and direct N -body models were later expanded upon by Hong et al. (2013), who showed that the cluster evolution is accelerated by not only the initial rotation but also the mass spectrum of the cluster. They also demonstrated that the total angular momentum and the total mass of the cluster both decrease rapidly, while a bar-like structure forms and persists in the cluster centre. The formation of a bar and its subsequent fairly rapid dissolution was already found earlier in the pioneer simulations by Akiyama and Sugimoto (1989). Furthermore, it was confirmed that there is no conflict with observed limits of Galactic globular cluster rotation by expanding upon earlier comparisons between the FP models and observations from Fiestas and Spurzem (2010) and Fiestas et al. (2006). Szölgyen et al. (2019), who initialised their N -model simulations with rotating King models from Longaretti and Lagoute (1996), found a process of anisotropic segregation of heavy masses towards the central region, forming a disk-like structure. This has been proposed earlier for galactic nuclei (Szölgyen & Kocsis, 2018) and studied in more detail in Szölgyen et al. (2021). The formation of such a disk is very likely linked to the gravothermal-gravogyro catastrophe and similar to the formation of the bar-like structure found by Akiyama and Sugimoto (1989) and Hong et al. (2013).

The work presented in this paper adds to the large body of theoretical work listed above. For the first time, we study the impact of initial bulk rotation, realistic stellar evolution mass loss models in combination with primordial binaries and stars drawn from a continuous IMF (Kroupa, 2001) and the impact of the tidal field

on the global dynamics of the star clusters. With these settings, we study the development, evolution and coupling of the gravothermal and gravogyro catastrophes using direct N -body methods during the pre- and post-core collapse phases of star cluster evolution over 1 Gyr.

10.3 Methods

10.3.1 N_{BODY6++GPU}

The rotating star cluster models are evolved using the state-of-the-art direct force integration code N_{BODY6++GPU}, which is optimised for high performance GPU-accelerated supercomputing (Nitadori & Aarseth, 2012; Spurzem, 1999; Wang et al., 2015). In the interest of brevity, all the details are given in Section 5.7 and the overall Chapter 5 and they will not be repeated here.

10.3.2 McLUSTER & FOPAX

Our initial N -body particle distribution and velocities are obtained in three steps.

Firstly, the star clusters are initialised with McLUSTER (Kamla, Leveque, et al., 2022; Küpper et al., 2011a; Leveque, Giersz, Banerjee, et al., 2022) with details given in Section 2.2.5. This code is used to either set up initial conditions for N -body computations or to generate artificial star clusters for direct investigation (Küpper et al., 2011a). The McLUSTER output models can be read directly into the N_{BODY6++GPU} as initial models (also other codes, e.g. MOCCA (Kamla, Leveque, et al., 2022)). This makes McLUSTER the perfect tool to initialise realistic star cluster simulations. The input parameters are given in the Section 10.4 and they can be found in Table 10.1. Secondly, we generate 2-D Fokker-Planck initial models as used in Einsel and Spurzem (1999), Kim et al. (2002), and Kim et al. (2004, 2008) with the Fokker-Planck code named FOPAX. These methods and the workings of the code are introduced in Chapter 1.2 and in particular in Section 7.1. The code produces a 2-D mesh based output of density ρ and velocity dispersions σ as a function of r and z based on the rotating King model $f(E, J_z)$ that are characterised by a pair of parameters (W_0, ω_0) (see Eq. 10.1) and Section 7.3.

Thirdly, a Monte Carlo rejection technique is then used to generate a discrete system of N particles following the known distributions of ρ and σ . The output is in N -body format (one line per particle, mass, and 3-D position, velocity data). This N -body distribution is combined with the McLUSTER N -body distribution and all data is scaled to standard Hénon units. As a result, we have an initial star cluster model that is a rotating King model N -body distribution with the chosen IMF and all relevant binary orbital parameter distributions conserved from McLUSTER.

It is important here that the dimensionless King model parameter W_0 is identical in both McLUSTER and FOPAX (In our set-up $W_0 = 6.0$). In this way, we create models ($W_0 = 6.0, \omega_0 \in [0.0, 0.6, 1.2, 1.8]$); see

Tab. 1 in Einsel and Spurzem (1999) for up to $\omega_0 = 1.0$) in the construction of the initially rotating N -body distributions of star cluster models presented in this paper. Models with $(W_0, \omega_0) = (6.0, 0.0)$ are identical to traditional King models with $W_0 = 6.0$.

Furthermore, the rotating King model initial distributions are initially more compact with increasing ω_0 (see Fig. 1 in Einsel and Spurzem (1999)). Therefore, the structural input parameters from McLUSTER, such as the half-mass radius r_h , are (slightly) changed in this step. Since the traditional calculation of the half-mass radii r_h and by extension also the Lagrangian radii r_{Lagr} rely on the assumption of spherical symmetry, which breaks down for the rotating models (and in general, also for initially spherical star clusters in tidal fields), they can only be used as an approximate or indicative measure for the global, structural evolution of the star clusters. All of this also implies that the initial half-mass relaxation times are smaller for increasing ω_0 (see Tab. 1 in Einsel and Spurzem (1999)).

10.4 Initial conditions

10.4.1 Star cluster parameters

The initial models from McLUSTER (Kamlah, Leveque, et al., 2022; Küpper et al., 2011a; Leveque, Giersz, Banerjee, et al., 2022) are constructed as smaller mock models of the Milky Way GC NGC3201 and are shown in Table 10.1. The initial number of objects is set to 10^5 with a binary fraction of 0.1. This yields a total number of stars of 1.1×10^5 . Our clusters have an initial cluster mass of $6.41 \times 10^4 M_\odot$. As sketched out above, we use a King density model with a King model parameter of $W_0 = 6.0$ (I. King, 1962). The model shows no initial mass segregation and is unfractal (Goodwin & Whitworth, 2004). The model is initially in virial equilibrium. The half-mass radius is set to $r_h = 1.85$ pc. As outlined in Section 10.3.2, the initial model from McLUSTER is then redistributed with a rotating King model, which are more compact than their non-rotating counterparts (Einsel & Spurzem, 1999). Therefore, the internal structural parameters such as the r_h and r_c change in this initialisation step from their original McLUSTER N -body distribution (see already Figure 10.1).

We use a Kroupa IMF (Kroupa et al., 2001) between $0.08 M_\odot$ and

Table 10.1: Initial parameters that are identical across all eight initial models for the Nbody6++GPU simulations.

| Quantity | Value |
|-------------------------------------|--|
| Particle number | 1.1×10^5 |
| Binary fraction f_b | 10.0% |
| Half mass radius r_h | 1.85 pc |
| Tidal radius r_{tid} | 65.59 pc |
| IMF | Kroupa IMF (Kroupa, 2001) ($0.08 - 150$) M_\odot |
| Density model | King model (I. King, 1962) $W_0 = 6.0$ |
| Eccentricity distribution $f(e)$ | Thermal ($f(e) \propto e^2$) |
| Semi-major axis distribution $f(a)$ | uniform in $\log(a)$ |
| mass ratio distribution $f(q)$ | uniform distribution of mass ratio ($0.1 < q < 1.0$) for $m > 5 M_\odot$. |

Table 10.2: Model identifiers (Model ID) for the eight N_{BODY}6++GPU simulations.

| Model ID | Stellar evolution? | ω_0 |
|----------------------|--------------------|------------|
| SEV ω_0 0.0 | yes | 0.0 |
| SEV ω_0 0.6 | yes | 0.6 |
| SEV ω_0 1.2 | yes | 1.2 |
| SEV ω_0 1.8 | yes | 1.8 |
| noSEV ω_0 0.0 | no | 0.0 |
| noSEV ω_0 0.6 | no | 0.6 |
| noSEV ω_0 1.2 | no | 1.2 |
| noSEV ω_0 1.8 | no | 1.8 |

150.0 M_\odot . The binaries are paired in their mass ratios q following (Kiminki et al., 2012; Kobulnicky et al., 2014; Sana et al., 2013; Sana & Evans, 2011), meaning that we have a uniform distribution of mass ratios ($0.1 < q < 1.0$) for $m > 5 M_\odot$ and random pairing for the remaining binaries. Their semi-major axes are distributed uniformly in log-scale between the sum of the radii of the two binary stars and 100 AU. The eccentricity distribution is thermal.

The cluster's absolute metallicity is set to $Z = 0.00051$. We put our cluster initial models on a circular orbit around the Galaxy of radius 13.3 kpc (according to (Cai et al., 2016) a circular orbit can be chosen such that the mass loss evolution of the cluster is similar compared to the eccentric orbit of NGC3201 (between 8.60 and 29.25 kpc, with eccentricity $e = 0.55$ according to Gaia DR2 data (Gaia Collaboration et al., 2018))) around a point-mass MW of mass $1.78 \times 10^{11} M_\odot$ (assuming a circular velocity $v_c = 240.0 \text{ kms}^{-1}$ at the Solar distance) (Bobylev & Bajkova, 2020; Gaia Collaboration et al., 2018). For our cluster models this yields an initial tidal radius of 65.59 pc. Therefore, the models are very tidally underfilling.

In the interest of aiding the discussion, we introduce model IDs for our eight individual runs, see Table 10.2. For example, the non-rotating model without stellar evolution is named noSEV ω_0 0.0, while the rotating model with $\omega_0 = 1.2$ and stellar evolution switched on is named SEV ω_0 1.2. The details of the stellar evolution parameters are discussed below. Furthermore, we will refer to the group of models without stellar evolution as noSEV models and to the group of models with stellar evolution as SEV models from here on after.

10.4.2 Stellar evolution parameters

We follow the level C stellar evolution as presented in Kamlah, Leveque, et al. (2022), which also describes the stellar evolution routines and parameters in detail. We use the metallicity-dependent winds following Belczynski et al. (2010), Vink and de Koter (2002, 2005), and Vink et al. (2001) across the full mass range. For the compact object evolution, we use remnant mass prescriptions following C. L. Fryer et al. (2012) and here we choose the delayed supernova (SNe) mechanism as the slow extreme of the convection-enhanced neutrino-driven SNe paradigm. We use standard momentum conserving fallback-scaled kicks (drawn from a Maxwellian distribution with a dispersion of 265.0 kms^{-1} from Hobbs et al. (2005)) for the neutron stars (NSs) and black holes (BHs) (Belczynski et al., 2008),

except for the NSs and BHs that are produced by the electron-capture SNe (ECSNe), accretion-induced collapse (AIC) and merger-induced collapse (MIC) (Gessner & Janka, 2018; Ivanova et al., 2008; Leung, Nomoto, & Suzuki, 2020; Podsiadlowski et al., 2004) and that are subject to low velocity kicks (drawn from a Maxwellian distribution with a dispersion of 3.0 km s^{-1} from Gessner and Janka (2018)). The BHs receive natal spins following the Geneva models (Banerjee et al., 2020; Banerjee, 2021a). The white dwarfs (WDs) receive natal kicks following Fellhauer et al. (2003) (drawn from a Maxwellian distribution with a dispersion of 2.0 km s^{-1} but, which is capped at 6.0 km s^{-1}). We switch on the (pulsational) pair instability SNe following Belczynski et al. (2016).

10.5 Results

10.5.1 Global dynamical evolution

Structural parameter evolution

We run each of the four initial models ($\omega_0 = 0.0, 0.6, 1.2, 1.8$) with NBODY6++GPU once with stellar evolution switched on (SEV models) and once without (noSEV models). Hence we have eight distinct simulations to compare and contrast. We discuss in the following Figure 10.1 to Figure 10.6, to get an overview on the global evolution of the simulated star clusters.

Figure 10.1 shows the total cluster mass M_{cl} (M_{\odot}), the tidal radius r_t (pc), the half mass radius r_h (pc), the mass of the core m_c (M_{\odot}) and the radius of the core r_c (pc) in the four panels, respectively. In NBODY6++GPU, particles (single or binary stars) are removed from the star cluster once they have reached a distance that is twice the *current* tidal radius far away from the density centre. They are called ‘escapers’ thereafter. The current tidal radius is then calculated using the *current* cluster mass. Escapers do not contribute to the current cluster mass. They are also not taken into account when calculating any of the other structural parameters of the star clusters, such as r_h or m_c .

First, we look at the time evolution of M_{cl} and r_t for all eight models. While M_{cl} and r_t decrease significantly due to stellar evolution mass loss in the SEV models, the noSEV models can only suffer mass loss through escaping stars, either through strong dynamical encounters or series of weak encounters. It is therefore unsurprising that in the presence of the additional mass loss mechanism through stellar evolution, the tidal radii of the respective SEV models exhibit a much faster decrease. We also observe that the noSEV appear to approach the SEV counterpart models in their tidal radii in the indicating that the cluster evolution is faster in the long-term. We need simulations longer than 1 Gyr to make a more qualified statement on this.

The half-mass radii r_h show an interesting evolution in time. While the evolution over the first couple of hundred Myrs is similar, the noSEV clearly diverge from the SEV models, which means the noSEV expand faster and more violently than the SEV models. This evolution is not mirrored by the core radius r_c evolution, which is

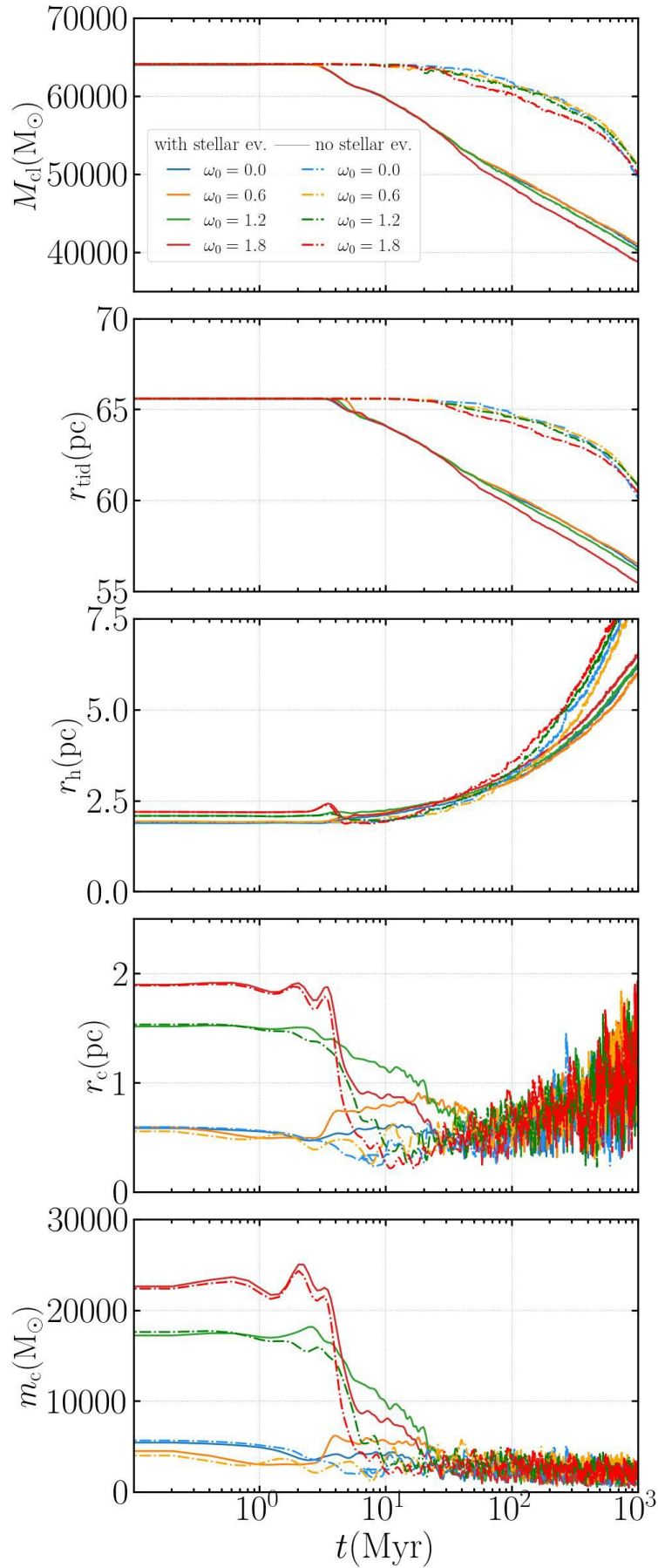


Figure 10.1: Plot showing the total cluster mass M_{cl} (M_\odot), the tidal radius r_t (pc), the half mass radius r_h (pc) and the mass of the core m_c (M_\odot) and the radius of the core r_c (pc) in the four panels for all eight simulations with and without stellar evolution for $\omega_0 = 0.0, 0.6, 1.2, 1.8$, respectively. The time axis is plotted logarithmically to show the details of the much more rapid early cluster evolution. The models with stellar evolution (SEV models) are plotted as solid lines and the models without stellar evolution (noSEV) runs are plotted as dash-dotted lines.

similar in the longer term leading up to 1 Gyr. There is one striking difference though. All noSEV models collapse faster and exhibit a stronger core collapse than their counterparts with stellar evolution. However, the mass in the core evolves similarly meaning that the core mass m_c (M_\odot) decreases faster and more strongly in all noSEV models. The evolution of the core radii and core masses are occur approximately synchronised, in all simulations.

The time evolution of the Lagrangian radii r_{Lagr} or more precisely, the radii of mass shells containing a certain percentage of the *current* total cluster mass (in this paper 1 %, 5 %, 10 %, 30 %, 50 %, and 90 % are shown), and the time evolution of the average stellar mass within these Lagrangian radii M_{av} are shown in [Figure 10.2](#) for the all eight simulations. Each of the four columns represents a rotational parameter ($\omega_0=0.0, 0.6, 1.2, 1.8$) and every second row shows the noSEV models on a light grey background. It appears that the core-collapse phase of the star cluster noSEV models is more extreme, while the overall collapse also happens earlier. This observation is especially clear in the plots of M_{av} in the bottom two rows of [Figure 10.2](#), which shows a much faster mass segregation in the noSEV than in the SEV models. Moreover, the expansion of the outer-most Lagrangian radii happens significantly faster in the noSEV than in the SEV models, which adds further evidence for a faster evolution of the noSEV models.

Overall, the discussion above can be related to the theorems described already in M. Hénon (1975) (see also Breen and Heggie (2013)). The evolution of the cluster system as a whole is governed by the energy flow through the half-mass radius r_h and it is independent of internal energy sources. The energy flow is approximately equal to $(GM_{\text{cl}}^2/r_h)/t_{r_h}$, where t_{r_h} is the half-mass relaxation time-scale and M_{cl} is the cluster mass, and this is equal to the energy generated at the centre of the cluster. In general, stellar evolution causes mass loss and results in an increase of r_h . Additionally, the loss of mass by interaction and relaxation for very massive stars (without evolution) causes an increase in r_h . Because in the case of no evolution we have more massive stars than in the case of evolution, the core collapses deeper and earlier. Mass loss through evolution slows down the collapse that then continues further. To stop the core collapse (no evolution), it is necessary to eject out some of the most massive binary systems and the most massive stars (as can be seen in the following figures). Then equilibrium occurs and both systems evolve similarly at the centre, generating similar energy. So if the mass of the system without stellar evolution is greater, then r_h must also be greater than in the case with stellar evolution.

Here, we also need to point out an important caveat: technically, as was also briefly outlined in [Section 10.3](#), it is not entirely accurate to use r_c , r_h and r_{Lagr} as measures for the global structure evolution of the rotating star cluster models that deviate too far from spherical symmetry. Instead of using Lagrangian mass shells, it would be better to sort the particles in terms of binding energy. This procedure would yield spheroids of equipotential surfaces. With these, we would then be able to calculate the respective radii along the principal axes of the spheroid, which is done below for the investigation of shape evolution of the star cluster models.

As was outlined in [Section 10.2](#), bulk rotation leaves an imprint on the shape of a star cluster. In general, the flattening of a rotating mass distribution can be calculated by transforming the principal axes of the moment of inertia tensor relative to the density centre of the mass distribution using different numbers of particles which are sorted by their binding energy (Theis & Spurzem, 1999). [Figure 10.3](#) shows the principal axis ratios of the intermediate to major axis ratio b/a and the minor to the major axis ratio c/a . Furthermore, following Theis and Spurzem (1999), we define a triaxiality parameter of the system

$$\tau = \frac{b - c}{a - c}, \quad (10.2)$$

which is shown in the bottom two rows of [Figure 10.3](#) (in this paper 10 %, 30 %, 50 %, and 90 % are shown). As in [Figure 10.2](#), the noSEV models are plotted in a light-grey background. We note that stochastic N -body noise disturbs the clean numbers. First, in the inner shells just the particle numbers are small. Second, our program does not have a fixed orientation for a , b and c ; the principal axes analysis always computes three principal axes and sorts them according to size. Therefore, stochastic noise always leads to b/a and c/a to be a bit smaller than unity, never greater. Stochastic noise in these quantities is also increased by the presence of massive stars, binaries, and fast evolving stellar masses (stellar evolution). For this reason, we have also refrained from plotting any shells below 50 % in this paper. We would need much larger particle numbers than 1.1×10^5 that we use in this work to have a more robust calculation that is less affected by these effects. Additionally, we note that the values of τ in [Figure 10.3](#) are unreliable, because the definition of tau is not suitable for nearly spherical systems with $b \sim c$ and $a \sim c$. Overall, the impact of the stellar evolution in combination with tidal field mass loss from the cluster is significant. While the SEV models return from the maximum triaxiality ($b \neq a \neq c$) at minimum c/a and b/a to axisymmetry ($b = a$, but $c \neq a$ and $c \neq b$), the star clusters without stellar evolution activated do not exhibit this evolution. In fact, all noSEV models show the initial maximum triaxiality earlier and more pronounced than the SEV models and while they then shortly after are attempting to return to axisymmetric configurations, they then show no, one or two consecutive triaxial "collapses" (τ in bottom row of [Figure 10.3](#)).

Furthermore, it is noteworthy that all shells from 10 % to 90 % are much more similar in their structure evolution for the noSEV compared with their counterparts in the SEV models, where there is more divergence between individual spheroidal shells. This is possibly related to the tidal field mass loss, meaning that if the tidal radius was (much) larger, the noSEV would show a similar evolution compared with the SEV models.

From [Figure 10.3](#) and [Figure 10.2](#) we can deduce the following cluster evolution qualitatively. Let us first look at the rotating clusters ($\omega_0 > 0.0$). First, there is a strong core collapse, which can be identified by the first maximum of the average mass in [Figure 10.2](#); it is earlier for noSEV runs, because they keep high stellar masses and thus experience fast mass segregation. For SEV runs heavy masses evolve fast, have strong mass loss, so collapse by mass

segregation is slower. It is interesting to note that approximately at the first core collapse there is a *minimum* value of triaxiality τ and δ shown in Figure 10.4 ($\delta = 1 - c/a$, a measure of flattening between the major and minor axes (a and c), it is 0 for spherical systems, and one for disk systems, see also Theis and Spurzem (1999)). That is followed a couple of Myrs later by a strong maximum in both τ and δ . We interpret this as follows: during collapse at high density the relaxation time is short, the system is developing towards sphericity and isotropy. Afterwards a radial orbit instability (ROI) is developing which produces the maximum of τ and δ ; the ROI is stronger for faster rotation, because we have less energy in the tangential unordered motion (tangential velocity dispersion becomes smaller compared to rotational velocity). Here, we did not examine in more detail the onset of ROI, the interested reader is referred to Theis and Spurzem (1999) and earlier references therein. For the non-rotating system there is also a core-collapse by mass segregation, faster in the noSEV case than with SEV; opposite to expectation the system develops some non-sphericity, in the case of noSEV ω_0 0.0.

Second, we find a phase of restoration of axisymmetry for the SEV models. The outermost shells exhibit oscillations in shape that are dampened over time, and the system returns to a stationary, flattened, axisymmetric state ($\tau \sim 1$, $\delta > 0$). It is interesting to note that the noSEV model does not return to axisymmetry, on the contrary it keeps some triaxiality during the last few 100 Myrs of our simulation. The effect is more pronounced for the rotating systems, but as discussed before, the values of τ for non-rotating models should be taken with care. Why this is the case is currently unclear. Possible speculative explanations are ongoing repeated ROI due to central core oscillations supported by the heavy masses, or interactions of the external tidal field, removing angular momentum (see Section 10.5.1).

Angular momentum evolution

We want to explore how the angular momentum is transported within the star cluster simulations and if and how this depends on the stellar evolution and initial bulk rotation strength. For this purpose, we divide the complete ZAMS particle set into four distinct mass groups (very low mass (v_{lm}), low mass (l_m), medium mass (m_m) and high mass (h_m):

$$M_{v_{lm}} : 0.08 M_{\odot} \leq m_{ZAMS} < 0.9 M_{\odot}$$

$$M_{l_m} : 0.9 M_{\odot} \leq m_{ZAMS} < 6 M_{\odot}$$

$$M_{m_m} : 6 M_{\odot} \leq m_{ZAMS} < 15 M_{\odot}$$

$$M_{h_m} : 15 M_{\odot} \leq m_{ZAMS} < 150 M_{\odot},$$

where m_{ZAMS} is the ZAMS stellar mass of a single star (this also means that a primordial binary star could have binary members that are in two different mass groups). The mass groups are chosen such that the stars from M_{h_m} become BHs, the stars from M_{m_m} become NSs, the stars from M_{l_m} become WDs and the stars from $M_{v_{lm}}$

remain as MSs for the simulation time, approximately. We can then follow the particles that originate from these mass groups through the full cluster evolution and compute their angular momentum across the full evolution. As a result, we are in a position to plot the time evolution of, for example, the square of the total angular momentum L^2 for each of the four mass groups and compare them to follow the angular momentum transfer. In Cartesian coordinates, L^2 for an individual star is simply given as quadratic sum of three components

$$L_x^2 = (yp_z - zp_y)^2, \quad (10.3)$$

$$L_y^2 = (zp_x - xp_z)^2, \quad (10.4)$$

$$L_z^2 = (xp_y - yp_x)^2, \quad (10.5)$$

which can then be done for all stars in each individual mass group. The sum of L^2 of all individual stars then gives the L_{group}^2 , the total sum of the square of the angular momentum.

All L_{group}^2 are divided by $L_{\omega_0 0.6, t=0}^2$, which is the square of the total angular momentum of the $\omega_0 0.6$ model(s) at $t = 0$ (the sum of all L_{group}^2 for the $\omega_0 0.6$ models divided by $L_{\omega_0 0.6, t=0}^2$ is one). We do this so that the models can be compared with each other more easily. $L_{\text{group}}^2 / L_{\omega_0 0.6, t=0}^2$ is shown in [Figure 10.5](#) for all models. M_{group} , which is the mass of all the stars (and compact objects) in the four groups as a function of time, is also shown in [Figure 10.5](#). First of all, we see that the total mass in each mass group evolves similarly at least initially across the SEV and across the noSEV models until stellar evolution and associated mass loss take over. With increasing initial bulk rotation, the mass loss from particularly the mass group of very low mass stars, M_{vlm} , is enhanced. This mass loss is assisted due to mass segregation and therefore, it is unsurprising that M_{vlm} is especially affected by this, because the member stars migrate to the cluster halo over time. The noSEV models lose mass only via tidal field mass loss or due to strong few-body encounters in the central high density region, which kick out stars and lift them up to escape energies. They also lose more mass by escaping stars than the SEV models (see [Figure 10.7](#) in [Section 10.5.2](#)). Due to stellar evolution, the SEV models lose mass in all mass groups much earlier during the simulation. It is especially striking in the medium mass M_{mm} and high mass M_{hm} groups, which predominantly produce NSs and BHs, respectively.

We now discuss the evolution of the angular momentum of the mass groups with the quantity $L_{\text{group}}^2 / L_{\omega_0 0.6, t=0}^2$, which reveals an important result that is particularly clear for increasing initial bulk rotation. From [Figure 10.7](#) we can qualitatively conclude the angular momentum loss and exchange - the angular momentum lost by the heavy mass group goes into cluster mass loss in the non- or slowly rotating case, only little is transferred to the light mass groups. The relative importance can be estimated from [Figure 10.7](#), which compares the mass loss for noSEV and SEV models. The interesting finding here is, however, that for the highly rotating systems a larger fraction of the heavy mass angular momentum is transferred to the light mass groups (but finally they also lose angular momentum due to general cluster mass loss). This is a signature of gravogyro

catastrophe.

The spikes in the $L_{\text{group}}^2/L_{\omega_0 0.6, t=0}^2$ curves are due to escaping stars or compact objects, which gain large amounts of angular momentum and then escape the cluster. It is important to keep in mind here that compact objects receive natal kicks in our simulations. Therefore, the number of these spikes is much higher in the SEV models (see in particular for the M_{mm}), because in the noSEV models, the stars can only escape through dynamical interactions. We can particularly see this in the evolution of the $L_{\text{mm}}^2/L_{\omega_0 0.6, t=0}^2$ and comparing it between the noSEV and SEV models. Remember that the objects from this group produce mostly NSs that receive very large natal kicks (several hundreds of kms^{-1}). We see that in the intermediate to long term of our simulations, the angular momentum loss from the SEV is much larger than that from the noSEV models, which becomes especially clear for the models with very large initial bulk rotation. While the noSEV models have a roughly constant angular momentum evolution above 100 Myr for the M_{vlm} , M_{lm} and M_{mm} mass groups, the SEV models show a clear decrease of angular momentum in all four mass groups. This effect is achieved through angular momentum loss through escaping stars and mass loss due to stellar evolution.

We also see for the noSEV models that when comparing [Figure 10.5](#) with [Figure 10.2](#) and [Figure 10.3](#), it becomes clearer that the noSEV models are unstable in their global evolution for all four runs ($\omega_0 = 0.0, 0.6, 1.2, 1.8$). By increasing the initial tidal radius in future simulations, this might be a very different situation.

Lastly, [Figure 10.5](#) reveals another important result. In the following discussion we focus on the M_{mm} mass group in the noSEV models. We can see that this group consistently has an almost constant mass (M_{group} ; with very small fluctuations). It appears that stars from this mass group are not ejected from the cluster. Furthermore, we see from $L_{\text{group}}^2/L_{\omega_0 0.6, t=0}^2$ for this mass group that its angular momentum effectively approaches zero after a couple of Myrs. This process can imply that the M_{mm} objects replace the depleting numbers of M_{hm} objects in the cluster centre in the mid- to long-term cluster evolution (see [Contentaetal2015](#) for the formation of a NS subsystem in the cluster centre).

Here, we also need to add an important caveat: the angular momenta are computed relative to the cluster density centre. However, since with have a tidal field the whole cluster experiences a (small) recoil every time a particle escapes by nature of momentum conservation. Therefore, the cluster density centre might move relative to the cluster centre of mass, which would have a (small) effect on the computation of the angular momentum.

Bar and disk formation of heavy mass objects

Here, we explore the spatial evolution of the high mass group M_{hm} . We want to know what happens to the shape of the distribution of these objects and how it is affected by initial bulk rotation and stellar evolution. In the SEV models this corresponds to the shape of the distribution of the BHs and their progenitor stars. [Figure 10.6](#) shows the 3-D spatial distribution of the stars and compact objects from M_{hm} at 0.0 Myr, 3.68 Myr, and 11.44 Myr from top to bottom,

respectively. This time is approximately the time of maximum triaxiality for the SEV ω_0 1.8 model (meaning approximately the simulation snapshot that is closest to maximum triaxiality). The bar formation of the BHs and their progenitor stars is clear in the SEV ω_0 1.2 and SEV ω_0 1.8 models (see also Hongetal2013 for more on bar formation). Their noSEV model counterparts, noSEV ω_0 1.2 and noSEV ω_0 1.8, also show the formation of a bar. It seems to be similar in spatial distribution, however, we know already from Figure 10.3 that the noSEV models do in fact yield slightly more maximally triaxial configurations. This overall process has also been referred to *anisotropic mass segregation* in Panamarev and Kocsis (2022) and Szölglyen et al. (2021). The noSEV ω_0 1.2 and noSEV ω_0 1.8 also attempt to return to axisymmetric configurations at 11.44 Myr. However, they seem to be slightly more concentrated than the SEV counterparts. We can infer on this from Figure 10.2. This effect is also due stellar evolution mass loss, which is in turn related to the natal kicks that the BHs experience. Therefore, it is natural that you can see larger spatial scattering in the distributions regardless of ω_0 compared to their noSEV model counterparts.

In summary, the initially rotating axisymmetric distribution of the M_{hm} objects becomes a bar that rotates around the z-axis and evolves toward a disc configuration over time (at least for the SEV models, see also Figure 10.3). This is strictly not the case for M_{hm} objects in the non-rotating ($\omega_0 = 0.0$) models. Here, the SEV and noSEV models stay spherical at least for the first 11.44 Myr of the simulations. However, we know from Figure 10.3 that also the noSEV ω_0 0.0 and noSEV ω_0 0.6 deviate from spherical symmetry over time. This deviation in the respective noSEV models is due to enhanced tidal field mass loss and tidal tails in the cluster (see discussion in Section 10.5.1 and Figure 10.4).

Young open clusters would be an ideal target for observations and further simulations to test this experimental result. In Pang, Tang, et al. (2022), elongated shapes of young clusters of *filamentary-type* might still carry the signal of a bar structure induced by rotation. However, the dynamical bar structure may blend with the inherent filamentary structure. We need to differentiate them carefully via kinematic data.

10.5.2 Escaper stars

The escapers from the simulations reveal more important information and are shown in Figure 10.7. In the following, we can study the temporal evolution of the number of escapers, n_{esc} . The SEV models initially lose more stars and compact objects than the noSEV models, but the noSEV models start losing stars significantly earlier, which is more apparent in the semi-logarithmic scaling in Figure 10.8, which is due to the faster evolution of the noSEV models (see also Section 10.5.1). The initially strong increase in the number of escapers is due to the large cluster mass reduction (potential) and increase of a number of stars called potential escapers. However, depending on the initial rotation, the noSEV models produce more escapers after a couple of Myr of simulation time. The runs with larger initial bulk rotation lose more stars, which is also the case

initially for the noSEV models. Here, the number of escapers of the runs without any rotation surpass the most strongly rotating run at about 600 Myr. We see a constant and almost linear rise of escaper numbers for the noSEV compared with the much flatter increase in escapers for the SEV models. We therefore confirm that the tidal field mass loss is much stronger for the noSEV models in the long-term, which can also be inferred from the time evolution of the total mass of the escapers, M_{esc} . The overall mass is larger and increases much faster in the noSEV than in the SEV models.

Interestingly, while the escaper numbers for the SEV models are very similar, the total mass loss is much larger for the SEV ω_0 1.8 models than for the SEV models that rotate less strongly initially. These numbers can be attributed mostly to the much larger number of initially escaping MS stars, n_{MSesc} , which is also shown in [Figure 10.7](#). The lower mass MS stars are driven onto large orbits around the density centre of the star cluster by having the angular momentum transported to them through the gravogyro catastrophe. We can also see this effect from [Figure 10.5](#), which is discussed in [Section 10.5.1](#). Interestingly, the SEV ω_0 0.6 retains many more MS stars than the SEV ω_0 0.0 model. This discrepancy is also mirrored by the number of escaping WDs, n_{WDesc} . For the other runs, SEV ω_0 1.2 and SEV ω_0 1.8, these are approximately similar over 1 Gyr. The number of escaping NS, n_{NSesc} , are practically identical. The reason for this is that the NSs that escape suffer from very large natal kicks and only those that form via ECSNe, AIC or MIC are retained in the cluster. Since the IMF is the same for all models, it is unsurprising that similar numbers are retained. This is not the case for the BHs. The plot for n_{BHesc} reveals that the SEV ω_0 1.8 models lose the largest number of BHs by a considerable margin. It might be suspected that n_{BHesc} should be similar for all models just like the evolution of n_{NSesc} . However, the double-core collapse hump in combination with the fallback-dependent scaling of the natal kicks produces a larger diversity (see also C. L. Fryer et al. (2012) and Kamlah, Leveque, et al. (2022)).

[Figure 10.8](#) shows the average mass of the escapers $m_{\text{esc,average}}$ for the SEV and noSEV models. Apart from the fact that stars escape the noSEV models earlier as was discussed above, $m_{\text{esc,average}}$ is much larger in the noSEV than in the SEV models. We define $m_{\text{esc,average}}$ as M_{esc} divided by n_{esc} at a specific point in time. Recall, that we use a IMF following Kroupa (2001) between (0.08 – 150) M_{\odot} (see [Table 10.1](#)). Our IMF produces an average ZAMS for our cluster of around 0.58 M_{\odot} . We see that the stars that escape the noSEV models are on average much more massive than the average star in the cluster. Due to the convective angular momentum transport, which happens extremely quickly and which is more dominant for increasing rotation (already after 0.1 Myr, see [Figure 10.5](#)), many (very) low mass, medium mass stars are removed along with high mass stars in the noSEV ω_0 1.8 model. This observation is mirrored in [Figure 10.7](#), where many more stars are removed for the noSEV ω_0 1.8 models initially than the other noSEV models. This effect brings down the average mass of the escapers. However, the noSEV ω_0 0.6 and the noSEV ω_0 1.2 produce remarkably similar evolution of $m_{\text{esc,average}}$. Averaging over more simulations would produce more reliable

results.

10.5.3 Binary stars

The temporal evolution of the number of binaries retained in the star clusters (both dynamical and primordial) can serve as a qualitative indicator for the number of dynamical interactions. [Figure 10.9](#) shows this number of binary stars n_b for all eight simulations. We first concentrate on the SEV models only. The SEV ω_0 1.8 have considerably lower numbers of binaries at 1 Gyr than the other models, which can mostly be attributed to escaping or disrupted binaries (by stellar evolution or dynamical encounters) in the very early simulations. The other simulations show a similar evolution of n_b with the notable exception that n_b for SEV ω_0 0.6 is larger than any of the other consistently over 1 Gyr. Now, comparing this with the evolution of n_b in the noSEV models, we find a different evolution. Here, the number of binaries show a lower scattering at 1 Gyr. Additionally, noSEV ω_0 1.8 appears to produce an intermediate number of retained binary stars and the noSEV ω_0 0.0 simulation produces the lowest numbers. To achieve greater clarity on this issue, we would need many simulations with different random realisations and look at the simulation ensemble average of the number of binaries for the different ω_0 values. We would then be in a position if this is not a random effect or if there is some systematic evolution occurring.

In the following discussion, we only consider the SEV models. The number of compact binaries, n_{cb} , reveals that the SEV ω_0 1.8 produce the lowest numbers of compact binaries retained in the cluster and the models with SEV ω_0 0.6 retain the largest numbers of compact binaries, thereby mirroring the overall number of binaries retained in the cluster. n_{cb} consists practically only of BHBH and WDWD binaries in our simulations, which is also why only the number of BHBH binaries, n_{BHBH} , and the number of WDWD binaries, n_{WDWD} , are shown in [Figure 10.9](#). Interestingly, there is a clear increase in the evolution of n_{BHBH} for the SEV ω_0 1.2 model. This is important because it could indicate that IMBH formation might be preferential at this initial bulk rotation (note that the maximum of this increase is already much later than the dissolution of the bar structure and occurs when the clusters are axisymmetric again, see also [Figure 10.3](#) and [Figure 10.6](#)). But it could also just be statistical fluctuation (compare this also to the smaller increases for the SEV ω_0 0.6 and SEV ω_0 1.8 models that occur later on). The number of BHs and BHBHs are both too low in our simulations to make a quantitative assessment on this. At 1 Gyr all simulations appear to converge at 5 or 6 BHBH binaries retained in the simulations. Our hypothesis here could be supported by the study of Brownian motion of BHs in (non-)rotating star clusters of [Webb et al. \(2019\)](#), who use very different initial conditions to the work presented here (Plummer distribution with 5×10^4 stars and rotation is induced by simply giving a fraction of stars some additional rotational velocity following [Lynden-Bell \(1960\)](#), which is not physical. Distribution functions from, e.g., [Einsel and Spurzem \(1999\)](#), [J. Goodman \(1983\)](#), [Longaretti and Lagoute \(1996\)](#), and [Varri and Bertin \(2012\)](#) should be used instead). They find that the orbits of BHs that receive velocity kicks of arbitrary origin

decay differently depending on the star cluster rotation. The larger the star cluster rotation, the earlier the orbits of the BHs circularise around the cluster centre due to the gain of angular momentum. As a result, dynamical friction becomes less effective in decaying the orbit. This may happen well before the BHs enter the so-called Brownian regime (e.g. Chatterjee et al. (2002) and Lingam (2018)), where any systematic orbit decay has stopped and the motion of the BHs is random. Due to the slowed down orbital decay with increasing rotation in the pre-Brownian motion regime, there could be more tidal capture events leading to larger BHBH abundances via three-body scatterings, where a MS star in a BHMS binary is exchanged with another BH (Webb et al., 2019).

The n_{WDWD} evolution mirrors that of n_{cb} , where n_{cb} is offset from n_{WDWD} mostly by n_{BHBH} . It is unsurprising that the n_{cb} is dominated by n_{WDWD} in the long-term and by n_{BHBH} in the beginning of simulation, because the massive stars evolve much faster than low mass stars and also our IMF contains many more low mass stars than high mass stars.

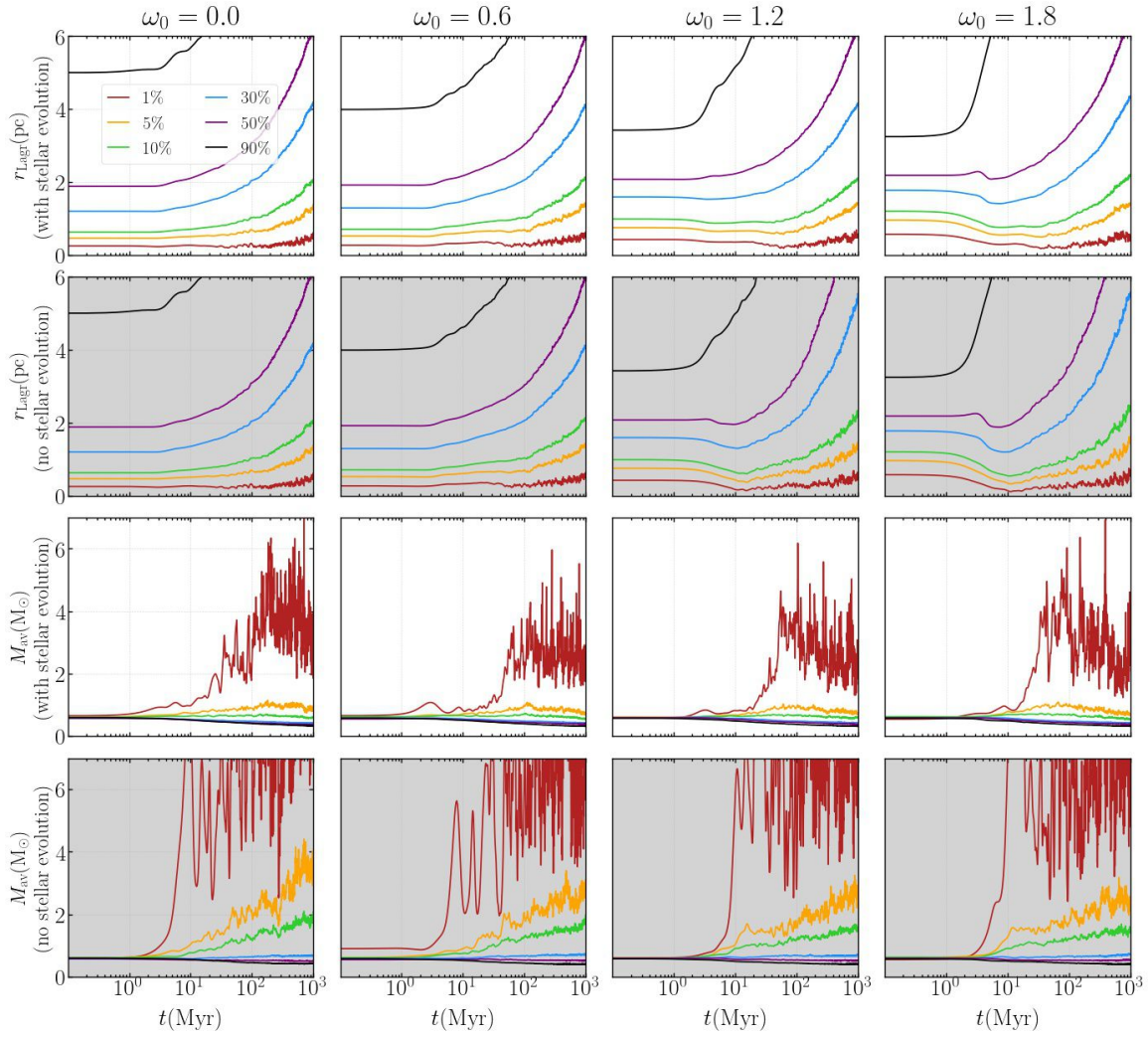


Figure 10.2: Plot showing the Lagrangian radii r_{Lagr} (pc) and the average mass M_{av} (M_\odot) within shells that contain 1%, 5%, 10%, 30%, 50%, and 90% of the total cluster mass at the current simulation time step for up to 1 Gyr. The time axis is plotted logarithmically to show the details of the much more rapid early cluster evolution. Each column represents one rotational parameter ω_0 of the rotating King model in ascending order from left to right ($\omega_0=0.0, 0.6, 1.2, 1.8$). The results from the runs *with* stellar evolution switched on (SEV models) are plotted on a white background, while the results from the simulations *without* stellar evolution (noSEV models) are highlighted in light grey.

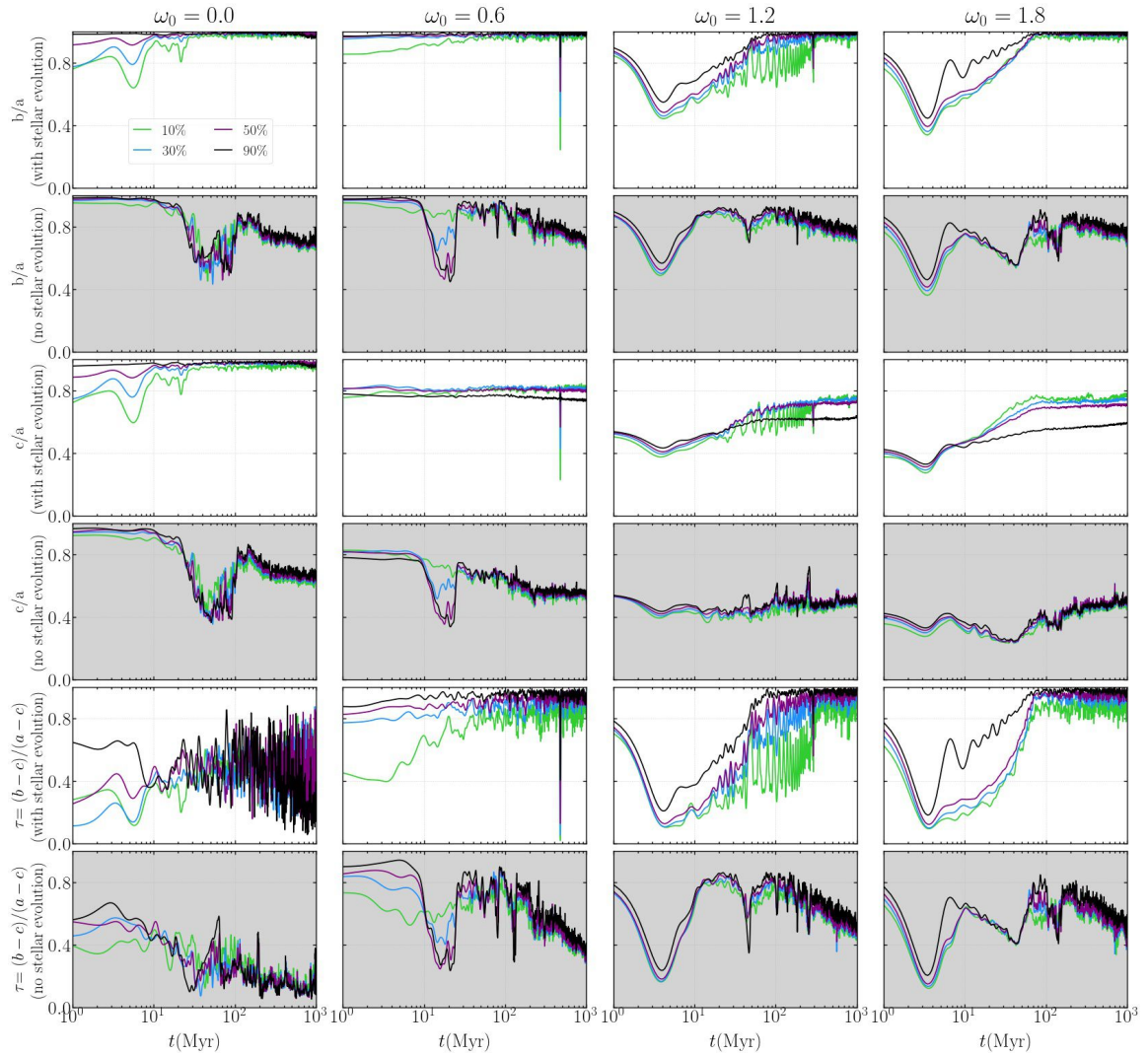


Figure 10.3: Plot showing the ratios of the principal axis of the moment of inertia tensor, b/a and c/a , as well as the triaxiality parameter $\tau = (b - c)/(a - c)$ within shells that contain 10%, 30%, 50%, and 90% of the total particle energy at the current simulation time step for up to 1 Gyr. The time axis is plotted logarithmically to show the details of the much more rapid early cluster evolution. Each column represents one rotational parameter ω_0 in ascending order from left to right ($\omega_0=0.0, 0.6, 1.2, 1.8$). The results from the runs *with* stellar evolution switched on (SEV models) are plotted on a white background, while the results from the simulations *without* stellar evolution (noSEV models) are highlighted in light grey.

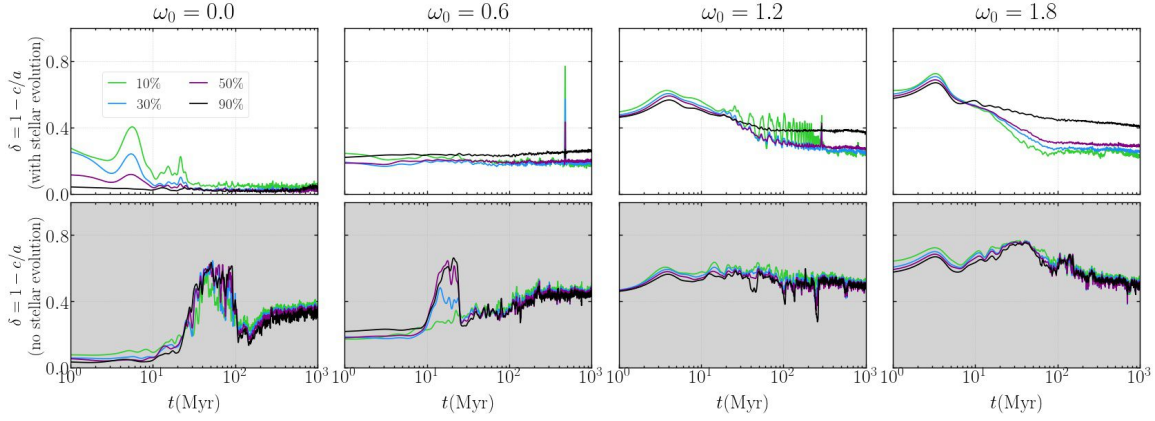


Figure 10.4: Plot showing the deviation from sphericity of the star cluster models, $\delta = 1 - c/a$, within shells that contain 10%, 30%, 50%, and 90% of the total particle energy at the current simulation time step for up to 1 Gyr. The time axis is plotted logarithmically to show the details of the much more rapid early cluster evolution. Each column represents one rotational parameter ω_0 in ascending order from left to right ($\omega_0=0.0, 0.6, 1.2, 1.8$). The results from the runs *with* stellar evolution switched on (SEV models) are plotted on a white background, while the results from the simulations *without* stellar evolution (noSEV models) are highlighted in light grey.

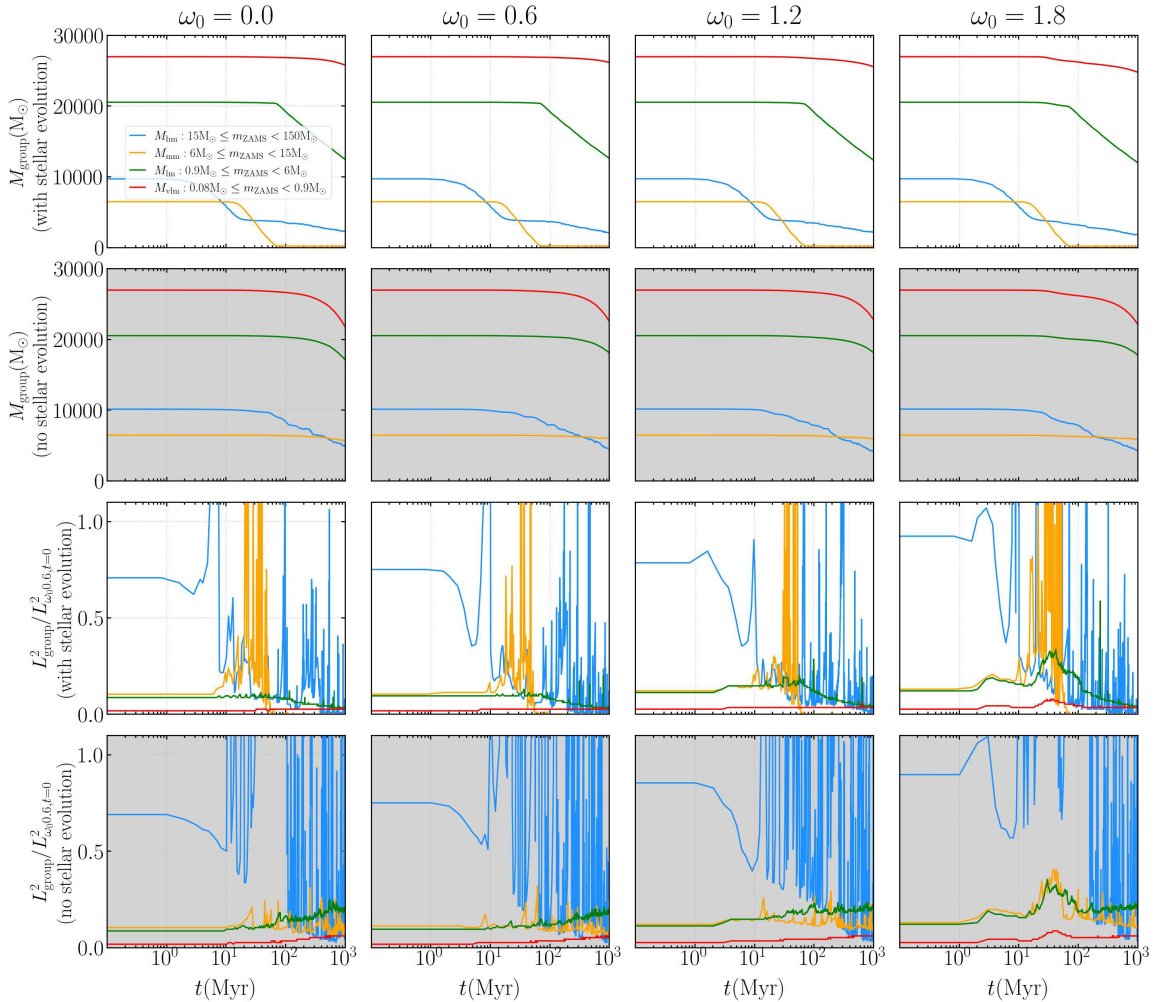


Figure 10.5: Plot showing the total mass of the four mass groups ($M_{\text{vlm}}, M_{\text{lm}}, M_{\text{mm}}, M_{\text{hm}}$) in the top two rows and the square of the total angular momentum for these groups divided by the square of the total angular momentum of the $\omega_0=0.6$ model(s) at $t=0$, $L_{\text{group}}^2 / L_{\omega_0=0.6, t=0}^2$, at the current simulation time step for up to 1 Gyr. The time axis is plotted logarithmically to show the details of the much more rapid early cluster evolution. Each column represents one rotational parameter ω_0 in ascending order from left to right ($\omega_0=0.0, 0.6, 1.2, 1.8$). The results from the runs *with* stellar evolution switched on (SEV models) are plotted on a white background, while the results from the simulations *without* stellar evolution (noSEV models) are highlighted in light grey.

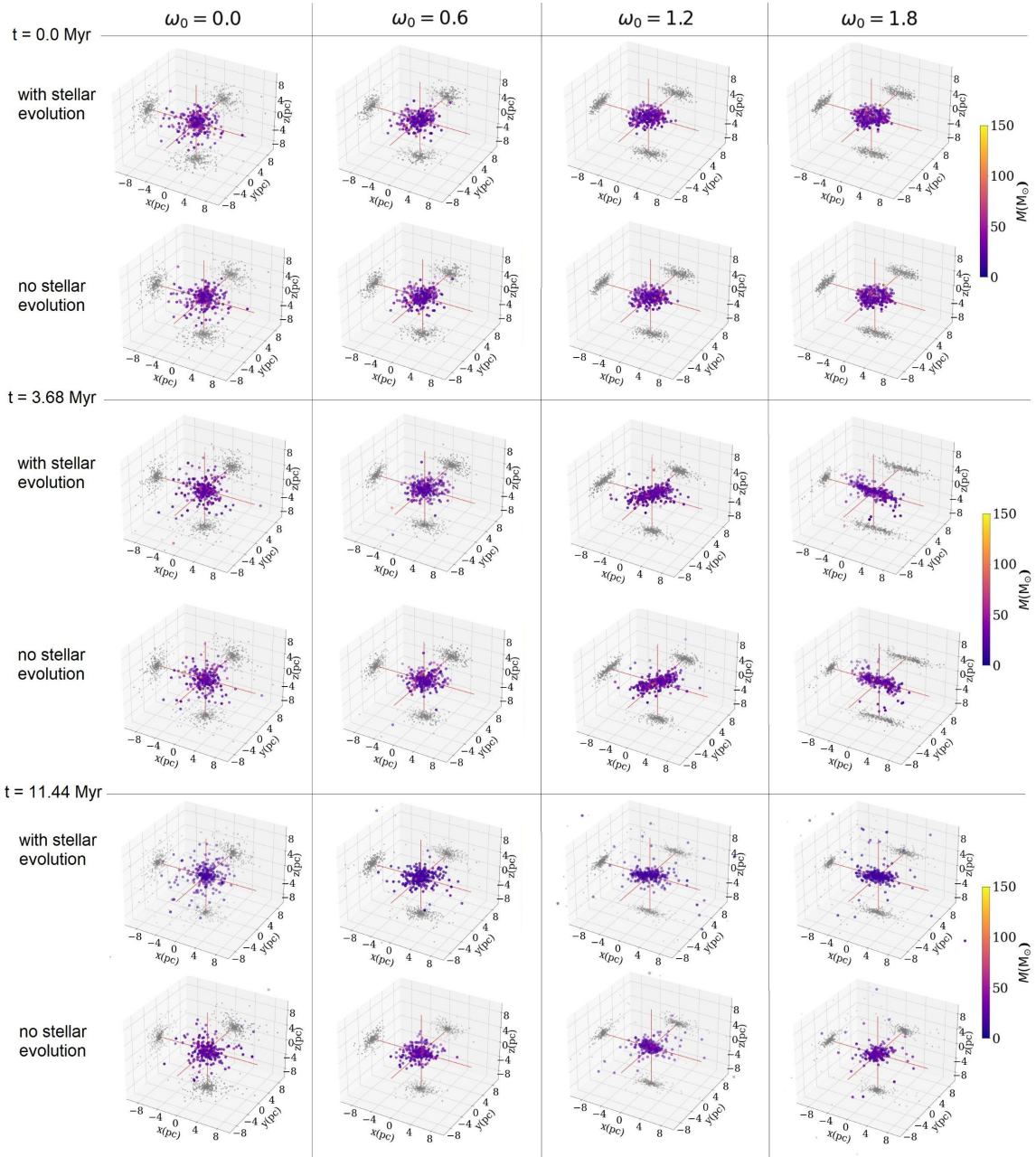


Figure 10.6: 3-D scatter plot showing the spatial distribution of the M_{hm} mass group in all eight simulations at 0.0 Myr, 3.68 Myr, and 11.44 Myr from the top to bottom in three separate rows with two sub-rows each; the top sub-row are always the models *with* stellar evolution (SEV models) and the bottom sub-row are always the models *without* stellar evolution (noSEV models). There are four columns and each one represents a rotational parameter ω_0 in ascending order of rotation from left to right. The stars and compact objects are color-coded by their mass between $0.0 M_{\odot}$ and $150.0 M_{\odot}$. The stars and BHs are also projected onto the three dimensional axes, which can be seen from the light-grey dots. We can clearly see the bar formation of the BHs and their progenitor stars in at $t=3.68$ Myr and the spatial reconfiguration of the M_{hm} objects to axisymmetric structures.

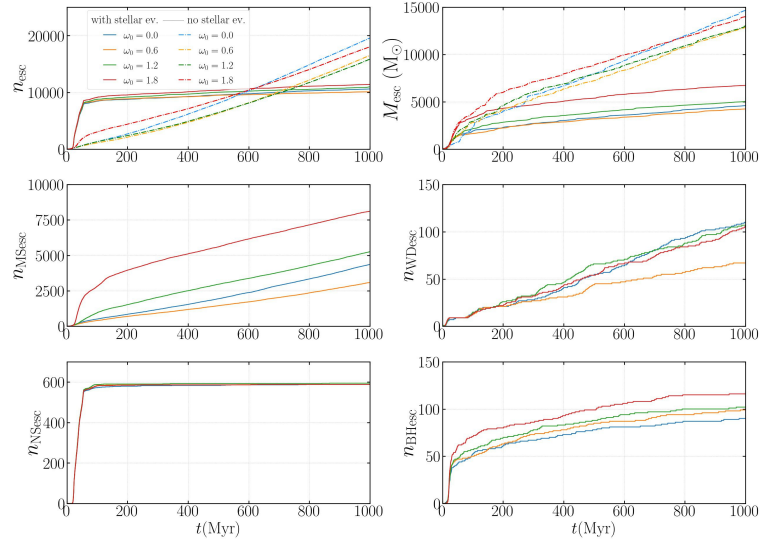


Figure 10.7: Plot showing over 1 Gyr the number of escapers, n_{esc} , the total mass evolution of the escapers, $M_{\text{esc}} (M_{\odot})$, the number of escaping MS stars, n_{MSesc} , the number of escaping WDs, n_{WDesc} , the number of escaping NSs, n_{NSesc} , and the number of escaping BHs, n_{BHesc} , respectively. The latter four are naturally only shown for the SEV models.

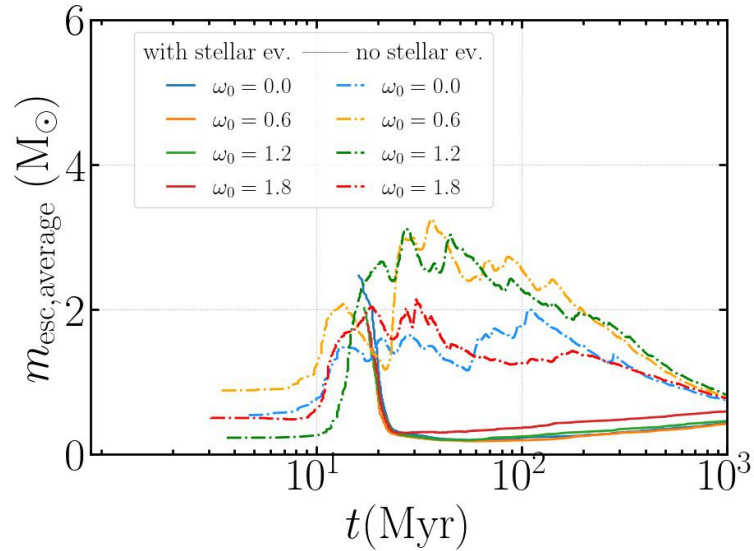


Figure 10.8: Plot showing the average mass of the escapers, $m_{\text{esc,average}}$, over 1 Gyr of cluster evolution.

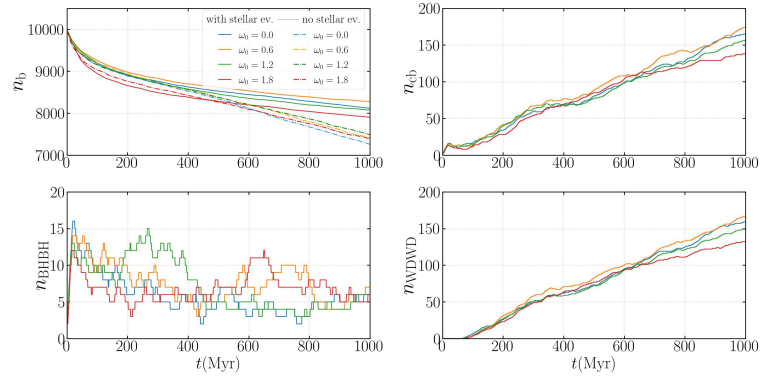


Figure 10.9: Plots showing the number of binary stars n_{b} , the number of compact binary stars n_{cb} , the number of binary black holes (BHBH) n_{BHBH} , the number of binary white dwarfs (WDWD) n_{WDWD} . For the plot of n_{b} both the SEV (solid lines) and the noSEV models (dash-dotted lines) are shown.

10.6 Summary, conclusion and perspective

10.6.1 Summary

For the first time we have studied the impact of initial bulk rotation, realistic stellar evolution mass loss models (Kamlah, Leveque, et al., 2022) in combination with primordial binaries and stars drawn from a continuous IMF (Kroupa, 2001) as well as a tidal field mass loss on the global dynamics of the star clusters and the development, evolution and coupling of the gravothermal and the gravogyro catastrophes using direct N -body methods. We have therefore expanded upon but also greatly surpassed any previous study on this phenomenon in astrophysical realism (Einsel & Spurzem, 1999; Ernst et al., 2007; Fiestas & Spurzem, 2010; Fiestas et al., 2006; Hong et al., 2013; Kim et al., 2002; Kim et al., 2004, 2008; Livernois et al., 2022; Szölggyen & Kocsis, 2018; Szölggyen et al., 2019, 2021; M. A. Tiongco et al., 2022; Wang et al., 2016).

In total, we have run eight simulations over 1 Gyr in total, four with stellar evolution (SEV models) and four without stellar evolution (noSEV models). In each subgroup of the two aforementioned groups, every individual model is distributed with a different rotating King model based on Einsel and Spurzem (1999). We use one non-rotating model ($\omega_0 = 0.0$) and three more models with increasing fractions of the initial total star cluster energy being stored in initial bulk rotational energy ($\omega_0 = 0.6, 1.2, 1.8$). We make the following observations:

- ▶ We obtain the same four phases in the early star cluster evolution that were previously observed in direct N -body simulations with low particle numbers by Akiyama and Sugimoto (1989) for both the runs with and without stellar evolution. Figure 10.2, Figure 10.3 and Figure 10.5 can be used in combination to deduce the following: we see a phase of violent relaxation that is followed by the gravogyro catastrophe of finite amplitude, where the amplitude depends on the degree of initial bulk rotation (see Figure 10.3). This gravogyro catastrophe then levels off and angular momentum is transported from the high mass stars (and compact objects) to the lower mass stars (and compact objects) (see Figure 10.5). Simultaneously, the system becomes gravothermally unstable and then collapses (see Figure 10.2). This is direct evidence for the coupling of the gravogyro and the gravothermal catastrophes that was first discussed by Hachisu (1979, 1982) and it is therefore appropriate to coin this process the gravothermal-gravogyro catastrophe. We also directly observe the predicted overall angular momentum loss from the cluster due to the tidal field in all models (Akiyama & Sugimoto, 1989).
- ▶ The SEV ω_0 1.2 and SEV ω_0 1.8 models evolve as follows: The BHs and their progenitor stars, which were distributed axisymmetrically initially, very quickly form a central bar, which rotates, as they transport angular momentum to lower mass stars and compact objects (see Figure 10.3, Figure 10.5 and Figure 10.6).

The bar then becomes an axisymmetric structure over longer time-scales. The outer halo stars (and compact objects) form a more spherical configuration in the long-term, while the stars (and compact objects) in the centre of the cluster form an axisymmetric structure that more slowly becomes spherical over time.

- ▶ The presence of stellar evolution and the tidal field of the star cluster impacts the aforementioned processes in a way that can be deduced mainly from [Figure 10.2](#), [Figure 10.3](#), [Figure 10.4](#) and [Figure 10.5](#). While the early dynamical evolution between the models with and without stellar evolution is similar qualitatively, the gravothermal-gravogyro catastrophe is stronger and happens slightly earlier in the noSEV models (see [Figure 10.1](#)). Most notably, the systems without stellar evolution evolve to similar configurations in the long-term (spherical halo of lower mass stars and compact objects with an axisymmetric centre of higher mass stars and compact objects), but are generally prohibited by doing so due to strong tidal field mass and angular momentum loss (see [Figure 10.1](#), [Figure 10.5](#), [Figure 10.4](#) and [Figure 10.7](#)). Instead they exhibit a second and even a third gravogyro collapse and approach a maximally triaxial state in the limit of 1 Gyr. It is an open question if this effect is dampened by larger initial tidal radius (see [Figure 10.1](#)).
- ▶ The noSEV $\omega_0 1.2$ and noSEV $\omega_0 1.8$ models also form a bar of the high mass stars that is more concentrated and more triaxial than the bar that forms with stellar evolution due to the lack of stellar evolution mass loss and compact object natal kicks. This bar becomes axisymmetric over time as well, but is also more compact than the counterparts in the SEV models (see [Figure 10.6](#)).
- ▶ The models *without* stellar evolution reveal that the M_{mm} mass group (see [Figure 10.5](#)) appear to replace the increasingly depleting numbers of M_{hm} objects in the cluster centre and form a subsystem there in the mid- to long-term cluster evolution. This result implies that mass segregation for the M_{hm} objects has effectively slowed down significantly at that point in simulation time.
- ▶ There is a significant increase in the number of BHBH binaries, n_{BHBH} , present in the SEV $\omega_0 1.2$ model (see [Figure 10.9](#)). There are also smaller increases in these numbers later on for the SEV $\omega_0 0.6$ and SEV $\omega_0 1.8$ models. However, it could also just be statistical fluctuation. This needs to be explored with further simulations and appropriate initial conditions that especially concern the IMF and the binary (orbital) parameters.

10.6.2 Conclusion

The inclusion of initial bulk rotation in direct N -body simulations of star clusters is still unusual, although it has been known for over

a century that star clusters even today show significant imprints of rotation, for example, in their shape (Bianchini et al., 2013b; C. W. Chen & Chen, 2010; Frenk & Fall, 1982; Harris, 1976; Harris, 1996; I. King, 1961; Kopal & Slouka, 1936; Kormendy, 1985; Lupton et al., 1987; Pease & Shapley, 1917; Shapley, 1930; Shapley & Sawyer, 1927; White & Shawl, 1987). This work therefore provides a bridge between observations and theory of the gravothermal-gravogyro catastrophe and the angular momentum and heat transport within a star cluster to much greater detail than any of the previous studies (see large body of work listed in Section 10.2). However, this is just another milestone on the road to unravel the impact of initial bulk rotation on realistic star clusters because many important questions are yet to be answered. Arca-Sedda et al. (2021), Rizzuto, Naab, Spurzem, Giersz, et al. (2021), and Rizzuto et al. (2022) have shown the formation and growth of an IMBH in a star cluster simulated by the same code as used here; so far our initial stellar density have been less than in their models. The question is what effect has rotation as in our models on the number and growth of IMBH in star clusters? This issue has only been briefly mentioned in Section:Binary stars2 of this paper and demands more simulations.

10.6.3 Perspective on future simulations

Reflecting on the discussion and conclusion above, there are several research objectives that require improvements on the simulations presented in this paper:

- ▶ Increasing the particle number will yield to better results on all sorts of statistics, but importantly in the context of this paper, the calculation of b/a , c/a and τ would be significantly improved, especially in the innermost spheroids of the star cluster models.
- ▶ Accordingly, increasing the binary fraction will yield more robust results on compact binary fractions and would enable us to make better and less speculative assessments on how initial bulk rotation affects compact binary formation.
- ▶ Increasing the density of the initial star cluster models will enable us to make assessments on the initial stellar merger rates of BH progenitor stars and subsequently IMBH formation.
- ▶ Extending our study to more flattened systems, to have a steady transition from spheroidal to disk systems. Our current initial models are not well-suited for disk systems, but e.g. Vergara et al. (2021) provide suitable disk rotating models. How do the gravothermal and gravogyro catastrophes proceed in disk systems? In this paper we still used the concept of Lagrangian radii, based on spherical systems (except when computing the principal axes a , b , c). The latter has been initiated by Theis and Spurzem (1999), it sorts the particles according to their energy in the system, rather than according to their distance (and spherical mass coordinate) from the

center, which means that the system is - in virial equilibrium - approximately subdivided using equipotential surfaces rather than spherical shells containing certain fractions of total mass. For strongly flattened systems it is necessary to compute quantities like average masses and velocity dispersions in such new spheroidal shells defined by equipotential surfaces.

- Using a realistic 3-D tidal field, which is possible to be treated with the `NBODY6++GPU` code version presented here, to study in detail how much angular momentum is carried away by escapers will enable us to assess how tidal shocks through galactic disk passages affect the rotating star cluster. We could then also compare the simulation results to recent cluster observations (e.g. from Pang, Li, et al. (2021) and Pang, Tang, et al. (2022)).

We are in the process of tackling some of these issues with direct N -body simulations and we expect many exciting results in the future. Among these, a recent work by Flammini Dotti et al. (2022) is shedding light on the impact of the initial bulk rotation on the ejection properties of free-floating planets and stars in rotating star clusters.

**THE EVOLUTION OF EXTREMELY MASSIVE,
(NON-)ROTATING POPULATION-III STAR
CLUSTERS**

Direct N -body simulations Population III star clusters

11

11.1 Abstract

We present results from eight direct N -body simulations, performed with `NBODY6++GPU`, representing extremely massive and rotating models of Population III star clusters with up to 1.01×10^5 stars. Our models feature primordial (hard) binaries, a continuous mass spectrum, differential rotation, and tidal mass loss induced by the overall gravitational field of a host galaxy. We include state-of-the-art fitting formulae for extremely massive, metal-poor Pop-III stars and general relativistic merger recoil kicks. We explore the impact of the above on the star cluster dynamics and merger rates between stars and compact objects. We observe (intermediate-mass) black hole formation below, within and above the pair instability mass gap and multi-generation black hole growth in all simulations. We confirm two of the hypothesized formation channels of galactic nuclei seed black hole formation: gravitational runaway mergers of black holes and of Pop-III stars, which core-collapse into intermediate-mass black holes thereafter. Higher initial star cluster bulk rotation potentially increases the merger rates of stars and compact objects, while the (compact) binary fractions decrease, because the combination of strong initial rotation and the mass and angular momentum removal by the tidal field lead to denser clusters and thus more dynamical interactions. After core-collapse of the cluster, which happens earlier the larger the initial rotation, a rotating, axisymmetric subsystem of intermediate mass black holes forms in the cluster centre, which is surrounded by rapidly expanding cluster halo of the lower mass stars and compact objects. Overall, we confirm the gravothermal-gravogyro catastrophe in the cluster simulations.

11.2 Introduction

There are three main formation channels of seed black holes (BHs) for galactic nuclei that are typically considered today (see the reviews by Greene et al., 2020; Rees, 1984, and sources therein):

1. First of all, gravitational runaway mergers between stars and compact objects happen throughout cosmic time in dense star clusters. They can be separated into a "fast" and a "slow" regime following Greene et al. (2020). In the fast regime (a couple of Myrs from star cluster formation and natal gas expulsion), gravitational runaway mergers can happen during early star cluster evolution, when stars evolve and merge either through binary stellar evolution or dynamical collisions (Gieles et al., 2018; Portegies Zwart & McMillan, 2002; Reinoso et al., 2018; Reinoso et al., 2021; Sakurai et al., 2017; Wang et al., 2022). The slow regime (around 100 Myr to Gyrs from

| | | |
|--------|---|-----|
| 11.1 | Abstract | 247 |
| 11.2 | Introduction | 247 |
| 11.3 | Methods | 251 |
| 11.3.1 | <code>NBODY6++GPU</code> | 251 |
| 11.3.2 | <code>MCLUSTER</code> & <code>FOPAX</code> | 252 |
| 11.3.3 | SSE, BSE and Pop-III stellar evolution | 252 |
| 11.3.4 | General relativistic merger recoil kicks | 255 |
| 11.4 | Initial conditions | 256 |
| 11.4.1 | Star cluster parameters | 256 |
| 11.4.2 | Stellar evolution param- eters | 258 |
| 11.5 | Results | 259 |
| 11.5.1 | Global dynamical evolution | 259 |
| 11.5.2 | Stars and compact objects | 268 |
| 11.5.3 | Binary stars | 271 |
| 11.5.4 | Collision and coales- cence events | 275 |
| 11.5.5 | Escaper stars | 278 |
| 11.6 | Summary, conclusion and perspective | 284 |
| 11.6.1 | Summary | 284 |
| 11.6.2 | Conclusion | 287 |

star cluster formation and natal gas expulsion) is populated by gravitational runaway mergers that occur between BHs. Gravitational runaway mergers of both kinds are postulated to produce intermediate mass BHs (IMBHs) with masses of order $10^2 M_{\odot}$ to $10^4 M_{\odot}$. Both the fast and the slow regimes have been confirmed extensively by simulations of dense star clusters using various methods and both mechanisms are instrumental to growing IMBHs (e.g. Arca Sedda & et al., 2023a, 2023b, 2023c; Arca Sedda, Mapelli, et al., 2020; Arca Sedda et al., 2019; Di Carlo, Mapelli, Bouffanais, et al., 2020; Di Carlo, Mapelli, Giacobbo, et al., 2020; Di Carlo et al., 2021; Giersz et al., 2015; Leveque, Giersz, Arca-Sedda, & Askar, 2022; Maliszewski et al., 2022; Rizzuto, Naab, Spurzem, Giersz, et al., 2021; Rizzuto et al., 2022; Rodriguez et al., 2019).

2. Secondly, massive Pop-III stars have been postulated to produce seed IMBHs with masses of order $10^2 M_{\odot}$ through direct collapse above the pair instability mass gap (e.g. Bromm, 2013; Bromm & Larson, 2004; Haemmerlé et al., 2020; Woosley, 2017). (Extremely massive) Pop-III stars can merge with other Pop-III stars in their host clusters before collapse to produce even more massive IMBHs above the pair-instability mass gap during the fast gravitational runaway merger phase, as outlined above (e.g. Katz et al., 2015; Reinoso et al., 2018; Reinoso et al., 2021; Sakurai et al., 2017; Tanikawa, Chiaki, et al., 2022; Wang et al., 2022).
3. Thirdly, the direct collapse of extremely massive gas clouds can result in extremely massive BHs of order $10^4 M_{\odot}$ to $10^6 M_{\odot}$ effectively bypassing all stellar evolution phases (e.g. Begelman, 2010; Begelman et al., 2006, 2008; Bromm & Loeb, 2003). We include here also the possibility of stars that form so massive ($10^5 - 10^6 M_{\odot}$) that they explode by general-relativistic instability Supernovae (SNe) (e.g. Sakurai et al., 2015; Shibata & Shapiro, 2002; Uchida et al., 2017). But we do not explore this channel in the work presented here.

As alluded to above, metal-poor Pop-III star clusters at high redshifts ($z \gtrsim 10$) hosting stellar populations with a top-heavy initial mass function (e.g. Sharda & Krumholz, 2022) are very strong candidates for the production of BH seeds for galactic nuclei and their nuclear star clusters (NSCs; Askar et al., 2021, 2022; Greene et al., 2020; Neumayer et al., 2020; Schleicher et al., 2022). The IMBHs that form in these clusters can grow even more massive through tidal disruption events over long time-scales (Sakurai et al., 2019). The single- and multi-generation mergers from the gravitational runaway process of BHs and other compact objects originating from Pop-III star clusters will be relevant GW detection events (Belczynski et al., 2017; Hartwig et al., 2016; Kinugawa et al., 2014, 2016, 2021a, 2021b; Ng et al., 2022; R. Schneider et al., 2000, 2002, 2003), especially for the proposed third-generation ground-based GW detectors, the Cosmic Explorer (CE Evans et al., 2021; Reitze et al., 2019), Einstein Telescope (ET; Liu & Bromm, 2020, 2021; Maggiore et al., 2020; Punturo et al., 2010a, 2010b; Sathyaprakash et al., 2012), and for future space-borne detec-

tors operating in the mHz and deci-Hz frequency bands, like the laser interferometer space antenna (LISA; Amaro-Seoane et al., 2013, 2017, 2022) or the decihertz gravitational wave observatory (DECIGO; Kawamura et al., 2011, 2021), where IMBHs are expected to be bright GW sources (see e.g. Amaro-Seoane, 2018; Amaro-Seoane et al., 2007; Arca Sedda, Berry, et al., 2020; Arca Sedda et al., 2021; Jani et al., 2020; M. C. Miller & Hamilton, 2002).

Using detailed BPS, Tanikawa, Susa, et al. (2021) conducted studies on the merger rate density of Pop-III binary BHs below, above, and in the pair-instability mass gap. They find that mergers between two low mass BHs (in their models, low mass means $M < 50 M_{\odot}$) independent of mass ratio and semi-major axis distributions of the primordial Pop-III binaries could be identified from the observed BHBH mergers by (Advanced) Laser Interferometer Gravitational-Wave Observatory ((a)LIGO; Aasi et al., 2015; B. P. Abbott, Abbott, Abbott, Abernathy, et al., 2018; B. P. Abbott et al., 2019), (Advanced) Virgo Interferometer ((a)Virgo; B. P. Abbott, Abbott, Abbott, Abernathy, et al., 2018; B. P. Abbott et al., 2019; Acernese et al., 2015) and by extension also Kamioka Gravitational Wave Detector (KAGRA; B. P. Abbott, Abbott, Abbott, Abernathy, et al., 2018; B. P. Abbott et al., 2020; Kagra Collaboration et al., 2019), although the predicted present-day (10 Gyr) merger rates would be comparatively low ($\sim 0.1 \text{ yr}^{-1} \text{ Gpc}^{-3}$) with regard to the merger rate density inferred by (a)LIGO/(a)Virgo observation of $(10-100) \text{ yr}^{-1} \text{ Gpc}^{-3}$ (B. P. Abbott et al., 2019). Similarly, mergers between a low mass BH and a high mass BH (in their models, high mass means $M > 130 M_{\odot}$ due to the pair instability mass gap) or mergers between two high mass BHs (combined merger rate of $\sim 0.01 \text{ yr}^{-1} \text{ Gpc}^{-3}$) will be detectable using the afore-mentioned currently available GW detectors according to Tanikawa, Susa, et al. (2021). However, the authors caution that if two conditions hold simultaneously, namely a wide minimum semi-major axis in primordial Pop-III binaries due stellar expansion in the protostellar phases and fast stellar rotation rates cause excitation of (quasi-)chemically homogeneous evolution, which would imply that they stay more compact than non-rotating counterparts due to mixed Helium throughout the star (e.g. de Mink et al., 2009; Maeder, 1987; Yoon & Langer, 2005).

Observations of Pop-III stars or their remnants or their host clusters remain elusive, because of the extreme distances from us. Recently, a possible detection of an extremely massive Pop-III star at $z = 6.2$ was announced by Schauer et al. (2022), but this detection needs follow-up studies to be conclusive. Earlier an observation with MUSE Deep Lensed Field (MDLF) targeting the Hubble Frontier Field (HFF) galaxy cluster MACS J0416 of a Pop-III stellar complex at $z = 6.629$ was claimed by Vanzella et al. (2020). In general, however, direct observations of Pop-III stars and their host clusters will remain elusive even considering the ground-breaking results expected from the James Webb Space Telescope (JWST; Katz et al., 2022; Rydberg et al., 2013). On the other hand, de Souza et al. (2013) claim that some hundred SNe detections by JWST may be enough to constrain the IMF of Pop-III stars. Schauer et al. (2020) provide a further discussion on this issue. In the future, the wide field near infra-red surveys by Euclid (Laureijs et al., 2011; Tanikawa, Moriya, et al., 2022)

and the Nancy Grace Roman Space Telescope (RST) are postulated to yield much better resolution than JWST on direct collapse BHs above the pair instability mass gap because of their greater fields of view (Lazar & Bromm, 2022; Vikaeus et al., 2022).

In the absence of unambiguous observations of Pop-III stars and their environments, it remains difficult to constrain the parameter spaces for Pop-III star and star cluster formation (e.g. Klessen, 2019). Fraser et al. (2017) attempted to fit an IMF to observed stars and collated detailed abundances of 29 Pop-III stars from the literature to infer the IMF. They found that the IMF is similar to those of Pop-I/-II populations. However, the authors cautioned against drawing strong conclusions due to low N statistic. Therefore, to constrain the IMF of Pop-III stars hydrodynamic models are often used to make for this deficiency (e.g. Chon & Omukai, 2020; Chon et al., 2021; Hirano et al., 2015; Hirano & Bromm, 2017, 2018a; Hirano et al., 2014; Latif et al., 2022; Sharda et al., 2021; Stacy et al., 2016; Sugimura et al., 2020; Susa, 2019; Susa et al., 2014). Similarly, the binary fraction and (initial) binary statistics of such star clusters is subject to significant uncertainty (Liu, Meynet, & Bromm, 2021; Stacy & Bromm, 2013). Furthermore, the Pop-III binary properties also depend on the environment, in which the star clusters, which hosts them, forms (e.g. Hirano & Bromm, 2018b; Sugimura et al., 2020).

The observational and theoretical uncertainties are inherited by the initial conditions of Pop-III star cluster simulations. One such parameter concerns the degree of initial Pop-III star cluster rotation. A set of direct N -body simulations of initially rotating Pop-III star clusters were performed by Vergara et al. (2021) ($N = 10^3 - 10^4$ and evolution only up to $t = 2$ Myr). They used Miyamoto-Nagai models with flattening and rotation and found that not only the collision rate increases with increasing bulk rotation, but additionally the number of escapers is reduced the larger the initial rotation is. The low particle numbers, the short simulation time and other simplifying assumptions, such as neglecting stellar evolution make it difficult to generalise these results. In general, for simulations in collisional dynamics of rotating star clusters, distribution functions from, e.g., Einsel and Spurzem (1999), J. Goodman (1983), Longaretti and Lagoute (1996), and Varri and Bertin (2012) are typically used. Kamlah, Spurzem, et al. (2022) recently ran simulations of Pop-I star clusters with rotating King models from Einsel and Spurzem (1999) (using the 2-D Fokker-Planck code FOPAX (Einsel & Spurzem, 1999; Kim et al., 2002; Kim et al., 2004, 2008)). Apart from the formation and dissolution of a rotating bar of BHs that is related to the gravothermal-gravogyro catastrophe (Akiyama & Sugimoto, 1989; Einsel & Spurzem, 1999; Hachisu, 1979, 1982; Hong et al., 2013; Kamlah, Spurzem, et al., 2022), they found a possible dependence of BHBH binary abundances³ on initial star cluster bulk rotation; for a fast rotating model (rotating King model $W_0 = 6.0$, $\omega_0 = 1.2$), they found significantly many more BHBH binaries during a phase of star cluster evolution when BHBH mergers in the aforementioned "slow" regime are relevant (Greene et al., 2020). Similarly, Webb et al. (2019) found that increased initial star cluster rotation precipitates the formation of circularised BHBH binaries. Since Pop-III are postulated

to harbour many more (IM)BHs than Pop-I star clusters, relative to their size, it is worthwhile to explore if these initial findings hold in Pop-III star clusters and we do this in the work presented here.

Furthermore, the lack of concrete observations of Pop-III stars adds uncertainty to their stellar evolution. The most impactful parameter that differentiates stars of same masses in Pop-I and Pop-III populations is the metallicity (therefore, Pop-III stars are also referred to as extreme metal poor (EMP) stars, e.g., in Tanikawa et al., 2020). The lower the metallicity, the weaker are radiation driven winds that affect massive stars. Generally, this statement also holds for pulsation-driven winds (Nakauchi et al., 2020). In the regime of $Z/Z_{\odot} < 10^{-4}$ both the winds become negligibly small. However, it has been suggested that Pop-III stars form with very high rotation rates, when the magnetic fields are negligible and thus there is negligible magnetic braking (Hirano & Bromm, 2018a; Stacy et al., 2011, 2013). The winds due to the weakened stellar magnetic field of such stars may be very powerful (Liu, Sibony, et al., 2021).

The internal evolution changes drastically the fewer metals reside within a Pop-III star and leads to lower opacities (Ekström et al., 2008). First of all, the lower the metallicity of a star, the more compact it is, because the line-driven radiation pressure diminishes. Furthermore, most massive Pop-I/-II stars are characterised by a red supergiant (RSG) evolutionary phase with convective envelopes, while most Pop-III stars end with a blue supergiant (BSG) phase that have radiative envelopes (Tanikawa et al., 2020). These properties affect stellar binary evolution. While Pop-I/Pop-II stars tend to undergo unstable mass transfer and CEE in the RSG phase, BSGs from Pop-III stars undergo stable mass transfer, so that less mass is ejected from the binary system. As a result, BHBH binaries from Pop-III stellar populations can be more massive than Pop-I/-II counterparts even ignoring wind mass loss making Pop-III star clusters a very attractive target of GW event detection and progenitor studies (e.g. Inayoshi et al., 2017; Kinugawa et al., 2021a, 2021b; Tanikawa, Chiaki, et al., 2022; Tanikawa, Kinugawa, et al., 2021; Tanikawa, Susa, et al., 2021; Tanikawa, Yoshida, Kinugawa, et al., 2021).

In this paper we present and discuss the results of eight direct N -body simulations of extremely massive and rotating Pop-III star clusters with and without self-consistent general relativistic (GR) merger recoil kicks. For the first time, we study the impact of initial bulk rotation, state-of-the-art Pop-III stellar evolution, GR merger recoil kicks in combination with primordial binaries and stars drawn from a continuous IMF and tidal field mass loss on the global dynamics of Pop-III star clusters and the formation of IMBHs and progenitor stars within them.

The paper is structured as follows: in Section 11.3 we discuss the methodology, the implementation of the GR recoil kicks and the Pop-III stellar evolution fitting formulae. In Section 11.4 we outline the initial conditions for the simulations. In Section 11.5 we present the simulation results and in Section 11.6 we summarize and conclude the work and we give a perspective on future work and open questions.

11.3 Methods

11.3.1 NBODY6++GPU

The rotating star cluster models are evolved using the state-of-the-art direct force integration code `NBODY6++GPU`, which is optimised for high performance GPU-accelerated supercomputing (Nitadori & Aarseth, 2012; Spurzem, 1999; Wang et al., 2015). In the interest of brevity, all the details are given in Section 5.7 and the overall Chapter 5 and they will not be repeated here.

11.3.2 McLUSTER & FOPAX

Our initial N -body particle distribution and velocities are obtained in three steps as described in Kamlah, Spurzem, et al. (2022), which is presented in Chapter 10 and Section 10.3.2. The procedure is reiterated here. Firstly, the star clusters are initialised with `McLUSTER` (Kamlah, Leveque, et al., 2022; Küpper et al., 2011a; Leveque, Giersz, Banerjee, et al., 2022). This code is used to either set up initial conditions for N -body computations or to generate artificial star clusters for direct investigation (Küpper et al., 2011a). The `McLUSTER` output models can be read directly into the `NBODY6++GPU` as initial models (also other codes, e.g., `MOCCA` in Kamlah, Leveque, et al., 2022). The input parameters can be found in Table 11.1.

Secondly, we generate 2-D Fokker-Planck initial models as used in Einsele and Spurzem (1999), Kim et al. (2002), and Kim et al. (2004, 2008) with the Fokker-Planck code named `FOPAX`. The code produces a 2-D mesh based output of density ρ and velocity dispersions σ as a function of r and z based on the rotating King model $f(E, J_z)$, and Section 7.3, that are characterised by a pair of parameters (W_0, ω_0):

$$f_{\text{rk}} \propto \left(e^{\beta E} - 1 \right) \times e^{-\beta \Omega_0 J_z} \quad (11.1)$$

, where $\beta = 1/(m\sigma_c^2)$ and the dimensionless angular velocity is given by $\omega_0 = \sqrt{9/4 \times \pi G n_c} \times \Omega_0$. σ_c, n_c are central one-dimensional velocity dispersion and the central density, respectively. Potential-density pairs (e.g. Binney & Tremaine, 2008b) for these models are created by relating β to the King parameter W_0 via $W_0 = \beta m(\psi - \psi_t)$, where ψ and ψ_t are the central King potential and the King potential at the truncation radius r_t as well as the number of stars and shells in the computation (for numerical and computational methods see also Cohn, 1979; Henyey et al., 1959; Spurzem, 1994, 1996).

Thirdly, a Monte Carlo rejection technique is then used to generate a discrete system of N particles following the known distributions of ρ and σ . The output is in N -body format (one line per particle, mass, and 3-D position, velocity data). This N -body distribution is combined with the `McLUSTER` N -body distribution and all data is scaled to standard Hénon units. As a result, we have an initial star cluster model that is a rotating King model N -body distribution with the chosen IMF and all relevant binary orbital parameter distributions conserved from `McLUSTER`.

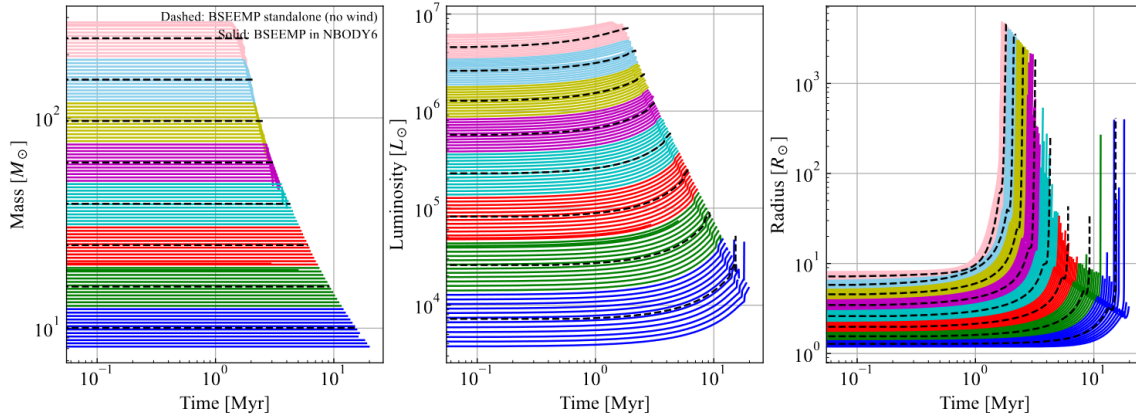


Figure 11.1: Plot showing the (functioning/fixed) Pop-III stellar evolution for stellar masses M (M_{\odot}), stellar luminosities L (L_{\odot}) and stellar radii R (R_{\odot}) for a simulation of 10^4 stars with and IMF from 8 to $300 M_{\odot}$ (only single ZAMS stars). The plot shows excellent agreement with the black dashed lines that are from pure BPS with the same fitting formulae from Tanikawa et al. (2020). In the broken version the stars with masses of 8 – $20 M_{\odot}$ simply did not evolve into compact objects.

11.3.3 SSE, BSE and Pop-III stellar evolution

In his work, we present the implementation into `NBODY6++GPU` of the extended fitting formulae derived from the fitting to 1-D HOSHI stellar evolution models (Takahashi et al., 2016, 2018, 2019; Yoshida et al., 2019) of extremely massive low metallicity (EMP; Pop-III) stars (Hijikawa et al., 2021; Tanikawa, Kinugawa, et al., 2021; Tanikawa, Susa, et al., 2021; Tanikawa et al., 2020). Thus, apart from Wang et al. (2022) we are among the first groups to combine direct N -body simulation with full Pop-III stellar evolution from Tanikawa et al. (2020). The fitting formulae by (Hurley et al., 2000), which are routinely extrapolated from $50 M_{\odot}$ to $100 M_{\odot}$, $150 M_{\odot}$ and even beyond that for Pop-I and Pop-II stellar populations (e.g. Kamlah, Leveque, et al., 2022; Kamlah, Spurzem, et al., 2022; Rizzuto, Naab, Spurzem, Giersz, et al., 2021; Rizzuto et al., 2022) cannot safely be used for Pop-III stellar populations with our initial conditions (see Table 11.1). At the metallicity that we adopt in this work, $Z/Z_{\odot} = 10^{-8}$, the fitting formulae by Tanikawa et al. (2020) are generally valid from $8 M_{\odot}$ to $1280 M_{\odot}$. We use the same extrapolation procedure for stars outside of this mass range as Wang et al. (2022). Extrapolation to high mass stars beyond $1280 M_{\odot}$ can be done for these formulae for several $10^3 M_{\odot}$ since for these large masses no abrupt changes in the fitting are expected (e.g. stellar luminosity is almost proportional to stellar mass and the stellar lifetime is constant). Extrapolation below $8 M_{\odot}$ is generally much more difficult, because here the stellar mass has a much greater influence on the stellar evolution. For stars with masses smaller than $8 M_{\odot}$ their evolution is fitted with the formulae from Hurley et al. (2000) for the lowest available metallicity of $Z/Z_{\odot} = 10^{-2}$. Very few stars are expected to end up in this mass range with our initial conditions (see already Table 11.1) and therefore, this does not present a strong constraint on the astrophysical realism of the simulations.

We emphasize that we still rely on the general stellar evolution routines by Hurley et al. (2000, 2002) that affect all stars with recent upgrades in `NBODY6++GPU` discussed in Kamlah, Leveque, et al. (2022) and sources therein, just not the fitting of the stellar parameters

above $8 M_{\odot}$ themselves. Adjustments have also been made, where necessary, to take into account the radically different behaviour of EMPs, for example in treatment of stellar winds, where it can be assumed that EMPs do not lose mass via winds and pulsations only if at all at our metallicity (Nakauchi et al., 2020).

We briefly reiterate the evolution of the stars for $Z/Z_{\odot} = 10^{-8}$ taken from Tanikawa et al. (2020). The stellar evolution is divided into five distinct phases in chronological order: Main Sequence (MS), Hertzsprung gap (HG), Core-Helium Burning (CHeB), Shell-Helium Burning (ShHeB) and the remnant phases of either NSs or BHs. Furthermore, Tanikawa et al. (2020) define the blue supergiant (BSG) and red supergiant (RSG) phases that relate to the surface, i.e. the effective temperature T_{eff} , of the stars. Stars with $\log_{10}(T_{\text{eff}}/K) \geq 3.65$ are classified as BSGs. Likewise, stars with $\log_{10}(T_{\text{eff}}/K) < 3.65$ are classified with RSGs. The BSG phase begins at ZAMS and ends when $\log_{10}(T_{\text{eff}}/K) < 3.65$. Subsequently, the RSG phase begins, which ends at the time of carbon ignition, which is the end point of the 1-D simulations used for the fitting formulae. For example, depending on T_{eff} a CHeB star can be a BSG or a RSG (see also Tab. 2 (in Tanikawa et al., 2020). For the metallicity of $Z/Z_{\odot} = 10^{-8}$, stars with masses of $13 \leq M/M_{\odot} < 50$ and end with BSG stars, while other stars become RSG stars at the ending time of their evolutions. Stars with $M/M_{\odot} < 13$ have entered into their ShHeB phases by the time they become RSG stars. On the other hand, stars with $M/M_{\odot} \geq 50$ still remain CHeB stars when they become RSG stars. In binary stars it is possible that the H envelope of the CHeB star is fully stripped by tides, Roche Lobe overflow (RLOF) or CEE changing the type of the star to a naked Helium MS (HeMS) star. For these stars, available fitting formulae of lowest metallicity of $Z/Z_{\odot} = 5 \times 10^{-3}$ from Hurley et al. (2000) are used instead.

In the results presented in this thesis, there is a mistake in the stellar evolution implementation, which was found just a few days before the final submission of the paper Kamlah et al. (2023, in prep.). Therefore, this chapter has the appearance of a fleshed out publication, which it technically is. We have decided **against** submitting the paper last minute. This bug has been solved, but new simulations are not in time for the production of the thesis or the paper, because they are very difficult. The bug is not so serious that all results have to be discarded and they can still be interpreted but with some caution. These models should be considered as prototype simulations of NBODY6++GPU coupled with full Pop-III stellar evolution and self-consistent GW merger recoil kicks and Since these models were a considerable part of my PhD work I have included them in the thesis. Furthermore, new simulations are ongoing.

The bug can be briefly summarised as follows: In the original code version of NBODY6++GPU, stars with masses of around $8 - 20 M_{\odot}$ do NOT evolve to NSs (and stay SheB stars; they are repeatedly rejuvenated) even if their lifetime exceeds 16 Myr. In fact, due to a mass loss criterion in they never change stellar types to a compact object if no other binary mass transfer happens that

moves them out of that mass range. [Figure 11.1](#) shows the fixed stellar evolution. The buggy stellar evolution implementation a large number of consequences. Among them are:

- ▶ Many NSs receive natal kicks that might eject them from the cluster leading to mass and particle loss and thus much faster cluster evolution and dissolution.
- ▶ Many NSs are missing that would otherwise possibly be potential members in BH-NS or NS-NS binaries and mergers, which have interesting and relevant GW signatures for detectors.
- ▶ There are many more ShHeB stars participating in binary evolution and that can feed BHs than there should be.

Nevertheless, I present these results because the Pop-III implementation (apart from the small bug) are a real novelty in the `NBODY6++GPU` code.

11.3.4 General relativistic merger recoil kicks

The latest studies of IMBH growth (e.g. Di Carlo, Mapelli, Bouffanais, et al., [2020](#); Di Carlo, Mapelli, Giacobbo, et al., [2020](#); Di Carlo et al., [2019, 2021](#); Rizzuto, Naab, Spurzem, Giersz, et al., [2021](#); Rizzuto et al., [2022](#)) and star cluster dynamics with `NBODY6++GPU` (e.g. Kamlah, Leveque, et al., [2022](#); Kamlah, Spurzem, et al., [2022](#)) do not include a general relativistic (GR) merger recoil treatment (in addition to missing PN terms). Arca-Sedda et al. ([2021](#)) do include the GR merger recoil kicks by a posteriori analysis, but this cannot replace a fully self-consistent modelling during the simulation. Another code from the *N*-body family `NBODY7` (S. J. Aarseth, [2012](#); Banerjee et al., [2020](#); Banerjee, [2021a](#)) and also the version of `NBODY6++GPU` presented in this paper contain a proper treatment of such velocity kicks, see also Arca Sedda et al. (in prep.). They depend on spins and mass ratio, and are caused due to asymmetric GW radiation during the final inspiral and merger process. Numerical relativity (NR) models (Campanelli et al., [2007](#); Hughes, [2009](#); Jiménez-Forteza et al., [2017](#); Rezzolla et al., [2008](#); van Meter et al., [2010](#)) have been used to formulate semi-analytic descriptions for MOCCA and `NBODY` codes (Arca-Sedda et al., [2021](#); Banerjee, [2021a, 2021b](#); Belczynski & Banerjee, [2020](#); Morawski et al., [2018, 2019](#)). For (nearly) non-spinning BHs (FULLER model), the kick velocity is smaller than for high spins. In the case of large mass ratios the kick velocity is much smaller than for small mass ratios (Morawski et al., [2018, 2019](#)) and therefore, in extreme cases these post-merger BHs might even be retained in open clusters (Baker et al., [2007, 2008](#); Baumgardt & Hilker, [2018](#); Portegies Zwart et al., [2010](#); Schödel et al., [2014](#)). For non-aligned natal spins and small mass ratios on the other hand, the asymmetry in the GW may produce GR merger recoils that reach thousands of kms^{-1} (Baker et al., [2008](#); van Meter et al., [2010](#)).

Generally, the orbital angular momentum of the BHBH dominates the angular momentum budget that contributes to the final spin vector of the post-merger BH and therefore, within limits, the final spin vector is mostly aligned with the orbital momentum vector

(Banerjee, 2021a). In the case of physical collisions and mergers during binary-single interactions, the orbital angular momentum is not dominating the momentum budget and thus the BH spin can still be low. Banerjee (2021a) also includes a treatment for random isotropic spin alignment of dynamically formed BHs. Additionally, Banerjee (2021a) assumes that the GR merger recoil kick velocity of NSNS and BHNS mergers (Arca Sedda, 2020; Chattopadhyay et al., 2021) to be zero but assigns merger recoil kick to BHBH merger products from numerical-relativity fitting formulae of van Meter et al. (2010) (which is updated in Banerjee (2021b)). The final spin of the merger product is then evaluated in the same way as a BHBH merger.

We implement numerical relativity fitting formulae for both the recoil kick velocity (Campanelli et al., 2007; Lousto et al., 2012) and the remnant mass and spin (Jiménez-Forteza et al., 2017). The implementation is explained in detail in Arca Sedda and et al. (2023a) in the DRAGON-II simulations (see also Arca Sedda & et al., 2023b, 2023c) and will not be repeated here (but see also section 2.5 and 2.6 in Arca Sedda, Mapelli, et al., 2020). The N_{BODY}6++GPU code versions used here and Arca Sedda and et al. (2023a) adopt the same implementation for the treatment of merging compact objects, but here we further implement stellar evolution recipes for Pop-III stars. We stress that these kicks apply to all compact object mergers, so also compact object binary mergers consisting of WDs and NSs. We note that this is one of areas of the code that we pointed out in Kamlah, Leveque, et al. (2022) that needed improvement and that is now completed.

11.4 Initial conditions

11.4.1 Star cluster parameters

Part of the initial model was constructed with MCLUSTER (Küpper et al., 2011a) with updates described in Kamlah, Leveque, et al. (2022) and Leveque, Giersz, Arca-Sedda, and Askar (2022). We create models that are much more massive and contain many more stars than earlier simulation studies of Pop-III star clusters (e.g. Sakurai

Table 11.1: Initial parameters that are identical across all eight initial models for the N_{BODY}6++GPU simulations.

| Quantity | Value |
|-------------------------------------|--|
| Particle number | 1.01×10^5 |
| Cluster mass | $8.135 \times 10^6 M_{\odot}$ |
| Cluster metallicity | $Z/Z_{\odot} = 10^{-8}$ |
| Binary fraction f_b | 1.0% |
| Half mass radius r_h | 1.00 pc |
| Tidal radius r_{tid} | 264.50 pc |
| IMF | flat (alpha=1) (8.0 – 300.0) M_{\odot} |
| Density model | King model (I. King, 1962) $W_0 = 6.0$ |
| Eccentricity distribution $f(e)$ | Thermal ($f(e) \propto e^2$) |
| Semi-major axis distribution $f(a)$ | uniform in $\log(a)$ between 10 AU and 100 AU |
| mass ratio distribution $f(q)$ | uniform distribution of mass ratio ($0.1 < q < 1.0$) for $m > 5 M_{\odot}$ |

Table 11.2: Model identifiers (Model ID) for the eight N_{BODY6++}GPU simulations.

| Model ID | GR kicks? | ω_0 |
|----------------------|-----------|------------|
| GRk ω_0 0.0 | yes | 0.0 |
| GRk ω_0 0.6 | yes | 0.6 |
| GRk ω_0 1.2 | yes | 1.2 |
| GRk ω_0 1.8 | yes | 1.8 |
| noGRk ω_0 0.0 | no | 0.0 |
| noGRk ω_0 0.6 | no | 0.6 |
| noGRk ω_0 1.2 | no | 1.2 |
| noGRk ω_0 1.8 | no | 1.8 |

et al. (2017), Vergara et al. (2021), and Wang et al. (2022)). The initial number of objects is set to 10^5 with a binary fraction of 0.01, which yields total number of stars of 1.01×10^5 . Our clusters have an initial cluster mass of $8.135 \times 10^6 M_\odot$. In McLUSTER, we use a King density model with a King model parameter of $w_0 = 6.0$ (I. R. King, 1966b). The model shows no initial mass segregation and is unfractal (Goodwin & Whitworth, 2004). The model is initially in virial equilibrium. The half-mass radius is set to $r_h=1$ pc. The initial model from McLUSTER is then redistributed with a rotating King model, which are more compact than their non-rotating counterparts (Einsel & Spurzem, 1999). Therefore, the internal structural parameters such as the r_h and r_c change in this initialisation step from their original McLUSTER N -body distribution (see already Figure 11.2).

We use a flat IMF between $8.0 M_\odot$ and $300.0 M_\odot$ (Lazar & Bromm, 2022). The binaries are paired in their mass ratios q following (Kiminki et al., 2012; Kobulnicky et al., 2014; Sana et al., 2012, 2013; Sana & Evans, 2011), meaning that we have a uniform distribution of mass ratio ($0.1 < q < 1.0$) for $m > 5 M_\odot$ and random pairing for the remaining binaries. Their semi-major axes are distributed uniformly between 10.0 AU and 100.0 AU. The eccentricity distribution is thermal.

The cluster's absolute metallicity is set to $Z/Z_\odot = 10^{-8}$ (Wang et al., 2022, also uses the fitting formulae for this metallicity), which is the lowest currently available metallicity for the stellar evolution fitting formulae from Tanikawa et al. (2020). We put our cluster initial models on a circular orbit around the galaxy of radius 13.3 kpc as was done in Kamlah, Spurzem, et al. (2022) (according to Cai et al. (2016) a circular orbit can be chosen such that the mass loss evolution of the cluster is similar compared to the eccentric orbit of NGC3201 (between 8.60 and 29.25 kpc, with eccentricity $e = 0.55$ according to Gaia DR2 data Gaia Collaboration et al., 2018) around a point-mass MW of mass $1.78 \times 10^{11} M_\odot$ (assuming a circular velocity $v_c = 240.0 \text{ km s}^{-1}$ at the Solar distance) (Bobylev & Bajkova, 2020; Gaia Collaboration et al., 2018). This set-up yields an initial tidal radius of 264.50 pc. Therefore, the models are very tidally underfilling. Keeping the star cluster models from Kamlah, Leveque, et al. (2022), Kamlah, Spurzem, et al. (2022) and this work on the same orbits around the same point-mass MW-like galaxy allow for better comparisons in follow-up studies.

We run the simulations up until 500 Myr for three reasons: firstly, the gravothermal-gravogyro catastrophe will have decreased in

amplitude and the star cluster will have undergone core-collapse, secondly, most of the ZAMS stars will have evolved to their final evolutionary stage, in particular the most massive ones and thirdly, star cluster environment changes are non-negligible and it is unlikely that Pop-III star clusters will continue their lives without merging with other clusters somewhere at some point (see, e.g., Arca-Sedda and Gualandris (2018)). The latter point implies that long-term simulations even beyond 10 Gyr of Pop-III star clusters such as presented in Wang et al. (2022), while they are very valuable, might not strictly be necessary.

In the interest of aiding the discussion, we introduce model IDs for our eight individual runs, see Table 11.2. For example, the non-rotating model without GR merger recoil kicks is named noGRk ω_0 0.0, while the rotating model with $\omega_0 = 1.2$ and GR merger recoil kicks is named GRk ω_0 1.2. The details of the full stellar evolution parameters are discussed below. Furthermore, we will refer to the group of models without GR merger recoil kicks as noGRk models and to the group of models with GR merger recoil kicks as GRk models from here on after.

11.4.2 Stellar evolution parameters

We largely follow the Level C stellar evolution as presented in Kamlah, Leveque, et al. (2022), which also describes the stellar evolution routines and parameters in detail, but we make adjustments in the code where necessary to account for Pop-III stellar evolution. Given the intrinsic properties of Pop-III stars at $Z/Z_\odot = 10^{-8}$, we assume no radiation-driven wind mass loss in our simulations (Tanikawa et al., 2020). We also assume no pulsation-driven (e.g. Nakauchi et al., 2020) or rotation-driven mass losses (e.g. Liu, Sibony, et al., 2021). For the compact object evolution, we use remnant mass prescriptions following C. L. Fryer et al. (2012) and here we choose the delayed SNe mechanism as the slow extreme of the convection-enhanced neutrino-driven SNe paradigm. We use collapse-asymmetry driven, fallback-scaled kicks (see e.g. Banerjee et al. (2020) and Kamlah, Leveque, et al. (2022); drawn from a Maxwellian distribution with a dispersion of 265.0 km s^{-1} from Hobbs et al. (2005)) for the NSs and BHs (Belczynski et al., 2008), except for the NSs that are produced by the ECSNe, AIC and MIC (Gessner & Janka, 2018; Ivanova et al., 2008; Leung, Nomoto, & Suzuki, 2020; Podsiadlowski et al., 2004) and that are subject to low velocity kicks (drawn from a Maxwellian with a dispersion of 3.0 km s^{-1} from Gessner & Janka, 2018). This setting produces velocity kicks of very low magnitude and when the fallback is 1, then the kicks are non-existent. The BHs receive natal spins following the Fuller models (Banerjee et al., 2020; Banerjee, 2021a; Kamlah, Leveque, et al., 2022), which implies natal spins of magnitude zero. We do not expect the production of WDs, but for the record, they would receive natal kicks following Fellhauer et al. (2003) (drawn from a Maxwellian with a dispersion of 2.0 km s^{-1} but, which is capped at 6.0 km s^{-1}). Importantly, we switch on the (pulsational) pair instability SNe following Belczynski et al. (2016), a process, which has recently been underpinned with observational evidence, see Woosley and Smith (2022).

It is worthwhile to briefly highlight the details of the (P)PSINe remnant mass prescriptions for the BHs that we use. The progenitor star in the He core mass range of $65.0 \leq m_{\text{He}}/M_{\odot} \leq 135.0$ is destroyed in the SNe explosion (leaving behind a massless remnant of type KW = 15). The maximum He core mass is set to $45.0 M_{\odot}$, below which the PISNe is not activated (Belczynski et al., 2016). In their scheme, the BH mass from a PPISNe is set to $40.5 M_{\odot}$ from $45.0 M_{\odot}$ minus a 10% neutrino mass loss (Timmes et al., 1996). In the range of $45.0 \leq m_{\text{He}}/M_{\odot} \leq 135.0$ the star is destroyed by PISNe. Above that m_{He} mass, we assume that the He core collapses directly into an IMBH and we model the remnant mass again following C. L. Fryer et al. (2012). To clarify, we refer to a BH with a mass above $100 M_{\odot}$ as an IMBH.

Lastly, concerning the runs with GR merger recoil kicks we briefly outline the settings. When there is a collision between two compact objects (in these simulations they will be NSs or BHs), then the merger product will have a spin drawn from a Maxwellian distribution with $\sigma = 0.2$. In the collision itself, there is a mass loss due to the emission of GWs. Therefore, the final merger product will have 0.985 times the sum of the masses of the compact objects that participated in the merger. The kick velocity is then calculated as described in Section 11.3.4.

11.5 Results

11.5.1 Global dynamical evolution

Structural parameter evolution

We run each of the four initial models ($\omega_0 = 0.0, 0.6, 1.2, 1.8$) with N_{BODY}6++GPU once with GR recoil kicks switched on (GRk models) and once without (noGRk models). Hence we have eight distinct simulations to compare and contrast. We note, that there should not be a large difference in the global evolution between the models with the same ω_0 with and without GR recoil kicks. Therefore, we should expect very similar evolution for identical initial bulk rotation. Furthermore, these simulations are just as much an investigation into the impact of initial bulk rotation on the Pop-III star cluster evolution, as it is a study of how GR recoil kicks impact the formation of IMBHs in these environments. In the following we discuss Figure 11.2 to Figure 11.6 to get an overview on the global evolution of the simulated star clusters.

Figure 11.2 shows the total cluster mass $M_{\text{cl}} (M_{\odot})$, the tidal radius r_{t} (pc), the half mass radius r_{h} (pc), the mass of the core $m_{\text{c}} (M_{\odot})$ and the radius of the core r_{c} (pc) in the four panels, respectively. In N_{BODY}6++GPU, particles (single or binary stars) are removed from the star cluster once they have reached a distance that is twice the *current* tidal radius far away from the density centre. They are called “escapers” thereafter. The current tidal radius is then calculated using the *current* cluster mass. Escapers do not contribute to the current cluster mass. They are also not taken into account when calculating any of the other structural parameters of the star clusters,

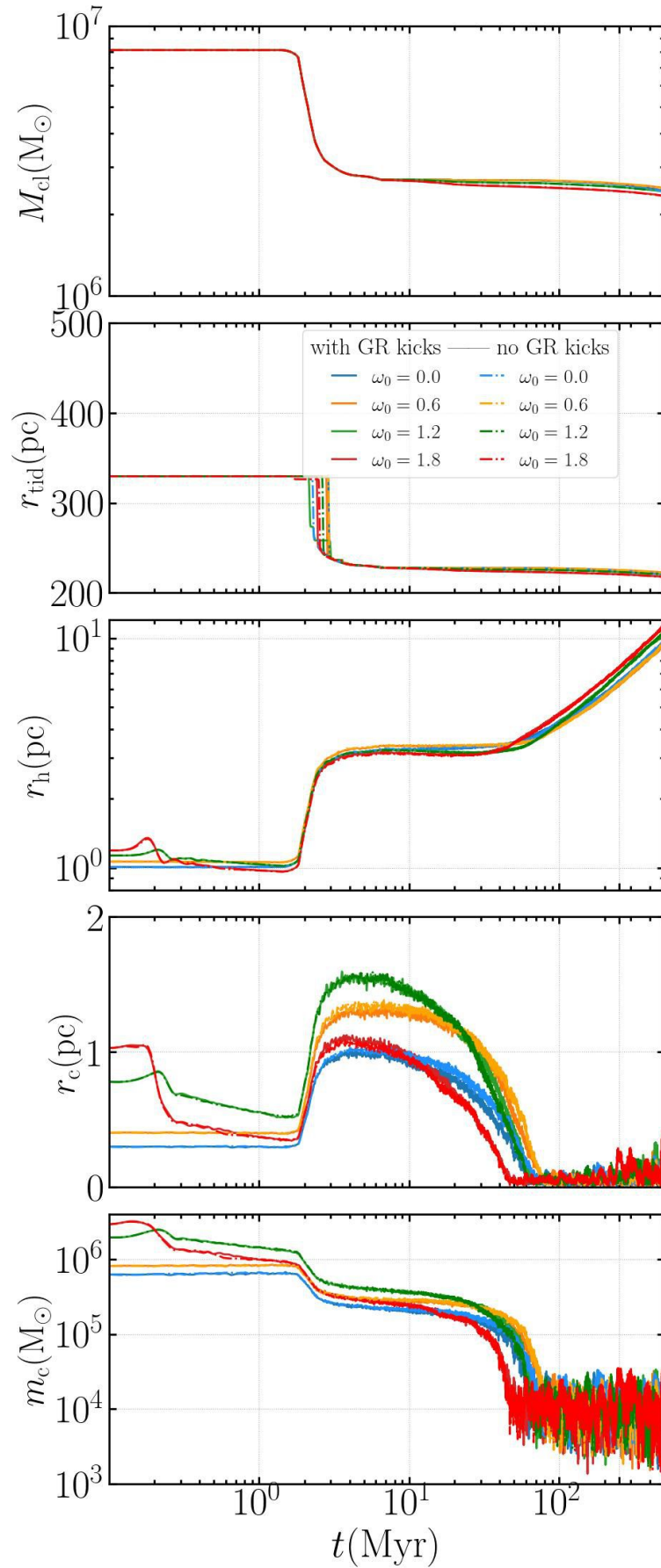


Figure 11.2: Plot showing the total cluster mass M_{cl} (M_{\odot}), the tidal radius r_t (pc), the half mass radius r_h (pc) and the mass of the core m_c (M_{\odot}) and the radius of the core r_c (pc) in the four panels for all eight simulations with and without GR recoil kicks for $\omega_0 = 0.0, 0.6, 1.2, 1.8$, respectively. The time axis is plotted logarithmically to show the details of the much more rapid early cluster evolution. The models with GR recoil kicks (GRk models) are plotted as solid lines and the models without GR recoil kicks (noGRk models) are plotted as dash-dotted lines.

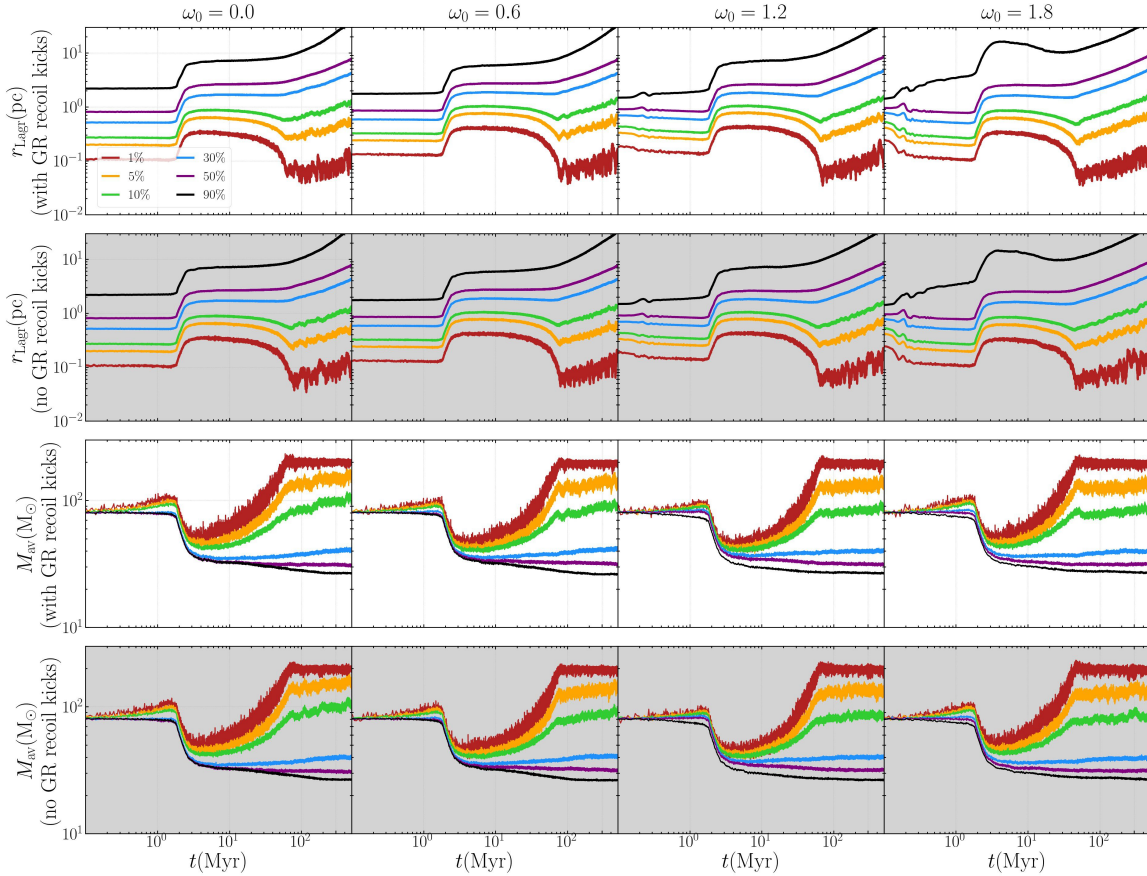


Figure 11.3: Plot showing the Lagrange radii r_{Lagr} (pc) and the average mass M_{av} (M_{\odot}) within shells that contain 1%, 5%, 10%, 30%, 50%, and 90% of the total cluster mass at the current simulation time step for up to 500 Myr. The time axis is plotted logarithmically to show the details of the much more rapid early cluster evolution. Each column represents one rotational parameter ω_0 of the rotating King model in ascending order from left to right ($\omega_0 = 0.0, 0.6, 1.2, 1.8$). The results from the runs *with* GR kicks switched on (GRk models) are plotted on a white background, while the results from the simulations *without* GR kicks (noGRk models) are highlighted in light grey.

such as r_h or m_c .

We identify a four phase evolution of the star cluster models:

- **Phase I:** First, we focus on the phase of star cluster evolution before the stellar evolution mass loss begins to dominate, so the time from 0 Myr to around 2 Myr. M_{cl} and r_t stay practically constant, because no mass loss from the cluster through escapers or stellar evolution is occurring. Depending on the degree of initial rotation measured by ω_0 , the remaining structural parameter in Figure 11.2 show many more variations. As already shown in Kamlah, Spurzem, et al. (2022) for Pop-I star cluster models initialised with rotating King models as presented here, the angular momentum transport can be extremely fast and generally happens earlier than the star cluster’s core-collapse; the larger the degree of initial rotation measured by ω_0 , the faster this evolution happens generally. In the Pop-III star clusters presented in this work, we also observe this fast angular momentum transport already from Figure 11.2. Within the first Myr already, the larger the initial rotation, the more pronounced is the temporary increase of r_h and decrease shortly after. The larger the initial rotation, the faster this evolution happens as well (compare the (no)GRk ω_0 1.2

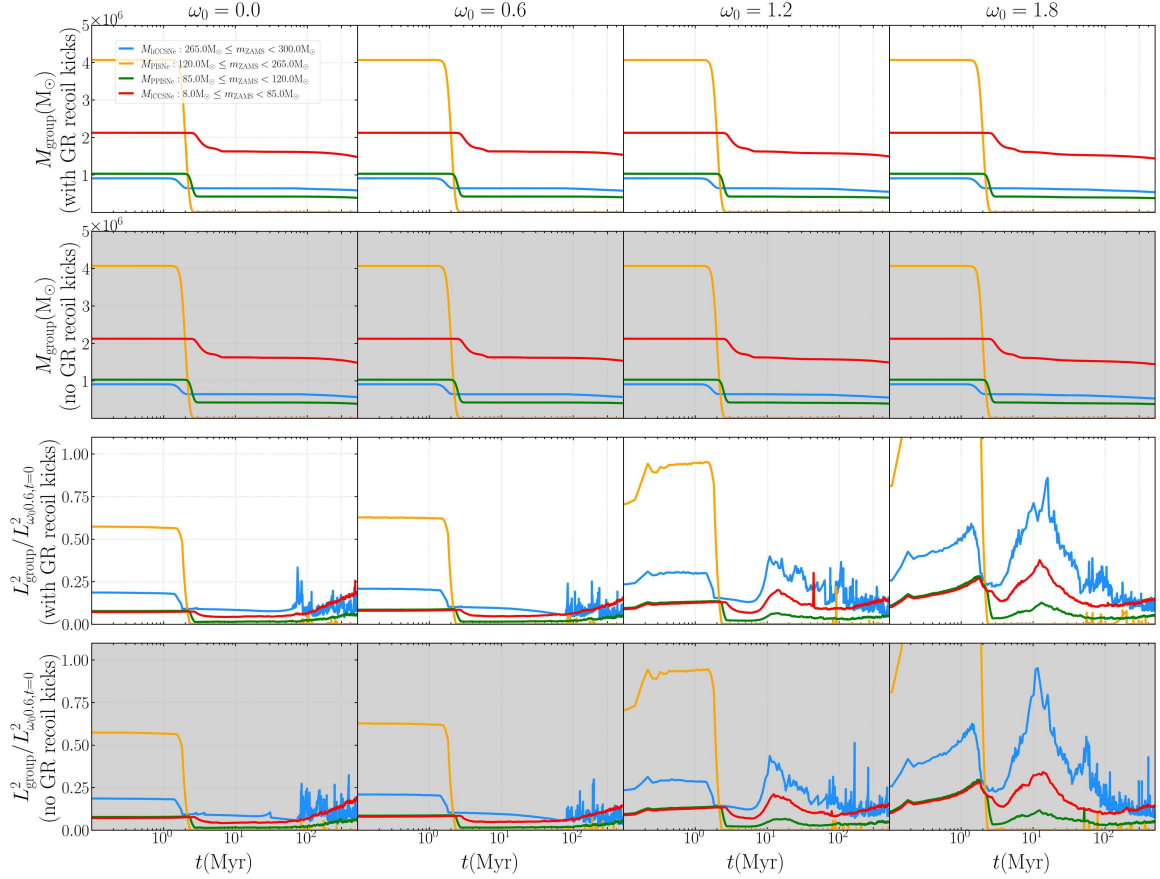


Figure 11.4: Plot showing the total mass of the four mass groups (M_{ICCSNe} is shown in red, M_{PPSiNe} is shown in green, M_{PISNe} is shown in orange and M_{hCCSNe} is shown in shown in blue) in the top two rows and the square of the total angular momentum divided by the square of the total angular momentum of the $\omega_0 0.6$ model(s) at $t = 0$, $L_{\text{group}}^2 / L_{\omega_0 0.6, t=0}^2$ for these groups L_{group}^2 at the current simulation time step for up to 500 Myr. The time axis is plotted logarithmically to show the details of the much more rapid early cluster evolution. Each column represents one rotational parameter ω_0 in ascending order from left to right ($\omega_0 = 0.0, 0.6, 1.2, 1.8$). The results from the runs *with* GR kicks switched on (GRk models) are plotted on a white background, while the results from the simulations *without* GR kicks (noGRk models) are highlighted in light grey.

with the (no)GRk $\omega_0 1.8$ models). This evolution is even more apparent in Figure 11.3, which shows the evolution of the Lagrangian radii r_{Lagr} within shells that contain 1%, 5%, 10%, 30%, 50%, and 90% of the total cluster mass at the current simulation time step. Each of the four columns represents a rotational parameter ($\omega_0 = 0.0, 0.6, 1.2, 1.8$) and every second row shows the noGRk models on a light grey background. Looking at the (no)GRk $\omega_0 1.8$ models in particular, we see the drastic impact of the degree of initial bulk rotation; the outermost r_{Lagr} is expanding heavily, while all others are generally shrinking up until 2 Myr except for the small bump (increase and decrease pattern) at around 0.1 Myr that is found in all r_{Lagr} . We still observe this evolution in the (no)GRk $\omega_0 1.2$ models to a lesser extent and slightly delayed compared with (no)GRk $\omega_0 1.8$ models. For the remaining (no)GRk $\omega_0 0.0$ and (no)GRk $\omega_0 0.6$ models, this evolution cannot be identified. For the (no)GRk $\omega_0 0.0$ and (no)GRk $\omega_0 0.6$ models, r_{h} stays approximately constant during the same time interval and until stellar evolution mass begins to dominate at around 2 Myr. This early evolution is also mirrored by r_{c} and m_{c} , where both

the (no)GRk ω_0 1.2 and the (no)GRk ω_0 1.8 exhibit fast increases with subsequent decreases in the respective models. Again, this evolution is more pronounced and happens earlier in the (no)GRk ω_0 1.8 with respect to the (no)GRk ω_0 1.2 models. In summary, the evolution of all models from (0-2) Myr is exclusively to the (missing) initial bulk rotation as tidal or stellar evolution mass losses are both not occurring here.

- Phase II: In the short second phase after around 2 Myr up until around 3 Myr, the star clusters begin to lose extreme amounts of mass due to stellar evolution, as can immediately be seen in the evolution of M_{cl} . This strong mass loss is a result of compact object formation, but in particular due to PISNe events, in which no BHs are produced and all the mass is immediately lost from the cluster. Further mass loss happens by escaping stars, either through compact object natal kicks and GR recoil kicks, strong dynamical encounters or by a series of weak dynamical encounters. It is worth mentioning that also the overall kinematic structure of the star cluster changes here due to many fallback-dependent natal kicks that are generally larger for lower mass BHs (see Kamlah, Leveque, et al., 2022). For a discussion on the escapers and their dependence on ω_0 , see Section 11.5.5. At the same time there is also a huge decrease in r_t and increase in r_h for all cluster models. The evolution of r_c at this stage reveals an interesting pattern: while in all models r_c increases simultaneously, the maxima between the (no)GRk ω_0 1.2 and (no)GRk ω_0 1.8. Furthermore, the core of the (no)GRk ω_0 1.8 models are (no)GRk ω_0 0.0 are similarly compact, with the (no)GRk ω_0 0.6 models exhibiting an intermediate maximum r_c . Simultaneous to the build up of the maximum in r_c , m_c decreases in all models to the same extent. We compare this with the average mass in the core M_{av} (M_{\odot}) within shells that contain 1%, 5%, 10%, 30%, 50%, and 90% of the total cluster mass at the current simulation time step that is shown in Figure 11.3. M_{av} (M_{\odot}) can be used as a measure of mass segregation in the cluster models. We see that here all models show similar segregation of masses into different shells independent of initial bulk rotation; for example, the minimum M_{av} in the 10% shell has similar values occurs at similar times, although we note that this quantity is subject to large statistical fluctuations.
- Phase III: The third phase of cluster evolution from around 3 Myr to time of gravothermal core-collapse varies in duration much more strongly than the previous phase, which can be seen most clearly the evolution of r_{Lagr} from Figure 11.3: for the (no)GRk ω_0 0.0 models, maximum core collapse happens at around 80 Myr, while for the (no)GRk ω_0 1.8 models it already happens at 50 Myr. For the (no)GRk ω_0 0.6, it happens at around 70 Myr and for the (no)GRk ω_0 1.2 models at around 60 Myr. Therefore, the larger the degree initial bulk rotation in our Pop-III star clusters, the earlier core collapse happens. This evolutionary pattern was already seen in, e.g., Akiyama

and Sugimoto (1989), Einsel and Spurzem (1999), Fiestas et al. (2012), Kamlah, Spurzem, et al. (2022), Kim et al. (2002), and Kim et al. (2004, 2008). Generally, as the central density becomes higher, the time scale of the gravothermal collapse becomes shorter. The degree of mass segregation at the time of core-collapse that can be seen in M_{av} from Figure 11.3 of the respective models also shows variations. Generally, for increasing ω_0 the models reach larger M_{av} in the 5% and 10% shells at the time of core-collapse. For the GRk ω_0 1.8 there is even a decrease of M_{av} in these shells shortly after, while all other models still show evolution of increasing M_{av} in the same shells to varying degrees. This finding implies that mass segregation happens earlier, the larger the degree of initial bulk rotation of the Pop-III star clusters is. For the (no)GRk ω_0 1.8, the star cluster expansion is so extreme that many stars already escape in this phase and before, so there is an actual decrease in $r_{\text{lagr}3}$ for 90 %, which is not present for the other models (see also Section 11.5.5).

- Phase IV: The fourth phase of the cluster evolution, which starts from the time of core-collapse to the end of the simulation at 500 Myr, is characterized by a self-similar evolution of the Lagrangian radii. This kind of evolution is dominated by binary energy generation in the star cluster center and subsequent expansion of the cluster. At 500 Myr, the larger the cluster initial bulk rotation, the more the cluster has expanded, which can be attributed to the earlier core-collapse in more rotating models, as the evolution of r_{Lagr} is very similar. The post-core collapse evolution shows that the full cluster has completely mass segregated, with M_{av} reaching around 200 M_{\odot} in the central cluster shells and around 30 M_{\odot} in the halo region of the cluster. By the same token, all quantities from Figure 11.2 exhibit similar long-term evolution. Longer simulation times could perhaps find larger differences here. The discussion above can also be understood by considering theorems surrounding energy flow through the half-mass radius r_h that are described in M. Hénon (1975) (see also Breen & Heggie, 2013).

In summary, we have seen from Figure 11.2 and Figure 11.3 the close connection between the two dominating processes in our star cluster simulations: the gravothermal-gravogyro catastrophe and Pop-III stellar evolution, in particular, the associated missing wind mass loss in combination with our supernovae and fallback-dependent natal kicks models. These processes are largely responsible for the four-phase evolution that we observe.

Angular momentum transport

While, the discussion on the structural parameters in the previous section already sketches extremely complex four-phase evolution of the Pop-III star clusters, in which different processes dominate

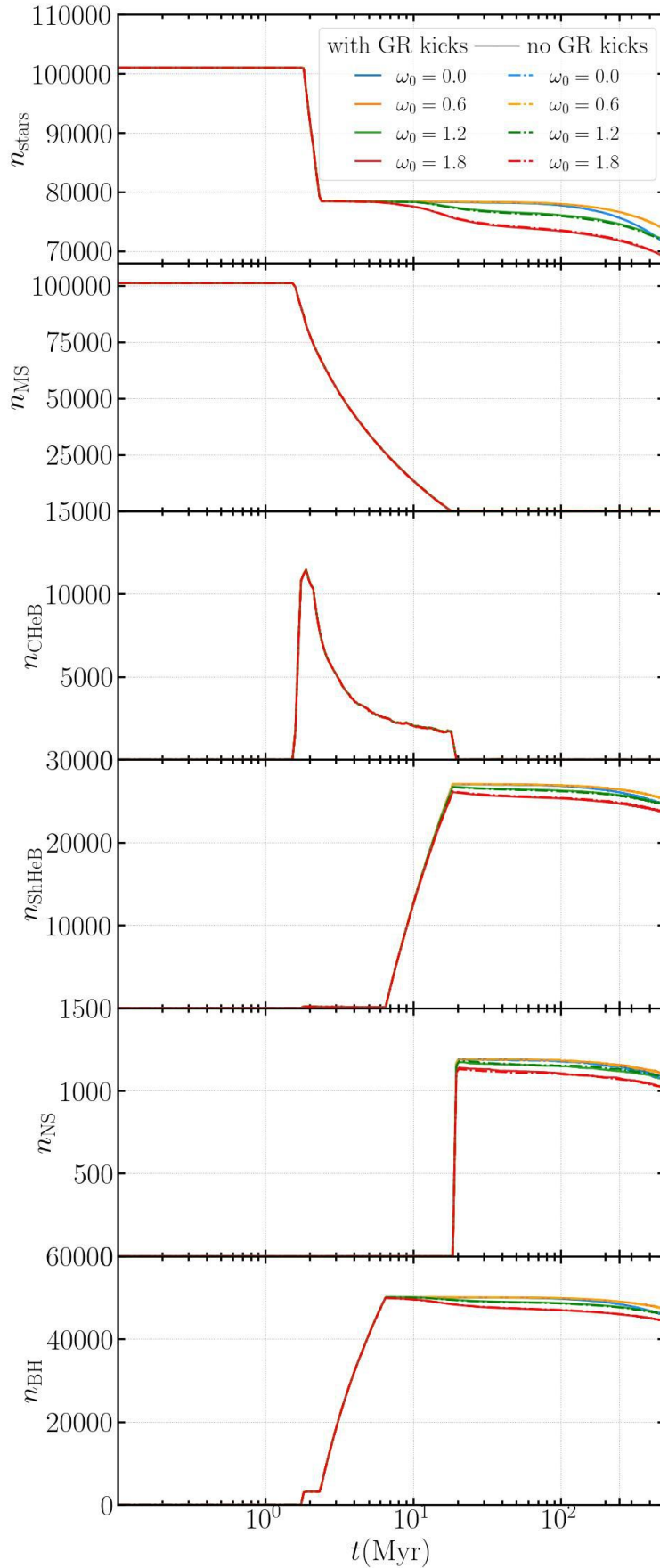
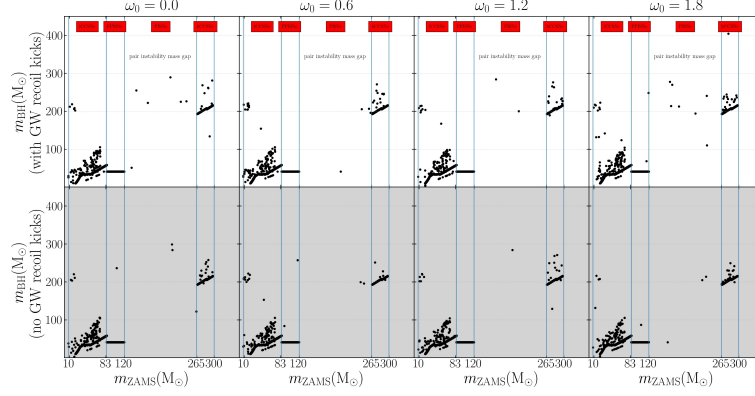


Figure 11.5: Plots showing the number of stars n_{stars} , the number MS stars n_{MS} , the number MS stars n_{CHeB} , the number ShHeB stars n_{ShHeB} , the number NS stars n_{NS} , the number BH stars n_{BH} in the six panels for all eight simulations with and without GR recoil kicks for $\omega_0 = 0.0, 0.6, 1.2, 1.8$, respectively. The time axis is plotted logarithmically to show the details of the much more rapid early cluster evolution. The models with GR recoil kicks (GRk models) are plotted as solid lines and the models without GR recoil kicks (noGRk models) are plotted as dash-dotted lines.

Table 11.3: Absolute numbers of stars, n_{stars} , ShHeB stars, n_{ShHeB} , NSs, n_{NS} and BHs, n_{BH} at 500 Myr for all eight $N_{\text{BODY6++GPU}}$ simulations. The column headers have been abbreviated - G corresponds to the GRK and noG corresponds to the noGRK models.

| Model ID | G ω_0 0.0 | G ω_0 0.6 | G ω_0 1.2 | G ω_0 1.8 | noG ω_0 0.0 | noG ω_0 0.6 | noG ω_0 1.2 | noG ω_0 1.8 |
|--------------------|------------------|------------------|------------------|------------------|--------------------|--------------------|--------------------|--------------------|
| n_{stars} | 71304 | 73726 | 71812 | 68975 | 71389 | 73569 | 71630 | 69130 |
| n_{ShHeB} | 24508 | 25240 | 24658 | 23592 | 24551 | 25230 | 24557 | 23698 |
| n_{NS} | 1085 | 1102 | 1066 | 1016 | 1071 | 1099 | 1079 | 1019 |
| n_{BH} | 45711 | 47384 | 46088 | 44367 | 45767 | 47240 | 45994 | 44413 |

**Figure 11.6:** Plots showing the initial-final-mass relation (IFMR) with the mass of the BH, m_{BH} (M_{\odot}), plotted against the m_{ZAMS} (M_{\odot}) of the progenitor ZAMS stars for all eight simulations with and without GR recoil kicks for $\omega_0 = 0.0, 0.6, 1.2, 1.8$. Each column represents one rotational parameter ω_0 in ascending order from left to right ($\omega_0 = 0.0, 0.6, 1.2, 1.8$). The results from the runs *with* GR merger recoil kicks switched on (GRK models) are plotted on a white background, while the results from the simulations *without* GR merger recoil kicks (noGRK models) are highlighted in light grey. The blue lines separate the following regions in m_{ZAMS} (M_{\odot}) (see also the red labels at the top of the plots): stars that explode by low mass core-collapse supernovae (lCCSNe), by pulsational pair instability supernovae (PPISNe), by pair instability supernovae (PISNe) and by high mass core-collapse supernovae, from left to right, respectively. We observe ImBH formation below, within and above the pair instability mass gap.

the star cluster evolution at different points in simulation time, and while we have already seen that clearly the initial star cluster rotation has a large impact on its global evolution, we want to explore how the angular momentum is transported within the star cluster simulations and if and how this depends on the stellar evolution, GR recoil kicks and initial bulk rotation strength. This analysis helps us to define the angular momentum transport between the stars and therefore, it helps us to see the gravogyro-gravothermal catastrophe more clearly. For this purpose, we divide the complete ZAMS particle set into four distinct mass groups (low mass core-collapse supernovae (lCCSNe), pulsational pair instability supernovae (PPISNe), pair instability supernovae (PISNe) and high mass core-collapse supernovae (hCCSNe)):

$$M_{\text{lCCSNe}} : 8.0 M_{\odot} \leq m_{\text{ZAMS}} < 85.0 M_{\odot}$$

$$M_{\text{PPISNe}} : 85.0 M_{\odot} \leq m_{\text{ZAMS}} < 120.0 M_{\odot}$$

$$M_{\text{PISNe}} : 120.0 M_{\odot} \leq m_{\text{ZAMS}} < 265.0 M_{\odot}$$

$$M_{\text{hCCSNe}} : 265.0 M_{\odot} \leq m_{\text{ZAMS}} < 300.0 M_{\odot},$$

where m_{ZAMS} is the ZAMS stellar mass of a single star (this also means that a primordial binary star could have binary members that are in two different mass groups). The mass groups are chosen such that the stars from M_{lCCSNe} core-collapse into BHs by CCSNe by low mass ZAMS stars of our IMF, the stars from M_{PPISNe} form BHs through PPISNe, the stars from M_{PISNe} form BHs through PISNe

and the stars from M_{HCCSNe} core-collapse into BHs again by CCSNe but this time from high mass ZAMS stars of our IMF, approximately. We can then follow the particles that originate from these mass groups through the full cluster evolution and compute their angular momentum across the full evolution. An analogous calculation was also done in Kamlah, Spurzem, et al. (2022) and the details will not be repeated here (the cluster initial conditions are very different in that study, so the separation of the mass m_{ZAMS} was also done differently).

For the mass groups we calculate L_{group}^2 of the individual mass groups in a similar fashion as described in Kamlah, Spurzem, et al. (2022). All L_{group}^2 are divided by $L_{\omega_0 0.6, t=0}^2$, which is the square of the total angular momentum of the $\omega_0 0.6$ model(s) at $t = 0$ (the sum of all L_{group}^2 for the $\omega_0 0.6$ models divided by $L_{\omega_0 0.6, t=0}^2$ is one). This division is done so that the models can be compared with each other more easily. These quantities are shown in Figure 11.4 along with M_{group} (M_{\odot}), which is the mass of all the stars (and compact objects) in the four groups as a function of time. Again, we look at the four-phase evolution that we have defined in Section 11.5.1:

- ▶ Phase I: this phase of star cluster evolution occurs before the stellar evolution mass loss begins to dominate, so the time from 0 Myr to around 2 Myr. Unsurprisingly, the evolution of M_{group} for the individual mass groups across all simulations is very similar. However, the evolution of $L_{\text{group}}^2/L_{\omega_0 0.6, t=0}^2$ exhibits much more variation here. For increasing ω_0 and especially for the (no)GRk $\omega_0 1.2$ and most notably for the (no)GRk $\omega_0 1.8$ models we see a large increase in all mass groups. This finding implies that the initially very compact star clusters expand rapidly overall and that many stars from all mass groups are migrating outwards relative to the cluster centre quickly, which explains the overall increase in $L_{\text{group}}^2/L_{\omega_0 0.6, t=0}^2$ for the $\omega_0 1.8$ model. This effect is supported by looking at the various structural radii that can be found in Figure 11.2 and Figure 11.3, which exhibit a large increase in their outermost radii with a simultaneous decrease in the innermost ones, which can be seen in particular for the (no)GRk $\omega_0 1.8$ models (refer to the discussion of the four-phase evolution in Section 11.5.1.)
- ▶ Phase II: in the short second phase after around 2 Myr up until around 3 Myr, the star clusters begin to lose extreme amounts of mass due to stellar evolution. It is mirrored in the evolution of M_{group} , all of which decrease enormously during this time. Note, that because stars from different mass groups evolve at different time-scales, this decrease happens progressively faster for increasing mass group. For the M_{PISNe} we now see the mass loss attributed to the PISNe from the cluster clearly and importantly, the huge loss of angular momentum as well, because before PISNe M_{PISNe} shows the largest angular momentum of all and after PISNe, this angular momentum has effectively diminished on all simulations. Therefore, with the loss of stars due to PISNe, a huge loss of rotational kinetic energy happens as well.

- ▶ Phase III: here, the cluster evolution occurs from around 3 Myr to time of gravothermal core-collapse, which generally occurs earlier for increasing, initial bulk rotation (see discussion in Section 11.5.1 and Figure 11.3). Depending on ω_0 there are radical differences between the models that are especially visible in the evolution of $L_{\text{hCCSNe}}^2/L_{\omega_0,0.6,t=0}^2$. Although, this quantity is decreasing initially after phase II, for increasing ω_0 instead of continuing to decrease even beyond phase III, for the (no)GRk ω_0 1.2 and (no)GRk ω_0 1.8 models, there is an extreme increase, which peaks at about 10-11 Myr. This increase is then followed by a generally less rapid decline in the case of the (no)GRk ω_0 1.2 models and by an equally quick drop in $L_{\text{hCCSNe}}^2/L_{\omega_0,0.6,t=0}^2$ in the (no)GRk ω_0 1.8 models. The evolution in $L_{\text{hCCSNe}}^2/L_{\omega_0,0.6,t=0}^2$ is mirrored by all other mass groups (naturally excluding M_{PISNe}). In the (no)GRk ω_0 1.8 models, there is a local minimum in $L_{\text{hCCSNe}}^2/L_{\omega_0,0.6,t=0}^2$ right at the time of core collapse. Figure 11.3 shows that at this point in time these respective models are essentially already fully mass segregated.
- ▶ Phase IV: Most Importantly we see in all models that while $L_{\text{hCCSNe}}^2/L_{\omega_0,0.6,t=0}^2$ declines, $L_{\text{lCCSNe}}^2/L_{\omega_0,0.6,t=0}^2$ increases. This finding implies that angular momentum is transported from highest mass BHs to the lowest mass BHs during this phase. Consequently, the lower mass BHs are slung out onto larger orbits around the cluster center, while a subsystem of IMBHs forms in the centre. We can also clearly see this happening in Figure 11.3. As explained in Section 11.5.1, we can deduce here that binary heating of IMBHs in the cluster centre is dominating the evolution of all star clusters at this point in simulation time.

In conclusion, we see a complex picture of angular momentum transport that is emerging in the star clusters, which is different to simulations of Pop-I star cluster that are initialised with rotating King models as well in Kamlah, Spurzem, et al. (2022). The main drivers of these differences are IMF and the Pop-III stellar evolution. However, the underlying gravitational processes that drive the evolution overall, namely the gravothermal and gravogyro catastrophes, can clearly be seen in both.

11.5.2 Stars and compact objects

To study the stellar abundances and the dependence on primarily the initial bulk rotation and also stellar evolution, we plot in Figure 11.5 the number of stars in the simulations, n_{stars} , the number of MS stars, n_{MS} , the number of CHEB stars, n_{CHEB} , the number of ShHeB stars, n_{ShHeB} , the number of NSs, n_{NS} , and the number of BHs, n_{BH} . n_{stars} shows that while the number of stars appears very similar in the first Myr in the pre-core collapse evolution and subsequently through the dramatic phase of compact formation, this is very different for the remaining pre-core collapse evolution until core collapse and also beyond. For the increasing ω_0 , the number of

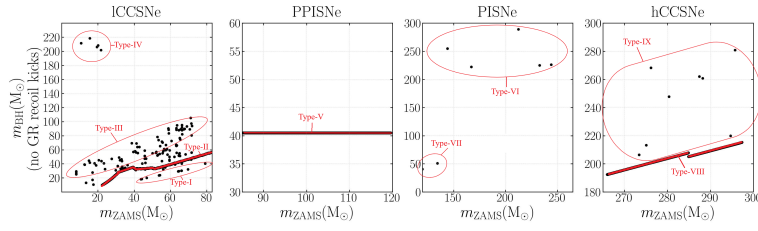


Figure 11.7: Plots showing the initial-final-mass relation (IFMR) with the mass of the BH, $m_{\text{BH}}(M_{\odot})$, plotted against the $m_{\text{ZAMS}}(M_{\odot})$ of the progenitor ZAMS stars for stars that explode by low mass core-collapse supernovae (ICCSNe), by pulsational pair instability supernovae (PPISNe), by pair instability supernovae (PISNe) and by high mass core-collapse supernovae, from left to right for the noGRk ω_0 0.0 simulation. We have marked in the different types of formation channels of (IM)BHs in red.

stars decreases more rapidly, which is especially apparent for the (no)GRk ω_0 1.8 models. This is a result of the gravothermal-gravogyro catastrophe in combination with tidal field mass loss, which can be inferred also from the fact that the GRk and noGRk exhibit effectively identical evolution in n_{stars} for the respective values of ω_0 .

There are no more MS stars in simulation after 11 Myr, which can be seen in the temporal evolution of n_{MS} . These evolve along the HG and become CHeB stars. At 11 Myr these CHeB stars (n_{CHeB}) have also already evolved into ShHeB stars, which have longer lifetimes, which can be seen from n_{ShHeB} . At about 11 Myr, all models start to produce over 1000 NSs (n_{NS}) and that number declines over the course of the simulation (this also happens to n_{ShHeB}) and this can be attributed to escapers as we will see in Section 11.5.5. Much earlier than 11 Myr at around 1.7 Myr, the simulations start the production of BHs and n_{BH} peaks before 10 Myr at around 50000.

For the BHs, we plot the initial-final-mass relation (IFMR), which can be seen Figure 11.6 and, which plots the BH mass $m_{\text{BH}}(M_{\odot})$ against the progenitor ZAMS star mass $m_{\text{ZAMS}}(M_{\odot})$. Figure 11.6 only contains BHs that are left inside the cluster at 500 Myr and have not escaped (yet). As a reminder, these ZAMS produce BHs by three mechanisms: core-collapse SNe of the low mass particles of our IMF (ICCSNe) from C. L. Fryer et al. (2012), pulsational pair instability SNe of the intermediate mass particles of our IMF (PPISNe) from Belczynski et al. (2016) and again core-collapse SNe of the extremely massive particles of our IMF (hCCSNe) C. L. Fryer et al. (2012). Importantly, the pair instability SNe from of the high particles of our IMF (PISNe) from Belczynski et al. (2016) leave no remnant BH. For details, see Kamlah, Leveque, et al. (2022) or Section 11.4.2. We mark these mass regions clearly by including blue vertical lines in Figure 11.6, where the pair instability mass gap is also clearly labelled. Crucially, the mergers between stars and BHs cause IMBH also within the pair instability mass gap for all models. We also see plenty of the IMBHs above the pair instability mass gap and stellar mass BHs and importantly, also IMBHs below the mass gap.

We identify several regimes of remnant masses of the (IM)BHs that are characterised by single and binary stellar evolution processes, respectively, and that can inspected in Figure 11.7:

- Type-I: These BHs are produced from primordial binaries. They all involve a stage during which the H-envelope is completely stripped off. As mentioned in Section 11.3.3, CHeB stars in binaries can be stripped partially or completely off their

envelopes via tides, Roche Lobe overflow (RLOF) or CEE. Thereafter, the naked HeMS that forms core-collapse into BHs. In some cases, both binary members undergo this evolution, meaning a MSMS binary forms a CHeBChEB binary and during CEE, the H-envelopes of both stars are stripped off leaving behind a HeMSHeMS binary. Thereafter, the HeMS core-collapse into BHs earlier or later depending on its He core mass. Finally, depending on the fallback of the stars and the result natal kick, a BHBH binary survives or does not. Crucially, there is no merger at any point during the evolution of the Type-I BHs and this is what differentiate these types from Type-III.

- ▶ Type-II: These BHs lie systematically above Type-I BHs and are all produced from single stellar evolution through the delayed core-collapse SNe mechanism by C. L. Fryer et al. (2012).
- ▶ Type-III: These BHs are also produced from primordial binaries and systematically lie above Type-II BHs. They form as a result of coalescence of a CHeB and a MS or two CHeBs during RLOF. Thereafter, the product CHeB star evolves quickly into a ShHeB star, which core-collapses into a BH.
- ▶ Type-IV: These IMBHs are dynamically formed exclusively. Every single one of these involves a stage of RLOF between an IMBH and a ShHeB stars. In the Nbody6++GPU code we use, the product of such a coalescence takes the name of the ShHeB star even if the mass of the participating IMBH is much larger. If it took the name of the IMBH, these mergers would show up in the lower mass end of the hCCSNe regime most likely or in the PISNe mass gap, if previous mergers are involved.
- ▶ Type-V: These BHs are produced through the PPISNe process. Some of our simulations produce IMBHs in this mass range, see Figure 11.6. For example, the GRk ω_0 0.0 model.
- ▶ Type-VI: These IMBHs are produced mainly through two channels: in the first one through hyperbolic collisions in dynamically formed MSMS binaries. The collision products then evolve into CHeB and ShHeB phases by single stellar evolution and core-collapse into BHs. In the second channel, a CHeB star forms a dynamical binary with a BH, which subsequently hyperbolically coalesce. Due to the definitions in Nbody6++GPU, the name of the lower mass particle in the merger is assigned to the merger product and therefore, these also appear in the PISNe mass gap.
- ▶ Type-VII: The third channel is the result of hyperbolic CE events in dynamically formed binaries made up of CHeB and or ShHeB stars. During the CE phase, the H-envelopes of the stars are stripped off and expelled. The cores merge and the product is a CHeB star following Hurley et al. (2002). The

Table 11.4: Absolute numbers of remaining binaries, n_b , compact binaries, n_{cb} , BHBH binaries, n_{BHBH} , binaries with a BH and a star, n_{BHstar} , and NS binaries, n_{NSb} , at 500 Myr for all eight N_{BODY}6++GPU simulations. The column headers have been abbreviated - G corresponds to the GRK and noG corresponds to the noGRK models.

| Model ID | G ω_0 0.0 | G ω_0 0.6 | G ω_0 1.2 | G ω_0 1.8 | noG ω_0 0.0 | noG ω_0 0.6 | noG ω_0 1.2 | noG ω_0 1.8 |
|--------------|------------------|------------------|------------------|------------------|--------------------|--------------------|--------------------|--------------------|
| n_b | 355 | 356 | 390 | 313 | 358 | 400 | 350 | 315 |
| n_{cb} | 220 | 212 | 250 | 195 | 228 | 263 | 214 | 192 |
| n_{BHBH} | 98 | 87 | 113 | 79 | 104 | 112 | 85 | 80 |
| n_{BHstar} | 106 | 111 | 118 | 101 | 109 | 129 | 117 | 98 |
| n_{NSb} | 16 | 14 | 19 | 15 | 15 | 22 | 12 | 14 |

product star then evolves into a ShHeB star and core-collapses into a BH.

- ▶ Type-VIII: These IMBHs form by single stellar evolution through core-collapse or rather the extension of the remnant mass functions of C. L. Fryer et al. (2012).
- ▶ Type-IX: These IMBHs form through dynamically formed binaries of MS or CHeB stars that undergo hyperbolic coalescence or coalescence following a CE event. The merger product takes the name of the more massive binary member.
- ▶ Type-X: There exist some rare cases of IMBHs with masses below Type-VIII IMBHs, all of which involve hyperbolic coalescence events between MS and CHeB stars during some significant proportion of the H-envelope from the CHeB star is lost. The product CHeB star of the coalescence evolves into a ShHeB and subsequently core-collapses into an IMBH.

This categorisation helps understand the different formation channels that are possible in our simulations using the fitting formulae of Pop-III stars from Tanikawa et al. (2020) and our initial conditions. We see also the impact of full dynamical simulation instead of simply relying on population synthesis, as many of the (IM)BHs that deviate from the single stellar evolution paths result from binary interaction in dynamically formed binaries.

As a summary of this section, within just 11 Myr and during the pre-core collapse phase (core-collapse happens at around 50 Myr depending on which model you look at, see also Figure 11.3), the Pop-III star clusters completely change their stellar make-up. This evolution is much more extreme than in Pop-I star clusters of comparable size (see e.g. Kamlah, Spurzem, et al. (2022)) owing to the extreme initial conditions. We have demonstrated that the star clusters with our initial conditions are all capable to produce IMBHs below, within and above the pair instability mass gap.

11.5.3 Binary stars

Compact binary fractions and general properties

The abundances of certain binary types and the temporal evolution of these reveal important information and can act as a tracer of the number of dynamical interactions in collisional stellar systems.

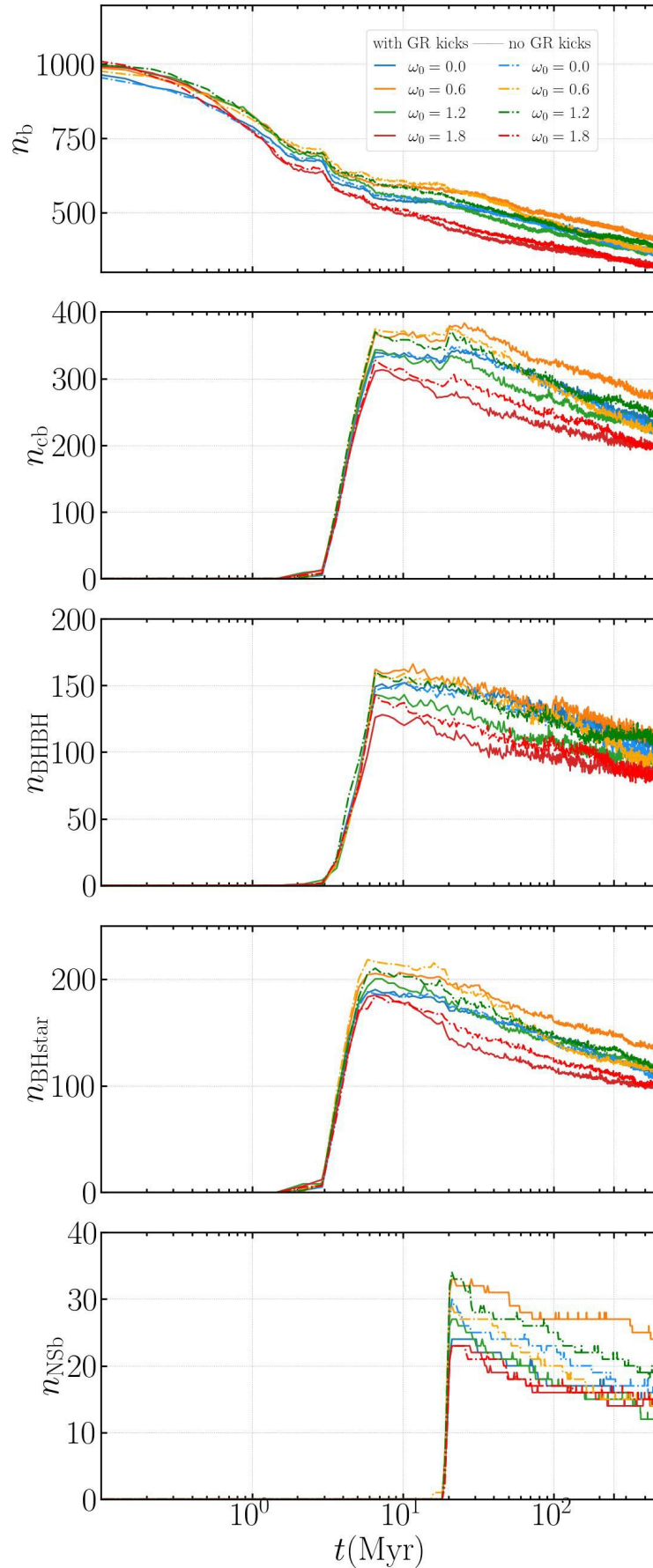


Figure 11.8: Plots showing the number of binary stars n_b , the number of compact binary stars n_{cb} , the number of binary black holes (BHBH) n_{BHBH} , the number of BH binaries with a stellar companion (BHstar) n_{BHstar} and the number of NS binaries n_{NSb} in the five panels for all eight simulations with and without GR recoil kicks for $\omega_0 = 0.0, 0.6, 1.2, 1.8$, respectively. The time axis is plotted logarithmically to show the details of the much more rapid early cluster evolution. The models with GR recoil kicks (GRk models) are plotted as solid lines and the models without GR recoil kicks (noGRk models) are plotted as dash-dotted lines.

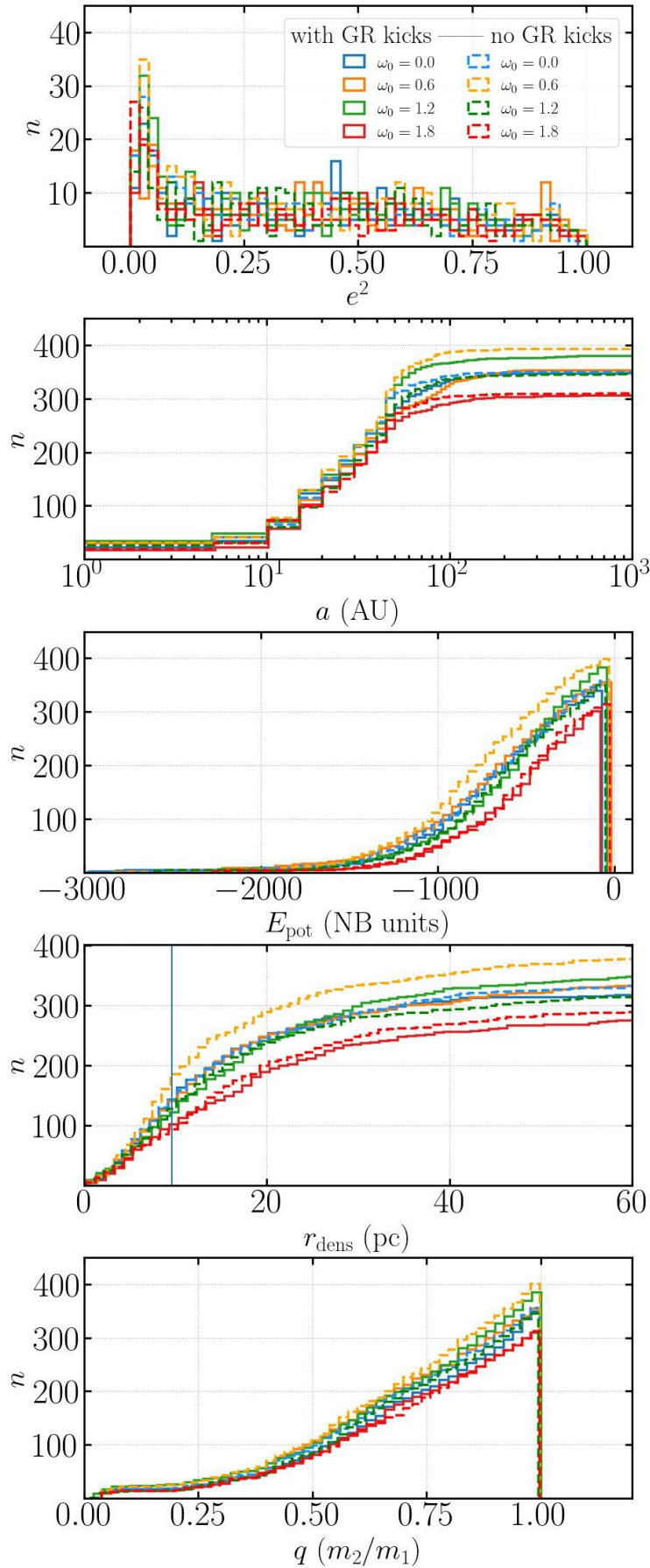


Figure 11.9: Plots showing several binary distributions from top to bottom at 500 Myr of simulation time: eccentricity squared, e^2 , cumulative semi-major axis, a (AU), cumulative binary potential energy, E_{pot} (NB units), cumulative distance to the cluster density centre, r_{dens} (pc) and mass ratio q (m_2/m_1), respectively. In the plot of r_{dens} , a blue vertical line has been added to show the half-mass radius, r_h (pc), of the noGRk $\omega_0=0.0$ model at 500 Myr (around 9.77 pc). The models with GR recoil kicks (GRk models) are plotted as solid lines and the models without GR recoil kicks (noGRk models) are plotted as dash-dotted lines.

Figure 11.8 shows the number of binary stars n_b , the number of compact binary stars n_{cb} , the number of binary black holes (BHBH) n_{BHBH} , the number of BH binaries with a stellar companion (BHstar) n_{BHstar} and the number of NS binaries n_{NSb} from top to bottom. The value of these quantities at 500 Myr can be inspected in Table 11.4. All binary abundances are lowest for the (no)GRk ω_0 1.8 models mirroring simulations of rotating star clusters with primordial binaries, stellar evolution and tidal field mass loss from Kamlah, Spurzem, et al. (2022). While we could insinuate similar trends with the (no)GRk ω_0 1.2, the situation is not so clear here and the abundances lie close to the (no)GRk ω_0 0.0 and (no)GRk ω_0 0.6 models. Interestingly, basically all abundances from the (no)GRk ω_0 0.6 models lie above those from the (no)GRk ω_0 0.0 models. In Section 11.5.5 we will prove this many the numbers of respective binaries. Figure 11.9 shows several properties of the binaries that are still found within the cluster tidal boundary at 500 Myr of simulation time. Going from top to bottom in Figure 11.9, we start with the square of the eccentricity, e^2 , where we see no significant differences in the shape of the distributions. All of these are bottom-heavy for circularised binaries. Similar statements can also be made about the cumulative distribution of the semi-major axes a (AU). The distribution here diverge at around 50 AU. While at this distance most of the binaries in the noGRk ω_0 1.8 simulations have been counted, this is not the case in particular for the noGRk ω_0 0.6 and the noGRk ω_0 1.2 simulations, but also to a lesser extent to all other simulations not yet explicitly stated. All of this implies that the noGRk ω_0 1.8 produce more dynamical interactions that disrupt wide binaries and as we already saw from Figure 11.8, this happens predominantly already before core-collapse. Looking at the cumulative distribution of the binary potential energies, E_{pot} (NB units), we see that there are significantly fewer hard binaries for the noGRk ω_0 1.8 simulations than the others. There are several possible reasons for this. For one, the hard binaries might have already collided or coalesced, see also Section 11.5.4. This statement can be substantiated by looking at Figure 11.8, Table 11.4, and Section 11.5.4. Secondly, these hard binaries might have escaped the runs with large initial rotation and this statement is underpinned by Figure 11.15 in Section 11.5.5. The latter effect implies that many potential coalescing or colliding binaries are kicked out early, which is not necessarily optimal for merging stars and black holes in these environments. These findings are further evidenced by the distribution of the binaries in relation to their distance to the star cluster density centres at 500 Myr, r_{dens} (pc), also shown in Figure 11.9. A vertical has been sketched in this figure, which shows the half-mass radius, r_h (pc), of the noGRk ω_0 0.0 model at 500 Myr. Looking back at Figure 11.3, we see that post core-collapse the evolution of the star clusters is dominated by binary heating in the centre as can be seen from the self-similar evolution of the Lagrangian radii, r_{Lagr} , in all simulations. Although, the post-core collapse evolution happens earlier in the cases of the increasing initial rotation mainly due to early core-collapse, which in turn is due to the gravothermal-gravogyro catastrophe, we see that at 500 Myr the distributions of the binaries across all simulations relative to the number of binaries retained in an individual star cluster. This

statement is particularly true within the distance of r_h (pc), of the noGRk ω_0 0.0 model at 500 Myr. At this point in simulation time, we do not observe more binaries that are also harder near the centre of the star cluster simulations if the initial bulk rotation is larger. Or in other words, the patterns in structural evolution, see [Figure 11.2](#) and [Figure 11.3](#), and angular momentum evolution, have largely been erased and the clusters evolve similarly in the long-term. This fact in turn has an equalizing effect on the distributions of the binaries that remain in the cluster at 500 Myr. The last quantity in [Figure 11.9](#) that is discussed is the distribution of the mass ratios q , where q is defined as the ratio of the mass of the secondary component, m_2 , and the mass of the primary component, m_1 , where $m_2 < m_1$ is always true. Here, we see discounting the fact that there are different numbers of binaries retained in the clusters at 500 Myr, that q is distributed virtually identically.

In general, we are dealing with low number statistics here as we only used 1000 binaries per simulation. While general trends emerge, we need more simulations to achieve fully reliable results.

11.5.4 Collision and coalescence events

We look at the coalescence and collision rates of binary stars and the properties thereof and we study how that depends on the initial bulk rotation. A *coalescence* for our purposes here means that at least one of the members is a star with a core and that the binary has a circular orbit before merging, while a *collision* means an actual physical collision, where none of the binary members is an evolved stellar type, but the member can also be a compact object. By nature of this definition, our initial conditions and the intrinsic properties of Pop-III stellar evolution we only record collisions between two BHs (BHBH), a MS star and a BH (MSBH) or two MS stars (MSMS). We have more variety for the coalescence events, with MS, HGs, CHeBs, ShHeBs, HeMSs, NSs and BHs facilitating these. We show the product masses of coalescence, m_{coal} (M_{\odot}), and collision, m_{coll} (M_{\odot}), in relation to the event's distance to the cluster density centre, r_{dens} (pc), in [Figure 11.10](#) for all simulations. The products of the coalescence events are colour-coded by their product stellar type. We do not observe any other stellar types here than MS, CHeB, ShHeB and BHs, although the two stars participating in the coalescence exhibit a larger variety than these four types. This finding is due to how collision and coalescence products and their stellar types are treated in Hurley et al. (2002) and which we still use currently (see (Kamlah, Leveque, et al., 2022)). The number counts of these are shown in [Table 11.5](#).

We first discuss the coalescence events (top two rows in [Figure 11.10](#)). We do not observe a significant difference in the spatial distribution of these events. Most of them occur within the central 2.5 pc of the star cluster, which is within the half mass radius r_h of the cluster for about 40 Myr of the cluster evolution, see [Figure 11.2](#). This result is further evidenced by the time at which the events plotted in [Figure 11.10](#) occur. In [Figure 11.11](#) we show the time-evolution of the cumulative number of the coalescence, n_{coal} (top two rows), and of the collision events, n_{coll} (bottom two rows), from the eight N -body

Table 11.5: Absolute numbers of coalescence and collision events occurring in all simulations. For the coalescence events (top four rows), the product star of the coalescing progenitor stars or compact objects is given in the ID (n_{MScoal} , n_{CHEBcoal} , $n_{\text{ShHeBcoal}}$, n_{BHcoal}), whereas for the collision events (bottom three rows), the progenitor stars or compact objects is given in the ID (n_{MSMScoll} , n_{MSBHcoll} , n_{BHBHcoll}). The total numbers of coalescence events, n_{totcoal} , and collision events, n_{totcoll} , and the sum of these two, $n_{\text{totevents}}$, are also shown for each simulation. The column headers have been abbreviated - G corresponds to the GRK and noG corresponds to the noGRK models.

| Model ID | G ω_0 0.0 | G ω_0 0.6 | G ω_0 1.2 | G ω_0 1.8 | noG ω_0 0.0 | noG ω_0 0.6 | noG ω_0 1.2 | noG ω_0 1.8 |
|------------------------|------------------|------------------|------------------|------------------|--------------------|--------------------|--------------------|--------------------|
| n_{MScoal} | 9 | 6 | 8 | 7 | 10 | 8 | 11 | 12 |
| n_{CHEBcoal} | 213 | 174 | 174 | 217 | 189 | 163 | 183 | 254 |
| $n_{\text{ShHeBcoal}}$ | 19 | 18 | 13 | 20 | 16 | 11 | 16 | 20 |
| n_{BHcoal} | 33 | 39 | 40 | 42 | 36 | 50 | 33 | 44 |
| n_{totcoal} | 274 | 237 | 235 | 284 | 251 | 232 | 243 | 330 |
| n_{MSMScoll} | 9 | 9 | 11 | 17 | 21 | 11 | 24 | 25 |
| n_{MSBHcoll} | 0 | 1 | 1 | 0 | 0 | 0 | 1 | 0 |
| n_{BHBHcoll} | 6 | 10 | 13 | 16 | 14 | 7 | 11 | 12 |
| n_{totcoll} | 15 | 20 | 25 | 33 | 35 | 19 | 35 | 37 |
| $n_{\text{totevents}}$ | 289 | 257 | 260 | 319 | 270 | 267 | 278 | 367 |

simulations. The large majority of the coalescence events already occur within 4 to 5 Myr of simulation time, so in the pre-core collapse phase of cluster evolution. Importantly, we have large number of coalescing events that populate the PISNe mass gap, which can still be made out from [Figure 11.10](#). The above provides further evidence that stellar mergers in very early star cluster evolution are capable of populating this region with BHs that subsequently form (see, e.g., [Ballone et al. \(2022\)](#) and [Costa et al. \(2022\)](#) for recent hydrodynamical simulations of stellar collisions on this topic). Due to our IMF and the intrinsic properties Pop-III stars and the non-existent wind mass loss in our simulations, we easily also populate the region above PISNe mass gap with BHs with much less "effort" than in young massive clusters (e.g. [Rizzuto et al. \(2022\)](#)).

We note that the vast majority of coalescence events produce CHEBs and these produce also the most massive products. Most of these are produced within the same couple of Myrs in all simulations. The larger the initial star cluster bulk rotation, the more of these coalescence events we have, approximately, see also [Figure 11.11](#). But we note that it is difficult to make such claims because of low number statistics. At the very least it can be treated indicatively. The number of stars that are accreted onto BHs, n_{BHcoal} , is similar for all simulations. The same can be said for $n_{\text{ShHeBcoal}}$ and n_{MScoal} . Importantly, these coalescence events also produce stars (mostly CHEB) with masses in and above the the pair instability mass gap. Additionally, there are some IMBHs in these pair instability mass gap, meaning that they have accreted stellar material and subsequently masses large enough to fill this gap.

The MSMS, BHMS and BHBH collisions reveal further important information. Here, we focus for the first time extensively on the inclusion of GR recoil kicks in combination with the initial star cluster bulk rotation. First of all, we note that all the models produce similar masses of IMBHs in collisions as can be seen from [Figure 11.10](#). The noGRK ω_0 1.2 is the notable exception with IMBHs that are close 1000 M_{\odot} . The counterpart to this model, i.e. GRK ω_0 1.2, does not produce these kind of masses. Notably, from [Figure 11.11](#), we could

draw a similar conclusion as for the number of coalescence events in relation to the initial bulk rotation: the larger the initial bulk rotation, the more MSMS and BHBH collisions we have. However, due to low number statistics it is difficult to make this claim. In the GRK models, we could certainly see such a trend. What is particularly interesting is that we get a multi-generation IMBH in the runs with GR kicks switched on.

In [Figure 11.12](#) we show the primary and secondary masses, m_1

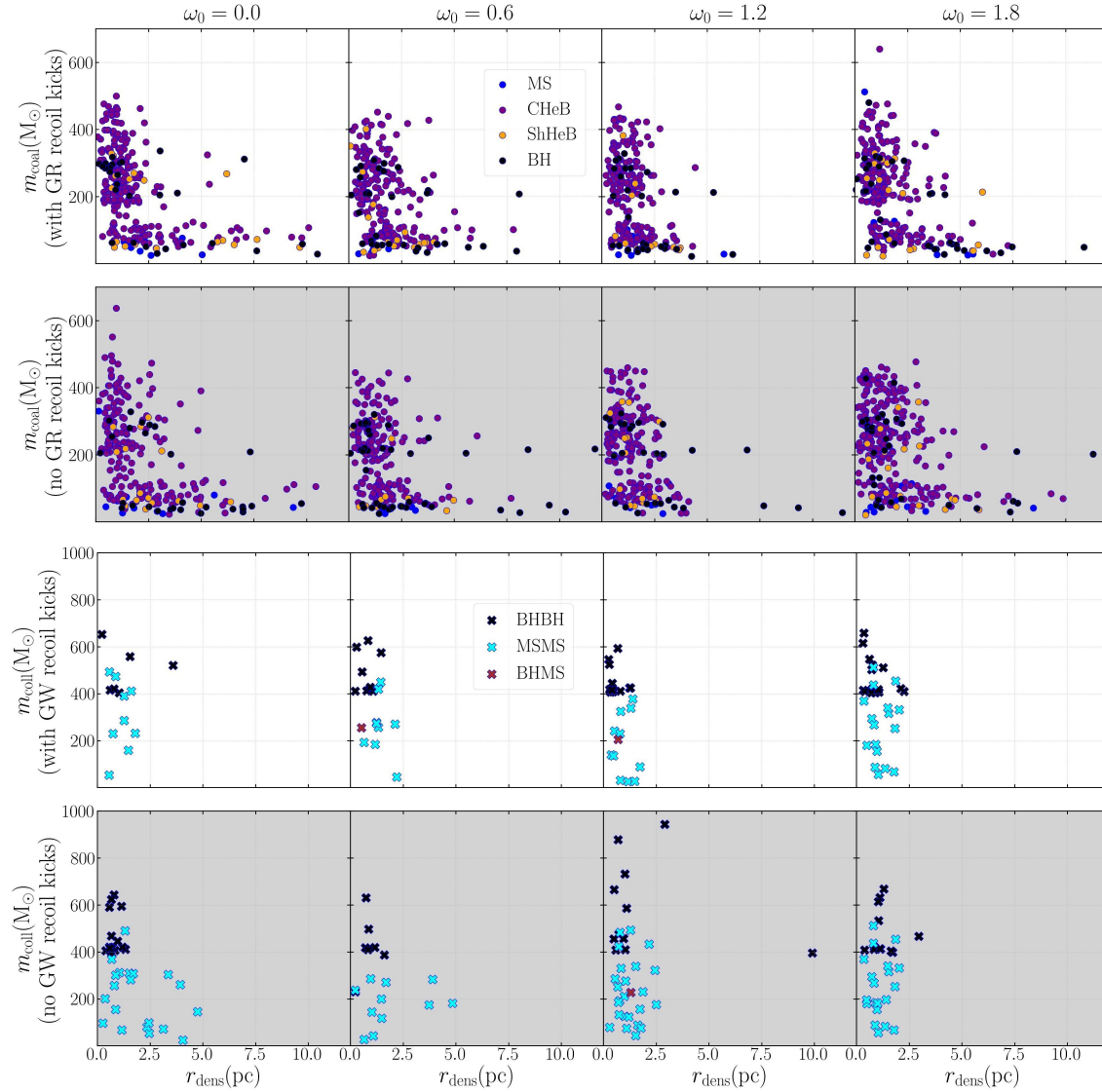


Figure 11.10: Plot showing all of the coalescence (top two rows) and all of the collision events (bottom two rows) from the eight N -body simulations, where the product masses of the coalescence event, $m_{\text{coal}} (M_{\odot})$, and the product masses of the collision events, $m_{\text{coll}} (M_{\odot})$, are plotted against the distance to the star cluster density centre r_{dens} (pc), where the events occurred. Each column represents one rotational parameter ω_0 in ascending order from left to right ($\omega_0 = 0.0, 0.6, 1.2, 1.8$). The results from the runs *with* GR merger recoil kicks switched on (GRK models) are plotted on a white background, while the results from the simulations *without* GR merger recoil kicks (noGRk models) are highlighted in light grey. The coalescence events that produce a main sequence (MS) star are plotted as blue dots, the ones that produce a core-Helium burning (CHeB) star as purple dots, the ones that produce a Shell Helium Burning (ShHeB) star as orange dots and the ones that result in black holes (BH) are plotted as black dots, respectively. The collision events between two BHs are shown as black crosses, the events between two MS stars are shown as cyan crosses and the ones between a BH and a MS are shown as violet crosses, respectively. The number counts for the events are given in [Table 11.5](#).

and m_2 ($m_1 > m_2$), respectively, of the MSMS, BHMS, and BHBH collisions in all eight simulations. We see here once again that the

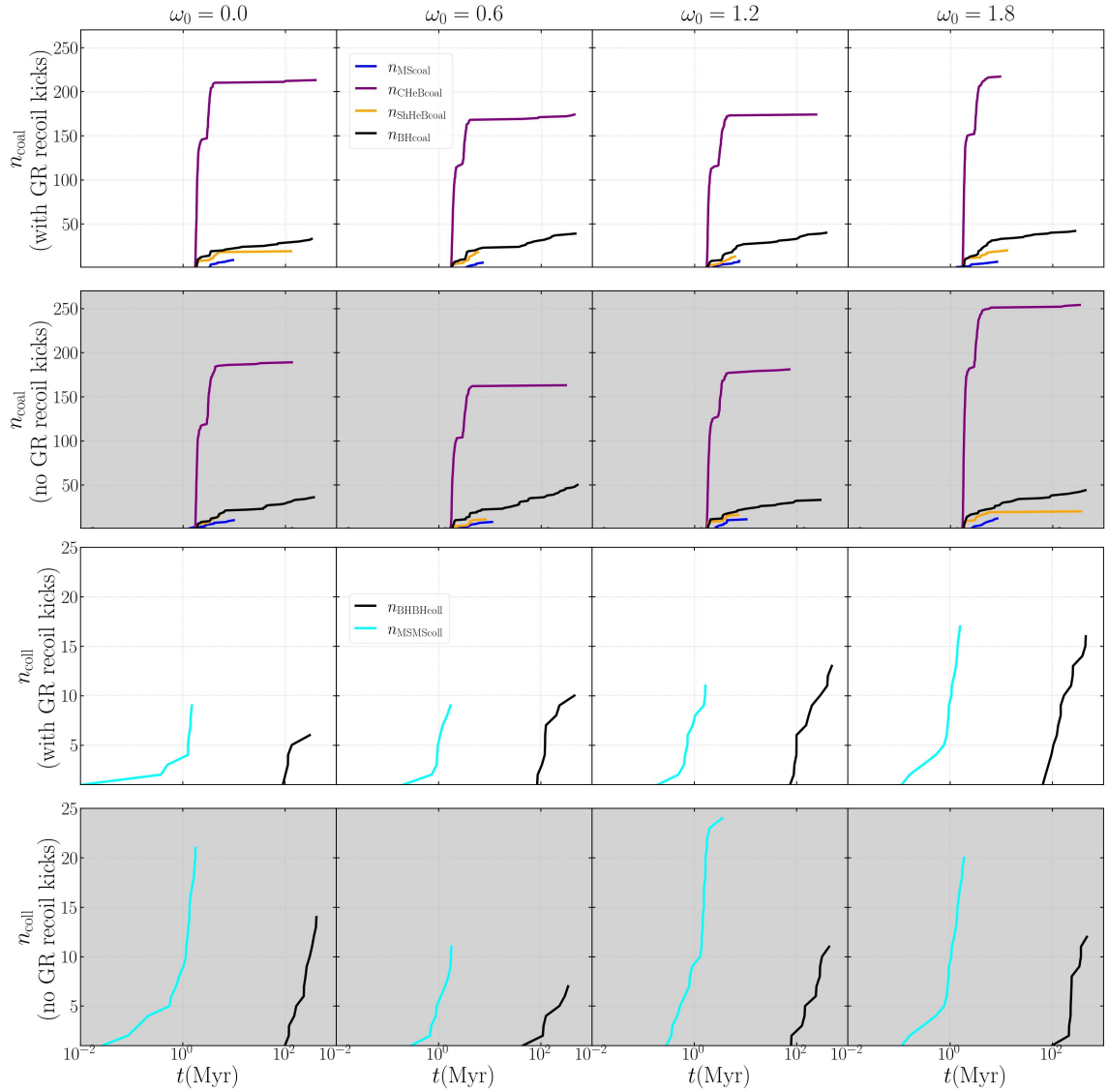


Figure 11.11: Plot showing the time-evolution of the cumulative number of the coalescence, n_{coal} (top two rows), and of the collision events, n_{coll} (bottom two rows), from the eight N -body simulations. Each column represents one rotational parameter ω_0 in ascending order from left to right ($\omega_0 = 0.0, 0.6, 1.2, 1.8$). The results from the runs *with* GR merger recoil kicks switched on (GRk models) are plotted on a white background, while the results from the simulations *without* GR merger recoil kicks (noGRk models) are highlighted in light grey. The time axis, t (Myr), is plotted logarithmically to better resolve the pre-core collapse evolution. The coalescence events that produce a main sequence (MS) star are plotted as blue lines, the ones that produce a core-Helium burning (CHeB) star as purple lines, the ones that produce a Shell Helium Burning (ShHeB) star as orange lines and the ones that result in black holes (BH) are plotted as black lines, respectively. The collision events between two BHs are shown as black lines, the events between two MS stars are shown as cyan lines, respectively. The number counts for the events are given in Table 11.5.

distributions are very similar across all simulations regardless of the initial rotation or the presence of GR recoil kicks. The red line denotes equal mass ratio collisions, i.e. $q = 1$. In theory following, e.g. Morawski et al. (2018, 2019), we would suspect that mergers would have very low relativistic (GR) recoil kick velocity, v_{GRk} , which would make them promising candidates for growing seed BHs for galactic nuclei. However, this is not always the case with our models of v_{GRk} . Figure 11.13 shows v_{GRk} (kms $^{-1}$) in relation to the mass ratio q of the participating compact objects, where $q < 1$. Most of these collisions are associated with v_{GRk} that lie above the respective cluster's escape speeds and will be kicked out as a result,

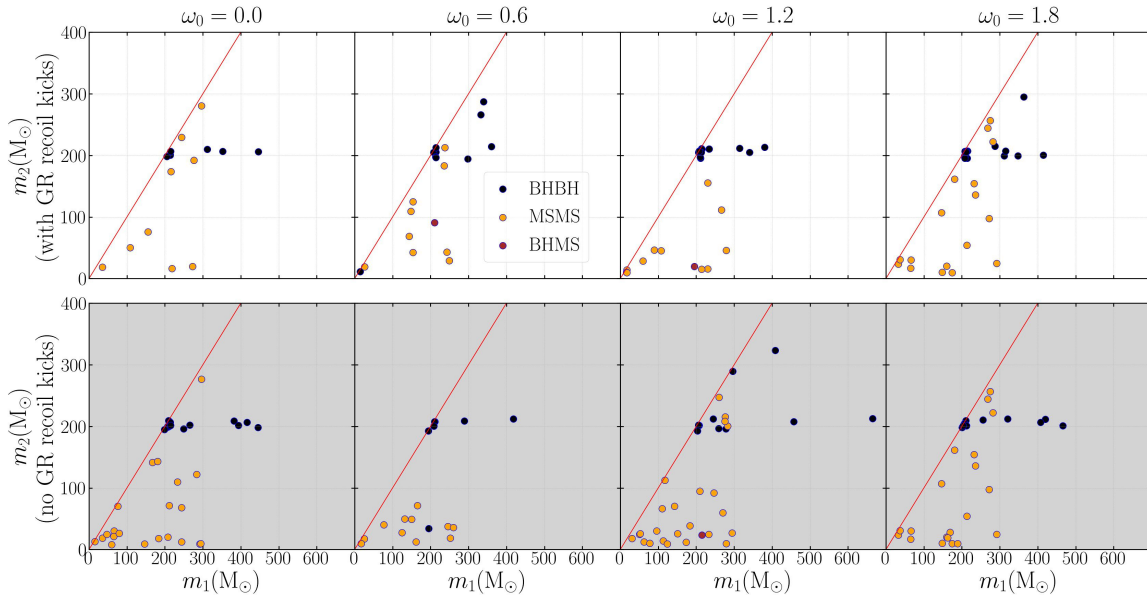


Figure 11.12: Plot showing the time primary and secondary masses, m_1 and m_2 ($m_1 > m_2$), respectively, of the MSMS collisions as orange, BHMS collisions as purple, and BHBH collisions as black dots in all eight simulations. Each column represents one rotational parameter ω_0 in ascending order from left to right ($\omega_0 = 0.0, 0.6, 1.2, 1.8$). The results from the runs *with* GR merger recoil kicks (GRk models) are plotted on a white background, while the results from the simulations *without* GR merger recoil kicks (noGRk models) are highlighted in light grey. The red line denotes equal mass ratio collisions, i.e. $q = 1$. The number counts for the events are given in Table 11.5.

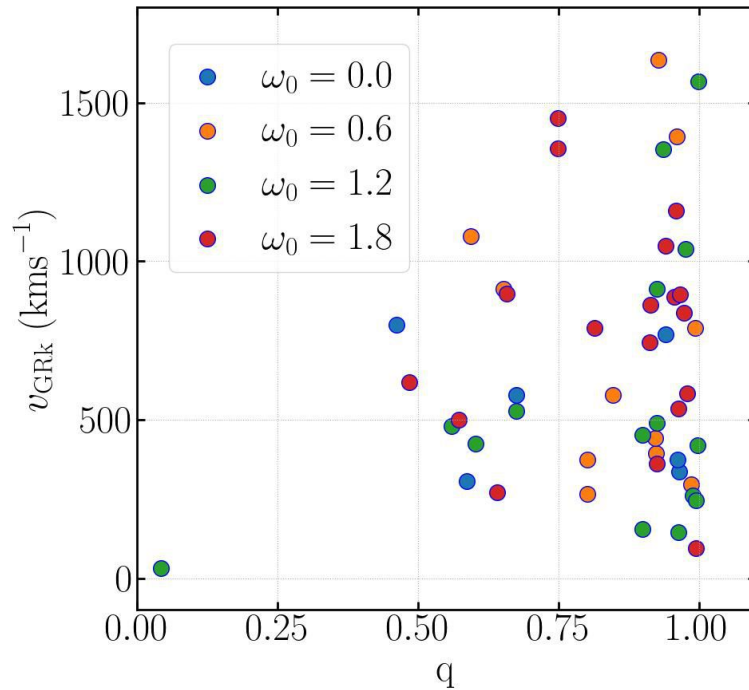


Figure 11.13: Plot showing general relativistic (GR) recoil kick velocity, v_{GRk} (km s^{-1}) in relation to the mass ratio q of the participating compact objects, where $q < 1$. All of these objects are BHBH mergers, except one, which is a merger between a BH and a NS. This merger can be identified by the extreme value of q and the low value of v_{GRk} (km s^{-1}).

Table 11.6: Table showing the number of escaping objects from all simulations at 500 Myr of simulation time (from top to bottom): total number of escaping single stars, $n_{\text{escsingles}}$, MS stars, n_{escMSs} , CHEB stars, n_{escCHEBs} , SheHeB stars, $n_{\text{escShHeBs}}$, NS, n_{escNSs} , and BHs, n_{escBHs} . Thereafter, the number of escaping objects in binaries are shown (from top to bottom): total number of escaping stars that are found in binaries, $n_{\text{escbinarymembers}}$, MS stars in binaries, n_{escMSb} , CHEB stars in binaries, n_{escCHEBb} , ShHeB stars in binaries, $n_{\text{escShHeBb}}$, NSs in binaries, n_{escNSb} , and BHs in binaries n_{escBHb} . The column headers have been abbreviated - G corresponds to the GRk and noG corresponds to the noGRk models.

| Model ID | G ω_0 0.0 | G ω_0 0.6 | G ω_0 1.2 | G ω_0 1.8 | noG ω_0 0.0 | noG ω_0 0.6 | noG ω_0 1.2 | noG ω_0 1.8 |
|-------------------------|------------------|------------------|------------------|------------------|--------------------|--------------------|--------------------|--------------------|
| $n_{\text{escsingles}}$ | 6903 | 4491 | 6334 | 8935 | 6796 | 4917 | 6689 | 8777 |
| $M_{\text{escsingles}}$ | 238416 | 173845 | 252120 | 342161 | 252089 | 192843 | 258546 | 343595 |
| n_{escMSs} | 79 | 82 | 181 | 454 | 91 | 74 | 171 | 459 |
| n_{escCHEBs} | 4 | 4 | 28 | 53 | 2 | 6 | 22 | 64 |
| $n_{\text{escShHeBs}}$ | 2482 | 1775 | 2283 | 3046 | 2448 | 1912 | 2431 | 2987 |
| n_{escNSs} | 107 | 84 | 109 | 133 | 116 | 96 | 103 | 119 |
| n_{escBHs} | 4310 | 2628 | 3914 | 5703 | 4230 | 2903 | 4133 | 5607 |
| $n_{\text{escbinmem}}$ | 90 | 102 | 180 | 180 | 108 | 112 | 146 | 190 |
| n_{escMSb} | 0 | 0 | 2 | 14 | 0 | 0 | 3 | 7 |
| n_{escCHEBb} | 0 | 0 | 0 | 2 | 1 | 0 | 0 | 3 |
| $n_{\text{escShHeBb}}$ | 29 | 20 | 44 | 49 | 16 | 6 | 37 | 43 |
| n_{escNSb} | 1 | 2 | 0 | 2 | 2 | 1 | 2 | 2 |
| n_{escBHb} | 60 | 80 | 134 | 113 | 89 | 105 | 104 | 135 |

even for mergers with q close to 1. Therefore, it is very hard to build up hierarchical merger chains in these systems with GR kicks. To grow the IMBHs into more massive seed black holes for galactic nuclei, there need to be additional processes that prevent escape of these BHs. Dark matter halos surrounding the Pop-III star clusters could provide enough additional mass as in Wang et al. (2022) (no GR kicks were used in these simulations), but there also models that do not require dark matter and rely on extreme gas inflow after several dozens of Myr to cause an extreme contraction of the cluster and the formation of such black holes as in Kroupa et al. (2020).

11.5.5 Escaper stars

The escapers from the simulations reveal more important information and are shown in Figure 11.14 for single escapers and in Figure 11.15 for binary escapers. The total numbers of the quantities shown in the aforementioned two figures at 500 Myr are given in Table 11.6. From the figures and the table, we can infer quickly that for increasing initial bulk rotation ω_0 both the noGRK and GRK models lose more escapers and also earlier in simulation time. This finding becomes particularly apparent from the (no)GRk ω_0 1.8 and the (no)GRk ω_0 1.2 models. However, the (no)GRk ω_0 0.6 models present notable exceptions to this claim. Here, the $n_{\text{escsingles}}$ and $n_{\text{escbinarymembers}}$ are smaller or similar to the non-rotating models, i.e. the (no)GRk ω_0 0.0 models. This evolution is mirrored by the mass of escaping singles $M_{\text{escsingles}}$ (M_{\odot}) with the (no)GRk ω_0 1.8 and the (no)GRk ω_0 1.2 models losing the most mass through escapers. This is an important observation, because the current cluster mass influences the evolution time-scales of the clusters. It also explains the evolution that is outlined in Section 11.5.1 and Section 11.5.1, where we implied that some proportion of the different evolutionary patterns of the star clusters is due to different initial bulk rotation in combination with

the tidal field mass loss.

Now, we focus on the abundances of certain stellar types that escape as single stars starting with MS stars, which are accounted for in [Figure 11.14](#) with n_{escMSs} . Here, in particular, we see that the large initial bulk rotation in the (no)GRk ω_0 1.8 models slings out hundreds more MSs than even from the (no)GRk ω_0 1.2 models. Most of these MSs will form BHs through ICCSNe subsequently in the field (see [Section 11.5.2](#)). Therefore, they are not available inside the cluster for hierarchical merger chains and therefore, this is an indication that although the extreme initial bulk rotation leads to an accelerated star cluster collapse and especially a gravogyro contraction in Phase I of star cluster evolution, see [Figure 11.3](#) and discussion in [Section 11.5.1](#), the simultaneous (note that the stars will have to travel to twice the current tidal radius before being counted as escapers and therefore, the actual escape process starts earlier than what is shown in the figure) escape of many progenitor stars of BHs can disrupt potential merger chains that would otherwise likely exist.

Next, we look at the evolved stellar phases starting with the escaping single CHeBs that are counted by n_{escCHeBs} . While the pattern is generally similar to what we observed for the single MSs, we note that there is less discrepancy between the (no)GRk ω_0 1.2 and (no)GRk ω_0 1.8 models here. Moreover, many of the escaping MSs will shortly after evolve to the CHeB stage and likewise many of the escaping CHeB will short evolve into ShHeB stars, see also [Figure 11.5](#) for the expected time-scales. After formation, most will remain in the ShHeB phase comparatively long. Looking again at [Figure 11.14](#), we see that for the escaping ShHeBs, which are counted by $n_{\text{escShHeBs}}$, the general pattern of escaper numbers in relation to ω_0 persists. However, although already somewhat apparent in the plot for n_{escMSs} , there is a very large increase in the escaper numbers later in the simulation (during Phase IV, i.e. the phase that is dominated by binary heating, see also [Section 11.5.1](#)). Moreover, in this phase $n_{\text{escShHeBs}}$ increases much more for the (no)GRk ω_0 0.0 simulations than for the (no)GRk ω_0 0.0 or the (no)GRk ω_0 1.2 models. In general by looking at [Table 11.6](#), we find that the (no)GRk ω_0 0.6 simulations consistently provide the lowest escaper abundances³ of single stars among all simulations for almost all stellar types.

Turning to the escapers of the compact remnants, we start with the NSs that are counted by n_{escNSs} , there are no significant differences between the simulations, except that the (no)GRk ω_0 0.6 models consistently produce the lowest numbers of single NSs that escape. This trend is reflected also when looking at the escaping single BHs, n_{escBHs} . Here, the (no)GRk ω_0 1.8 models stand out significantly with the largest number of escapers by a significant margin at 500 Myr of simulation time, see [Table 11.6](#). Interestingly, the (no)GRk ω_0 0.0 models show an the most acceleration in loss of single BHs compared with all the other models thereby mirroring similar trends in other aforementioned stellar types, see [Figure 11.5](#). It is important to keep in mind that since the kicks that we use are fallback dependent (see [Section 11.4.2](#)), the flat IMF between $8 M_{\odot}$ and $300 M_{\odot}$ (see [Section ??](#)) and the absent mass loss in the BH progenitor stars in our models, the dominant fraction of BHs have so much fallback that the kick velocity approaches 0 km s^{-1} .

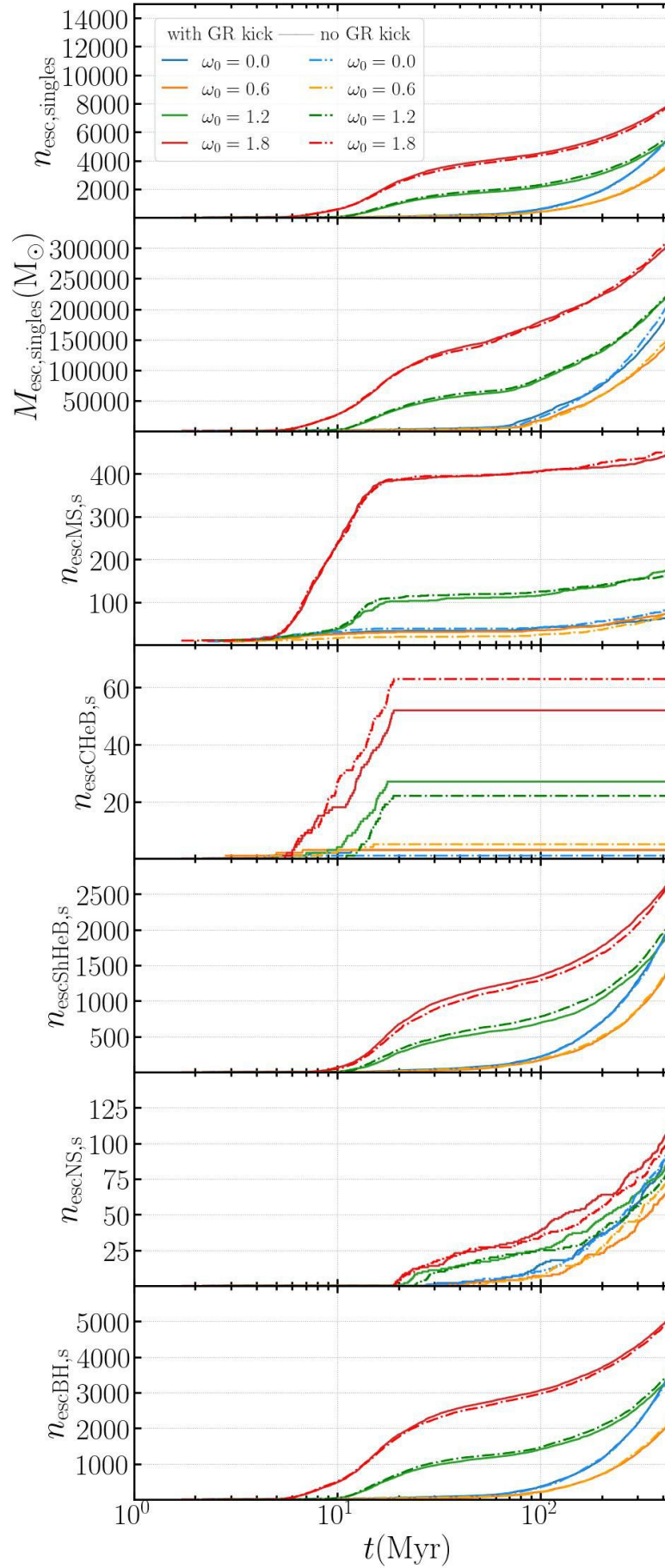


Figure 11.14: Plots showing the cumulative numbers of escaping single stars $n_{\text{esc,singles}}$, the total mass of the $M_{\text{esc,singles}} (M_{\odot})$, the cumulative numbers of escaping single MS stars $n_{\text{escMS,s}}$, of escaping single CHEB stars $n_{\text{escCHEB,s}}$, of escaping single ShHeB stars $n_{\text{escShHeB,s}}$, of escaping single NSs $n_{\text{escNS,s}}$ and of escaping single BHs $n_{\text{escBH,s}}$ in the seven simulations with and without GR recoil kicks for $\omega_0 = 0.0, 0.6, 1.2, 1.8$, respectively. The time axis is plotted on a logarithmic scale to show the details of the much more rapid early cluster evolution. The models with GR recoil kicks (GRK models) are plotted as solid lines and the models without GR recoil kicks (noGRK models) are plotted as dash-dotted lines.

The main takeaways that we can draw from looking at the single escaping stars and compact objects are that the (no)GRk ω_0 1.8 at 500 Myr have lost the most objects and mass by a large margin. However, the (mass) loss from the (no)GRk ω_0 0.0 models appears to be accelerating in the long-term beyond the end of the simulations and even overtaking the (no)GRk ω_0 1.8 models. Interestingly, (no)GRk ω_0 0.6 models exhibit the least amount of mass loss and the lowest numbers of stars and compact objects lost of all simulations. We now turn the number of escaping binary stars, the temporal evolution of which is shown in Figure 11.15 with the abundances listed in Table 11.4. Here, the number of stars that are found in binaries, which are counted by $n_{\text{escbinarymembers}}$, show significant differences. Especially, the (no)GRk ω_0 1.2 and (no)GRk ω_0 1.8 models produce escaping binary stars much earlier and also lead to similar abundances in the long-term of 500 Myr that are about two times the number of binaries that have escaped for the (no)GRk ω_0 0.0 and (no)GRk ω_0 0.6 simulations. Interestingly, the latter two sets of simulations do not show the strong deviations in the long-term as was observed in Figure 11.5 for the single escapers, but stay remarkably similar.

We now look at the various stellar types excluding compact objects. Starting with the MSs found in binaries that are counted by n_{escMSb} . Only the (no)GRk ω_0 1.2 and (no)GRk ω_0 1.8 simulations lose MS stars in binaries. Virtually all of them are from primordial binaries and would possibly merger with their companion inside the cluster if they had not escaped. Most of them, however, are not very massive and would not produce IMBHs. Relatively speaking, these escaper numbers are also low. For the CHeB stars, which are counted with n_{escBHb} , the numbers are even lower. Things get more interesting when discussing the numbers of escaping ShHeB stars in binaries, which are counted by $n_{\text{escShHeBb}}$. Here, we see that the (no)GRk ω_0 1.2 and (no)GRk ω_0 1.8 models suffer from about twice as many losses of these types and much earlier on than the (no)GRk ω_0 0.0 and (no)GRk ω_0 0.6 simulations. Again, it is remarkable that the trends in deviating escaper numbers of the (no)GRk ω_0 0.0 and (no)GRk ω_0 0.6 simulations are not apparent here either. We might observe them in the longer term. Many of the BHBH binaries that escape later in the simulation consist of two IMBHs that will not be available for hierarchical mergers inside the clusters. Therefore, it can be argued here that in the large initial bulk rotation in the (no)GRk ω_0 1.2 and (no)GRk ω_0 1.8 models is counterproductive in forming seed black holes for galactic nuclei at least in the simulations presented here.

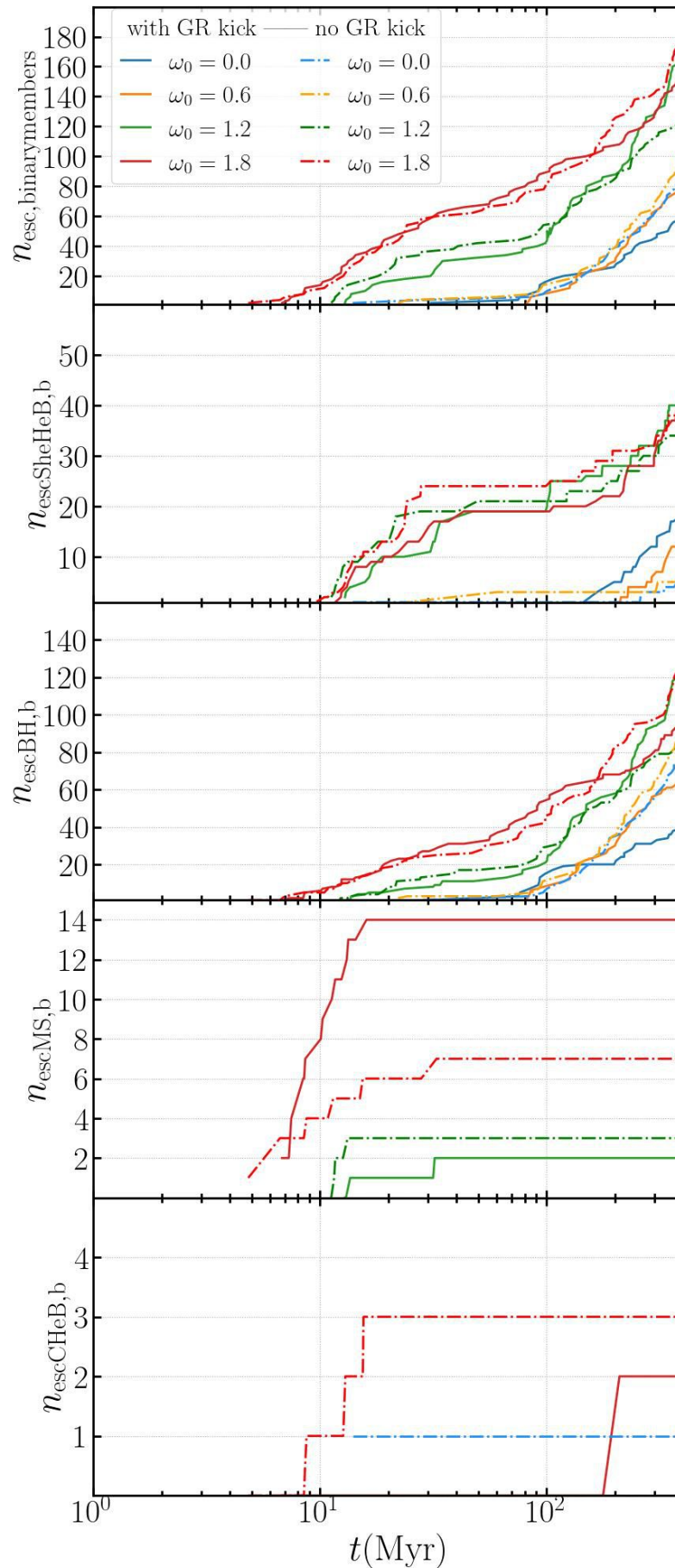


Figure 11.15: Plots showing the cumulative numbers of escaping binary member stars, $n_{\text{esc,binarymember}}$, $n_{\text{esc,MS,b}}$, CHeB stars in binaries, $n_{\text{esc,CHeB,b}}$, ShHeB stars in binaries, $n_{\text{esc,ShHeB,b}}$, and BHs in binaries, $n_{\text{esc,BH,b}}$ in eight simulations with and without GR recoil kicks for $\omega_0 = 0.0, 0.6, 1.2, 1.8$, respectively. The time axis is logarithmic to show the details of the much more rapid early cluster evolution. The models with GR recoil kicks (GRK) are plotted as solid lines and the models without GR recoil kicks (noGRK models) are plotted as dash-dotted lines.

11.6 Summary, conclusion and perspective

11.6.1 Summary

For the first time we have investigated impact of initial bulk rotation, Pop-III stellar evolution models (Tanikawa et al., 2020) ($Z/Z_{\odot} = 10^{-8}$) in combination with stellar evolution processes that affect all stars (Kamlah, Leveque, et al., 2022) and general relativistic (GR) merger recoil kicks by Arca Sedda et al. (in prep.) in combination with primordial binaries and stellar masses drawn from a flat IMF (of extremely massive stars between $(8.0 - 300.0) M_{\odot}$) as well as a tidal field mass loss on the global dynamics of the star clusters using direct N -body methods. Here we focused particularly on formation and evolution of the the gravothermal-gravogyro catastrophe, coalescence and collision rates between stars and compact objects, IMBH formation with and without GR merger recoil kicks and escaping single stars and binaries. This paper adds to the large body of work on rotating star cluster models (see e.g. Einsel and Spurzem (1999), Ernst et al. (2007), Fiestas and Spurzem (2010), Fiestas et al. (2006), Hong et al. (2013), Kamlah, Spurzem, et al. (2022), Kim et al. (2002), Kim et al. (2004, 2008), Livernois et al. (2022), Szölgyen and Kocsis (2018), Szölgyen et al. (2019, 2021), M. A. Tiongco et al. (2022), and Vergara et al. (2021)) and explores a completely new avenue by the inclusion of self-consistent Pop-III stellar evolution and GR merger recoil kicks.

In total, we have run eight simulations over 500 Myr, four with GR merger recoil kicks (GRk models) and four without (noGRk models). In each sub-group of the two aforementioned groups, any individual model is distributed with a different rotating King model from Einsel and Spurzem (1999). We use one non-rotating model ($\omega_0 = 0.0$) and three more models with increasing fractions of initial total star cluster energy being stored in initial bulk rotational energy ($\omega_0 = 0.6, 1.2, 1.8$). We make the following observations:

- ▶ The global, dynamical evolution of the Pop-III star clusters can be divided into four distinct evolutionary phases that are dominated by certain physical processes, which can be concluded mostly from Figure 11.2, Figure 11.3 and Figure 11.4:
 - Phase I: this phase of star cluster evolution occurs before the stellar evolution mass loss begins to dominate, so the time from 0 Myr to around 2 Myr. The transport of angular momentum transport for increasing ω_0 is clearly visible (Figure 11.4). For increasing ω_0 and especially for the (no)GRk ω_0 1.2 and most notably for the (no)GRk ω_0 1.8 models we see a large increase in all mass groups. This finding implies that the initially very compact star clusters expand rapidly overall and that many stars from all mass groups are migrating outwards relative to the cluster centre quickly leading also to large numbers of escapers initially (see Figure 11.14 and Figure 11.15), which explains the overall increase in $L_{\text{group}}^2/L_{\omega_0 0.6, t=0}^2$ for the ω_0 1.8 model. The effect thereof on the other structural parameters, such as r_{Lagr} (see Figure 11.3) can immediately

be seen. Within the first Myr already, the larger the initial rotation, the more pronounced is the temporary increase of r_h and decrease shortly after, while the innermost r_{Lagr} contract. The larger the initial rotation, the faster this evolution happens as well generally (with the exception of the (no)GRk ω_0 0.6 models). This contraction also leads to more dynamical interactions and the dissolution of many primordial binaries (see [Figure 11.8](#)).

- Phase II: in the short second phase after around 2 Myr up until around 3 Myr, the star clusters begin to lose extreme amounts of mass due to stellar evolution most importantly through the formation of compact objects in the ICCSNe, PPISNe and hCCSNe and massless remnants in the PISNe regime (see discussion in [Section 11.5.2](#), [Figure 11.6](#) and [Figure 11.7](#)). The impact of this evolution can immediately be seen, e.g., in the large decrease in M_{av} and indirectly in the simultaneously occurring large expansion of the r_{Lagr} (see [Figure 11.3](#)).
- Phase III: during this phase the cluster evolution occurs from around 3 Myr to time of gravothermal core-collapse, which generally occurs earlier for increasing, initial bulk rotation (see discussion in [Section 11.5.1](#) and [Figure 11.3](#)). This evolutionary pattern was already seen in, e.g., Akiyama and Sugimoto (1989), Einsel and Spurzem (1999), Fiestas et al. (2012), Kamlah, Spurzem, et al. (2022), Kim et al. (2002), and Kim et al. (2004, 2008). For the (no)GRk ω_0 1.2 and (no)GRk ω_0 1.8 models, there is an extreme increase in $L_{\text{hCCSNe}}^2/L_{\omega_0,0.6,t=0}^2$, which peaks at about 10-11 Myr followed by a slightly less rapid drop (see [Figure 11.4](#)). In the (no)GRk ω_0 1.8 models, there is a local minimum in $L_{\text{hCCSNe}}^2/L_{\omega_0,0.6,t=0}^2$ right at the time of core collapse. [Figure 11.3](#) shows that at this point in time these respective models are essentially already fully mass segregated and IMBH subsystem has formed at the centre of all clusters. For the (no)GRk ω_0 1.8, the star cluster expansion in this phase is so extreme that many stars already escape in this phase and before (see [Figure 11.14](#) and [Figure 11.15](#)), so there is an actual decrease in $r_{\text{Lagr}3}$ for 90 %, which is not present for the other models (see [Figure 11.3](#)).
- Phase IV: this phase starts from the time of core-collapse to the end of the simulation at 500 Myr, is characterized by a self-similar evolution of the Lagrangian radii. The overall evolution is remarkably similar across all simulations. This kind of evolution is dominated by binary energy generation in the star cluster center and subsequent expansion of the cluster (see e.g. Breen and Heggie (2013) and M. Hénon (1975))). In this phase, $L_{\text{hCCSNe}}^2/L_{\omega_0,0.6,t=0}^2$ declines, $L_{\text{ICCSNe}}^2/L_{\omega_0,0.6,t=0}^2$ increases (see [Figure 11.4](#)). This finding implies that angular momentum is transported

from highest mass BHs to the lowest mass BHs and lower mass remaining stars (see [Figure 11.5](#) during this phase. During this phase the escaper rates for the (no)GRK ω_0 0.0 models overtake the (no)GRK ω_0 0.6 significantly, which means that binary energy generation should be more efficient in the non-rotating models. At 500 Myr and the end of the simulations, the binary distributions of the binaries remaining inside the cluster appear very similar, although the number of binaries for models with increasing initial rotation are generally slightly lower (see [Figure 11.8](#) and [Figure 11.9](#)). The binary fractions are dominated by remaining BHBH and BHstar binaries in the cluster, but there also some NS binaries surviving in the cluster ([Figure 11.8](#)).

- ▶ We find a possible dependence of initial Pop-III star cluster rotation and the merger rates between stars and compact objects, when looking at [Figure 11.11](#). In particular, for the GRK models, we can draw see this indicatively. In [Table 11.5](#) we see that the total number of coalescence and collision events is consistently largest in the (no)GRK ω_0 1.8 simulations. Concerning the BHBH collisions, large initial rotation does also seem to precipitate these, with the largest number of collisions found (no)GRK ω_0 1.8 simulations. However, we note that it is difficult to make such claims because of low number statistics in terms of events.
- ▶ We form IMBHs below, within and above the pair instability (PISNe) mass gap (see [Figure 11.6](#) and [Figure 11.7](#)) in all simulations. The largest mass of an IMBH that we form is $943.19 M_{\odot}$ and originates from the noGRK ω_0 1.2 simulation (see also [Figure 11.12](#)). While IMBHs can be formed above the PISNe mass gap through core-collapse SNe, in all other regimes, binary processes must occur. Most of these IMBHs are produced by hyperbolic collisions between MSs and BHs or coalescences between CHeB and SheHeBs with BHs. Additionally, mergers between MS stars that make up primordial massive primordial binaries produce IMBHs. Many of the BHs in our simulations that lie in mass below the regime of single stellar evolution involve common envelope phases, during which H-envelopes are stripped from the CHeB star(s) in binaries, which is followed by a coalescence that produces a CHeB star, which evolves into a ShHeB star and subsequently core-collapses into a BH.

11.6.2 Conclusion

In general, we are presented with a delicate balance between gravothermal-gravogyro contraction of the cluster system that generally appears to cause more mergers initially and the removal of high mass particles, binaries and others due to the excess initial angular momentum that might precipitate further IMBH formation and BH mergers. There might be extra mechanisms at work that

are not present in our simulations to contain (IM)BHs inside the cluster beyond simply making the clusters more compact initially or including more hard primordial binaries. Firstly, we did not include dark matter in our simulations, for example, we could assume dark matter mini-halos surrounding our Pop-III star clusters initially as is done in Wang et al. (2022) (note that that these simulations did not account for rotation or GR merger recoil kicks). These mini-halos might provide enough mass for escaping objects to back-scatter and fall back into the cluster. Alternatively, gas inflow without the need of dark matter might provide additional mass and also friction so that the Pop-III star clusters contract beyond what would be expected by gravothermal-gravogyro evolution alone. This additional contraction could trigger a total collapse of the central, rotation IMBH subsystem that also forms in our simulations and produce very massive seed black holes for galactic nuclei (see Kroupa (2020) for more details on this theory in general). Nevertheless, this work provides important progress on the question of how initial rotation of Pop-III star clusters can shape their evolution and influence merger rates between stars and compact objects.

SUMMARY, CONCLUSION AND OUTLOOK

In my thesis and my work presented here I have focused mostly on the simulations of star clusters with direct N -body methods with `NBODY6++GPU`, secondly on the different stellar evolution fitting formulae and processes with the traditional SSE and Pop-III fitting formulae and thirdly on the Hénon-type Monte-Carlo methods with MOCCA and comparisons with direct N -body simulations again using `NBODY6++GPU`.

[Chapter 9](#) that is based on my first-author publication in Kamlah, Leveque, et al. (2022) is centered around the research question (see also [Section 1.1](#))

How do different simulation methods of star clusters compare when using updated stellar evolution methods?

I make the central following observations (see also [Section 9.6](#)):

- ▶ The MOCCA models evolve faster / age faster dynamically than the `NBODY6++GPU` counterparts, which is associated with a smaller mass loss from the `NBODY6++GPU` models. This is because of larger (gravitational) energy generation in the star cluster cores of the MOCCA models and primordial binaries become 'active' earlier here. It is also related to the treatment of escaping stars in the tidally underfilling star cluster models, see also [Section 2.3.4](#): while in `NBODY6++GPU`, the stars are removed (escape) from the star cluster when they are two current tidal radii afar from the cluster density centre, in MOCCA the escape criterion is quite different, see also [Chapter 6](#), where a star with high enough energy is immediately removed from simulations. The crucial point here is the immediate removal. In the `NBODY6++GPU` simulations the stars travel for a considerable time before removal. However, even worse, these stars can scatter back into the star cluster. These effects in combination with the higher energy generation in the cores of the star clusters in the MOCCA models lead to the faster evolution. We need to be careful with tidally underfilling star cluster models when doing such comparisons in the future, as the different tidal treatment has an enormous impact on the star clusters. In fact, MOCCA models should generally not be tidally underfilling.
- ▶ The MOCCA star cluster cores are centrally more dense, which leads to more dynamical interactions (see also above) and faster star cluster evolution. This is especially reflected in the binary fractions, which are consistently higher for `NBODY6++GPU` models. Moreover, the MOCCA models have a consistently larger BSS fractions, which is a further indication of more dynamical interactions between stars.

- ▶ Subtle differences in the updated stellar evolution parameters and implementations lead to slightly different IFMRs between the MOCCA and N_{BODY6++GPU} models, with the MOCCA models producing remnant masses slightly above those of the N_{BODY6++GPU} simulations. Otherwise, the agreement is excellent.
- ▶ The fallback-scaled kick distributions for NSs and BHs likewise show excellent agreement for all masses across all simulations. All simulations retain NSs formed from an ECSNe, AIC or MIC and despite their very low natal kicks of 3.0 km s^{-1} , some do escape all simulations. Retention fractions are similar across all simulations with the exception of the HeWDs, where most are retained in the MOCCA simulations, in contrast to N_{BODY6++GPU} where virtually all of them escape with large escape speeds. All of the escaped HeWDs originate from ZAMS binaries in both the MOCCA and the N_{BODY6++GPU} simulations. Many more COWDs from single ZAMS stars escape the MOCCA simulations than the N_{BODY6++GPU} simulations and the escape speeds are also much more similar and in many cases much lower than those of the N_{BODY6++GPU} runs. COWDs from ZAMS binaries escape all the simulations in similar numbers. The same statements can be made about the ONeWDs. The reasons why the v_{esc} distributions are so dissimilar cannot be attributed only to the WD kicks in the N_{BODY6++GPU} simulations, because the natal kicks are of very low velocity dispersion. Further studies with MOCCA and N_{BODY6++GPU} on the effects that WD natal kicks have on binary stability and WD production and retention fraction in OCs, GCs and NSCs should be done going forward to shed more light on this particular aspect using the two modelling methods. We leave this riddle to future simulations.

Attempting to answer the research question above we find from the detailed comparison a good agreement between the two modelling methods (N_{BODY6++GPU} and MOCCA), which provides mutual support for both methods in star cluster simulations and the stellar evolution implementations in both codes. However, there are also some significant differences in the global evolution of the star cluster simulations with the two modelling methods. The conclusion here relates to our initial models, the density of the star cluster cores and the treatment of unbound stars in MOCCA vs. N_{BODY6++GPU} simulations. In the future, we strongly suggest to not choose massively tidally underfilling initial cluster models with extremely large tidal radii.

In [Chapter 10](#) that is based on my first-author publication in Kamlah, Spurzem, et al. (2022) focuses on the following research question (see also [Section 1.1](#)):

How does stellar evolution (mass loss) impact the global dynamics of (non-)rotating star clusters?

I make the following observations (see also [Section 10.6](#)):

- ▶ We obtain the same four phases in the early star cluster evolution that were previously observed in direct N -body simulations with low particle numbers by Akiyama and Sugimoto (1989) for both the runs with and without stellar evolution: we see a phase of violent relaxation that is followed by the gravogyro catastrophe of finite amplitude, where the amplitude depends on the degree of initial bulk rotation. This gravogyro catastrophe then levels off and angular momentum is transported from the high mass stars (and compact objects) to the lower mass stars (and compact objects). Simultaneously, the system becomes gravothermally unstable and then collapses. This is direct evidence for the coupling of the gravogyro, see [Section 2.3.2](#), and the gravothermal catastrophes, see [Section 2.3.1](#), and it is therefore appropriate to coin this process the gravothermal-gravogyro catastrophe. We also directly observe the predicted overall angular momentum loss from the cluster due to the tidal field in all models.
- ▶ The highly rotating models with stellar evolution evolve as follows: the BHs and their progenitor stars, which were distributed axisymmetrically initially, very quickly (on dynamical time-scales) form a central bar, which rotates, as they transport angular momentum to lower mass stars and compact objects. The bar then becomes an axisymmetric structure over longer time-scales. The outer halo stars (and compact objects) form a more spherical configuration in the long-term, while the stars (and compact objects) in the centre of the cluster form an axisymmetric structure that more slowly becomes spherical over time. The model counterparts without stellar evolution also form a rotating bar of the high mass stars that is more concentrated and more triaxial than the bar that forms with stellar evolution due to the lack of stellar evolution mass loss and compact object natal kicks and this bar also becomes axisymmetric over time.
- ▶ The presence of stellar evolution and the tidal field of the star cluster impacts the aforementioned processes in the following fashion: while the early dynamical evolution between the models with and without stellar evolution is similar qualitatively, the gravothermal-gravogyro catastrophe is stronger and happens slightly earlier in the models without stellar evolution. Most notably, the systems without stellar evolution evolve to similar configurations in the long-term (spherical halo of lower mass stars and compact objects with an axisymmetric centre of higher mass stars and compact objects), but are generally prohibited by doing so due to strong tidal field mass and angular momentum loss. Instead they exhibit a second and even a third gravogyro collapse and approach a maximally triaxial state in the limit of 1 Gyr. It is an open question if this effect is dampened by larger initial tidal radius and this is left for future studies.

- ▶ The models *without* stellar evolution reveal that the medium-mass group appear to replace the increasingly depleting numbers of high mass objects in the cluster centre and form a subsystem there in the mid- to long-term cluster evolution. This result implies that mass segregation for the high mass objects has effectively slowed down significantly at that point in simulation time.
- ▶ There is a significant increase in the number of BH-BH binaries present in the in the second-most rotating star cluster model. However, it could also just be statistical fluctuation. This needs to be explored with further simulations and appropriate initial conditions that especially concern the IMF and the binary (orbital) parameters.

Again reflecting on the research question tackled here, stellar evolution leads to a delay in the evolution of the gravothermal-gravogyro catastrophes and the amplitude is also smaller. In the simulations, the post-core collapse evolution for the highly rotating models without stellar evolution are characterised by repeated gravothermal-gravogyro catastrophes due to tidal field mass and angular momentum loss similar to gravothermal oscillations found in simulations earlier. Due to the large mass loss in the models with stellar evolution, this effect is dampened significantly. Besides other exciting phenomena such as the bar formation in the star clusters that is inhabited by BHs, we can conclude that stellar evolution mass loss has an enormous impact on rotating star clusters and the right choice of stellar evolution prescriptions has large consequences on the dynamical evolution of them. On the flipside, initial star cluster rotation is important in the actual evolution of star clusters and should be included in simulations, although this is still unusual.

In [Chapter 11](#) which is based on my publication Kamlah et al. (2023, in prep.), I tackle this research question (see also [Section 1.1](#)):

Can massive seed black holes for galactic nuclei form in extremely metal-poor star clusters and does initial star cluster rotation influence this process?

Here, I make the central observations (see also [Section 11.6.1](#)):

- ▶ The global, dynamical evolution of the extremely metal-poor (Pop-III) star clusters can be divided into four distinct evolutionary phases that are dominated by certain physical processes:
 - Phase I: this phase of star cluster evolution occurs before the stellar evolution mass loss begins to dominate, so the time from 0 Myr to around 2 Myr. The transport of angular momentum transport for increasing initial star cluster rotation is clearly visible. The initially very compact star clusters expand rapidly and many stars from all mass groups are migrate outwards relative to the cluster

centre quickly leading also to large numbers of escaping stars early on. Within the first Myr already, the larger the initial rotation, the more pronounced is the temporary increase of the half-mass radii and decrease shortly after, while the innermost Lagrangian radii contract. The larger the initial rotation, the faster this evolution happens as well generally. Unsurprisingly the initial contraction also leads to more dynamical interactions and the dissolution of many primordial binaries as the central star cluster density increases rapidly.

- Phase II: in the short second phase after around 2 Myr up until around 3 Myr, the star clusters begin to lose extreme amounts of mass due to stellar evolution most importantly through the formation of compact objects in the core-collapse regime below and above the pair instability mass gap as well as the pulsational pair instability SNe regime. The impact of this evolution can immediately be seen, e.g., in the large decrease in the average mass in mass shells and indirectly in the simultaneously occurring large expansion of the Lagrangian radii.
 - Phase III: during this phase the cluster evolution occurs from around 3 Myr to time of gravothermal core-collapse, which generally occurs earlier for increasing, initial bulk rotation. This evolutionary pattern was already observed in my work in Kamlah, Spurzem, et al. (2022), see also the discussion above and the sources therein.
 - Phase IV: this phase starts from the time of core-collapse to the end of the simulation at 500 Myr and it is characterized by a self-similar evolution of the Lagrangian radii. The overall evolution is remarkably similar across all simulations. This kind of evolution is dominated by binary energy generation in the star cluster center and subsequent expansion of the cluster. This finding implies that angular momentum is transported from highest mass BHs to the lowest mass BHs and lower mass remaining stars here. During this phase the escaper rates for the non-rotating models overtake the models with second lowest rotation significantly, which means that binary energy generation should be more efficient in the non-rotating models. At 500 Myr and the end of the simulations, the binary distributions of the binaries remaining inside the cluster appear very similar, although the number of binaries for models with increasing initial rotation are generally slightly lower. The binary fractions are dominated by remaining BH-BH and BH-star binaries in the cluster, but there also some NS binaries surviving in the cluster.
- We find a possible dependence of initial Pop-III star cluster rotation and the merger rates between stars and compact objects, particularly for the models with general relativistic merger

recoil kicks. We see that the total number of coalescence and collision events is consistently largest in simulations with the largest initial rotation. Concerning the BH-BH collisions, large initial rotation does also seem to precipitate these, with the largest number of collisions found in simulations with the largest initial rotation. However, we note that it is difficult to make such claims because of low number statistics in terms of events.

- We form IMBHs below, within and above the pair instability mass gap in all simulations. The largest mass of an IMBH that we form is $943.19 M_{\odot}$ and originates from the simulation without general relativistic merger recoil kicks with the second-largest initial rotation. While IMBHs can be formed above the PISNe mass gap through core-collapse SNe, in all other regimes, binary processes must occur. Most of these IMBHs are produced by hyperbolic collisions between MSs and BHs or coalescences between CHeB and ShHeBs with BHs. Additionally, mergers between MS stars that make up primordial massive primordial binaries produce IMBHs. Many of the BHs in our simulations that lie in mass below the regime of single stellar evolution involve common envelope phases, during which H-envelopes are stripped from the CHeB star(s) in binaries, which is followed by a coalescence that produces a CHeB star, which evolves into a ShHeB star and subsequently core-collapses into a BH.

Returning to the research question tackled, it has been found that in extremely metal-poor star clusters can all form massive seed black holes for galactic nuclei above the pair instability mass gap by coalescence and collision events between primordial stars and BHs, so-called gravitational runaway mergers. We have achieved this even though we have not used dark matter haloes to artificially enhance the gravitational potential or with gas infall to increase the potential and support dynamical friction and thus mass segregation of massive black holes. It appears that the larger the initial rotation of the star clusters is, the more efficiently this process can happen, although many more simulations are needed to make concrete statements about this.

Conclusion 13

This thesis has dealt with a large variety of astrophysical issues from pure stellar evolution to special phenomena surrounding self-gravitating many-body systems that are collisional, which in nature are represented by young and massive, globular, or nuclear star clusters. To explore these issues, I have used simulations and here mostly direct N -body (NBODY6++GPU) and secondly Hénon-type Monte-Carlo (MOCCA) simulations of star clusters. The stellar evolution was modelled exclusively with fitting formulae, although I have employed two distinct sets of these in work: for Pop-I / Pop-II stars, I have used the traditional SSE formulae and for the Pop-III simulations I have used special, new sets for extremely metal-poor and massive stars. The initialisation of the star clusters has happened using MCLUSTER and the rotation of star cluster has been derived from FOPAX modelling. Overall, using these techniques, I have managed to tackle all the research questions that I outlined in the beginning and which I have summarised again in the preceding [Chapter 12](#).

I have demonstrated repeatedly that the combination of full stellar evolution with collisional dynamics can lead to exciting research surrounding the dynamical evolution of dense star clusters of various make-ups and across cosmic time. From the formation and evolution of exotic stellar and compact binaries, such as Blue Stragglers, Cataclysmic Variables, X-ray binaries, and many others to double-degenerate binaries, such as BH-BH and the elusive BH-NS binaries, to the abundances of compact objects and their dynamical properties an extremely diverse array of astrophysically fascinating populations can be modelled for large metallicity and mass ranges. Therefore, the simulations of collisional stellar systems with modern production codes are the ideal laboratory to study stellar evolution in dense stellar environments. My simulations can be used to give predictions for theoreticians and observers alike on the properties, abundances and dynamics of gravitational wave sources from star clusters (and field) across cosmic time. As was stated in Spurzem and Kamlah (2023), (my) simulations of collisional stellar systems are important and useful tools for unravelling our cosmic history in the age of multi-messenger astronomy. They are at the crossroads of many seemingly disparate astrophysical research fields, much like the simulation target, star clusters, are a fundamental building block in a hierarchy of cosmological structure formation.

I have also shown that we need more comparisons between direct N -body and Monte-Carlo simulations as well as code comparisons between codes that follow the same approach, for example, NBODY6++GPU vs. PETAR vs. BIFROST for direct N -body simulations and MOCCA vs. CMC for Monte-Carlo models. Similarly, concerning the implementation of stellar evolution in star cluster simulations, comparisons between fitting formulae and interpolation between tables should be undertaken, for example SSE/BSE vs. SEVN2.0 vs. METISSE. These comparative studies are necessary to guarantee the quality of simulation results, because they are ultimately used to

interpret and explain star cluster observations, which also brings me to the last point I would like to make. It would be very worthwhile in the future to have many more studies that use observations across the electro-magnetic and gravitational wave spectra and simulations of star clusters side by side, for example to take observational data from modern star cluster observations to set up initial conditions for star cluster observations and interpret the results from both a theoretical and observational perspective with experts in both fields. In such an almost cross-disciplinary approach the quality of simulations and the interpretation of the results could possibly be enhanced significantly and these simulations might also be ultimately be more useful to the entire astrophysical community.

While I have illuminated some of the areas of the rich and fascinating physics surrounding star clusters, this by no means that some key questions are conclusively answered. In fact, it is the other way around. In all of my publications I call for more in-depth star cluster simulations or more stellar evolution updates. It remains that many exciting discoveries are yet to be made.

Concerning the stellar evolution, we are in the process of updating a large number of astrophysical processes in our SSE & BSE implementations in `NBODY6++GPU` & `MCLUSTER` and to a lesser extent `MOCCA`. Apart of the self-consistent general relativistic merger recoil kicks final post-merger spins and the Pop-III stellar evolution fitting formulae that are already completed in `NBODY6++GPU`, more updates will be made: the evolution of the Cataclysmics Variables around the orbital period gap, updated factors for wind velocities that depend on the stellar types, pulsars and magnetic fields, winds for extremely massive stars and pulsation-driven mass loss and core radii for certain stellar types. We want to ultimately synchronise that implementation of the stellar evolution with `MOCCA`, which has some of these updates already fully functional (because the implementation in that code is much simpler than in `NBODY6++GPU`). We want to keep the same updates in `MCLUSTER` to use that as a standalone BPS code and for setting up star cluster initial conditions for multiple stellar populations.

We are also in the process exploring the impact of star cluster initial rotation further. Currently, the computation of key quantities can be measured better. We now use the sorting of the particles according to their energy in the system for all quantities beyond the principal axis ratios, rather than according to their distance (and spherical mass coordinate) from the center, which means that the system is - in virial equilibrium - approximately subdivided using equipotential surfaces rather than spherical shells containing certain fractions of total mass. For strongly flattened systems it is necessary to compute quantities like average masses and velocity dispersions in such new spheroidal shells defined by equipotential surfaces. This treatment is still experimental and requires much testing. Moreover, I am currently testing rotating stellar disks represented by rotating Miyamoto-Nagai models that are extremely flat with the aim of isolating the gravogyro and gravothermal catastrophes or at least to dampen the coupling between them. In the team we are also comparing rotating King and Miyamoto-Nagai models. While the details are completely beyond the scope of this thesis it is important to state that in line with my conclusion from [Chapter 13](#) that all models and modelling methods (since the Miyamoto-Nagai models are set up by an entirely different methodology) should be exposed to frequent comparisons and double-checking.

Moreover, now that the Pop-III stellar evolution implementation in direct N -body has been completed and corrected many more exciting studies are underway. I am testing extremely massive Pop-III star clusters that could represent the nuclear star clusters of the

first galaxies in the Universe. We are planning to combine this with gas infall to see if we can form SMBHs in these clusters. Furthermore, we want to explore in more depth how star cluster rotation in combination with stellar evolution can assist gravitational runaway mergers. Through these simulations we can make statements about the necessity of dark matter to increase the gravitational potential and we will yield first simulation data for observations of such star clusters for missions like JWST.

Finally, we should all be excited by the constant improvements on the hardware side. New components of computing nodes speeding up data transfer beyond more and more powerful GPUs and CPUs will make it possible for direct N -body simulation to finally break into the 10^7 particle regime with binary stars, i.e. the regimes of NSCs. We will see which code will achieve this feat with the most promising being NBODY6++GPU, PETAR and BIFROST. Possibly special purpose-built computers like the GRAPE machines will be necessary to reach this goal. All in all, the future holds many exciting discoveries for the simulation scene and by extension the astrophysics community as a whole and I am grateful to have been a part of that journey in the past couple of years.

APPENDIX

A.1 Publications used in this thesis either published or submitted

Arca Sedda M., **Kamlah A.W.H.**, Spurzem R., Giersz M., Berczik P., Rastello S., Iorio G., Mapelli M., Gatto M. & Grebel E. (2023), "The DRAGON-II simulations - I: evolution of single and binary compact objects in star clusters with up to 1 million stars", *Monthly Notices of the Royal Astronomical Society*, to be submitted

Arca Sedda M., **Kamlah A.W.H.**, Leveque A., Rizzuto F.P., Naab T., Spurzem R., Giersz M. & Berczik P. (2023), "The DRAGON-II simulations - II: formation mechanisms, mass, and spins of intermediate-mass black holes in star clusters with up to 1 million stars", *Monthly Notices of the Royal Astronomical Society*, to be submitted

Spurzem R. & **Kamlah A.W.H.** (2023), "Computational Methods for Collisional Stellar Systems", *Living Reviews in Computational Astrophysics*, submitted

Flammini-Dotti F., Kouwenhoven M.B.N., **Kamlah A.W.H.** & Spurzem R. (2023), "Planetary Systems in Star Clusters III: Escape of stars and planets in rotating star clusters", *Monthly Notices of the Royal Astronomical Society*, submitted

Hoyer N., Pinna F., **Kamlah A.W.H.**, Nogueras-Lara F., Feldmeier-Krause A., Neumayer, N., Sormani M. C., Boquien M., Emsellem E., Seth A., Klessen R.S., Williams T.G. (+21 more co-authors) (2023), "PHANGS-JWST First Results: A combined HST and JWST analysis of the nuclear star cluster in NGC 628", Accepted for publication by *ApJL*

Li Z.-M., Kayastha B., **Kamlah A.W.H.**, Berczik P., Deng Y.-Y. & Spurzem R. (2022), "Fractions of Compact Object Binaries in Star Clusters: Theoretical Predictions", *Research in Astronomy and Astrophysics*, RAA-2022-0297

Kamlah A.W.H., Leveque A., Spurzem R., Arca Sedda M., Askar A., Banerjee S., Berczik P., Giersz, M., Hurley, J., Belloni, D., Kühmichel, L. & Wang L. (2022), "Preparing the next gravitational million-body simulations: evolution of single and binary stars in NBODY6++GPU, MOCCA, and MCLUSTER", *Monthly Notices of the Royal Astronomical Society*, Volume 511, Issue 3, pp.4060-4089

Kamlah A.W.H., Spurzem R., Arca Sedda M., Askar A., Banerjee S., Berczik P., Giersz, M., Hurley, J., Belloni, D., Kühmichel, L. & Wang L. (2022), "The impact of stellar evolution on rotating star clusters: the gravothermal-gravogyro catastrophe and the formation of a bar of black holes", *Monthly Notices of the Royal Astronomical Society*, Volume 516, Issue 3, pp.3266-3283

A.2 Publications used that are in writing as of submission of PhD thesis

Kamlah A.W.H., Tanikawa A., Arca Sedda M., Giersz, M., Neumayer N. & Spurzem R. (2023), "Direct N -body simulations of extremely massive and initially rotating Population III star clusters I: Global evolution", *Monthly Notices of the Royal Astronomical Society*, to be submitted

Arca Sedda M., **Kamlah A.W.H.**, Leveque A., Rizzuto F.P., Naab T., Spurzem R., Giersz M. & Berczik P. (2023), "The DRAGON-II simulations - III: compact binary mergers, their properties, and the PISNe rate", *Monthly Notices of the Royal Astronomical Society*, to be submitted

Shukirgaliyev B., Berczik P., Otebay A., Kalambay M., **Kamlah A.W.H.**, Tleukhanov Y., Abdikamalov E., Banerjee S. (2023), "Evolution of open clusters with or without black holes", *Astronomy and Astrophysics*, to be submitted

Bibliography

Here are the references in alphabetic order.

- Aarseth, S. J. (1963). Dynamical evolution of clusters of galaxies, I. *MNRAS*, 126, 223. <https://doi.org/10.1093/mnras/126.3.223>
- Aarseth, S. J. (1971). Direct Integration Methods of the N-Body Problem (Papers appear in the Proceedings of IAU Colloquium No. 10 Gravitational N-Body Problem (ed. by Myron Lecar), R. Reidel Publ. Co. , Dordrecht-Holland.) *ApSS*, 14(1), 118–132. <https://doi.org/10.1007/BF00649199>
- Aarseth, S. J. (1972). Direct Integration Methods of the N-Body Problem. In M. Lecar (Ed.), *Iau colloq. 10: Gravitational n-body problem* (p. 373, Vol. 31). https://doi.org/10.1007/978-94-010-2870-7_36
- Aarseth, S. J. (1979). An N-body integration method in co-moving coordinates. In V. G. Szebehely (Ed.), *Instabilities in dynamical systems. applications to celestial mechanics* (pp. 69–80, Vol. 47).
- Aarseth, S. J. (1985). Direct methods for N-body simulations. *Multiple time scales*, 377–418.
- Aarseth, S. J. (1994). Direct methods for N-body simulations. In G. Contopoulos, N. K. Spyrou, & L. Vlahos (Eds.), *Galactic dynamics and n-body simulations* (pp. 277–312, Vol. 433).
- Aarseth, S. J. (1996). N-Body Simulations of Open Clusters with Binary Evolution. In E. F. Milone & J. .-. Mermilliod (Eds.), *The origins, evolution, and destinies of binary stars in clusters* (p. 423, Vol. 90).
- Aarseth, S. J. (2003a). Black hole binary dynamics. *Ap&SS*, 285(2), 367–372. <https://doi.org/10.1023/A:1025492510715>
- Aarseth, S. J., Henon, M., & Wielen, R. (1974). A Comparison of Numerical Methods for the Study of Star Cluster Dynamics. *A&A*, 37(1), 183–187.
- Aarseth, S. J., & Lecar, M. (1975). Computer simulations of stellar systems. *ARAA*, 13, 1–88. <https://doi.org/10.1146/annurev.aa.13.090175.000245>
- Aarseth, S. J., Lin, D. N. C., & Palmer, P. L. (1993). Evolution of Planetesimals. II. Numerical Simulations. *ApJ*, 403, 351. <https://doi.org/10.1086/172208>
- Aarseth, S. J., & Zare, K. (1974). A Regularization of the Three-Body Problem. *Celestial Mechanics*, 10(2), 185–205. <https://doi.org/10.1007/BF01227619>
- Aarseth, S. (1967). On a collisionless method in stellar dynamics. I. *Les Nouvelles Méthodes de la Dynamique Stellaire*, 47.
- Aarseth, S. J. (1999a). Star Cluster Simulations: the State of the Art. *CeMDA*, 73, 127–137. <https://doi.org/10.1023/A:1008390828807>
- Aarseth, S. J. (1999b). From NBODY1 to NBODY6: The Growth of an Industry. *PASP*, 111(765), 1333–1346. <https://doi.org/10.1086/316455>
- Aarseth, S. J. (2003b). *Gravitational N-Body Simulations*.
- Aarseth, S. J. (2012). Mergers and ejections of black holes in globular clusters. *MNRAS*, 422(1), 841–848. <https://doi.org/10.1111/j.1365-2966.2012.20666.x>
- Aarseth, S. J., Tout, C. A., & Mardling, R. A. (2008). *The Cambridge N-Body Lectures* (Vol. 760). <https://doi.org/10.1007/978-1-4020-8431-7>
- Aasi, J., Abadie, J., Abbott, B. P., Abbott, R., Abbott, T., & Abernathy, M. R. e. a. (2015). Characterization of the LIGO detectors during their sixth science run. *Classical and Quantum Gravity*, 32(11), Article 115012, 115012. <https://doi.org/10.1088/0264-9381/32/11/115012>
- Abbott, B. P., Abbott, R., Abbott, T. D., Abernathy, M. R., Acernese, F., & et al. (2016). Observation of Gravitational Waves from a Binary Black Hole Merger. *PhRvL*, 116(6), Article 061102, 061102. <https://doi.org/10.1103/PhysRevLett.116.061102>
- Abbott, B. P., Abbott, R., Abbott, T. D., Abernathy, M. R., Acernese, F., & et al. (2018). Prospects for observing and localizing gravitational-wave transients with Advanced LIGO, Advanced Virgo and KAGRA. *LRR*, 21(1), Article 3, 3. <https://doi.org/10.1007/s41114-018-0012-9>

- Abbott, B. P., Abbott, R., Abbott, T. D., Abraham, S., Acernese, F., & et al. (2019). Binary Black Hole Population Properties Inferred from the First and Second Observing Runs of Advanced LIGO and Advanced Virgo. *ApJL*, 882(2), Article L24, L24. <https://doi.org/10.3847/2041-8213/ab3800>
- Abbott, B. P., Abbott, R., Abbott, T. D., Abraham, S., Acernese, F., & et al. (2020). Prospects for observing and localizing gravitational-wave transients with Advanced LIGO, Advanced Virgo and KAGRA. *LRR*, 23(1), Article 3, 3. <https://doi.org/10.1007/s41114-020-00026-9>
- Abbott, B. P., Abbott, R., Abbott, T. D., Acernese, F., Ackley, K., & Adams, C. e. a. (2018). Search for Substellar-Mass Ultracompact Binaries in Advanced LIGO's First Observing Run. *PRL*, 121(23), Article 231103, 231103. <https://doi.org/10.1103/PhysRevLett.121.231103>
- Abbott, B. P., Abbott, R., Abbott, T. D., Acernese, F., Ackley, K., & et al. (2017a). GW170817: Observation of Gravitational Waves from a Binary Neutron Star Inspiral. *PhRvL*, 119(16), Article 161101, 161101. <https://doi.org/10.1103/PhysRevLett.119.161101>
- Abbott, B. P., Abbott, R., Abbott, T. D., Acernese, F., Ackley, K., & et al. (2017b). Multi-messenger Observations of a Binary Neutron Star Merger. *ApJL*, 848(2), Article L12, L12. <https://doi.org/10.3847/2041-8213/aa91c9>
- Abbott, R., Abbott, T. D., Abraham, S., Acernese, F., Ackley, K., & et al. (2020a). GW190814: Gravitational Waves from the Coalescence of a 23 Solar Mass Black Hole with a 2.6 Solar Mass Compact Object. *ApJL*, 896(2), Article L44, L44. <https://doi.org/10.3847/2041-8213/ab960f>
- Abbott, R., Abbott, T. D., Abraham, S., Acernese, F., Ackley, K., & et al. (2020b). GW190521: A Binary Black Hole Merger with a Total Mass of 150 M_{\odot} . *PhRvL*, 125(10), Article 101102, 101102. <https://doi.org/10.1103/PhysRevLett.125.101102>
- Acernese, F., Agathos, M., Agatsuma, K., Aisa, D., Allemandou, N., & Allocca, A. e. a. (2015). Advanced Virgo: a second-generation interferometric gravitational wave detector. *Classical and Quantum Gravity*, 32(2), Article 024001, 024001. <https://doi.org/10.1088/0264-9381/32/2/024001>
- Agrawal, P., Hurley, J., Stevenson, S., Szécsi, D., & Flynn, C. (2020). The fates of massive stars: exploring uncertainties in stellar evolution with METISSE. *MNRAS*, 497(4), 4549–4564. <https://doi.org/10.1093/mnras/staa2264>
- Agrawal, P., Stevenson, S., Szécsi, D., & Hurley, J. (2021). A systematic study of super-Eddington envelopes in massive stars. *arXiv e-prints*, Article arXiv:2112.02801, arXiv:2112.02801.
- Ahmad, A., & Cohen, L. (1973). A numerical integration scheme for the N-body gravitational problem. *Journal of Computational Physics*, 12, 389–402. [https://doi.org/10.1016/0021-9991\(73\)90160-5](https://doi.org/10.1016/0021-9991(73)90160-5)
- Akiyama, K., & Sugimoto, D. (1989). Evolution of a self-gravitating many-body system with rotation. *PASJ*, 41(5), 991–1003.
- Allison, R. J., Goodwin, S. P., Parker, R. J., Portegies Zwart, S. F., de Grijs, R., & Kouwenhoven, M. B. N. (2009). Using the minimum spanning tree to trace mass segregation. *MNRAS*, 395(3), 1449–1454. <https://doi.org/10.1111/j.1365-2966.2009.14508.x>
- Alongi, M., Bertelli, G., Bressan, A., Chiosi, C., Fagotto, F., Greggio, L., & Nasi, E. (1993). Evolutionary sequences of stellar models with semiconvection and convective overshoot. I. $Z=0.008$. *A&AS*, 97, 851–871.
- Amaro-Seoane, P., Eichhorn, C., Porter, E. K., & Spurzem, R. (2010). Binaries of massive black holes in rotating clusters: dynamics, gravitational waves, detection and the role of eccentricity. *MNRAS*, 401(4), 2268–2284. <https://doi.org/10.1111/j.1365-2966.2009.15842.x>
- Amaro-Seoane, P. (2018). Detecting intermediate-mass ratio inspirals from the ground and space. *PhRvD*, 98(6), Article 063018, 063018. <https://doi.org/10.1103/PhysRevD.98.063018>
- Amaro-Seoane, P., Andrews, J., Arca Sedda, M., Askar, A., Balasov, R., Bartos, I., Bavera, S. S., Bellovary, J., Berry, C. P. L., Berti, E., Bianchi, S., Blecha, L., Blondin, S., Bogdanović, T., Boissier, S., Bonetti, M., Bonoli, S., Bortolas, E., Breivik, K., . . . Vigna-Gómez, A. (2022). Astrophysics with the Laser Interferometer Space Antenna. *arXiv e-prints*, Article arXiv:2203.06016, arXiv:2203.06016.
- Amaro-Seoane, P., Aoudia, S., Babak, S., Binétruy, P., Berti, E., Bohé, A., Caprini, C., Colpi, M., Cornish, N. J., Danzmann, K., Dufaux, J.-F., Gair, J., Hinder, I., Jennrich, O., Jetzer, P., Klein, A., Lang, R. N., Lobo, A., Littenberg, T., . . . Wardell, B. (2013). eLISA: Astrophysics and cosmology in the millihertz regime. *GW Notes*, 6, 4–110.

- Amaro-Seoane, P., Audley, H., Babak, S., Baker, J., Barausse, E., & et al. (2017). Laser Interferometer Space Antenna. *arXiv*, Article arXiv:1702.00786, arXiv:1702.00786.
- Amaro-Seoane, P., Gair, J. R., Freitag, M., Miller, M. C., Mandel, I., Cutler, C. J., & Babak, S. (2007). TOPICAL REVIEW: Intermediate and extreme mass-ratio inspirals—astrophysics, science applications and detection using LISA. *Classical and Quantum Gravity*, *24*(17), R113–R169. <https://doi.org/10.1088/0264-9381/24/17/R01>
- Amaro-Seoane, P., Glaschke, P., & Spurzem, R. (2014). Hybrid methods in planetesimal dynamics: formation of protoplanetary systems and the mill condition. *MNRAS*, *445*(4), 3755–3769. <https://doi.org/10.1093/mnras/stu1734>
- Anderson, J., & King, I. R. (2000). Toward High-Precision Astrometry with WFPC2. I. Deriving an Accurate Point-Spread Function. *PASP*, *112*(776), 1360–1382. <https://doi.org/10.1086/316632>
- Anderson, J., Sarajedini, A., Bedin, L. R., King, I. R., Piotto, G., & et al. (2008). The Acs Survey of Globular Clusters. V. Generating a Comprehensive Star Catalog for each Cluster. *AJ*, *135*(6), 2055–2073. <https://doi.org/10.1088/0004-6256/135/6/2055>
- Anderson, J., & van der Marel, R. P. (2010). New Limits on an Intermediate-Mass Black Hole in Omega Centauri. I. Hubble Space Telescope Photometry and Proper Motions. *ApJ*, *710*(2), 1032–1062. <https://doi.org/10.1088/0004-637X/710/2/1032>
- Antonini, F. (2013). Origin and Growth of Nuclear Star Clusters around Massive Black Holes. *The Astrophysical Journal*, *763*(1), 62. <https://doi.org/10.1088/0004-637X/763/1/62>
- Antonini, F. (2014). On the Distribution of Stellar Remnants around Massive Black Holes: Slow Mass Segregation, Star Cluster Inspirals, and Correlated Orbits. *The Astrophysical Journal*, *794*(2), 106. <https://doi.org/10.1088/0004-637X/794/2/106>
- Antonini, F., & Gieles, M. (2020). Merger rate of black hole binaries from globular clusters: Theoretical error bars and comparison to gravitational wave data from GWTC-2. *PRD*, *102*(12), Article 123016, 123016. <https://doi.org/10.1103/PhysRevD.102.123016>
- Antonov, V. A. (1960). Remarks on the Problem of Stability in Stellar Dynamics. *AZH*, *37*, 918.
- Antonov, V. A. (1961). Remarks on the Problem of Stability in Stellar Dynamics. *SOVAST*, *4*, 859.
- Antonov, V. A. (1962). *Solution of the problem of stability of stellar system Emden's density law and the spherical distribution of velocities.*
- Arca Sedda, M., & et al. (2023a). The DRAGON II simulations - I: evolution of single and binary compact objects in star clusters with up to 1 million stars [in prep.]. *MNRAS*.
- Arca Sedda, M., & et al. (2023b). The DRAGON II simulations - II: formation and merger of intermediate-mass black holes and compact stellar objects in star clusters with up to 1 million stars [in prep.]. *MNRAS*.
- Arca Sedda, M., & et al. (2023c). The DRAGON II simulations - III: formation and merger of intermediate-mass black holes and compact stellar objects in star clusters with up to 1 million stars [in prep.]. *MNRAS*.
- Arca Sedda, M. (2020). Dissecting the properties of neutron star-black hole mergers originating in dense star clusters. *CmPhy*, *3*(1), Article 43, 43. <https://doi.org/10.1038/s42005-020-0310-x>
- Arca Sedda, M., Amaro Seoane, P., & Chen, X. (2021). Merging stellar and intermediate-mass black holes in dense clusters: implications for LIGO, LISA, and the next generation of gravitational wave detectors. *A&A*, *652*, Article A54, A54. <https://doi.org/10.1051/0004-6361/202037785>
- Arca Sedda, M., Askar, A., & Giersz, M. (2018). MOCCA-Survey Database - I. Unravelling black hole subsystems in globular clusters. *MNRAS*, *479*(4), 4652–4664. <https://doi.org/10.1093/mnras/sty1859>
- Arca Sedda, M., Askar, A., & Giersz, M. (2019). MOCCA-SURVEY Database I. Intermediate mass black holes in Milky Way globular clusters and their connection to supermassive black holes. *arXiv*, Article arXiv:1905.00902, arXiv:1905.00902.
- Arca Sedda, M., Berry, C. P. L., Jani, K., Amaro-Seoane, P., Auclair, P., & et al. (2020). The missing link in gravitational-wave astronomy: discoveries waiting in the decihertz range. *CQGrA*, *37*(21), Article 215011, 215011. <https://doi.org/10.1088/1361-6382/abb5c1>
- Arca Sedda, M., Gualandris, A., Do, T., Feldmeier-Krause, A., Neumayer, N., & Erkal, D. (2020). On the Origin of a Rotating Metal-poor Stellar Population in the Milky Way Nuclear Cluster. *ApJL*, *901*(2), Article L29, L29. <https://doi.org/10.3847/2041-8213/abb245>

- Arca Sedda, M., Mapelli, M., Spera, M., Benacquista, M., & Giacobbo, N. (2020). Fingerprints of Binary Black Hole Formation Channels Encoded in the Mass and Spin of Merger Remnants. *ApJ*, 894(2), Article 133, 133. <https://doi.org/10.3847/1538-4357/ab88b2>
- Arca-Sedda, M., & Capuzzo-Dolcetta, R. (2017). The MEGaN project - I. Missing formation of massive nuclear clusters and tidal disruption events by star clusters-massive black hole interactions. *Monthly Notices of the Royal Astronomical Society*, 471(1), 478–490. <https://doi.org/10.1093/mnras/stx1586>
- Arca-Sedda, M., & Gualandris, A. (2018). Gravitational wave sources from inspiralling globular clusters in the Galactic Centre and similar environments. *MNRAS*, 477(4), 4423–4442. <https://doi.org/10.1093/mnras/sty922>
- Arca-Sedda, M., Rizzuto, F. P., Naab, T., Ostriker, J., Giersz, M., & Spurzem, R. (2021). Breaching the Limit: Formation of GW190521-like and IMBH Mergers in Young Massive Clusters. *ApJ*, 920(2), Article 128, 128. <https://doi.org/10.3847/1538-4357/ac1419>
- Askar, A., Davies, M. B., & Church, R. P. (2021). Formation of supermassive black holes in galactic nuclei - I. Delivering seed intermediate-mass black holes in massive stellar clusters. *MNRAS*, 502(2), 2682–2700. <https://doi.org/10.1093/mnras/stab113>
- Askar, A., Davies, M. B., & Church, R. P. (2022). Formation of supermassive black holes in galactic nuclei - II. Retention and growth of seed intermediate-mass black holes. *MNRAS*, 511(2), 2631–2647. <https://doi.org/10.1093/mnras/stab3741>
- Askar, A., Giersz, M., Pych, W., & Dalessandro, E. (2018). COCOA code for creating mock observations of star cluster models. *MNRAS*, 475(3), 4170–4185. <https://doi.org/10.1093/mnras/sty101>
- Askar, A., Szkudlarek, M., Gondek-Rosińska, D., Giersz, M., & Bulik, T. (2017). MOCCA-SURVEY Database - I. Coalescing binary black holes originating from globular clusters. *MNRAS*, 464(1), L36–L40. <https://doi.org/10.1093/mnras/lfw177>
- Bahcall, J. N., & Wolf, R. A. (1976). Star distribution around a massive black hole in a globular cluster. *ApJ*, 209, 214–232. <https://doi.org/10.1086/154711>
- Baker, J. G., Boggs, W. D., Centrella, J., Kelly, B. J., McWilliams, S. T., & et al. (2007). Modeling Kicks from the Merger of Nonprecessing Black Hole Binaries. *ApJ*, 668(2), 1140–1144. <https://doi.org/10.1086/521330>
- Baker, J. G., Boggs, W. D., Centrella, J., Kelly, B. J., McWilliams, S. T., & et al. (2008). Mergers of nonspinning black-hole binaries: Gravitational radiation characteristics. *PhRvD*, 78(4), Article 044046, 044046. <https://doi.org/10.1103/PhysRevD.78.044046>
- Ballone, A., Costa, G., Mapelli, M., & MacLeod, M. (2022). Formation of black holes in the pair-instability mass gap: Hydrodynamical simulation of a massive star collision. *arXiv*, Article arXiv:2204.03493, arXiv:2204.03493.
- Ballone, A., Mapelli, M., Di Carlo, U. N., Torniamenti, S., Spera, M., & et al. (2020). Evolution of fractality and rotation in embedded star clusters. *MNRAS*, 496(1), 49–59. <https://doi.org/10.1093/mnras/staa1383>
- Ballone, A., Torniamenti, S., Mapelli, M., Di Carlo, U. N., Spera, M., & et al. (2021). From hydrodynamics to N-body simulations of star clusters: mergers and rotation. *MNRAS*, 501(2), 2920–2933. <https://doi.org/10.1093/mnras/staa3763>
- Banerjee, S., Belczynski, K., Fryer, C. L., Berczik, P., Hurley, J. R., & et al. (2020). BSE versus StarTrack: Implementations of new wind, remnant-formation, and natal-kick schemes in NBODY7 and their astrophysical consequences. *A&A*, 639, Article A41, A41. <https://doi.org/10.1051/0004-6361/201935332>
- Banerjee, S. (2018). Stellar-mass black holes in young massive and open stellar clusters and their role in gravitational-wave generation - II. *MNRAS*, 473(1), 909–926. <https://doi.org/10.1093/mnras/stx2347>
- Banerjee, S. (2021a). Stellar-mass black holes in young massive and open stellar clusters - IV. Updated stellar-evolutionary and black hole spin models and comparisons with the LIGO-Virgo O1/O2 merger-event data. *MNRAS*, 500(3), 3002–3026. <https://doi.org/10.1093/mnras/staa2392>
- Banerjee, S. (2021b). Binary black hole mergers from young massive clusters in the pair-instability supernova mass gap. *arXiv e-prints*, Article arXiv:2109.14612, arXiv:2109.14612.
- Barniske, A., Oskinova, L. M., & Hamann, W. -. (2008). Two extremely luminous WN stars in the Galactic center with circumstellar emission from dust and gas. *A&A*, 486(3), 971–984. <https://doi.org/10.1051/0004-6361:200809568>

- Baumgardt, H. (2001). Scaling of N-body calculations. *MNRAS*, 325(4), 1323–1331. <https://doi.org/10.1046/j.1365-8711.2001.04272.x>
- Baumgardt, H., & Hilker, M. (2018). A catalogue of masses, structural parameters, and velocity dispersion profiles of 112 Milky Way globular clusters. *MNRAS*, 478(2), 1520–1557. <https://doi.org/10.1093/mnras/sty1057>
- Baumgardt, H., Kroupa, P., & Parmentier, G. (2008). The influence of residual gas expulsion on the evolution of the Galactic globular cluster system and the origin of the Population II halo. *MNRAS*, 384(3), 1231–1241. <https://doi.org/10.1111/j.1365-2966.2007.12811.x>
- Baumgardt, H., De Marchi, G., & Kroupa, P. (2008). Evidence for Primordial Mass Segregation in Globular Clusters. *ApJ*, 685(1), 247–253. <https://doi.org/10.1086/590488>
- Baumgardt, H., & Makino, J. (2003). Dynamical evolution of star clusters in tidal fields. *MNRAS*, 340(1), 227–246. <https://doi.org/10.1046/j.1365-8711.2003.06286.x>
- Baym, G., Furusawa, S., Hatsuda, T., Kojo, T., & Togashi, H. (2019). New Neutron Star Equation of State with Quark-Hadron Crossover. *ApJ*, 885(1), Article 42, 42. <https://doi.org/10.3847/1538-4357/ab441e>
- Baym, G., Hatsuda, T., Kojo, T., Powell, P. D., Song, Y., & et al. (2018). From hadrons to quarks in neutron stars: a review. *RPPh*, 81(5), Article 056902, 056902. <https://doi.org/10.1088/1361-6633/aaae14>
- Begelman, M. C. (2010). Evolution of supermassive stars as a pathway to black hole formation. *MNRAS*, 402(1), 673–681. <https://doi.org/10.1111/j.1365-2966.2009.15916.x>
- Begelman, M. C., Rossi, E. M., & Armitage, P. J. (2008). Quasi-stars: accreting black holes inside massive envelopes. *MNRAS*, 387(4), 1649–1659. <https://doi.org/10.1111/j.1365-2966.2008.13344.x>
- Begelman, M. C., Volonteri, M., & Rees, M. J. (2006). Formation of supermassive black holes by direct collapse in pre-galactic haloes. *MNRAS*, 370(1), 289–298. <https://doi.org/10.1111/j.1365-2966.2006.10467.x>
- Bekki, K., & Freeman, K. C. (2003). Formation of ω Centauri from an ancient nucleated dwarf galaxy in the young Galactic disc. *MNRAS*, 346(2), L11–L15. <https://doi.org/10.1046/j.1365-2966.2003.07275.x>
- Bekki, K., & Chiba, M. (2001). Formation of the Galactic Stellar Halo. I. Structure and Kinematics. *ApJ*, 558(2), 666–686. <https://doi.org/10.1086/322300>
- Belczynski, K., & Banerjee, S. (2020). Formation of low-spinning 100 M_{\odot} black holes. *A&A*, 640, Article L20, L20. <https://doi.org/10.1051/0004-6361/202038427>
- Belczynski, K., Heger, A., Gladysz, W., Ruitter, A. J., Woosley, S., & et al. (2016). The effect of pair-instability mass loss on black-hole mergers. *A&A*, 594, Article A97, A97. <https://doi.org/10.1051/0004-6361/201628980>
- Belczynski, K., Klencik, J., Fields, C. E., Olejak, A., Berti, E., & et al. (2020). Evolutionary roads leading to low effective spins, high black hole masses, and O1/O2 rates for LIGO/Virgo binary black holes. *A&A*, 636, Article A104, A104. <https://doi.org/10.1051/0004-6361/201936528>
- Belczynski, K., Bulik, T., Fryer, C. L., Ruitter, A., Valsecchi, F., & et al. (2010). On the Maximum Mass of Stellar Black Holes. *ApJ*, 714(2), 1217–1226. <https://doi.org/10.1088/0004-637X/714/2/1217>
- Belczynski, K., Kalogera, V., & Bulik, T. (2002). A Comprehensive Study of Binary Compact Objects as Gravitational Wave Sources: Evolutionary Channels, Rates, and Physical Properties. *ApJ*, 572(1), 407–431. <https://doi.org/10.1086/340304>
- Belczynski, K., Kalogera, V., Rasio, F. A., Taam, R. E., Zezas, A., & et al. (2008). Compact Object Modeling with the StarTrack Population Synthesis Code. *ApJS*, 174(1), 223–260. <https://doi.org/10.1086/521026>
- Belczynski, K., Ryu, T., Perna, R., Berti, E., Tanaka, T. L., & et al. (2017). On the likelihood of detecting gravitational waves from Population III compact object binaries. *MNRAS*, 471(4), 4702–4721. <https://doi.org/10.1093/mnras/stx1759>
- Belloni, D., Askar, A., Giersz, M., Kroupa, P., & Rocha-Pinto, H. J. (2017). On the initial binary population for star cluster simulations. *MNRAS*, 471(3), 2812–2828. <https://doi.org/10.1093/mnras/stx1763>
- Belloni, D., Giersz, M., Rivera Sandoval, L. E., Askar, A., & Ciecieląg, P. (2019). MOCCA-SURVEY database I. Accreting white dwarf binary systems in globular clusters - IV. Cataclysmic variables - properties of bright and faint populations. *MNRAS*, 483(1), 315–331. <https://doi.org/10.1093/mnras/sty3097>
- Belloni, D., Giersz, M., Rocha-Pinto, H. J., Leigh, N. W. C., & Askar, A. (2017). MOCCA-SURVEY database I. Accreting white dwarf binary systems in globular clusters - II. Cataclysmic variables - progenitors and population at birth. *MNRAS*, 464(4), 4077–4095. <https://doi.org/10.1093/mnras/stw2516>

- Belloni, D., Kroupa, P., Rocha-Pinto, H. J., & Giersz, M. (2018). Dynamical equivalence, the origin of the Galactic field stellar and binary population, and the initial radius-mass relation of embedded clusters. *MNRAS*, 474(3), 3740–3745. <https://doi.org/10.1093/mnras/stx3034>
- Belloni, D., Mikołajewska, J., Ilkiewicz, K., Schreiber, M. R., Giersz, M., & et al. (2020). On the absence of symbiotic stars in globular clusters. *MNRAS*, 496(3), 3436–3447. <https://doi.org/10.1093/mnras/staa1714>
- Belloni, D., Schreiber, M. R., Pala, A. F., Gänsicke, B. T., Zorotovic, M., & et al. (2020). Evidence for reduced magnetic braking in polars from binary population models. *MNRAS*, 491(4), 5717–5731. <https://doi.org/10.1093/mnras/stz3413>
- Belloni, D., Schreiber, M. R., Zorotovic, M., Ilkiewicz, K., Hurley, J. R., & et al. (2018). No cataclysmic variables missing: higher merger rate brings into agreement observed and predicted space densities. *MNRAS*, 478(4), 5626–5637. <https://doi.org/10.1093/mnras/sty1421>
- Belloni, D., Zorotovic, M., Schreiber, M. R., Leigh, N. W. C., Giersz, M., & et al. (2017). mocca-SURVEY database I. Accreting white dwarf binary systems in globular clusters - III. Cataclysmic variables - implications of model assumptions. *MNRAS*, 468(2), 2429–2446. <https://doi.org/10.1093/mnras/stx575>
- Benacquista, M. J., & Downing, J. M. B. (2013). Relativistic Binaries in Globular Clusters. *LRR*, 16(1), Article 4, 4. <https://doi.org/10.12942/lrr-2013-4>
- Berczik, P., Spurzem, R., Zhong, S., Wang, L., Nitadori, K., Hamada, T., & Veles, A. (2013). Up to 700k GPU cores, Kepler, and the Exascale future for simulations of star clusters around black holes [Procs. of 28th Intl. Supercomputing Conf. ISC 2013, Leipzig, Germany]. In J. M. Kunkel, T. Ludwig, & H. Meuer (Eds.), *Supercomputing* (pp. 13–25, Vol. 7905).
- Bestenlehner, J. M. (2020). Mass loss and the Eddington parameter: a new mass-loss recipe for hot and massive stars. *MNRAS*, 493(3), 3938–3946. <https://doi.org/10.1093/mnras/staa47410.48550/arXiv.2002.05168>
- Bestenlehner, J. M., Crowther, P. A., Caballero-Nieves, S. M., Schneider, F. R. N., Simón-Díaz, S., & et al. (2020). The R136 star cluster dissected with Hubble Space Telescope/STIS - II. Physical properties of the most massive stars in R136. *MNRAS*, 499(2), 1918–1936. <https://doi.org/10.1093/mnras/staa2801>
- Bettwieser, E. (1983). A numerical method for the study of the gravothermal instability in star clusters. *MNRAS*, 203, 811–831. <https://doi.org/10.1093/mnras/203.3.811>
- Bettwieser, E., & Spurzem, R. (1986). Anisotropy in stellar dynamics. *AAP*, 161(1), 102–112.
- Bettwieser, E., & Sugimoto, D. (1984). Post-collapse evolution and gravothermal oscillation of globular clusters. *MNRAS*, 208, 493–509. <https://doi.org/10.1093/mnras/208.3.493>
- Bialas, D., Lisker, T., Olczak, C., Spurzem, R., & Kotulla, R. (2015). On the occurrence of galaxy harassment. *A&A*, 576, Article A103, A103. <https://doi.org/10.1051/0004-6361/201425235>
- Bianchini, P., Ibata, R., & Famaey, B. (2019). Exploring the Outskirts of Globular Clusters: The Peculiar Kinematics of NGC 3201. *ApJL*, 887(1), Article L12, L12. <https://doi.org/10.3847/2041-8213/ab58d1>
- Bianchini, P., van de Ven, G., Norris, M. A., Schinnerer, E., & Varri, A. L. (2016a). A novel look at energy equipartition in globular clusters. *MNRAS*, 458(4), 3644–3654. <https://doi.org/10.1093/mnras/stw552>
- Bianchini, P., van de Ven, G., Norris, M. A., Schinnerer, E., & Varri, A. L. (2016b). A novel look at energy equipartition in globular clusters. *MNRAS*, 458(4), 3644–3654. <https://doi.org/10.1093/mnras/stw552>
- Bianchini, P., van der Marel, R. P., del Pino, A., Watkins, L. L., Bellini, A., & et al. (2018). The internal rotation of globular clusters revealed by Gaia DR2. *MNRAS*, 481(2), 2125–2139. <https://doi.org/10.1093/mnras/sty2365>
- Bianchini, P., Varri, A. L., Bertin, G., & Zocchi, A. (2013a). Rotating Globular Clusters. *ApJ*, 772(1), Article 67, 67. <https://doi.org/10.1088/0004-637X/772/1/67>
- Bianchini, P., Varri, A. L., Bertin, G., & Zocchi, A. (2013b). Rotating Globular Clusters. *ApJ*, 772(1), Article 67, 67. <https://doi.org/10.1088/0004-637X/772/1/67>
- Biermann, L. (1932). Untersuchungen über den inneren Aufbau der Sterne. IV. Konvektionszonen im Innern der Sterne. (Veröffentlichungen der Universitäts-Sternwarte Göttingen, Nr. 27.) Mit 5 Abbildungen. *ZA*, 5, 117.
- Binney, J., & Tremaine, S. (2008a). *Galactic Dynamics: Second Edition*.

- Binney, J., & Tremaine, S. (2008b). *Galactic Dynamics: Second Edition*.
- Blanchet, L. (2014). Gravitational Radiation from Post-Newtonian Sources and Inspiralling Compact Binaries. *LRR*, 17(1), Article 2, 2. <https://doi.org/10.12942/lrr-2014-2>
- Bobylev, V. V., & Bajkova, A. T. (2020). Kinematic properties of young intermediate- and low-mass stars from the gaia dr2 catalogue. *Astronomy Reports*, 64(12), 1042–1049. <https://doi.org/10.1134/s1063772920120033>
- Böhm-Vitense, E. (1958). Über die Wasserstoffkonvektionszone in Sternen verschiedener Effektivtemperaturen und Leuchtkräfte. Mit 5 Textabbildungen. *ZA*, 46, 108.
- Bondi, H., & Hoyle, F. (1944). On the mechanism of accretion by stars. *MNRAS*, 104, 273. <https://doi.org/10.1093/mnras/104.5.273>
- Bonetti, M., Haardt, F., Sesana, A., & Barausse, E. (2016). Post-Newtonian evolution of massive black hole triplets in galactic nuclei - I. Numerical implementation and tests. *MNRAS*, 461(4), 4419–4434. <https://doi.org/10.1093/mnras/stw1590>
- Bonetti, M., Sesana, A., Barausse, E., & Haardt, F. (2018). Post-Newtonian evolution of massive black hole triplets in galactic nuclei - III. A robust lower limit to the nHz stochastic background of gravitational waves. *MNRAS*, 477(2), 2599–2612. <https://doi.org/10.1093/mnras/sty874>
- Bonnell, I. A., Larson, R. B., & Zinnecker, H. (2007). The Origin of the Initial Mass Function. In B. Reipurth, D. Jewitt, & K. Keil (Eds.), *Protostars and planets v* (p. 149).
- Boshkayev, K., Rueda, J. A., Ruffini, R., & Siutsou, I. (2013). On General Relativistic Uniformly Rotating White Dwarfs. *ApJ*, 762(2), Article 117, 117. <https://doi.org/10.1088/0004-637X/762/2/117>
- Boylan-Kolchin, M. (2018). The Little Engines That Could? Globular clusters contribute significantly to reionization-era star formation. *MNRAS*, 479(1), 332–340. <https://doi.org/10.1093/mnras/sty1490>
- Breen, P. G., & Hoggie, D. C. (2013). Dynamical evolution of black hole subsystems in idealized star clusters. *MNRAS*, 432(4), 2779–2797. <https://doi.org/10.1093/mnras/stt628>
- Breivik, K., Coughlin, S., Zevin, M., Rodriguez, C. L., Kremer, K., & et al. (2020). COSMIC Variance in Binary Population Synthesis. *ApJ*, 898(1), Article 71, 71. <https://doi.org/10.3847/1538-4357/ab9d85>
- Breivik, K., Mingarelli, C. M. F., & Larson, S. L. (2020). Constraining Galactic Structure with the LISA White Dwarf Foreground. *ApJ*, 901(1), Article 4, 4. <https://doi.org/10.3847/1538-4357/abab99>
- Brem, P., Amaro-Seoane, P., & Spurzem, R. (2013). Relativistic mergers of compact binaries in clusters: the fingerprint of the spin. *MNRAS*, 434(4), 2999–3007. <https://doi.org/10.1093/mnras/stt1220>
- Bressan, A., Fagotto, F., Bertelli, G., & Chiosi, C. (1993). Evolutionary Sequences of Stellar Models with New Radiative Opacities. II. $Z = 0.02$. *A&AS*, 100, 647.
- Bromm, V. (2013). Formation of the first stars. *Reports on Progress in Physics*, 76(11), Article 112901, 112901. <https://doi.org/10.1088/0034-4885/76/11/112901>
- Bromm, V., Coppi, P. S., & Larson, R. B. (2002). The Formation of the First Stars. I. The Primordial Star-forming Cloud. *ApJ*, 564(1), 23–51. <https://doi.org/10.1086/323947>
- Bromm, V., & Larson, R. B. (2004). The First Stars. *ARA&A*, 42(1), 79–118. <https://doi.org/10.1146/annurev.astro.42.053102.134034>
- Bromm, V., & Loeb, A. (2003). Formation of the First Supermassive Black Holes. *ApJ*, 596(1), 34–46. <https://doi.org/10.1086/377529>
- Brott, I., Evans, C. J., Hunter, I., de Koter, A., Langer, N., Dufton, P. L., Cantiello, M., Trundle, C., Lennon, D. J., de Mink, S. E., Yoon, S. .-, & Anders, P. (2011). Rotating massive main-sequence stars. II. Simulating a population of LMC early B-type stars as a test of rotational mixing. *AAP*, 530, Article A116, A116. <https://doi.org/10.1051/0004-6361/201016114>
- Burrows, A., & Hayes, J. (1996). Pulsar Recoil and Gravitational Radiation Due to Asymmetrical Stellar Collapse and Explosion. *PhRvL*, 76(3), 352–355. <https://doi.org/10.1103/PhysRevLett.76.352>
- Cai, M. X., Gieles, M., Hoggie, D. C., & Varri, A. L. (2016). Evolution of star clusters on eccentric orbits. *MNRAS*, 455(1), 596–602. <https://doi.org/10.1093/mnras/stv2325>
- Camacho, J., Torres, S., García-Berro, E., Zorotovic, M., Schreiber, M. R., & et al. (2014). Monte Carlo simulations of post-common-envelope white dwarf + main sequence binaries: comparison with the SDSS DR7 observed sample. *A&A*, 566, Article A86, A86. <https://doi.org/10.1051/0004-6361/201323052>
- Cameron, A. G. W., & Mock, M. (1967). Stellar Accretion and X-ray Emission. *Natur*, 215(5100), 464–466. <https://doi.org/10.1038/215464a0>

- Campanelli, M., Lousto, C., Zlochower, Y., & Merritt, D. (2007). Large Merger Recoils and Spin Flips from Generic Black Hole Binaries. *ApJL*, 659(1), L5–L8. <https://doi.org/10.1086/516712>
- Campbell, C. G. (1984). Tidal effects in twin-degenerate binaries. *MNRAS*, 207, 433–443. <https://doi.org/10.1093/mnras/207.3.433>
- Cantat-Gaudin, T., Jordi, C., Vallenari, A., Bragaglia, A., Balaguer-Núñez, L., Soubiran, C., Bossini, D., Moitinho, A., Castro-Ginard, A., Krone-Martins, A., Casamiquela, L., Sordo, R., & Carrera, R. (2018). A Gaia DR2 view of the open cluster population in the Milky Way. *A&A*, 618, Article A93, A93. <https://doi.org/10.1051/0004-6361/201833476>
- Cantat-Gaudin, T., Vallenari, A., Zaggia, S., Bragaglia, A., Sordo, R., Drew, J. E., Eisloffel, J., Farnhill, H. J., Gonzalez-Solares, E., Greimel, R., Irwin, M. J., Kupcu-Yoldas, A., Jordi, C., Blomme, R., Sampedro, L., Costado, M. T., Alfaro, E., Smiljanic, R., Magrini, L., . . . Worley, C. C. (2014). The Gaia-ESO Survey: Stellar content and elemental abundances in the massive cluster NGC 6705. *AAP*, 569, Article A17, A17. <https://doi.org/10.1051/0004-6361/201423851>
- Chabrier, G. (2003). Galactic Stellar and Substellar Initial Mass Function. *PASP*, 115(809), 763–795. <https://doi.org/10.1086/376392>
- Chandrasekhar, S. (1943a). Dynamical Friction. I. General Considerations: the Coefficient of Dynamical Friction. *ApJ*, 97, 255. <https://doi.org/10.1086/144517>
- Chandrasekhar, S. (1943b). Dynamical Friction. II. The Rate of Escape of Stars from Clusters and the Evidence for the Operation of Dynamical Friction. *ApJ*, 97, 263. <https://doi.org/10.1086/144518>
- Chandrasekhar, S. (1943c). Dynamical Friction. III. a More Exact Theory of the Rate of Escape of Stars from Clusters. *ApJ*, 98, 54. <https://doi.org/10.1086/144544>
- Chandrasekhar, S. (1939). *An introduction to the study of stellar structure*.
- Chandrasekhar, S. (1942). *Principles of stellar dynamics*.
- Chang, J. S., & Cooper, G. (1970). A Practical Difference Scheme for Fokker-Planck Equations. *Journal of Computational Physics*, 6(1), 1–16. [https://doi.org/10.1016/0021-9991\(70\)90001-X](https://doi.org/10.1016/0021-9991(70)90001-X)
- Chatterjee, P., Hernquist, L., & Loeb, A. (2002). Dynamics of a Massive Black Hole at the Center of a Dense Stellar System. *ApJ*, 572(1), 371–381. <https://doi.org/10.1086/340224>
- Chattopadhyay, D., Stevenson, S., Hurley, J. R., Bailes, M., & Broekgaarden, F. (2021). Modelling neutron star-black hole binaries: future pulsar surveys and gravitational wave detectors. *MNRAS*, 504(3), 3682–3710. <https://doi.org/10.1093/mnras/stab973>
- Chattopadhyay, D., Stevenson, S., Hurley, J. R., Rossi, L. J., & Flynn, C. (2020). Modelling double neutron stars: radio and gravitational waves. *MNRAS*, 494(2), 1587–1610. <https://doi.org/10.1093/mnras/staa756>
- Chen, C. W., & Chen, W. P. (2010). Morphological Distortion of Galactic Globular Clusters. *ApJ*, 721(2), 1790–1819. <https://doi.org/10.1088/0004-637X/721/2/1790>
- Chen, Y., Bressan, A., Girardi, L., Marigo, P., Kong, X., & et al. (2015). PARSEC evolutionary tracks of massive stars up to 350 M_{\odot} at metallicities $0.0001 \leq Z \leq 0.04$. *MNRAS*, 452(1), 1068–1080. <https://doi.org/10.1093/mnras/stv1281>
- Cherepashchuk, A. M., Belinski, A. A., Dodin, A. V., & Postnov, K. A. (2021). Discovery of orbital eccentricity and evidence for orbital period increase of SS433. *MNRAS*, 507(1), L19–L23. <https://doi.org/10.1093/mnras/507.1/l19>
- Chernoff, D. F., & Weinberg, M. D. (1990). Evolution of Globular Clusters in the Galaxy. *ApJ*, 351, 121. <https://doi.org/10.1086/168451>
- Chon, S., & Omukai, K. (2020). Supermassive star formation via super competitive accretion in slightly metal-enriched clouds. *MNRAS*, 494(2), 2851–2860. <https://doi.org/10.1093/mnras/staa863>
- Chon, S., Omukai, K., & Schneider, R. (2021). Transition of the initial mass function in the metal-poor environments. *MNRAS*, 508(3), 4175–4192. <https://doi.org/10.1093/mnras/stab2497>
- Church, R. P., Tout, C. A., & Hurley, J. R. (2009). N-body Simulations with Live Stellar Evolution. *PASA*, 26(1), 92–102. <https://doi.org/10.1071/AS08062>
- Claeys, J. S. W., Pols, O. R., Izzard, R. G., Vink, J., & Verbunt, F. W. M. (2014). Theoretical uncertainties of the Type Ia supernova rate. *A&A*, 563, Article A83, A83. <https://doi.org/10.1051/0004-6361/201322714>
- Claret, A. (1995). Stellar models for a wide range of initial chemical compositions until helium burning. I. From $X=0.60$ to $X=0.80$ for $Z=0.02$. *A&AS*, 109, 441–446.

- Claret, A., & Gimenez, A. (1995). Stellar models for a wide range of initial chemical compositions until helium burning. II. From $X=0.63$ to $X=0.80$, for $Z=0.01$. *A&AS*, 114, 549.
- Claret, A., & Torres, G. (2016). The dependence of convective core overshooting on stellar mass. *A&A*, 592, Article A15, A15. <https://doi.org/10.1051/0004-6361/201628779>
- Clark, G. W. (1975). X-ray binaries in globular clusters. *ApJL*, 199, L143–L145. <https://doi.org/10.1086/181869>
- Cohn, H. (1979). Numerical integration of the Fokker-Planck equation and the evolution of star clusters. *ApJ*, 234, 1036–1053. <https://doi.org/10.1086/157587>
- Cohn, H. (1980). Late core collapse in star clusters and the gravothermal instability. *ApJ*, 242, 765–771. <https://doi.org/10.1086/158511>
- Cojocaru, R., Rebassa-Mansergas, A., Torres, S., & García-Berro, E. (2017). The population of white dwarf-main sequence binaries in the SDSS DR 12. *MNRAS*, 470(2), 1442–1452. <https://doi.org/10.1093/mnras/stx1326>
- Costa, G., Ballone, A., Mapelli, M., & Bressan, A. (2022). Formation of black holes in the pair-instability mass gap: evolution of a post-collision star. *arXiv*, Article arXiv:2204.03492, arXiv:2204.03492.
- Cummings, J. D., Kalirai, J. S., Tremblay, P. .-, Ramirez-Ruiz, E., & Choi, J. (2018). The White Dwarf Initial-Final Mass Relation for Progenitor Stars from 0.85 to 7.5 M_{\odot} . *ApJ*, 866(1), Article 21, 21. <https://doi.org/10.3847/1538-4357/aadfd610.48550/arXiv.1809.01673>
- De, S., MacLeod, M., Everson, R. W., Antoni, A., Mandel, I., & et al. (2020). Common Envelope Wind Tunnel: The Effects of Binary Mass Ratio and Implications for the Accretion-driven Growth of LIGO Binary Black Holes. *ApJ*, 897(2), Article 130, 130. <https://doi.org/10.3847/1538-4357/ab9ac6>
- de Boer, T. J. L., Gieles, M., Balbinot, E., Hénault-Brunet, V., Sollima, A., & et al. (2019). Globular cluster number density profiles using Gaia DR2. *MNRAS*, 485(4), 4906–4935. <https://doi.org/10.1093/mnras/stz651>
- de Mink, S. E., Cantiello, M., Langer, N., Pols, O. R., Brott, I., & et al. (2009). Rotational mixing in massive binaries. Detached short-period systems. *A&A*, 497(1), 243–253. <https://doi.org/10.1051/0004-6361/200811439>
- de Souza, R. S., Ciardi, B., Maio, U., & Ferrara, A. (2013). Dark matter halo environment for primordial star formation. *MNRAS*, 428(3), 2109–2117. <https://doi.org/10.1093/mnras/sts181>
- de Vries, N., Portegies Zwart, S., & Figueira, J. (2014). The evolution of triples with a Roche lobe filling outer star. *MNRAS*, 438(3), 1909–1921. <https://doi.org/10.1093/mnras/stt1688>
- Decin, L. (2020). Evolution and Mass Loss of Cool Ageing Stars: a Daedalean Story. *arXiv e-prints*, Article arXiv:2011.13472, arXiv:2011.13472.
- Dehnen, W. (2000). A Very Fast and Momentum-conserving Tree Code. *ApJl*, 536(1), L39–L42. <https://doi.org/10.1086/312724>
- Dehnen, W., & Hernandez, D. M. (2017). Symplectic fourth-order maps for the collisional N -body problem. *MNRAS*, 465(1), 1201–1217. <https://doi.org/10.1093/mnras/stw2758>
- Dejonghe, H., & de Zeeuw, T. (1988). Analytic Axisymmetric Galaxy Models with Three Integrals of Motion. *ApJ*, 333, 90. <https://doi.org/10.1086/166727>
- Dewi, J. D. M., & Tauris, T. M. (2000). On the energy equation and efficiency parameter of the common envelope evolution. *A&A*, 360, 1043–1051.
- Di Carlo, U. N., Giacobbo, N., Mapelli, M., Pasquato, M., Spera, M., & et al. (2019). Merging black holes in young star clusters. *MNRAS*, 487(2), 2947–2960. <https://doi.org/10.1093/mnras/stz1453>
- Di Carlo, U. N., Mapelli, M., Bouffanais, Y., Giacobbo, N., Santoliquido, F., & et al. (2020). Binary black holes in the pair instability mass gap. *MNRAS*, 497(1), 1043–1049. <https://doi.org/10.1093/mnras/staa1997>
- Di Carlo, U. N., Mapelli, M., Giacobbo, N., Spera, M., Bouffanais, Y., & et al. (2020). Binary black holes in young star clusters: the impact of metallicity. *MNRAS*, 498(1), 495–506. <https://doi.org/10.1093/mnras/staa2286>
- Di Carlo, U. N., Mapelli, M., Pasquato, M., Rastello, S., Ballone, A., Dall’Amico, M., Giacobbo, N., Iorio, G., Spera, M., Torniamenti, S., & Haardt, F. (2021). Intermediate-mass black holes from stellar mergers in young star clusters. *MNRAS*, 507(4), 5132–5143. <https://doi.org/10.1093/mnras/stab2390>
- Dosopoulou, F., & Antonini, F. (2017). Dynamical Friction and the Evolution of Supermassive Black Hole Binaries: The Final Hundred-parsec Problem. *ApJ*, 840(1), Article 31, 31. <https://doi.org/10.3847/1538-4357/aa6b58>

- Downing, J. M. B. (2012). Is there a size difference between red and blue globular clusters? *MNRAS*, 425(3), 2234–2243. <https://doi.org/10.1111/j.1365-2966.2012.21680.x>
- Downing, J. M. B., Benacquista, M. J., Giersz, M., & Spurzem, R. (2010). Compact binaries in star clusters - I. Black hole binaries inside globular clusters. *MNRAS*, 407(3), 1946–1962. <https://doi.org/10.1111/j.1365-2966.2010.17040.x>
- Downing, J. M. B., Benacquista, M. J., Giersz, M., & Spurzem, R. (2011). Compact binaries in star clusters - II. Escapers and detection rates. *MNRAS*, 416(1), 133–147. <https://doi.org/10.1111/j.1365-2966.2011.19023.x>
- Doyle, T. F., Shara, M. M., Lessing, A. M., & Zurek, D. (2019). A Hubble Space Telescope Survey for Novae in the Globular Clusters of M87. *ApJ*, 874(1), Article 65, 65. <https://doi.org/10.3847/1538-4357/ab0490>
- Drozda, P., Belczynski, K., O’Shaughnessy, R., Bulik, T., & Fryer, C. L. (2020). Black hole - neutron star mergers: the first mass gap and kilonovae. *arXiv*, Article arXiv:2009.06655, arXiv:2009.06655.
- Duquennoy, A., & Mayor, M. (1991). Multiplicity among solar-type stars in the solar neighbourhood. II - Distribution of the orbital elements in an unbiased sample. *A&A*, 500, 337–376.
- Duquennoy, A., Mayor, M., & Halbwachs, J. -. (1991). Multiplicity among solar type stars in the solar neighbourhood. I. CORAVEL radial velocity observations of 291 stars. *A&AS*, 88, 281–324.
- Eggenberger, P., Meynet, G., Maeder, A., Hirschi, R., Charbonnel, C., & et al. (2008). The Geneva stellar evolution code. *Ap&SS*, 316(1-4), 43–54. <https://doi.org/10.1007/s10509-007-9511-y>
- Eggleton, P. P. (1983). Approximations to the radii of Roche lobes. *ApJ*, 268, 368–369. <https://doi.org/10.1086/160960>
- Eggleton, P. P. (1996). Combining Stellar Evolution and Stellar Dynamics. In P. Hut & J. Makino (Eds.), *Dynamical evolution of star clusters: Confrontation of theory and observations* (p. 213, Vol. 174).
- Eggleton, P. P., Faulkner, J., & Flannery, B. P. (1973). An Approximate Equation of State for Stellar Material. *A&A*, 23, 325.
- Eggleton, P. (2006). *Evolutionary Processes in Binary and Multiple Stars*.
- Eggleton, P. P. (1971). The evolution of low mass stars. *MNRAS*, 151, 351. <https://doi.org/10.1093/mnras/151.3.351>
- Eggleton, P. P. (1972). Composition changes during stellar evolution. *MNRAS*, 156, 361. <https://doi.org/10.1093/mnras/w156.3.361>
- Eggleton, P. P. (1973). A numerical treatment of double shell source stars. *MNRAS*, 163, 279. <https://doi.org/10.1093/mnras/163.3.279>
- Eggleton, P. P., Fitchett, M. J., & Tout, C. A. (1989). The Distribution of Visual Binaries with Two Bright Components. *ApJ*, 347, 998. <https://doi.org/10.1086/168190>
- Eggleton, P. P., Kiseleva, L. G., & Hut, P. (1998). The Equilibrium Tide Model for Tidal Friction. *ApJ*, 499(2), 853–870. <https://doi.org/10.1086/305670>
- Einsel, C. (1997). *Dynamische entwicklung rotierender sternsysteme* [Doctoral dissertation, Christian-Albrechts-Universität zu Kiel] [Shaker Verlag, ISBN 3-8265-2230-5].
- Einsel, C., & Spurzem, R. (1999). Dynamical evolution of rotating stellar systems - I. Pre-collapse, equal-mass system. *MNRAS*, 302(1), 81–95. <https://doi.org/10.1046/j.1365-8711.1999.02083.x>
- Ekström, S., Georgy, C., Eggenberger, P., Meynet, G., Mowlavi, N., & et al. (2012). Grids of stellar models with rotation. I. Models from 0.8 to 120 M_{\odot} at solar metallicity ($Z = 0.014$). *A&A*, 537, Article A146, A146. <https://doi.org/10.1051/0004-6361/201117751>
- Ekström, S., Meynet, G., Chiappini, C., Hirschi, R., & Maeder, A. (2008). Effects of rotation on the evolution of primordial stars. *A&A*, 489(2), 685–698. <https://doi.org/10.1051/0004-6361:200809633>
- Eldridge, J. J., & Tout, C. A. (2004). The progenitors of core-collapse supernovae. *MNRAS*, 353(1), 87–97. <https://doi.org/10.1111/j.1365-2966.2004.08041.x>
- Elson, R., Hut, P., & Inagaki, S. (1987). Dynamical evolution of globular clusters. *ARA&A*, 25, 565–601. <https://doi.org/10.1146/annurev.aa.25.090187.003025>
- Elson, R. A. W., Fall, S. M., & Freeman, K. C. (1987). The Structure of Young Star Clusters in the Large Magellanic Cloud. *ApJ*, 323, 54. <https://doi.org/10.1086/165807>
- Ernst, A., Glaschke, P., Fiestas, J., Just, A., & Spurzem, R. (2007). N-body models of rotating globular clusters. *MNRAS*, 377(2), 465–479. <https://doi.org/10.1111/j.1365-2966.2007.11602.x>

- Erwin, P., & Gadotti, D. A. (2012). Do Nuclear Star Clusters and Supermassive Black Holes Follow the Same Host-Galaxy Correlations? *Advances in Astronomy*, 2012, Article 946368, 946368. <https://doi.org/10.1155/2012/946368>
- Evans, M., Adhikari, R. X., Afle, C., Ballmer, S. W., Biscoveanu, S., & et al. (2021). A Horizon Study for Cosmic Explorer: Science, Observatories, and Community. *arXiv*, Article arXiv:2109.09882, arXiv:2109.09882.
- Event Horizon Telescope Collaboration, e. a. (2019). First M87 Event Horizon Telescope Results. IV. Imaging the Central Supermassive Black Hole. *ApJ*, 875(1), Article L4, L4. <https://doi.org/10.3847/2041-8213/ab0e85>
- Everson, R. W., MacLeod, M., De, S., Macias, P., & Ramirez-Ruiz, E. (2020). Common Envelope Wind Tunnel: Range of Applicability and Self-similarity in Realistic Stellar Envelopes. *ApJ*, 899(1), Article 77, 77. <https://doi.org/10.3847/1538-4357/aba75c>
- Fagotto, F., Bressan, A., Bertelli, G., & Chiosi, C. (1994a). Evolutionary sequences of stellar models with new radiative opacities. III. $Z=0.0004$ and $Z=0.05$. *A&AS*, 104, 365–376.
- Fagotto, F., Bressan, A., Bertelli, G., & Chiosi, C. (1994b). Evolutionary sequences of stellar models with new radiative opacities. IV. $Z=0.004$ and $Z=0.008$. *A&AS*, 105, 29–38.
- Fahrion, K., Müller, O., Rejkuba, M., Hilker, M., Lyubenova, M., van de Ven, G., Georgiev, I. Y., Lelli, F., Pawlowski, M. S., & Jerjen, H. (2020). Metal-poor nuclear star clusters in two dwarf galaxies near Centaurus A suggestion formation from the in-spiraling of globular clusters. *Astronomy & Astrophysics*, 634, A53. <https://doi.org/10.1051/0004-6361/201937120>
- Faucher-Giguère, C.-A., & Kaspi, V. M. (2006). Birth and Evolution of Isolated Radio Pulsars. *ApJ*, 643(1), 332–355. <https://doi.org/10.1086/501516>
- Faye, G., Blanchet, L., & Buonanno, A. (2006). Higher-order spin effects in the dynamics of compact binaries. I. Equations of motion. *PhRvD*, 74(10), Article 104033, 104033. <https://doi.org/10.1103/PhysRevD.74.104033>
- Feldmeier, A., Neumayer, N., Seth, A., Schödel, R., Lützgendorf, N., de Zeeuw, P. T., Kissler-Patig, M., Nishiyama, S., & Walcher, C. J. (2014). Large scale kinematics and dynamical modelling of the Milky Way nuclear star cluster. *A&A*, 570, Article A2, A2. <https://doi.org/10.1051/0004-6361/201423777>
- Feldmeier-Krause, A., Kerzendorf, W., Do, T., Nogueras-Lara, F., Neumayer, N., Walcher, C. J., Seth, A. C., Schödel, R., de Zeeuw, P. T., Hilker, M., Lützgendorf, N., Kuntschner, H., & Kissler-Patig, M. (2020). Asymmetric spatial distribution of subsolar metallicity stars in the Milky Way nuclear star cluster. *Monthly Notices of the Royal Astronomical Society*, 494(1), 396–410. <https://doi.org/10.1093/mnras/staa703>
- Feldmeier-Krause, A., Zhu, L., Neumayer, N., van de Ven, G., de Zeeuw, P. T., & Schödel, R. (2017). Triaxial orbit-based modelling of the Milky Way Nuclear Star Cluster. *MNRAS*, 466(4), 4040–4052. <https://doi.org/10.1093/mnras/stw3377>
- Fellhauer, M., & Kroupa, P. (2005). Star Cluster Survival in Star Cluster Complexes under Extreme Residual Gas Expulsion. *ApJ*, 630(2), 879–886. <https://doi.org/10.1086/432110>
- Fellhauer, M., Lin, D. N. C., Bolte, M., Aarseth, S. J., & Williams, K. A. (2003). The White Dwarf Deficit in Open Clusters: Dynamical Processes. *ApJL*, 595(1), L53–L56. <https://doi.org/10.1086/379005>
- Fellhauer, M. (2008). Dynamical Friction. In S. J. Aarseth, C. A. Tout, & R. A. Mardling (Eds.), *The cambridge n-body lectures* (p. 171, Vol. 760). https://doi.org/10.1007/978-1-4020-8431-7_7
- Fernández, R. (2010). The Spiral Modes of the Standing Accretion Shock Instability. *ApJ*, 725(2), 1563–1580. <https://doi.org/10.1088/0004-637X/725/2/156310.48550/arXiv.1003.1730>
- Ferraro, F. R., Mucciarelli, A., Lanzoni, B., Pallanca, C., Lapenna, E., Origlia, L., Dalessandro, E., Valenti, E., Beccari, G., Bellazzini, M., Vesperini, E., Varri, A., & Sollima, A. (2018). MIKIS: The Multi-instrument Kinematic Survey of Galactic Globular Clusters. I. Velocity Dispersion Profiles and Rotation Signals of 11 Globular Clusters. *ApJ*, 860(1), Article 50, 50. <https://doi.org/10.3847/1538-4357/aabe2f>
- Fewell, M. P. (1995). The atomic nuclide with the highest mean binding energy. *American Journal of Physics*, 63(7), 653–658. <https://doi.org/10.1119/1.17828>
- Fiestas, J., Porth, O., Berczik, P., & Spurzem, R. (2012). Evolution of growing black holes in axisymmetric galaxy cores. *MNRAS*, 419(1), 57–69. <https://doi.org/10.1111/j.1365-2966.2011.19670.x>
- Fiestas, J., & Spurzem, R. (2010). Dynamical evolution of rotating dense stellar systems with embedded black holes. *MNRAS*, 405(1), 194–208. <https://doi.org/10.1111/j.1365-2966.2010.16479.x>

- Fiestas, J., Spurzem, R., & Kim, E. (2006). 2D Fokker-Planck models of rotating clusters. *MNRAS*, 373(2), 677–686. <https://doi.org/10.1111/j.1365-2966.2006.11036.x>
- Flammini Dotti, F., Kouwenhoven, M. B. N., Kamlah, A. W. H., & Spurzem, R. (2022). *MNRAS submitted*.
- Forbes, D. A., Read, J. I., Gieles, M., & Collins, M. L. M. (2018). Extending the globular cluster system-halo mass relation to the lowest galaxy masses. *MNRAS*, 481(4), 5592–5605. <https://doi.org/10.1093/mnras/sty2584>
- Fragione, G., & Banerjee, S. (2020). Demographics of Neutron Stars in Young Massive and Open Clusters. *ApJL*, 901(1), Article L16, L16. <https://doi.org/10.3847/2041-8213/abb671>
- Fragione, G., & Kocsis, B. (2020). Effective spin distribution of black hole mergers in triples. *MNRAS*, 493(3), 3920–3931. <https://doi.org/10.1093/mnras/staa443>
- Fragione, G., & Loeb, A. (2019). Black hole-neutron star mergers from triples. *MNRAS*, 486(3), 4443–4450. <https://doi.org/10.1093/mnras/stz1131>
- Fragos, T., Willems, B., Kalogera, V., Ivanova, N., Rockefeller, G., Fryer, C. L., & Young, P. A. (2009). Understanding Compact Object Formation and Natal Kicks. II. The Case of XTE J1118 + 480. *ApJ*, 697(2), 1057–1070. <https://doi.org/10.1088/0004-637X/697/2/1057>
- Fragos, T., Andrews, J. J., Ramirez-Ruiz, E., Meynet, G., Kalogera, V., Taam, R. E., & Zezas, A. (2019). The complete evolution of a neutron-star binary through a common envelope phase using 1d hydrodynamic simulations. *The Astrophysical Journal*, 883(2), L45. <https://doi.org/10.3847/2041-8213/ab40d1>
- Frank, J., & Rees, M. J. (1976). Effects of massive black holes on dense stellar systems. *MNRAS*, 176, 633–647. <https://doi.org/10.1093/mnras/176.3.633>
- Fraser, M., Casey, A. R., Gilmore, G., Heger, A., & Chan, C. (2017). The mass distribution of Population III stars. *MNRAS*, 468(1), 418–425. <https://doi.org/10.1093/mnras/stx480>
- Fregeau, J. M., Cheung, P., Portegies Zwart, S. F., & Rasio, F. A. (2004). Stellar collisions during binary-binary and binary-single star interactions. *MNRAS*, 352(1), 1–19. <https://doi.org/10.1111/j.1365-2966.2004.07914.x>
- Fregeau, J. M., Joshi, K. J., Portegies Zwart, S. F., & Rasio, F. A. (2002). Mass Segregation in Globular Clusters. *ApJ*, 570(1), 171–183. <https://doi.org/10.1086/339576>
- Fregeau, J. M., & Rasio, F. A. (2007). Monte Carlo Simulations of Globular Cluster Evolution. IV. Direct Integration of Strong Interactions. *ApJ*, 658(2), 1047–1061. <https://doi.org/10.1086/511809>
- Freitag, M., & Benz, W. (2001). A new Monte Carlo code for star cluster simulations. I. Relaxation. *A&A*, 375, 711–738. <https://doi.org/10.1051/0004-6361:20010706>
- Freitag, M., & Benz, W. (2002). A new Monte Carlo code for star cluster simulations. II. Central black hole and stellar collisions. *A&A*, 394, 345–374. <https://doi.org/10.1051/0004-6361:20021142>
- Freitag, M. (2008). Monte-Carlo Models of Collisional Stellar Systems. In S. J. Aarseth, C. A. Tout, & R. A. Mardling (Eds.), *The cambridge n-body lectures* (p. 123, Vol. 760). https://doi.org/10.1007/978-1-4020-8431-7_5
- Frenk, C. S., & Fall, S. M. (1982). An ellipticity-age relation for globular clusters in the Large Magellanic Cloud - I. Measurements. *MNRAS*, 199, 565–580. <https://doi.org/10.1093/mnras/199.3.565>
- Fryer, C. L., Woosley, S. E., & Heger, A. (2001). Pair-Instability Supernovae, Gravity Waves, and Gamma-Ray Transients. *ApJ*, 550(1), 372–382. <https://doi.org/10.1086/319719>
- Fryer, C., & Kalogera, V. (1997). Double Neutron Star Systems and Natal Neutron Star Kicks. *ApJ*, 489(1), 244–253. <https://doi.org/10.1086/304772>
- Fryer, C. L. (2004). Neutron Star Kicks from Asymmetric Collapse. *ApJ*, 601(2), L175–L178. <https://doi.org/10.1086/382044>
- Fryer, C. L., Belczynski, K., Wiktorowicz, G., Dominik, M., Kalogera, V., & et al. (2012). Compact Remnant Mass Function: Dependence on the Explosion Mechanism and Metallicity. *ApJ*, 749(1), Article 91, 91. <https://doi.org/10.1088/0004-637X/749/1/91>
- Fryer, C. L., & Kusenko, A. (2006). Effects of Neutrino-driven Kicks on the Supernova Explosion Mechanism. *ApJS*, 163(2), 335–343. <https://doi.org/10.1086/500933>
- Fryer, C. L., & Young, P. A. (2007). Late-Time Convection in the Collapse of a 23 M_{Solar} Star. *ApJ*, 659(2), 1438–1448. <https://doi.org/10.1086/513003>

- Fukushige, T., & Heggie, D. C. (2000). The time-scale of escape from star clusters. *MNRAS*, 318(3), 753–761. <https://doi.org/10.1046/j.1365-8711.2000.03811.x>
- Fuller, G. M., Kusenko, A., Mocioiu, I., & Pascoli, S. (2003). Pulsar kicks from a dark-matter sterile neutrino. *PhRvD*, 68(10), Article 103002, 103002. <https://doi.org/10.1103/PhysRevD.68.103002>
- Fuller, J., & Ma, L. (2019). Most Black Holes Are Born Very Slowly Rotating. *ApJL*, 881(1), Article L1, L1. <https://doi.org/10.3847/2041-8213/ab339b>
- Fuller, J., Piro, A. L., & Jermyn, A. S. (2019). Slowing the spins of stellar cores. *MNRAS*, 485(3), 3661–3680. <https://doi.org/10.1093/mnras/stz514>
- Funato, Y., Hut, P., McMillan, S., & Makino, J. (1996). Time-Symmetrized Kustaanheimo-Stiefel Regularization. *AJ*, 112, 1697. <https://doi.org/10.1086/118136>
- Gabriel, M., Noels, A., Montalbán, J., & Miglio, A. (2014). Proper use of Schwarzschild Ledoux criteria in stellar evolution computations. *A&A*, 569, Article A63, A63. <https://doi.org/10.1051/0004-6361/201423442>
- Gaia Collaboration, Helmi, A., van Leeuwen, F., McMillan, P. J., Massari, D., & et al., A. (2018). Gaia data release 2 - kinematics of globular clusters and dwarf galaxies around the milky way. *A&A*, 616, A12. <https://doi.org/10.1051/0004-6361/201832698>
- Geller, A. M., Leigh, N. W. C., Giersz, M., Kremer, K., & Rasio, F. A. (2019). In Search of the Thermal Eccentricity Distribution. *ApJ*, 872(2), Article 165, 165. <https://doi.org/10.3847/1538-4357/ab0214>
- Genzel, R., Eisenhauer, F., & Gillessen, S. (2010). The Galactic Center massive black hole and nuclear star cluster. *Reviews of Modern Physics*, 82(4), 3121–3195. <https://doi.org/10.1103/RevModPhys.82.3121>
- Georgiev, I. Y., Böker, T., Leigh, N., Lützgendorf, N., & Neumayer, N. (2016). Masses and scaling relations for nuclear star clusters, and their co-existence with central black holes. *MNRAS*, 457(2), 2122–2138. <https://doi.org/10.1093/mnras/stw093>
- Gerhard, O. (2001). The Galactic Center HE I Stars: Remains of a Dissolved Young Cluster? *ApJL*, 546(1), L39–L42. <https://doi.org/10.1086/318054>
- Gessner, A., & Janka, H.-T. (2018). Hydrodynamical Neutron-star Kicks in Electron-capture Supernovae and Implications for the CRAB Supernova. *ApJ*, 865(1), Article 61, 61. <https://doi.org/10.3847/1538-4357/aadbae>
- Geyer, E. H., Hopp, U., & Nelles, B. (1983). Ellipticity variations within some globular clusters of the galaxy and the Magellanic Clouds. *A&A*, 125, 359–367.
- Giacobbo, N., & Mapelli, M. (2018). The progenitors of compact-object binaries: impact of metallicity, common envelope and natal kicks. *MNRAS*, 480(2), 2011–2030. <https://doi.org/10.1093/mnras/sty1999>
- Giacobbo, N., & Mapelli, M. (2019). Erratum: The progenitors of compact-object binaries: impact of metallicity, common envelope and natal kicks. *MNRAS*, 486(2), 2494–2495. <https://doi.org/10.1093/mnras/stz892>
- Giacobbo, N., Mapelli, M., & Spera, M. (2018). Merging black hole binaries: the effects of progenitor’s metallicity, mass-loss rate and Eddington factor. *MNRAS*, 474(3), 2959–2974. <https://doi.org/10.1093/mnras/stx2933>
- Gieles, M., Athanassoula, E., & Portegies Zwart, S. F. (2007). The effect of spiral arm passages on the evolution of stellar clusters. *MNRAS*, 376(2), 809–819. <https://doi.org/10.1111/j.1365-2966.2007.11477.x>
- Gieles, M., Charbonnel, C., Krause, M. G. H., Hénault-Brunet, V., Agertz, O., & et al. (2018). Concurrent formation of supermassive stars and globular clusters: implications for early self-enrichment. *MNRAS*, 478(2), 2461–2479. <https://doi.org/10.1093/mnras/sty1059>
- Gieles, M., & Zocchi, A. (2015). A family of lowered isothermal models. *MNRAS*, 454(1), 576–592. <https://doi.org/10.1093/mnras/stv1848>
- Giersz, M., & Heggie, D. C. (1994a). Statistics of N-Body Simulations - Part One - Equal Masses Before Core Collapse. *MNRAS*, 268, 257. <https://doi.org/10.1093/mnras/268.1.257>
- Giersz, M., & Heggie, D. C. (1994b). Statistics of N-Body Simulations - Part Two - Equal Masses after Core Collapse. *MNRAS*, 270, 298. <https://doi.org/10.1093/mnras/270.2.298>
- Giersz, M., Leigh, N., Hypki, A., Askar, A., & Lützgendorf, N. (2016). Formation mechanisms of IMBH in globular clusters. *MmSAI*, 87, 555.
- Giersz, M., & Spurzem, R. (1994). Comparing direct N-body integration with anisotropic gaseous models of star clusters. *MNRAS*, 269, 241. <https://doi.org/10.1093/mnras/269.2.241>

- Giersz, M. (1998). Monte Carlo simulations of star clusters - I. First Results. *MNRAS*, 298(4), 1239–1248. <https://doi.org/10.1046/j.1365-8711.1998.01734.x>
- Giersz, M. (2001). Monte Carlo simulations of star clusters - II. Tidally limited, multimass systems with stellar evolution. *MNRAS*, 324(1), 218–230. <https://doi.org/10.1046/j.1365-8711.2001.04337.x>
- Giersz, M., & Heggie, D. C. (1996). Statistics of N-body simulations - III. Unequal masses. *MNRAS*, 279(3), 1037–1056. <https://doi.org/10.1093/mnras/279.3.1037>
- Giersz, M., & Heggie, D. C. (1997). Statistics of N-body simulations - IV. Unequal masses with a tidal field. *MNRAS*, 286(3), 709–731. <https://doi.org/10.1093/mnras/286.3.709>
- Giersz, M., Heggie, D. C., & Hurley, J. R. (2008). Monte Carlo simulations of star clusters - IV. Calibration of the Monte Carlo code and comparison with observations for the open cluster M67. *MNRAS*, 388(1), 429–443. <https://doi.org/10.1111/j.1365-2966.2008.13407.x>
- Giersz, M., Heggie, D. C., Hurley, J. R., & Hypki, A. (2013). MOCCA code for star cluster simulations - II. Comparison with N-body simulations. *MNRAS*, 431(3), 2184–2199. <https://doi.org/10.1093/mnras/stt307>
- Giersz, M., Leigh, N., Hypki, A., Lützgendorf, N., & Askar, A. (2015). MOCCA code for star cluster simulations - IV. A new scenario for intermediate mass black hole formation in globular clusters. *MNRAS*, 454(3), 3150–3165. <https://doi.org/10.1093/mnras/stv2162>
- Giersz, M., Leigh, N., Marks, M., Hypki, A., & Askar, A. (2014). Monte Carlo modelling of globular star clusters - many primordial binaries, IMBH formation. *arXiv*, Article arXiv:1411.7603, arXiv:1411.7603.
- Giesers, B., Dreizler, S., Husser, T.-O., Kamann, S., Anglada Escudé, G., Brinchmann, J., Carollo, C. M., Roth, M. M., Weilbacher, P. M., & Wisotzki, L. (2018). A detached stellar-mass black hole candidate in the globular cluster NGC 3201. *MNRAS*, 475(1), L15–L19. <https://doi.org/10.1093/mnras/slx203>
- Giesers, B., Kamann, S., Dreizler, S., Husser, T.-O., Askar, A., Göttgens, F., Brinchmann, J., Latour, M., Weilbacher, P. M., Wendt, M., & Roth, M. M. (2019). A stellar census in globular clusters with MUSE: Binaries in NGC 3201. *AAP*, 632, Article A3, A3. <https://doi.org/10.1051/0004-6361/201936203>
- Glaschke, P., Amaro-Seoane, P., & Spurzem, R. (2014). Hybrid methods in planetesimal dynamics: description of a new composite algorithm. *MNRAS*, 445(4), 3620–3649. <https://doi.org/10.1093/mnras/stu1558>
- Gnedin, O. Y., & Ostriker, J. P. (1997). Destruction of the Galactic Globular Cluster System. *ApJ*, 474(1), 223–255. <https://doi.org/10.1086/303441>
- Goodman, J. (1983). Core collapse with strong encounters. *ApJ*, 270, 700–710. <https://doi.org/10.1086/161161>
- Goodman, J. J. (1983). *Dynamical Relaxation in Stellar Systems*. [Doctoral dissertation, Princeton Univ., NJ].
- Goodman, J., Heggie, D. C., & Hut, P. (1993). On the Exponential Instability of N-Body Systems. *ApJ*, 415, 715. <https://doi.org/10.1086/173196>
- Goodman, J., & Hut, P. (1993). Binary–Single-Star Scattering. V. Steady State Binary Distribution in a Homogeneous Static Background of Single Stars. *ApJ*, 403, 271. <https://doi.org/10.1086/172200>
- Goodwin, S. P., & Kroupa, P. (2005). Limits on the primordial stellar multiplicity. *AAP*, 439(2), 565–569. <https://doi.org/10.1051/0004-6361:20052654>
- Goodwin, S. P., & Whitworth, A. P. (2004). The dynamical evolution of fractal star clusters: The survival of substructure. *A&A*, 413, 929–937. <https://doi.org/10.1051/0004-6361:20031529>
- Gräfener, G., & Hamann, W. -. (2008). Mass loss from late-type WN stars and its Z-dependence. Very massive stars approaching the Eddington limit. *A&A*, 482(3), 945–960. <https://doi.org/10.1051/0004-6361:20066176>
- Gratton, R. G., Carretta, E., & Bragaglia, A. (2012). Multiple populations in globular clusters. Lessons learned from the Milky Way globular clusters. *AAPR*, 20, Article 50, 50. <https://doi.org/10.1007/s00159-012-0050-3>
- GRAVITY Collaboration, Abuter, R., Amorim, A., Bauböck, M., Berger, J. P., Bonnet, H., Brandner, W., Clénet, Y., Coudé Du Foresto, V., de Zeeuw, P. T., Deen, C., Dexter, J., Duvert, G., Eckart, A., Eisenhauer, F., Förster Schreiber, N. M., Garcia, P., Gao, F., Gendron, E., . . . Yazici, S. (2018). Detection of orbital motions near the last stable circular orbit of the massive black hole SgrA*. *A&A*, 618, Article L10, L10. <https://doi.org/10.1051/0004-6361/201834294>
- Greene, J. E., Strader, J., & Ho, L. C. (2020). Intermediate-Mass Black Holes. *ARA&A*, 58, 257–312. <https://doi.org/10.1146/annurev-astro-032620-021835>

- Grillmair, C. J., & Dionatos, O. (2006). A 22° Tidal Tail for Palomar 5. *ApJL*, 641(1), L37–L39. <https://doi.org/10.1086/503744>
- Grudić, M. Y., Guszejnov, D., Hopkins, P. F., Lamberts, A., Boylan-Kolchin, M., Murray, N., & Schmitz, D. (2018). From the top down and back up again: star cluster structure from hierarchical star formation. *MNRAS*, 481(1), 688–702. <https://doi.org/10.1093/mnras/sty2303>
- Grudić, M. Y., Hafen, Z., Rodriguez, C. L., Guszejnov, D., Lamberts, A., Wetzel, A., Boylan-Kolchin, M., & Faucher-Giguère, C.-A. (2023). Great balls of FIRE - I. The formation of star clusters across cosmic time in a Milky Way-mass galaxy. *MNRAS*, 519(1), 1366–1380. <https://doi.org/10.1093/mnras/stac3573>
- Grudić, M. Y., Hopkins, P. F., Faucher-Giguère, C.-A., Quataert, E., Murray, N., & Kereš, D. (2018). When feedback fails: the scaling and saturation of star formation efficiency. *MNRAS*, 475(3), 3511–3528. <https://doi.org/10.1093/mnras/sty035>
- Guerrero, M. A., & Miranda, L. F. (2012). NGC 6778: a disrupted planetary nebula around a binary central star. *A&A*, 539, Article A47, A47. <https://doi.org/10.1051/0004-6361/201117923>
- Hachisu, I. (1979). Gravogyro Catastrophe of Self-Gravitating and Rotating Systems. *PASJ*, 31, 523–540.
- Hachisu, I. (1982). Gravothermal and Gravogyro Catastrophes of Rotating and Self-Gravitating Gaseous Disks. *PASJ*, 34, 313.
- Hachisu, I., Nakada, Y., Nomoto, K., & Sugimoto, D. (1978). Gravothermal Catastrophe of Finite Amplitude. *Progress of Theoretical Physics*, 60(2), 393–402. <https://doi.org/10.1143/PTP.60.393>
- Hachisu, I., & Sugimoto, D. (1978). Gravothermal Catastrophe and Negative Specific Heat of Self-Gravitating Systems. *Progress of Theoretical Physics*, 60(1), 123–135. <https://doi.org/10.1143/PTP.60.123>
- Haemmerlé, L., Mayer, L., Klessen, R. S., Hosokawa, T., Madau, P., & Bromm, V. (2020). Formation of the First Stars and Black Holes. *SSR*, 216(4), Article 48, 48. <https://doi.org/10.1007/s11214-020-00673-y>
- Hamann, W. .-, & Koesterke, L. (1998). Spectrum formation in clumped stellar winds: consequences for the analyses of Wolf-Rayet spectra. *A&A*, 335, 1003–1008.
- Hamers, A. S., Pols, O. R., Claeys, J. S. W., & Nelemans, G. (2013). Population synthesis of triple systems in the context of mergers of carbon-oxygen white dwarfs. *MNRAS*, 430(3), 2262–2280. <https://doi.org/10.1093/mnras/stt046>
- Hamers, A. S., & Safarzadeh, M. (2020). Was GW190412 Born from a Hierarchical 3 + 1 Quadruple Configuration? *ApJ*, 898(2), Article 99, 99. <https://doi.org/10.3847/1538-4357/ab9b27>
- Han, Z., Podsiadlowski, P., & Eggleton, P. P. (1995). The formation of bipolar planetary nebulae and close white dwarf binaries. *MNRAS*, 272(4), 800–820. <https://doi.org/10.1093/mnras/272.4.800>
- Hansen, B. M. S., & Phinney, E. S. (1997). The pulsar kick velocity distribution. *MNRAS*, 291(3), 569–577. <https://doi.org/10.1093/mnras/291.3.569>
- Harris, W. E. (1976). Spatial structure of the globular cluster system and the distance to the galactic center. *AJ*, 81, 1095–1116. <https://doi.org/10.1086/111991>
- Harris, W. E. (1996). A Catalog of Parameters for Globular Clusters in the Milky Way. *AJ*, 112, 1487. <https://doi.org/10.1086/118116>
- Harris, W. E., Blakeslee, J. P., & Harris, G. L. H. (2017). Galactic Dark Matter Halos and Globular Cluster Populations. III. Extension to Extreme Environments. *ApJ*, 836(1), Article 67, 67. <https://doi.org/10.3847/1538-4357/836/1/67>
- Hartwig, T., Volonteri, M., Bromm, V., Klessen, R. S., Barausse, E., Magg, M., & Stacy, A. (2016). Gravitational waves from the remnants of the first stars. *MNRAS*, 460(1), L74–L78. <https://doi.org/10.1093/mnrasl/slw074>
- Hayashi, C. (1961). Stellar evolution in early phases of gravitational contraction. *PASJ*, 13, 450–452.
- Heggie, D. C. (1974). A Global Regularisation of the Gravitational N-Body Problem. *CeMec*, 10(2), 217–241. <https://doi.org/10.1007/BF01227621>
- Heggie, D. C. (1975). Binary evolution in stellar dynamics. *MNRAS*, 173, 729–787. <https://doi.org/10.1093/mnras/173.3.729>
- Heggie, D. C. (1984). Post-collapse evolution of a gaseous cluster model. *MNRAS*, 206, 179–195. <https://doi.org/10.1093/mnras/206.1.179>
- Heggie, D., & Hut, P. (2003). *The Gravitational Million-Body Problem: A Multidisciplinary Approach to Star Cluster Dynamics*.

- Heggie, D. C., & Giersz, M. (2014). MOCCA code for star cluster simulations - III. Stellar-mass black holes in the globular cluster M22. *MNRAS*, 439(3), 2459–2467. <https://doi.org/10.1093/mnras/stu102>
- Hellström, C., & Mikkola, S. (2010). Explicit algorithmic regularization in the few-body problem for velocity-dependent perturbations. *Celestial Mechanics and Dynamical Astronomy*, 106(2), 143–156. <https://doi.org/10.1007/s10569-009-9248-8>
- Hénon, M. (1961). Sur l'évolution dynamique des amas globulaires. *AnAp*, 24, 369.
- Hénon, M. (1971). Monte Carlo Models of Star Clusters (Part of the Proceedings of the IAU Colloquium No. 10, held in Cambridge, England, August 12-15, 1970.) *APSS*, 13(2), 284–299. <https://doi.org/10.1007/BF00649159>
- Hénon, M. (1972a). Monte Carlo Models of Star Clusters. In M. Lecar (Ed.), *Iau colloq. 10: Gravitational n-body problem* (p. 44, Vol. 31). https://doi.org/10.1007/978-94-010-2870-7_6
- Hénon, M. (1972b). The Monte Carlo Method. In M. Lecar (Ed.), *Iau colloq. 10: Gravitational n-body problem* (p. 406, Vol. 31). https://doi.org/10.1007/978-94-010-2870-7_38
- Hénon, M. (1975). Two Recent Developments Concerning the Monte Carlo Method. In A. Hayli (Ed.), *Dynamics of the solar systems* (p. 133, Vol. 69).
- Hénon, M. H. (1971). The Monte Carlo Method (Papers appear in the Proceedings of IAU Colloquium No. 10 Gravitational N-Body Problem (ed. by Myron Lecar), R. Reidel Publ. Co., Dordrecht-Holland.) *APSS*, 14(1), 151–167. <https://doi.org/10.1007/BF00649201>
- Heney, L. G., Wilets, L., Böhm, K. H., Lelevier, R., & Levee, R. D. (1959). A Method for Automatic Computation of Stellar Evolution. *ApJ*, 129, 628. <https://doi.org/10.1086/146661>
- Higgins, E. R., Sander, A. A. C., Vink, J. S., & Hirschi, R. (2021). Evolution of Wolf-Rayet stars as black hole progenitors. *MNRAS*, 505(4), 4874–4889. <https://doi.org/10.1093/mnras/stab1548>
- Higgins, E. R., & Vink, J. S. (2019). Massive star evolution: rotation, winds, and overshooting vectors in the mass-luminosity plane. I. A calibrated grid of rotating single star models. *AAP*, 622, Article A50, A50. <https://doi.org/10.1051/0004-6361/201834123>
- Hijikawa, K., Tanikawa, A., Kinugawa, T., Yoshida, T., & Umeda, H. (2021). On the population III binary black hole mergers beyond the pair-instability mass gap. *MNRAS.tmp*. <https://doi.org/10.1093/mnras/slab052>
- Hillier, D. J., Davidson, K., Ishibashi, K., & Gull, T. (2001). On the Nature of the Central Source in η Carinae. *ApJ*, 553(2), 837–860. <https://doi.org/10.1086/320948>
- Hills, J. G. (1975). Possible power source of Seyfert galaxies and QSOs. *Nature*, 254(5498), 295–298. <https://doi.org/10.1038/254295a0>
- Hillwig, T. C., Gies, D. R., Huang, W., McSwain, M. V., Stark, M. A., van der Meer, A., & Kaper, L. (2004). Identification of the Mass Donor Star's Spectrum in SS 433. *ApJ*, 615(1), 422–431. <https://doi.org/10.1086/423927>
- Hirano, S., Hosokawa, T., Yoshida, N., Omukai, K., & Yorke, H. W. (2015). Primordial star formation under the influence of far ultraviolet radiation: 1540 cosmological haloes and the stellar mass distribution. *MNRAS*, 448(1), 568–587. <https://doi.org/10.1093/mnras/stv044>
- Hirano, S., & Bromm, V. (2017). Formation and survival of Population III stellar systems. *MNRAS*, 470(1), 898–914. <https://doi.org/10.1093/mnras/stx1220>
- Hirano, S., & Bromm, V. (2018a). Angular momentum transfer in primordial discs and the rotation of the first stars. *MNRAS*, 476(3), 3964–3973. <https://doi.org/10.1093/mnras/sty487>
- Hirano, S., & Bromm, V. (2018b). Angular momentum transfer in primordial discs and the rotation of the first stars. *MNRAS*, 476(3), 3964–3973. <https://doi.org/10.1093/mnras/sty487>
- Hirano, S., Hosokawa, T., Yoshida, N., Umeda, H., Omukai, K., & et al. (2014). One Hundred First Stars: Protostellar Evolution and the Final Masses. *ApJ*, 781(2), Article 60, 60. <https://doi.org/10.1088/0004-637X/781/2/60>
- Hobbs, G., Lorimer, D. R., Lyne, A. G., & Kramer, M. (2005). A statistical study of 233 pulsar proper motions. *MNRAS*, 360(3), 974–992. <https://doi.org/10.1111/j.1365-2966.2005.09087.x>
- Hoffman, L., & Loeb, A. (2007). Dynamics of triple black hole systems in hierarchically merging massive galaxies. *MNRAS*, 377(3), 957–976. <https://doi.org/10.1111/j.1365-2966.2007.11694.x>

- Hong, J., Askar, A., Giersz, M., Hypki, A., & Yoon, S.-J. (2020). MOCCA-SURVEY Database I: Binary black hole mergers from globular clusters with intermediate mass black holes. *MNRAS*, 498(3), 4287–4294. <https://doi.org/10.1093/mnras/staa2677>
- Hong, J., de Grijs, R., Askar, A., Berczik, P., Li, C., & et al. (2017). The dynamical origin of multiple populations in intermediate-age clusters in the Magellanic Clouds. *MNRAS*, 472(1), 67–77. <https://doi.org/10.1093/mnras/stx1954>
- Hong, J., Kim, E., Lee, H. M., & Spurzem, R. (2013). Comparative study between N-body and Fokker-Planck simulations for rotating star clusters - II. Two-component models. *MNRAS*, 430(4), 2960–2972. <https://doi.org/10.1093/mnras/stt099>
- Hong, J., Vesperini, E., Askar, A., Giersz, M., Szkudlarek, M., & et al. (2018). Binary black hole mergers from globular clusters: the impact of globular cluster properties. *MNRAS*, 480(4), 5645–5656. <https://doi.org/10.1093/mnras/sty2211>
- Hong, J., Vesperini, E., Askar, A., Giersz, M., Szkudlarek, M., & et al. (2020). Erratum: Binary black hole mergers from globular clusters: the impact of globular cluster properties. *MNRAS*, 491(4), 5793–5793. <https://doi.org/10.1093/mnras/stz3454>
- Hong, J., Vesperini, E., Belloni, D., & Giersz, M. (2017). Dynamical formation of cataclysmic variables in globular clusters. *MNRAS*, 464(2), 2511–2516. <https://doi.org/10.1093/mnras/stw2595>
- Hopkins, A. M. (2018). The Dawes Review 8: Measuring the Stellar Initial Mass Function. *PASA*, 35, Article e039, e039. <https://doi.org/10.1017/pasa.2018.29>
- Hoyer, N., Neumayer, N., Georgiev, I. Y., Seth, A. C., & Greene, J. E. (2021). The nucleation fraction of local volume galaxies. *MNRAS*, 507(3), 3246–3266. <https://doi.org/10.1093/mnras/stab2277>
- Hoyer, N., Pinna, F., Kamlah, A. W. H., Nogueras-Lara, F., Feldmeier-Krause, A., Neumayer, N., Sormani, M. C., Boquien, M., Emsellem, E., Seth, A. C., Klessen, R. S., Williams, T. G., Schinnerer, E., Barnes, A. T., Leroy, A. K., Bonoli, S., Kruijssen, J. M. D., Neumann, J., Sánchez-Blázquez, P., . . . Hassani, H. (2022). PHANGS-JWST First Results: A combined HST and JWST analysis of the nuclear star cluster in NGC 628. *arXiv e-prints*, Article arXiv:2211.13997, arXiv:2211.13997.
- Huang, K.-W., & Koposov, S. E. (2021). Search for globular clusters associated with the Milky Way dwarf galaxies using Gaia DR2. *MNRAS*, 500(1), 986–997. <https://doi.org/10.1093/mnras/staa3297>
- Huang, S.-Y., Spurzem, R., & Berczik, P. (2016). Performance analysis of parallel gravitational N-body codes on large GPU clusters. *Research in Astronomy and Astrophysics*, 16(1), Article 11, 11. <https://doi.org/10.1088/1674-4527/16/1/011>
- Hubble, E. P. (1926). Extragalactic nebulae. *ApJ*, 64, 321–369. <https://doi.org/10.1086/143018>
- Hughes, S. A. (2009). Gravitational Waves from Merging Compact Binaries. *ARA&A*, 47(1), 107–157. <https://doi.org/10.1146/annurev-astro-082708-101711>
- Humphreys, R. M., & Davidson, K. (1979). Studies of luminous stars in nearby galaxies. III. Comments on the evolution of the most massive stars in the Milky Way and the Large Magellanic Cloud. *ApJ*, 232, 409–420. <https://doi.org/10.1086/157301>
- Humphreys, R. M., & Davidson, K. (1994). The Luminous Blue Variables: Astrophysical Geysers. *PASP*, 106, 1025. <https://doi.org/10.1086/133478>
- Hurley, J. R. (2008a). N - Body Binary Evolution. In S. J. Aarseth, C. A. Tout, & R. A. Mardling (Eds.), *The cambridge n-body lectures* (p. 321, Vol. 760). https://doi.org/10.1007/978-1-4020-8431-7_12
- Hurley, J. R. (2008b). N-Body Stellar Evolution. In S. J. Aarseth, C. A. Tout, & R. A. Mardling (Eds.), *The cambridge n-body lectures* (p. 283, Vol. 760). https://doi.org/10.1007/978-1-4020-8431-7_10
- Hurley, J. R., Pols, O. R., & Tout, C. A. (2000). Comprehensive analytic formulae for stellar evolution as a function of mass and metallicity. *MNRAS*, 315(3), 543–569. <https://doi.org/10.1046/j.1365-8711.2000.03426.x>
- Hurley, J. R., Pols, O. R., & Tout, C. A. (2013). SSE: Single Star Evolution.
- Hurley, J. R., & Shara, M. M. (2003). White Dwarf Sequences in Dense Star Clusters. *ApJ*, 589(1), 179–198. <https://doi.org/10.1086/374637>
- Hurley, J. R., Tout, C. A., & Pols, O. R. (2002). Evolution of binary stars and the effect of tides on binary populations. *MNRAS*, 329(4), 897–928. <https://doi.org/10.1046/j.1365-8711.2002.05038.x>

- Husser, T.-O., Kamann, S., Dreizler, S., Wendt, M., Wulff, N., & et al. (2016). MUSE crowded field 3D spectroscopy of over 12 000 stars in the globular cluster NGC 6397. I. The first comprehensive HRD of a globular cluster. *A&A*, 588, Article A148, A148. <https://doi.org/10.1051/0004-6361/201526949>
- Hut, P. (1980). Stability of tidal equilibrium. *A&A*, 92(1-2), 167–170.
- Hut, P. (1981). Tidal evolution in close binary systems. *A&A*, 99, 126–140.
- Hut, P. (1985). Binary formation and interactions with field stars. In J. Goodman & P. Hut (Eds.), *Dynamics of star clusters* (pp. 231–247, Vol. 113).
- Hut, P., Makino, J., & McMillan, S. (1995). Building a Better Leapfrog. *ApJL*, 443, L93. <https://doi.org/10.1086/187844>
- Hypki, A., & Giersz, M. (2013). MOCCA code for star cluster simulations - I. Blue stragglers, first results. *MNRAS*, 429(2), 1221–1243. <https://doi.org/10.1093/mnras/sts415>
- Hypki, A., Giersz, M., Hong, J., Leveque, A., Askar, A., & et al. (2022). MOCCA: Dynamics and evolution of binary stars of multiple stellar populations in tidally filling and underfilling globular star clusters. *arXiv*, Article arXiv:2205.05397, arXiv:2205.05397.
- Ibata, R. A., Lewis, G. F., & Martin, N. F. (2016). Feeling the Pull: a Study of Natural Galactic Accelerometers. I. Photometry of the Delicate Stellar Stream of the Palomar 5 Globular Cluster. *ApJ*, 819(1), Article 1, 1. <https://doi.org/10.3847/0004-637X/819/1/1>
- Ibata, R. A., Lewis, G. F., Thomas, G., Martin, N. F., & Chapman, S. (2017). Feeling the Pull: A Study of Natural Galactic Accelerometers. II. Kinematics and Mass of the Delicate Stellar Stream of the Palomar 5 Globular Cluster. *ApJ*, 842(2), Article 120, 120. <https://doi.org/10.3847/1538-4357/aa7514>
- Inagaki, S., & Hachisu, I. (1978). Thermodynamic Stability of Rotating Gaseous Cylinders. I. Stability Analysis by Linear Series. *PASJ*, 30, 39–56.
- Inagaki, S., & Lynden-Bell, D. (1983). Self-similar solutions for post-collapse evolution of globular clusters. *MNRAS*, 205, 913–930. <https://doi.org/10.1093/mnras/205.4.913>
- Inayoshi, K., Hirai, R., Kinugawa, T., & Hotokezaka, K. (2017). Formation pathway of Population III coalescing binary black holes through stable mass transfer. *MNRAS*, 468(4), 5020–5032. <https://doi.org/10.1093/mnras/stx757>
- Ivanova, N., Heinke, C. O., Rasio, F. A., Belczynski, K., & Fregeau, J. M. (2008). Formation and evolution of compact binaries in globular clusters - II. Binaries with neutron stars. *MNRAS*, 386(1), 553–576. <https://doi.org/10.1111/j.1365-2966.2008.13064.x>
- Ivanova, N., Justham, S., Chen, X., De Marco, O., Fryer, C. L., & et al. (2013). Common envelope evolution: where we stand and how we can move forward. *A&ARv*, 21, Article 59, 59. <https://doi.org/10.1007/s00159-013-0059-2>
- Ivanova, N., & Nandez, J. L. A. (2016). Common envelope events with low-mass giants: understanding the transition to the slow spiral-in. *MNRAS*, 462(1), 362–381. <https://doi.org/10.1093/mnras/stw1676>
- Ivanova, N. (2016). Evolution of binaries with compact objects in globular clusters. In Y. Meiron, S. Li, F. -. Liu, & R. Spurzem (Eds.), *Star clusters and black holes in galaxies across cosmic time* (pp. 203–212, Vol. 312). <https://doi.org/10.1017/S1743921315007826>
- Ivanova, N. (2018). On the Use of Hydrogen Recombination Energy during Common Envelope Events. *ApJL*, 858(2), Article L24, L24. <https://doi.org/10.3847/2041-8213/aac101>
- Ivanova, N., Justham, S., & Ricker, P. (2020). *Common envelope evolution*. IOP Publishing. <https://doi.org/10.1088/2514-3433/abb6f0>
- Ivanova, N. (2019). Common Envelope Physics. *KITP Conference: Merging Visions: Exploring Compact-Object Binaries with Gravity and Light*, Article 7, 7.
- Izzard, R. G., Dray, L. M., Karakas, A. I., Lugaro, M., & Tout, C. A. (2006). Population nucleosynthesis in single and binary stars. I. Model. *AAP*, 460(2), 565–572. <https://doi.org/10.1051/0004-6361/20066129>
- Izzard, R. G., Glebbeek, E., Stancliffe, R. J., & Pols, O. R. (2009). Population synthesis of binary carbon-enhanced metal-poor stars. *AAP*, 508(3), 1359–1374. <https://doi.org/10.1051/0004-6361/200912827>
- Izzard, R. G., Tout, C. A., Karakas, A. I., & Pols, O. R. (2004). A new synthetic model for asymptotic giant branch stars. *MNRAS*, 350(2), 407–426. <https://doi.org/10.1111/j.1365-2966.2004.07446.x>
- Jani, K., Shoemaker, D., & Cutler, C. (2020). Detectability of intermediate-mass black holes in multiband gravitational wave astronomy. *Nature Astronomy*, 4, 260–265. <https://doi.org/10.1038/s41550-019-0932-7>

- Jeřábková, T., Hasani Zonoozi, A., Kroupa, P., Beccari, G., Yan, Z., Vazdekis, A., & Zhang, Z. -. (2018). Impact of metallicity and star formation rate on the time-dependent, galaxy-wide stellar initial mass function. *AAP*, 620, Article A39, A39. <https://doi.org/10.1051/0004-6361/201833055>
- Jiménez-Forteza, X., Keitel, D., Husa, S., Hannam, M., Khan, S., & et al. (2017). Hierarchical data-driven approach to fitting numerical relativity data for nonprecessing binary black holes with an application to final spin and radiated energy. *PhRvD*, 95(6), Article 064024, 064024. <https://doi.org/10.1103/PhysRevD.95.064024>
- Jordan, I., George C., Perets, H. B., Fisher, R. T., & van Rossum, D. R. (2012). Failed-detonation Supernovae: Subluminous Low-velocity Ia Supernovae and their Kicked Remnant White Dwarfs with Iron-rich Cores. *ApJL*, 761(2), Article L23, L23. <https://doi.org/10.1088/2041-8205/761/2/L23>
- Joshi, K. J., Rasio, F. A., & Portegies Zwart, S. (2000). Monte Carlo Simulations of Globular Cluster Evolution. I. Method and Test Calculations. *ApJ*, 540(2), 969–982. <https://doi.org/10.1086/309350>
- Joyce, M., & Chaboyer, B. (2018). Not All Stars Are the Sun: Empirical Calibration of the Mixing Length for Metal-poor Stars Using One-dimensional Stellar Evolution Models. *ApJ*, 856(1), Article 10, 10. <https://doi.org/10.3847/1538-4357/aab200>
- Kagra Collaboration, Akutsu, T., Ando, M., Arai, K., Arai, Y., & et al. (2019). KAGRA: 2.5 generation interferometric gravitational wave detector. *NatAs*, 3, 35–40. <https://doi.org/10.1038/s41550-018-0658-y>
- Kamann, S., Bastian, N., Gossage, S., Baade, D., Cabrera-Ziri, I., & et al. (2020). How stellar rotation shapes the colour-magnitude diagram of the massive intermediate-age star cluster NGC 1846. *MNRAS*, 492(2), 2177–2192. <https://doi.org/10.1093/mnras/stz3583>
- Kamann, S., Bastian, N., Husser, T. .-, Martocchia, S., Usher, C., & et al. (2018). Cluster kinematics and stellar rotation in NGC 419 with MUSE and adaptive optics. *MNRAS*, 480(2), 1689–1695. <https://doi.org/10.1093/mnras/sty1958>
- Kamann, S., Bastian, N. J., Gieles, M., Balbinot, E., & Hénault-Brunet, V. (2019). Linking the rotation of a cluster to the spins of its stars: the kinematics of NGC 6791 and NGC 6819 in 3D. *MNRAS*, 483(2), 2197–2206. <https://doi.org/10.1093/mnras/sty3144>
- Kamann, S., Giesers, B., Bastian, N., Brinchmann, J., Dreizler, S., & et al. (2020). The binary content of multiple populations in NGC 3201. *A&A*, 635, Article A65, A65. <https://doi.org/10.1051/0004-6361/201936843>
- Kamann, S., Husser, T. .-, Brinchmann, J., Emsellem, E., Weilbacher, P. M., & et al. (2016). MUSE crowded field 3D spectroscopy of over 12 000 stars in the globular cluster NGC 6397. II. Probing the internal dynamics and the presence of a central black hole. *A&A*, 588, Article A149, A149. <https://doi.org/10.1051/0004-6361/201527065>
- Kamann, S., Husser, T. .-, Dreizler, S., Emsellem, E., Weilbacher, P. M., & et al. (2018). A stellar census in globular clusters with MUSE: The contribution of rotation to cluster dynamics studied with 200 000 stars. *MNRAS*, 473(4), 5591–5616. <https://doi.org/10.1093/mnras/stx2719>
- Kamlah, A. W. H., Leveque, A., Spurzem, R., Arca Sedda, M., Askar, A., Banerjee, S., Berczik, P., Giersz, M., Hurley, J., Belloni, D., Kühmichel, L., & Wang, L. (2022). Preparing the next gravitational million-body simulations: evolution of single and binary stars in NBODY6++GPU, MOCCA, and MCLUSTER. *MNRAS*, 511(3), 4060–4089. <https://doi.org/10.1093/mnras/stab3748>
- Kamlah, A. W. H., Spurzem, R., Berczik, P., Arca Sedda, M., Flammini Dotti, F., & et al. (2022). The impact of stellar evolution on rotating star clusters: the gravothermal-gravogyro catastrophe and the formation of a bar of black holes. *arXiv*, Article arXiv:2205.04470, arXiv:2205.04470.
- Kamlah, A. W. H., Tanikawa, A., Arca Sedda, M., Giersz, M., Neumayer, N., & Spurzem, R. (2023). Direct N-body simulations of extremely massive and initially rotating Population III star clusters [in prep.].
- Kandrup, H. E., Mahon, M. E., & Smith, J., Haywood. (1994). On the Sensitivity of the N-Body Problem toward Small Changes in Initial Conditions. IV. *ApJ*, 428, 458. <https://doi.org/10.1086/174259>
- Katz, H., Kimm, T., Ellis, R. S., Devriendt, J., & Slyz, A. (2022). The Challenges of Identifying Population III Stars in the Early Universe. *arXiv*, Article arXiv:2207.04751, arXiv:2207.04751.
- Katz, H., Sijacki, D., & Haehnelt, M. G. (2015). Seeding high-redshift QSOs by collisional runaway in primordial star clusters. *MNRAS*, 451(3), 2352–2369. <https://doi.org/10.1093/mnras/stv1048>
- Kawamura, S., Ando, M., Seto, N., Sato, S., Musha, M., Kawano, I., Yokoyama, J., Tanaka, T., Ioka, K., Akutsu, T., Takashima, T., Agatsuma, K., Araya, A., Aritomi, N., Asada, H., Chiba, T., Eguchi, S., Enoki, M.,

- Fujimoto, M.-K., . . . Zhu, Z.-H. (2021). Current status of space gravitational wave antenna DECIGO and B-DECIGO. *Progress of Theoretical and Experimental Physics*, 2021(5), Article 05A105, 05A105. <https://doi.org/10.1093/ptep/ptab019>
- Kawamura, S., Ando, M., Seto, N., Sato, S., Nakamura, T., Tsubono, K., Kanda, N., Tanaka, T., Yokoyama, J., Funaki, I., Numata, K., Ioka, K., Takashima, T., Agatsuma, K., Akutsu, T., Aoyanagi, K.-s., Arai, K., Araya, A., Asada, H., . . . Sun, K.-X. (2011). The Japanese space gravitational wave antenna: DECIGO. *Classical and Quantum Gravity*, 28(9), Article 094011, 094011. <https://doi.org/10.1088/0264-9381/28/9/094011>
- Kerr, R. P. (1963). Gravitational Field of a Spinning Mass as an Example of Algebraically Special Metrics. *PhRvL*, 11(5), 237–238. <https://doi.org/10.1103/PhysRevLett.11.237>
- Khalisi, E., Amaro-Seoane, P., & Spurzem, R. (2007). A comprehensive NBODY study of mass segregation in star clusters: energy equipartition and escape. *MNRAS*, 374(2), 703–720. <https://doi.org/10.1111/j.1365-2966.2006.11184.x>
- Kiel, P. D., & Hurley, J. R. (2006). Populating the Galaxy with low-mass X-ray binaries. *MNRAS*, 369(3), 1152–1166. <https://doi.org/10.1111/j.1365-2966.2006.10400.x>
- Kiel, P. D., & Hurley, J. R. (2009). Populating the Galaxy with pulsars - II. Galactic dynamics. *MNRAS*, 395(4), 2326–2346. <https://doi.org/10.1111/j.1365-2966.2009.14711.x>
- Kiel, P. D., Hurley, J. R., & Bailes, M. (2010). The long and the short of it: modelling double neutron star and collapsar Galactic dynamics. *MNRAS*, 406(1), 656–672. <https://doi.org/10.1111/j.1365-2966.2010.16717.x>
- Kiel, P. D., Hurley, J. R., Bailes, M., & Murray, J. R. (2008). Populating the Galaxy with pulsars - I. Stellar and binary evolution. *MNRAS*, 388(1), 393–415. <https://doi.org/10.1111/j.1365-2966.2008.13402.x>
- Kim, E., Einsel, C., Lee, H. M., Spurzem, R., & Lee, M. G. (2002). Dynamical evolution of rotating stellar systems - II. Post-collapse, equal-mass system. *MNRAS*, 334(2), 310–322. <https://doi.org/10.1046/j.1365-8711.2002.05420.x>
- Kim, E., Lee, H. M., & Spurzem, R. (2004). Dynamical evolution of rotating stellar systems - III. The effect of the mass spectrum. *MNRAS*, 351(1), 220–236. <https://doi.org/10.1111/j.1365-2966.2004.07776.x>
- Kim, E., Yoon, I., Lee, H. M., & Spurzem, R. (2008). Comparative study between N-body and Fokker-Planck simulations for rotating star clusters - I. Equal-mass system. *MNRAS*, 383(1), 2–10. <https://doi.org/10.1111/j.1365-2966.2007.12524.x>
- Kiminki, D. C., Kobulnicky, H. A., Ewing, I., Bagley Kiminki, M. M., Lundquist, M., & et al. (2012). Additional Massive Binaries in the Cygnus OB2 Association. *ApJ*, 747(1), Article 41, 41. <https://doi.org/10.1088/0004-637X/747/1/41>
- King, A. R., & Kolb, U. (1995). Consequential Angular Momentum Loss and the Period Gap of Cataclysmic Variables. *ApJ*, 439, 330. <https://doi.org/10.1086/175176>
- King, I. R. (1981). The Dynamics of Globular Clusters. *QJRAS*, 22, 227.
- King, I. (1961). The shape of a rotating star cluster. *AJ*, 66, 68. <https://doi.org/10.1086/108376>
- King, I. (1962). The structure of star clusters. I. an empirical density law. *AJ*, 67, 471. <https://doi.org/10.1086/108756>
- King, I. R. (1966a). The structure of star clusters. III. Some simple dynamical models. *AJ*, 71, 64. <https://doi.org/10.1086/109857>
- King, I. R. (1966b). The structure of star clusters. IV. Photoelectric surface photometry in nine globular clusters. *AJ*, 71, 276. <https://doi.org/10.1086/109918>
- King, I. R. (2008). The Simple Underlying Dynamics of Globular Clusters. In E. Vesperini, M. Giersz, & A. Sills (Eds.), *Dynamical evolution of dense stellar systems* (pp. 131–140, Vol. 246). <https://doi.org/10.1017/S1743921308015470>
- Kinugawa, T., Inayoshi, K., Hotokezaka, K., Nakauchi, D., & Nakamura, T. (2014). Possible indirect confirmation of the existence of pop III massive stars by gravitational wave. *MNRAS*, 442(4), 2963–2992. <https://doi.org/10.1093/mnras/stu1022>
- Kinugawa, T., Miyamoto, A., Kanda, N., & Nakamura, T. (2016). The detection rate of inspiral and quasi-normal modes of Population III binary black holes which can confirm or refute the general relativity in the strong gravity region. *MNRAS*, 456(1), 1093–1114. <https://doi.org/10.1093/mnras/stv2624>

- Kinugawa, T., Nakamura, T., & Nakano, H. (2021a). Formation of binary black holes similar to GW190521 with a total mass of $\sim 150 M_{\odot}$ from Population III binary star evolution. *MNRAS*, 501(1), L49–L53. <https://doi.org/10.1093/mnras/slaa191>
- Kinugawa, T., Nakamura, T., & Nakano, H. (2021b). Gravitational waves from Population III binary black holes are consistent with LIGO/Virgo O3a data for the chirp mass larger than $\sim 20 M_{\odot}$. *MNRAS*, 504(1), L28–L33. <https://doi.org/10.1093/mnras/slab032>
- Kippenhahn, R., Weigert, A., & Weiss, A. (2012). *Stellar Structure and Evolution*. <https://doi.org/10.1007/978-3-642-30304-3>
- Klessen, R. (2019). Formation of the first stars. In M. Latif & D. Schleicher (Eds.), *Formation of the first black holes* (pp. 67–97). https://doi.org/10.1142/9789813227958_0004
- Knigge, C. (2006). The donor stars of cataclysmic variables. *MNRAS*, 373(2), 484–502. <https://doi.org/10.1111/j.1365-2966.2006.11096.x>
- Knigge, C., Baraffe, I., & Patterson, J. (2011). The Evolution of Cataclysmic Variables as Revealed by Their Donor Stars. *ApJS*, 194(2), Article 28, 28. <https://doi.org/10.1088/0067-0049/194/2/28>
- Kobulnicky, H. A., & Fryer, C. L. (2007). A New Look at the Binary Characteristics of Massive Stars. *ApJ*, 670(1), 747–765. <https://doi.org/10.1086/522073>
- Kobulnicky, H. A., Kiminki, D. C., Lundquist, M. J., Burke, J., Chapman, J., & et al. (2014). Toward Complete Statistics of Massive Binary Stars: Penultimate Results from the Cygnus OB2 Radial Velocity Survey. *ApJS*, 213(2), Article 34, 34. <https://doi.org/10.1088/0067-0049/213/2/34>
- Kobulnicky, H. A., Smullen, R. A., Kiminki, D. C., Runnoe, J. C., Wood, E. S., & et al. (2012). A Fresh Catch of Massive Binaries in the Cygnus OB2 Association. *ApJ*, 756(1), Article 50, 50. <https://doi.org/10.1088/0004-637X/756/1/50>
- Köhler, K., Langer, N., de Koter, A., de Mink, S. E., Crowther, P. A., Evans, C. J., Gräfener, G., Sana, H., Sanyal, D., Schneider, F. R. N., & Vink, J. S. (2015). The evolution of rotating very massive stars with LMC composition. *AAP*, 573, Article A71, A71. <https://doi.org/10.1051/0004-6361/201424356>
- Kokubo, E., Yoshinaga, K., & Makino, J. (1998). On a time-symmetric Hermite integrator for planetary N-body simulation. *MNRAS*, 297(4), 1067–1072. <https://doi.org/10.1046/j.1365-8711.1998.01581.x>
- Kopal, Z. (1978). *Dynamics of close binary systems*. <https://doi.org/10.1007/978-94-009-9780-6>
- Kopal, Z., & Slouka, H. (1936). Axial Rotation of Globular Star Clusters. *Natur*, 137(3467), 621. <https://doi.org/10.1038/137621a0>
- Koribalski, B. S., Wang, J., Kamphuis, P., Westmeier, T., Staveley-Smith, L., Oh, S. .-, Lopez-Sanchez, A. R., Wong, O. I., Ott, J., de Blok, W. J. G., & Shao, L. (2018). The Local Volume H I Survey LVHIS. *MNRAS*, 478(2), 1611–1648. <https://doi.org/10.1093/mnras/sty479>
- Kormendy, J. (1985). Families of ellipsoidal stellar systems and the formation of dwarf elliptical galaxies. *ApJ*, 295, 73–79. <https://doi.org/10.1086/163350>
- Kormendy, J., & Ho, L. C. (2013). Coevolution (Or Not) of Supermassive Black Holes and Host Galaxies. *ARA&A*, 51(1), 511–653. <https://doi.org/10.1146/annurev-astro-082708-101811>
- Kouwenhoven, M. B. N., Brown, A. G. A., Portegies Zwart, S. F., & Kaper, L. (2007). The primordial binary population. II. Recovering the binary population for intermediate mass stars in Scorpius OB2. *A&A*, 474(1), 77–104. <https://doi.org/10.1051/0004-6361:20077719>
- Kremer, K., Chatterjee, S., Rodriguez, C. L., & Rasio, F. A. (2018). Accreting Black Hole Binaries in Globular Clusters. *ApJ*, 852(1), Article 29, 29. <https://doi.org/10.3847/1538-4357/aa99df>
- Kremer, K., Rodriguez, C. L., Amaro-Seoane, P., Breivik, K., Chatterjee, S., & et al. (2019). Post-Newtonian dynamics in dense star clusters: Binary black holes in the LISA band. *PhRvD*, 99(6), Article 063003, 063003. <https://doi.org/10.1103/PhysRevD.99.063003>
- Kremer, K., Rui, N. Z., Weatherford, N. C., Chatterjee, S., Fragione, G., & et al. (2021). White Dwarf Subsystems in Core-Collapsed Globular Clusters. *arXiv*, Article arXiv:2104.11751, arXiv:2104.11751.
- Kremer, K., Spera, M., Becker, D., Chatterjee, S., Di Carlo, U. N., & et al. (2020). Populating the Upper Black Hole Mass Gap through Stellar Collisions in Young Star Clusters. *ApJ*, 903(1), Article 45, 45. <https://doi.org/10.3847/1538-4357/abb945>
- Kremer, K., Ye, C. S., Chatterjee, S., Rodriguez, C. L., & Rasio, F. A. (2018). How Black Holes Shape Globular Clusters: Modeling NGC 3201. *ApJL*, 855(2), Article L15, L15. <https://doi.org/10.3847/2041-8213/aab26c>

- Kremer, K., Ye, C. S., Rui, N. Z., Weatherford, N. C., Chatterjee, S., & et al. (2020). Modeling Dense Star Clusters in the Milky Way and Beyond with the CMC Cluster Catalog. *ApJS*, 247(2), Article 48, 48. <https://doi.org/10.3847/1538-4365/ab7919>
- Kroupa, P. (2005). The Fundamental Building Blocks of Galaxies. In C. Turon, K. S. O'Flaherty, & M. A. C. Perryman (Eds.), *The three-dimensional universe with gaia* (p. 629, Vol. 576).
- Kroupa, P. (1995a). Inverse dynamical population synthesis and star formation. *MNRAS*, 277, 1491. <https://doi.org/10.1093/mnras/277.4.1491>
- Kroupa, P. (1995b). The dynamical properties of stellar systems in the Galactic disc. *MNRAS*, 277, 1507. <https://doi.org/10.1093/mnras/277.4.1507>
- Kroupa, P. (2001). On the variation of the initial mass function. *MNRAS*, 322(2), 231–246. <https://doi.org/10.1046/j.1365-8711.2001.04022.x>
- Kroupa, P. (2008). Initial Conditions for Star Clusters. In S. J. Aarseth, C. A. Tout, & R. A. Mardling (Eds.), *The cambridge n-body lectures* (p. 181, Vol. 760). https://doi.org/10.1007/978-1-4020-8431-7_8
- Kroupa, P. (2009). The influence of star clusters on galactic disks: new insights in star-formation in galaxies. In J. Andersen, Nordströara, B. m, & J. Bland-Hawthorn (Eds.), *The galaxy disk in cosmological context* (pp. 209–220, Vol. 254). <https://doi.org/10.1017/S1743921308027610>
- Kroupa, P. (2011). The universality hypothesis: binary and stellar populations in star clusters and galaxies. In J. Alves, B. G. Elmegreen, J. M. Girart, & V. Trimble (Eds.), *Computational star formation* (pp. 141–149, Vol. 270). <https://doi.org/10.1017/S1743921311000305>
- Kroupa, P. (2020). The systematically varying stellar IMF. In A. Bragaglia, M. Davies, A. Sills, & E. Vesperini (Eds.), *Star clusters: From the milky way to the early universe* (pp. 117–121, Vol. 351). <https://doi.org/10.1017/S1743921319007749>
- Kroupa, P., Aarseth, S., & Hurley, J. (2001). The formation of a bound star cluster: from the Orion nebula cluster to the Pleiades. *MNRAS*, 321(4), 699–712. <https://doi.org/10.1046/j.1365-8711.2001.04050.x>
- Kroupa, P., & Jerabkova, T. (2018). The Impact of Binaries on the Stellar Initial Mass Function. *arXiv e-prints*, Article arXiv:1806.10605, arXiv:1806.10605.
- Kroupa, P., & Jerabkova, T. (2019). The Salpeter IMF and its descendants. *NatAs*, 3, 482–484. <https://doi.org/10.1038/s41550-019-0793-0>
- Kroupa, P., Subr, L., Jerabkova, T., & Wang, L. (2020). Very high redshift quasars and the rapid emergence of supermassive black holes. *MNRAS*, 498(4), 5652–5683. <https://doi.org/10.1093/mnras/staa2276>
- Kroupa, P., Tout, C. A., & Gilmore, G. (1993). The Distribution of Low-Mass Stars in the Galactic Disc. *MNRAS*, 262, 545–587. <https://doi.org/10.1093/mnras/262.3.545>
- Kroupa, P., Weidner, C., Pflamm-Altenburg, J., Thies, I., Dabringhausen, J., & et al. (2013). The Stellar and Sub-Stellar Initial Mass Function of Simple and Composite Populations. In T. D. Oswalt & G. Gilmore (Eds.), *Planets, stars and stellar systems. volume 5: Galactic structure and stellar populations* (p. 115, Vol. 5). https://doi.org/10.1007/978-94-007-5612-0_4
- Kruckow, M. U. (2020). Masses of double neutron star mergers. *A&A*, 639, Article A123, A123. <https://doi.org/10.1051/0004-6361/202037519>
- Kruckow, M. U., Neunteufel, P. G., Di Stefano, R., Gao, Y., & Kobayashi, C. (2021). A Catalog of Potential Post-Common Envelope Binaries. *ApJ*, 920(2), Article 86, 86. <https://doi.org/10.3847/1538-4357/ac13ac>
- Kruckow, M. U., Tauris, T. M., Langer, N., Kramer, M., & Izzard, R. G. (2018). Progenitors of gravitational wave mergers: binary evolution with the stellar grid-based code COMBINE. *MNRAS*, 481(2), 1908–1949. <https://doi.org/10.1093/mnras/sty2190>
- Krujissen, J. M. D. (2014). Globular cluster formation in the context of galaxy formation and evolution. *Classical and Quantum Gravity*, 31(24), Article 244006, 244006. <https://doi.org/10.1088/0264-9381/31/24/244006>
- Krumholz, M. R., McKee, C. F., & Bland-Hawthorn, J. (2019). Star Clusters Across Cosmic Time. *ARA&A*, 57, 227–303. <https://doi.org/10.1146/annurev-astro-091918-104430>
- Kudritzki, R. P., Pauldrach, A., Puls, J., & Abbott, D. C. (1989). Radiation-driven winds of hot stars. VI. Analytical solutions for wind models including the finite cone angle effect. *A&A*, 219, 205–218.
- Kudritzki, R. P., & Reimers, D. (1978). On the absolute scale of mass-loss in red giants. II. Circumstellar absorption lines in the spectrum of alpha Sco B and mass-loss of alpha Sco A. *A&A*, 70, 227–239.

- Kuhn, M. A., Hillenbrand, L. A., Sills, A., Feigelson, E. D., & Getman, K. V. (2019). Kinematics in Young Star Clusters and Associations with Gaia DR2. *ApJ*, 870(1), Article 32, 32. <https://doi.org/10.3847/1538-4357/aaef8c>
- Kupi, G., Amaro-Seoane, P., & Spurzem, R. (2006). Dynamics of compact object clusters: a post-Newtonian study. *MNRAS*, 371(1), L45–L49. <https://doi.org/10.1111/j.1745-3933.2006.00205.x>
- Küpper, A. H. W., Maschberger, T., Kroupa, P., & Baumgardt, H. (2011a). McLuster: A Tool to Make a Star Cluster.
- Küpper, A. H. W., Maschberger, T., Kroupa, P., & Baumgardt, H. (2011b). Mass segregation and fractal substructure in young massive clusters - I. The McLuster code and method calibration. *MNRAS*, 417(3), 2300–2317. <https://doi.org/10.1111/j.1365-2966.2011.19412.x>
- Kuranov, A. G., & Postnov, K. A. (2006). Neutron stars in globular clusters: Formation and observational manifestations. *AstL*, 32(6), 393–405. <https://doi.org/10.1134/S106377370606003X>
- Kuranz, C. C., Park, H. .-, Huntington, C. M., Miles, A. R., Remington, B. A., Plewa, T., Trantham, M. R., Robey, H. F., Shvarts, D., Shimony, A., Raman, K., MacLaren, S., Wan, W. C., Doss, F. W., Kline, J., Flippo, K. A., Malamud, G., Handy, T. A., Prisbrey, S., . . . Drake, R. P. (2018). How high energy fluxes may affect Rayleigh-Taylor instability growth in young supernova remnants. *Nature Communications*, 9, Article 1564, 1564. <https://doi.org/10.1038/s41467-018-03548-7>
- Kustaanheimo, P., & Stiefel, E. (1965). Perturbation theory of Kepler motion based on spinor regularization. *J. Reine Angew. Math.*, 218, 204–219.
- Kuzma, P. B., Ferguson, A. M. N., Varri, A. L., Irwin, M. J., Bernard, E. J., Tolstoy, E., Peñarrubia, J., & Zucker, D. B. (2022). Forward and back: kinematics of the Palomar 5 tidal tails. *MNRAS*, 512(1), 315–327. <https://doi.org/10.1093/mnras/stac381>
- Lada, C. J., & Lada, E. A. (2003). Embedded Clusters in Molecular Clouds. *ARA&A*, 41, 57–115. <https://doi.org/10.1146/annurev.astro.41.011802.094844>
- Lada, C. J., Lombardi, M., & Alves, J. F. (2010). On the Star Formation Rates in Molecular Clouds. *ApJ*, 724(1), 687–693. <https://doi.org/10.1088/0004-637X/724/1/687>
- Lahén, N., Naab, T., Johansson, P. H., Elmegreen, B., Hu, C.-Y., & et al. (2020). Structure and Rotation of Young Massive Star Clusters in a Simulated Dwarf Starburst. *ApJ*, 904(1), Article 71, 71. <https://doi.org/10.3847/1538-4357/abc001>
- Langer, N., Schürmann, C., Stoll, K., Marchant, P., Lennon, D. J., & et al. (2020). Properties of OB star-black hole systems derived from detailed binary evolution models. *A&A*, 638, Article A39, A39. <https://doi.org/10.1051/0004-6361/201937375>
- Lanzoni, B., Ferraro, F. R., Mucciarelli, A., Pallanca, C., Lapenna, E., Origlia, L., Dalessandro, E., Valenti, E., Bellazzini, M., Tiongco, M. A., Varri, A. L., Vesperini, E., & Beccari, G. (2018). The Strong Rotation of M5 (NGC 5904) as Seen from the MikiS Survey of Galactic Globular Clusters. *ApJ*, 861(1), Article 16, 16. <https://doi.org/10.3847/1538-4357/aac26a>
- Lanzoni, B., Ferraro, F. R., Mucciarelli, A., Pallanca, C., Tiongco, M. A., Varri, A., Vesperini, E., Bellazzini, M., Dalessandro, E., Origlia, L., Valenti, E., Sollima, A., Lapenna, E., & Beccari, G. (2018). The ESO Multi-instrument Kinematic Survey (MikiS) of Galactic Globular Clusters: Solid-body Rotation and Anomalous Velocity Dispersion Profile in NGC 5986. *ApJ*, 865(1), Article 11, 11. <https://doi.org/10.3847/1538-4357/aad810>
- Larson, R. B. (1981). Turbulence and star formation in molecular clouds. *MNRAS*, 194, 809–826. <https://doi.org/10.1093/mnras/194.4.809>
- Larson, R. B. (1970a). A method for Computing the evolution of star clusters. *MNRAS*, 147, 323. <https://doi.org/10.1093/mnras/147.4.323>
- Larson, R. B. (1970b). The evolution of star clusters. *MNRAS*, 150, 93. <https://doi.org/10.1093/mnras/150.1.93>
- Latif, M. A., Whalen, D., & Khochfar, S. (2022). The birth mass function of population III stars. *The Astrophysical Journal*, 925(1), 28. <https://doi.org/10.3847/1538-4357/ac3916>
- Latour, M., Husser, T. .-, Giesers, B., Kamann, S., Göttgens, F., & et al. (2019). A stellar census in globular clusters with MUSE: multiple populations chemistry in NGC 2808. *A&A*, 631, Article A14, A14. <https://doi.org/10.1051/0004-6361/201936242>
- Lattimer, J. M., & Prakash, M. (2004). The Physics of Neutron Stars. *Sci*, 304(5670), 536–542. <https://doi.org/10.1126/science.1090720>

- Lattimer, J. M. (2012). The Nuclear Equation of State and Neutron Star Masses. *ARNPS*, 62(1), 485–515. <https://doi.org/10.1146/annurev-nucl-102711-095018>
- Laureijs, R., Amiaux, J., Arduini, S., Auguères, J. .-, Brinchmann, J., & et al. (2011). Euclid Definition Study Report. *arXiv*, Article arXiv:1110.3193, arXiv:1110.3193.
- Lazar, A., & Bromm, V. (2021). Probing the initial mass function of the first stars with transients. *arXiv e-prints*, Article arXiv:2110.11956, arXiv:2110.11956.
- Lazar, A., & Bromm, V. (2022). Probing the initial mass function of the first stars with transients. *MNRAS*, 511(2), 2505–2514. <https://doi.org/10.1093/mnras/stac176>
- Lecar, M., & Aarseth, S. J. (1986). A Numerical Simulation of the Formation of the Terrestrial Planets. *ApJ*, 305, 564. <https://doi.org/10.1086/164269>
- Leung, S.-C., Blinnikov, S., Ishidoshiro, K., Kozlov, A., & Nomoto, K. (2020). Pulsational Pair-instability Supernovae. II. Neutrino Signals from Pulsations and Their Detection by Terrestrial Neutrino Detectors. *ApJ*, 889(2), Article 75, 75. <https://doi.org/10.3847/1538-4357/ab6211>
- Leung, S.-C., Nomoto, K., & Blinnikov, S. (2019). Pulsational Pair-instability Supernovae. I. Pre-collapse Evolution and Pulsational Mass Ejection. *ApJ*, 887(1), Article 72, 72. <https://doi.org/10.3847/1538-4357/ab4fe5>
- Leung, S.-C., Nomoto, K., & Suzuki, T. (2020). Electron-capture Supernovae of Super-AGB Stars: Sensitivity on Input Physics. *ApJ*, 889(1), Article 34, 34. <https://doi.org/10.3847/1538-4357/ab5d2f>
- Leveque, A., Giersz, M., Arca-Sedda, M., & Askar, A. (2022). MOCCA-Survey Database: Extra Galactic Globular Clusters. II. Milky Way and Andromeda. *arXiv*, Article arXiv:2206.03967, arXiv:2206.03967.
- Leveque, A., Giersz, M., Banerjee, S., Vesperini, E., Hong, J., & et al. (2022). A Monte Carlo study of early gas expulsion and evolution of star clusters: new simulations with the MOCCA code in the AMUSE framework. *arXiv*, Article arXiv:2206.03404, arXiv:2206.03404.
- Leveque, A., Giersz, M., & Paolillo, M. (2021). MOCCA Survey Database: extra Galactic globular clusters. I. Method and first results. *MNRAS*, 501(4), 5212–5228. <https://doi.org/10.1093/mnras/staa4027>
- Li, C., de Grijs, R., Deng, L., Geller, A. M., Xin, Y., & et al. (2016a). Formation of new stellar populations from gas accreted by massive young star clusters. *Natur*, 529(7587), 502–504. <https://doi.org/10.1038/nature16493>
- Li, C., de Grijs, R., Deng, L., Geller, A. M., Xin, Y., & et al. (2016b). Erratum: Formation of new stellar populations from gas accreted by massive young star clusters. *Natur*, 539(7627), 123. <https://doi.org/10.1038/nature19336>
- Li, Z.-M., Kayastha, B., Kamlah, A., Berczik, P., Deng, Y.-Y., & Spurzem, R. (2023). Fractions of Compact Object Binaries in Star Clusters: Theoretical Predictions. *Research in Astronomy and Astrophysics*, 23(2), Article 025019, 025019. <https://doi.org/10.1088/1674-4527/aca94f>
- Linares, M. (2020). Super-Massive Neutron Stars and Compact Binary Millisecond Pulsars. *Multifrequency Behaviour of High Energy Cosmic Sources - XIII. 3-8 June 2019. Palermo*, Article 23, 23.
- Linares, M. (2018). Compact Binary Pulsar Search (COBIPULSE): First results. *42nd COSPAR Scientific Assembly*, 42, Article E1.3-27-18, E1.3-27-18.
- Lingam, M. (2018). Black hole Brownian motion in a rotating environment. *MNRAS*, 473(2), 1719–1735. <https://doi.org/10.1093/mnras/stx2531>
- Liu, B., & Bromm, V. (2020). The Population III Origin of GW190521. *ApJ*, 903(2), Article L40, L40. <https://doi.org/10.3847/2041-8213/abc552>
- Liu, B., & Bromm, V. (2021). Gravitational waves from the remnants of the first stars in nuclear star clusters. *MNRAS*, 506(4), 5451–5467. <https://doi.org/10.1093/mnras/stab2028>
- Liu, B., Meynet, G., & Bromm, V. (2021). Dynamical evolution of population III stellar systems and the resulting binary statistics. *MNRAS*, 501(1), 643–663. <https://doi.org/10.1093/mnras/staa3671>
- Liu, B., Sibony, Y., Meynet, G., & Bromm, V. (2021). Stellar winds and metal enrichment from fast-rotating Population III stars. *MNRAS*, 506(4), 5247–5267. <https://doi.org/10.1093/mnras/stab2057>
- Livernois, A. R., Vesperini, E., Varri, A. L., Hong, J., & Tiongco, M. (2022). Long-term evolution of multimass rotating star clusters. *MNRAS*, 512(2), 2584–2593. <https://doi.org/10.1093/mnras/stac651>
- Longaretti, P. .-, & Lagoute, C. (1996). Rotating globular clusters. II. Relaxation and evaporation. *AAP*, 308, 453–464.

- Louis, P. D., & Spurzem, R. (1991). Anisotropic gaseous models for the evolution of star clusters. *MNRAS*, 251, 408–426. <https://doi.org/10.1093/mnras/251.3.408>
- Lousto, C. O., Zlochower, Y., Dotti, M., & Volonteri, M. (2012). Gravitational recoil from accretion-aligned black-hole binaries. *PhRvD*, 85(8), Article 084015, 084015. <https://doi.org/10.1103/PhysRevD.85.084015>
- Lupton, R. H., & Gunn, J. E. (1987). Three-Integral Models of Globular Clusters. *AJ*, 93, 1106. <https://doi.org/10.1086/114394>
- Lupton, R. H., Gunn, J. E., & Griffin, R. F. (1987). Dynamical Studies of Globular Clusters Based on Photoelectric Radial Velocities of Individual Stars and on the Observed Mass Function. II. M13. *AJ*, 93, 1114. <https://doi.org/10.1086/114395>
- Lurie, J. C., Vyhmeister, K., Hawley, S. L., Adilia, J., Chen, A., Davenport, J. R. A., Jurić, M., Puig-Holzman, M., & Weisenburger, K. L. (2017). Tidal Synchronization and Differential Rotation of Kepler Eclipsing Binaries. *AJ*, 154(6), Article 250, 250. <https://doi.org/10.3847/1538-3881/aa974d>
- Lynden-Bell, D. (1960). Can spherical clusters rotate? *MNRAS*, 120, 204. <https://doi.org/10.1093/mnras/120.3.204>
- Lynden-Bell, D. (1962a). Stellar dynamics: Exact solution of the self-gravitation equation. *MNRAS*, 123, 447. <https://doi.org/10.1093/mnras/123.5.447>
- Lynden-Bell, D. (1962b). The stability and vibrations of a gas of stars. *MNRAS*, 124, 279. <https://doi.org/10.1093/mnras/124.4.279>
- Lynden-Bell, D. (1999). Negative Specific Heat in Astronomy, Physics and Chemistry. *Physica A Statistical Mechanics and its Applications*, 263(1-4), 293–304. [https://doi.org/10.1016/S0378-4371\(98\)00518-4](https://doi.org/10.1016/S0378-4371(98)00518-4)
- Lynden-Bell, D., & Eggleton, P. P. (1980). On the consequences of the gravothermal catastrophe. *MNRAS*, 191, 483–498. <https://doi.org/10.1093/mnras/191.3.483>
- Lynden-Bell, D., & Wall, C. T. C. (1962). On the gravitational collapse of a cold rotating gas cloud. *Proceedings of the Cambridge Philosophical Society*, 58(4), 709. <https://doi.org/10.1017/S0305004100040767>
- Lynden-Bell, D., & Wood, R. (1968). The gravo-thermal catastrophe in isothermal spheres and the onset of red-giant structure for stellar systems. *MNRAS*, 138, 495. <https://doi.org/10.1093/mnras/138.4.495>
- MacAlpine, G. M., Ecklund, T. C., Lester, W. R., Vanderveer, S. J., & Strolger, L.-G. (2007). A Spectroscopic Study of Nuclear Processing and the Production of Anomalously Strong Lines in the Crab Nebula. *AJ*, 133(1), 81–88. <https://doi.org/10.1086/509504>
- Madrid, J. P., Leigh, N. W. C., Hurley, J. R., & Giersz, M. (2017). Mass evaporation rate of globular clusters in a strong tidal field. *MNRAS*, 470(2), 1729–1737. <https://doi.org/10.1093/mnras/stx1350>
- Maeder, A. (1987). Changes of surface chemistry for standard massive star evolution : cartography in the HR diagram. *A&A*, 173, 247–262.
- Maeder, A., & Meynet, G. (1989). Grids of evolutionary models from 0.85 to 120M : observational tests and the mass limits. *AAP*, 210, 155–173.
- Maggiore, M., Van Den Broeck, C., Bartolo, N., Belgacem, E., Bertacca, D., & et al. (2020). Science case for the Einstein telescope. *JCAP*, 2020(3), Article 050, 050. <https://doi.org/10.1088/1475-7516/2020/03/050>
- Makino, J. (1991). Optimal Order and Time-Step Criterion for Aarseth-Type N-Body Integrators. *ApJ*, 369, 200. <https://doi.org/10.1086/169751>
- Makino, J. (1999). Yet Another Fast Multipole Method without Multipoles-Pseudoparticle Multipole Method. *Journal of Computational Physics*, 151(2), 910–920. <https://doi.org/10.1006/jcph.1999.6226>
- Makino, J., & Aarseth, S. J. (1992). On a Hermite Integrator with Ahmad-Cohen Scheme for Gravitational Many-Body Problems. *PASJ*, 44, 141–151.
- Makino, J., Fukushige, T., Koga, M., & Namura, K. (2003). GRAPE-6: Massively-Parallel Special-Purpose Computer for Astrophysical Particle Simulations. *PASJ*, 55, 1163–1187. <https://doi.org/10.1093/pasj/55.6.1163>
- Makino, J., Taiji, M., Ebisuzaki, T., & Sugimoto, D. (1997). GRAPE-4: A Massively Parallel Special-Purpose Computer for Collisional N-Body Simulations. *ApJ*, 480(1), 432–446. <https://doi.org/10.1086/303972>
- Maliszewski, K., Giersz, M., Gondek-Rosinska, D., Askar, A., & Hypki, A. (2022). MOCCA-SURVEY Database II - Properties of Intermediate Mass Black Holes escaping from star clusters. *MNRAS.tmp*. <https://doi.org/10.1093/mnras/stac1728>
- Manchester, R. N., Hobbs, G. B., Teoh, A., & Hobbs, M. (2005). The Australia Telescope National Facility Pulsar Catalogue. *AJ*, 129(4), 1993–2006. <https://doi.org/10.1086/428488>

- Mapelli, M. (2018a). The Maxwell's demon of star clusters. *arXiv*, Article arXiv:1807.07944, arXiv:1807.07944.
- Mapelli, M. (2018b). Astrophysics of stellar black holes. *arXiv*, Article arXiv:1809.09130, arXiv:1809.09130.
- Mapelli, M., Santoliquido, F., Bouffanais, Y., Arca Sedda, M., Giacobbo, N., & et al. (2020). Hierarchical mergers in young, globular and nuclear star clusters: black hole masses and merger rates. *arXiv*, Article arXiv:2007.15022, arXiv:2007.15022.
- Mapelli, M., Spera, M., Montanari, E., Limongi, M., Chieffi, A., & et al. (2020). Impact of the Rotation and Compactness of Progenitors on the Mass of Black Holes. *ApJ*, 888(2), Article 76, 76. <https://doi.org/10.3847/1538-4357/ab584d>
- Mardling, R., & Aarseth, S. (1999). Dynamics and Stability of Three-Body Systems. In B. A. Steves & A. E. Roy (Eds.), *The dynamics of small bodies in the solar system, a major key to solar system studies* (p. 385, Vol. 522).
- Mardling, R. A. (1995a). The Role of Chaos in the Circularization of Tidal Capture Binaries. I. The Chaos Boundary. *ApJ*, 450, 722. <https://doi.org/10.1086/176178>
- Mardling, R. A. (1995b). The Role of Chaos in the Circularization of Tidal Capture Binaries. II. Long-Time Evolution. *ApJ*, 450, 732. <https://doi.org/10.1086/176179>
- Mardling, R. A., & Aarseth, S. J. (2001). Tidal interactions in star cluster simulations. *MNRAS*, 321(3), 398–420. <https://doi.org/10.1046/j.1365-8711.2001.03974.x>
- Marks, M., Janson, M., Kroupa, P., Leigh, N., & Thies, I. (2015). M-dwarf binaries as tracers of star and brown dwarf formation. *MNRAS*, 452(1), 1014–1025. <https://doi.org/10.1093/mnras/stv1361>
- Marks, M., & Kroupa, P. (2011). Dynamical population synthesis: constructing the stellar single and binary contents of galactic field populations. *MNRAS*, 417(3), 1702–1714. <https://doi.org/10.1111/j.1365-2966.2011.19519.x>
- Marks, M., Kroupa, P., Dabringhausen, J., & Pawlowski, M. S. (2012). Evidence for top-heavy stellar initial mass functions with increasing density and decreasing metallicity. *MNRAS*, 422(3), 2246–2254. <https://doi.org/10.1111/j.1365-2966.2012.20767.x>
- Martinazzi, E., Pieres, A., Kepler, S. O., Costa, J. E. S., Bonatto, C., & et al. (2014). Probing mass segregation in the globular cluster NGC 6397. *MNRAS*, 442(4), 3105–3111. <https://doi.org/10.1093/mnras/stu1032>
- Maschberger, T. (2013). On the function describing the stellar initial mass function. *MNRAS*, 429(2), 1725–1733. <https://doi.org/10.1093/mnras/sts479>
- Matzner, C. D., & McKee, C. F. (2000). Efficiencies of Low-Mass Star and Star Cluster Formation. *ApJ*, 545(1), 364–378. <https://doi.org/10.1086/317785>
- Mazeh, T. (2008). Observational Evidence for Tidal Interaction in Close Binary Systems. In M. -. Goupil & J. P. Zahn (Eds.), *Eas publications series* (pp. 1–65, Vol. 29). <https://doi.org/10.1051/eas:0829001>
- Mazzali, P. A., Röpkke, F. K., Benetti, S., & Hillebrandt, W. (2007). A Common Explosion Mechanism for Type Ia Supernovae. *Sci*, 315(5813), 825. <https://doi.org/10.1126/science.1136259>
- McDonald, I., & Zijlstra, A. A. (2015). Mass-loss on the red giant branch: the value and metallicity dependence of Reimers' η in globular clusters. *MNRAS*, 448(1), 502–521. <https://doi.org/10.1093/mnras/stv007>
- McKee, C. F., & Ostriker, E. C. (2007). Theory of Star Formation. *ARA&A*, 45(1), 565–687. <https://doi.org/10.1146/annurev.astro.45.051806.110602>
- McMillan, S. L. W. (1986). The Vectorization of Small-N Integrators. In P. Hut & S. L. W. McMillan (Eds.), *The use of supercomputers in stellar dynamics* (p. 156, Vol. 267). <https://doi.org/10.1007/BFb0116406>
- McMillan, S. L. W., & Aarseth, S. J. (1993). An O(N N) Integration Scheme for Collisional Stellar Systems. *ApJ*, 414, 200. <https://doi.org/10.1086/173068>
- Meakin, C. A., & Arnett, D. (2006). Active Carbon and Oxygen Shell Burning Hydrodynamics. *ApJL*, 637(1), L53–L56. <https://doi.org/10.1086/500544>
- Meakin, C. A., & Arnett, D. (2007). Anelastic and Compressible Simulations of Stellar Oxygen Burning. *ApJ*, 665(1), 690–697. <https://doi.org/10.1086/519372>
- Meibom, S., & Mathieu, R. D. (2005). A Robust Measure of Tidal Circularization in Coeval Binary Populations: The Solar-Type Spectroscopic Binary Population in the Open Cluster M35. *ApJ*, 620(2), 970–983. <https://doi.org/10.1086/427082>
- Meng, X., Chen, X., & Han, Z. (2008). Initial-final mass relationship for stars of different metallicities. *A&A*, 487(2), 625–635. <https://doi.org/10.1051/0004-6361:2007884110.48550/arXiv.0710.2397>
- Merritt, D. (2015). Gravitational Encounters and the Evolution of Galactic Nuclei. I. Method. *ApJ*, 804(1), Article 52, 52. <https://doi.org/10.1088/0004-637X/804/1/52>

- Mestel, L. (1968a). Magnetic braking by a stellar wind-I. *MNRAS*, 138, 359. <https://doi.org/10.1093/mnras/138.3.359>
- Mestel, L. (1968b). Magnetic braking by a stellar wind-II. *MNRAS*, 140, 177. <https://doi.org/10.1093/mnras/140.2.177>
- Mestel, L., & Spruit, H. C. (1987). On magnetic braking of late-type stars. *MNRAS*, 226, 57–66. <https://doi.org/10.1093/mnras/226.1.57>
- Michie, R. W. (1963). The dynamics of spherical stellar systems, III. *MNRAS*, 126, 331. <https://doi.org/10.1093/mnras/126.4.331>
- Michie, R. W. (1962). Dynamics of Spherical Stellar Systems: Properties of Theoretical Models, and Comparison with Clusters and Elliptical Galaxies. *AJ*, 67, 582. <https://doi.org/10.1086/108880>
- Mikkola, S., & Aarseth, S. J. (1990). A chain regularization method for the few-body problem. *Celestial Mechanics and Dynamical Astronomy*, 47(4), 375–390.
- Mikkola, S., & Aarseth, S. J. (1993). An Implementation of N-Body Chain Regularization. *Celestial Mechanics and Dynamical Astronomy*, 57(3), 439–459. <https://doi.org/10.1007/BF00695714>
- Mikkola, S., & Aarseth, S. J. (1998). An efficient integration method for binaries in N-body simulations. *NA*, 3(5), 309–320. [https://doi.org/10.1016/S1384-1076\(98\)00018-9](https://doi.org/10.1016/S1384-1076(98)00018-9)
- Mikkola, S., & Merritt, D. (2008). Implementing Few-Body Algorithmic Regularization with Post-Newtonian Terms. *AJ*, 135(6), 2398–2405. <https://doi.org/10.1088/0004-6256/135/6/2398>
- Mikkola, S., & Tanikawa, K. (1999a). Explicit Symplectic Algorithms For Time-Transformed Hamiltonians. *Celestial Mechanics and Dynamical Astronomy*, 74(4), 287–295. <https://doi.org/10.1023/A:1008368322547>
- Mikkola, S., & Tanikawa, K. (1999b). Algorithmic regularization of the few-body problem. *MNRAS*, 310(3), 745–749. <https://doi.org/10.1046/j.1365-8711.1999.02982.x>
- Miller, M. C., & Hamilton, D. P. (2002). Production of intermediate-mass black holes in globular clusters. *MNRAS*, 330(1), 232–240. <https://doi.org/10.1046/j.1365-8711.2002.05112.x>
- Miller, R. H. (1964). Irreversibility in Small Stellar Dynamical Systems. *ApJ*, 140, 250. <https://doi.org/10.1086/147911>
- Milone, A. P., Marino, A. F., Bedin, L. R., Anderson, J., Apai, D., & et al. (2017). The HST large programme on ω Centauri - I. Multiple stellar populations at the bottom of the main sequence probed in NIR-Optical. *MNRAS*, 469(1), 800–812. <https://doi.org/10.1093/mnras/stx836>
- Milone, A. P., Marino, A. F., Da Costa, G. S., Lagioia, E. P., D'Antona, F., & et al. (2020). Multiple populations in globular clusters and their parent galaxies. *MNRAS*, 491(1), 515–531. <https://doi.org/10.1093/mnras/stz2999>
- Milone, A. P., Marino, A. F., Mastrobuono-Battisti, A., & Lagioia, E. P. (2018). Gaia unveils the kinematics of multiple stellar populations in 47 Tucanae. *MNRAS*, 479(4), 5005–5011. <https://doi.org/10.1093/mnras/sty1873>
- Milone, A. P., Marino, A. F., Piotto, G., Bedin, L. R., Anderson, J., & et al. (2013). A WFC3/HST View of the Three Stellar Populations in the Globular Cluster NGC 6752. *ApJ*, 767(2), Article 120, 120. <https://doi.org/10.1088/0004-637X/767/2/120>
- Milone, A. P., Marino, A. F., Renzini, A., D'Antona, F., Anderson, J., & et al. (2018). The Hubble Space Telescope UV legacy survey of galactic globular clusters - XVI. The helium abundance of multiple populations. *MNRAS*, 481(4), 5098–5122. <https://doi.org/10.1093/mnras/sty2573>
- Milone, A. P., Marino, A. F., Renzini, A., Li, C., Jang, S., & et al. (2020). A chromosome map to unveil stellar populations with different magnesium abundances. The case of ω Centauri. *MNRAS*, 497(3), 3846–3859. <https://doi.org/10.1093/mnras/staa2119>
- Milone, A. P., Piotto, G., Bedin, L. R., Cassisi, S., Anderson, J., & et al. (2012). Luminosity and mass functions of the three main sequences of the globular cluster NGC 2808. *A&A*, 537, Article A77, A77. <https://doi.org/10.1051/0004-6361/201116539>
- Milone, A. P., Piotto, G., Bedin, L. R., King, I. R., Anderson, J., & et al. (2012). Multiple Stellar Populations in 47 Tucanae. *ApJ*, 744(1), Article 58, 58. <https://doi.org/10.1088/0004-637X/744/1/58>
- Milone, A. P., Piotto, G., Renzini, A., Marino, A. F., Bedin, L. R., & et al. (2017). The Hubble Space Telescope UV Legacy Survey of Galactic globular clusters - IX. The Atlas of multiple stellar populations. *MNRAS*, 464(3), 3636–3656. <https://doi.org/10.1093/mnras/stw2531>

- Milone, A. P., Vesperini, E., Marino, A. F., Hong, J., van der Marel, R., & et al. (2020). The Hubble Space Telescope UV Legacy Survey of Galactic globular clusters - XXI. Binaries among multiple stellar populations. *MNRAS*, 492(4), 5457–5469. <https://doi.org/10.1093/mnras/stz3629>
- Milone, A. P. (2020). Thirteen facts that you need to know on multiple populations in globular clusters. In A. Bragaglia, M. Davies, A. Sills, & E. Vesperini (Eds.), *Star clusters: From the milky way to the early universe* (pp. 251–260, Vol. 351). <https://doi.org/10.1017/S1743921319010044>
- Milone, A. P., & Marino, A. F. (2022). Multiple Populations in Star Clusters. *arXiv*, Article arXiv:2206.10564, arXiv:2206.10564.
- Moe, M., & Di Stefano, R. (2017). Mind Your Ps and Qs: The Interrelation between Period (P) and Mass-ratio (Q) Distributions of Binary Stars. *ApJS*, 230(2), Article 15, 15. <https://doi.org/10.3847/1538-4365/aa6fb6>
- Morawski, J., Giersz, M., Askar, A., & Belczynski, K. (2018). MOCCA-SURVEY Database I: Assessing GW kick retention fractions for BH-BH mergers in globular clusters. *MNRAS*, 481(2), 2168–2179. <https://doi.org/10.1093/mnras/sty2401>
- Morawski, J., Giersz, M., Askar, A., & Belczynski, K. (2019). Erratum to: MOCCA-SURVEY Database I: Assessing GW kick retention fractions for BH-BH mergers in globular clusters. *MNRAS*, 486(3), 3402–3402. <https://doi.org/10.1093/mnras/stz1074>
- Myeong, G. C., Evans, N. W., Belokurov, V., Sanders, J. L., & Koposov, S. E. (2018a). Discovery of new retrograde substructures: the shards of ω Centauri? *MNRAS*, 478(4), 5449–5459. <https://doi.org/10.1093/mnras/sty1403>
- Myeong, G. C., Evans, N. W., Belokurov, V., Sanders, J. L., & Koposov, S. E. (2018b). The Sausage Globular Clusters. *ApJL*, 863(2), Article L28, L28. <https://doi.org/10.3847/2041-8213/aad7f7>
- Myeong, G. C., Vasiliev, E., Iorio, G., Evans, N. W., & Belokurov, V. (2019). Evidence for two early accretion events that built the Milky Way stellar halo. *MNRAS*, 488(1), 1235–1247. <https://doi.org/10.1093/mnras/stz1770>
- Nakauchi, D., Inayoshi, K., & Omukai, K. (2020). Pulsation-driven Mass Loss from Massive Stars behind Stellar Mergers in Metal-poor Dense Clusters. *ApJ*, 902(1), Article 81, 81. <https://doi.org/10.3847/1538-4357/abb463>
- Nardiello, D., Libralato, M., Piotto, G., Anderson, J., Bellini, A., Aparicio, A., Bedin, L. R., Cassisi, S., Granata, V., King, I. R., Lucertini, F., Marino, A. F., Milone, A. P., Ortolani, S., Platais, I., & van der Marel, R. P. (2018). The Hubble Space Telescope UV Legacy Survey of Galactic Globular Clusters - XVII. Public Catalogue Release. *MNRAS*, 481(3), 3382–3393. <https://doi.org/10.1093/mnras/sty2515>
- Neumayer, N., Seth, A., & Böker, T. (2020). Nuclear star clusters. *A&ARv*, 28(1), Article 4, 4. <https://doi.org/10.1007/s00159-020-00125-0>
- Newmark, N. M. (1959). A method of computation for structural dynamics. *Journal of the Engineering Mechanics Division*, 85(3), 67–94. <https://doi.org/10.1061/JMCEA3.0000098>
- Ng, K. K. Y., Franciolini, G., Berti, E., Pani, P., Riotto, A., & et al. (2022). Constraining high-redshift stellar-mass primordial black holes with next-generation ground-based gravitational-wave detectors. *arXiv*, Article arXiv:2204.11864, arXiv:2204.11864.
- Nieuwenhuijzen, H., & de Jager, C. (1990). Parametrization of stellar rates of mass loss as functions of the fundamental stellar parameters M , L , and R . *A&A*, 231, 134–136.
- Nitadori, K., & Aarseth, S. J. (2012). Accelerating NBODY6 with graphics processing units. *MNRAS*, 424(1), 545–552. <https://doi.org/10.1111/j.1365-2966.2012.21227.x>
- Nitadori, K., & Makino, J. (2008). Sixth- and eighth-order Hermite integrator for N-body simulations. *NewA*, 13(7), 498–507. <https://doi.org/10.1016/j.newast.2008.01.010>
- Nomoto, K. (1984). Evolution of 8–10 solar mass stars toward electron capture supernovae. I - Formation of electron-degenerate O + NE + MG cores. *ApJ*, 277, 791–805. <https://doi.org/10.1086/161749>
- Nomoto, K. (1987). Evolution of 8–10 M_{sun} Stars toward Electron Capture Supernovae. II. Collapse of an O + NE + MG Core. *ApJ*, 322, 206. <https://doi.org/10.1086/165716>
- Nomoto, K., & Kondo, Y. (1991). Conditions for Accretion-induced Collapse of White Dwarfs. *ApJL*, 367, L19. <https://doi.org/10.1086/185922>
- Offner, S. S. R., & Chaban, J. (2017). Impact of Protostellar Outflows on Turbulence and Star Formation Efficiency in Magnetized Dense Cores. *ApJ*, 847(2), Article 104, 104. <https://doi.org/10.3847/1538-4357/aa8996>

- Oh, S., Kroupa, P., & Pflamm-Altenburg, J. (2015). Dependency of Dynamical Ejections of O Stars on the Masses of Very Young Star Clusters. *ApJ*, 805(2), Article 92, 92. <https://doi.org/10.1088/0004-637X/805/2/92>
- Olejak, A., Belczynski, K., Bulik, T., & Sobolewska, M. (2020). Synthetic catalog of black holes in the Milky Way. *A&A*, 638, Article A94, A94. <https://doi.org/10.1051/0004-6361/201936557>
- Olejak, A., Belczynski, K., & Ivanova, N. (2021). The impact of common envelope development criteria on the formation of LIGO/Virgo sources. *arXiv*, Article arXiv:2102.05649, arXiv:2102.05649.
- Ordenes-Briceño, Y., Puzia, T. H., Eigenthaler, P., Taylor, M. A., Muñoz, R. P., Zhang, H., Alamo-Martínez, K., Ribbeck, K. X., Grebel, E. K., Ángel, S., Côté, P., Ferrarese, L., Hilker, M., Lançon, A., Mieske, S., Miller, B. W., Rong, Y., & Sánchez-Janssen, R. (2018). The Next Generation Fornax Survey (NGFS). IV. Mass and Age Bimodality of Nuclear Clusters in the Fornax Core Region. *ApJ*, 860(1), Article 4, 4. <https://doi.org/10.3847/1538-4357/aac1b8>
- Ott, C. D. (2009). Probing the core-collapse supernova mechanism with gravitational waves. *Classical and Quantum Gravity*, 26(20), Article 204015, 204015. <https://doi.org/10.1088/0264-9381/26/20/204015>
- Paczynski, B. (1976). Common Envelope Binaries. In P. Eggleton, S. Mitton, & J. Whelan (Eds.), *Structure and evolution of close binary systems* (p. 75, Vol. 73).
- Padmanabhan, T. (1990). Statistical mechanics of gravitating systems. *Phys. Rep.*, 188(5), 285–362. [https://doi.org/10.1016/0370-1573\(90\)90051-3](https://doi.org/10.1016/0370-1573(90)90051-3)
- Palla, F., Randich, S., Pavlenko, Y. V., Flaccomio, E., & Pallavicini, R. (2007). Old Stars in Young Clusters: Lithium-depleted Low-Mass Stars of the Orion Nebula Cluster. *ApJL*, 659(1), L41–L44. <https://doi.org/10.1086/516733>
- Panamarev, T., Just, A., Spurzem, R., Berczik, P., Wang, L., & et al. (2019). Direct N-body simulation of the Galactic centre. *MNRAS*, 484(3), 3279–3290. <https://doi.org/10.1093/mnras/stz208>
- Panamarev, T., & Kocsis, B. (2022). A numerical study of stellar discs in galactic nuclei. *arXiv*, Article arXiv:2207.06398, arXiv:2207.06398.
- Pang, X., Li, Y., Tang, S.-Y., Pasquato, M., & Kouwenhoven, M. B. N. (2020). Different Fates of Young Star Clusters after Gas Expulsion. *ApJL*, 900(1), Article L4, L4. <https://doi.org/10.3847/2041-8213/abad28>
- Pang, X., Li, Y., Yu, Z., Tang, S.-Y., Dinnbier, F., & et al. (2021). 3D Morphology of Open Clusters in the Solar Neighborhood with Gaia EDR 3: Its Relation to Cluster Dynamics. *ApJ*, 912(2), Article 162, 162. <https://doi.org/10.3847/1538-4357/abeaac>
- Pang, X., Shu, Q., Wang, L., & Kouwenhoven, M. B. N. (2022). Investigating the UV-excess in star clusters with N-body simulations: predictions for future CSST observations. *arXiv*, Article arXiv:2207.00772, arXiv:2207.00772.
- Pang, X., Tang, S.-Y., Li, Y., Yu, Z., Wang, L., Li, J., Li, Y., Wang, Y., Wang, Y., Zhang, T., Pasquato, M., & Kouwenhoven, M. B. N. (2022). 3D Morphology of Open Clusters in the Solar Neighborhood with Gaia EDR3 II: Hierarchical Star Formation Revealed by Spatial and Kinematic Substructures. *arXiv e-prints*, Article arXiv:2204.06000, arXiv:2204.06000.
- Pang, X., Yu, Z., Tang, S.-Y., Hong, J., Yuan, Z., & et al. (2021). Disruption of Hierarchical Clustering in the Vela OB2 Complex and the Cluster Pair Collinder 135 and UBC7 with Gaia EDR3: Evidence of Supernova Quenching. *arXiv*, Article arXiv:2106.07658, arXiv:2106.07658.
- Pasetto, S., Chiosi, C., Cropper, M., & Grebel, E. (2018). New theory of stellar convection without the mixing-length parameter: New stellar atmosphere model. *Journal of Physics: Conference Series*, 940, 012020. <https://doi.org/10.1088/1742-6596/940/1/012020>
- Pattabiraman, B., Umbreit, S., Liao, W.-k., Choudhary, A., Kalogera, V., & et al. (2013). A Parallel Monte Carlo Code for Simulating Collisional N-body Systems. *ApJS*, 204(2), Article 15, 15. <https://doi.org/10.1088/0067-0049/204/2/15>
- Paxton, B., Bildsten, L., Dotter, A., Herwig, F., Lesaffre, P., & et al. (2011). Modules for Experiments in Stellar Astrophysics (MESA). *ApJS*, 192(1), Article 3, 3. <https://doi.org/10.1088/0067-0049/192/1/3>
- Paxton, B., Cantiello, M., Arras, P., Bildsten, L., Brown, E. F., & et al. (2013). Modules for Experiments in Stellar Astrophysics (MESA): Planets, Oscillations, Rotation, and Massive Stars. *ApJS*, 208(1), Article 4, 4. <https://doi.org/10.1088/0067-0049/208/1/4>
- Paxton, B., Marchant, P., Schwab, J., Bauer, E. B., Bildsten, L., & et al. (2015). Modules for Experiments in Stellar Astrophysics (MESA): Binaries, Pulsations, and Explosions. *ApJS*, 220(1), Article 15, 15. <https://doi.org/10.1088/0067-0049/220/1/15>

- Paxton, B., Marchant, P., Schwab, J., Bauer, E. B., Bildsten, L., & et al. (2016). Erratum: “Modules for Experiments in Stellar Astrophysics (MESA): Binaries, Pulsations, and Explosions” (2015, ApJS, 220, 15). *ApJS*, 223(1), Article 18, 18. <https://doi.org/10.3847/0067-0049/223/1/18>
- Paxton, B., Schwab, J., Bauer, E. B., Bildsten, L., Blinnikov, S., & et al. (2018). Modules for Experiments in Stellar Astrophysics (MESA): Convective Boundaries, Element Diffusion, and Massive Star Explosions. *ApJS*, 234(2), Article 34, 34. <https://doi.org/10.3847/1538-4365/aaa5a8>
- Paxton, B., Smolec, R., Schwab, J., Gautschy, A., Bildsten, L., & et al. (2019). Modules for Experiments in Stellar Astrophysics (MESA): Pulsating Variable Stars, Rotation, Convective Boundaries, and Energy Conservation. *ApJS*, 243(1), Article 10, 10. <https://doi.org/10.3847/1538-4365/ab2241>
- Pease, F. G., & Shapley, H. (1917). On the distribution of stars in twelve globular clusters. *ApJ*, 45, 225–243. <https://doi.org/10.1086/142324>
- Peters, P. C. (1964). Gravitational Radiation and the Motion of Two Point Masses. *PhRv*, 136(4B), 1224–1232. <https://doi.org/10.1103/PhysRev.136.B1224>
- Peters, P. C., & Mathews, J. (1963). Gravitational Radiation from Point Masses in a Keplerian Orbit. *PhRv*, 131(1), 435–440. <https://doi.org/10.1103/PhysRev.131.435>
- Pflamm-Altenburg, J., & Kroupa, P. (2006). A highly abnormal massive star mass function in the Orion Nebula cluster and the dynamical decay of trapezium systems. *MNRAS*, 373(1), 295–304. <https://doi.org/10.1111/j.1365-2966.2006.11028.x>
- Pflamm-Altenburg, J., & Kroupa, P. (2007). Captured older stars as the reason for apparently prolonged star formation in young star clusters. *MNRAS*, 375(3), 855–860. <https://doi.org/10.1111/j.1365-2966.2006.11294.x>
- Piatti, A. E., Illesca, D. M. F., Massara, A. A., Chiarpotti, M., Roldán, D., Morón, M., & Bazzoni, F. (2023). Assessing the physical reality of Milky Way open cluster candidates. *MNRAS*, 518(4), 6216–6222. <https://doi.org/10.1093/mnras/stac3479>
- Piotto, G., Milone, A. P., Bedin, L. R., Anderson, J., King, I. R., Marino, A. F., Nardiello, D., Aparicio, A., Barbuy, B., Bellini, A., Brown, T. M., Cassisi, S., Cool, A. M., Cunial, A., Dalessandro, E., D’Antona, F., Ferraro, F. R., Hidalgo, S., Lanzoni, B., . . . Zoccali, M. (2015). The Hubble Space Telescope UV Legacy Survey of Galactic Globular Clusters. I. Overview of the Project and Detection of Multiple Stellar Populations. *AJ*, 149(3), Article 91, 91. <https://doi.org/10.1088/0004-6256/149/3/91>
- Plummer, H. C. (1911). On the problem of distribution in globular star clusters. *MNRAS*, 71, 460–470. <https://doi.org/10.1093/mnras/71.5.460>
- Plummer, H. C. (1915). The distribution of stars in globular clusters. *MNRAS*, 76, 107–121. <https://doi.org/10.1093/mnras/76.2.107>
- Podsiadlowski, P., Langer, N., Poelarends, A. J. T., Rappaport, S., Heger, A., & et al. (2004). The Effects of Binary Evolution on the Dynamics of Core Collapse and Neutron Star Kicks. *ApJ*, 612(2), 1044–1051. <https://doi.org/10.1086/421713>
- Pols, O. R., Schröder, K.-P., Hurley, J. R., Tout, C. A., & Eggleton, P. P. (1998). Stellar evolution models for $Z = 0.0001$ to 0.03 . *MNRAS*, 298(2), 525–536. <https://doi.org/10.1046/j.1365-8711.1998.01658.x>
- Pols, O. R., Tout, C. A., Eggleton, P. P., & Han, Z. (1995). Approximate input physics for stellar modelling. *MNRAS*, 274(3), 964–974. <https://doi.org/10.1093/mnras/274.3.964>
- Pols, O. R., Tout, C. A., Schroder, K.-P., Eggleton, P. P., & Manners, J. (1997). Further critical tests of stellar evolution by means of double-lined eclipsing binaries. *MNRAS*, 289(4), 869–881. <https://doi.org/10.1093/mnras/289.4.869>
- Portegies Zwart, S. F., Belleman, R. G., & Geldof, P. M. (2007). High-performance direct gravitational N-body simulations on graphics processing units. *Nature*, 12(8), 641–650. <https://doi.org/10.1016/j.newast.2007.05.004>
- Portegies Zwart, S. F., & McMillan, S. L. W. (2002). The Runaway Growth of Intermediate-Mass Black Holes in Dense Star Clusters. *ApJ*, 576(2), 899–907. <https://doi.org/10.1086/341798>
- Portegies Zwart, S. F., McMillan, S. L. W., & Gieles, M. (2010). Young Massive Star Clusters. *ARA&A*, 48, 431–493. <https://doi.org/10.1146/annurev-astro-081309-130834>
- Postnov, K. A., & Yungelson, L. R. (2014). The Evolution of Compact Binary Star Systems. *LRR*, 17(1), Article 3, 3. <https://doi.org/10.12942/lrr-2014-3>

- Prendergast, K. H., & Tomer, E. (1970). Self-Consistent Models of Elliptical Galaxies. *AJ*, 75, 674. <https://doi.org/10.1086/111008>
- Preto, M., Merritt, D., & Spurzem, R. (2004). N-Body Growth of a Bahcall-Wolf Cusp around a Black Hole. *ApJl*, 613(2), L109–L112. <https://doi.org/10.1086/425139>
- Punturo, M., Abernathy, M., Acernese, F., Allen, B., Andersson, N., & et al. (2010a). The third generation of gravitational wave observatories and their science reach. *CQGra*, 27(8), Article 084007, 084007. <https://doi.org/10.1088/0264-9381/27/8/084007>
- Punturo, M., Abernathy, M., Acernese, F., Allen, B., Andersson, N., & et al. (2010b). The Einstein Telescope: a third-generation gravitational wave observatory. *CQGra*, 27(19), Article 194002, 194002. <https://doi.org/10.1088/0264-9381/27/19/194002>
- Quillen, A. C., Minchev, I., Bland-Hawthorn, J., & Haywood, M. (2009). Radial mixing in the outer Milky Way disc caused by an orbiting satellite. *MNRAS*, 397(3), 1599–1606. <https://doi.org/10.1111/j.1365-2966.2009.15054.x>
- Quinlan, G. D., & Tremaine, S. (1992). On the reliability of gravitational N-body integrations. *MNRAS*, 259(3), 505–518. <https://doi.org/10.1093/mnras/259.3.505>
- Railton, A. D., Tout, C. A., & Aarseth, S. J. (2014). Pre-Mainsequence Stellar Evolution in N-Body Models. *PASA*, 31, Article e017, e017. <https://doi.org/10.1017/pasa.2014.10>
- Ramos-Almendares, F., Sales, L. V., Abadi, M. G., Doppel, J. E., Muriel, H., & Peng, E. W. (2020). Simulating the spatial distribution and kinematics of globular clusters within galaxy clusters in illustris. *MNRAS*, 493(4), 5357–5368. <https://doi.org/10.1093/mnras/staa551>
- Rantala, A., Naab, T., & Springel, V. (2021). frost: a momentum-conserving CUDA implementation of a hierarchical fourth-order forward symplectic integrator. *MNRAS*, 502(4), 5546–5562. <https://doi.org/10.1093/mnras/stab057>
- Rantala, A., Pihajoki, P., Mannerkoski, M., Johansson, P. H., & Naab, T. (2020). MSTAR - a fast parallelized algorithmically regularized integrator with minimum spanning tree coordinates. *MNRAS*, 492(3), 4131–4148. <https://doi.org/10.1093/mnras/staa084>
- Rappaport, S., Verbunt, F., & Joss, P. C. (1983). A new technique for calculations of binary stellar evolution application to magnetic braking. *ApJ*, 275, 713–731. <https://doi.org/10.1086/161569>
- Rasio, F. A., Tout, C. A., Lubow, S. H., & Livio, M. (1996). Tidal Decay of Close Planetary Orbits. *ApJ*, 470, 1187. <https://doi.org/10.1086/177941>
- Rastello, S., Mapelli, M., Di Carlo, U. N., Iorio, G., Ballone, A., Giacobbo, N., Santoliquido, F., & Torniamenti, S. (2021). Dynamics of binary black holes in low-mass young star clusters. *MNRAS*, 507(3), 3612–3625. <https://doi.org/10.1093/mnras/stab2355>
- Rebassa-Mansergas, A., Nebot Gómez-Morán, A., Schreiber, M. R., Gänsicke, B. T., Schwöpe, A., & et al. (2012). Post-common envelope binaries from SDSS - XIV. The DR7 white dwarf-main-sequence binary catalogue. *MNRAS*, 419(1), 806–816. <https://doi.org/10.1111/j.1365-2966.2011.19923.x>
- Rees, M. J. (1984). Black Hole Models for Active Galactic Nuclei. *ARA&A*, 22, 471–506. <https://doi.org/10.1146/annurev.aa.22.090184.002351>
- Reimers, D. (1975). Circumstellar absorption lines and mass loss from red giants. *MSRSL*, 8, 369–382.
- Reina-Campos, M., Hughes, M. E., Kruijssen, J. M. D., Pfeffer, J. L., Bastian, N., & et al. (2020). The mass fraction of halo stars contributed by the disruption of globular clusters in the E-MOSAICS simulations. *MNRAS*, 493(3), 3422–3428. <https://doi.org/10.1093/mnras/staa483>
- Reina-Campos, M., Kruijssen, J. M. D., Pfeffer, J. L., Bastian, N., & Crain, R. A. (2019). Formation histories of stars, clusters, and globular clusters in the E-MOSAICS simulations. *MNRAS*, 486(4), 5838–5852. <https://doi.org/10.1093/mnras/stz1236>
- Reina-Campos, M., Trujillo-Gomez, S., Deason, A. J., Kruijssen, J. M. D., Pfeffer, J. L., & et al. (2021). Globular clusters as tracers of the dark matter halo: insights from the E-MOSAICS simulations. *arXiv*, Article arXiv:2106.07652, arXiv:2106.07652.
- Reinoso, B., Schleicher, D. R. G., Fellhauer, M., Klessen, R. S., & Boekholt, T. C. N. (2018). Collisions in primordial star clusters. Formation pathway for intermediate mass black holes. *AAP*, 614, Article A14, A14. <https://doi.org/10.1051/0004-6361/201732224>
- Reinoso, B., Leigh, N. W. C., Barrera-Retamal, C. M., Schleicher, D., Klessen, R. S., & Stutz, A. M. (2021). The mean free path approximation and stellar collisions in star clusters: Numerical exploration of the ana-

- lytic rates and the role of perturbations on binary star mergers. *arXiv e-prints*, Article arXiv:2111.03119, arXiv:2111.03119.
- Reitze, D., Adhikari, R. X., Ballmer, S., Barish, B., Barsotti, L., & et al. (2019). Cosmic Explorer: The U.S. Contribution to Gravitational-Wave Astronomy beyond LIGO. *Bulletin of the American Astronomical Society*, 51, Article 35, 35.
- Renaud, F., Gieles, M., & Boily, C. M. (2011). Evolution of star clusters in arbitrary tidal fields. *MNRAS*, 418(2), 759–769. <https://doi.org/10.1111/j.1365-2966.2011.19531.x>
- Rezzolla, L., Barausse, E., Dorband, E. N., Pollney, D., Reisswig, C., & et al. (2008). Final spin from the coalescence of two black holes. *PhRvD*, 78(4), Article 044002, 044002. <https://doi.org/10.1103/PhysRevD.78.044002>
- Ritter, H. (1988). Turning on and off mass transfer in cataclysmic binaries. *A&A*, 202, 93–100.
- Rizzuto, F. P., Naab, T., Spurzem, R., Arca-Sedda, M., Giersz, M., & et al. (2022). Black hole mergers in compact star clusters and massive black hole formation beyond the mass gap. *MNRAS*, 512(1), 884–898. <https://doi.org/10.1093/mnras/stac231>
- Rizzuto, F. P., Naab, T., Spurzem, R., Arca-Sedda, M., Giersz, M., Ostriker, J. P., & Banerjee, S. (2021). Black hole mergers in compact star clusters and massive black hole formation beyond the mass-gap. *arXiv e-prints*, Article arXiv:2108.11457, arXiv:2108.11457.
- Rizzuto, F. P., Naab, T., Spurzem, R., Giersz, M., Ostriker, J. P., & et al. (2021). Intermediate mass black hole formation in compact young massive star clusters. *MNRAS*, 501(4), 5257–5273. <https://doi.org/10.1093/mnras/staa3634>
- Rodriguez, C. L., Amaro-Seoane, P., Chatterjee, S., Kremer, K., Rasio, F. A., & et al. (2018). Post-Newtonian dynamics in dense star clusters: Formation, masses, and merger rates of highly-eccentric black hole binaries. *PhRvD*, 98(12), Article 123005, 123005. <https://doi.org/10.1103/PhysRevD.98.123005>
- Rodriguez, C. L., Weatherford, N. C., Coughlin, S. C., Amaro-Seoane, P., Breivik, K., & et al. (2022). Modeling Dense Star Clusters in the Milky Way and beyond with the Cluster Monte Carlo Code. *ApJS*, 258(2), Article 22, 22. <https://doi.org/10.3847/1538-4365/ac2edf>
- Rodriguez, C. L., Zevin, M., Amaro-Seoane, P., Chatterjee, S., Kremer, K., & et al. (2019). Black holes: The next generation—repeated mergers in dense star clusters and their gravitational-wave properties. *PhRvD*, 100(4), Article 043027, 043027. <https://doi.org/10.1103/PhysRevD.100.043027>
- Rosenbluth, M. N., MacDonald, W. M., & Judd, D. L. (1957). Fokker-Planck Equation for an Inverse-Square Force. *Physical Review*, 107(1), 1–6. <https://doi.org/10.1103/PhysRev.107.1>
- Ruiter, A. J., Ferrario, L., Belczynski, K., Seitzzahl, I. R., Crocker, R. M., & Karakas, A. I. (2019). On the formation of neutron stars via accretion-induced collapse in binaries. *Monthly Notices of the Royal Astronomical Society*, 484(1), 698–711. <https://doi.org/10.1093/mnras/stz001>
- Rydberg, C.-E., Zackrisson, E., Lundqvist, P., & Scott, P. (2013). Detection of isolated Population III stars with the James Webb Space Telescope. *MNRAS*, 429(4), 3658–3664. <https://doi.org/10.1093/mnras/sts653>
- Ryon, J. E., Gallagher, J. S., Smith, L. J., Adamo, A., Calzetti, D., Bright, S. N., Cignoni, M., Cook, D. O., Dale, D. A., Elmegreen, B. E., Fumagalli, M., Gouliermis, D. A., Grasha, K., Grebel, E. K., Kim, H., Messa, M., Thilker, D., & Ubeda, L. (2017). Effective Radii of Young, Massive Star Clusters in Two LEGUS Galaxies. *ApJ*, 841(2), Article 92, 92. <https://doi.org/10.3847/1538-4357/aa719e>
- Saeedi, S., Liu, T., Knies, J., Sasaki, M., Becker, W., Bulbul, E., Dennerl, K., Freyberg, M., Laktionov, R., & Merloni, A. (2022). eROSITA study of the globular cluster 47 Tucanae. *A&A*, 661, Article A35, A35. <https://doi.org/10.1051/0004-6361/202141612>
- Saio, H., & Nomoto, K. (1985). Evolution of a merging pair of C + O white dwarfs to form a single neutron star. *A&A*, 150(1), L21–L23.
- Saio, H., & Nomoto, K. (1998). Inward Propagation of Nuclear-burning Shells in Merging C-O and He White Dwarfs. *ApJ*, 500(1), 388–397. <https://doi.org/10.1086/305696>
- Saio, H., & Nomoto, K. (2004). Off-Center Carbon Ignition in Rapidly Rotating, Accreting Carbon-Oxygen White Dwarfs. *ApJ*, 615(1), 444–449. <https://doi.org/10.1086/423976>
- Sakurai, Y., Hosokawa, T., Yoshida, N., & Yorke, H. W. (2015). Formation of primordial supermassive stars by burst accretion. *MNRAS*, 452(1), 755–764. <https://doi.org/10.1093/mnras/stv1346>
- Sakurai, Y., Yoshida, N., & Fujii, M. S. (2019). Growth of intermediate mass black holes by tidal disruption events in the first star clusters. *MNRAS*, 484(4), 4665–4677. <https://doi.org/10.1093/mnras/stz315>

- Sakurai, Y., Yoshida, N., Fujii, M. S., & Hirano, S. (2017). Formation of intermediate-mass black holes through runaway collisions in the first star clusters. *MNRAS*, 472(2), 1677–1684. <https://doi.org/10.1093/mnras/stx2044>
- Salaris, M., & Cassisi, S. (2017). Chemical element transport in stellar evolution models. *Royal Society Open Science*, 4(8), Article 170192, 170192. <https://doi.org/10.1098/rsos.170192>
- Salpeter, E. E. (1955). The Luminosity Function and Stellar Evolution. *ApJ*, 121, 161. <https://doi.org/10.1086/145971>
- Sana, H., de Mink, S. E., de Koter, A., Langer, N., Evans, C. J., & et al. (2012). Binary Interaction Dominates the Evolution of Massive Stars. *Sci*, 337(6093), 444. <https://doi.org/10.1126/science.1223344>
- Sana, H., de Mink, S. E., de Koter, A., Langer, N., Evans, C. J., & et al. (2013). Multiplicity of massive O stars and evolutionary implications. In G. Pugliese, A. de Koter, & M. Wijburg (Eds.), *370 years of astronomy in utrecht* (p. 141, Vol. 470).
- Sana, H., & Evans, C. J. (2011). The multiplicity of massive stars. In C. Neiner, G. Wade, G. Meynet, & G. Peters (Eds.), *Active ob stars: Structure, evolution, mass loss, and critical limits* (pp. 474–485, Vol. 272). <https://doi.org/10.1017/S1743921311011124>
- Sánchez-Janssen, R., Côté, P., Ferrarese, L., Peng, E. W., Roediger, J., Blakeslee, J. P., Emsellem, E., Puzia, T. H., Spengler, C., Taylor, J., Álamo-Martínez, K. A., Boselli, A., Cantiello, M., Cuillandre, J.-C., Duc, P.-A., Durrell, P., Gwyn, S., MacArthur, L. A., Lançon, A., . . . Toloba, E. (2019). The Next Generation Virgo Cluster Survey. XXIII. Fundamentals of Nuclear Star Clusters over Seven Decades in Galaxy Mass. *ApJ*, 878(1), Article 18, 18. <https://doi.org/10.3847/1538-4357/aaf4fd>
- Sander, A. A. C., Vink, J. S., & Hamann, W. -. (2020). Driving classical Wolf-Rayet winds: a Γ - and Z-dependent mass-loss. *MNRAS*, 491(3), 4406–4425. <https://doi.org/10.1093/mnras/stz3064>
- Sander, A. A. C., & Vink, J. S. (2020). On the nature of massive helium star winds and Wolf-Rayet-type mass-loss. *MNRAS*, 499(1), 873–892. <https://doi.org/10.1093/mnras/staa2712>
- Santoliquido, F., Mapelli, M., Bouffanais, Y., Giacobbo, N., Di Carlo, U. N., & et al. (2020). The Cosmic Merger Rate Density Evolution of Compact Binaries Formed in Young Star Clusters and in Isolated Binaries. *ApJ*, 898(2), Article 152, 152. <https://doi.org/10.3847/1538-4357/ab9b78>
- Sanyal, D., Grassitelli, L., Langer, N., & Bestenlehner, J. M. (2015). Massive main-sequence stars evolving at the Eddington limit. *AAP*, 580, Article A20, A20. <https://doi.org/10.1051/0004-6361/201525945>
- Sathyaprakash, B., Abernathy, M., Acernese, F., Ajith, P., Allen, B., & et al. (2012). Scientific objectives of Einstein Telescope. *CQGra*, 29(12), Article 124013, 124013. <https://doi.org/10.1088/0264-9381/29/12/124013>
- Schaller, G., Schaerer, D., Meynet, G., & Maeder, A. (1992). New grids of stellar models from 0.8 to 120 M_{sun} at $Z=0.020$ and $Z=0.001$. *A&AS*, 96, 269.
- Schauer, A. T. P., Bromm, V., Drory, N., & Boylan-Kolchin, M. (2022). On the probability of the extremely lensed $z=6.2$ Earendel source being a Population-III star. *arXiv*, Article arXiv:2207.02863, arXiv:2207.02863.
- Schauer, A. T. P., Drory, N., & Bromm, V. (2020). The Ultimately Large Telescope: What Kind of Facility Do We Need to Detect Population III Stars? *ApJ*, 904(2), Article 145, 145. <https://doi.org/10.3847/1538-4357/abbc0b>
- Scheck, L., Janka, H. .-, Foglizzo, T., & Kifonidis, K. (2008). Multidimensional supernova simulations with approximative neutrino transport. II. Convection and the advective-acoustic cycle in the supernova core. *A&A*, 477(3), 931–952. <https://doi.org/10.1051/0004-6361:20077701>
- Scheck, L., Plewa, T., Janka, H. .-, Kifonidis, K., & Müller, E. (2004). Pulsar Recoil by Large-Scale Anisotropies in Supernova Explosions. *PhRvL*, 92(1), Article 011103, 011103. <https://doi.org/10.1103/PhysRevLett.92.011103>
- Schleicher, D. R. G., Reinoso, B., Latif, M., Klessen, R. S., Vergara, M. Z. C., & et al. (2022). Origin of supermassive black holes in massive metal-poor protoclusters. *MNRAS*, 512(4), 6192–6200. <https://doi.org/10.1093/mnras/stac926>
- Schneider, F. R. N., Podsiadlowski, P., & Müller, B. (2021). Pre-supernova evolution, compact-object masses, and explosion properties of stripped binary stars. *A&A*, 645, Article A5, A5. <https://doi.org/10.1051/0004-6361/202039219>
- Schneider, J., Amaro-Seoane, P., & Spurzem, R. (2011). Higher-order moment models of dense stellar systems: applications to the modelling of the stellar velocity distribution function. *MNRAS*, 410(1), 432–454. <https://doi.org/10.1111/j.1365-2966.2010.17454.x>

- Schneider, R., Ferrara, A., Ciardi, B., Ferrari, V., & Matarrese, S. (2000). Gravitational wave signals from the collapse of the first stars. *MNRAS*, 317(2), 385–390. <https://doi.org/10.1046/j.1365-8711.2000.03596.x>
- Schneider, R., Ferrara, A., Natarajan, P., & Omukai, K. (2002). First stars, very massive black holes, and metals. *ApJ*, 571(1), 30–39. <https://doi.org/10.1086/339917>
- Schneider, R., Ferrara, A., Salvaterra, R., Omukai, K., & Bromm, V. (2003). Low-mass relics of early star formation. *Nature*, 422(6934), 869–871. <https://doi.org/10.1038/nature01579>
- Schödel, R., Feldmeier, A., Neumayer, N., Meyer, L., & Yelda, S. (2014). The nuclear cluster of the Milky Way: our primary testbed for the interaction of a dense star cluster with a massive black hole. *CQGra*, 31(24), Article 244007, 244007. <https://doi.org/10.1088/0264-9381/31/24/244007>
- Schreiber, M. R., Gänsicke, B. T., Rebassa-Mansergas, A., Nebot Gomez-Moran, A., Southworth, J., & et al. (2010). Post common envelope binaries from SDSS. VIII. Evidence for disrupted magnetic braking. *A&A*, 513, Article L7, L7. <https://doi.org/10.1051/0004-6361/201013990>
- Schreiber, M. R., Zorotovic, M., & Wijnen, T. P. G. (2016). Three in one go: consequential angular momentum loss can solve major problems of CV evolution. *MNRAS*, 455(1), L16–L20. <https://doi.org/10.1093/mnras/slv144>
- Schroder, K.-P., Pols, O. R., & Eggleton, P. P. (1997). A critical test of stellar evolution and convective core ‘overshooting’ by means of zeta Aurigae systems. *MNRAS*, 285(4), 696–710. <https://doi.org/10.1093/mnras/285.4.696>
- Schröder, K. P., & Cuntz, M. (2005). A New Version of Reimers’ Law of Mass Loss Based on a Physical Approach. *ApJL*, 630(1), L73–L76. <https://doi.org/10.1086/491579>
- Seth, A. C., Blum, R. D., Bastian, N., Caldwell, N., & Debattista, V. P. (2008). The Rotating Nuclear Star Cluster in NGC 4244. *ApJ*, 687(2), 997–1003. <https://doi.org/10.1086/591935>
- Shapley, H. (1930). *Star Clusters* (Vol. 2).
- Shapley, H., & Sawyer, H. B. (1927). Apparent Diameters and Ellipticities of Globular Clusters. *Harvard College Observatory Bulletin*, 852, 22–26.
- Shara, M. M., & Hurley, J. R. (2002). Star Clusters as Type Ia Supernova Factories. *ApJ*, 571(2), 830–842. <https://doi.org/10.1086/340062>
- Sharda, P., Federrath, C., Krumholz, M. R., & Schleicher, D. R. G. (2021). Magnetic field amplification in accretion discs around the first stars: implications for the primordial IMF. *MNRAS*, 503(2), 2014–2032. <https://doi.org/10.1093/mnras/stab531>
- Sharda, P., & Krumholz, M. R. (2022). When did the initial mass function become bottom-heavy? *MNRAS*, 509(2), 1959–1984. <https://doi.org/10.1093/mnras/stab2921>
- Shibata, M., & Shapiro, S. L. (2002). Collapse of a Rotating Supermassive Star to a Supermassive Black Hole: Fully Relativistic Simulations. *ApJL*, 572(1), L39–L43. <https://doi.org/10.1086/341516>
- Shu, Q., Pang, X., Flammini Dotti, F., Kouwenhoven, M. B. N., Arca Sedda, M., & et al. (2021). The Long-term Evolution of Main-sequence Binaries in DRAGON Simulations. *ApJS*, 253(1), Article 14, 14. <https://doi.org/10.3847/1538-4365/abcfb8>
- Sicilia, A., Lapi, A., Boco, L., Spera, M., Di Carlo, U. N., Mapelli, M., Shankar, F., Alexander, D. M., Bressan, A., & Danese, L. (2021). The Black Hole Mass Function Across Cosmic Times I. Stellar Black Holes and Light Seed Distribution. *arXiv e-prints*, Article arXiv:2110.15607, arXiv:2110.15607.
- Siess, L., Izzard, R. G., Davis, P. J., & Deschamps, R. (2013). BINSTAR: a new binary stellar evolution code. Tidal interactions. *A&A*, 550, Article A100, A100. <https://doi.org/10.1051/0004-6361/201220327>
- Smith, R., Fellhauer, M., Candlish, G. N., Wojtak, R., Farias, J. P., & Blańa, M. (2013). Ursa Major II - reproducing the observed properties through tidal disruption. *MNRAS*, 433(3), 2529–2544. <https://doi.org/10.1093/mnras/stt925>
- Smith, R., Fellhauer, M., Goodwin, S., & Assmann, P. (2011). Surviving infant mortality in the hierarchical merging scenario. *MNRAS*, 414(4), 3036–3043. <https://doi.org/10.1111/j.1365-2966.2011.18604.x>
- Sollima, A., Baumgardt, H., & Hilker, M. (2019). The eye of Gaia on globular clusters kinematics: internal rotation. *MNRAS*, 485(1), 1460–1476. <https://doi.org/10.1093/mnras/stz505>
- Sollima, A., Bellazzini, M., Smart, R. L., Correnti, M., Pancino, E., Ferraro, F. R., & Romano, D. (2009). The non-peculiar velocity dispersion profile of the stellar system ω Centauri. *MNRAS*, 396(4), 2183–2193. <https://doi.org/10.1111/j.1365-2966.2009.14864.x>

- Spengler, C., Côté, P., Roediger, J., Ferrarese, L., Sánchez-Janssen, R., Toloba, E., Liu, Y., Guhathakurta, P., Cuillandre, J.-C., Gwyn, S., Zirm, A., Muñoz, R., Puzia, T., Lançon, A., Peng, E. W., Mei, S., & Powalka, M. (2017). Virgo Redux: The Masses and Stellar Content of Nuclei in Early-type Galaxies from Multiband Photometry and Spectroscopy. *ApJ*, 849(1), Article 55, 55. <https://doi.org/10.3847/1538-4357/aa8a78>
- Spera, M., & Mapelli, M. (2017). Very massive stars, pair-instability supernovae and intermediate-mass black holes with the sevn code. *MNRAS*, 470(4), 4739–4749. <https://doi.org/10.1093/mnras/stx1576>
- Spera, M., Mapelli, M., & Bressan, A. (2015). The mass spectrum of compact remnants from the PARSEC stellar evolution tracks. *MNRAS*, 451(4), 4086–4103. <https://doi.org/10.1093/mnras/stv1161>
- Spera, M., Mapelli, M., Giacobbo, N., Trani, A. A., Bressan, A., & et al. (2019). Merging black hole binaries with the SEVN code. *MNRAS*, 485(1), 889–907. <https://doi.org/10.1093/mnras/stz359>
- Spitzer, J., L. (1975). Dynamical Theory of Spherical Stellar Systems with Large N (invited Paper). In A. Hayli (Ed.), *Dynamics of the solar systems* (p. 3, Vol. 69).
- Spitzer, J., L., & Mathieu, R. D. (1980). Random gravitational encounters and the evolution of spherical systems. VIII - Clusters with an initial distribution of binaries. *ApJ*, 241, 618–636. <https://doi.org/10.1086/158376>
- Spitzer, J., L., & Shull, J. M. (1975a). Random gravitational encounters and the evolution of spherical systems. VI. Plummer's model. *ApJ*, 200, 339–342. <https://doi.org/10.1086/153793>
- Spitzer, J., L., & Shull, J. M. (1975b). Random gravitational encounters and the evolution of spherical systems. VII. Systems with several mass groups. *ApJ*, 201, 773–782. <https://doi.org/10.1086/153943>
- Spitzer, J., Lyman. (1940). The stability of isolated clusters. *MNRAS*, 100, 396. <https://doi.org/10.1093/mnras/100.5.396>
- Spitzer, J., Lyman, & Chevalier, R. A. (1973). Random Gravitational Encounters and the Evolution of Spherical Systems. V. Gravitational Shocks. *ApJ*, 183, 565–582. <https://doi.org/10.1086/152247>
- Spitzer, J., Lyman, & Hart, M. H. (1971a). Random Gravitational Encounters and the Evolution of Spherical Systems. I. Method. *ApJ*, 164, 399. <https://doi.org/10.1086/150855>
- Spitzer, J., Lyman, & Hart, M. H. (1971b). Random Gravitational Encounters and the Evolution of Spherical Systems. II. Models. *ApJ*, 166, 483. <https://doi.org/10.1086/150977>
- Spitzer, J., Lyman, & Shapiro, S. L. (1972). Random Gravitational Encounters and the Evolution of Spherical Systems. III. Halo. *ApJ*, 173, 529. <https://doi.org/10.1086/151442>
- Spitzer, J., Lyman, & Thuan, T. X. (1972). Random Gravitational Encounters and the Evolution of Spherical Systems. IV Isolated Systems of Identical Stars. *ApJ*, 175, 31. <https://doi.org/10.1086/151537>
- Spitzer, L. (1987). *Dynamical evolution of globular clusters*.
- Spruit, H. C. (2002). Dynamo action by differential rotation in a stably stratified stellar interior. *AAP*, 381, 923–932. <https://doi.org/10.1051/0004-6361:20011465>
- Spurzem, R. (1994). Gravo-thermal Oscillations. In V. G. Gurzadyan & D. Pfenniger (Eds.), *Ergodic concepts in stellar dynamics* (p. 170, Vol. 430). <https://doi.org/10.1007/BFb0058104>
- Spurzem, R. (1996). Fluid Techniques and Evolution of Anisotropy. In P. Hut & J. Makino (Eds.), *Dynamical evolution of star clusters: Confrontation of theory and observations* (p. 111, Vol. 174).
- Spurzem, R. (1999). Direct N-body Simulations. *Journal of Computational and Applied Mathematics*, 109, 407–432.
- Spurzem, R. (2001). Rotation and Relaxation in Dense Star Clusters and Galactic Nuclei. In S. Deiters, B. Fuchs, A. Just, R. Spurzem, & R. Wielen (Eds.), *Dynamics of star clusters and the milky way* (p. 75, Vol. 228).
- Spurzem, R., Giersz, M., Takahashi, K., & Ernst, A. (2005). Anisotropic gaseous models of tidally limited star clusters: comparison with other methods. *MNRAS*, 364(3), 948–960. <https://doi.org/10.1111/j.1365-2966.2005.09631.x>
- Spurzem, R., & Kamlah, A. W. H. (2023). Computational Methods for Collisional Stellar Systems. *LRCA*.
- Spurzem, R., & Takahashi, K. (1995). Comparison between Fokker-Planck and gaseous models of star clusters in the multi-mass case revisited. *MNRAS*, 272(4), 772–784. <https://doi.org/10.1093/mnras/272.4.772>
- Stacy, A., & Bromm, V. (2013). Constraining the statistics of Population III binaries. *MNRAS*, 433(2), 1094–1107. <https://doi.org/10.1093/mnras/stt789>
- Stacy, A., Bromm, V., & Lee, A. T. (2016). Building up the Population III initial mass function from cosmological initial conditions. *MNRAS*, 462(2), 1307–1328. <https://doi.org/10.1093/mnras/stw1728>

- Stacy, A., Bromm, V., & Loeb, A. (2011). Rotation speed of the first stars. *MNRAS*, 413(1), 543–553. <https://doi.org/10.1111/j.1365-2966.2010.18152.x>
- Stacy, A., Greif, T. H., Klessen, R. S., Bromm, V., & Loeb, A. (2013). Rotation and internal structure of Population III protostars. *MNRAS*, 431(2), 1470–1486. <https://doi.org/10.1093/mnras/stt264>
- Stacy, A., Pawlik, A. H., Bromm, V., & Loeb, A. (2012). Effect of Population III multiplicity on dark star formation. *MNRAS*, 421(1), 894–907. <https://doi.org/10.1111/j.1365-2966.2011.20373.x>
- Stevenson, S., Berry, C. P. L., & Mandel, I. (2017). Hierarchical analysis of gravitational-wave measurements of binary black hole spin-orbit misalignments. *MNRAS*, 471(3), 2801–2811. <https://doi.org/10.1093/mnras/stx1764>
- Stevenson, S., Vigna-Gómez, A., Mandel, I., Barrett, J. W., Neijssel, C. J., & et al. (2017). Formation of the first three gravitational-wave observations through isolated binary evolution. *NatCo*, 8, Article 14906, 14906. <https://doi.org/10.1038/ncomms14906>
- Stodółkiewicz, J. S. (1982). Dynamical evolution of globular clusters. I. *ACTAA*, 32(1-2), 63–91.
- Stodółkiewicz, J. S. (1986). Dynamical evolution of globular clusters. II - Binaries Method. *ACTAA*, 36(1), 19–41.
- Šubr, L., Kroupa, P., & Baumgardt, H. (2008). A new method to create initially mass segregated star clusters in virial equilibrium. *MNRAS*, 385(3), 1673–1680. <https://doi.org/10.1111/j.1365-2966.2008.12993.x>
- Sugimura, K., Matsumoto, T., Hosokawa, T., Hirano, S., & Omukai, K. (2020). The Birth of a Massive First-star Binary. *ApJL*, 892(1), Article L14, L14. <https://doi.org/10.3847/2041-8213/ab7d37>
- Sun, J., Leroy, A. K., Schruba, A., Rosolowsky, E., Hughes, A., & et al. (2018). Cloud-scale Molecular Gas Properties in 15 Nearby Galaxies. *ApJ*, 860(2), Article 172, 172. <https://doi.org/10.3847/1538-4357/aac326>
- Susa, H. (2019). Merge or Survive: Number of Population III Stars per Minihalo. *ApJ*, 877(2), Article 99, 99. <https://doi.org/10.3847/1538-4357/ab1b6f>
- Susa, H., Hasegawa, K., & Tominaga, N. (2014). The Mass Spectrum of the First Stars. *ApJ*, 792(1), Article 32, 32. <https://doi.org/10.1088/0004-637X/792/1/32>
- Szécsi, D., Langer, N., Yoon, S.-C., Sanyal, D., de Mink, S., Evans, C. J., & Dermine, T. (2015). Low-metallicity massive single stars with rotation. Evolutionary models applicable to I Zwicky 18. *AAP*, 581, Article A15, A15. <https://doi.org/10.1051/0004-6361/201526617>
- Szécsi, D., Wunsch, R., Agrawal, P., & Langer, N. (2020). ‘Bonn’ Optimized Stellar Tracks (BoOST). Simulated Populations of Massive and Very Massive Stars for Astrophysical Applications. *arXiv e-prints*, Article arXiv:2004.08203, arXiv:2004.08203.
- Szölgvény, A., & Kocsis, B. (2018). Black Hole Disks in Galactic Nuclei. *PRL*, 121(10), Article 101101, 101101. <https://doi.org/10.1103/PhysRevLett.121.101101>
- Szölgvény, A., Máthé, G., & Kocsis, B. (2021). Resonant Dynamical Friction in Nuclear Star Clusters: Rapid Alignment of an Intermediate-mass Black Hole with a Stellar Disk. *ApJ*, 919(2), Article 140, 140. <https://doi.org/10.3847/1538-4357/ac13ab>
- Szölgvény, A., Meiron, Y., & Kocsis, B. (2019). Anisotropic Mass Segregation in Rotating Globular Clusters. *ApJ*, 887(2), Article 123, 123. <https://doi.org/10.3847/1538-4357/ab50bb>
- Takahashi, K., Sumiyoshi, K., Yamada, S., Umeda, H., & Yoshida, T. (2019). The Evolution toward Electron Capture Supernovae: The Flame Propagation and the Pre-bounce Electron-Neutrino Radiation. *ApJ*, 871(2), Article 153, 153. <https://doi.org/10.3847/1538-4357/aaf8a8>
- Takahashi, K., Yoshida, T., & Umeda, H. (2018). Stellar Yields of Rotating First Stars. II. Pair-instability Supernovae and Comparison with Observations. *ApJ*, 857(2), Article 111, 111. <https://doi.org/10.3847/1538-4357/aab95f>
- Takahashi, K., Yoshida, T., Umeda, H., Sumiyoshi, K., & Yamada, S. (2016). Exact and approximate expressions of energy generation rates and their impact on the explosion properties of pair instability supernovae. *MNRAS*, 456(2), 1320–1331. <https://doi.org/10.1093/mnras/stv2649>
- Takahashi, K. (1995). Fokker-Planck Models of Star Clusters with Anisotropic Velocity Distributions I. Pre-Collapse Evolution. *PASJ*, 47, 561–573. <https://doi.org/10.48550/arXiv.astro-ph/9507040>
- Tamura, N., Sharples, R. M., Arimoto, N., Onodera, M., Ohta, K., & Yamada, Y. (2006a). A Subaru/Suprime-Cam wide-field survey of globular cluster populations around M87 - I. Observation, data analysis and luminosity function. *MNRAS*, 373(2), 588–600. <https://doi.org/10.1111/j.1365-2966.2006.11067.x>

- Tamura, N., Sharples, R. M., Arimoto, N., Onodera, M., Ohta, K., & Yamada, Y. (2006b). A Subaru/Suprime-Cam wide-field survey of globular cluster populations around M87 - II. Colour and spatial distribution. *MNRAS*, 373(2), 601–612. <https://doi.org/10.1111/j.1365-2966.2006.11059.x>
- Tang, J., & Joyce, M. (2021). Revised Best Estimates for the Age and Mass of the Methuselah Star HD 140283 Using MESA and Interferometry and Implications for 1D Convection. *RNAAS*, 5(5), Article 117, 117. <https://doi.org/10.3847/2515-5172/ac01ca>
- Tanikawa, A., Chiaki, G., Kinugawa, T., Suwa, Y., & Tominaga, N. (2022). Can Population III stars be major origins of both merging binary black holes and extremely metal poor stars? *PASJ*, 74(3), 521–532. <https://doi.org/10.1093/pasj/psac010>
- Tanikawa, A., Kinugawa, T., Yoshida, T., Hijikawa, K., & Umeda, H. (2021). Population III Binary Black Holes: Effects of convective overshooting on formation of GW190521. *MNRAS.tmp*. <https://doi.org/10.1093/mnras/stab1421>
- Tanikawa, A., Moriya, T. J., Tominaga, N., & Yoshida, N. (2022). Euclid detectability of pair instability supernovae in binary population synthesis models consistent with merging binary black holes. *arXiv*, Article arXiv:2204.09402, arXiv:2204.09402.
- Tanikawa, A., Susa, H., Yoshida, T., Trani, A. A., & Kinugawa, T. (2021). Merger Rate Density of Population III Binary Black Holes Below, Above, and in the Pair-instability Mass Gap. *ApJ*, 910(1), Article 30, 30. <https://doi.org/10.3847/1538-4357/abe40d>
- Tanikawa, A., Yoshida, T., Kinugawa, T., Takahashi, K., & Umeda, H. (2020). Fitting formulae for evolution tracks of massive stars under extreme metal-poor environments for population synthesis calculations and star cluster simulations. *MNRAS*, 495(4), 4170–4191. <https://doi.org/10.1093/mnras/staa1417>
- Tanikawa, A., Yoshida, T., Kinugawa, T., Trani, A. A., Hosokawa, T., Susa, H., & Omukai, K. (2021). Merger rate density of binary black holes through isolated Population I, II, and III binary star evolution. *arXiv e-prints*, Article arXiv:2110.10846, arXiv:2110.10846.
- Tauris, T. M. (2015). Maximum speed of hypervelocity stars ejected from binaries. *MNRAS*, 448, L6–L10. <https://doi.org/10.1093/mnrasl/slu189>
- Tauris, T. M., Kramer, M., Freire, P. C. C., Wex, N., Janka, H. .-, & et al. (2017). Formation of Double Neutron Star Systems. *ApJ*, 846(2), Article 170, 170. <https://doi.org/10.3847/1538-4357/aa7e89>
- Tauris, T. M., Langer, N., Moriya, T. J., Podsiadlowski, P., Yoon, S. .-, & et al. (2013). Ultra-stripped Type Ic Supernovae from Close Binary Evolution. *ApJL*, 778(2), Article L23, L23. <https://doi.org/10.1088/2041-8205/778/2/L23>
- Tauris, T. M., Langer, N., & Podsiadlowski, P. (2015). Ultra-stripped supernovae: progenitors and fate. *MNRAS*, 451(2), 2123–2144. <https://doi.org/10.1093/mnras/stv990>
- Tauris, T. M., van den Heuvel, E. P. J., & Savonije, G. J. (2000). Formation of Millisecond Pulsars with Heavy White Dwarf Companions: Extreme Mass Transfer on Subthermal Timescales. *ApJL*, 530(2), L93–L96. <https://doi.org/10.1086/312496>
- Team COMPAS, : Riley, J., Agrawal, P., Barrett, J. W., Boyett, K. N. K., Broekgaarden, F. S., Chattopadhyay, D., Gaebel, S. M., Gittins, F., Hirai, R., Howitt, G., Justham, S., Khandelwal, L., Kummer, F., Lau, M. Y. M., Mandel, I., de Mink, S. E., Neijssel, C., . . . Willcox, R. (2021). Rapid stellar and binary population synthesis with COMPAS. *arXiv e-prints*, Article arXiv:2109.10352, arXiv:2109.10352.
- Theis, C., & Spurzem, R. (1999). On the evolution of shape in N-body simulations. *A&A*, 341, 361–370.
- Thompson, T. A. (2011). Accelerating Compact Object Mergers in Triple Systems with the Kozai Resonance: A Mechanism for “Prompt” Type Ia Supernovae, Gamma-Ray Bursts, and Other Exotica. *ApJ*, 741(2), Article 82, 82. <https://doi.org/10.1088/0004-637X/741/2/82>
- Thompson, T. A., Fabian, A. C., Quataert, E., & Murray, N. (2015). Dynamics of dusty radiation-pressure-driven shells and clouds: fast outflows from galaxies, star clusters, massive stars, and AGN. *MNRAS*, 449(1), 147–161. <https://doi.org/10.1093/mnras/stv246>
- Thorne, K. S., & Żytkow, A. N. (1977). Stars with degenerate neutron cores. I. Structure of equilibrium models. *ApJ*, 212, 832–858. <https://doi.org/10.1086/155109>
- Timmes, F. X., Woosley, S. E., & Weaver, T. A. (1996). The Neutron Star and Black Hole Initial Mass Function. *ApJ*, 457, 834. <https://doi.org/10.1086/176778>
- Tiongco, M., Collier, A., & Varri, A. L. (2021). Central dynamics of multimass rotating star clusters. *MNRAS*, 506(3), 4488–4498. <https://doi.org/10.1093/mnras/stab1968>

- Tiongco, M. A., Vesperini, E., & Varri, A. L. (2016a). Velocity anisotropy in tidally limited star clusters. *MNRAS*, 455(4), 3693–3701. <https://doi.org/10.1093/mnras/stv2574>
- Tiongco, M. A., Vesperini, E., & Varri, A. L. (2016b). Kinematical evolution of tidally limited star clusters: the role of retrograde stellar orbits. *MNRAS*, 461(1), 402–411. <https://doi.org/10.1093/mnras/stw1341>
- Tiongco, M. A., Vesperini, E., & Varri, A. L. (2017). Kinematical evolution of tidally limited star clusters: rotational properties. *MNRAS*, 469(1), 683–692. <https://doi.org/10.1093/mnras/stx853>
- Tiongco, M. A., Vesperini, E., & Varri, A. L. (2018). The complex kinematics of rotating star clusters in a tidal field. *MNRAS*, 475(1), L86–L90. <https://doi.org/10.1093/mnrasl/sly009>
- Tiongco, M. A., Vesperini, E., & Varri, A. L. (2019). Kinematical evolution of multiple stellar populations in star clusters. *MNRAS*, 487(4), 5535–5548. <https://doi.org/10.1093/mnras/stz1595>
- Tiongco, M. A., Vesperini, E., & Varri, A. L. (2022). Early dynamical evolution of rotating star clusters in a tidal field. *MNRAS*, 512(2), 1584–1597. <https://doi.org/10.1093/mnras/stac643>
- Tominaga, N., Blinnikov, S. I., & Nomoto, K. (2013). Supernova Explosions of Super-asymptotic Giant Branch Stars: Multicolor Light Curves of Electron-capture Supernovae. *ApJL*, 771(1), Article L12, L12. <https://doi.org/10.1088/2041-8205/771/1/L12>
- Toonen, S., & Nelemans, G. (2013). The effect of common-envelope evolution on the visible population of post-common-envelope binaries. *A&A*, 557, Article A87, A87. <https://doi.org/10.1051/0004-6361/201321753>
- Toonen, S., Portegies Zwart, S., Hamers, A. S., & Bandopadhyay, D. (2020). The evolution of stellar triples. The most common evolutionary pathways. *A&A*, 640, Article A16, A16. <https://doi.org/10.1051/0004-6361/201936835>
- Toonen, S. (2019). Evolution of Hierarchical Triplets. *KITP Conference: Merging Visions: Exploring Compact-Object Binaries with Gravity and Light*, Article 9, 9.
- Torniamenti, S., Bertin, G., & Bianchini, P. (2019). A simple two-component description of energy equipartition and mass segregation for anisotropic globular clusters. *A&A*, 632, Article A67, A67. <https://doi.org/10.1051/0004-6361/201935878>
- Tout, C. A., Wickramasinghe, D. T., Liebert, J., Ferrario, L., & Pringle, J. E. (2008). Binary star origin of high field magnetic white dwarfs. *MNRAS*, 387(2), 897–901. <https://doi.org/10.1111/j.1365-2966.2008.13291.x>
- Tout, C. A. (2008a). Binary Stars. In S. J. Aarseth, C. A. Tout, & R. A. Mardling (Eds.), *The cambridge n-body lectures* (p. 297, Vol. 760). https://doi.org/10.1007/978-1-4020-8431-7_11
- Tout, C. A. (2008b). Stellar Evolution. In S. J. Aarseth, C. A. Tout, & R. A. Mardling (Eds.), *The cambridge n-body lectures* (p. 261, Vol. 760). https://doi.org/10.1007/978-1-4020-8431-7_9
- Tout, C. A., Aarseth, S. J., Pols, O. R., & Eggleton, P. P. (1997). Rapid binary star evolution for N-body simulations and population synthesis. *MNRAS*, 291(4), 732–748. <https://doi.org/10.1093/mnras/291.4.732>
- Trabucchi, M., Wood, P. R., Montalbán, J., Marigo, P., Pastorelli, G., & Girardi, L. (2019). Modelling long-period variables - I. A new grid of O-rich and C-rich pulsation models. *MNRAS*, 482(1), 929–949. <https://doi.org/10.1093/mnras/sty2745>
- Trani, A. A., & Spera, M. (2023). Modeling gravitational few-body problems with tsunami and okinami. *IAU Symposium*, 362, 404–409. <https://doi.org/10.1017/S1743921322001818>
- Trani, A. A., Rieder, S., Tanikawa, A., Iorio, G., Martini, R., & et al. (2022). Revisiting Common Envelope Evolution – A New Semi-Analytic Model for N-body and Population Synthesis Codes. *arXiv*, Article arXiv:2205.13537, arXiv:2205.13537.
- Tremaine, S. D., Ostriker, J. P., & Spitzer, L. (1975). The formation of the nuclei of galaxies. I. M31. *The Astrophysical Journal*, 196, 407–411. <https://doi.org/10.1086/153422>
- Uchida, H., Shibata, M., Yoshida, T., Sekiguchi, Y., & Umeda, H. (2017). Gravitational collapse of rotating supermassive stars including nuclear burning effects. *PhRvD*, 96(8), Article 083016, 083016. <https://doi.org/10.1103/PhysRevD.96.083016>
- Urquhart, J. S., König, C., Giannetti, A., Leurini, S., Moore, T. J. T., Eden, D. J., Pillai, T., Thompson, M. A., Braiding, C., Burton, M. G., Csengeri, T., Dempsey, J. T., Figura, C., Froebrich, D., Menten, K. M., Schuller, F., Smith, M. D., & Wyrowski, F. (2018). ATLASGAL - properties of a complete sample of Galactic clumps. *MNRAS*, 473(1), 1059–1102. <https://doi.org/10.1093/mnras/stx2258>

- van Meter, J. R., Miller, M. C., Baker, J. G., Boggs, W. D., & Kelly, B. J. (2010). Test of a General Formula for Black Hole Gravitational Wave Kicks. *ApJ*, 719(2), 1427–1432. <https://doi.org/10.1088/0004-637X/719/2/1427>
- Vanzella, E., Calura, F., Meneghetti, M., Castellano, M., Caminha, G. B., Mercurio, A., Cupani, G., Rosati, P., Grillo, C., Gilli, R., Mignoli, M., Fiorentino, G., Arcidiacono, C., Lombini, M., & Cortecchia, F. (2019). Massive star cluster formation under the microscope at $z = 6$. *MNRAS*, 483(3), 3618–3635. <https://doi.org/10.1093/mnras/sty3311>
- Vanzella, E., Calura, F., Meneghetti, M., Mercurio, A., Castellano, M., Caminha, G. B., Balestra, I., Rosati, P., Tozzi, P., De Barros, S., Grazian, A., D’Ercole, A., Ciotti, L., Caputi, K., Grillo, C., Merlin, E., Pentericci, L., Fontana, A., Cristiani, S., & Coe, D. (2017). Paving the way for the JWST: witnessing globular cluster formation at $z > 3$. *MNRAS*, 467(4), 4304–4321. <https://doi.org/10.1093/mnras/stx351>
- Vanzella, E., Meneghetti, M., Caminha, G. B., Castellano, M., Calura, F., Rosati, P., Grillo, C., Dijkstra, M., Gronke, M., Sani, E., Mercurio, A., Tozzi, P., Nonino, M., Cristiani, S., Mignoli, M., Pentericci, L., Gilli, R., Treu, T., Caputi, K., . . . Balestra, I. (2020). Candidate Population III stellar complex at $z = 6.629$ in the MUSE Deep Lensed Field. *MNRAS*, 494(1), L81–L85. <https://doi.org/10.1093/mnrasl/slaa041>
- Vanzella, E., Adamo, A., Annibali, F., Annunziatella, M., Bartosch Caminha, G., Bergamini, P., Calura, F., Caputi, K., Castellano, M., Comastri, A., Dickinson, M., Gilli, R., Grillo, C., Gronke, M., Gruppioni, C., Meneghetti, M., Mercurio, A., Mignoli, M., Nonino, M., . . . Sani, E. (2021). Constraining the nature of the first stellar complexes: globular cluster precursors and Population III stellar clusters at z 6–7.
- Varri, A. L., & Bertin, G. (2012). Self-consistent models of quasi-relaxed rotating stellar systems. *AAP*, 540, Article A94, A94. <https://doi.org/10.1051/0004-6361/201118300>
- Vasiliev, E. (2015). A new Monte Carlo method for dynamical evolution of non-spherical stellar systems. *MNRAS*, 446(3), 3150–3161. <https://doi.org/10.1093/mnras/stu2360>
- Vasiliev, E. (2019). Proper motions and dynamics of the Milky Way globular cluster system from Gaia DR2. *MNRAS*, 484(2), 2832–2850. <https://doi.org/10.1093/mnras/stz171>
- Vasilyev, V., Ludwig, H. .-, Freytag, B., Lemasle, B., & Marconi, M. (2018). Spectroscopic properties of a two-dimensional time-dependent Cepheid model. II. Determination of stellar parameters and abundances. *AAP*, 611, Article A19, A19. <https://doi.org/10.1051/0004-6361/201732201>
- Vassiliadis, E., & Wood, P. R. (1993). Evolution of Low- and Intermediate-Mass Stars to the End of the Asymptotic Giant Branch with Mass Loss. *ApJ*, 413, 641. <https://doi.org/10.1086/173033>
- Vennes, S., Nemeth, P., Kawka, A., Thorstensen, J. R., Khalack, V., & et al. (2017). An unusual white dwarf star may be a surviving remnant of a subluminous Type Ia supernova. *Sci*, 357(6352), 680–683. <https://doi.org/10.1126/science.aam8378>
- Vergara, M. Z. C., Schleicher, D. R. G., Boekholt, T. C. N., Reinoso, B., Fellhauer, M., Klessen, R. S., & Leigh, N. W. C. (2021). Stellar collisions in flattened and rotating Population III star clusters. *A&A*, 649, Article A160, A160. <https://doi.org/10.1051/0004-6361/202140298>
- Vikaeus, A., Whalen, D. J., & Zackrisson, E. (2022). Finding Lensed Direct-collapse Black Holes and Supermassive Primordial Stars. *ApJL*, 933(1), Article L8, L8. <https://doi.org/10.3847/2041-8213/ac7802>
- Vink, J. S. (2021). Theory and Diagnostics of Hot Star Mass Loss. *arXiv e-prints*, Article arXiv:2109.08164, arXiv:2109.08164.
- Vink, J. S., & de Koter, A. (2002). Predictions of variable mass loss for Luminous Blue Variables. *A&A*, 393, 543–553. <https://doi.org/10.1051/0004-6361:20021009>
- Vink, J. S., & de Koter, A. (2005). On the metallicity dependence of Wolf-Rayet winds. *AAP*, 442(2), 587–596. <https://doi.org/10.1051/0004-6361:20052862>
- Vink, J. S., de Koter, A., & Lamers, H. J. G. L. M. (2001). Mass-loss predictions for O and B stars as a function of metallicity. *A&A*, 369, 574–588. <https://doi.org/10.1051/0004-6361:20010127>
- von Hoerner, S. (1960). Die numerische Integration des n-Körper-Problemes für Sternhaufen. I. *ZAP*, 50, 184–214.
- von Hoerner, S. (1963). Die numerische Integration des n-Körper-Problems für Sternhaufen, II. *ZAP*, 57, 47–82.
- von Hoerner, S. (2001). How it All Started. In S. Deiters, B. Fuchs, A. Just, R. Spurzem, & R. Wielen (Eds.), *Dynamics of star clusters and the milky way* (p. 11, Vol. 228).

- Wang, L., Fujii, M. S., & Tanikawa, A. (2021). Impact of initial mass functions on the dynamical channel of gravitational wave sources. *MNRAS*, 504(4), 5778–5787. <https://doi.org/10.1093/mnras/stab1157>
- Wang, L., & Hernandez, D. M. (2021). On the reliability of simulations of collisional stellar systems. *arXiv e-prints*, Article arXiv:2104.10843, arXiv:2104.10843.
- Wang, L., Iwasawa, M., Nitadori, K., & Makino, J. (2020). PETAR: a high-performance N-body code for modelling massive collisional stellar systems. *MNRAS*, 497(1), 536–555. <https://doi.org/10.1093/mnras/staa1915>
- Wang, L., Kroupa, P., Takahashi, K., & Jerabkova, T. (2020). The possible role of stellar mergers for the formation of multiple stellar populations in globular clusters. *MNRAS*, 491(1), 440–454. <https://doi.org/10.1093/mnras/stz3033>
- Wang, L., Nitadori, K., & Makino, J. (2020a). SDAR: Slow-Down Algorithmic Regularization code for solving few-body problems.
- Wang, L., Nitadori, K., & Makino, J. (2020b). A slow-down time-transformed symplectic integrator for solving the few-body problem. *MNRAS*, 493(3), 3398–3411. <https://doi.org/10.1093/mnras/staa480>
- Wang, L., Spurzem, R., Aarseth, S., Giersz, M., Askar, A., & et al. (2016). The DRAGON simulations: globular cluster evolution with a million stars. *MNRAS*, 458(2), 1450–1465. <https://doi.org/10.1093/mnras/stw274>
- Wang, L., Spurzem, R., Aarseth, S., Nitadori, K., Berczik, P., & et al. (2015). NBODY6++GPU: ready for the gravitational million-body problem. *MNRAS*, 450(4), 4070–4080. <https://doi.org/10.1093/mnras/stv817>
- Wang, L., Tanikawa, A., & Fujii, M. (n.d.). Gravitational wave of intermediate-mass black holes in Population III star clusters. *MNRAS submitted*.
- Wang, L., Tanikawa, A., & Fujii, M. (2022). Gravitational wave of intermediate-mass black holes in Population III star clusters. *MNRAS*, 515(4), 5106–5120. <https://doi.org/10.1093/mnras/stac2043>
- Warren, J. S., Hughes, J. P., & Badenes, C. (2005). First Results from a Principal Component Analysis of Tycho's SNR: Evidence for Cosmic Ray Ion Acceleration. *American Astronomical Society Meeting Abstracts*, 207, Article 172.12, 172.12.
- Weatherford, N. C., Fragione, G., Kremer, K., Chatterjee, S., Ye, C. S., & et al. (2021). Black Hole Mergers from Star Clusters with Top-heavy Initial Mass Functions. *ApJL*, 907(2), Article L25, L25. <https://doi.org/10.3847/2041-8213/abd79c>
- Weatherford, N. C., Kiroğlu, F., Fragione, G., Chatterjee, S., Kremer, K., & Rasio, F. A. (2022). Stellar Escape from Globular Clusters I: Escape Mechanisms and Properties at Ejection. *arXiv e-prints*, Article arXiv:2211.16523, arXiv:2211.16523. <https://doi.org/10.48550/arXiv.2211.16523>
- Webb, J. J., & Bovy, J. (2019). Searching for the GD-1 stream progenitor in Gaia DR2 with direct N-body simulations. *MNRAS*, 485(4), 5929–5938. <https://doi.org/10.1093/mnras/stz867>
- Webb, J. J., Leigh, N. W. C., Serrano, R., Bellovary, J., Ford, K. E. S., & et al. (2019). The evolution of kicked stellar-mass black holes in star cluster environments - II. Rotating star clusters. *MNRAS*, 488(3), 3055–3066. <https://doi.org/10.1093/mnras/stz1896>
- Webbink, R. F. (1984). Double white dwarfs as progenitors of R Coronae Borealis stars and type I supernovae. *ApJ*, 277, 355–360. <https://doi.org/10.1086/161701>
- Webbink, R. F. (1985). Stellar evolution and binaries. In J. E. Pringle & R. A. Wade (Eds.), *Interacting binary stars* (p. 39).
- Webbink, R. F. (2003). Contact Binaries. In S. Turcotte, S. C. Keller, & R. M. Cavallo (Eds.), *3d stellar evolution* (p. 76, Vol. 293).
- Weisskopf, M. C., Tananbaum, H. D., Van Speybroeck, L. P., & O'Dell, S. L. (2000). Chandra X-ray Observatory (CXO): overview. In J. E. Truemper & B. Aschenbach (Eds.), *X-ray optics, instruments, and missions iii* (pp. 2–16, Vol. 4012). <https://doi.org/10.1117/12.39154510.48550/arXiv.astro-ph/0004127>
- White, R. E., & Shawl, S. J. (1987). Axial Ratios and Orientations for 100 Galactic Globular Star Clusters. *ApJ*, 317, 246. <https://doi.org/10.1086/165273>
- Whyte, C. A., & Eggleton, P. P. (1980). Comments on the evolution and origin of cataclysmic binaries. *MNRAS*, 190, 801–823. <https://doi.org/10.1093/mnras/190.4.801>

- Willems, B., Henninger, M., Levin, T., Ivanova, N., Kalogera, V., McGhee, K., Timmes, F. X., & Fryer, C. L. (2005). Understanding Compact Object Formation and Natal Kicks. I. Calculation Methods and the Case of GRO J1655-40. *ApJ*, 625(1), 324–346. <https://doi.org/10.1086/429557>
- Wilson, C. P. (1975). Dynamical models of elliptical galaxies. *AJ*, 80, 175–187. <https://doi.org/10.1086/111729>
- Wong, T.-W., Valsecchi, F., Ansari, A., Fragos, T., Glebbeek, E., Kalogera, V., & McClintock, J. (2014). Understanding Compact Object Formation and Natal Kicks. IV. The Case of IC 10 X-1. *ApJ*, 790(2), Article 119, 119. <https://doi.org/10.1088/0004-637X/790/2/119>
- Wong, T.-W., Valsecchi, F., Fragos, T., & Kalogera, V. (2012). Understanding Compact Object Formation and Natal Kicks. III. The Case of Cygnus X-1. *ApJ*, 747(2), Article 111, 111. <https://doi.org/10.1088/0004-637X/747/2/111>
- Woosley, S. E. (2017). Pulsational Pair-instability Supernovae. *ApJ*, 836(2), Article 244, 244. <https://doi.org/10.3847/1538-4357/836/2/244>
- Woosley, S. E., & Heger, A. (2021). The Pair-instability Mass Gap for Black Holes. *ApJL*, 912(2), Article L31, L31. <https://doi.org/10.3847/2041-8213/abf2c4>
- Woosley, S. E., & Smith, N. (2022). SN 1961V: A Pulsational Pair-Instability Supernova. *arXiv*, Article arXiv:2205.06386, arXiv:2205.06386.
- Wuchterl, G., & Tscharnuter, W. M. (2003). From clouds to stars. Protostellar collapse and the evolution to the pre-main sequence I. Equations and evolution in the Hertzsprung-Russell diagram. *AAP*, 398, 1081–1090. <https://doi.org/10.1051/0004-6361:20021707>
- Yan, Z., Jeřábková, T., & Kroupa, P. (2021). Downsizing revised: Star formation timescales for elliptical galaxies with an environment-dependent IMF and a number of SNIa. *A&A*, 655, Article A19, A19. <https://doi.org/10.1051/0004-6361/202140683>
- Ye, C. S., Kremer, K., Chatterjee, S., Rodriguez, C. L., & Rasio, F. A. (2019). Millisecond Pulsars and Black Holes in Globular Clusters. *ApJ*, 877(2), Article 122, 122. <https://doi.org/10.3847/1538-4357/ab1b21>
- Ye, C. S., Kremer, K., Rodriguez, C. L., Rui, N. Z., Weatherford, N. C., Chatterjee, S., Fragione, G., & Rasio, F. A. (2022). Compact Object Modeling in the Globular Cluster 47 Tucanae. *ApJ*, 931(2), Article 84, 84. <https://doi.org/10.3847/1538-4357/ac5b0b>
- Yoon, S. .-, Dierks, A., & Langer, N. (2012). Evolution of massive Population III stars with rotation and magnetic fields. *AAP*, 542, Article A113, A113. <https://doi.org/10.1051/0004-6361/201117769>
- Yoon, S. .-, & Langer, N. (2005). Evolution of rapidly rotating metal-poor massive stars towards gamma-ray bursts. *A&A*, 443(2), 643–648. <https://doi.org/10.1051/0004-6361:20054030>
- Yoon, S. .-, Langer, N., & Norman, C. (2006). Single star progenitors of long gamma-ray bursts. *Nuovo Cimento B Serie*, 121(12), 1631–1632. <https://doi.org/10.1393/ncb/i2007-10344-4>
- Yoshida, T., Takiwaki, T., Kotake, K., Takahashi, K., Nakamura, K., & et al. (2019). One-, Two-, and Three-dimensional Simulations of Oxygen-shell Burning Just before the Core Collapse of Massive Stars. *ApJ*, 881(1), Article 16, 16. <https://doi.org/10.3847/1538-4357/ab2b9d>
- Yoshida, T., Umeda, H., Maeda, K., & Ishii, T. (2016). Mass ejection by pulsational pair instability in very massive stars and implications for luminous supernovae. *MNRAS*, 457(1), 351–361. <https://doi.org/10.1093/mnras/stv3002>
- Zahn, J. P. (1970). Forced Oscillations in Close Binaries. The Adiabatic Approximation. *A&A*, 4, 452.
- Zahn, J. P. (1974). Rotational Instabilities and Stellar Evolution. In P. Ledoux, A. Noels, & A. W. Rodgers (Eds.), *Stellar instability and evolution* (p. 185, Vol. 59).
- Zahn, J. P. (1975). The dynamical tide in close binaries. *A&A*, 41, 329–344.
- Zahn, J. P. (1977). Reprint of 1977A&A....57..383Z. Tidal friction in close binary stars. *A&A*, 500, 121–132.
- Zahn, J. P. (1989). Tidal evolution of close binary stars. I - Revisiting the theory of the equilibrium tide. *A&A*, 220(1-2), 112–116.
- Zahn, J. P. (1991). Convective penetration in stellar interiors. *A&A*, 252, 179–188.
- Zahn, J. P. (1992). Circulation and turbulence in rotating stars. *A&A*, 265, 115–132.
- Zavala, R. T., Hummel, C. A., Boboltz, D. A., Ojha, R., Shaffer, D. B., Tycner, C., Richards, M. T., & Hutter, D. J. (2010). The Algol Triple System Spatially Resolved at Optical Wavelengths. *ApJL*, 715(1), L44–L48. <https://doi.org/10.1088/2041-8205/715/1/L44>
- Zick, T., Weisz, D., & Kriek, M. (2020). Star Cluster Formation Through Cosmic Time: The Low- High-Redshift Connection. *American Astronomical Society Meeting Abstracts #235*, 235, Article 156.01, 156.01.

- Zick, T. O., Kriek, M., Shapley, A. E., Reddy, N. A., Freeman, W. R., & et al. (2018). The MOSDEF Survey: Stellar Continuum Spectra and Star Formation Histories of Active, Transitional, and Quiescent Galaxies at $1.4 < z < 2.6$. *ApJL*, 867(1), Article L16, L16. <https://doi.org/10.3847/2041-8213/aae887>
- Zick, T. O., Weisz, D. R., & Boylan-Kolchin, M. (2018). Globular clusters in high-redshift dwarf galaxies: a case study from the Local Group. *MNRAS*, 477(1), 480–490. <https://doi.org/10.1093/mnras/sty662>
- Zinnecker, H., & Yorke, H. W. (2007). Toward Understanding Massive Star Formation. *ARA&A*, 45(1), 481–563. <https://doi.org/10.1146/annurev.astro.44.051905.092549>
- Zorotovic, M., Schreiber, M. R., Gänsicke, B. T., & Nebot Gómez-Morán, A. (2010). Post-common-envelope binaries from SDSS. IX: Constraining the common-envelope efficiency. *A&A*, 520, Article A86, A86. <https://doi.org/10.1051/0004-6361/200913658>
- Zorotovic, M., Schreiber, M. R., Parsons, S. G., Gänsicke, B. T., Hardy, A., & et al. (2016). Detached cataclysmic variables are crossing the orbital period gap. *MNRAS*, 457(4), 3867–3877. <https://doi.org/10.1093/mnras/stw246>